Metal Chalcogenides, Chalcophosphates and Halides for Energy Conversion and Environmental Remediation

A Thesis

Submitted for the Degree of

Doctor of philosophy

By

EKASHMI RATHORE

New Chemistry Unit

Jawaharlal Nehru Centre for Advanced Scientific Research

(*A deemed University*)

Bangalore, India

June 2021

Dedication

I dedicate this thesis to all the women scientists, those who always face a special series of gender-related barriers to entry and success in scientific careers that persist, despite recent advances. I dedicate this thesis to my lovely family for giving me an opportunity to be that woman in science. I dedicate this thesis to my found family for standing through ups and downs, and for all their support, love, and prayers. I dedicate this thesis to the omnipresent divine force that drives me to do the best despite the odds. I dedicate this thesis to every single person who made me a better person in some way or the other.

Declaration

I hereby declare that this thesis entitled "*Metal Chalcogenides, Chalcophosphates and Halides for Energy Conversion and Environmental Remediation*" is an authentic record of research work that has been carried out by me at Solid State Chemistry Laboratory, New Chemistry Unit, Jawaharlal Nehru Centre for Advanced Scientific Research, Bangalore, India under supervision of Prof. Kanishka Biswas. This work has not been submitted elsewhere for the award of any degree or diploma.

In keeping with the general practices of reporting scientific observations, due acknowledgments have been made wherever the work described is based on the findings of other investigators in a collaborative pursuit. Any omission which might have occurred by oversight or error in judgment is regretted.

Date: 01-06-2021
Bangalore, India

Ekashmi Rathore

Prof. Kanishka Biswas
Associate Professor
New Chemistry Unit
Jawaharlal Nehru Centre for
Advanced Scientific Research
Bangalore, India -560064

Email :kanishka@jncasr.ac.in
Phone: +91-80-22082678 (office)
+91-9902063469(mobile)
FAX : +91-80-2208-2627
Web: http://www.jncasr.ac.in/kanishka/

Certificate

I hereby certify that the work described in this thesis titled "*Metal Chalcogenides, Chalcophosphates and Halides for Energy Conversion and Environmental Remediation*" has been carried out by Ms. Ekashmi Rathore at Solid State Chemistry Laboratory, New Chemistry Unit, Jawaharlal Nehru Centre for Advanced Scientific Research, Bangalore, India under my supervision and that it has not been submitted elsewhere for the award of any degree or diploma.

Date: 01-06-2021
Bangalore, India

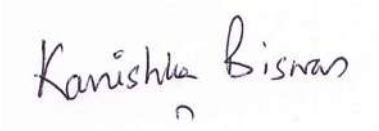

Prof. Kanishka Biswas
(Research Supervisor)

Acknowledgments

Completion of my Ph.D. thesis necessitated a lot of guidance and support from many people. I take this opportunity to mention a few of them. However, my sincere thanks extend to everyone who has played a role in making this dream a reality.

Firstly, I thank my research supervisor, Prof. Kanishka Biswas for suggesting me research problems and guiding me throughout. He has been a constant source of inspiration for me to build up new ideas and carry out experiments. I greatly admire his enthusiasm for science. His enthusiasm makes a mark upon the young heart, urging them to perform as best as one could. I express my hearty gratitude to him for giving me an opportunity to work under his guidance. I also thank him for all the valuable suggestions, freedom, and motivating words in times of need. I thank Prof. C. N. R. Rao, FRS for his generous support and encouragement throughout my stay in JNCASR.

I thank Prof. A. Singh, Prof. W. G. Zeier, Prof. U. V. Waghmare, Prof. A. Soni, Dr. K. Nakajima, Dr. B. Saha, Dr. R. Juneja, Dr. M. Kofu, Dr. J. Pandey, Ms. R. Arora, Ms. Dheemahi for the fruitful scientific collaborations and all the insightful discussions.

I thank Dr. A. Govindraj, Prof. Eswaramoorthy, Prof. Sebastian, Dr. Gopal, Dr. Amritroop, Dr. Manjeet, Dr. Dheeraj, Dr. Jiaul, Dr. Soumyabrata, Dr. Saurav, Dr. Manoj for creating an initial spark of research during MS lab experiments, summer project, semester projects.

I thank all my beloved labmates: Dr. S. Guin, Dr. M. Jana, Dr. S. Roychowdhury, Dr. A. Banik, Dr. Manisha, Dr. T. Ghosh, Dr. S. Shidaling, Dr. P. Pal, Dr. S. Perumal, Dr. K. Kundu, Dr. P. Dutta, Dr. Archana, Dr. J. Pradhan, Mr. K. Maji, Mr. M. Dutta, Mr. A. Sarkar, Ms. S. Chandra, Mr. P. Acharyya, Mr. D. Sarkar, Mr. A. Bhui, Mr. R. Pathak, Mr. A. Das, Mr. A. Das, and Mr. S. Das for their cheerful company and help on various occasions.

I thank Prof. Ramananda Chakrabarti (IISc), Prof. Mrinmoy De (IISc), Prof. T. K. Maji (JNCASR), Prof. Eshwarmoorthy (JNCASR), Prof. A. Sunderasan (JNCASR), and their students, Anupam, Rahul, Utpal, Subrata, Tarandeep, Arunava, Soumita, Subhajit, Suchismita, Swaraj, Mr. Subrata Nijitha, Prem, Dr. Jay Ghatak, Dr. Badri for helping me in ICP-MS, Zeta-Potential, Cyclic-Voltammetry, Surface-Area, Low-Temperature Resistivity Measurements, TEM Data Analysis. I have learned a lot whenever I had a meeting with them or a discussion with them.

The constant assistance and friendly nature of the technical staff helped me doing my experiments smoothly. Here, I acknowledge Ms. Selvi, Mrs. Usha, Ms. Minakshi, Dr. Jay, Mr. Kanan, Mr. Anil, Mr. Vasu, Mr. Rahul, Mr. Shiva, Mr. Jagdish, Mr. N. Kishore, Mr. Dileep, and Mr. Gowda for their technical help. I am thankful to all the academic, administrative, technical, security, complab, and health center staff for making our campus life smooth and easy.

I express my deep gratitude to all my high school and undergraduate teachers for training me to be disciplined, teaching the basics of science, and growing my interest in chemistry.

I express my love and affection to lovable found family buddies, Manjeet, Ankit, Priti, Aditi, Raagya, Pragya, Mohit, Uma, Mahesh, Aakaksha Di, Shruthi, Ashish, Ankur, Himanshi, Ayuk. I am thankful to my friends from DAE School, Pranidhi, Kiran, Saloni, Danish; my friends from Hindu College, Krishnav, Shubham, Nikita, Mona, Shikha, Ashima, Deepika, Ankita, Aparna, Amit; my friends from travel clubs: Laila, Anshu, Sheetal, Jaydeep, Rohit, Himanshu, my friends from Jagriti Yatra, Nawaz, Harshikha, Pratik, Peyush, Hemant, Radhika. Thanks for being there to share my happiness as well as sorrow.

Simple words of thanks are never enough to convey feelings to my family members who have supported me and placed their trust and faith in all activities. Their love, endurance, and utmost patience are the backbone of my future. I am grateful to you all for whatever you gave me.

Preface

Metal chalcogenides/chalcophosphates/ halides present an important platform for exploring various intriguing properties. This Ph.D. thesis presents the design and synthesis of various metal chalcogenides, layered chalcophosphates/ halides for their application in thermoelectric energy conversion, water purification, and fundamental understanding of the charge transfer mechanism in the all-inorganic halide perovskite heterostructures. The thesis work is divided into four parts (1- 4), containing one, five, four, and two chapters respectively.

Part 1 presents a brief introduction to metal chalcogenides/chalcophosphates/ halide perovskites for energy conversion and environmental remediation, covering the summary of thermoelectrics, ion-exchange, intercalation, water purification, synthesis, detailed characterizations, and measurement techniques.

With the apparent burgeoning energy crisis, alternative sources of energy are in greater need of a sustainable future. Thermoelectrics which can convert waste heat arising from industries, power plants, and automobiles into a usable form, electricity; have the potential to be a game-changer in this critical energy shortage. **Part 2** of my thesis is related to energy conversion and is focused on the design and synthesis of metal chalcogenides for high-performance thermoelectric energy conversion. It is divided into five chapters. **Chapter 2.1** discusses the influence of the periodic table in designing solid-state metal chalcogenides for thermoelectric energy conversion. **Chapter 2.2** focuses on stabilizing cubic $AgBiS_2$ at room temperature and understanding the origin of ultralow thermal conductivity in n-type cubic $AgBiS_2$ caused by the soft vibrations and local structure distortion in [011] direction induced by the Bi $6s^2$ lone pair. In ch**apter 2.3**, electrical transport properties have been enhanced in Bi excess samples of $AgBiSe_2$ by modulation doping using microstructures of topological semi-metal Bi_4Se_3 which injects the charge carriers to the precipitates of Bi_4Se_3 from the $AgBiSe_2$ matrix and results in a large improvement of carrier mobility. **Chapter 2.4** reports the highest zT of 1.45 in low-cost and earth-abundant element-based lead sulfide thermoelectric material, an

alternative to champion lead chalcogenides, PbTe, and PbSe. Ge doping in PbS synergistically brings out extremely low lattice thermal conductivity (κ_{lat}) in PbS via endotoxic nano precipitates of Pb_2GeS_4 which scatter heat-carrying phonon and the electrical conductivity increases due to enhanced covalency in chemical bonding. **Chapter 2.5** reports the synthesis of superconductive Chevrel phase compound $SnMo_6S_8$ and discusses the origin of ultra-low thermal conductivity arising from tin rattler atoms.

Clean and fresh water is pivotal to the existence of life. However, the world's supply of fresh water is dwindling and the contaminant levels are increasing rapidly. **Part 3** of my thesis is related to the environment and is focused on water purification using layered materials. It is divided into four chapters. In **chapter 3.1**, we have captured toxic lead (II) from water, efficiently and selectively from ppb level using layered metal chalcophosphate, $K_{0.48}Mn_{0.76}PS_3$. H2O (K-MPS-1). This material is stable in 2-12 pH and can remove lead even from 1 ppb level. **Chapter 3.2** reports the selective and ppb level removal of toxic mercury (II) from water using the composite of high surface area graphene oxide and tin sulfide which induces selectivity towards Hg(II) adsorption. The material is stable in pH 0.5-11 and can remove Hg(II) even from 0.3 ppb level. I have designed a prototype tea bag with the composite which can remove 99.9 % Hg(II) from water. In **chapter 3.3**, I have designed and synthesized nature-inspired coral-like morphology of CoAl-Layered Double Hydroxide and removed hexavalent chromium (VI) from the water up to 4.5 ppb level. This material works in a broad pH range of 1.93-12.22, can be regenerated and recycled. With these great properties, we designed a low-cost column for the treatment of effluent discharge, with 1 weight % of material and 99 weight % sand and removed ~99% Cr(VI). **Chapter 3.4** reports the removal of radionuclide Cesium from water by the ion-exchange process using K-MPS-1. Sorption of Cs(I) is reversible, shows fast kinetics and removal occurs in ppb level. In summary, this part of the thesis has described the removal of heavy metal ions, Pb(II), Hg(II), Cr(VI), and radionuclides of Cs(I) using layered materials.

All-inorganic halide perovskites have created a sensation in diverse optoelectronic applications like photovoltaics, photodetectors, light-emitting diodes, and lasers and we have seen phenomenal growth in research efforts to understand the photodynamics, luminescent properties, and stabilization of different phases of perovskites.

Heterostructures of inorganic halide perovskites with mixed-dimensional inorganic nanomaterials have shown great potential not only in the field of optoelectronic energy devices and photocatalysis but also for improving our fundamental understanding of the charge transfer across the heterostructure interface. In **part 4**, I have designed heterostructures of $CsPbBr_3$ and studied the optical properties of the heterostructures. **Chapter 4.1** focuses on studying the charge transfer, the driving force for synthesis, photoluminescence quenching, and photo-conductivity in the heterostructure of $CsPbBr_3$ nanocrystals with nitrogen-doped carbon dots. In **chapter 4.2**, we have synthesized the heterostructure of $CsPbBr_3$ nanocrystals with few layers of layered metal oxy-chalcogenide, Bi_2O_2Se, and studied the photoluminescence quenching mechanism

Contents

PART 1

A Brief Introduction to Metal Chalcogenides, Chalcophosphates and Halides for Energy Conversion and Environment Remediation

Part 1

A Brief Introduction to Metal Chalcogenides, Chalcophosphates and Halides for Energy Conversion and Environment Remediation

1.1. Introduction

Today, energy consumption in the world contributes to pollution, environmental deterioration, and the emission of global greenhouse gases. This increase in consumption of energy is driven by the population growth and economic development that tends to increase energy use per capita. Thus, the unavoidable upsurge in population in the near future and the economic development that will necessarily occur in many countries, pose serious implications for the environment. At the same time, the depletion of fossil fuels and other resources which generate electricity are escalating evidently. Hence all developed and developing countries are trying serious attempts to find out various ways to meet energy shortfall around the globe. The current sources of energy are insufficient but global energy demand will surely upsurge more rapidly, and it may raise many folds by the end of this century. The energy crisis and the endlessly fluctuating cost of petroleum have moved researchers' attention toward new sustainable and renewable energy sources and materials. Hence alternative, eco-friendly sustainable energy resources are highly essential. The use of renewable resources such as solar, biomass, wind, and geothermal energy has been on the rise for the past few decades. Although efforts are being made to increase the use of these sources, renewable energy still accounts for not more than 20% of the electricity generated. Among all the renewable resources available on the earth, solar energy is part of the solution to the problem of dwindling fossil-fuel reserves. However, only a minuscule fraction of the available solar energy is used in electricity generation due to the cost of solar energy production and implementation and performance of solar power plants in the face of weather uncertainties. Hence, optimizing the resources to produce efficient power at low cost

and finding alternative methods to generate electricity is the need of the hour. The best possible way is to develop new technologies which can increase the output power of the existing fuels and for that the use of alternative energy sources (renewable sources; wind, solar, biomass, and others) and improvement of the thermal management is necessary. Thermoelectric materials can convert waste heat into electricity without any moving parts. **Part 2** of my thesis is related to energy conversion and is focused on the design and synthesis of metal chalcogenides for high-performance thermoelectric energy conversion (Figure 1.1).

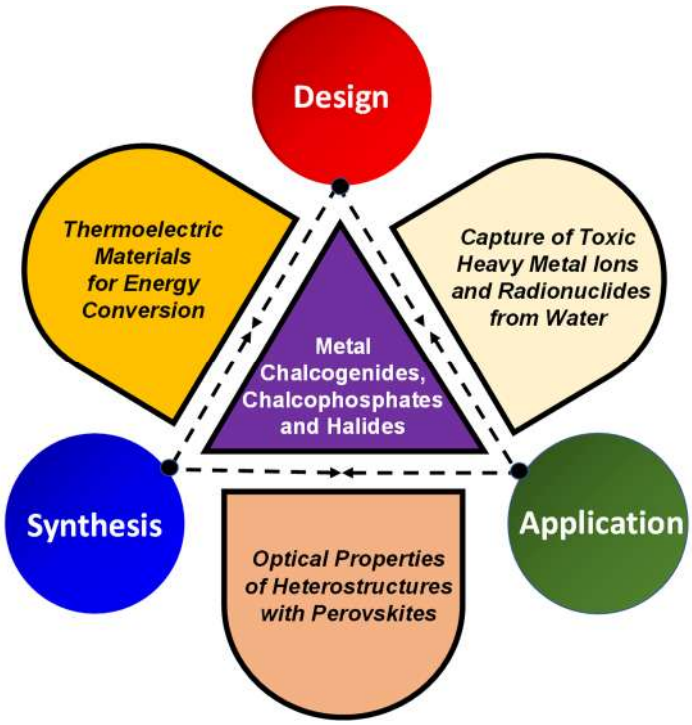

Figure 1.1. *Illustration showing the use of metal chalcogenides, chalcophosphates, and halide perovskites for energy conversion and environmental remediation.*

The rapid step of industrialization and its subsequent by-products have affected the environment by producing hazardous wastes and poisonous gas fumes and smokes, which have been released to the environment. Conventional technologies have been used to treat all types of organic and toxic waste by adsorption, biological oxidation, chemical oxidation, and incineration. The treatment of pollutants in water and air is a great challenge and the development of new adsorbents is important for environmental remediation. Environmental remediation technologies involve chemical degradation (via ozone/UV radiation/H_2O_2 oxidation, photocatalytic degradation, supercritical water

oxidation, sonochemical degradation, the electrochemical method, the electron beam process, and enzymatic treatment methods), use of metals/metal oxides (e.g. silver, iron, gold, iron oxides, titanium oxides, etc.), nanofiltration by membranes, nanofiber media, sorbents (e.g. clay, zeolites, layered materials, etc.), carbon materials (graphene, graphene-oxide, carbon nanotubes, etc.), polymer-supported nanocomposites, etc.[1] However, selective and low parts per billion level removal of organic and toxic waste remains a challenge to be solved. **Part 3** of my thesis is related to the environment and is focused on water purification using layered materials (Figure 1.1).

In this chapter, I will discuss metal chalcogenides, layered materials, metal chalcophosphates, and heterostructures of halide perovskites for their application in energy conversion and environmental remediation. I have discussed some relevant basics, synthesis, and characterization techniques at the end to provide a background to my thesis work.

1.2. Metal Chalcogenides

Chalcogenides constitute one of the most important classes in the field of chemistry, exhibiting rich compositional and structural diversity on par with oxides and organic compounds. Chalcogenides are compounds that contain at least one chalcogen Q atom (Q = S/ Se/ Te) in a chemically reduced state compared to its elemental form. Chalcogenides bear few chemical resemblances to oxides, but there are big dissimilarities in chemical character and physical properties among them which are significant enough to warrant a separate treatment of the chalcogenides as a distinct class of materials. These differences must, of course, originate from the differences between the oxygen atom on the one hand and the atoms of S, Se, Te on the other. Some important differences in the atomic properties of oxygen and the chalcogen are:[2]

1. The chalcogen atoms are larger (and also heavier) than oxygen atoms.
2. The chalcogens are less electronegative than oxygen.
3. The chalcogens have d orbitals of accessible energy (3d for S, 4d for Se and 5d for Te), while oxygen has not. These differences in the atomic properties cause differences in the bonding of metals to S, Se, and Te relative to the metal-to-oxygen bond. Some of these differences are:

4. The metal-to-chalcogen bonds are more covalent than metal-to-oxygen bonds (a consequence of (2))
5. The metal-to-chalcogen bonds often involve the d orbitals of the chalcogen, while this is not possible for the bonding to oxygen (a consequence of (3)).
6. The chalcogenides are more polarizable than oxide ions (a consequence of (1) and (3)).

Metal chalcogenides are at the cutting edge of many research areas. Some examples include nonlinear optics,[3] optical information storage,[4] photovoltaic energy conversion, thermoelectric energy conversion,[5–8] radiation detectors,[9] thin-film electronics,[10] spintronics,[11] fast-ion conductivity,[12] rechargeable batteries,[13] catalysis,[14] novel magnetism,[15] unconventional superconductivity,[16] and science in two dimensions.[17] In recent times, the scientific community has witnessed sensational discoveries pertinent to metal chalcogenides such as quantum spin Hall Effect,[18] topological insulators,[19–22] topological crystalline insulators,[22,23] non-saturating magnetoresistance,[24] and many others which will have huge implications, especially in the fields of spintronics and (Opto) electronics. We are currently in the midst of an impressive expansion in solid-state chalcogenide chemistry with emphasis on the synthesis of materials with new compositions and structures on the one hand, and exploration of their novel properties on the other. Most of the aforementioned applications and phenomena are associated with chalcogenides of transition metals and main group p-block metals.

The following sections will brief structural aspects and novel properties pertinent to these metal chalcogenides of type I-V-VI_2, IV-VI, Chevrel phases, and layered oxychalcogenides, along with some relevant basics at the end to provide a background to my thesis work.

1.2.1. Chalcogenides of Type I-V-VI_2

Ternary chalcogenide materials have drawn tremendous attention in recent years because of potential applications in photovoltaic, TE, and photo-thermal areas. They have been studied on a large scale due to their optical phase-change and photovoltaic applications.[25,26] A part of my Ph.D. research work is based on improving the thermoelectric properties of $AgBiS_2$ and $AgBiSe_2$ belonging to this class of ternary

chalcogenide materials. The ternary chalcogenide materials of type (I-V-VI_2) are based on the ternary semiconducting compounds with the general formula ABX_2. "A" denotes the group I element which can be Cu, Ag or Au or an alkali metal, "B" denotes the group V element can be P, As, Sb or Bi, and the "X" represents the group VI element can be S, Se, or Te. They are derived from PbX by replacing Pb^{2+} with equal amounts of A^+ and B^+ leading to ABX_2. They exhibit sodium chloride or rocksalt-type structure. The most common examples belonging to this class of compounds are $AgSbSe_2$, $AgSbTe_2$, $AgSbS_2$, $AgBiS_2$, $AgBiSe_2$.[27–30] In the rocksalt I-V-VI_2 semiconductors, the external *s* electrons and part of the *p* electrons are non-bonding and are believed to form a shell of a relatively large radius. This is the fundamental reason for the large anharmonicity of the bonds in this group of materials and that leads to low lattice thermal conductivity.[31] For example, the valence electronic configuration of Sb in $AgSbSe_2$ is $5s^2\ 5p^3$, where only $5p^3$ electrons take part in bond formation with the Se valence electrons while the $5s^2$ electrons of Sb form a lone pair (Figure 1.2).[32]

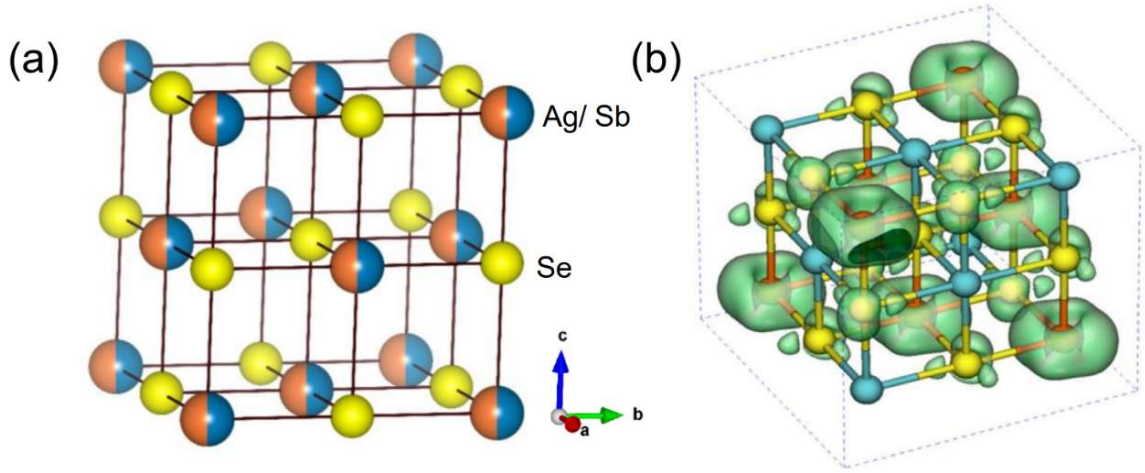

Figure 1.2. *(a) Crystal structure of cubic rock salt $AgSbSe_2$ with disordered Ag/Sb positions. (b) Schematic representation of the presence of stereochemically active lone pair on Sb atom. Figure 1.2b is reproduced from ref. 31 © 2013 RSC.*

The origin of anharmonicity in the Sb-Se bond is the electrostatic repulsion between the stereochemically active lone pair of Sb and the valence bonding charge of Se. the lone pair on the group V element plays an important role in deforming the lattice vibrations, which results in intrinsically low lattice thermal conductivity κ_{lat} in these compounds. The valence electronic configuration of the group V element in I-V-VI_2

compounds is $ns^2 np^3$, where only np^3 electrons are involved in the bond formation with group VI element valence electrons, while the ns^2 electrons of the group V element remain as a lone pair. The electrostatic repulsion between the stereochemically active lone pair of group V elements and the valence bonding charge of the chalcogen atom results in strong anharmonicity in the bonding arrangement.

$AgSbSe_2$, a homolog of $AgSbTe_2$ containing earth-abundant elements, has attracted our attention for thermoelectric investigation.[29,31] At room temperature, $AgSbSe_2$ crystallizes in a cubic rock salt structure (space group, $Fm\bar{3}m$) with disordered Ag and Sb positions (Figure 1.2a). The presence of stereochemically active $5s^2$ lone pair on the Sb atom results in strong anharmonicity in the Sb-Se bond (Figure 1.2b).[31][30] Grüneisen parameter (γ) is a direct measurement of anharmonicity. The compounds with a high degree of anharmonicity in bonding exhibit high γ value. Theoretical investigations by Heremans and co-workers showed that the γ value is higher in the case of $AgSbSe_2$ ($\gamma = 3.4$) compared to those of $AgSbTe_2$ ($\gamma = 2.3$) and $AgBiSe_2$ ($\gamma = 2.5$).[31] $AgSbSe_2$ possesses the lowest lattice thermal conductivity among all the I-V-VI_2 compounds in the 10-300 K range. In addition to low thermal conductivity, $AgSbSe_2$ is a narrow band gap semiconductor with a favorable valence band structure composed of 12 half-pockets located at the X-point of the Brillouin zone.[33–35] The thermoelectric performance of $AgSbSe_2$ can, therefore, be enhanced significantly by the convergence of many valleys through proper carrier engineering.[36,37]

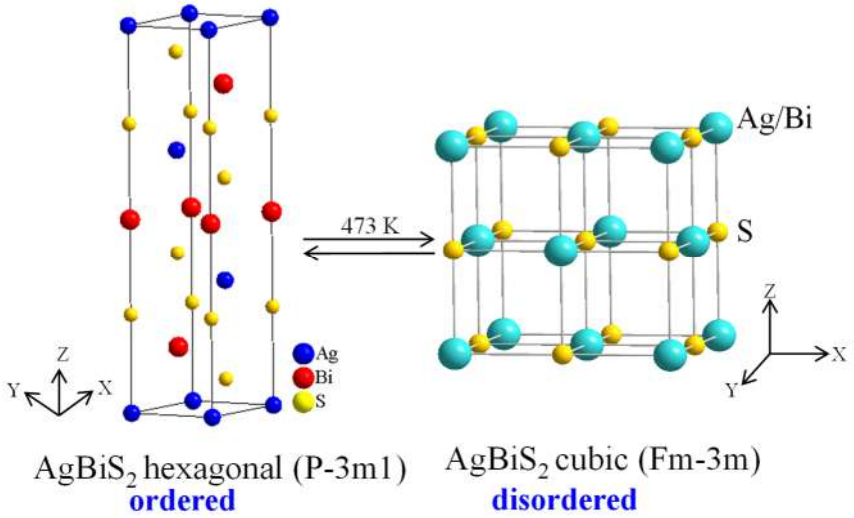

Figure 1.3. *Phase-transition in bulk $AgBiS_2$ from ordered hexagonal at room temperature to disordered cubic phase after 473 K.*

$AgBiS_2$ crystallizes in a hexagonal crystal structure (space group, $P\bar{3}m1$) at room temperature, which transforms to a cation disordered rock salt structure (space group, $Fm\bar{3}m$) at ~473 K (Figure 1.3). The nanocrystalline cubic phase of $AgBiS_2$ prefers a cation-ordered structure, whereas bulk cubic $AgBiS_2$ prefers a disordered structure.[38]

Positron annihilation spectroscopy indicates the Ag vacancy as the native defect in $AgBiS_2$. The concentration of the Ag vacancy is higher in the nanocrystal compared to that in the bulk at room temperature. A significant rise in the Ag vacancy concentration was evidenced during the order-disorder phase transition at 610 K in nanocrystalline $AgBiS_2$. Shuttling of an Ag atom in a vacant or an interstitial site at higher temperatures due to the formation of more Ag vacancies plays a key role in the transition from an ordered to a locally disordered structure in nanocrystalline cubic $AgBiS_2$. This indeed increases the entropy of the system at higher vacancy concentration, which, in turn, results in an unusual rise in thermopower (contributed by both transport and S presence). Synthesis of a new metastable phase in the nanoscale, mechanistic understanding of the order-disorder phase transition, and associated unusual properties not only enrich the fundamental solid-state inorganic but also should assist chemists in understanding the exotic properties associated with the phase transition.[38] In **chapter 2.2**, we have synthesized and stabilized the high-temperature cubic phase of bulk $AgBiS_2$ at room temperature and discussed the origin of ultra-low lattice thermal conductivity and thermoelectric properties. We have studied the effect of $6s^2$ lone pair of Bi, which cause local distortion along the crystallographic [011] direction in bulk $AgBiS_2$ that leads to strong lattice anharmonicity stems from arises from locally distorted structure.[39]

In the *p*-type family, $AgSbSe_2$ and in *n*-type family, $AgBiSe_2$ have been established to be the most promising candidates for thermoelectric performance. At room temperature, $AgBiSe_2$ crystallizes in a cento-symmetric cation-ordered hexagonal structure with space group $P\bar{3}m1$ and lattice parameter a = 4.194 Å, c = 19.65 Å. It shows two structural transitions at higher temperatures. The hexagonal (a) to rhombohedral (b) (space group $R\bar{3}m$, a = 7.022 Å) transition takes place at ~460 K (Figure 1.4).[40,41] During a–b transition, the cation sublattice remains ordered, but a slight atomic displacement and an elongation of the unit cell in the (001) direction of the hexagonal lattice take place. The ordered rhombohedral (b) to cation-disordered cubic (c) (space group Fm-3m, a = 5.832 Å) phase transition takes place at ~580 K.

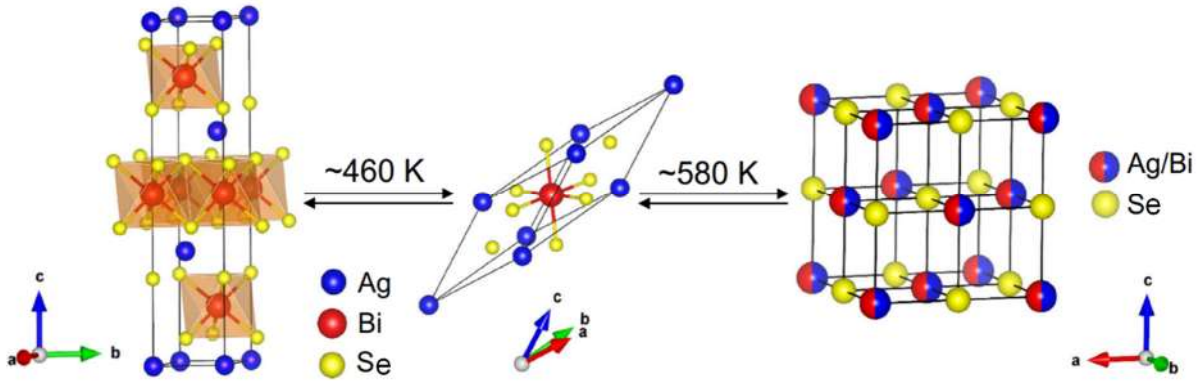

Figure 1.4. *Temperature-dependent structural phase transitions in $AgBiSe_2$. The room-temperature hexagonal and the intermediate rhombohedral phases are cation-ordered structures. The high-temperature cubic phase is a cation-disordered structure.*

In **chapter 2.3**, we have synthesized $AgBiSe_2$ and improved the carrier mobilities of Bi- excess samples of $AgBiSe_2$ by modulation doping. We have observed enhancement in the thermoelectric performance of $AgBiSe_2$ and it is discussed in depth in **chapter 2.3**.[41]

1.2.2. IV-VI Sulfides

Recently, sulfides of group IV metal (metal = Ge, Sn, Pb) have opened up opportunities in the field of thermoelectric to design sustainable electronic and photonic materials due to the earth-abundant, low-cost, and environmentally friendly features. Sulfur is a beneficial alternative, firstly due to its low cost.[42–46] Cost per kg in U.S. $ is 0.15, 44, 82, for S, Se, Te, respectively (Figure 1.5).[47,48] The price of S is much less than the price of Te and Se.[47] Secondly, the terrestrial abundance of Te is only 1 ppb and for Se is 50 ppb while for S it is 3.50×10^5 ppb. [47] Annual production in the metric ton is 8.0×10^4 for S, 2.80×10^3 for Se, and 4.40×10^2 for Te, while the estimated amount in reserves (metric ton) is $>6.0 \times 10^{11}$ for S, 9.9×10^4 for Se, and 3.1×10^4 for Te. Thus, sulfur has longer-term price stability and is an inexpensive sustainable alternative. Thirdly, it is non-toxic as compared to Te with high values of LD50, i.e., 2000 mg/kg for S and ~100 mg/kg for Te. LD50 (lethal dose) is defined as the dose given per unit mass of the test subject which is enough to kill half of the test subjects within the next 14 days.[48] Lower is the value of LD50, higher is the toxicity.

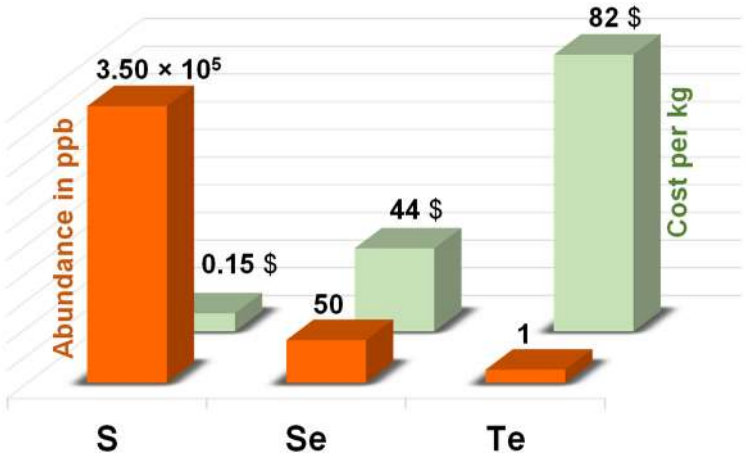

Figure 1.5. *Abundance and cost per kg of chalcogenides to design thermoelectric materials.*

Sulfur-based systems are known to have intrinsic *n*-type nature due to S^{2-} vacancy. Sulfides usually have low zT values due to their high lattice thermal conductivity. Sulfur's light atomic weight (32.06 g/mol) is primarily responsible for such a high value of lattice thermal conductivity. Also, the strong ionic character results in low carrier mobilities.[49–51] The polarizability of S^{2-} is high (10.2×10^{-24} cm^3), comparable with that of heavier Se (10.5×10^{-24} cm^3) and Te (14×10^{-24} cm^3), but more than lighter congener, O^{2-} (3.88×10^{-24} cm^3) or neighbor Cl^- (3.66×10^{-24} cm^3).[47]

High polarizability values help in achieving anisotropic bonding that can lead to low-dimensional structures which can offer high thermoelectric performance, while a polarizable sublattice of anion also assists cation diffusion.[47] The successful practical application for sulfur-based thermoelectrics require mitigation of many challenges such as volatility of S at high temperature due to the low melting point of S (115.4 °C), light atomic weights, and intrinsically un-optimized carrier concentrations that limit the performances of metal sulfides.[48] In this section 1.2.2, I have discussed the thermoelectric properties of IV-VI class-based PbS which have gained huge attention in recent times.

High symmetry lead chalcogenides have shown the high thermoelectric figure of merit zT, in the temperatures range 500 K to 900 K.[7,46,52–56] The continuous research throughout the past 20 years has given rise to the high zT values in both n and p-type lead chalcogenides due to exceptional electrical and thermal transport properties. Recently, the in-depth considerate research in the complex valence band structure of

lead chalcogenides has directed to put forward potential strategies of band engineering to advance the thermoelectric performance. Lead chalcogenides have principal valence band maximum located at L point in Brillouin zone (L band, with band degeneracy N_v= 4), secondary valence band maximum along Σ direction (Σ band, N_v= 12), and conduction band minimum located at L point (Figure 1.6a).[36] This large N_v provides multiple conducting channels for high electrical conductivity without affecting the Seebeck coefficient.[57] By optimizing charge carrier concentration, band engineering through band Convergence, tuning Fermi levels, reducing deformation potential coefficient, low effective mass, lead chalcogenides have shown a high peak figure of merit zT.[36] Due to a similar band structure with different band offset among lead chalcogenides, the formation of solid solution among PbX(X = S, Se, Te) can be used as an effective approach to tune band offset for electronic performance enhancement.

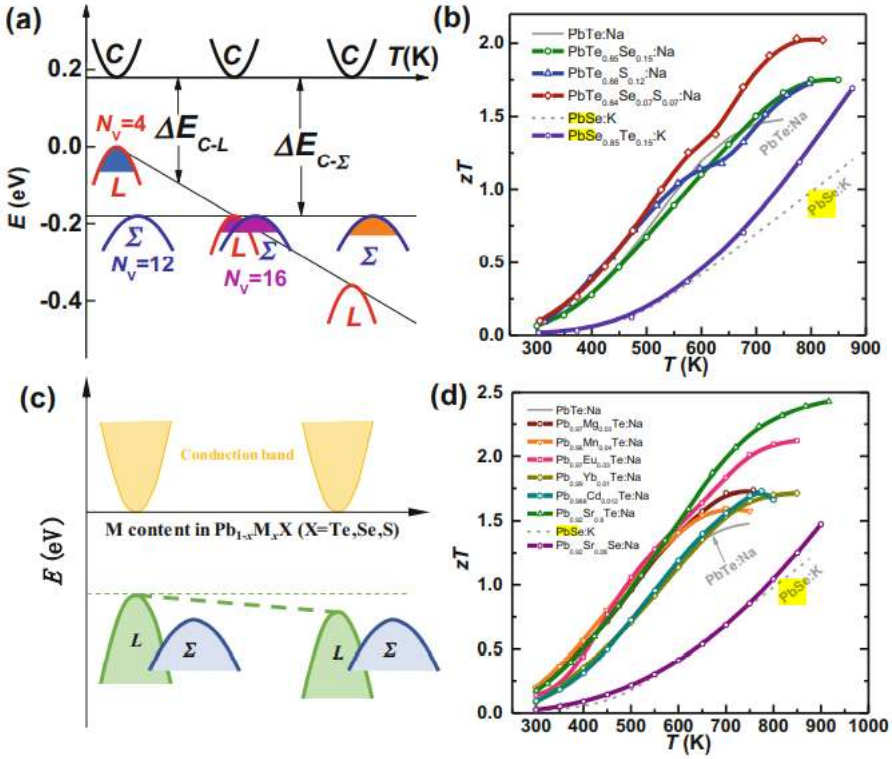

Figure 1.6. *(a) Schematic diagram of temperature-induced band convergence of L and Σ bands in PbTe; (b) temperature-dependent thermoelectric figure of merit ZT of solid solutions within lead chalcogenides; (c) schematic diagram of tuning band offset between L and Σ bands through alloying with MX (M can be but not limited to Mg, Mn, Cd, Sr, Eu, Yb, X= Te, Se, S); (d) temperature-dependent ZT of lead chalcogenides through alloying with MX. Reproduced with permission from ref. 57 © 2019 Springer.*

Figure 1.6b shows the improvement in ZT through this approach. In a typical case, Te is partially substituted by Se in PbTe to increase in convergence temperature of L and Σ bands, resulting in significant improvement in ZT at high temperatures, with the additional help of reduced κ_L by alloying defects for phonon scattering.[37] Further alloying with PbS, the thermoelectric performance of PbTe can be further improved.[58] In addition, alloying with MTe (M= Mg, Cd, Mn, Eu, Yb, Sr)[59–63] can tune effectively the band offset between L and Σ bands as well, usually accompanied by an increase in the bandgap, as schematically shown in Figure 1.6c. Improvements in ZT have also been demonstrated in these alloys, as shown in Figure 1.6d.

With the awareness of using commercial energy harvesting devices and the concern about the scarcity and cost of Te, the interest in IV-VI sulfides has returned. PbS has been least explored in terms of thermoelectric properties, even though it has an almost similar crystal structure and energy band configuration in comparison to high-performing PbTe or PbSe. This is due to the high lattice thermal conductivity (2.75 Wm^{-1} K^{-1} at 300 K) of PbS which leads to a low figure of merit. However, by implementing new strategies by taking an account for band structure and microstructure engineering, the potential of zT enhancement in PbS can be explored. [64]

Figure 1.7a shows that the lattice thermal conductivities of pristine PbS (the blue solid line in the figure) can be significantly reduced by solid solution point defect scattering alone (given for *n*-type and *p*-type variants respectively as the dotted and solid brown lines in the figure), where the room-temperature lattice thermal conductivity of pristine PbS is reduced by ~ 40% in the case of *p*-type $Pb_{0.975}Na_{0.025}S$[64] and 10% for n-type $PbS_{0.98}Cl_{0.02}$,[49] respectively. Subsequent research has demonstrated that nanostructuring with Bi_2S_3 (given as the dotted green line in Figure 1.7a) results in an additional ~30% reduction of the lattice thermal conductivity for *n*-type $PbS_{0.98}Cl_{0.02}$. Further introduction of mesostructures (given for *n*-type and *p*-type variants respectively as the dotted and solid red lines in Figure 1.7) led to an additional suppression of lattice thermal conductivity by ~40% and ~25% for *p*-type $Pb_{0.975}Na_{0.025}S$-SrS and *n*-type $PbS_{0.98}Cl_{0.02}$-Bi_2S_3, respectively. [65]

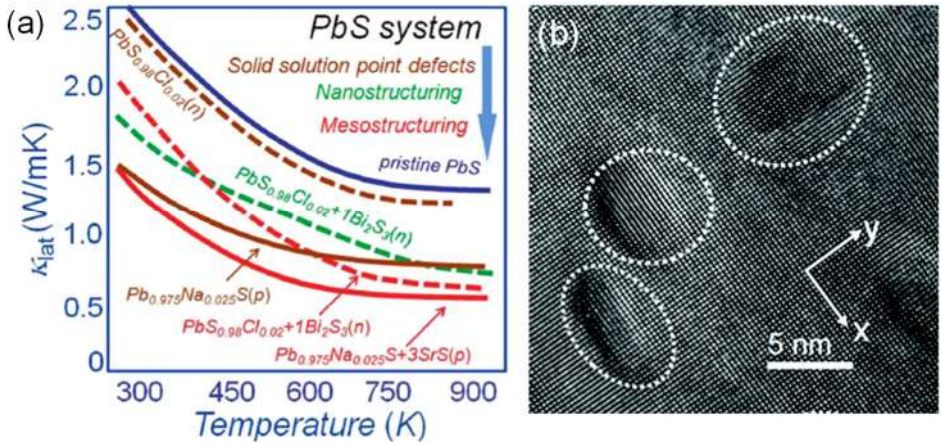

Figure 1.7. *(a) Temperature dependence of the lattice thermal conductivity for the multiple-scale hierarchically architectured PbS system. The blue-colored line represents the pristine PbS material, the brown-colored lines depict the effects of solid solution point defects, the green-colored line depicts the effect of point defects + nanostructures, and the red-colored lines depict the effects of all hierarchical architectures together (point defects + nanostructures + mesostructures). The solid lines represent p-type materials and the dotted lines represent n-type materials and (b) high magnification TEM image of* $Pb_{0.975}Na_{0.025}S$ *with 3.0% SrS sample. Reproduced from ref. 48, 65 © Elsevier and ACS.*

1.2.3. Chevrel Phases

The ternary molybdenum chalcogenides $M_xT_6X_8$ (X = chalcogen), known as Chevrel phases, constitute an outstanding family of materials presenting spectacular physical and chemical properties. These compounds have known to be extensively studied since their discovery by Chevrel and Sergent and the subsequent reports by Matthias *et al.* of their superconducting properties in the 1970's.[66,67] The remarkable features are closely related to the amazing capability of the crystal structure to host a large number of elements, covering all ranges of their chemical nature. The generic formula is $M_xT_6X_8$, where M can be monovalent, divalent, or trivalent elements, with x varying from 0-4, depending essentially on their ionic size and T is the main cation that can be transition metal like Mo, Nb, Ta, Re, W or others. The X anion, a chalcogen (S, Se, or Te), can be partially substituted by halogen elements, even by oxygen.[68] The atomic arrangement of the host in $M_xT_6X_8$ is the stacking of T_6X_8 blocks composed of the octahedral cluster of T atoms inside the anion cube.[68] From three types of cavities,

formed between T_6X_8 blocks (Figure 1.8), only two of them (cavities 1 and 2) can be filled by cations of ternary metals, because of a strong repulsion of the Mo atoms does not allow the occupation of cavity 3. The cation position in the crystal structure depends mainly on its size. The big cations such as Pb^{2+} or Sn^{2+} (with a radius larger than 1 Å) occupy the center of the large cubic cavity 1, whereas the insertion of relatively small cations such as Cu^{+} or Li^{+} (with a radius smaller than 1 Å) leads to the deformation of the cubic anion environments around cations to the tetrahedral ones. These cavities form three-dimensional channels that are available for cation transport.[68] In classic Chevrel phases, such as Cu- or Li-containing compounds, two types of the tetrahedral sites are used to describe the position of the small cations in the crystal structure: (1) so-called inner sites in cavity 1 that form a pleated ring and (2) outer sites in cavity 2 with a quasioctahedral arrangement.[68]

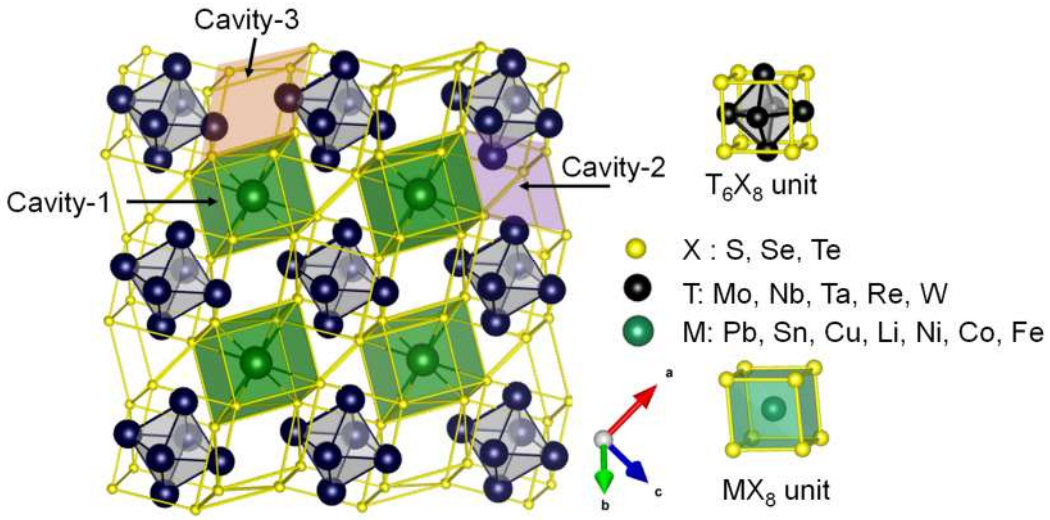

Figure 1.8. *Stacking view of T_6X_8 units and MS_8 cubic sites of rhombohedral with space group $R\bar{3}$. Shaded regions in green, purple, and orange denote three different types of cavities in MT_6X_8 crystal structure.*

Chevrel phases possess outstanding superconducting properties, in particular, high transition temperatures (T_C up to 14 or 15 K) and remarkable high critical fields H_{C2} (reaching 60 T at zero temperature).[68] New properties have come due to the possibility to leach and replace some cations in the crystal structure, opening a broad range of applications based on the electrochemical properties of these materials.[69–71] As

such, Chevrel phases appear very promising as cathode materials, and applications to batteries have come up.[72] Also, the presence of sulfur in these compounds and their high stability during synthesis, make them to be adequate materials for the hydrodesulfurization of thiophene and/or decomposition of nitrogen oxides, among others, and, therefore, are promising materials to be used as catalysts. Moving on, new applications have recently been investigated in sulfides, selenides, and tellurides.[72] Chevrel phases; they concern a new generation of thermoelectrical devices since these materials may present low thermal conductivity and high figures of merit.[73] In **chapter 2.5** we have studied the origin of ultra-low lattice thermal conductivity in $SnMo_6S_8$ arising from Sn rattler atoms, which creates an anharmonicity in the system.

1.3. Layered Materials

Bulk layered materials have been studied extensively in the past several decades because of their unique structural features, and physical and chemical properties.[74] Materials with layered structures remain an extensively investigated subject in current chemistry and physics due to their interesting properties.[75,76] The valuable properties of layered inorganic solids and the possibility of modification by various post-synthesis treatments have attracted a lot of attention for many years. Layered materials typically exhibit strong in-plane covalent bonding and weak out-of-plane van der Waals interactions through the interlayer gap.[77] They exhibit a wide range of electronic band structures from insulators, semiconductors, metals, superconductors to topological insulators. Hence, layered phases present new physical and chemical properties that are not commonly encountered in three-dimensional materials.[78–80] Many of these properties are strongly related to the nature and extent of interactions between the layers, hence reflects the type of behavior that falls between two and three-dimensional systems.[81] Research into the basic science of layered solids has intensified in the last decade due to several emerging applications in catalysis, adsorption, photovoltaics, and medicine.[82] Most of the promising technological applications, however, deal with intercalation compounds of layered inorganic solids. These intercalated materials have various applications, for instance as thermoelectrics, catalysts, sorbents for water purification, ion exchange, electrochromic displays, electrodes for secondary batteries (Li-ion batteries), and components for fuel cells.[81] In this section we have discussed, tin sulfide

and bismuth oxychalcogenides whose properties have been studied in-depth in **chapters 3.2** and **4.2**.

1.3.1. Layered Metal Chalcogenides

Layered metal dichalcogenides have attracted significant interest as a family of single- and few-layer materials that show new physics and are of interest for device applications. Layered metal dichalcogenides have attracted significant interest as a family of single- and few-layer materials that show new physics and are of interest for device applications.[83] SnS_2 crystallizes in a CdI_2-type layered structure, in which S–Sn–S trilayers with internal covalent bonding are held together by van der Waals forces.[84] SnS_2 occurs in different polytypes with the same structure of the S–Sn–S layers but different interlayer stacking. SnS_2 has been reported to have outstanding properties for applications in photocatalysis, electrochemical capacitors and batteries, and supercapacitors. I have studied and exploited this layered SnS_2 by forming composites with graphene oxide to introduce selectivity towards the sorption of mercury (Hg^{2+}) ions from water in **chapter 3.2**. I have used the hard and soft acids and bases (HSAB) principle to capture heavy metal ions in **part 3** of my thesis.

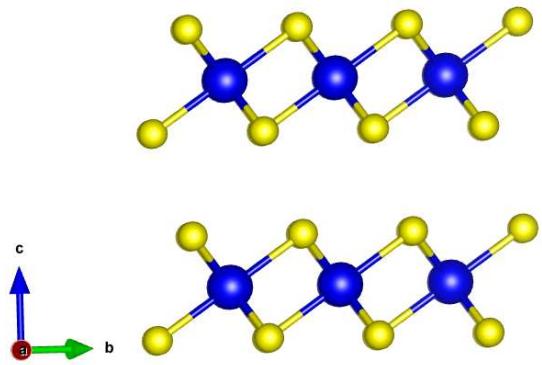

Figure 1.9. *The layered structure of tin disulfide (SnS_2).*

Recently, the layered oxy-chalcogenide material Bi_2O_2Se has emerged as fascinating 2D semiconductor material with excellent environmental stability in the air. The material is known for its extremely high carrier mobility (>20000 $cm^2V^{-1}s^{-1}$ at 2 K) with very low effective mass (0.14 m_0), indirect size tuneable band gap (bulk band gap ~0.8 eV) which is excellent for electronic and optoelectronic applications.[85,86] Top-gated

field-effect transistor based on 2D Bi_2O_2Se crystal shows high Hall mobility value (up to 450 $cm^2V^{-1}s^{-1}$), high current on/off ratio ($>10^6$), and ideal subthreshold swing value ($\approx$65 mV dec^{-1}) at room temperature. The photodetector based on 2D Bi_2O_2Se has high sensitivity over the wide spectral range from visible to infrared regions. Therefore, bismuth oxychalcogenide is a good candidate material for high-performance electronics and optoelectronics.[87]

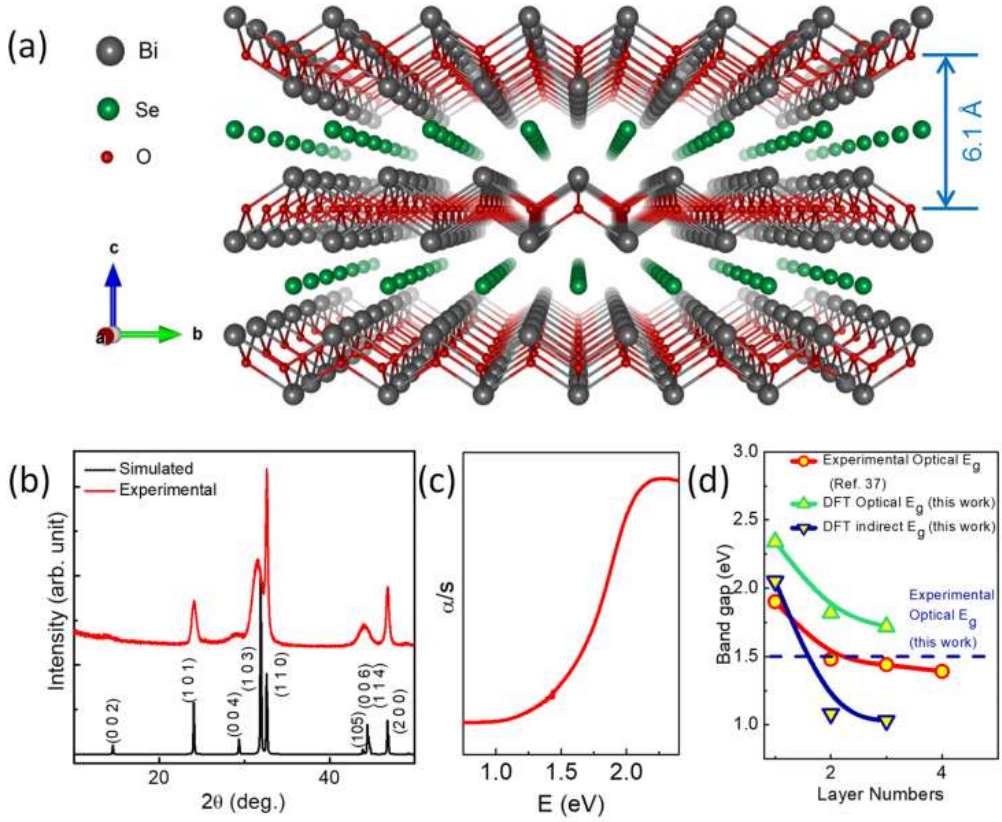

Figure 1.10. *(a) Layered crystal structure of Bi_2O_2Se showing alternative stacks of $[Bi_2O_2]^{2+}$ and Se^{2-} layers. (b) XRD pattern of the synthesized Bi_2O_2Se nanosheets after vacuum drying (c) Optical absorption spectrum of Bi_2O_2Se nanosheets showing band gap of 1.5 eV. (d) Experimental and theoretical optical band gap variation with layer numbers for a Bi_2O_2Se nanosheet. This figure has been reproduced with permission from ref. 87 © 2019 ACS.*

In previous research work, chemical vapor deposition was regularly used to obtain Bi_2O_2Se material with high purity and good crystallinity, however, the preparation conditions were harsh due to high reaction temperature. Recently, from our group, Tanmoy et.al, have designed ultrathin ferroelectric Bi_2O_2Se nanosheets and

demonstrated a simple and scalable solution-based synthesis to prepare self-assembled charged nanosheets of Bi_2O_2Se.[87] The obtained nanosheets are ultrathin (~2 nm), single crystalline, and free-standing in nature. Bi_2O_2Se, with the absence of a well-defined van der Waals (vdW) gap, however, intrinsically distinguishes itself from the family of vdW solids. The tetragonal structure (I4/mmm space group, a = 3.88 Å, c = 12.16 Å) of Bi_2O_2Se is formed by the alternate stacking of positively charged $[Bi_2O_2]^{2+}$ and negatively charged Se^{2-} layers along the crystallographic c-direction (Figure 1.10a). Although Bi_2O_2Se has a layered crystal structure, the interlayer interaction is of the electrostatic type which arises out of positively charged $[Bi_2O_2]^{2+}$ and negatively charged Se^{2-} stacking layers and is stronger than vdW interaction.[87]

The next sensation in this field is to make heterostructures as semiconductor heterostructures are considered as the basic building blocks for high-performance modern optoelectronic devices, such as light-emitting diodes, solar cells, and photodetectors.[88] 2D vdW layered semiconductor materials have attracted great research interest due to their unique physical properties, atomic thin geometry, and dangling-band-free surfaces, which facilitate the formation of heterostructures based on the layered materials via vdW interaction that is free of constraints on the strict lattice match. Although the heterostructures constructed by two distinct 2D materials (2D/2D heterostructures) are promising to satisfy the demands of portability and wearability for next-generation electronics and optoelectronics, the limited number of 2D materials confines their extensive applications in multifunctional devices.[88,89] As a consequence, intensive efforts have been devoted to integrating 2D materials with disparate dimensional structures to form the mixed-dimensional vdW heterostructures, including 2D/0D (quantum dot), 2D/1D (nanowire), and 2D/3D (bulk), where the charge transport behaviors are affected by not only the heterojunction types but also the heterojunction geometry. Such mixed-dimensional vdW heterostructures offer new opportunities to design promising applications with high performance and multifunctionality.[89] In **part 4** of my thesis, I have synthesized heterostructures of $CsPbBr_3$ nanocrystals with 0-D nitrogen-doped carbon dots (**chapter 4.1**) and 2-D nanosheets of Bi_2O_2Se (**chapter 4.2**) and studied the charge-transfer and photoluminescence quenching.

1.4. Metal Chalcophosphates

Transition metal chalcophosphate MPX_3 (M = Mg, V, Mn, Fe, Co, Ni, Zn, Pd, and Cd; X= S, Se) are semiconducting two-dimensional material. Several phases of MPS_3 were first reported by Friedel.[90] The first transition metal series adopts the $FePS_3$ structure that is based on a cubic close-packed anion array with alternate layers of vacant cationic sites. Within the layer, the cationic sites are occupied by M^{2+} cations and P_2 pairs, as shown in Figure 1.11.

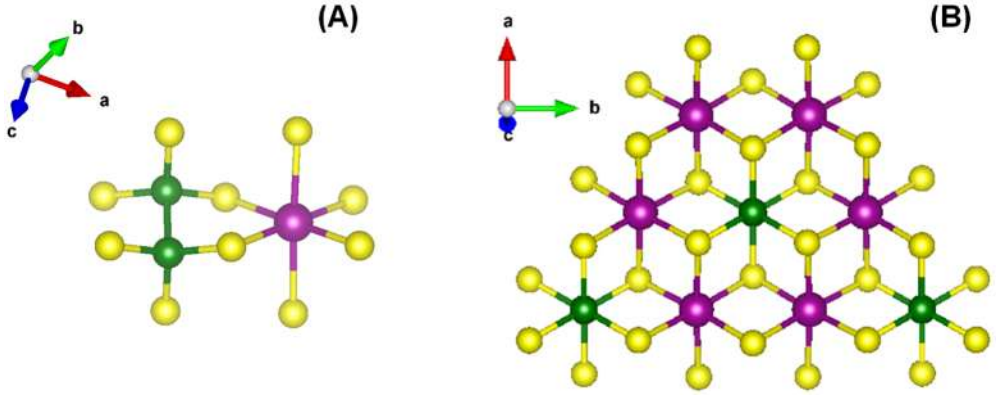

Figure 1.11. *MPS_3 structure showing the connection of P_2S_6 and MPS_6 octahedra and (B) ordered arrangement within a single layer. Violet, green and yellow are metal, phosphorous and sulfur atoms.*

Each P_2S_6 octahedron is surrounded by six MS_6 octahedra and each MS_6 octahedron has 3 each of MS_6 and P_2S_6 neighbors. The general composition can be written as $M_{2/3}(P_2)_{1/3}S_2$ to emphasize the structural relationship to the dichalcogenides.[78,81] The host lattice of MPS_3 is either a semiconductor or insulator and the transition metal compounds have magnetic properties characteristic of high-spin octahedral cations. At lower temperatures, the antiferromagnetic order is observed but the susceptibility maxima are broad, indicative of the strong two-dimensional nature of the magnetic interactions.[91]

1.4.1. Ion-exchange in MPS_3

In the cation-exchange process, the electrical charge of the cationic guest species entering the host lattice is counterbalanced by the loss of intralayer M^{2+} ions. An important feature of the ion exchange chemistry in MPS_3 class is that it yields intercalates which are generally air-stable, well crystallized.

The K^+ ions of a $K_{2x}Mn_{1-x}PS_3$ pre-intercalate are exchanged with the tetrafluoroborate salt $(TTF)_3(BF_4)_2$ in acetonitrile medium. The compound obtained under these conditions was formulated as $Mn_{0.83}PS_3$-$(TTF)_{0.42}K_{0.10}(solv)_y$.[92] Polyethylene oxide, $(C_2H_4O)_n$ [PEO], a polymer has also been intercalated in $MnPS_3$.[93] Intercalation of potentially reactive transition-metal complexes like $Cr(en)_3Cl_3$, $Ru(bpy)_3Cl_3$ and cyclopentadienylcarbnyl(diphos)iron monocation leads to dramatic modification in magnetic properties.[94] New hetero-metallic materials, $Cu_{0.2}Mn_{0.8}PS_3 \cdot 0.25H_2O$, $Co_{0.2}Mn_{0.8}PS_3 \cdot 0.25H_2O$, $Ni_{0.2}Mn_{0.8}PS_3 \cdot 0.25H_2O$ and $Zn_{0.2}Mn_{0.8}PS_3 \cdot 0.25H_2O$, with an ordered distribution of the secondary metal ions have also been synthesized and shows improved magnetic properties.[95] Cationic complexes $[M(salen)]^+$ ($M=Mn^{3+}$, Fe^{3+},Co^{3+}; salen=N,N-ethylene-bis(salicylal-diamine)) also accommodates themselves in the space between the layers of MPS_3.[96] Intercalation compound, $Mn_{0.84}PS_3(phen)_{0.64}$ (phen=1,10-phenanthroline) exhibits bulk spontaneous magnetization below 36 K.[96] Polymer-inorganic intercalation nano-composite based on a C_{60}-containing poly-(ethylene oxide) (C_{60}-PEO) into layered $MnPS_3$ have shown a magnetic phase transition from paramagnetism to ferrimagnetism at about 40 K.[97] Interestingly, aminoacid intercalates, $Mn_{0.83}PS_3(His)_{0.34}$, $Mn_{0.83}PS_3(Lys)_{0.35}$ and $Mn_{0.88}PS_3(Arg)_{0.25}$ are the first example of a magnetic bioorganic/inorganic material synthesized by inserting a biomolecule into a layered inorganic host.[98] I have used $K_{2x}Mn_{1-x}PS_3$ as an adsorbent for the removal of lead ions and cesium ions in **chapters 3.1** and **3.4**.

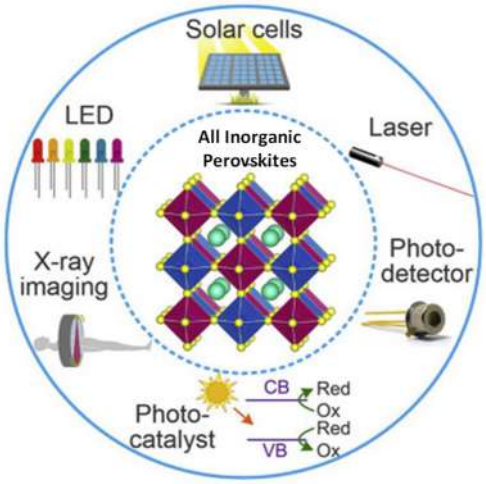

Figure 1.12. *Illustration showing applications of all inorganic perovskites in photocatalysis, X-ray imaging, photovoltaics, photodetectors, light-emitting diodes, and lasers. Reproduced with permission from ref. 99 © 2018 Cell.*

1.5. Heterostructures of Inorganic Halides Perovskites

All-inorganic halide perovskites have created a sensation in diverse optoelectronic applications like photovoltaics, photodetectors, light-emitting diodes, and lasers and we have seen phenomenal growth in research efforts to understand the photodynamics, luminescent properties, and stabilization of different phases of perovskites.[99] Lead-based halide perovskites have emerged as excellent semiconductors for a broad range of optoelectronic applications, such as photovoltaics, lighting, lasing, and photon detection (Figure 1.12).The rocketing improvement of efficiency is attributed to the suitable direct bandgap, strong absorption coefficient, long-range charge diffusion length, balanced electron-hole mobility, high dielectric constant, excellent carrier mobility and small exciton binding energy of halide perovskites.

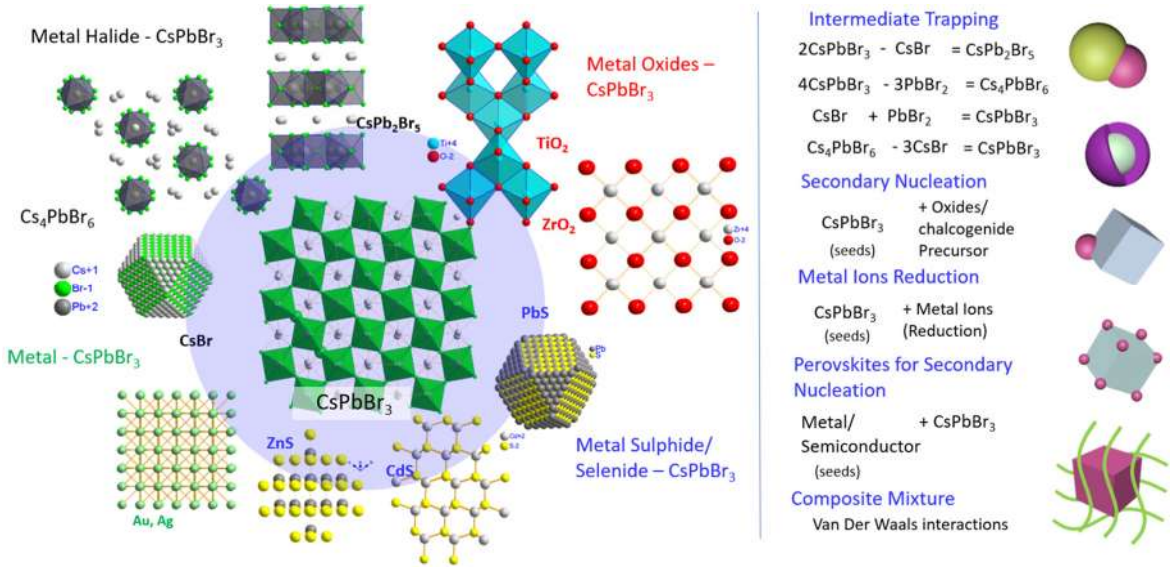

Figure 1.13. *Schematic presentation of different nanostructures coupled with $CsPbBr_3$ perovskite nanocrystals. This includes metal halides and perovskite–perovskite-type, metal oxide–perovskite, metal chalcogenide–perovskite, and metal (0)–perovskite heterostructures. The right panel presents the formation processes of heterostructures which include intermediate trapping during phase transformation, secondary nucleations of oxides/chalcogenides/metals on perovskites seeds, and also nucleation of perovskites on seed materials. Shapes obtained in different heterostructures include dimers, core/shell, dimers involving seed cubes, decorated nanocubes, and composites. This image is adapted from ref. 100 © 2020 ACS.*

Heterostructures of inorganic halide perovskites with mixed-dimensional inorganic nanomaterials have shown great potential not only in the field of optoelectronic energy devices and photocatalysis but also for improving our fundamental understanding of the charge transfer across the heterostructure interface. Bringing together two nanostructures of different materials in a single building block can create a new platform where both can share their electronic and optical characteristics. Enhancement in optoelectronic properties, photo-response and efficient CO_2 reduction capability has been achieved by the formation of heterostructures between 2D layered materials (graphene oxide, MXene and phosphorene), metal chalcogenide semiconductors (ZnS, CdS, CdSe, PbS, PbSe) and $CsPbBr_3$ nanocrystals (NCs).[100,101] Combining all such inorganic heterostructures of perovskites, atomic models showing different phases of materials associated with $CsPbBr_3$, the most widely studied perovskite nanocrystals are presented in Figure 1.13. In addition, all the combining methods of their heterostructure formation, which include intermediate trapping; secondary nucleation of the inorganic material on perovskites or vice versa; and possible heterostructures in the form of heterodimers, core/shell, decorated nanocrystals, and van der Waal's interacted composites[100] have been listed in Figure 1.13.

In **part 4** of my thesis, I have focused on designing heterostructures of $CsPbBr_3$, studying the optical properties of the synthesized heterostructures, and understanding the mechanism of charge transfer. In **chapter 4.1**, I have investigated the driving force for the synthesis of a heterostructure of $CsPbBr_3$ nanocrystals with nitrogen-doped carbon dots, the charge transfer mechanism responsible for photoluminescence quenching, and photoconductivity. In addition, I have synthesized the heterostructure of $CsPbBr_3$ nanocrystals with few layers of layered metal oxy-chalcogenide, Bi_2O_2Se, and studied the photoluminescence quenching mechanism in **chapter 4.2**.

1.6. Energy Conversion and Environmental Remediation

This Ph.D. thesis presents the design and synthesis of various metal chalcogenides, layered chalcophosphates/ halides for their application in thermoelectric energy conversion, water purification, and a fundamental understanding of the charge transfer mechanism in the all-inorganic halide perovskite heterostructures. In this

section, I have elaborated on applications related to thermoelectrics and water purification.

1.6.1. Thermoelectrics

Over decades, the continuous depletion of existing energy sources has become a serious problem due to the huge consumption rate. Fossil fuels, the primary source of energy are going to be exhausted in near future. So, it is the prime time to think of some alternative, sustainable energy sources. The best possible way is to develop new technologies which can increase the output power of the existing fuels and for that the use of alternative energy sources (renewable sources; wind, solar, biomass, and others) and improvement of the thermal management is necessary. Thermoelectric (TE) materials, by virtue of a unique combination of electrical and thermal properties, can convert thermal gradients into electrical energy or vice-versa and are posited to play a significant role in energy management.[6,8,102] The thermoelectric materials and devices are successful in recycling the waste heat energy which is produced in large amounts through automobile exhaust, domestic heating exhaust, and industrial processes. Interestingly, thermoelectric devices are all-solid-state devices well equipped without any mobile parts thus making them tailor-made for small-scale power generation and distribution. For the past 40 years, thermoelectric generators are consistently providing power in remote terrestrial and extra-terrestrial locations (radioisotope thermoelectric generators, RTGs in Voyager 1, Vo yager 2, Galileo, Ulysses, Cassini, and New Horizons spacecraft).[103,104] Efforts are already underway to mount the thermoelectric device in the exhaust stream of cars to utilize the waste heat, thereby improving fuel efficiency. Recently large multinational car companies like BMW, Ford, Renault and Honda have shown their interest in exhaust heat recovery, developing systems that make use of thermoelectric generators.[105]

When a temperature gradient (ΔT) is applied to a TE couple consisting of n-type and p-type elements, the mobile charge carriers (electrons in n-type and holes in p-type) at the hot end diffuse to the cold end, producing a potential difference (ΔV). This effect is known as the Seebeck effect, where $S = \Delta V/\Delta T$ is defined as the Seebeck coefficient, which forms the basis of TE power generation. (Figure 1.14a). Conversely, when a potential difference is applied to a TE couple, carriers bring heat from one side

to the other so that one side gets cooler while the other gets hotter, an effect known as the Peltier effect (Figure 1.14a) which forms the basis of TE refrigeration.[106] The TE conversion efficiency of a TE material is a function of a dimensionless figure of merit, zT, given by

$$zT = \left(\frac{\sigma S^2}{\kappa_e + \kappa_L}\right) T \qquad \text{Eq. 1.1.}$$

where σ is the electrical conductivity, S is the Seebeck coefficient, κ_e and κ_L are the electronic and thermal conductivities respectively, and T is the absolute temperature. An ideal thermoelectric material should have high electrical conductivity similar to metals, a large Seebeck coefficient as in semiconductors, and ultra-low thermal conductivity like glasses (Figure 1.14b). It is always challenging for the chemists to design a single TE material that meets all the above criteria; moreover, the high interdependence of all the above properties poses an inherent limit to the maximum zT that can be attained in a given material.

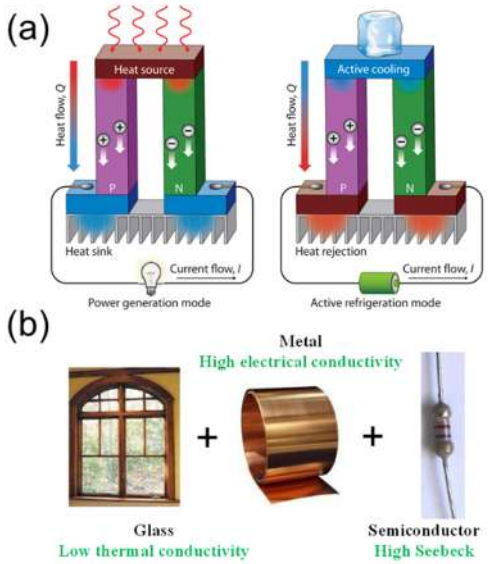

Figure 1.14. *(a) Schematic illustrations of a thermoelectric (TE) module for active refrigeration-Peltier effect (left) and power generation-Seebeck effect (right). (b) TE material should have glass like low thermal conductivity, metal like high electrical conductivity and semiconductor like high Seebeck coefficient. (a) reproduced with permission from ref. 106 © 2010 NPG.*

Two approaches are employed to boost zT viz. enhancement of power factor (σS^2) and reduction of thermal conductivity. Some strategies to enhance power factor include: a) engineering of carrier-concentration through chemical doping, b) enhancement of effective carrier mass (m*) and hence, the Seebeck coefficient either via distortion of the density of states near Fermi level by resonant impurity levels or, the convergence of multiple valence/conduction band extrema and c) enhancement of carrier mobility by modulation-doping. On the other hand, thermal conductivity is suppressed traditionally through a) point defects, b) endotoxic nanoscale precipitates in the host matrix and c) mesoscale grain boundaries.[102] Sometimes all the above three are incorporated in what is referred to as hierarchical architectures where the atomic scale, nanoscale, and mesoscale defects would scatter phonons with a broad range of wavelengths (Figure 1.15).

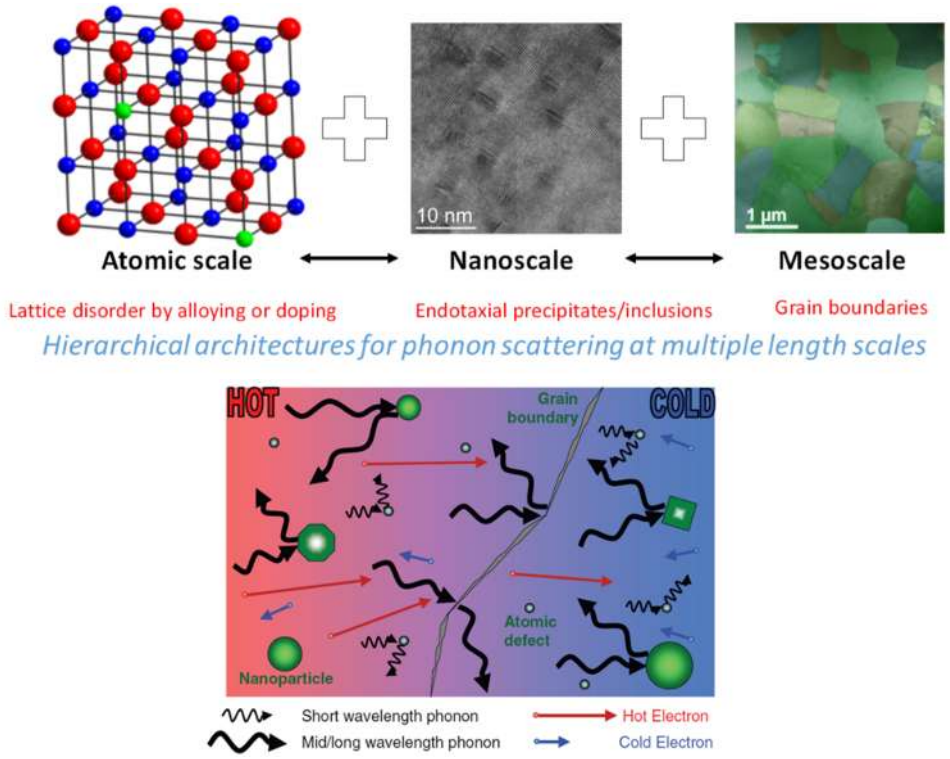

Figure 1.15. *Illustration of extrinsic approaches to reduce lattice thermal conductivity by atomic-scale point defects, endotaxial nanostructures, and mesoscale grain boundaries in hierarchical architectures based on PbTe that lead to an all-scale phonon scattering (upper panel). Point defects scatter short-wavelength phonons. Nanoparticles are effective at scattering mid-long wavelength phonons while grain boundaries predominantly scatter the long-wavelength phonons. Schematic illustration of phonon-scattering by atomic defects, nanoparticles and grain boundaries in a solid (lower panel). The upper panel is adapted from ref. 102 © 2012 NPG and the lower panel is reproduced with permission from ref. 8 © 2010 Wiley.*

The all-scale hierarchical architecting is promising especially for the lead chalcogenides. However, in addition to a scattering of phonons, an undesirable scattering of carriers can occur limiting the overall zT in most other TE materials. In this respect, materials with intrinsically low thermal conductivity are, therefore, practically more attractive being robust to impurities, doping, grain sizes etc. Solids with intrinsically low lattice thermal conductivity have gained popularity because of independent control over electric transport[39,107–112] (Figure 1.16).

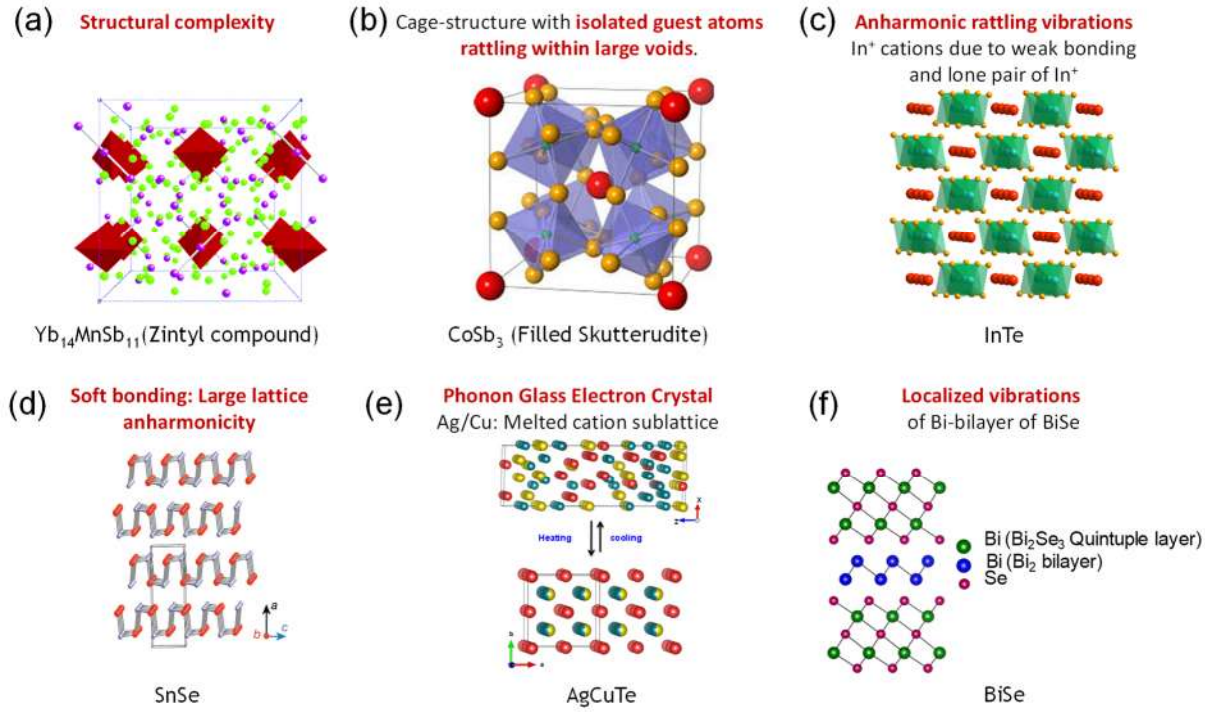

Figure 1.16. *Illustration of intrinsic approaches to reduce lattice thermal conductivity via the introduction of (a) structural complexity in $Yb_{14}MnSb_{11}$(Zintyl compound), (b) isolated guest atoms rattling within large voids of cage-structures of filled skutteride like $CoSb_3$, (c) anharmonic rattling vibrations of In^+ cations due to weak bonding and lone pair of In^+ in InTe, (d) soft bonding that creates large lattice anharmonicity in SnSe, (e) Ag/Cu melted cation sublattice in AgCuTe that behaves like phonon glass electron crystal and (f) localized vibrations of Bi-bilayer of BiSe. Reproduced from ref. 107-112. © 2006 ACS, 2014 PNAS, 2018 ACS, 2018 Wiley, 2017 ACS.*

Slack had originally proposed "phonon-glass electron-crystal" (PGEC) where the electron and phonon transport channels are decoupled, thus facilitating an independent

control of electronic and thermal properties. As the name suggests, a PGEC crystal should possess glass-like low thermal conductivity coexistent with crystal-like high electrical conductivity. PGEC concept has inspired several investigations and led to a significant increase in zT in several classes of compounds such as skutterudites,[113] clathrates,[114] etc. The latter can be doped with guest-fillers that preferably occupy the intrinsic over-sized structural voids. These guest atoms, not being bonded to the host matrix, randomly rattle within the voids producing localized low-frequency optical vibrations. The latter can couple with the heat-carrying acoustic phonons of the host and lead to ineffective thermal transport via "phonon resonant scattering"[115] or lowering of acoustic phonon group velocities. Other intrinsic factors leading to low thermal conductivity include large unit cells,[107] complex crystal structures,[116] cation-disorder,[117] liquid-like atomic motion,[118] and weak multicentre bonds[119] as shown in Figure 1.16. Lattice anharmonicity is a universal feature that leads to low lattice thermal conductivity due to anharmonic phonon- phonon scattering.

Part 2 of my thesis is related to energy conversion and is focused on the design and synthesis of metal chalcogenides for high-performance thermoelectric energy conversion. In **chapter 2.1**, I have discussed the influence of the periodic table in designing solid-state metal chalcogenides for thermoelectric energy conversion. As mentioned before, in certain lone pair containing compounds of I-V-VI_2 class, the lattice vibrations can be rendered strongly anharmonic by the deformation of electron lone-pairs. **Chapter 2.2** is focused on understanding the origin of ultralow thermal conductivity in n-type cubic $AgBiS_2$ caused by the soft vibrations and local structure distortion in [011] direction induced by the Bi $6s^2$ lone pair. In **chapter 2.3**, I have enhanced electrical transport properties in Bi excess samples of $AgBiSe_2$ by modulation doping using microstructures of topological semi-metal Bi_4Se_3 which injects the charge carriers to the precipitates of Bi_4Se_3 from the $AgBiSe_2$ matrix and that results in a large improvement of carrier mobility. In **chapter 2.4**, I have synergistically modulated both electronic and thermal properties and obtained the highest zT of 1.45 in low-cost and earth-abundant element-based lead sulfide thermoelectric material which is an alternative to champion lead chalcogenides, PbTe, and PbSe. Ge doping in PbS synergistically brings out extremely low lattice thermal conductivity (κ_{lat}) in PbS via endotoxic nano precipitates of Pb_2GeS_4 which scatter heat-carrying phonon and the

electrical conductivity increases due to enhanced covalency in chemical bonding. In **chapter 2.5**, I have studied Chevrel phase compound $SnMo_6S_8$, which has an interesting complex structure, where Sn atoms rattle in the channels formed between the Mo_6S_8 cubane and SnS_8. This creates anharmonicity and has been studied in-depth to understand the origin of ultra-low lattice thermal conductivity in superconductive $SnMo_6S_8$.

1.6.2. Water Purification

Clean and fresh water is essential to the survival of life. However, the world's supply of fresh water is diminishing, and the contaminant levels are increasing rapidly. The treatment of several types of aqueous wastes, such as industrial and nuclear waste effluents, is of most important concern for countries all over the world. Toxic heavy metal ions (Hg^{2+}, Pb^{2+}, Cd^{2+}, and Tl^{+}) and radionuclides (^{137}Cs, ^{89}Sr, ^{235}U, ^{59}Fe, ^{57}Co, ^{65}Zn, *etc.*) are key pollutants in these types of waste and cause severe danger to humans and other species.[120] Traditional inexpensive methods such as precipitation of the ions from solutions are not satisfactorily effective to reduce the concentration of these ions below the acceptable toxic legal limits. For example, it is difficult to reduce the concentration of Hg^{2+} ions below 10 to 50 ppb by precipitation using Na_2S. These levels are 20 to 100-times higher than the legally accepted limits defined by the European Union (1 ppb) and USA-EPA (2 ppb).[120,121] On the contrary, the treatment of nuclear effluents is even more complicated due to the harsh conditions of nuclear waste like inhomogeneous samples, extreme pH, and very high salt concentrations. Cost-effective removal of radioactive elements and reduction of long-term storage space is vital to enable safer and inexpensive operation of nuclear energy.

1.6.2.1. Ion-exchange and Intercalation

Ion exchange is well established as a reasonably inexpensive and highly effective technique for the removal of numerous types of toxic ions from aqueous waste solutions. Ion-exchange is a chemical reaction in which intercalated ions of a compound with an open-network or layered structure are exchanged with different ions contained in a medium with which it is in contact. Certain inorganic materials can react with ionic solutions to selectively remove one ionic component and replace it with other ions from the solution, with the result being new materials. Ion-exchangers are insoluble solid

materials with exchangeable cations or anions. When ion-exchanger is in contact with an electrolyte solution, a stoichiometrically equivalent amount of other ions of the same sign can be exchanged.[122]

$$\text{Cation exchange: } 2NaX + CaCl_2\,(aq) \rightleftharpoons CaX_2 + 2NaCl\,(aq)$$

$$\text{Anion exchange: } 2XCl + Na_2SO_4\,(aq) \rightleftharpoons X_2SO_4 + 2NaCl\,(aq)$$

The ion-exchange process, based on topotactic reactions, can result in a material crystallographically analogous to the parent phase but with a new chemical composition.

Intercalation is a solid-state reaction that involves the chemical or thermal reversible inclusion or insertion of a guest species (ion or molecule) into a layered inorganic solid host. The structure of the host remains unchanged or is only slightly altered in the guest-host complex (intercalate). The reaction does not involve diffusive rearrangement of the host and therefore is considered to be a topotactic reaction.[81] A wide variety of intercalated structures can form including ordered vacancy compounds because of the specificity of the interactions between the guest atoms and host lattice. The reversible ion-electron transfer reaction is described as

$$x\mathrm{A}^+ + xe^- + [\mathrm{Host}] \rightleftharpoons \mathrm{A}_x^+[\mathrm{Host}]^{x-}$$

where A is an alkali metal and x is the molar intercalation fraction.

In the intercalation reaction of transition metal dichalcogenides, guest species are inserted into the octahedral, tetrahedral, or trigonal prismatic sites between the chalcogenide layers. Alkali metal intercalation in TMDs is carried out electrochemically by using TMDs as a cathode and the alkali metal as an anode in presence of a non-aqueous solution of the alkali metal salt as the electrolyte.[123–125]

$$\mathrm{Na/NaI\ –propylene\ carbonate/MX_2\ (X{=}S,\ Se,\ Te)}$$

$$\mathrm{Li/LiClO_4\text{-}dioxolane/MX_2}$$

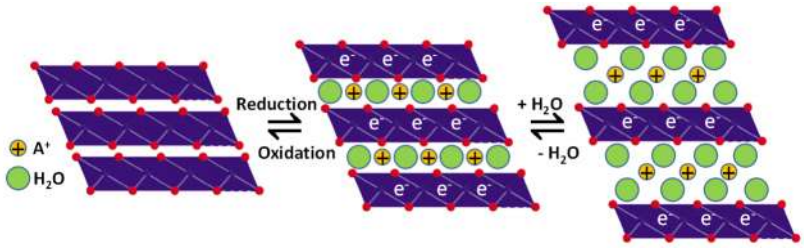

Figure 1.17 *Schematic illustration of hydrated phase formation by redox intercalation in aqueous electrolyte: (a) host lattice MX_2 and (b) monolayer hydrate $A_x^+(H_2O)_y[MX_2]^{x-}$ and (c) bilayer hydrate.*

Direct alkali metal intercalation in TMDs (A_xMX_2, M=V, Nb, Ta) is achieved by heating elements in sealed tubes around 1070 K which forms hydrated phases, $A_x(H_2O)_yMX_2$ similar to layered oxides which are illustrated in Figure 1.17.[125] Mg^{2+} is known to sandwich between TiS_2 using organometallic reagents. Lewis base type molecules such as ammonia, amines, amides, pyridine, organometallic cations such as cobaltocene, chromocene have also been known to intercalate in TMDs.[126,127]

1.6.2.2. Mechanism of Ion-Exchange Reactions

Ion-exchange is an adsorption phenomenon where the mechanism of adsorption is electrostatic. Electrostatic forces hold ions to charged functional groups on the surface of the ion-exchanger. The adsorbed ions replace ions that are on the surface of the ion-exchanger on a 1:1 charge basis. England *et al.* revealed that ion exchange occurs even when the diffusion coefficients are as small as ~10-12 cm^2/s.[128] Figure 1.18 explains the general mechanism of ion exchange reactions. Ion-exchange occurs at considerable rates in stoichiometric solid topochemical which enables the synthesis of metastable phases that are inaccessible by high-temperature reactions.[129]

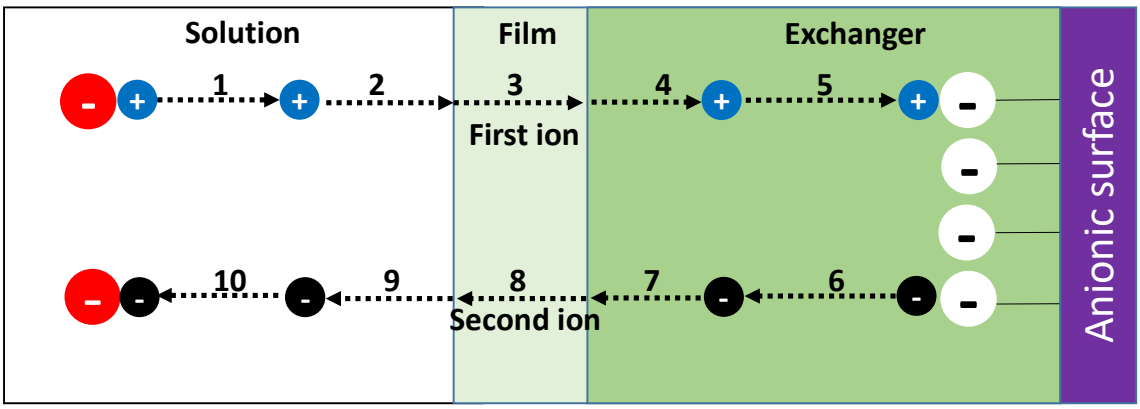

Figure 1.18. *Mechanism of the ion-exchange process.(1) dissociation of the dissolved complexes containing the first ion; (2) diffusion of the first ion from solution towards the inter-phase film; (3) diffusion of the first ion through the inter-phase film; (4) diffusion of the first ion inside the material phase; (5) association between the first ion and functional group; (6) dissociation of the associates between the second ion and functional group; (7) diffusion of the second ion inside the material phase towards the surface; (8) diffusion of the second ion through the interphase film; (9) diffusion and random distribution of the second ion in the solution; (10) formation of the second ion complexes in the solution.*

1.6.2.3. Mechanism of Intercalation Reactions

During intercalation two main effects take place. One is a change of preferential crystallographic parameters without destruction of the original structure and the other is the charge transfer which can affect the electronic properties of the host strongly. It is believed that the driving force for intercalation reaction comes from the tendency for charge transfer. The charge transfer takes place from the guest to the host layered compound's conduction band, thus electron-donating species can act generally as a guest. The host spans the range of electronic conductivity from insulators such as MoO_3, clays, zeolites through semiconductors such as graphite and transition metal dichalcogenides to metallic nature such as $LaNi_5$.[78,79]

Both kinetics and thermodynamics play a crucial role in the formation of these intercalated compounds. During a reaction, expansion of host lattice takes place due to nucleation of a new phase which is followed by diffusion of guest species into host lattice. Staging helps to minimize the energy required for expansion. The staging phenomenon is observed only in layered compounds. When an odd number of stages are found, it appears that in going from one stage to another an entire layer of guests should exit and re-intercalate (Figure 1.19). Lower guest concentration leads to higher stages.[80,130]

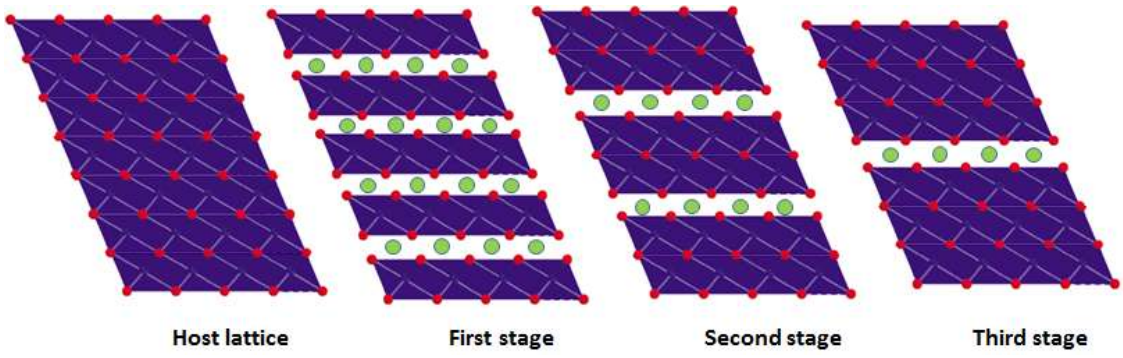

Figure 1.19. *Schematic representation of different staging in intercalation compounds. Guest molecules are green spheres.*

Clays and zeolites are common and rich cation exchangers but they suffer from low selectivity and capacity for toxic heavy metal ions in the occurrence of high salt concentrations or under acidic conditions.[120] Clay minerals have structures comprising complex layers made by condensing two types of sub-layers. In one type, silicon is tetrahedrally coordinated, $Si_2O_3(OH)_2$, and in the other aluminum is octahedral,

$Al(OH)_6$. The sub-layers are connected to produce two different structure types that are illustrated by kaolinite, which has the ideal composition $Al_2Si_2O_5(OH)_4$ and contains one octahedral and one tetrahedral layer (1:1), and pyrophyllite, $Al_2(Si_4O_{10})(OH)_2$, which has one octahedral and two tetrahedral layers (2:1) (see Figure 1.20).[131] In addition, these materials are unstable in severe alkaline or acidic conditions (due to immediate dissolution of aluminum/silicon ions) of nuclear wastes. Other oxidic sorbents, such as titanates, silicates, and manganese oxides, can survive under the conditions of nuclear waste; however, they show decreased selectivity for radioactive ions in the presence of high salt concentrations (*e.g.* Cs^+ absorption by manganese oxides), or they are selective for radioactive ions only within a narrow pH range (*e.g.* Sr^{2+} absorption by sodium titanate).[120]

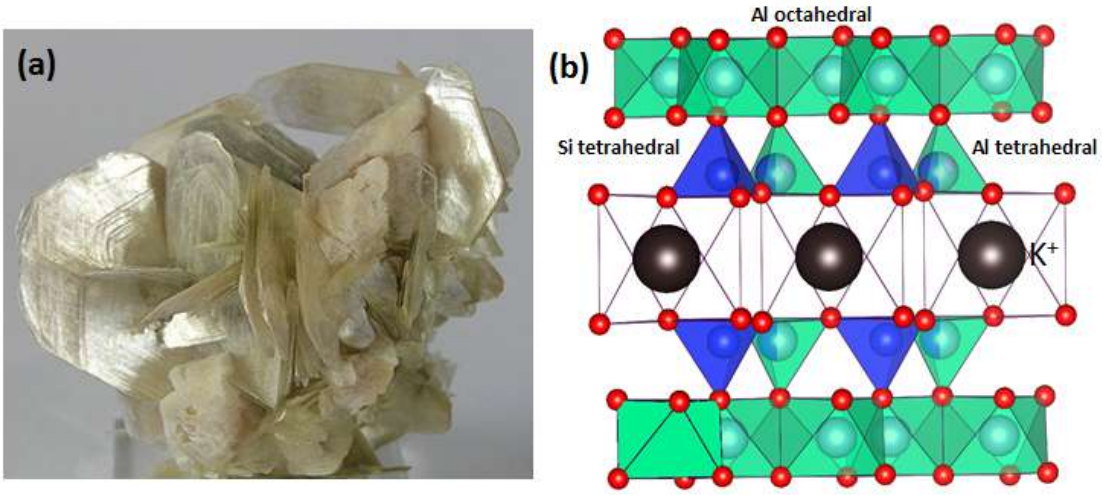

Figure 1.20. *(a) Muscovite ($KAl_2(Si_3AlO_{10})(OH)_2$) and (b) Structure of Muscovite, where red and black are oxygen and potassium. Potassium is intercalated between the layers of pyrophyllite ($Al_2(Si_4O_{10})(OH)_2$). Figure 1.20a has been taken from google images.*

Organic resins, with functional groups appropriate for the absorption of particular ions, are widely used for water decontamination. But these purely organic materials have limited chemical, radiolytic and thermal stability.[132] Although resins demonstrate an amorphous porous structure they cannot show the molecular sieve separation properties of ordered porous inorganic materials such as zeolites. Functionalized silica-based materials have shown extraordinary selectivity and binding affinity for a range of heavy metal ions. For example, thiol-functionalized mesoporous materials are renowned for their extraordinary capability to rapidly absorb Hg^{2+} from water solutions. But silica-

based materials cannot be utilized for remediation of extreme alkaline or acidic wastewater (*e.g.* nuclear waste) because of their instability under such conditions.[133]

Metal-organic frameworks (MOFs) with functional groups which have a high affinity for toxic or radioactive ions appear to be possible sorbents for various remediation processes. The advancement of these sorbents is still in its early stages.[134,135] From the above discussion, it is obvious that "perfect" sorbents that can withstand the harsh conditions of various types of wastes, are highly selective for toxic or radioactive ions, and are affordable are still mysterious. The search for new sorbent materials is therefore important.

Lately, metal sulfide ion exchangers (MSIEs) with labile extra-framework cations have become apparent as a new class of potential sorbents. These materials display a range of structures, ranging from two-dimensional layered and three-dimensional crystalline frameworks to porous materials and aerogels. These materials are growing as an effective sorbent for the purification of water contaminated with various heavy metal ions (*e.g.* Hg^{2+}, Pb^{2+}, Cd^{2+}, Ni^{2+}, and Co^{2+}) as well as ions relevant to nuclear waste (*e.g.* UO_2^{2+}, Cs^+, and Sr^{2+}).[120] The distinctive attributes of MSIEs occur from their soft S^{2-} ligands, which provide these materials with natural selectivity for soft or comparatively soft metal ions. MSIEs with a soft basic framework do not involve the insertion of any specific functional groups. They display extraordinary absorption properties for soft metal ions, exceptional to those of the best sulfur-functionalized materials. Moreover, hard ions such as H^+, Na^+, and Ca^{2+} only feebly interact with the soft S^{2-} ligands of MSIEs, thus affecting their ion exchange properties to a less significant degree than those of traditional oxidic materials. Therefore, MSIEs can be useful for metal ion absorption over a wide pH range and in the existence of high salt concentration.[120] In this section, I have discussed a few most important MSIEs in terms of their synthesis, structural characteristics, and metal ion absorption properties which will provide some directions and perspectives for future research on this new family of ion-exchangers.

1.6.2.4. Alkali-Ion Intercalated Metal Disulfides

In 1979, R. Schöllhorn *et al.* reported alkali-ion intercalated metal disulfides, specifically hydrated layered Sn sulfide phases $A_x(H_2O)_y[SnS_2]^{x-}$ (A^+=K^+, Rb^+, Cs^+)

which show facile ion-exchange properties for a series of inorganic cations, such as Li^+, Na^+, Mg^{2+}, Ca^{2+}, $Ni^{2+,}$ etc.[136,137]

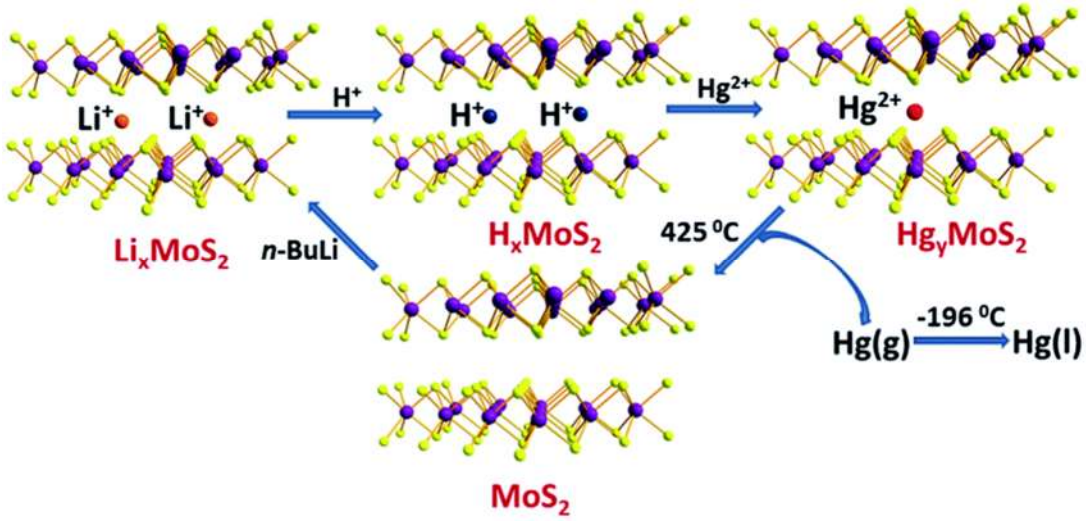

Figure 1.21. *Suggested mechanism of Hg^{2+} absorption/desorption for the Li_xMoS_2 material. Mo, purple; S, yellow. Reproduced from ref. 120 © 2016 RSC.*

In 1999, A.E. Gash *et al.* showed that $LixMoS_2$ ($0.25 \leq x \leq 1.9$) binds to $Hg^{2+,}Zn^{2+}$,Pb^{2+} and Cd^{2+} in acidic conditions in order $Hg^{2+} > Pb^{2+} > Cd^{2+} > Zn^{2+}$. The mechanism for Hg^{2+} binding is shown in Figure.1.21 where the second step is favorable due to the higher affinity of the soft basic MoS_2^{x-} for soft acid Hg^{2+} in comparison to hard hydronium ions.

1.6.2.5. KMS and LHMS Materials

$K_{2x}M_xSn_{3-x}S_6$ (KMS) compounds, reported by M. G. Kanatzidis and coworkers are derivatives of SnS_2 with partial substitution of Sn^{4+} by M^{2+} (M= Mn^{2+} or Mg^{2+}) ions.[138–143] These materials have general formula $K_{2x}M_xSn_{3-x}S_6$ (M=Mn^{2+}, KMS-1; M=Mg^{2+}, KMS-2; x=0.5-1), where interlayer spacing is filled with K^+ ions can be exchanged with radioactive Cs^+ , Sr^{2+}, Ni^{2+} and UO_2^{2+} and cations like Rb^+, Hg^{2+}, Pb^{2+}, Cd^{2+}, Ag^+, Hg^{2+} and Cu^{2+}. Figure 1.12 describes the representation of ion-exchange in KMS-1 by Rb^+ and Cs^+. When KMS-1 is treated with strongly acidic solutions, hydronium ions replace potassium ions and form layered hydrogen metal sulfide compound (LHMS-1) with general formula $H_{2x}Mn_xSn_{3-x}S_6$ (x=0.11-0.25).[141] LHMS-1 has achieved almost 100% Hg^{2+} removal under extremely acidic solutions which can be useful for removing Hg^{2+} from acid wastewater.

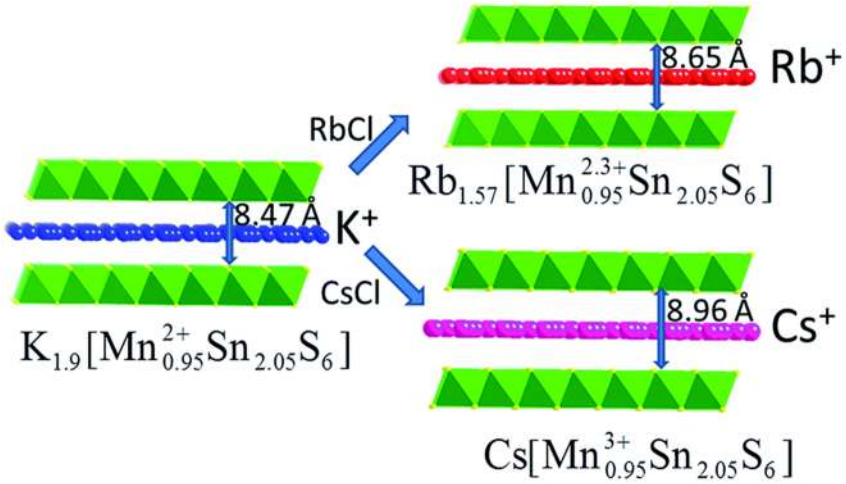

Figure 1.22. *Representations of the crystal structures of KMS-1 and its Rb^+ and Cs^+-exchanged analogs and the interlayer spacing. Reproduced from ref. 120 © 2016 RSC.*

1.6.2.6. Materials based on the $Sn_3S_7^{2-}$ net

J. B. Praise and coworkers reported the first compound based on $Sn_3S_7^{2-}$, $(TMA)_2(Sn_3S_7)*H_2O$ (TMA^+=tetramethylammonium ion).[144] Figure 1.13 shows a microporous framework consisting of edge-sharing Sn_3S_4 semi cubes connected by twelve SnS_5 trigonal bipyramids, where TMA^+ and guest water species present between the layers can be exchanged with Ag^+. Recently, FJSM-SnS, $(Me_2NH_2)_{4/3}(Me_3NH)_{2/3}Sn_3S_7*1.25H_2O$ reported by X. H. Qi *et. al.* has proven to be an effective ion-exchanger for Cs^+ and Sr^{2+}.[145]

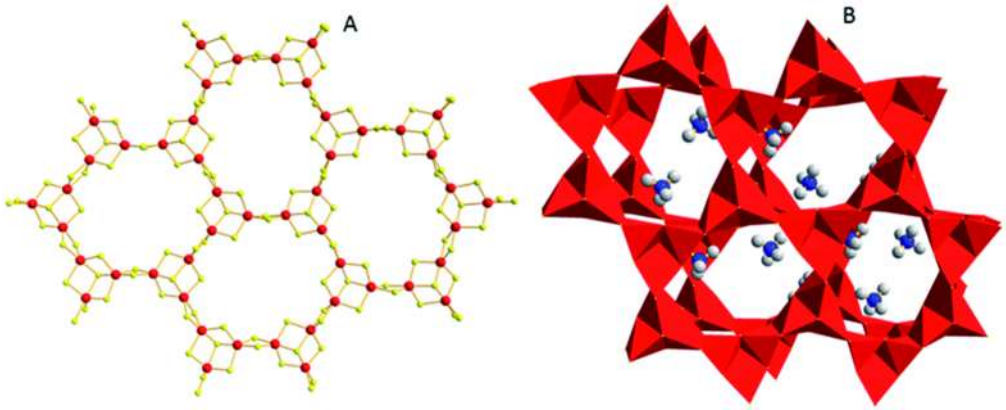

Figure 1.23. *(A) The structure of $(TMA)_2(Sn_3S_7)*H_2O$ (Sn, red; S, yellow). (B) The arrangement of two adjacent layers (with a polyhedral representation) and the TMA^+ cations (C, grey; N, blue) located in the interlayer space (guest water molecules were omitted for clarity). Reproduced from ref.120 © 2016 RSC.*

1.6.2.7. KTS materials

Tin sulfide layered material, $K_2Sn_4S_9$ (KTS-1) consists of $Sn_4S_9^{2-}$ cluster connected through S^{2-} bridges to form the layered structure perforated with large holes, and the interlayer space is filled with highly disordered cations (see Figure 1.24).[146] K^+ ion of KTS-1 has been exchanged with Cs^+ and heavy metal ions like Hg^{2+}, $Pb^{2+,}$ and Cd^{2+}. KTS-3 ($K_{2x}Sn_{4-x}S_{8-x}$) with SnS_6 octahedra are connected with SnS_4 units and the interlayer space is filled with disordered K^+ ions.[147] KTS-3 has been found as an excellent ion-exchanger for Cs^+, $Sr^{2+,}$ and UO_2^{2+}.[148]

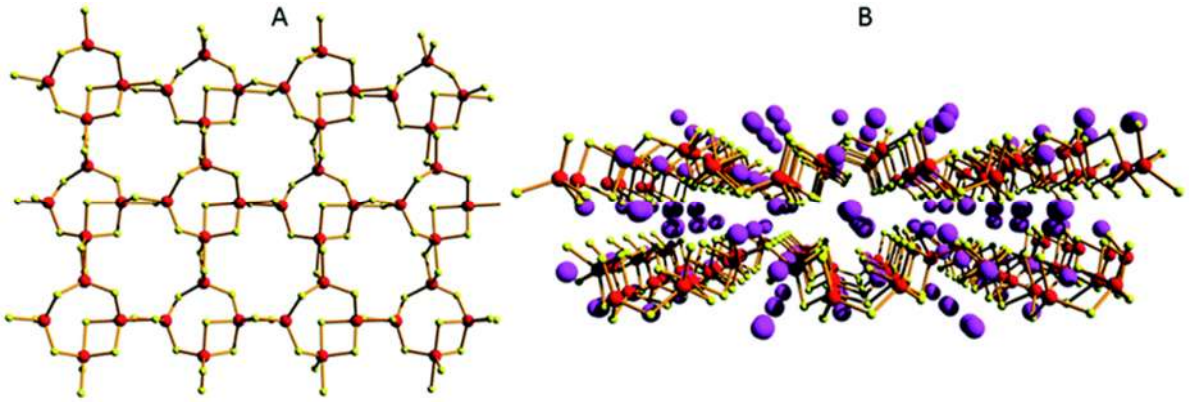

Figure 1.24. *(A) Part of the $Sn_4S_9^{2-}$ layer (Sn, red; S, yellow). (B) The arrangement of two adjacent layers with the cations (Cs^+, pink) filling the interlayer space. Reproduced from ref. 120 © RSC.*

1.6.2.8. Layered Sulfides with Trivalent Metal Ions

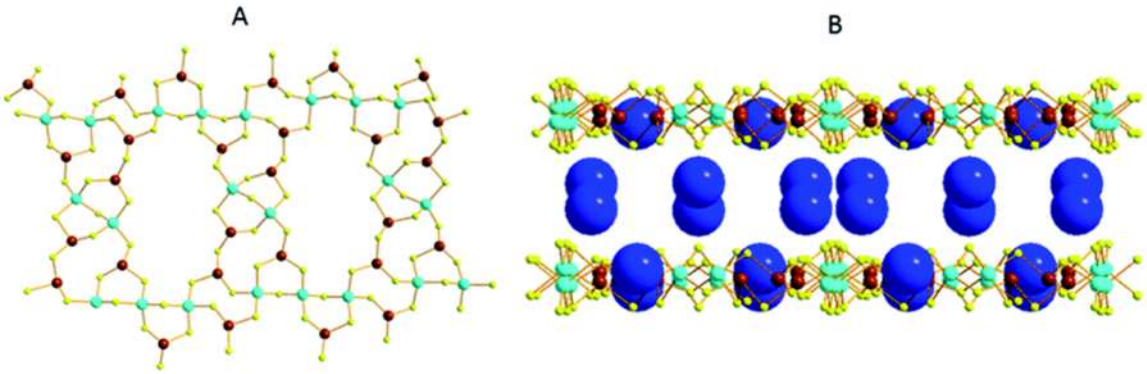

Figure 1.25 *(A) Part of the $[In_5Sb_6S_{19}]^{5-}$ layer viewed down the b-axis. (B) Packing of the layers with the N atoms of dipropylammonium cations showing as large balls (C and H atoms were omitted for clarity). In, cyan; Sb, brown; N, blue; S, yellow. Reproduced from ref.120 © 2016 RSC.*

Layered sulfide materials with trivalent ions like In^{3+} or Ga^{3+} tend to prefer tetrahedral coordination and Sb^{3+} adopts trigonal pyramidal coordination geometry. InSbS ($[(CH_3CH_2CH_2)_2NH_2]_5In_5Sb_6S_{19}*1.45H_2O$) composed of corner shared InS_4 tetrahedral, bridged by SbS_3 trigonal pyramidal units and Sb_2S_6 dimers with large holes which can accommodate organic counter ions (see figure 1.25). Facile ion-exchange for Cs^+ and Rb^+ has been explored by N. Ding and M. G. Kanatzidis.[149]

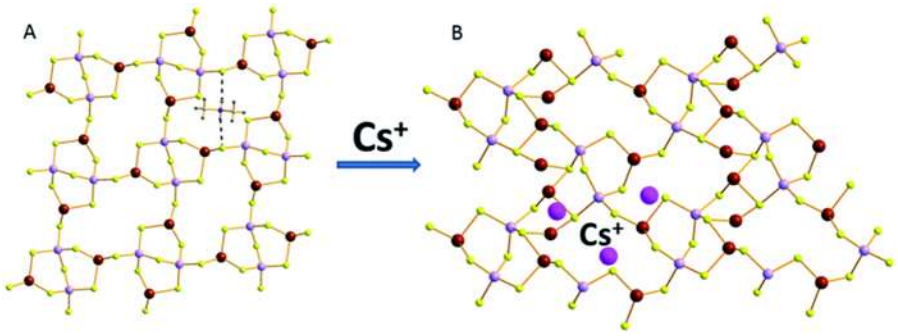

Figure 1. 26. *(A) Part of the layer of GaSbS-1. The dashed lines represent hydrogen bonding interactions between the dimethylammonium ions and the layer. (B) Part of the layer of GaSbS-2 and some of the interlayer Cs^+ ions. Ga, purple; Sb, brown; S, yellow; Cs, pink. Reproduced from ref. 120 © 2016 RSC.*

GaSbS-1 ($[CH_2NH_2]_2Ga_2Sb_2S_7*H_2O$) comprises of two corner-shared GaS_4 tetrahedra which are bridged by two SbS_3 trigonal pyramidal units forming an open window of size 11.36×4.28 $Å^2$. Dimethyl ammonium cations, present in the interlayer space by the interaction of N-H with S^{2-} via hydrogen bonding, can be exchanged with Cs^+ leading to the closing of the windows and the size changes to 11.85×3.69 $Å^2$. This mechanism is similar to insect capturing by the Venus flytrap plant. [150]

1.6.2.9. Polysulfide and MoS_4^{2-} Intercalated LDH

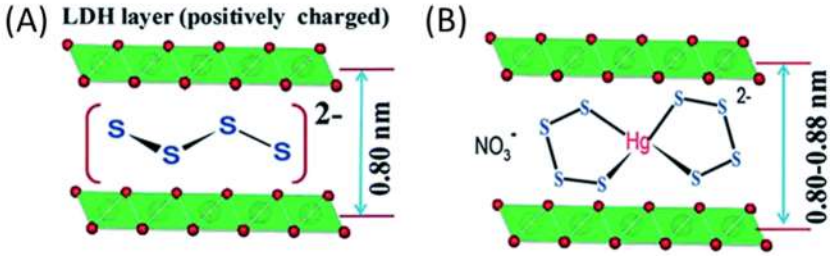

Figure 1.27 *(a) Arrangement of $[S_4]^{2-}$ groups in the interlayer space of the LDH material and (b) Proposed binding of metal ions with the polysulfide unit. Metal, green; O, red. Reproduced from ref.121 © 2016 RSC.*

Recently, S. Ma *et. al.* designed a new type of layered double hydroxides (LDHs) intercalated by polysulfide $[S_x]^{2-}$ groups (Figure 1.27a). They can be ion-exchanged with series of metal ions, such as Ni^{2+}, Co^{2+}, Cu^{2+}, Cd^{2+}, Hg^{2+}, Pb^{2+}, Zn^{2+}, $UO_2^{2+}$and Ag^+.[151–153] The mechanism of metal ion-exchange is dependent on the metal ion: LDH(S_x) molar ratio. The $[S_x]^{2-}$ groups act as a second host for the incoming ions, shown in Figure 1.27b.

Intercalated layered inorganic solids are a new class of ion-exchangers, which seem highly promising for environmental remediation applications. As the anthropogenic release of heavy metals and radioactive discharges into the environment is becoming a global epidemic, there is a need to develop efficient ion-exchange materials to remove the heavy metals and radioactive species from waste waters. Clays, layered double hydroxides, alkali-intercalated metal sulfides like Li_xMoS_2, KMS-1, KMS-2, KTS-1, protonated acid metal sulfide like LHMS-1, layered sulfides with trivalent metal ions in the framework, etc. have been studied extensively to capture heavy metals like Pb^{2+}, Cd^{2+}, Hg^{2+}, Ni^{2+}, Co^{2+} and radioactive species like Sr^{2+}, Cs^+, UO_2^{2+}.

However, these materials suffer from pH instability as they decompose in extreme pH conditions, low capacity, low distribution coefficients, inability to distinguish between other cations like Na^+, Mg^{2+}, K^+, Ca^{2+}, etc, and inability to capture heavy metals from low ppb level contamination. So, it is challenging to find a novel stable layered material that can work in a wide pH range with fast kinetics, large ion-removal capacity and is capable of selectively removing heavy metal and radioactive species from water which are present in trace (ppb) amounts.

Part 3 of my thesis is dedicated to water purification. I have focused on selective removal of heavy metals like Pb^{2+}, Hg^{2+}, and Cr^{6+} and radioactive species, Cs^+ by using potassium intercalated layered metal chalcophosphates, graphene oxide-tin sulfide composites, layered double hydroxides, etc. I have done a detailed study of adsorbents, in terms of determination of the mechanism of removal, adsorption capacity, low-ppb removal, pH stability, kinetics, competitive ion study, and design of products like tea bags, cartridge like a column for practical application for the treatment of effluent wastes.

1.7. Synthesis

The materials in this thesis are synthesized by below-mentioned methods.

1.7.1 Sealed Tube Method

When the products or reactants are susceptible to air or water or are volatile, evacuated quartz tubes are utilized. The majority of chalcogenides have been manufactured by sealed tube reactions in vacuum (10^{-3} -10^{-5} Torr) by employing high-temperature melt cooling and alkali metal polychalcogenide fluxs A_2Q_n (Q= S, Se, Te) at low temperature. Chalcogens generally have low boiling temperature and thus evacuated tube is essential to avoid boiling off and being lost from the reaction vessel. Phase diagrams are useful to understand at which temperature a particular phase is stable and how it can be synthesized via high-temperature methods.

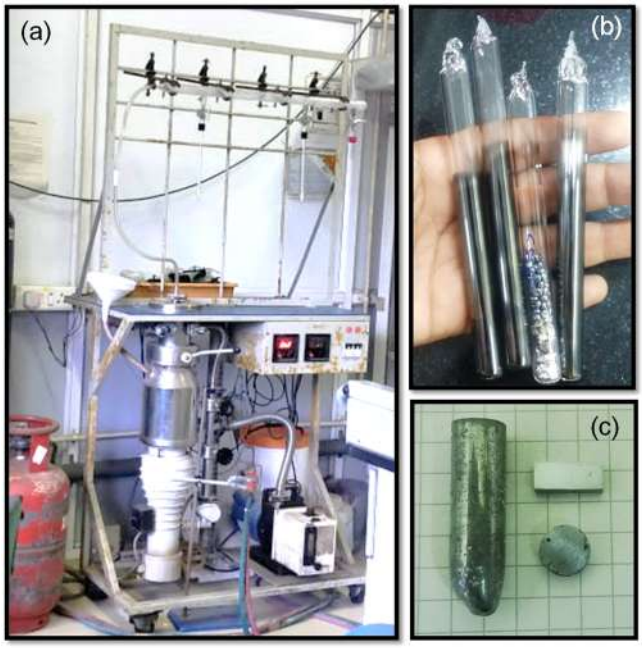

Figure 1.28. *Synthesis using the sealed-tube method: photographs showing (a) sealing-line, (b) uncoated and carbon-coated quartz sealed tubes with stochiometric amounts of elements for the synthesis of metal chalcogenides and (c) synthesized ingots cut into the bar and coin shapes for the measurement of thermoelectric properties.*

In the high-temperature method, suitable stochiometric amounts of elemental metals and chalcogens are heated above the melting point of desired compounds in vacuum-sealed tubes, followed by cooling the reaction mixture at different cooling rates

depending on the reaction conditions. Products of the reactions are thermodynamically/kinetically stable polycrystalline ingots or single crystals.

In order to prepare high performance thermoelectric materials, we have done spark plasma sintering (SPS) of the melt grown ingots in SPS-211Lx, Fuji Electronic Industrial Co., Ltd. The SPS process and geometrical configuration of the punches, mould and powder are illustrated in figure 1.29. Powders to be consolidated, are placed in a die and heated by applying the electric current. The melt grown ingots were first ground into fine powders using a mortar and pestle to reduce the grains size in an inert glove box. This powder was then pressed into cylindrical shape by SPS method (SPS-211Lx, Fuji Electronic Industrial Co., Ltd.) at specific temperature and pressure under vacuum (Figure 1.10). Highly dense (~ ≥ 98% of theoretical density) disk-shaped pellets with ~ 10 mm diameter and ~ 10 mm thickness were obtained. I have used this seal tube method to synthesize samples of $AgBiS_2$, $AgBiSe_2$, PbS, and $SnMo_6S_8$ and made pellets using SPS in **part 2** and $MnPS_3$ in **part 3** of my thesis.

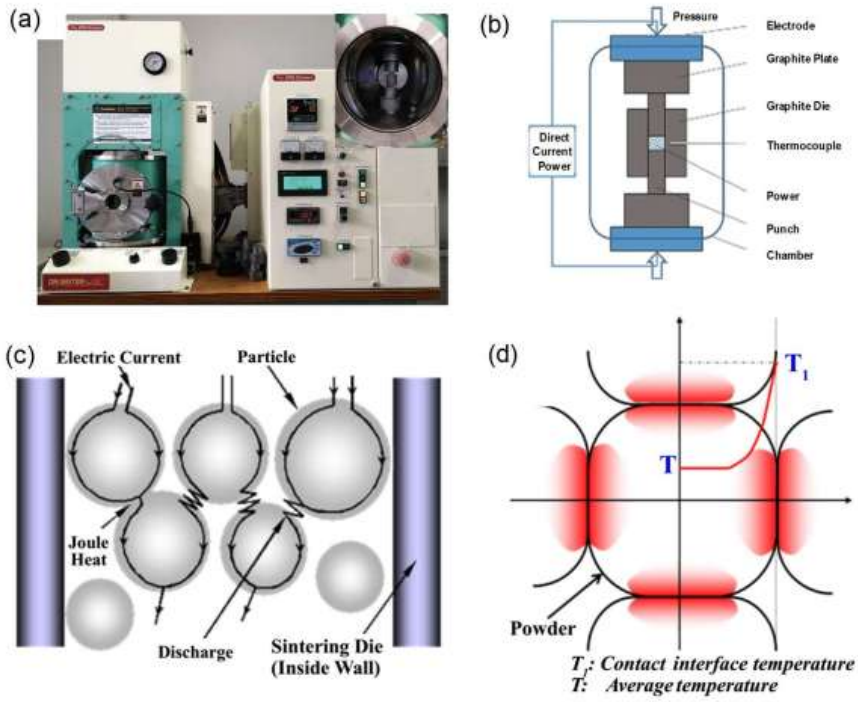

Figure 1.29. *(a) Photograph of SPS-211Lx instrument. The inset image shows sitering chamber. (b) Schematic illustration of a spark plasma sintering equipment. (c) Possible electric current path through powder particles inside the die. (d) The temperature image on powder particles surface. Contact surface temperature (T1) differs significantly from average temperature (T). Reproduced from ref. 154 © 2016 Springer.*

1.7.2 Solvothermal Method

Solvothermal as the name suggests uses solvents, heat, and capping agents to synthesize chalcogenides, composites with various morphologies. The solvothermal method involves heating the reactants and solvent in a closed vessel, called autoclave. An autoclave is usually constructed from thick stainless steel to withstand high pressures and is fitted with safety valves; it may be lined with nonreactive materials such as Teflon. The pressure generated in the vessel due to the solvent vapors elevates the boiling point of the solvent. Typically, solvothermal methods make use of various organic solvents such as ethanol, toluene, long-chain organic molecule (oleic acid, octadecene, oleylamine), and water.

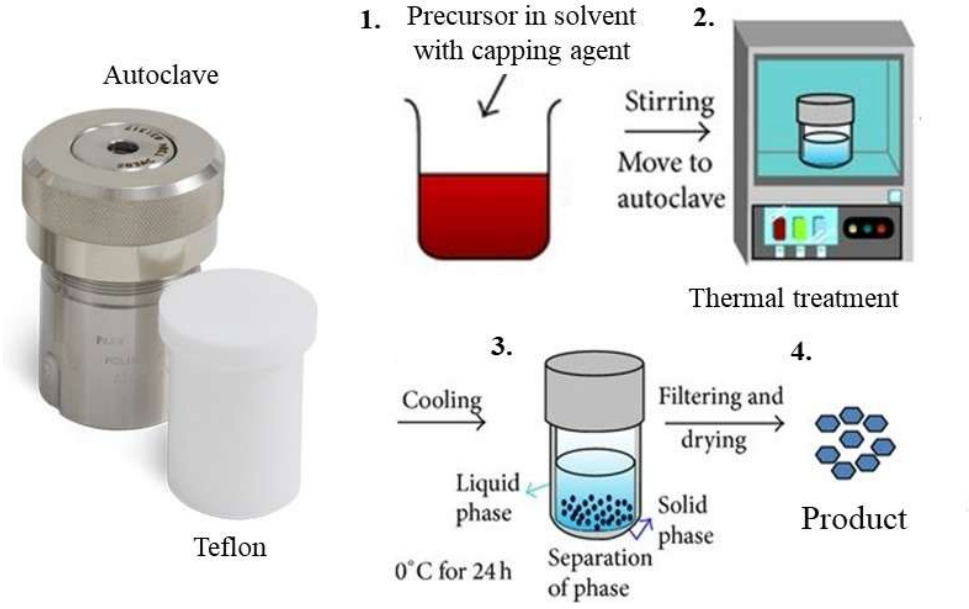

Figure 1.30. *Solvothermal synthesis technique scheme involving the use of teflon autoclave with thick stainless-steel covering.*

Capping agents can produce different morphologies. This method has been widely used to synthesize zeolites, inorganic open-framework structures, layered double hydroxides, layered materials, nanocrystals, quantum dots, and other solid materials. In the past few years, solvothermal synthesis has emerged to become the chosen method to synthesize nanocrystals of inorganic materials. By employing a metal salt, elemental Te/Se/S, and a reducing agent, it is possible to produce metal chalcogenide nanocrystals.

Control over size is possible by the slow release of sulfide or selenide ions.[154,155] Solvothermal methods can be used to make composites and functionalization of graphene-oxide, clays, etc. I have used this method to synthesize graphene oxide-tin sulfide composites in **chapter 3.2**, Co-Al layered double hydroxides in **chapter 3.3** for the removal of mercuric and chromate ions from water.

1.7.3. Schlenk Line Method.

To synthesize extremely air-sensitive compounds, Schlenk line, also known as vacuum gas manifold techniques. It comprises of a duplex of glass tubes with several ports connected side-by-side, which together is called a manifold. One manifold is connected to a source of purified inert gas (Ar, N_2), while the other is connected to a vacuum pump (Figure 1.31).

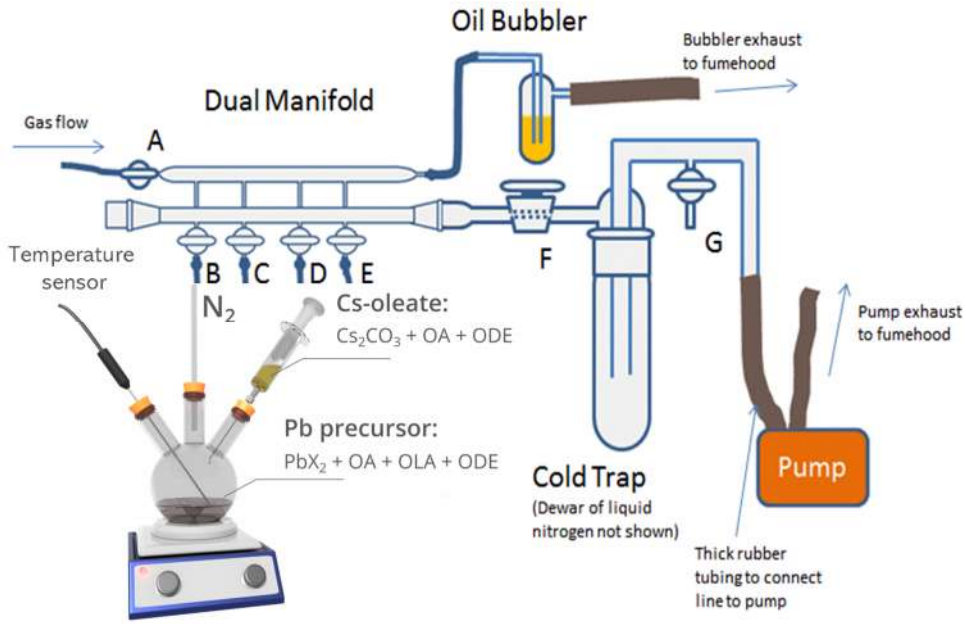

Figure 1.31. *Synthesis of $CsPbBr_3$ nano-crystals by hot-injection Schlenk line synthesis technique.*

The inert gas line is vented through an oil bubbler. Liquid nitrogen or dry-ice/acetone cold trap generally use in the connector line of the pump and manifold to prevent the contamination of the vacuum pump oil from solvent vapors and gaseous reaction products. Special stopcocks or Teflon taps allow vacuum or inert gas to be selected without the need for placing the sample on a separate line. I have used the

Schlenk line for the synthesis of $CsPbBr_3$ nanocrystals by the hot-injection method in **part 4** of my thesis.

1.8. Characterizations

Characterization refers to the broad and general process by which a material's structure and properties are probed and measured. It is a fundamental process in the field of chemistry, without which no scientific understanding of engineering materials could be established. Following characterization techniques are used in the present thesis.

1.8.1. Powder X-ray Diffraction (PXRD)

Powder X-ray diffraction is the most used technique in solid-state inorganic chemistry for analysis and evaluating phase purity to determining the structure. In this thesis, both lab source X-ray and synchrotron X-ray have been used for structural characterization. In the laboratory, X-rays are generated in a cathode tube. In this technique, a tungsten filament was heated to produce electrons and the electron beam was then accelerated towards an anode by applying a voltage (~30-40 kV). When electrons have sufficient energy to dislodge inner shell electrons of the target material, characteristic X-ray spectra are produced. These spectra consist of several components, the most common being K_α and K_β. K_α consists of $K_{\alpha1}$ and $K_{\alpha2}$. $K_{\alpha1}$ has a slightly shorter wavelength and twice intensity than $K_{\alpha2}$. The specific wavelengths are characteristic of the target material (Cu, Fe, Mo, Cr). Cu is the most common target material use for laboratory X-ray. Filtering out of K_β radiation by foils or crystal monochromators is required to produce monochromatic X-rays. For Cu radiation, a sheet of Ni foil is a very effective filter, but it is difficult to remove $K_{\alpha2}$ from $K_{\alpha1}$ because of the close wavelength. The filtering process in laboratory X-ray leads to a reduction in intensity and hence it is difficult to detect low-intensity peaks in laboratory X-ray diffraction. In addition, it is difficult to distinguish peak splitting when peaks appear closely. These limitations can be ruled out in synchrotron X-ray. Synchrotron radiation is emitted when charged particles such as electrons, traveling at relativistic speeds, are forced to change direction on passing through a magnetic field. To generate synchrotron radiation, electrons or positrons are accelerated to speeds close to that of light and circulate in ultra-high vacuum tubes or storage rings, guided by arrays of magnets. X-ray diffraction obeys

Bragg's law, which states that constructive interference would occur if the path difference between the x-rays scattered from parallel planes were an integer number of the wavelength of radiation. If the planes of atoms, separated by a distance d, make an angle θ with the incident beam, then the path difference would be $2d\sin\theta$. So, for constructive interference, the Braggs law must be satisfied

i.e., $n\lambda = 2d\sin\theta$ n = 1, 2, 3, ……

λ= wavelength of the x-ray radiation

In my thesis, room-temperature powder X-ray diffraction experiments on the samples are carried out using Bruker D8 Advance diffractometer using Cu-K_α radiation having wavelength 1.5406 Å. Powder or precipitates of the sample were placed on a glass plate sample holder during measurement. To understand the local structure in **chapter 2.2,** synchrotron X-ray scattering data for pair distribution function analysis are collected by a I15-1 instrument at the Diamond Light Source (UK) at room temperature. High-energy X-rays (λ= 0.161669 Å, 76.6 keV, bent Laue monochromator) and PerkinElmer 1611 CP3 area detector were used for data collection.

1.8.2. Transmission Electron Microscopy (TEM)

TEM is a crucial tool in material science for the characterization of the microscopic structure of materials. A TEM image represents a two-dimensional projection of a three-dimensional object. TEM operates on the same basic principles as the light microscope, however, uses electrons as a "light source" that makes it possible to get a resolution of about a thousand times better than a visible light microscope. Instead of glass lenses focusing the light in the light microscope, the TEM uses electromagnetic lenses to focus the electrons into a very thin beam. The electron beam then travels through the specimen you want to study. When the electron beam passes through an ultrathin specimen, it gets absorbed or diffracted through the specimen. Some of the electrons are scattered and disappear from the beam depending on the density of the material present in the focused region. A "shadow image" is formed by the interaction of the electrons transmitted through the specimen focused onto a fluorescent screen or a photographic film or by a sensor such as a charge-coupled device (CCD). TEM study allows to focus electron beam to any part of specimen and electron diffraction data from a different area of the specimen can give us more details about the accurate local structure of the sample. TEM samples for the solid-state materials are

prepared by conventional mechanical and tripod polishing. A large electron transparent area is obtained by subsequent Ar ion milling in the precision ion polishing system (PIPS) with an ion energy of 4.5 eV and beam angle of 7 deg. The thickness is restricted to 40-50 μm. Bright-field imaging, diffraction pattern, HRTEM imaging is carried out in aberration-corrected FEI TITAN3™ 80–300kV transmission electron microscope. This technique has been used to understand Pb_2GeS_4 nano precipitates which scatters the heat-carrying phonons in Ge doped PbS samples and lowers the thermal conductivity in **chapter 2.4**.

For nanocrystals, TEM samples were prepared by drop-casting very dilute well-dispersed sample solution (solvent: water or organic solvent: hexane, toluene, ethanol) onto a carbon-coated grid (Cu grid). The grid is dried under IR lamp to evaporate the solvent before imaging. TEM imaging was performed using JEOL (JEM3010) TEM microscope, operating at 300 kV, and FEI TECNAI G2 T20 operating at 200 kV. In **part 3** of my thesis, I have used this technique to characterize SnS_2 nanocrystals on graphene-oxide sheets in **chapter 3.2**, hollow structures of layered-double hydroxides in **chapter 3.3**. In **part 4** of my thesis, I have used this tool to characterize heterostructures in depth.

1.8.3. Field Emission Scanning Electron Microscopy (FESEM)

Like TEM microscope, FESEM microscope also uses electrons as a light source. The electrons are liberated by a field emission source. The object is scanned by electrons according to a zig-zag pattern. Within the high vacuum column, the primary electrons are finely focused to produce a narrow scan beam which then bombards on the surface of the sample. As a result, secondary electrons are emitted from the sample. By scanning the sample and collecting the secondary electrons that are emitted using a detector, an image displaying the topography of the surface is created. This technique is useful for looking at particle size, crystal morphology, magnetic domains, and surface defects. Using backscattered electrons (BSE) detection mode in FESEM it is possible to obtain compositional maps of a sample, as heavy elements (high atomic number) backscatter electrons more strongly than light elements (low atomic number), and thus appear brighter in the image. Samples for FESEM imaging has been prepared by drop-casting very dilute well-dispersed sample solution (solvent: water or organic solvent: hexane, toluene, ethanol) onto an alumina or silicon wafer. Before imaging, the sample was then

dried under IR lamp to evaporate the solvent. FESEM imaging was performed using a NOVA NANO SEM 600 (FEI) microscope operated at 15 kV. I have used this technique to understand the micro-precipitates in **chapters 2.3 and chapter 2.4**. This technique has been helpful to visualize the adsorbents of different morphology and understand what happens to adsorbents after the adsorption of heavy metal ions or radionuclides in **part** 3.

1.8.4. Energy Dispersive X-ray Analysis (EDX)

EDX is an analytical technique used for the elemental or compositional analysis of a sample. EDX makes use of the X-ray spectrum emitted by a solid sample bombarded with a focused beam of electrons to obtain the elemental analysis. For EDX analysis an X-ray detector integrated with the FESEM or TEM instrument, which detects and converts X-ray into electronic signals. Qualitative analysis involves the identification of the lines in the spectrum and quantitative for each element in the sample involves measurement of x-ray intensities. We have performed EDX analysis with EDX Genesis instrument attached to the FESEM column. The STEM-EDX technique has been used for elemental mapping. I have used this technique extensively in my thesis to understand qualitatively the adsorption of heavy metal ions.

1.8.5. X-ray Photoelectron Spectroscopy (XPS)

XPS is a surface analytical technique, which measures the elemental composition, empirical formula, chemical state, and electronic state of the elements in a material. The technique is based on Einstein's idea about the photoelectric effect. The sample analysis is conducted in an ultrahigh vacuum chamber (~10^{-10} torr) to prevent contamination of the surface and aid an accurate analysis of the sample. When an X-ray beam directs to the sample surface, the energy of the X-ray photon is absorbed completely by the core electron of an atom. The ionizing radiation is usually a monochromatic X-ray (Mg K_α, 1254 eV, or Al K_α, 1487 eV). If the photon energy, E_{photon}, is large enough, the core electron will then escape from the atom and emit out of the surface. The emitted electron with the kinetic energy of $E_{kinetic}$ is referred to as the photoelectron. The binding energy, $E_{binding}$ of the core electron is given by the Einstein relationship:

$$E_{photon} = E_{binding} + E_{kinetic} + \phi \quad (1.14)$$

$$E_{binding} = E_{photon} - (E_{kinetic} + \phi)$$

where ϕ is the work function of the spectrometer, about few eV(~ 4-5 eV). $E_{kinetic}$ is determined utilizing a high-resolution electron spectrometer. Since core electrons are close to the nucleus and have the binding energies characteristic of a certain chemical environment, XPS allows determining the atomic compositions of a sample or the chemical state of a certain element. On a modern instrument, the detection limits for most of the elements are in the parts per thousand range. However, using special condition parts per million (ppm) level detection is possible. XPS measurements were performed with a Mg-Kα (1253.6 eV) X-ray source with a relative composition detection better than 0.1% on an Omicron Nanotechnology spectrometer. Throughout my thesis, I have used this technique to understand the bonding between the metal ion and oxidation states of elements.

1.8.6. Inductively Coupled Plasma Atomic Emission Spectroscopy (ICP-AES)

ICP-AES is an analytical technique used to determine the elemental composition of a sample. An ICP-AES system is composed of two basic parts: (i) the inductively coupled plasma source and (ii) the atomic emission spectrometry detector. This technique is based on Atomic Emission Spectroscopy. First, a stable, high-temperature plasma of about 7000 - 8000K is generated by an intense electromagnetic field, created using a high-power radio frequency signal flowing in the coil. Argon gas is generally used to create the plasma. Sample introduced into the ICP should be liquid form. For solid samples, the sample should be dissolved completely in millipore water in an acidic medium (2-5%). The sample solution is introduced into the nebulizer chamber into the central channel of the plasma. The sample solution is quickly vaporized at the central channel due to very high temperatures (~8000 K). Therefore, molecule breaks up into individual elements as free atoms. The collisional excitation within the plasma imparts additional energy to the atoms, promoting them to excited states. In addition, sufficient energy is often available to convert the atoms to ions and subsequently promote the ions to excited states. Both the atomic and ionic excited state species may then relax to the ground state via the emission of a photon. Every element has its characteristics emission spectrum and hence 36 Introduction to a thermoelectrics element type is determined based on the wavelength of the photons. The concentration of each element is determined based on the intensity of photons. In this thesis, we have used Perkin Elmer

optima 7000 DV ICP-OES machine to determine the elemental concentration in our samples. Samples were dissolved in 2-5% (V/V) aqua regia (HNO_3: HCl = 1: 3)/ water solution, and different elemental concentrations were measured against high purity is known standards. I have used this technique extensively in **part-3** of my thesis to measure the initial and final concentrations of the metal ions in the parts per million (ppm) range.

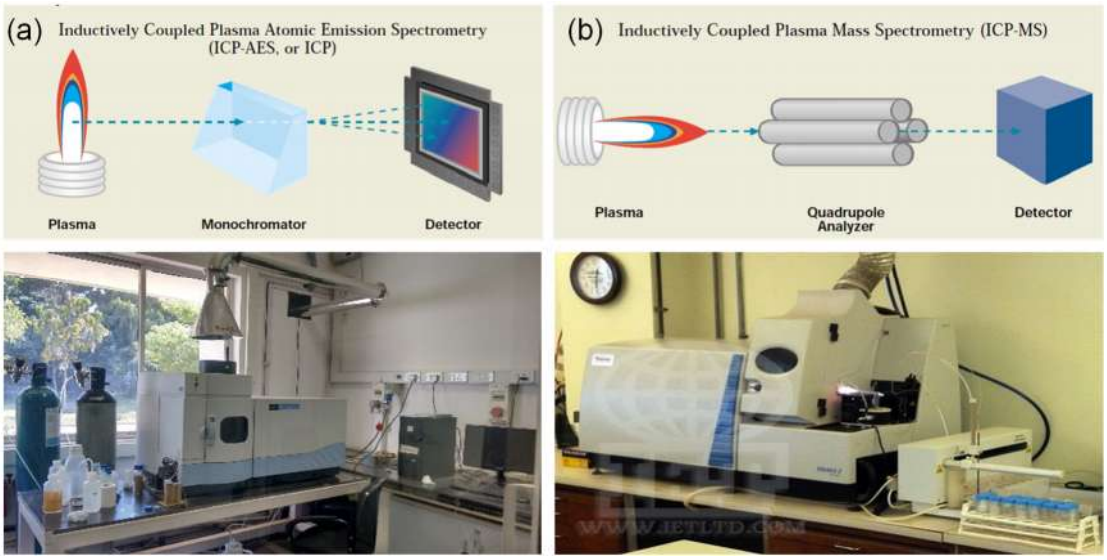

Figure 1.32. *Schematic representation and photograph of (a) ICP-AES and (b) ICP-MS.*

1.8.7 Inductively Coupled Plasma Mass Spectroscopy (ICP-MS)

Inductively coupled plasma mass spectrometry (ICP-MS) is a type of mass spectrometry that uses inductively coupled plasma to ionize the sample. It atomizes the sample and creates atomic and small polyatomic ions, which are then detected. It is known and used for its ability to detect metals and several non-metals in liquid samples at very low concentrations. It can detect different isotopes of the same element, which makes it a versatile tool in Isotopic labeling. Compared to atomic absorption spectroscopy, ICP-MS has greater speed, precision, and sensitivity. The ions from the plasma are extracted through a series of cones into a mass spectrometer, usually a quadrupole. The ions are separated on the basis of their mass-to-charge ratio and a detector receives an ion signal proportional to the concentration. The concentration of a sample can be determined through calibration with certified reference material such

as single or multi-element reference standards. ICP-MS also lends itself to quantitative determinations through isotope dilution, a single-point method based on an isotopically enriched standard. This technique has been used to measure the concentration of metal ion at parts per billion (ppb) level. ICP-MS have been helpful to understand the low ppb removal of heavy metal ions by adsorbents and is discussed in **part 3** of my thesis. ICP-MS studies have been helpful to show the novelty of designed adsorbents to capture heavy metal ions from ppb level.

1.8.8. Optical Band Gap

In my thesis, the diffuse reflectance method has been used for the determination of the band gap of the solid powder material. Diffuse reflectance is an excellent sampling tool for powdered or crystalline materials. When radiation is directed onto the surface of a solid sample, two types of reflection can occur specular reflection and diffuse reflection. The specular component is the radiation that reflects directly off the sample surface according to the normal reflection law; angle of reflection equals the angle of incidence. Diffuse reflection is the radiation that penetrates into the sample and then emerges at all angles after suffering multiple reflections and refractions by the sample particles. A diffuse reflection accessory is designed so the diffusely reflected energy is optimized, and the specular component is minimized. The optical system collects the scattered radiation and directs it to the detector. In 1931, Kubelka and Munk derived a theory of diffuse reflection and the function is given by:

$$f(R) = \frac{(1-R)^2}{2R} = \frac{\alpha}{\Lambda} \qquad \text{Eq. 1.2.}$$

where R is the absolute reflectance of the sample, α and Λ are the absorption and scattering coefficients. The Kubelka-Munk theory predicts a linear relationship between spectral intensity and sample concentration under conditions of constant scattering coefficient and infinite sample dilution. Therefore, the sample must be ground uniformly fine size and sample thickness should be low (~3 mm) if quantitatively valid measurements are desired. Using diffuse reflection spectroscopy, samples can be analyzed either directly or as dispersions in nonabsorbing matrices (e.g. alkali halides such as KBr) for qualitative analysis. It eliminates the time-consuming process of pressing pellets for transmission measurements. Apart from this, it has several other advantages:

(i) Very high sensitivity (ppm levels)

(ii) Ability to analyze most non-reflective materials

(iii) Ability to analyze irregular surfaces or coatings.

In my thesis, to probe the optical energy gap of the synthesized compounds, diffuse reflectance measurements were performed on finely ground powders at room temperature. The spectra were recorded using a Perkin-Elmer Lambda 900, UV/Vis/NIR spectrometer.

1.8.9. Thermogravimetric Analysis (TGA)

TGA analysis is a method in which the mass of a sample is measured over time with changes in temperature in a specified trend. This measurement provides information about physical phenomena such as mass changes, temperature stability, oxidation/reduction behavior, decomposition, corrosion studies, and compositional analysis. It is suitable for use with all types of solid materials, including organic or inorganic materials. TGA is the act of heating a mixture to a high enough temperature so that one of the components decomposes into a gas, which dissociates into the air. If the compounds in the mixture that remain are known, then the percentage by mass can be determined by taking the weight of what is left in the mixture and dividing it by the initial mass. Knowing the mass of the original mixture and the total mass of impurities liberated upon heating, the stoichiometric ratio can be used to calculate the percent mass of the substance in a sample.

In my thesis, TGA was performed using a TGA/DSC 2STAR instrument in the temperature range of 300–900 K under nitrogen atmosphere with a ramp rate of 5 K min^{-1}. I have used TGA to calculate the amount of water present in different adsorbents, calculate the molecular formula of adsorbents used and understand the mechanism of adsorption in **part 3** of my thesis.

1.8.10. Differential Scanning Calorimetry (DSC)

DSC is a thermo-analytical technique in which the difference in the amount of heat released or absorbed by a sample is compared with that of inert reference material during a programmed change of temperature. The sample and reference are maintained at the same temperature during heating and temperature are monitored with a thermocouple. The temperatures of the sample and reference remain the same until some thermal event, such as melting, decomposition or change in the crystal structure, occurs, in which case the sample temperature either lags behind (if the change is endothermic) or leads (if the change is exothermic) the reference temperature. The extra heat input

to the sample (or to the reference if the sample undergoes an exothermic change) required to maintain this balance is measured and thus change in enthalpy measured directly.

We have performed DSC measurement using a NETZSCH DSC 200F3 instrument with a heating/cooling rate of 20 K/ min in N_2 atmosphere. The temperature ranges for the measurement have been given in the relevant chapters in **part 2** of my thesis.

1.8.11. Raman Spectroscopy

Raman spectroscopy is a spectroscopic technique for the structural characterization of inorganic or organic samples. This technique is based on the inelastic scattering of monochromatic light. A change in the molecular polarizability with respect to the vibrational coordinate corresponding to the rovibronic state is required for a molecule to exhibit a Raman effect. Normally a laser source such as Nd: YAG with a fixed wavelength of 532 nm, an argon ion laser at 514 nm or a He–Ne laser at 633 nm a laser use for the light source. During the irradiation process, the photons of the laser light interact with molecular vibrations, phonons or other excitations in the system and the molecule is promoted to a much higher energy state. This results in the molecule being in a so-called virtual energy state for a short period of time and then relax back, giving either Rayleigh scatter with exactly the same energy and wavelength as the incident light (the molecule returns to its initial vibrational state). A very small amount of the scattered light (~10-6 times the incident light intensity) is shifted in energy either lower (Stokes) or higher (anti-Stokes) energy than the incident photon due to interactions between the incident electromagnetic waves and the vibrational energy levels of the molecules. In Raman scattering, Stokes lines are more intense than anti-Stokes because only molecules that are vibrationally excited before irradiation can give anti-Stokes line. Therefore, in Raman spectroscopy, only Stokes line is normally measured. Raman spectra are plotted with respect to the frequency of light such that the Rayleigh band (frequency of laser) lies at 0 cm^{-1}. Plotting the intensity of this "shifted" light versus frequency results in a Raman spectrum of the sample.

In **part 3** of my thesis, room temperature Raman spectroscopic measurement were carried out on powered samples with HORIBA LABRAM HR800 spectrometer. The excitation wavelength of the laser was 514 nm. Temperature-dependent micro-

Raman measurements in **part 2** of my thesis were performed using Horiba Jobin-Yvon LabRAM HR evolution Raman spectrometer in backscattering geometry with solid-state laser excitation ~ 785 nm, 1800 gr/mm grating and Peltier cooled CCD detector. Temperature-dependent Raman study was performed using Montana cryostat in the range of 3 - 300 K under collaboration with Prof. Ajay Soni, IIT Mandi, India. The results have been discussed in **chapter 2.5** of my thesis.

1.8.12.Hall Effect

Measurement of the Hall effect gives an important source of information about the conduction type, especially in semiconductors. From conductivity measurement, it is not possible to separate the number of current carriers, n, from their mobility, μ. Combined hall and conductivity measurement enable the separation of n and μ. If a current of I amperes flows through a solid in one direction and a magnetic field B oersteds are applied at a right angle to the direction of current flow, a potential difference is developed across the sample in the direction perpendicular to B and I. This is because the magnetic field causes the electrons to follow curved paths and therefore one side of the material becomes depleted in electrons compare to the other side. The unequal electron concentration across the sample causes an electric field to build by until an equilibrium situation is reached where the tendency for electrons to deflect is balanced by the Hall potential acting in the opposite direction. Hall coefficient (R_H), charge carrier density (n), and carrier mobility (μ) for a material can be calculated using the following equations:

$$\rho_H = \frac{R \times L \times T}{W} \qquad \text{Eq. 1.3.}$$

$$R_H = \frac{R \times T}{B} \times 10^8 cm^3\, C^{-1} \qquad \text{Eq. 1.4.}$$

$$n = \frac{1}{R_H \times e} cm^{-3} \qquad \text{Eq. 1.5.}$$

$$\mu = \frac{\sigma}{n \times e} \qquad \text{Eq. 1.6.}$$

ρ_H is the measured Hall resistivity [Ω*m]; R is the Hall resistance (Ω); L, W, T are the dimensions of the sample (cm), respectively. n is the charge carrier density (cm^{-3}); e = 1.6×10^{-19} C, σ and μ are the conductivity and carrier mobility.

In my thesis hall measurement has been done in using an ECOPIA HMS 3000 system and also using PPMS (Physical Property Measurement System, Quantum Design, USA) with a variable magnetic field up to 5 Tesla. I have used custom-built equipment developed by Excel Instruments where up to a magnetic field of 0.57 T and 50mA dc-current is used.

1.9. Thermoelectric Measurements

In **part 2** of my thesis, I have done thermoelectric measurements extensively and the details of electronic and thermal transport measurements are discussed below.

1.9.1. Electronic Transport

The power factor of the zT expression depends on the product of the Seebeck coefficient and the electrical conductivity. The Seebeck coefficient is the ratio of a resulting electric field gradient to an applied temperature gradient. In a typical measurement, the temperature is varied around a constant average temperature and the slope of the voltage (V) vs. temperature difference (ΔT) curve gives the Seebeck coefficient (the slope method) or just V/ΔT is measured (single point measurement). Either a specific temperature difference is stabilized before each measurement (steady-state), which takes longer, or measurements are conducted continuously while the temperature difference is varied slowly (quasi-steady-state). Little difference was found between steady-state and quasi-steady-state measurements when good thermal and electrical contact is ensured. The employed temperature difference should be kept small, but too small will lead to decreased accuracy. Usually, 4-20 K (or 2-10 K) is appropriate for the full temperature span. In the present thesis, temperature-dependent Seebeck coefficient measurement has been done using the most popular commercial instruments ULVAC ZEM 3 RIKO using off-axis 4-point geometry under low-pressure helium (He) atmosphere (Figure 1.33(a)). In the off-axis, 4-point geometry, the thermocouples, and voltage leads are pressed against the sides of the sample (Figure 1.33(b)). The instrument uses the slope method to extract the Seebeck coefficient from steady-state measurements. In the slope method, the measured raw data is corrected for constant

offset voltages by using the slope of several (ΔT, V) points for extracting the Seebeck coefficient. The typical sample for measurement has a rectangular shape with the dimensions of 2 mm × 2 mm × 8 mm and ΔT values 5, 10, 15 K have been used in the measurement. The error in the measurement is ~5%. In a typical measurement, the sample is set in a vertical position between the upper and lower electrode blocks in the heating furnace. For temperature-dependent measurement, the sample was first heated to a specified temperature using an infrared (IR) furnace. Thereafter a temperature gradient across the sample was created by heating the lower part of it with a heater. Seebeck coefficient is measured by measuring the upper and lower temperatures T1 and T2 with the thermocouples pressed against the side of the sample, followed by measurement of voltage (ΔV) between the same wires on one side of the thermocouple.

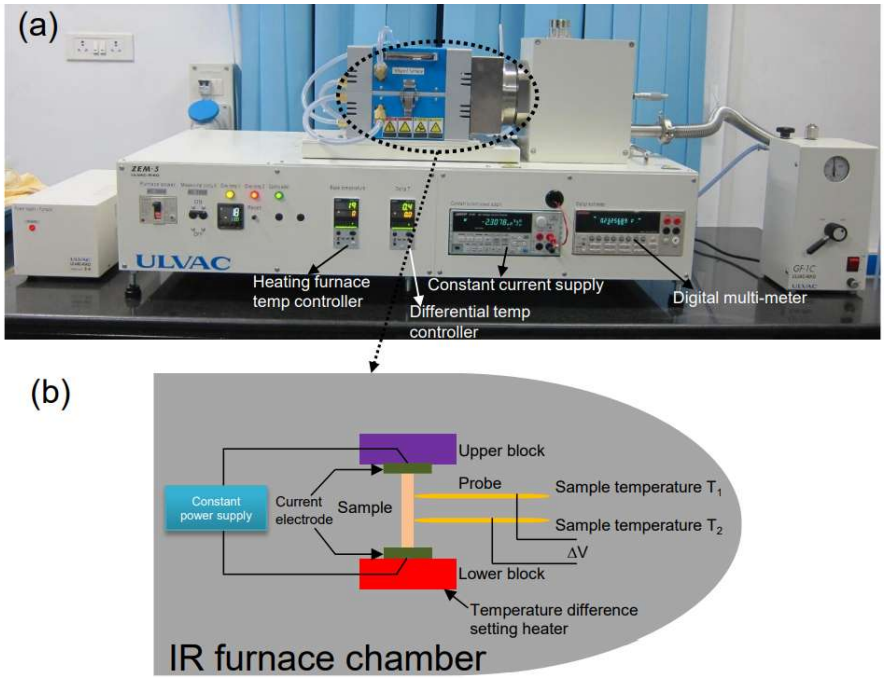

Figure 1.33. *(a) Photograph of ULVAC ZEM 3 RIKO instrument (b) Schematic representation of sample chamber in ULVAC ZEM 3 RIKO.*

The electrical conductivity, σ is measured using the four-probe method. Temperature-dependent σ has been measured concurrently during Seebeck measurement in ULVAC ZEM 3 RIKO. For the measurement, a constant current I is applied to both ends of the sample to measure the voltage V between the thermocouple. By knowing

the resistance of the sample, R (R = V/I), we can calculate σ from resistivity (ρ) of the sample using the following equation:

$$\rho = R \times \frac{A}{l}$$

$$\sigma = \frac{1}{\rho}$$

where A is the sample cross-section and l is the distance between probes.

1.9.2. Thermal Transport

The flash diffusivity method most frequently is used for the determination of thermal conductivity (κtotal) of material. Non-contact, non-destructive, easy sample preparation, applicability for a wide range of diffusivity values with excellent accuracy and reproducibility make this method more advantageous than the direct method.

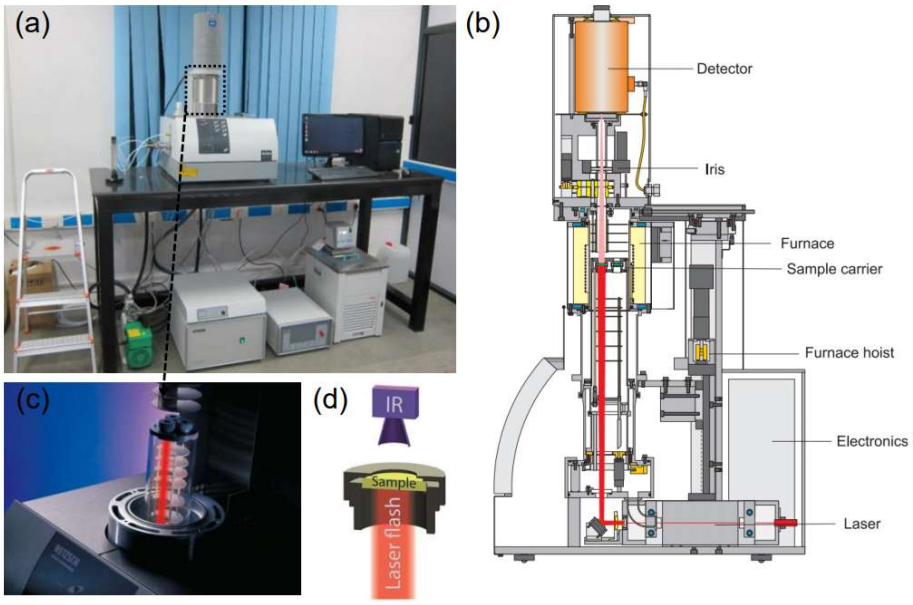

Figure 1. 34. *(a) Photograph of NETZSCH LFA-457 instrument. In (b) diffident component of the instrument. (c) and (d) show schematic of a short laser pulse is applied to the bottom of a sample (shown in a sample holder) and the resulting temperature rise on the top is monitored with an IR detector.*

In the flash diffusivity method, the thermal conductivity is calculated as $\kappa_{total} = DC_p\rho$, where D is thermal diffusivity, ρ is density, and C_p is the constant pressure heat capacity. In this method, the sample is mounted on a carrier system, which is located in a furnace. After the sample reaches a predetermined temperature, a short heat pulse from a pulsed laser is applied to one side of a thin sample, resulting inhomogeneous heating. The relative temperature increase on the rear face of the sample is then measured as a function of time by an IR detector. The temperature will rise to a maximum, after which it will decay. The time for the temperature to increase to half-maximum, $t_{1/2}$, is used to calculate the thermal diffusivity using equation

$$D = 0.1388 \times \frac{l^2}{t_{1/2}}$$

where D is thermal diffusivity in cm^2/sec, l is the thickness.

In **part 2** of my thesis, temperature-dependent thermal transport measurement has been done using the most popular NETZSCH LFA-457 instrument in N_2 atmosphere (Figure 1.34(a)). Coins with ~8 mm diameter and ~2 mm thickness were used for all the measurements. The samples were coated with a thin layer of graphite (~5 μm) in order to enhance the absorption of laser energy and emission of IR radiation to the detector. It also increases the signal-to-noise ratio. The error for the κtotal measurement is ~5%. The samples were placed inside SiC sample holder to mount on the carrier system (Figure 1.18(c)). A Nd-Glass pulsed laser source of wavelength 1054 nm has been used for all the measurements. To measure the increased temperature on the rear face of the sample a liquid N_2 cooled InSb IR detector has been used. The density (ρ) was determined using the dimensions and mass of the sample and Cp, was derived indirectly using a standard sample (pyroceram). The thermal diffusivity data were analyzed using a Cowan model with pulse correction to account for heat losses on the sample faces.

1.10. Inelastic Neutron Scattering (INS)

Inelastic neutron scattering is an experimental technique commonly used in condensed matter research to study atomic and molecular motion as well as magnetic and crystal field excitations. It distinguishes itself from other neutron scattering techniques by resolving the change in kinetic energy that occurs when the collision between neutrons and the sample is an inelastic one. The inelastic scattering of neutrons, as the name of the technique implies, involves processes in which neutrons incident on

a sample experience an exchange of energy with the matter, resulting in a shift in energy/wavelength of the exiting neutrons relative to the incident ones. Ruminating on the origin of energy exchanges between neutrons and matter, one realizes that the collisions between neutrons and atomic nuclei can lead to atomic motion within material lattices and if certain quantized lattice vibrations (phonons) are resonantly excited, then energy will be transferred from the neutrons to the matter. By detecting the energy shifts of the scattered neutrons, then, much knowledge can be acquired about the fundamental atomic and molecular motions taking place in various materials.[156]

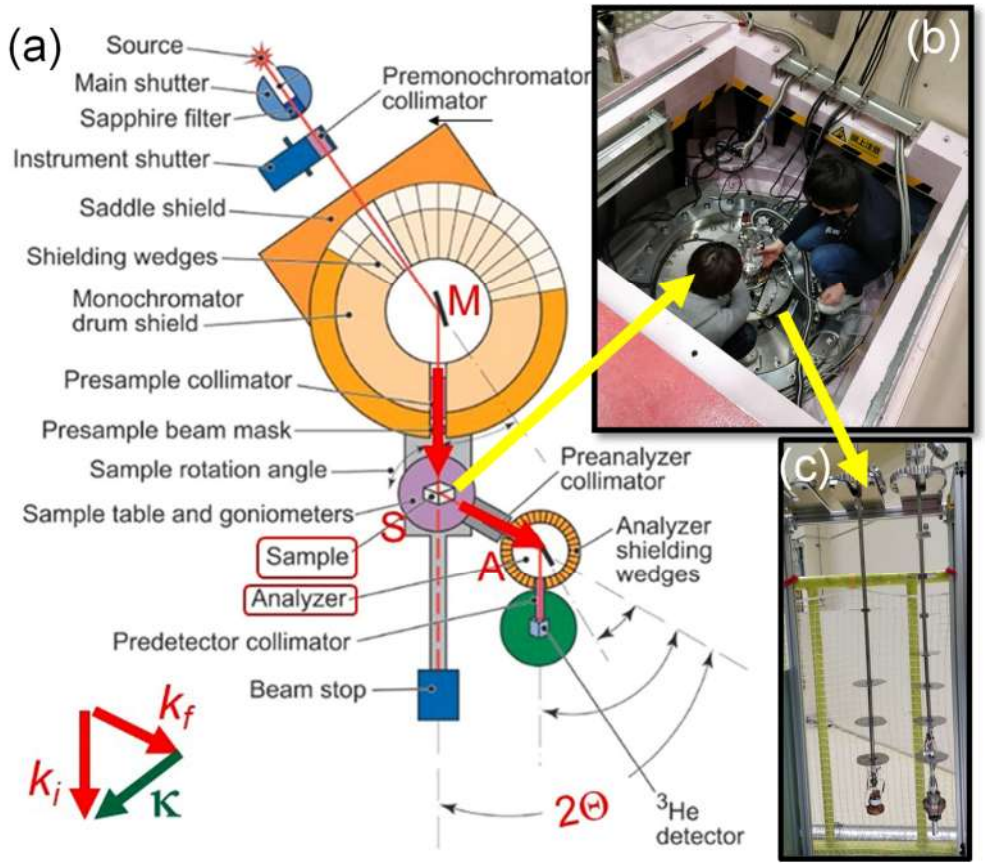

Figure 1.35. *(a) Experimental setup for inelastic neutron scattering, (b) sample chamber and (c) sample holders for the experiments done at BL-14, AMATERAS, Japan. (a) is reproduced from ref. 156. © 2018 M & C Publishers.*

In my PhD work, I have collaborated with Prof. Kenji Nakajima, J-PARC, Japan to understand low thermal conductivity in Ge doped PbS samples using inelastic neutron

scattering experiments and the results are discussed in **chapter 2.4**. I have calculated temperature-dependent experimental DOS by analyzing the obtained temperature-dependent INS data. Cold neutron disc chopper spectrometer BL14 AMATERAS at the J-PARC in Japan, has been used to perform multi-E_i time-of-flight INS measurements. E_i of 42.00 and 15.2 meV were selected. Powder samples of $Pb_{0.90}Ge_{0.10}S$ were encased in a thin-walled aluminum cylinder with a diameter of 14 mm. $Pb_{0.90}Ge_{0.10}S$ data were collected at 8-600 K and a top-loading cryofurnace was used to control temperatures. The data reduction and visualization were accomplished using UTSUSEMI version 0.3.7.

The neutron-weighted general density of state (GDOS) was calculated by using the integration results of

$$G(Q,E) = S(Q,E)\left[1 - e^{\frac{-E}{\kappa_B T}}\right]E$$

where $\left[1 - e^{\frac{-E}{\kappa_B T}}\right]$ =<n>+1 describes the Bose population factor and G(E) $\propto$ S(E)*E/(<n>+1) for E>0. The integration Q region was 3.2–5.2 $Å^{-1}$ for E = 42.0 meV and 1.8-3.2 $Å^{-1}$ for E = 15.2 meV. The peak broadening or change in full width at half maximum (FWHM) was calculated as, FWHM(T)-FWHM(8K). The peak positions and the line width of acoustic phonons were calculated by the Gaussian fitting using fityk and the data was plotted using OriginPro 8.5. To get the scattering rate from the fitted data, the 8 K data was used as a standard to observe the change in parameters with the temperature change. The phonon scattering was then obtained by adding Gaussian widths in quadrature, $\sigma_{scat} = \sqrt{\sigma_T^2 - \sigma_{8K}^2}$, where σ_{8K} is the width at base temperature 8 K, σ_T is the width at the higher temperature.[157] We calculated phonon lifetime from the extracted width using, $\tau^{-1} = 2.355\pi\sigma_{scat}$, where τ is an inverse lifetime.

1.11. Scope of the Thesis

Metal chalcogenides/chalcophosphates/ halides present an important platform for exploring various intriguing properties. This Ph.D. thesis presents the design and synthesis of various metal chalcogenides, layered chalcophosphates/ halides for their application in thermoelectric energy conversion, water purification, and fundamental understanding of the charge transfer mechanism in the all-inorganic halide perovskite heterostructures. Apart from the present introductory part (**Part 1**), my thesis work is divided into four parts (2- 4), containing one, five, four, and two chapters respectively.

Part 2 of my thesis is directed towards high-performance thermoelectric energy conversion. With the apparent burgeoning energy crisis, alternative sources of energy are in greater need of a sustainable future. Thermoelectrics which can convert waste heat arising from industries, power plants, and automobiles into a usable form, electricity; have the potential to be a game-changer in this critical energy shortage. In **Part 2** of my thesis, I have discussed energy conversion and is focused on the design and synthesis of metal chalcogenides for high-performance thermoelectric energy conversion. It is divided into five chapters. In **chapter 2.1**, I have discussed the influence of the periodic table in designing solid-state metal chalcogenides for thermoelectric energy conversion. **Chapter 2.2** focuses on stabilizing cubic $AgBiS_2$ at room temperature and understanding the origin of ultralow thermal conductivity in n-type cubic $AgBiS_2$ caused by the soft vibrations and local structure distortion in [011] direction induced by the Bi $6s^2$ lone pair. In **chapter 2.3**, I have enhanced the electrical transport properties in Bi excess samples of $AgBiSe_2$ by modulation doping using microstructures of topological semi-metal Bi_4Se_3 which injects the charge carriers to the precipitates of Bi_4Se_3 from the AgBiSe2 matrix and results in a large improvement of carrier mobility. In **chapter 2.4** I have reported the highest zT of 1.45 in low-cost and earth-abundant element-based lead sulfide, PbS thermoelectric material, an alternative to champion lead chalcogenides, PbTe, and PbSe. Ge doping in PbS synergistically brings out extremely low lattice thermal conductivity (κ_L) in PbS via endotoxic nano precipitates of Pb_2GeS_4 which scatter heat-carrying phonon and the electrical conductivity increases due to enhanced covalency in chemical bonding. In **chapter 2.5**, I have reported the synthesis of superconductive Chevrel phase compound $SnMo_6S_8$ and discussed the origin of ultra-low thermal conductivity arising from tin rattler atoms.

Part 3 of my thesis is related to the environment and is focused on water purification using layered materials. Clean and fresh water is pivotal to the existence of life. However, the world's supply of fresh water is dwindling and the contaminant levels are increasing rapidly. In **chapter 3.1**, I have captured toxic lead (II) from water, efficiently and selectively from ppb level using layered metal chalcophosphate, $K_{0.48}Mn_{0.76}PS_3$. H_2O (K-MPS-1). This material is stable in 2-12 pH and can remove lead even from 1 ppb level. In **chapter 3.2**, I have studied the selective and ppb level removal of toxic mercury (II) from water using the composite of high surface area graphene oxide

and tin sulfide which induces selectivity towards Hg(II) adsorption. The material is stable in pH 0.5-11 and can remove Hg(II) even from 0.3 ppb level. I have designed a prototype tea bag with the composite which can remove 99.9 % Hg(II) from water. In **chapter 3.3**, I have synthesized nature-inspired coral-like morphology of CoAl-Layered Double Hydroxide and used it to remove hexavalent chromium (VI) from the water up to 4.5 ppb level in a broad pH range of 1.93-12.22. Interestingly, it can be regenerated and recycled. With these great properties, I have designed a low-cost column for the treatment of effluent discharge, with 1 weight % of material and 99 weight % sand and removed ~99% Cr(VI). In **chapter 3.4**, I have discussed the removal of radionuclide Cesium from water by the ion-exchange process using K-MPS-1. Ion-exchange of Cs(I) is reversible, shows fast kinetics and removal occurs in ppb level. In summary, this part of the thesis has described the removal of heavy metal ions, Pb(II), Hg(II), Cr(VI), and radionuclides of Cs(I) using layered materials.

Part 4 of my thesis is directed towards the synthesis of heterostructures and understanding the charge-transfer mechanism. All-inorganic halide perovskites have created a sensation in diverse optoelectronic applications like photovoltaics, photodetectors, light-emitting diodes, and lasers and we have seen phenomenal growth in research efforts to understand the photodynamics, luminescent properties, and stabilization of different phases of perovskites. Heterostructures of inorganic halide perovskites with mixed-dimensional inorganic nanomaterials have shown great potential not only in the field of optoelectronic energy devices and photocatalysis but also for improving our fundamental understanding of the charge transfer across the heterostructure interface. In **part 4**, I have designed heterostructures of $CsPbBr_3$ and studied the optical properties of the heterostructures. **Chapter 4.1** focuses on studying the charge transfer, the driving force for synthesis, photoluminescence quenching, and photo-conductivity in the heterostructure of $CsPbBr_3$ nanocrystals with nitrogen-doped carbon dots. In **chapter 4.2**, I have synthesized the heterostructure of $CsPbBr_3$ nanocrystals with few layers of layered metal oxy-chalcogenide, Bi_2O_2Se, and studied the photoluminescence quenching mechanism.

To summarize, my thesis is directed towards high-performance thermoelectric energy conversion (**Part 2**), water purification (**Part-3**) and designing new heterostructures (**Part 4**). My thesis addresses the current important challenges in the

world and has societal importance. I have employed different synthesis routes to synthesize important metal chalcogenides, metal chalcophosphates, various layered materials, and halide perovskites heterostructures and examined their properties.

1.12. References

[1] M. M. Khin, A. S. Nair, V. J. Babu, R. Murugan, S. Ramakrishna, *Energy Environ. Sci.* **2012**, *5*, 8075–8109.

[2] F. Jellinek, *React. Solids* **1988**, *5*, 323–339.

[3] H. Lin, L. Chen, L.-J. Zhou, L.-M. Wu, *J. Am. Chem. Soc.* **2013**, *135*, 12914–12921.

[4] S. Hudgens, B. Johnson, *MRS Bull.* **2004**, *29*, 829–832.

[5] S. C. Riha, B. A. Parkinson, A. L. Prieto, *J. Am. Chem. Soc.* **2009**, *131*, 12054–12055.

[6] J. R. Sootsman, D. Y. Chung, M. G. Kanatzidis, *Angew. Chemie Int. Ed.* **2009**, *48*, 8616–8639.

[7] G. Tan, L.-D. Zhao, M. G. Kanatzidis, *Chem. Rev.* **2016**, *116*, 12123–12149.

[8] C. J. Vineis, A. Shakouri, A. Majumdar, M. G. Kanatzidis, *Adv. Mater.* **2010**, *22*, 3970–3980.

[9] A. Rogalski, *Reports Prog. Phys.* **2005**, *68*, 2267.

[10] B. Radisavljevic, A. Radenovic, J. Brivio, V. Giacometti, A. Kis, *Nat. Nanotechnol.* **2011**, *6*, 147–150.

[11] J. J. Cha, J. R. Williams, D. Kong, S. Meister, H. Peng, A. J. Bestwick, P. Gallagher, D. Goldhaber-Gordon, Y. Cui, *Nano Lett.* **2010**, *10*, 1076–1081.

[12] N. Kamaya, K. Homma, Y. Yamakawa, M. Hirayama, R. Kanno, M. Yonemura, T. Kamiyama, Y. Kato, S. Hama, K. Kawamoto, *Nat. Mater.* **2011**, *10*, 682–686.

[13] F. Cheng, J. Liang, Z. Tao, J. Chen, *Adv. Mater.* **2011**, *23*, 1695–1715.

[14] D. Merki, X. Hu, *Energy Environ. Sci.* **2011**, *4*, 3878–3888.

[15] J. M. Caron, J. R. Neilson, D. C. Miller, K. Arpino, A. Llobet, T. M. McQueen, *Phys. Rev. B* **2012**, *85*, 180405.

[16] S. Medvedev, T. M. McQueen, I. A. Troyan, T. Palasyuk, M. I. Eremets, R. J. Cava, S. Naghavi, F. Casper, V. Ksenofontov, G. Wortmann, *Nat. Mater.* **2009**, *8*, 630–633.

[17] H. S. S. Ramakrishna Matte, A. Gomathi, A. K. Manna, D. J. Late, R. Datta, S. K. Pati, C. N. R. Rao, *Angew. Chemie Int. Ed.* **2010**, *49*, 4059–4062.

[18] M. König, S. Wiedmann, C. Brüne, A. Roth, H. Buhmann, L. W. Molenkamp, X.-L. Qi, S.-C. Zhang, *Science* **2007**, *318*, 766–770.

[19] D. Hsieh, Y. Xia, D. Qian, L. Wray, J. H. Dil, F. Meier, J. Osterwalder, L. Patthey, J. G. Checkelsky, N. P. Ong, *Nature* **2009**, *460*, 1101–1105.

[20] D. Kong, Y. Cui, *Nat. Chem.* **2011**, *3*, 845–849.

[21] L. Müchler, F. Casper, B. Yan, S. Chadov, C. Felser, *Phys. status solidi (RRL)–Rapid Res. Lett.* **2013**, *7*, 91–100.

[22] T. H. Hsieh, H. Lin, J. Liu, W. Duan, A. Bansil, L. Fu, *Nat. Commun.* **2012**, *3*, 1–7.
[23] L. Fu, *Phys. Rev. Lett.* **2011**, *106*, 106802.
[24] M. N. Ali, J. Xiong, S. Flynn, J. Tao, Q. D. Gibson, L. M. Schoop, T. Liang, N. Haldolaarachchige, M. Hirschberger, N. P. Ong, *Nature* **2014**, *514*, 205–208.
[25] L. Yu, R. S. Kokenyesi, D. A. Keszler, A. Zunger, *Adv. Energy Mater.* **2013**, *3*, 43–48.
[26] R. Detemple, D. Wamwangi, M. Wuttig, G. Bihlmayer, *Appl. Phys. Lett.* **2003**, *83*, 2572–2574.
[27] K. Wang, C. Steimer, R. Detemple, D. Wamwangi, M. Wuttig, *Appl. Phys. A* **2005**, *81*, 1601–1605.
[28] J. Wernick, *J. Phys. Chem. Solids* **1957**, *3*, 157–159.
[29] D. T. Morelli, V. Jovovic, J. P. Heremans, *Phys. Rev. Lett.* **2008**, *101*, 35901.
[30] S. Geller, J. H. Wernick, *Acta Crystallogr.* **1959**, *12*, 46–54.
[31] M. D. Nielsen, V. Ozolins, J. P. Heremans, *Energy Environ. Sci.* **2013**, *6*, 570–578.
[32] S. N. Guin, K. Biswas, *J. Mater. Chem. C* **2015**, *2*, DOI: 10.1039/c5tc01429h.
[33] K. Hoang, S. D. Mahanti, J. R. Salvador, M. G. Kanatzidis, *Phys. Rev. Lett.* **2007**, *99*, 156403.
[34] J.-H. Song, A. J. Freeman, T. K. Bera, I. Chung, M. G. Kanatzidis, *Phys. Rev. B* **2009**, *79*, 245203.
[35] K. Wojciechowski, M. Schmidt, J. Tobola, M. Koza, A. Olech, R. Zybała, *J. Electron. Mater.* **2010**, *39*, 2053–2058.
[36] Y. Pei, H. Wang, G. J. Snyder, *Adv. Mater.* **2012**, *24*, 6125.
[37] Y. Pei, X. Shi, A. LaLonde, H. Wang, L. Chen, G. J. Snyder, *Nature* **2011**, *473*, 66.
[38] S. N. Guin, K. Biswas, *Chem. Mater.* **2013**, *25*, 3225–3231.
[39] E. Rathore, R. Juneja, S. P. Culver, N. Minafra, A. K. Singh, W. G. Zeier, K. Biswas, *Chem. Mater.* **2019**, *31*, 2106–2113.
[40] S. N. Guin, V. Srihari, K. Biswas, *J. Mater. Chem. A* **2015**, *3*, 648–655.
[41] E. Rathore, S. N. Guin, K. Biswas, *Bull. Mater. Sci.* **2020**, *43*, 1–7.
[42] M. Cagnoni, D. Führen, M. Wuttig, *Adv. Mater.* **2018**, *30*, 1801787.
[43] A. A. Khan, I. Khan, I. Ahmad, Z. Ali, *Mater. Sci. Semicond. Process.* **2016**, *48*, 85–94.
[44] X. Zhou, Q. Zhang, L. Gan, H. Li, J. Xiong, T. Zhai, *Adv. Sci.* **2016**, *3*, 1600177.
[45] A. Shafique, Y.-H. Shin, *Sci. Rep.* **2017**, *7*, 506.
[46] J. He, M. G. Kanatzidis, V. P. Dravid, *Mater. Today* **2013**, *16*, 166–176.

[47] A. V Powell, *J. Appl. Phys.* **2019**, *126*, 100901.

[48] Z.-H. Ge, L.-D. Zhao, D. Wu, X. Liu, B.-P. Zhang, J.-F. Li, J. He, *Mater. Today* **2016**, *19*, 227.

[49] H. Wang, E. Schechtel, Y. Pei, G. J. Snyder, *Adv. Energy Mater.* **2013**, *3*, 488.

[50] H. Xie, X. Su, G. Zheng, T. Zhu, K. Yin, Y. Yan, C. Uher, M. G. Kanatzidis, X. Tang, *Adv. Energy Mater.* **2017**, 1–14.

[51] M. Beaumale, T. Barbier, Y. Bréard, S. Hébert, Y. Kinemuchi, E. Guilmeau, *J. Appl. Phys.* **2017**, *043704*, DOI 10.1063/1.4863141.

[52] Y. Xiao, L.-D. Zhao, *Science* **2020**, *367*, 1196–1197.

[53] X.-L. Shi, J. Zou, Z.-G. Chen, *Chem. Rev.* **2020**, *120*, 7399–7515.

[54] O. Delaire, J. Ma, K. Marty, A. F. May, M. A. McGuire, M. H. Du, D. J. Singh, A. Podlesnyak, G. Ehlers, M. D. Lumsden, B. C. Sales, *Nat. Mater.* **2011**, *10*, 614–619.

[55] E. S. Bozin, C. D. Malliakas, P. Souvatzis, T. Proffen, N. a. Spaldin, M. G. Kanatzidis, S. J. L. Billinge, *Science* **2010**, *330*, 1660–1663.

[56] A. Banik, S. Roychowdhury, K. Biswas, *ChemComm* **2018**, *54*, 6573–6590.

[57] S. Skipidarov, M. Nikitin, *Novel Thermoelectric Materials and Device Design Concepts*, Springer, **2019**.

[58] R. J. Korkosz, T. C. Chasapis, S. Lo, J. W. Doak, Y. J. Kim, C.-I. Wu, E. Hatzikraniotis, T. P. Hogan, D. N. Seidman, C. Wolverton, V. P. Dravid, M. G. Kanatzidis, *J. Am. Chem. Soc.* **2014**, *136*, 3225.

[59] Y. Pei, A. D. LaLonde, N. A. Heinz, X. Shi, S. Iwanaga, H. Wang, L. Chen, G. J. Snyder, *Adv. Mater.* **2011**, *23*, 5674.

[60] Y. Pei, A. D. LaLonde, N. A. Heinz, G. J. Snyder, *Adv. Energy Mater.* **2012**, *2*, 670–675.

[61] Y. Pei, H. Wang, Z. M. Gibbs, A. D. LaLonde, G. J. Snyder, *NPG Asia Mater.* **2012**, *4*, e28–e28.

[62] Z. Jian, Z. Chen, W. Li, J. Yang, W. Zhang, Y. Pei, *J. Mater. Chem. C* **2015**, *3*, 12410–12417.

[63] G. Tan, F. Shi, S. Hao, L.-D. Zhao, H. Chi, X. Zhang, C. Uher, C. Wolverton, V. P. Dravid, M. G. Kanatzidis, *Nat. Commun.* **2016**, *7*, 12167.

[64] L.-D. Zhao, J. He, C.-I. Wu, T. P. Hogan, X. Zhou, C. Uher, V. P. Dravid, M. G. Kanatzidis, *J. Am. Chem. Soc.* **2012**, *134*, 7902–7912.

[65] L.-D. Zhao, S.-H. Lo, J. He, H. Li, K. Biswas, J. Androulakis, C.-I. Wu, T. P. Hogan, D.-Y. Chung, V. P. Dravid, M. G. Kanatzidis, *J. Am. Chem. Soc.* **2011**, *133*, 20476–20487.

[66] B. T. Matthias, M. Marezio, E. Corenzwit, A. S. Cooper, H. E. Barz, *Science*

1972, *175*, 1465–1466.

[67] R. Chevrel, M. Sergent, J. Prigent, *J. Solid State Chem.* **1971**, *3*, 515–519.

[68] R. Chevrel, M. Sergent, in *Supercond. Ternary Compd. I*, Springer, **1982**, pp. 25–86.

[69] J. M. Tarascon, G. W. Hull, P. Marsh, T. Haar, *J. Solid State Chem.* **1987**, *66*, 204–224.

[70] Z. Kaidi, S. Belin, C. Boulanger, J.-M. Lecuire, M. Sergent, R. Chevrel, *J. Solid State Chem.* **1999**, *147*, 199–210.

[71] W. R. McKinnon, J. R. Dahn, *Phys. Rev. B* **1985**, *31*, 3084–3087.

[72] O. Peña, *Phys. C Supercond. its Appl.* **2015**, *514*, 95–112.

[73] T. Caillat, J.-P. Fleurial, G. J. Snyder, *Solid State Sci.* **1999**, *1*, 535–544.

[74] C. N. R. Rao, H. S. S. Ramakrishna Matte, U. Maitra, *Angew. Chemie Int. Ed.* **2013**, *52*, 13162–13185.

[75] P. R. Wallace, *Phys. Rev.* **1947**, *71*, 622.

[76] R. W. Keyes, *Phys. Rev.* **1953**, *92*, 580.

[77] M. Chhowalla, H. S. Shin, G. Eda, L.-J. Li, K. P. Loh, H. Zhang, *Nat. Chem.* **2013**, *5*, 263–275.

[78] M. Stanley Whittingham, A. J. Jacobson, *Intercalation Chemistry*, Academic Press, New York, **1982**.

[79] C. N. R. Rao, J. Gopalakrishnan, *New Directions in Solid State Chemistry*, Cambridge University Press, **1997**.

[80] C. N. R. Rao, K. Biswas, *Essentials of Inorganic Materials Synthesis*, John Wiley & Sons, **2015**.

[81] A. J. Jacobson, L. F. Nazar, *Intercalation Chemistry*, **2006**.

[82] A. Clearfield, *Chem. Rev.* **1988**, *88*, 125–148.

[83] M.-R. Gao, Y.-F. Xu, J. Jiang, S.-H. Yu, *Chem. Soc. Rev.* **2013**, *42*, 2986–3017.

[84] C. Julien, M. Eddrief, I. Samaras, M. Balkanski, *Mater. Sci. Eng. B* **1992**, *15*, 70–72.

[85] J. Wu, H. Yuan, M. Meng, C. Chen, Y. Sun, Z. Chen, W. Dang, C. Tan, Y. Liu, J. Yin, *Nat. Nanotechnol.* **2017**, *12*, 530–534.

[86] J. Wu, C. Tan, Z. Tan, Y. Liu, J. Yin, W. Dang, M. Wang, H. Peng, *Nano Lett.* **2017**, *17*, 3021–3026.

[87] T. Ghosh, M. Samanta, A. Vasdev, K. Dolui, J. Ghatak, T. Das, G. Sheet, K. Biswas, *Nano Lett.* **2019**, *19*, 5703–5709.

[88] M. Velický, P. S. Toth, *Appl. Mater. Today* **2017**, *8*, 68–103.

[89] K. S. Novoselov, A. Mishchenko, A. Carvalho, A. H. Castro Neto, *Science* **2016**, *353*, aac9439.

[90] R. Brec, *Solid State Ionics* **1986**, *22*, 3–30.
[91] A. R. Wildest S J Kennedy, T. J. Hickst, *Condens. Matter* **1994**, *6*, 335–341.
[92] A. Lkaustic, J. P. Audibre, P. G. Lacroix, R. C16ment, L. Lomas, A. Michalowicz, W. R. Dunham, A. H. Francis, *Chem. Mater* **1996**, *7*, 1103–1111.
[93] C. O. Oriakhi, M. M. Lerner, *Chem. Mater* **1996**, *8*, 2016–2022.
[94] R. Clement, *J. Am. Chem. Soc.* **1981**, *103*, 6998–7000.
[95] P. Fuentealba, C. Cortés, N. Audebrand, E. Le Fur, V. Paredes-García, D. Venegas-Yazigi, J. Manzur, E. Spodine, *Dalt. Trans. Commun. Cite this Dalt. Trans* **2015**, *44*, 12493–12496.
[96] X. Zhang, H. Zhou, X. Su, X. Chen, C. Yang, J. Qin, M. Inokuchi, *J. Alloys Compd.* **2007**, *432*, 247–252.
[97] C. Yang, X. Chen, J. Qin, K. Yakushi, Y. Nakazawa, K. Ichimura, *J. Solid State Chem.* **2000**, *150*, 281–285.
[98] H. Zhou, X. Su, X. Zhang, X. Chen, C. Yang, J. Qin, M. Inokuchi, *Mater. Res. Bull.* **2006**, *41*, 2161–2167.
[99] X.-G. Zhao, D. Yang, J.-C. Ren, Y. Sun, Z. Xiao, L. Zhang, *Joule* **2018**, *2*, 1662–1673.
[100] S. Bera, N. Pradhan, *ACS Energy Lett.* **2020**, *5*, 2858–2872.
[101] P. V Kamat, N. Pradhan, K. Schanze, P. S. Weiss, J. Buriak, P. Stang, T. W. Odom, G. Hartland, *ACS Energy Lett.* **2020**, 2253–2255.
[102] K. Biswas, J. He, I. D. Blum, C.-I. Wu, T. P. Hogan, D. N. Seidman, V. P. Dravid, M. G. Kanatzidis, *Nature* **2012**, *489*, 414–418.
[103] J.-P. Fleurial, *Jom* **2009**, *61*, 79–85.
[104] J. Yang, T. Caillat, *MRS Bull.* **2006**, *31*, 224–229.
[105] B. Orr, A. Akbarzadeh, M. Mochizuki, R. Singh, *Appl. Therm. Eng.* **2016**, *101*, 490–495.
[106] J.-F. Li, W.-S. Liu, L.-D. Zhao, M. Zhou, *NPG Asia Mater.* **2010**, *2*, 152.
[107] S. R. Brown, S. M. Kauzlarich, F. Gascoin, G. J. Snyder, *Chem. Mater.* **2006**, *18*, 1873–1877.
[108] W. Qiu, L. Xi, P. Wei, X. Ke, J. Yang, W. Zhang, *Proc. Natl. Acad. Sci.* **2014**, *111*, 15031-15035.
[109] M. K. Jana, K. Biswas, *ACS Energy Lett.* **2018**, *3*, 1315–1324.
[110] M. G. Kanatzidis, *Nature* **2014**, *508*, 373–377.
[111] S. Roychowdhury, M. K. Jana, J. Pan, S. N. Guin, D. Sanyal, U. V Waghmare, K. Biswas, *Angew. Chemie Int. Ed.* **2018**, 2–7.
[112] M. Samanta, K. Pal, P. Pal, U. V. Waghmare, K. Biswas, *J. Am. Chem. Soc.* **2017**, 140, 5866-5872

[113] X. Shi, J. Yang, J. R. Salvador, M. Chi, J. Y. Cho, H. Wang, S. Bai, J. Yang, W. Zhang, L. Chen, *J. Am. Chem. Soc.* **2011**, *133*, 7837–7846.

[114] T. Takabatake, K. Suekuni, T. Nakayama, E. Kaneshita, *Rev. Mod. Phys.* **2014**, *86*, 669–716.

[115] H. Euchner, S. Pailhès, L. T. K. Nguyen, W. Assmus, F. Ritter, A. Haghighirad, Y. Grin, S. Paschen, M. de Boissieu, *Phys. Rev. B* **2012**, *86*, 224303.

[116] G. J. Snyder, E. S. Toberer, *Nat. Mater.* **2008**, *7*, 105.

[117] S. N. Guin, A. Chatterjee, D. S. Negi, R. Datta, K. Biswas, *Energy Environ. Sci.* **2013**, *6*, 2603–2608.

[118] H. Liu, X. Shi, F. Xu, L. Zhang, W. Zhang, L. Chen, Q. Li, C. Uher, T. Day, G. J. Snyder, *Nat. Mater.* **2012**, *11*, 422–425.

[119] S. Wang, J. Yang, L. Wu, P. Wei, J. Yang, W. Zhang, Y. Grin, **2015**, DOI 10.1021/cm504398d.

[120] M. J. Manos, M. G. Kanatzidis, *Chem. Sci.* **2016**, *7*, 4804–4824.

[121] M. J. Manos, N. Ding, M. G. Kanatzidis, *Proc. Natl. Acad. Sci. U. S. A.* **2008**, *105*, 3696–9.

[122] F. G. Helfferich, *Ion Exchange*, Courier Corporation, **1962**.

[123] J. Rouxel, *Rev. Inorg. Chem* **1979**, *1*, 245–279.

[124] M. S. Whittingham, *Prog. Solid State Chem.* **1978**, *12*, 41–99.

[125] R. Schöllhorn, *Angew. Chemie Int. Ed. English* **1980**, *19*, 983–1003.

[126] M. J. McKelvy, W. S. Glaunsinger, *Annu. Rev. Phys. Chem.* **1990**, *41*, 497–523.

[127] M. B. Dines, *Science* **1975**, *188*, 1210–1211.

[128] W. A. England, J. B. Goodenough, P. J. Wiseman, *J. Solid State Chem.* **1983**, *49*, 289–299.

[129] M. L. T. Cossio, L. F. Giesen, G. Araya, M. L. S. Pérez-Cotapos, R. L. VERGARA, M. Manca, R. A. Tohme, S. D. Holmberg, T. Bressmann, D. R. Lirio, J. S. Román, R. G. Solís, S. Thakur, S. N. Rao, E. L. Modelado, A. D. E. La, C. Durante, U. N. A. Tradición, M. En, E. L. Espejo, D. E. L. A. S. Fuentes, U. A. De Yucatán, C. M. Lenin, L. F. Cian, M. J. Douglas, L. Plata, F. Héritier, *Ion Exchnange Materials Properties and Application*, **2012**.

[130] N. Daumas, A. Herold, *Comptes Rendus Hebd. Des Seances L Acad. Des Sci. Ser. C* **1969**, *268*, 373.

[131] A. C. D. Newman, *Chemistry of Clays and Clay Minerals*, Wiley, **1987**.

[132] S. Rapti, A. Pournara, D. Sarma, I. T. Papadas, G. S. Armatas, A. C. Tsipis, T. Lazarides, M. G. Kanatzidis, M. J. Manos, *Chem. Sci.*, **2016**, 7, 2427-2436.

[133] Q. Sun, B. Aguila, J. Perman, L. D. Earl, C. W. Abney, Y. Cheng, H. Wei, N. Nguyen, L. Wojtas, S. Ma, *J. Am. Chem. Soc.* **2017**, *139*, 2786–2793.

[134] C. W. Abney, J. C. Gilhula, K. Lu, W. Lin, *Adv. Mater.* **2014**, *26*, 7993–7997.
[135] H.-R. Fu, Z.-X. Xu, J. Zhang, *Chem. Mater.* **2015**, *27*, 205–210.
[136] C. O. Oriakhi, M. M. Lerner, *Layer. Mater.* **2004**, 509.
[137] R. Schöllhorn, W. Roer, K. Wagner, *Monatshefte für Chemie/Chemical Mon.* **1979**, *110*, 1147–1152.
[138] A. E. Gash, A. L. Spain, L. M. Dysleski, C. J. Flaschenriem, A. Kalaveshi, P. K. Dorhout, S. H. Strauss, *Environ. Sci. Technol.* **1998**, *32*, 1007–1012.
[139] M. J. Manos, M. G. Kanatzidis, *J. Am. Chem. Soc.* **2009**, *131*, 6607.
[140] M. J. Manos, M. G. Kanatzidis, *Chem. Eur. J.* **2009**, *15*, 4779–4784.
[141] M. J. Manos, V. G. Petkov, M. G. Kanatzidis, *Adv. Funct. Mater.* **2009**, *19*, 1087–1092.
[142] M. J. Manos, M. G. Kanatzidis, *J. Am. Chem. Soc.* **2012**, *134*, 16441–16446.
[143] J. L. Mertz, Z. H. Fard, C. D. Malliakas, M. J. Manos, M. G. Kanatzidis, *Chem. Mater.* **2013**, *25*, 2116–2127.
[144] J. B. Parise, Y. Ko, J. Rijssenbeek, D. M. Nellis, K. Tan, S. Koch, *J. Chem. Soc. Chem. Commun.* **1994**, 527.
[145] X.-H. Qi, K.-Z. Du, M.-L. Feng, J.-R. Li, C.-F. Du, B. Zhang, X.-Y. Huang, *J. Mater. Chem. A* **2015**, *3*, 5665–5673.
[146] G. A. Marking, M. Evain, V. Petricek, M. G. Kanatzidis, *J. Solid State Chem.* **1998**, *141*, 17–28.
[147] M. G. Kanatzidis, J. L. Mertz, E. Manos, *Chalcogenide Compounds for the Remediation of Nuclear and Heavy Metal Wastes,US Patent, US2011290735-A1.*, **2011**.
[148] D. Sarma, C. D. Malliakas, K. S. Subrahmanyam, S. M. Islam, M. G. Kanatzidis, *Chem. Sci.* **2016**, *7*, 1121–1132.
[149] N. Ding, M. G. Kanatzidis, *Chem. Mater.* **2007**, *19*, 3867–3869.
[150] N. Ding, M. G. Kanatzidis, *Nat. Chem.* **2010**, *2*, 187–191.
[151] S. Ma, Q. Chen, H. Li, P. Wang, S. M. Islam, Q. Gu, X. Yang, M. G. Kanatzidis, *J. Mater. Chem. A* **2014**, *2*, 10280–10289.
[152] L. Ma, Q. Wang, S. M. Islam, Y. Liu, S. Ma, M. G. Kanatzidis, *J. Am. Chem. Soc.* **2016**, *138*, 2858–2866.
[153] S. Ma, L. Huang, L. Ma, Y. Shim, S. M. Islam, P. Wang, L.-D. Zhao, S. Wang, G. Sun, X. Yang, *J. Am. Chem. Soc.* **2015**, *137*, 3670–3677.
[154] C. N. R. Rao, P. J. Thomas, G. U. Kulkarni, *Synth. Prop. Appl. Springer, Berlin* **2007**.
[155] L. E. Smart, E. A. Moore, *Solid State Chemistry: An Introduction*, CRC Press, **2012**.

[156] R. S. Fishman, J. A. Fernandez-Baca, T. Rõõm, *Spin-Wave Theory and Its Applications to Neutron Scattering and THz Spectroscopy*, Morgan & Claypool Publishers, **2018**.

[157] M. Dutta, M. Samanta, T. Ghosh, D. J. Voneshen, K. Biswas, *Angew. Chemie Int. Ed.* **2020**, *133,* 4305-4311.

PART 2

Design and Synthesis of Metal Chalcogenides for High Performance Thermoelectric Materials

Chapter 2.1

Influence of periodic table in designing solid-state metal chalcogenides for thermoelectric energy conversion[†]

[†] *Paper based on this has been published as* ***E. Rathore****, M. Dutta, K. Biswas, J. Chem. Sci.* ***2019,*** *131, 116.*

Chapter 2.1

Influence of periodic table in designing solid-state metal chalcogenides for thermoelectric energy conversion†

Summary: *With the noticeable burgeoning energy crisis, alternative sources of energies are in a greater need for a sustainable future. Thermoelectrics can convert waste heat arising from industries, power plants and automobiles into a usable form, electricity. Thermoelectric materials have the potential to be a game-changer in this critical energy shortage and energy management. The efficiency of thermoelectric materials which is given by the dimensionless figure of merit is tricky to manipulate due to the complicated interrelationships of electronic and thermal transport parameters. But with the proper understanding of a material and with the aid of periodic table, one can manoeuvre the shortcomings which hinder its efficiency. In this chapter, we discuss how the properties of materials can be manipulated just by understanding the elements of the periodic table and how each element in their respective position in the periodic table influences the outcome of high performing thermoelectric material.*

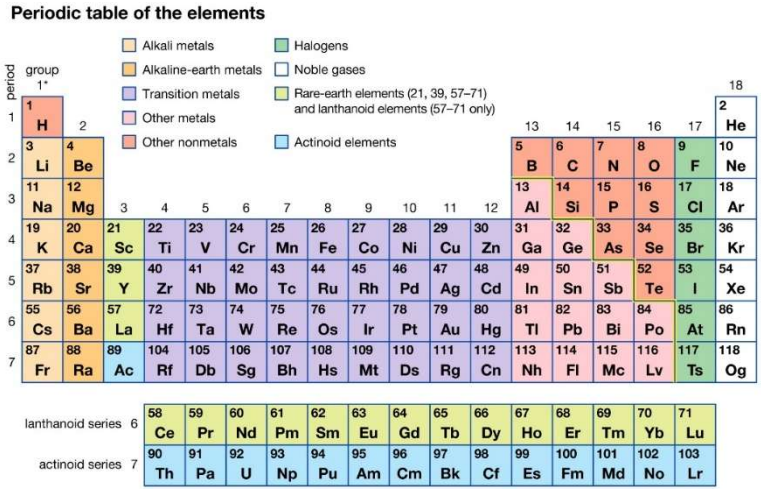

†*Paper based on this has been published as* ***E. Rathore****, M. Dutta, K. Biswas, J. Chem. Sci.* ***2019,*** *131, 116.*

2.1.1. Introduction

The growing demand of energy has given rise to a tremendous scope for research in thermoelectrics. Thermoelectric materials can convert waste heat into electricity. High thermoelectric (TE) performance is observed in materials with high Seebeck coefficient, S, low electrical resistivity, ρ (high electrical conductivity, σ) and low thermal conductivity, κ_{tot}.[1-5] The thermoelectric figure of merit couples these necessary attributes of good TE material into one factor as given by

$$ZT = \frac{\sigma S^2 T}{(\kappa_{ele}+\kappa_{lat})} \qquad \text{Eq. 2.1.1.}$$

where κ_{ele} and κ_{lat} correspond to electrical and lattice contributions respectively, of the total thermal conductivity, κ_{tot}. These physical properties are strongly interdependent on each other and thus makes it challenging to design high performance TE materials. To understand the fundamental material properties, assuming carrier concentration, a more prominent term called the TE quality factor, β is preferred.[1]

$$\beta = \frac{N_v}{m_i^* \kappa_{lat}} \qquad \text{Eq. 2.1.2.}$$

Large valley degeneracy, N_v which essentially relates to the number of similar energy states around conduction band minima or valence band maxima, contributes to a large number of conduction pathways for charge carriers for electronic transport and low inertial effective mass, m_i^* along the direction of conduction pathway. Effective mass is defined as the relative mass of the charge carriers with respect to the mass of free electron. Thus, effective mass being closer to the mass of free electron means the electrical conduction is much greater and can hence improve the mobility ($\mu = e\tau / m_i^*$). For single valley, $m^*_{band} = m_i^*$ and the contribution of m_i^* is related to density of states effective mass m^*_{DOS} via m^*_{band} as[5]

$$m^*_{DOS} = m^*_{band} N_v^{2/3} \qquad \text{Eq. 2.1.3.}$$

High Seebeck coefficient can either be due to large m^*_{band} or large N_v. However, large m^*_{band} increases scattering and decrease the mobility of electrons as it is related to m_i^*.

The band gap between the valence and conduction band plays an important role in TE performance of a material. When the temperature increases, the electronic carriers are thermally excited across the bandgap and the minority carriers start to neutralize the majority carriers, leading to origin of low thermo-power and high thermal conductivity due to bipolar conduction. Thus, bandgap regulates the maximum suitable operating temperature and figure of merit of TE material.[1, 6] Figure 2.1.1 describes the band gap of a crystalline solid with hypothetical composition AB by Molecular Orbital Theory (MOT). The band gap, bonding energy or strength of bonding interactions, energy difference between atomic orbitals, width of valence and conduction band is given by E_g, B^*, $2A^*$, W_{VB}, W_{CB}, respectively.

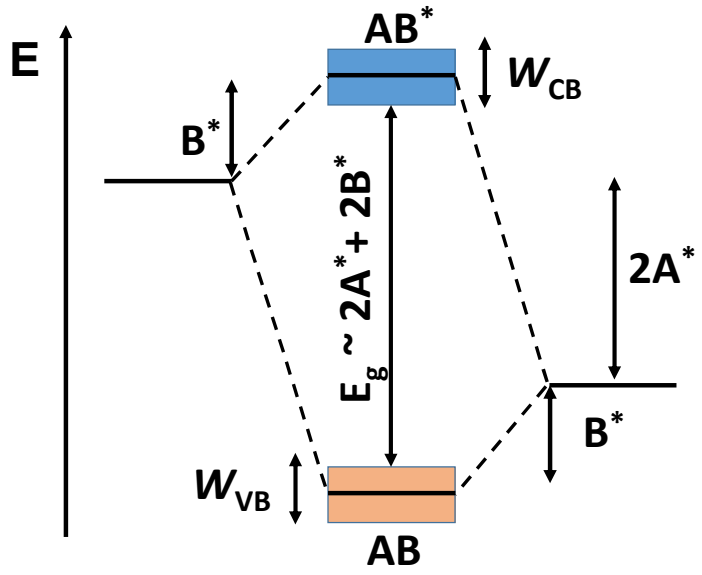

Figure 2.1.1. *Molecular orbital (MO) diagram of AB, where E_g is bandgap, A^* is energy difference of atomic orbitals, W is width of conduction and valence band, B^* is strength of bonding interactions.*

In simple MO of AB, B^* is the subsequent energy from stabilization of molecular bonding orbitals and destabilization of antibonding orbital compared to atomic orbitals. B^* can be expressed in terms of orbital overlap interaction, V and A^* as[7-8]:

$$B^* = \sqrt{V^2 + A^{*2}} - A^* \qquad \text{Eq. 2.1.4.}$$

Larger A^* will lead to weaker covalent bonding energy, B^*. V is indirectly proportional to the square of distance, d which can describe the valence shell interactions. According to Koopman's theorem, higher is the electronegativity, lower is A^*.[9] Large difference in electronegativity (EN) between element A with small EN and B with large EN results in larger band gap. Orbital character of bands is also influenced by EN difference. In ionic solids with large A^*, the valence band states will have anion B character and conduction band states will have cation A element character.

The electronic properties in semiconductors are governed by the width of an electronic band W.[2] Figure 2.1.1 shows that increased width W can lead to reduction of the band gap and it is possible to tune the electronic properties. If $W > B^* + A^*$, AB and AB* MO orbitals of AB will merge to form an overlapping band and result into metal or semimetal. For polar compounds ($A^* \neq 0$), W tends to drop with an increase in A^* as the overlap, V becomes less effective due the rise in the energy difference between the neighboring orbitals leading to large band gaps in ionic compounds. Smaller dispersion (narrow band) arise from factors like longer bonds, high degree of polarity or dispersed f- orbitals which have lower overlap than p- or s- interactions. Narrow band in energy space corresponds to wide parabola in k-space, a large DOS and a high m^*_{band} which is expected in large electronegative difference ionic compounds.[8]

Arguably the most important parameter in the thermoelectric figure of merit is that of thermal conductivity. The total thermal conductivity (κ_{tot}) is a summation of two types of heat propagators. One of the heat propagators are the free charge carriers, and the amount of heat propagation by them is given by κ_{ele}; while the other is heat transport via lattice vibration (or phonons) which is denoted as κ_{lat}. Since high κ_{ele} is a resultant of high σ by virtue of their relation using Wiedemann-Franz Law (i.e., $\kappa_{ele} = L\sigma T$, L = Lorentz number), reducing κ_{ele} is not a popular choice and thus reducing κ_{lat} is seen as an important avenue to achieve high performance in thermoelectrics. As a matter of fact, almost all high performing thermoelectric materials possess low thermal conductive parent compound and is often considered to be the backbone in designing superior, highly efficient thermoelectric material.[10-12] Periodic table more often than not dictates how the material will transport heat and along with keen chemical intuition, one often designs compounds showing low thermal conductive materials. For example, the tellurides of Ge to Pb in group 14 (i.e., GeTe, SnTe and PbTe), we see a decreasing

trend in the κ_{tot} of the material. We have discussed about the influence of periodic table in generating low thermal conductive materials in more detail in later part of our review.

Thus, we can say that the electronic and thermal transport are linked to bonding character, band gap, bonding strength, bond length, effective mass, orbital overlap and lone-pair anharmonicity; all of them can be understood just by a thorough understanding of the elements and their position on the periodic table. In this chapter, we will discuss the importance that the periodic table plays in shaping the thermoelectric properties of materials.

2.1.2. Periodic Trends in Electronic Properties

2.1.2.1. Band Gap

Band gap is one of the contributing factors in determining the electrical conductivity (σ) of a semiconductor. Generally, materials with low band gap shows high σ and decreases with increasing band gap. In case of PbQ (Q = chalcogenides, S, Se and Te), the band gap for PbSe (0.27 eV) < PbTe (0.31 eV) < PbS (0.40 eV). The electrical conductivity too shows the same trend as (σ(PbSe) > σ(PbTe) > σ(PbS)).[13] For thermoelectrics, the materials should possess band gap which is falls in the semi-conducting region in terms of band edge (i.e., neither very low metallic gap or high band gap as that of an insulator). Often σ is governed by the mobility of the major carriers in the material. Carrier mobility, μ is low for bands with heavy mass m^*_{band}, leading to the low electrical conductivity ($\sigma = ne\mu$). This difference between the valence band and conduction band relies upon several factors like electronegativity, presence of stereochemical lone pairs and temperature etc. and are known play a crucial role in determining the electrical conductivity of a material.

2.1.2.2. Role of Electronegativity

The difference in electronegativity can be helpful in tuning the band gaps and thereby the electronic mobility as $E_g \sim 2A^* + 2B^*$ and A^* depends on electronegativity. Larger is the electronegativity difference more will be band gap. For example, in $AgBiSe_{2-x}X_x$ (X = Cl, Br, I) the electrical conductivity for pristine $AgBiSe_2$ is around 63 Scm^{-1}. On doping aliovalent halogens, the band gap is seen to widen up (from ~ 0.6 eV) due higher electronegativity of halogens (χ_{Cl} (3.16) > χ_{Br} (2.96) > χ_I (2.66)) as compared to selenium (χ_{Se} = 2.55) which causes more ionic character in M-X bond than

that of M-Se bond.[14] As a result, the σ increases to 376 Scm^{-1} at room temperature for 4 mol% Cl doped $AgBiSe_2$. For 4 mol% Br and I doped $AgBiSe_2$, σ value is 337 Scm^{-1} and 196 Scm^{-1} respectively at room temperature.[14] The σ trend for aliovalent halogen doped $AgBiSe_2$ mirrors the electronegativity trend down the Group 17 of the periodic table. Thus, proper knowledge of periodic table and their corresponding electronegativity aids in realizing high thermoelectric performance in n-type $AgBiSe_2$.[14] Similarly for PbSe, ongoing down Group 13, (i.e., B, Al, Ga), σ is seen to increase from 8.72 (10^2 Scm^{-1}) in case of B doped PbSe to around 38.5 (10^2 Scm^{-1}) for Ga doped PbSe.[15] Here too, the periodic trend is observed, as down the group the electronegativity decreases which increases the propensity of Group 13 elements to donate excess electrons and thereby increase the carrier concentration which in turn increases the σ of n-type PbSe.

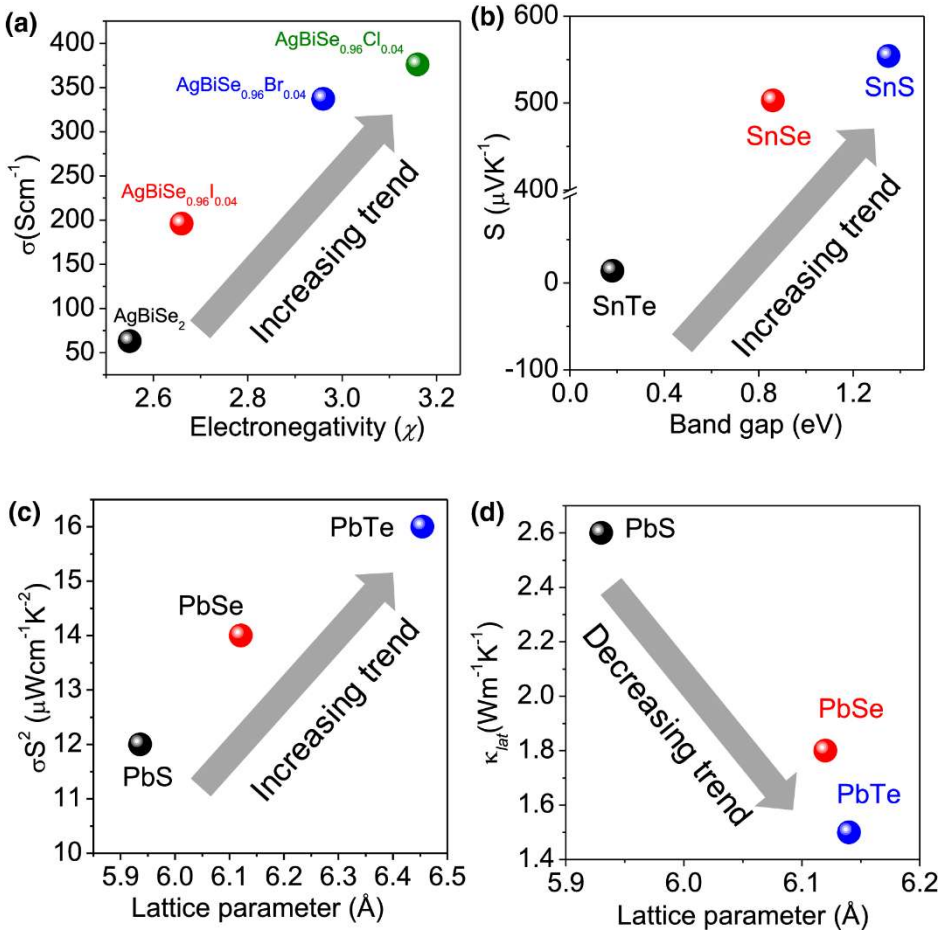

Figure 2.1.2. *Periodic trends of (a) electrical conductivity (σ), (b) Seebeck coefficient (S), (c) Power factor (σS^2) and (d) lattice thermal conductivity (κ_{lat}) for some metal chalcogenides.*

2.1.2.3. Effect of Lone-pairs

In the elements of group 13, 14 and 15, the lone pair of electrons play an important role in electronic properties of thermoelectric materials. As we move down the group in p-block elements, the s^2 lone pair experiences a greater effective nuclear force and as a result tends to become inert in nature. In group 13, as the element becomes heavier from Ga to Tl, the lone pair becomes more stabilized in In^+ than in Ga^+. In case of group 14 and 15, Pb^{2+} and Bi^{3+} have very stable lone pair and it is difficult to form Pb^{4+} and Bi^{5+}. This enormous stability of s^2 lone pairs is due to relativistic effects which reduce the size of s-orbital and bring the electron near to nucleus. In semiconductors, containing Tl, Ge, Sn, Pb, Sb and Bi, the stereochemical expression of ns^2 lone pair, increases the band gap as it stabilizes in energy.[2] Depending upon the chalcogenides bonded to these metal ions, the lone pair is either stereochemically expressed or quenched. Down the group, there is tendency for quenching of lone pair and adopting high local symmetry. This concept can be realized in many examples and it is listed in Table 2.1. In Bi_2S_3, SnSe, Sb_2Se_3 and GeS the lone pair stereochemically expresses, causes strong distortion and lowering of structural symmetry which lowers the energy of the orbitals significantly and thereby increasing the bandgap. Thus, the lone pairs become a contributing factor in estimating the band gap of a system and its influence on the electrical conductivity.

Table 2.1: Comparison of band gaps of chalcogenide-based semiconductors.

Semiconductor	Crystal structure (symmetry)	Band Gap (eV)
Bi_2S_3	Orthorhombic (low)	1.30
Bi_2Se_3	Rhombohedral (high)	0.30
SnSe	Orthorhombic (low)	0.80
SnTe	Cubic (high)	0.18
Sb_2Se_3	Orthorhombic (low)	1.10
Sb_2Te_3	Rhombohedral (high)	0.11
GeSe	Orthorhombic (low)	1.07
GeTe	Rhombohedral (high)	0.6

2.1.2.4. Seebeck Coefficient

Seebeck coefficient is related to electrical conductivity by Mott equation (Eq 5). S is the measure of variation of $\sigma(E)$ above and below the Fermi surfaces. $\sigma(E)$ is proportional the DOS at E if scattering of electrons is independent of energy. A larger slope (d $\ln\sigma(E)/\mathrm{d}E$) where DOS changes rapidly, will contribute to larger thermopower.[1]

$$S = \frac{\pi}{3}\frac{k^2T}{e}\left[\frac{d\ln\sigma(E)}{dE}\right]_{E=E_f} \qquad \text{Eq. 2.1.5.}$$

Also, S is expressed in relation to density of state effective mass (m^*) of the carrier by the equation below:[16]

$$S = \frac{8\pi^2 k_B^2 T}{3eh^2}\, m^*_{DOS}\left[\frac{\pi}{3n}\right]^{2/3} \qquad \text{Eq. 2.1.6.}$$

and density of states is given by:

$$g(E) = \frac{[m^*_{DOS}]^{3/2}\sqrt{2E}}{\hbar^3\pi^2} \qquad \text{Eq. 2.1.7.}$$

In SnQ, down the Group 16, the band edge decreases, SnS having a band gap of 1.35 eV[17] decreases to 0.86 eV for SnSe[18] to around 0.18 eV for SnTe[19]. This band edge decrease also is seen to increase the S value for SnQ. SnTe having S value of ~ 14 μVK^{-1} is much lower than SnSe (~ 503 μVK^{-1}) or SnS (554 μVK^{-1}) at ambient temperatures and the trend is continuous and in line with the periodic table trend.[19-20] Thus, here also periodic table showS a tremendous influence in monitoring the Seebeck coefficient of thermoelectric materials. It is to be noted that PbQ (Q = S/Se/Te) does not follow the trend of decreasing band gap with increasing atomic number. Chalcogenides of Sn and Ge which resides on the same Group 14 follows the normal trend. This anomaly in PbQ may have to do with relativistic effects and an extensive spin-orbit coupling which renders it impossible to predict the band gap just from a simplified MO model and general trends.

2.1.2.5. Power Factor

In PbQ, (Q = S, Se, Te), the room temperature power factor increases from ~12 $\mu W\ cm^{-1}\ K^{-2}$ for PbS to ~14 $\mu W\ cm^{-1}\ K^{-2}$ for PbSe and ~16 $\mu W\ cm^{-1}\ K^{-2}$ for PbTe. This is directly related to the size of the anion going down the group and the lattice

parameter (Figure 2.1.2c).[13] A similar trend is observed in MSe (M = Pb, Sn, Ge) series, where the room temperature power factor increases from ~1.2×10^{11} W mK^{-2} s^{-1} for PbSe to ~4×10^{11} W mK^{-2} s^{-1} for SnSe and ~8×10^{11} W mK^{-2} s^{-1} for GeSe due more overlapping factor.[16]

2.1.3. Periodic Trends in Thermal Conductivity

Achieving a high thermoelectric figure of merit often relies on materials having low κ_{lat}.[3, 10, 21] Often an overlooked parameter in the figure of merit equation, but with recent developments in the field of thermoelectrics, κ_{lat} is often regarded as the defining parameter to achieve superior thermoelectric performance. SnSe, for example, has achieved ultrahigh ZT (> 2.5) in both n- and p-type conduction owing to the impressively low κ_{lat} values (κ_{lat} 0.2 – 0.3 Wm^{-1}K^{-1} at 773 K) in both single crystalline and polycrystalline forms.[10, 21-23] The most extensive work on achieving κ_{lat} in materials are via introducing micro and/or nanostructuring in the matrix,[3, 11] while recent scientific explorations focusses on looking at the intrinsic bonding inhomogeneity[24-26] and enhanced anharmonicity[27-28] to lower the phonon propagation in materials. Here, however we will focus on the influence of chemical bonds and nature of phonon propagation trending with periodic table and will develop an understanding how the periodic table shapes up the κ_{lat} of certain high performing materials.

Kinetic theory predicts that the κ_{lat} of material can be quantified approximately using the equation $\kappa_{lat} = \frac{1}{3} C_v v_m l$; where C_v is the specific heat at constant volume, l is the mean free path length for phonons and v_m is the mean speed of sound. v_m depicts the speed of phonon waves propagating through a lattice and is given by $v_m \sim \sqrt{k/M}$, where k is the spring constant and M is its molar mass. Thus, high bond strength results in high spring constant and eventually a higher κ_{lat} as envisaged earlier by Ioffe and Spitzer.[1]

Pb based chalcogenides, PbQ (i.e., Q = Te, Se and S) which adopt a rock-salt type structure, on going down Group 16, the v_m decreases. As a result, the κ_{lat} trend also depicts this periodic trend of decreasing v_m. PbS have a κ_{lat} of ~ 2.6 Wm^{-1}K^{-1} at room temperature and going down the group it decreases to ~ 1.8 Wm^{-1}K^{-1} and ~ 1.5 Wm^{-1}K^{-1} for PbSe and PbTe respectively at room temperature.[13] However, for Ge based chalcogenides, we don't observe such trend in κ_{lat} values. GeTe have a κ_{lat} value of ~ 3.0 Wm^{-1}K^{-1} at room temperature, while GeSe possess much lower κ_{lat} values of 1.76 Wm^{-}

$^{1}K^{-1}$ at room temperature. GeS possesses κ_{lat} slightly higher than that of GeSe but lower than GeTe.[29] The difference in trend here can be understood in terms of understanding the structure and the energy of the valence electrons of Ge 4*p* and 4*s* orbitals relative to the chalcogenides *np* orbitals. Ongoing down the Group 16, the electronegativity of the Q decreases (i.e., χ_S (2.58) > χ_{Se} (2.55) > χ_{Te} (2.1)) and as a result, the energy of the *p* orbitals on the Q increases (Figure 2.1.3). For GeTe, the difference in energy between 4*s* of Ge and 5*p* of Te is high enough for any significant overlap between them, and hence remains in relatively higher symmetry as compared to GeSe and GeS. Se and S whose 4*p* and 3*p* respectively are lower in energy can form significant bonding interaction with the Ge 4*s* and as a result the lone pairs on Ge stereochemically expresses themselves which drives the structure to a lower symmetric layered structure (Figure 2.1.3). This stereochemically active lone pairs induces lattice anharmonicity which in turn lowers the κ_{lat} of GeSe and GeS as compared to GeTe. For SnQ, Sn based chalcogenides shows similar trend as that of GeQ. SnTe have κ_{lat} of ~ 3.6 $Wm^{-1}K^{-1}$ at room temperature which is significantly higher than that of SnSe (0.46 $Wm^{-1}K^{-1}$) and SnS (~0.9 $Wm^{-1}K^{-1}$) at room temperature.[19] The reason for such trend is in line with the GeQ. However, SnTe at room temperature procures rock-salt structure contrary to GeTe which is rhombohedral in nature. The reason being the difference energy states of 4*s* for Ge and 5*s* in case of Sn. The energy gap between 5*s* of Sn and 5*p* of Te is too much to have any meaningful interaction and thus the stereochemical nature of $5s^2$ lone pairs are suppressed and the structural distortion do not take place (Figure 2.1.3) unlike GeTe.

Comparing MTe compounds now (M = Ge, Sn, Pb), we observe that the structure changes from rhombohedral in case of GeTe, to cubic in case of SnTe and PbTe. This is a direct result of the amount of interaction between *ns* orbitals of M and 5*p* of Te. The trend here directly relates to the work done by Waghmare *et al.* wherein they explored the interaction between anion *p* and cation *s* and their corresponding distortion from the rocksalt structure.[30] PbQ on the other hand all resides as rock-salt type structure. That is due to the relativistic effect on $6s^2$ lone pairs which stabilizes them to a much greater extent.[31] Although in case of PbQ and SnTe, the bonding interaction among them is not significant, there remains a substantial quantity of *s* character in the anti-bonding state. As a result, the structure although attains a globally cubic structure but locally it distorts due to trivial but finite contribution from the ns^2 lone pairs on Sn and Pb which is observed from the local structure determining technique

Pair Distribution Function.[32-33] This result in local off-centering of cation in these materials (ie., PbQ and SnTe) which lowers their thermal conductivity from the ideal one and also gives rise to lone pair induced anharmonicity in the lattice which is also responsible for scattering of phonons in the lattice and lowering of κ_{lat}. Thus, periodic table enables a chemist to logically intuit the outcome of κ_{lat} in a material and thereby enhance the probability for furnishing high performing thermoelectric materials.

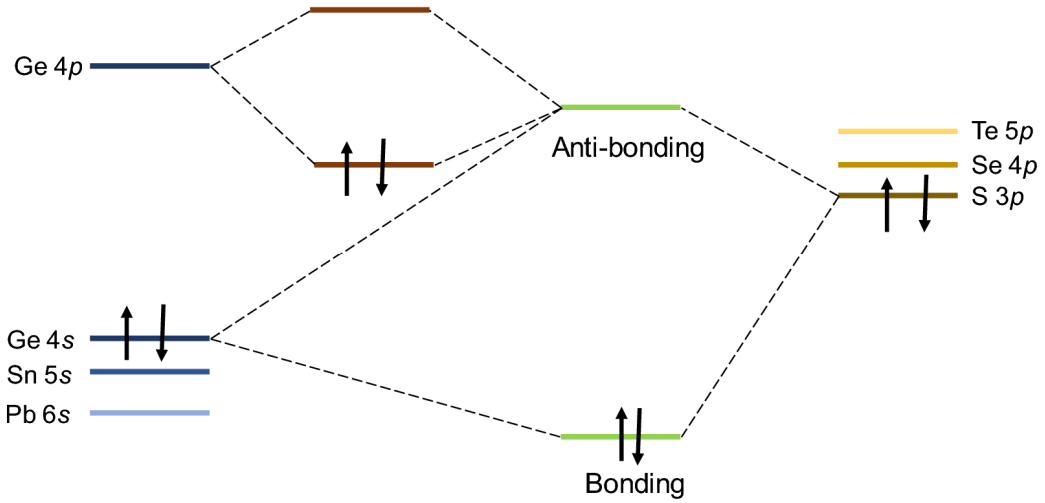

Figure 2.1.3. *Modified MO diagram showing the interaction of ns orbitals of Ge (Sn, Pb) with np orbitals of S (Se, Te). The corresponding interaction results in an opening of band gap as the anti-bonding orbital interacts with 4p orbital of Ge.*

2.1.4. Figure of Merit

The thermoelectric figure of merit (zT) which accounts for both the aforementioned properties (i.e., electronic and thermal) leads to high efficient values for heavier elements (i.e., Pb and Te). As seen from the above discussions, that the high how periodic properties optimizes the properties which shows that PbTe show high electronic properties but surprisingly low thermal properties. The factors influencing for such high efficiency in PbTe directly arises from the optimal band gap of ~ 0.3 eV and low κ_{lat} of 1.5 $Wm^{-1}K^{-1}$. As a result, PbTe shows high thermoelectric zT values (ZT ~2.0) with very high device efficiencies using appropriate dopants.[3, 34-36] The use of dopants to stimulate higher thermoelectric properties are directly governed by position in the periodic table and one can easily engineer the properties influencing the ZT value by proper intuition and knowledge of the periodic table.

2.1.5. Cost Issue

Apart from low thermal conductivity and good thermoelectric performance, there is also need of earth abundant, non-toxic, and low-cost constituent elements. The leading advanced thermoelectric materials are mainly based on Pb, Ge, Se, Te. There is a need of exploring attractive potential alternatives due to the toxicity of Pb, Se, extreme scarcity of Te, cost issues related to Ge. Extensive research on inexpensive sulfur which has long-price stability and abundance is required. Down the group, as the element becomes heavier, it become less abundant and costly.

2.1.6. Conclusion

In conclusion, the advances in thermoelectric materials have come a long way since its inception in the late 1940s. A plethora of new techniques like formation of resonant level, band convergence, formation of hierarchical architectures skyrocketed the development in this field. A ZT >2 which was inconceivable in the past have been achieved and now with the aid of theoretical guidance and materials genome project, a vast plethora of new materials with potential to furnish highly efficient thermoelectric materials are being generated. But even all these new techniques rely on the periodic table to dictate their performance. Without the periodic table, attaining such high ZT values would not have been possible. It guides a scientist to look into the right direction and with a proper knowledge and keen understanding of the periodic table one can easily attain a right dopant to improve on the already known thermoelectric materials or even better furnish a new and high performing one. But one must keep in mind that even with all the prowess of the periodic table, it alone is not sufficient to cater into the scientific query for high performing thermoelectric materials. Integrating the knowledge obtained from periodic table with theoretical calculations and the chemical intuition to apply the required techniques like nano-structuring will pave a long way to develop materials having superior thermoelectric performances.

2.1.7. References

[1] W. G. Zeier, A. Zevalkink, Z. M. Gibbs, G. Hautier, M. G. Kanatzidis, G. J. Snyder, *Angew. Chem. Int. Ed.* **2016**, 55, 6826.

[2] L.-D. Zhao, V. P. Dravid, M. G. Kanatzidis, *Energy Environ. Sci.* **2014**, 7, 251.

[3] K. Biswas, J. He, I. D. Blum, C.-I. Wu, T. P. Hogan, D. N. Seidman, V. P. Dravid, M. G. Kanatzidis, *Nature* **2012,** 489, 414.

[4] J. R. Sootsman, D. Y. Chung, M. G. Kanatzidis, *Angew. Chem. Int. Ed.* **2009**, 48, 8616.

[5] G. Tan, L.-D. Zhao, M. G. Kanatzidis, *Chem. Rev.* **2016**, 116, 12123.

[6] Z. M. Gibbs, H. Kim, H. Wang, R. L. White, F. Drymiotis, M. Kaviany, G. J. Snyder, *Appl. Phy. Lett.* **2013**, 103, 262109.

[7] W. A. Harrison, *Pure Appl. Chem.* **1989**, 61, 2161.

[8] G. S. Rohrer, *Structure and Bonding in Crystalline Materials* Cambridge University Press: Cambridge. **2001**

[9] T. Koopmans, *Physica* **1934,** 1, 104.

[10] L.-D. Zhao, S.-H. Lo, Y. Zhang, H. Sun, G. Tan, C. Uher, C. Wolverton, V. P. Dravid, M. G. Kanatzidis, *Nature* **2014**, 508, 373.

[11] M. Samanta, K. Biswas, *J. Am. Chem. Soc.* **2017**, 139, 9382.

[12] T. Zhu, Y. Liu, C. Fu, J. P. Heremans, J. G. Snyder, X. Zhao, *Ad. Mater.* **2017**, 29 1605884.

[13] Y.-L. Pei,Y. Liu, *J. Alloys Compd.* **2012,** 514, 40.

[14] S. N. Guin, V. Srihari, K. Biswas, *J. Mater. Chem. A* **2015**, 3, 648.

[15] Q. Zhang, F. Cao, K. Lukas, W. Liu, K. Esfarjani, C. Opeil, D. Broido, D. Parker, D. J. Singh, G. Chen, Z. Ren, *J. Am. Chem. Soc.* **2012**, 134, 17731.

[16] G. Ding, J. Li, G. Gao, *RSC Adv.* **2015**, 5, 91974.

[17] W. Albers, C. Haas, H. J. Vink, J. D. Wasscher, *J. Appl. Phys.* **1961**, 32 2220.

[18] Y. Zhou, L.-D. Zhao, *Adv. Mater.* **2017**, 29, 1702676.

[19] A. Banik, S. Roychowdhury, K. Biswas, *Chem. Commun.* **2018**, 54, 6573.

[20] Y.-M. Han, J. Zhao, M. Zhou, X.-X. Jiang, H.-Q. Leng, L.-F. Li, *J. Mater. Chem. A* **2015**, 3, 4555.

[21] S. Chandra, K. Biswas, *J. Am. Chem. Soc.* **2019**, 141, 6141.

[22] C. Chang, M. Wu, D. He, Y. Pei, C.-F. Wu, X. Wu, H. Yu, F. Zhu, K. Wang, Y. Chen, L. Huang, J.-F. Li, J. He, L.-D. Zhao, *Science* **2018**, 360, 778.

[23] Y. K. Lee, Z. Luo, S. P. Cho, M. G. Kanatzidis, I. Chung, *Joule* **2019**, 3, 719.

[24] M. Dutta, K. Pal, U.V. Waghmare,K. Biswas, *Chem. Sci.* **2019**, 10, 4905

[25] M. K. Jana, K. Pal, A.Warankar, P. Mandal, U. V. Waghmare, K. Biswas, *J. Am. Chem. Soc.* **2017**, 139, 4350.

[26] M. Samanta, K. Pal, P. Pal, U. V. Waghmare, K. Biswas, *J. Am. Chem. Soc.* **2018**, 140 5866.

[27] D. T. Morelli, V. Jovovic, J. P. Heremans, *Phys. Rev. Lett.* **2008**,101, 035901.

[28] S. N. Guin, A. Chatterjee, D. S. Negi, R. Datta, K. Biswas, *Energy Environ. Sci.* **2013**, 6 2603.

[29] S. Roychowdhury, M. Samanta, S. Perumal, K. Biswas, *Chem. Mater.* **2018**, 30, 5799.

[30] U. V. Waghmare, N. A. Spaldin, H. C. Kandpal, R. Seshadri, *Phys. Rev. B* **2003**, 67, 125111.

[31] A. Walsh, D. J .Payne, R. G. Egdell, G. W. Watson, *Chem. Soc. Rev.* **2011**, 40, 4455.

[32] K. R. Knox, E. S. Bozin, C. D. Malliakas, M. G. Kanatzidis and S. J. L. Billinge, *Phys. Rev. B* **2014,** 89, 014102.

[33] E. S. Božin, C. D. Malliakas, P. Souvatzis, T. Proffen, N. A. Spaldin, M. G. Kanatzidis and S. J. L. Billinge, *Science* **2010,** 330, 1660.

[34] K. Biswas, J. He, Q. Zhang, G. Wang, C. Uher, V. P. Dravid, M. G. Kanatzidis *Nat. Chem.* **2011**, 3, 160.

[35] J. Androulakis, C.-H. Lin, H. -J. Kong, C. Uher, C.-I. Wu, T. Hogan, B. A. Cook, T. Caillat, K. M. Paraskevopoulos, M. G. Kanatzidis, *J. Am. Chem. Soc.* **2007,** 129, 9780.

[36] J. Zhang, D. Wu, D. He, D. Feng, M. Yin, X. Qin, J. He, *Adv. Mater.* **2017**, 29, 1703148.

Chapter 2.2

Origin of Ultralow Thermal Conductivity in n-Type Cubic Bulk $AgBiS_2$: Soft Ag Vibrations and Local Structural Distortion Induced by the Bi $6s^2$ Lone Pair†

†*Paper based on this has been published as* ***E. Rathore****, R. Juneja, A. Singh, K. Biswas, Chem. Mater.* ***2019****, 31, 6, 2106.*

Chapter 2.2

Origin of Ultralow Thermal Conductivity in n-Type Cubic Bulk $AgBiS_2$: Soft Ag Vibrations and Local Structural Distortion Induced by the Bi $6s^2$ Lone Pair†

Summary: *Crystalline solids with ultralow thermal conductivity are essential for thermal barrier coating and thermoelectric energy conversion. Nontoxic n-type bulk cubic $AgBiS_2$ exhibits exceptionally low lattice thermal conductivity (κ_{lat}) of 0.68-0.48 W/mK in the temperature range 298- 820 K, which is near to its theoretical minimum (κ_{min}). The low κ_{lat} is attributed to soft vibrations of predominantly Ag atoms and significant lattice anharmonicity due to local structural distortions along the [011] direction, arising from the stereochemically active $6s^2$ lone pair of Bi, as suggested by synchrotron X-ray pair distribution function (PDF) analysis. Heat capacity of $AgBiS_2$ shows a broad hump at low temperatures due to the Ag-induced low energy Einstein modes as also evidenced from phonon dispersion calculated by first principles density functional theory (DFT). Low energy optical phonons contributed by Ag and Bi couple strongly with the heat carrying acoustic phonons, thereby decreasing the κ_{lat} to a low value. A maximum thermoelectric figure of merit of ~0.7 is achieved at 820 K for bulk spark plasma sintered n-type $AgBiS_2$.*

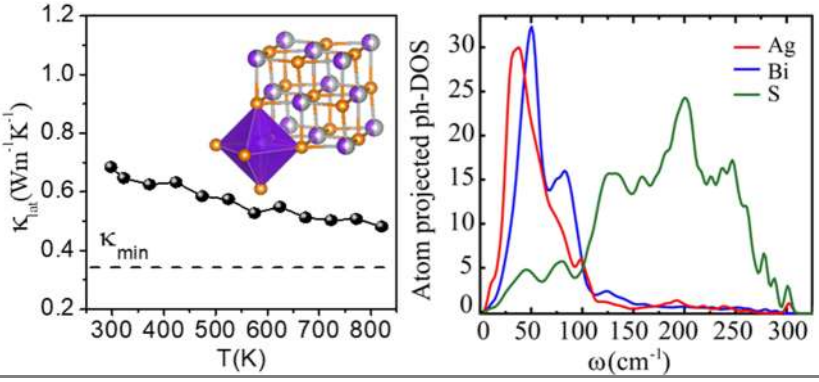

†*Paper based on this has been published as* ***E. Rathore****, R. Juneja, A. Singh, K. Biswas, Chem. Mater.* ***2019****, 31, 6, 2106.*

2.2.1. Introduction

The discovery of crystalline solids with low thermal conductivity is paramount for the development of thermoelectric materials, thermal barrier coatings and thermal energy management.[1-3] Substantial reductions in lattice thermal conductivity (κ_{lat}) of solids are usually achieved using extrinsic approaches for phonon scattering, *e.g.* nanostructuring[4-5] and all-scale hierarchial architecturing,[6-7] however, such methods introduce scattering of the charge carriers and slash the carrier mobility. On the contrary, solids with intrinsically low κ_{lat} have gained popularity due to the independent control over the electrical transport.[8] Intrinsically low κ_{lat} have been achieved for solids with complex crystal structures (*e.g.* skutterudites[9-10] or clathrates[11-12]), anharmonic ratting or soft phonon modes,[13-19] liquid-like cation disordering in superionic substructures,[20-25] as well as layered structures with lattice anharmonicity.[3,26]

Besides having low thermal conductivity and good electronic performance, thermoelectric energy conversion also demands earth abundant, non-toxic, and low-cost constituent elements, as leading advanced thermoelectric materials are mainly based on PbTe.[6,7,27-29] Researchers are currently exploring attractive potential alternatives for PbTe based on metal sulfides due to the toxicity of Pb and the extreme scarcity of Te.[30-40] For example, sulfur (S) is inexpensive, has longer-term price stability, and is 1000 times more abundant than Te.[35,38] Typically, sulfides have low thermoelectric figures of merit (zT) because of the low atomic weight of S, leading to high thermal conductivity, as well as the strong ionic character of sulfides inducing low carrier mobilities.[41-43] Nevertheless, metal sulfides have recently shown great promise as thermoelectric materials, though the performance attained with *n*-type sulfides[36,44-46] is still inferior to *p*-type sulfides.[47-48] An exception to this is ternary bulk silver bismuth sulfide, $AgBiS_2$, which belongs to the I-V-VI_2 class of compounds (where I = Cu/Ag/Au V = As/Sb/Bi and VI = S/Se/Te). $AgBiS_2$ generally crystallizes in the hexagonal structure (space group, $P\bar{3}m1$), which transforms into the cubic cation-disordered rock salt structure (space group $Fm\bar{3}m$) at 473 K (Figure 2.2.1).[37,49,50] Notably, the possible stereochemical activity of the $6s^2$ lone pair of Bi may create a locally-distorted structure, thereby inducing significant lattice anharmonicity. Previously, we have obtained moderate thermoelectric performance in solution phase synthesized cubic nanocrystals of $AgBiS_2$ with a zT of only ~0.2 at 810 K.[37] However, the thermal conductivity and advanced

thermoelectric properties of the bulk cubic $AgBiS_2$ phase are still unexplored. Furthermore, while studying the structure and chemical bonding of $AgBiS_2$ several questions arise. For example, what is local structure in cubic $AgBiS_2$? Is it different from the globally cubic structure? Additionally, the $6s^2$ lone pairs on Bi are know to distort the local structure, which is exploited in ferroelectric materials, *e.g.* $BiMnO_3$,[51] and thus, the implications of the ns^2 lone pair induced local structural distortions on the ultra-low κ_{lat} should also be investigated.

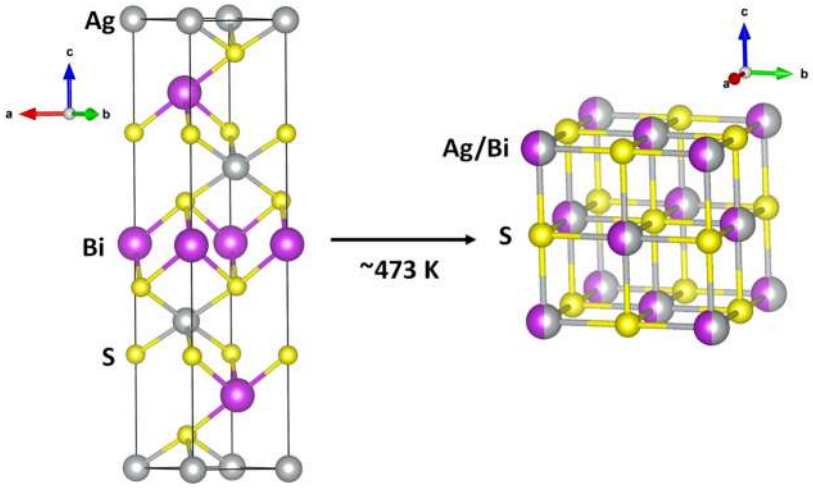

Figure 2.2.1 *Phase transition in $AgBiS_2$: room temperature hexagonal structure (space group, $P\bar{3}m1$) transforms into the cubic cation-disordered rock salt structure (space group $Fm\bar{3}m$) at 473 K.*

In this chapter, we demonstrate the ultra-low lattice thermal conductivity of 0.68-0.48 W/mK in the temperature range of 300–820 K in *n*-type non-toxic bulk cubic $AgBiS_2$. The measured low sound velocities indicate significant inhibition of phonon propagation in the crystal lattice. Low-temperature (2-30 K) heat capacity measurements show evidence of low energy Einstein modes (optical phonon modes), which is due to the soft vibration of Ag and Bi in $AgBiS_2$. This is further confirmed by first principle density functional theoretical (DFT) calculations of the phonon dispersion, which shows that low lying optical phonons generated mainly by Ag and Bi couple with heat carrying acoustic phonons, thereby decreasing κ_{lat} down to its theoretical minimum. Moreover, the local structure of $AgBiS_2$, as derived from synchrotron X-ray pair distribution function (PDF) analysis, is different from its global cubic structure. The

stereochemically active $6s^2$ lone pair of Bi distorts the local structure along the [011] direction, creating significant lattice anharmonicity, which results in a significant suppression of κ_{lat}. A maximum thermoelectric figure of merit (zT) of ~0.7 at 823 K is achieved in *n*-type bulk $AgBiS_2$.

2.2.2. Methods

2.2.2.1. Reagents. Elemental silver (Ag, 99.9999%, metal basis, Sigma Aldrich), elemental bismuth (Bi, 99.9999%, metal basis, Sigma Aldrich) and elemental sulfur (S, 99.999%, metal basis, Alfa Aesar) were used for synthesis without further purification.

2.2.2.2. Synthesis. Ingots (~7g) of pristine $AgBiS_2$ were synthesized by melting reaction of stoichiometric amounts of high-purity Ag, Bi and S in quartz tubes which were sealed under high vacuum (~ 10^{-5} Torr). The sealed tubes were slowly heated up to 723 K over 12 h, then heated up to 1173 K in 4 h, soaked for 10 h, and eventually nitrogen quenched to room temperature. The nitrogen quenched samples were crushed and ground with pestle and mortar. The powders were then transferred into a graphite die of 15 mm diameter and compressed before inserting the die assembly into a SPS system (SPS211-LX, Dr. Sinter Lab). The sintering-chamber was first evacuated to 10^{-3} Torr and then the powders were fused by pulsed electric current sintering at 873 K for 5 min under an axial pressure of 45 MPa. The SPS processed pellet is cut using a low-speed diamond saw and polished using a polisher for further electrical and thermal transport measurement. The density of the samples was found to be ~ 99% of the theoretical value of pristine $AgBiS_2$.

2.2.2.3. Powder X-ray diffraction. Power X-ray diffraction patterns for finely powder samples and the spark-plasma sintered pellets were recorded using a Cu K_α (λ = 1.5406 Å) radiation source on a Bruker D8 diffractometer.

2.2.2.4. Band Gap. To determine the room temperature optical band gaps, diffuse reflectance measurements were carried out over the range of 600 nm to 2500 nm using a Perkin Elmer Lambda 900, UV/Vis/NIR spectrometer in reflectance mode. Absorption (α/S) data were estimated from reflectance data using the Kubelka–Munk equation: $\alpha/S = (1- R)^2/(2R)$, where R is the reflectance, and α and S are the absorption and

scattering coefficient, respectively. The energy band gaps were obtained from a α/S vs. E (eV) plot.

2.2.2.5. Transmission Electron Microscopy (TEM). The high-resolution images and electron diffraction pattern of the as-synthesized materials were obtained using FEI TECNAI G2 20 STWIN TEM instrument (operating at 200 kV).

2.2.2.6. Electrical Transport. Electrical conductivity and Seebeck coefficients were measured concurrently under a helium atmosphere from room temperature to 823 K on a ULVAC RIKO ZEM-3 instrument system. The sample for the measurement is parallelepiped with dimensions of ~2 mm × 2 mm × 8 mm. Heating and cooling cycles gave repeatable electrical properties for a given sample. Electrical transport is measured in the same direction of thermal conductivity.

2.2.2.7. Thermal Transport. The thermal diffusivity (D) was measured by laser flash method (Netzsch LFA-457) from room temperature to 823 K. It was performed on carbon-coated square samples of 10 mm × 10 mm dimension and 2 mm thickness under a N_2 atmosphere. Temperature-dependent heat capacity, C_p, was derived using the standard sample (pyroceram) in LFA457. Cowan model with pulse correction was used to analyze the thermal diffusivity data. The total thermal conductivity, κ_{total}, was estimated using the formula: $\kappa_{\text{total}} = DC_p\rho$, where ρ is the density.

2.2.2.8. Heat Capacity Measurement. Low temperature (2−200 K) specific heat of $AgBiS_2$ is measured in Physical Property Measurement System (PPMS).

2.2.2.9. Sound Velocity Measurement. This part of the work has been performed in collaboration with Prof. Wolfgang Zeier's group in University of Muenster, Germany. Pulse-echo speed of sound measurements were performed on consolidated discs using an Epoch 600 (Olympus) with 5 MHz transducers for the longitudinal and transverse speeds of sound. The obtained longitudinal and transverse speeds of sound v_l and v_t can then be used to calculate the mean speed of sound v_m, as well as the Debye temperature Θ_D via Eq. 1–2[52-53]:

$$v_m{}^3 = \frac{3}{v_l{}^{-3} + 2v_t{}^{-3}} \qquad \text{Eq. 2.2.1.}$$

$$\Theta_D = \frac{v_m\, h}{2\pi k_B}\left(\frac{6\pi^2}{V}\right)^{1/3} \qquad \text{Eq. 2.2.2.}$$

The obtained longitudinal and transverse speeds of sound can be also used to calculate the Poisson ratio v_p and the Grüneisen parameter γ via Equations 3-4[54]:

$$v_p = \frac{1 - 2\left(v_t/v_l\right)^2}{2 - 2\left(v_t/v_l\right)^2} \qquad \text{Eq. 2.2.3.}$$

$$\gamma = \frac{3}{2}\cdot\frac{1 + v_p}{2 - 3v_p} \qquad \text{Eq. 2.2.4.}$$

The Grüneisen parameter gives direct information about the degree of anharmonicity in the lattice vibrations. Increased anharmonicity in the lattice vibrations results in a larger Grüneisen parameter for the system.[55]

2.2.2.10. Computational Methods. This part of the work has been performed in collaboration with Prof. Abhishek K Singh's group in IISC, Bangalore, India. The first principles calculations were performed using density functional theory (DFT)[56] as implemented in the Vienna *Ab initio* Simulation Package (VASP).[57-58] The ion-electron interactions were represented by Projector augmented wave (PAW)[59-60] pseudopotentials. The exchange and correlation part of the total energy was approximated using Perdew-Burke-Ernzerhof (PBE)[61] generalized gradient approximation. The special quasirandom structure (SQS) was generated using the Monte Carlo SQS tool as implemented in Alloy Theoretical Automated Toolkit (ATAT).[62] The structure was fully relaxed by employing a conjugate gradient scheme until the components of Hellmann-Feynman forces on the atoms were less than 0.0001 eV/Å. The calculation of harmonic interatomic force constants and the Grüneisen parameters was performed using on a 2x2x2 supercell using the Phonopy code.[63]A strict energy convergence of 10^{-8} eV and energy cut-off 400 eV was used to obtain accurate phonon frequencies.

$AgBiS_2$ crystallizes in Fm-3m space group, where the sulfur atoms occupy 4b (0.5, 0.5, 0.5) Wyckoff positions. Ag and Bi atoms can randomly occupy any of the 4a (0, 0, 0) sites, therefore, the modeled structure is generated using the special quasirandom structure (SQS) algorithm.[64-65] In the 2x2x2 supercell having 32 S, 16 Ag and 16 Bi

atoms, the 4a Wyckoff sites are occupied by the S atoms, whereas half of 4b sites are occupied by the Ag and remaining half of the sites are occupied by the Bi atoms. The SQS unit cell is shown in Figure 2.2.4a, with optimized lattice parameters are a=b=c= 11.54 Å.

2.2.2.11. X-ray Pair Distribution Function (PDF) Analysis. This part of the work has been performed in collaboration with Prof. Wolfgang Zeier's group in University of Muenster, Germany. Capillaries made of borosilicate glass with an outer diameter of 1.5 mm were filled in an argon glovebox and flame-sealed. X-ray scattering data suitable for pair distribution function and diffraction analysis were collected at room temperature using the I15-1 instrument at the Diamond Light Source (UK) beamline. High-energy X-rays ($\lambda = 0.161669$ Å, 76.6 keV, bent Laue monochromator) were used in combination with a PerkinElmer 1611 CP3 area detector.

Pair distribution function $G(r)$ data were extracted from the raw diffraction data using the PDFgetX2 software.[66] The collected data were first corrected for background, sample absorption, and Compton scattering. Then, normalized structure functions $[S(Q)]$ were obtained. Finally, $S(Q)$ was Fourier-transformed to yield $G(r)$. A maximum scattering vector (Q_{max}) of 28 $Å^{-1}$ was employed in the Fourier transform. Structural refinements were carried out using the PDFgui software.[67] The local crystal structure of $AgBiS_2$ was refined in both the $Fm\bar{3}m$ and $P1$ space groups, with the latter being employed to allow for structural distortions. It should also be noted that, back projections of the collected total scattering data were optimized to eliminate significant contributions from terminal ripples.

When modeling the experimental PDF over the r range of 2.5–25.5 Å, the following parameters were refined: (1) scale factor, (2) lattice parameters (3) correlated motion factor and (4) atomic isotropic displacement parameters. Additionally, upon reducing the symmetry to the $P1$ space group, the fractional atomic coordinates of Ag and Bi were also allowed to refine. The R_w indicator was employed to assess the quality of the refined structural models.[68]

2.2.3. Results and Discussions

Crystalline ingots of pristine cubic $AgBiS_2$ were synthesized by melting the elements at 1173 K in evacuated sealed quartz tubes and quenching the reactions using liquid nitrogen. The powder X-ray diffraction patterns can be indexed as pure cubic $AgBiS_2$ (space group, $Fm\bar{3}m$, Figure 2.2.2a).

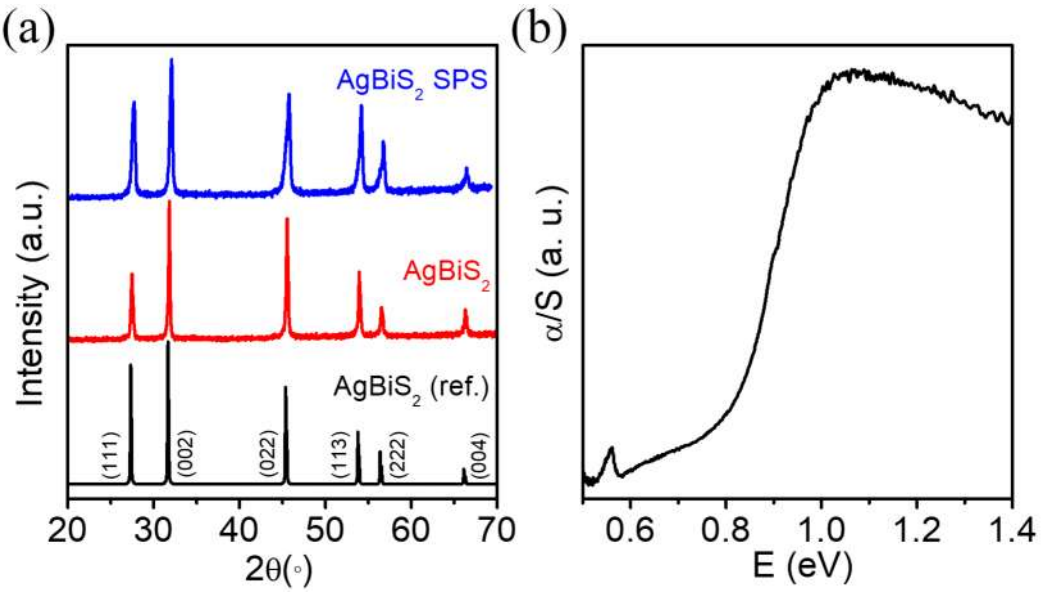

Figure 2.2.2. *(a) Powder XRD pattern of $AgBiS_2$ powdered sample and spark plasma sintered pellet (b) electronic absorption spectrum of $AgBiS_2$ obtained from diffused reflectance spectroscopy.*

The powdered samples were densified using SPS at 873 K and the diffraction pattern of the SPS pellet shows the retention of the cubic structure of $AgBiS_2$. An optical band gap of about 0.8 eV was obtained for cubic $AgBiS_2$ using diffuse reflectance spectroscopy (Figure 2.2.2b).

Figure 2.2.3a depicts the temperature-dependent lattice thermal conductivity (κ_{lat}) of cubic $AgBiS_2$ measured in the 300−820 K range. Bulk $AgBiS_2$ exhibits an ultra-low κ_{lat} of 0.68 W/mK at 300 K, which decreases to 0.48 W/mK at 820 K, *i.e.* close to the calculated theoretical lattice thermal conductivity minimum ($\kappa_{min} \sim 0.34$ W/mK), estimated using Cahill's model[69]:

$$\kappa_{min} = \frac{3}{2}\left(\frac{\pi}{6}\right)^{1/3} k_B \, v_m V^{-2/3} \qquad \text{Eq. 2.2.5.}$$

where k_B, v_m, and V is Boltzmann constant, mean sound velocity (1659 ± 85 m/s), and volume per atom.

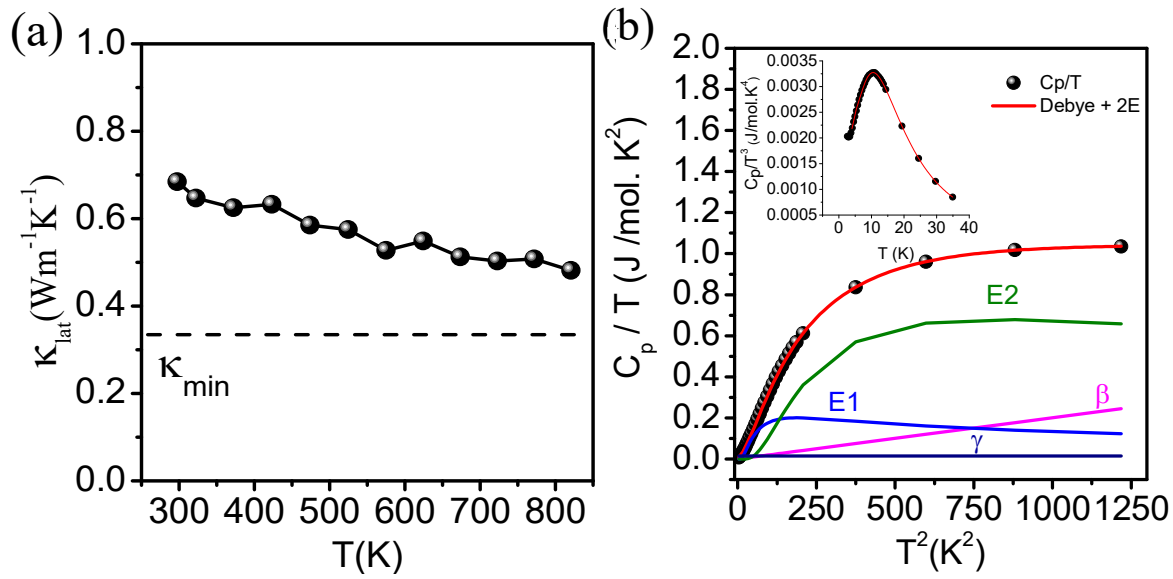

Figure 2.2.3. *(a) κ_{lat} of $AgBiS_2$ measured between 300 and 820 K. The dashed line is the theoretical κ_{min} of $AgBiS_2$ (b) C_p/T vs T^2 plot in 2–35 K range. The solid red line is calculated using combined Debye–Einstein model. The individual contributions from electronic (γ), Debye (β) and the two Einstein terms (E1, E2) are also plotted. Inset shows plot of Cp/T^3 vs T plot.*

The longitudinal and transverse sound velocities measured are 3047 ± 85 m/s and 1476 ± 13 m/s respectively. These low velocities of sound indicate the material has soft bonding interactions, which can be linked to phonon-interactions and propagation in crystals.[33] The Grüneisen parameter (γ), obtained from the sound velocity measurement via Eq. 4, is 2.1 ± 0.1 which is higher than the standard thermoelectric materials such as PbTe (1.65 to 1.94)[70-71] and Bi_2Te_3 (1.49)[72] but lower than that of SnSe (3.13).[71] This indicates significant lattice anharmonicity in $AgBiS_2$.[55]

In order to better understand the mechanism for the ultra-low κ_{lat} of $AgBiS_2$ and to investigate the occurrence of independent Einstein oscillator modes (*e.g.* soft or low energy vibration modes), the low temperature heat capacity (C_p) of $AgBiS_2$ was measured (Figure 2.2.3b), and fitted, using the C_p/T vs T^2 plot, to a combined Debye-Einstein model:[17, 23, 73]

$$\frac{C_p}{T} = \gamma + \beta T^2 + \sum_n \left(A_n \left(\Theta_{E_n}\right)^2 . \ (T^2)^{-3/2} \ . \ \frac{e^{\Theta_{E_n}/T}}{\left(e^{\Theta_{E_n}/T} - 1\right)^2} \right) \qquad \text{Eq. 2.2.6}$$

where the first term, γ, denotes the electronic contribution, the second term, $\beta = B.\left(12\pi^4 N_A \kappa_B / 5\right).(\Theta_D)^{-3}$, offers the contribution from the Debye mode and k_B, N_A, and Θ_D are the Boltzmann constant, Avogadro number, and Debye temperature, respectively. Herein, B is calculated by $B = 1 - \Sigma_n A_n/3NR$, where R is the universal gas constant (8.314 J $mole^{-1}K^{-1}$) and N is the number of atoms per formula unit. The last term in Eq. 6 provides the contribution from the Einstein oscillator modes, where A_n corresponds to the Einstein prefactor of the n^{th} Einstein mode, Θ_{En}. The low temperature C_p in the range of 2-35 K of $AgBiS_2$ cannot be effectively fitted solely with the Debye contribution and requires a minimum of two Einstein modes whose characteristic temperatures are estimated from the fits to be $\Theta_{E1} = 35.61$ K (i.e. ~25 cm^{-1}), $\Theta_{E2} = 73.94$ K (~51 cm^{-1}). The calculated Debye temperature (Θ_D) for $AgBiS_2$ is 182 K, which is close to the value of 175.9 ± 1.2 K that obtained from the sound velocity measurements. The other derived parameters are provided in the Table 2.2.1 below

.

Table 2.2.1. *Parameters obtained by modeling low temperature Cp/T vs T^2 data of $AgBiS_2$ by using combined Debye-Einstein equation.*

Parameters	Derived values
$\gamma/10^{-2}$ (J $mol^{-1}K^{-2}$)	1.40 ± 0.17
$B/10^{-4}$ (J $mol^{-1}K^{-4}$)	2.00 ± 0.11
A_1 (J $mol^{-1}K^{-1}$)	4.69 ± 0.42
Θ_{E1} (K)	35.61 ± 0.96 (~ 25 cm^{-1})
A_2 (J mol^{-1} K^{-1})	32.97 ± 0.54
Θ_{E2} (K)	73.94 ± 0.99 (~ 51 cm^{-1})
Θ_D (K)	181.9 (~ 126 cm^{-1})
R^2	0.99984

A broad hump is observed in the C_p/T^3 vs T (inset in Figure 2.2.3b), which cannot be accounted for solely by the Debye model, but can be fitted well with the combined Debye-Einstein model. The broad peak resembles the Boson-like hump observed in disordered glasses, whereas recently in $TlInTe_2$ and BiSe,[17,13] it was ascribed to an excess phonon density of states (PDOS) due to low energy vibrations of a selective sub-lattice, observed in low temperature heat capacity measurements. In $AgBiS_2$, an excess contribution to C_p at low temperatures arises due to low-energy optical phonon modes from soft vibrations of Ag and/or Bi. These soft vibrations behave like Einstein oscillators, as confirmed by our first-principles DFT calculation of the phonon dispersion (*vide infra*). The low energy optical phonon modes scatter the heat-carrying acoustic phonons, thereby suppressing κ_{lat} in $AgBiS_2$.

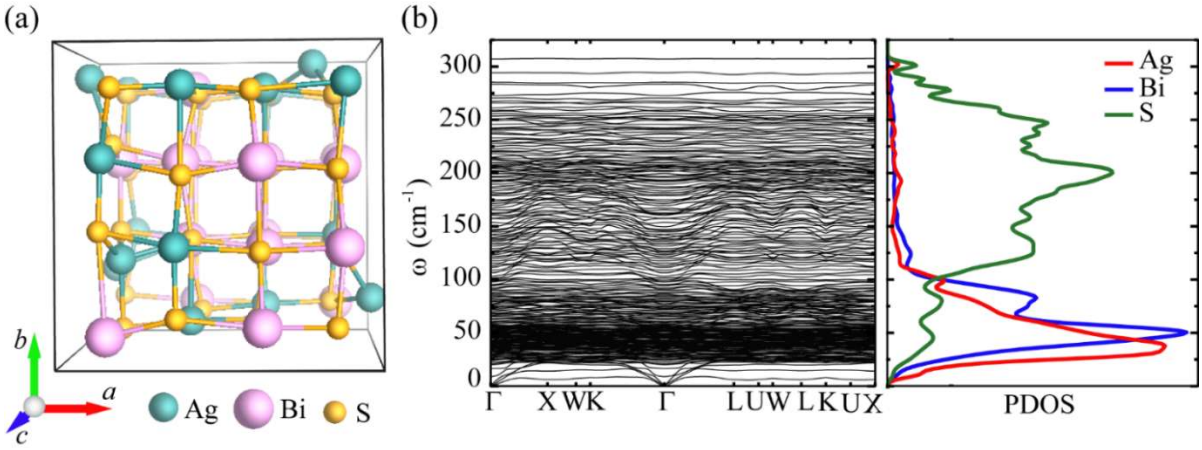

Figure 2.2.4. *(a) The SQS unit cell of modeled $AgBiS_2$, (b) calculated phonon dispersion and atom-projected phonon density of states (PDOS) for $AgBiS_2$.*

The modeled structure of $AgBiS_2$ generated using the special quasirandom structure (SQS) algorithm is shown above in Figure 2.2.4a. The calculated phonon dispersion and atomic projected phonon density of states (PDOS) are also shown in Figure 2.2.4b. The absence of any negative frequencies imply the dynamic stability of the system. Furthermore, the phonon density of states shows that both Ag and Bi strongly contribute to the low-frequency regime below 100 cm^{-1}, whereas the lighter S atoms contribute dominantly to the high-frequency regime (see right panel in Figure 2.2.4b). The PhDOS for the Ag and Bi atoms exhibit clear peaks around ~35.6 cm^{-1} and

~48.4 cm^{-1}, which are in close agreement with the two Einstein modes (Θ_{E1} = 35.6 K i.e., ~25 cm^{-1}, Θ_{E2} = 73.9 K i.e ~51 cm^{-1}) obtained from the experimental temperature-dependent C_p data of $AgBiS_2$. Thus, low energy optical phonon modes arise predominately from the soft vibrations of Ag and partially from Bi in $AgBiS_2$, which play a significant role in lowering its κ_{lat}.

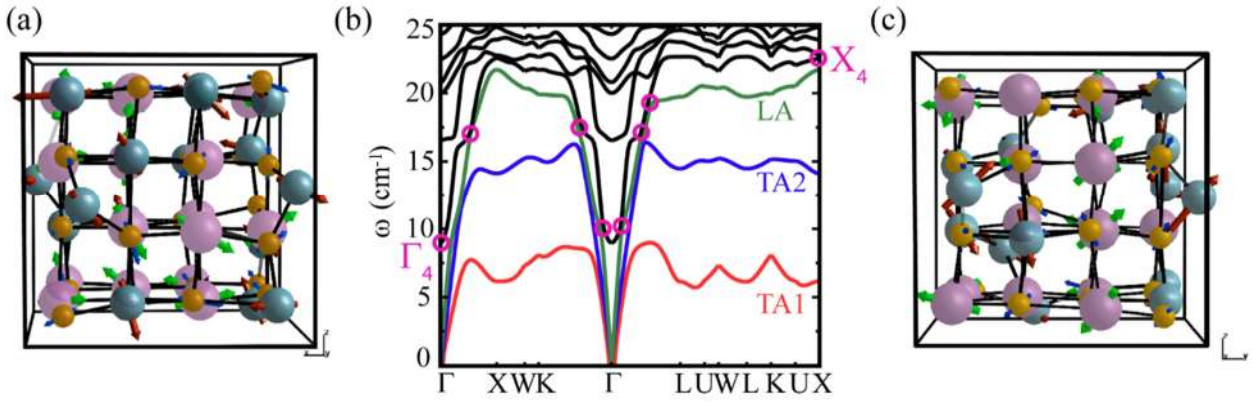

2.2.5. *(a) and (c) snapshots of lowest frequency optical modes at Γ and X point, respectively. The cyan, violet, and yellow color represent Ag, Bi and S atoms, respectively. (b) Expanded view of phonon dispersion in low-frequency regime.*

Figure 2.2.5b shows the zoomed region of the low-frequency phonon modes of $AgBiS_2$, where the first three acoustic branches are shown in red, blue and green, respectively and the black curves correspond to the optical phonon branches. The low-lying optical branches avoid crossing with the acoustic branches, as shown by the magenta circles in Figure 2.2.5b. The avoided-crossing is the hallmark of the presence of soft vibrational modes, which arise from the Ag (predominantly) and Bi atoms. As an example, snapshots of two such modes at X_4 and Γ_4 points with corresponding Eigen displacements are given in Figure 2.2.5a and c. The amplitude of these Eigen modes is quite large at the avoided crossing points, which is indicative of a large anharmonicity. To gain further insight into the origin of these soft vibration modes, the potential energies from displacing Ag, Bi and S atoms from their equilibrium positions in the x-, y- and z-directions have also been calculated (see Figure 2.2.6). The displacement-dependent average potential energies clearly show a relatively flat potential well for Ag atoms and a steep potential well for the S atoms. This implies that the Ag atoms can

be more easily excited out of their equilibrium positions relative to the other component elements, thereby further substantiating the fact that soft vibrations are more pronounced by Ag atoms in $AgBiS_2$.

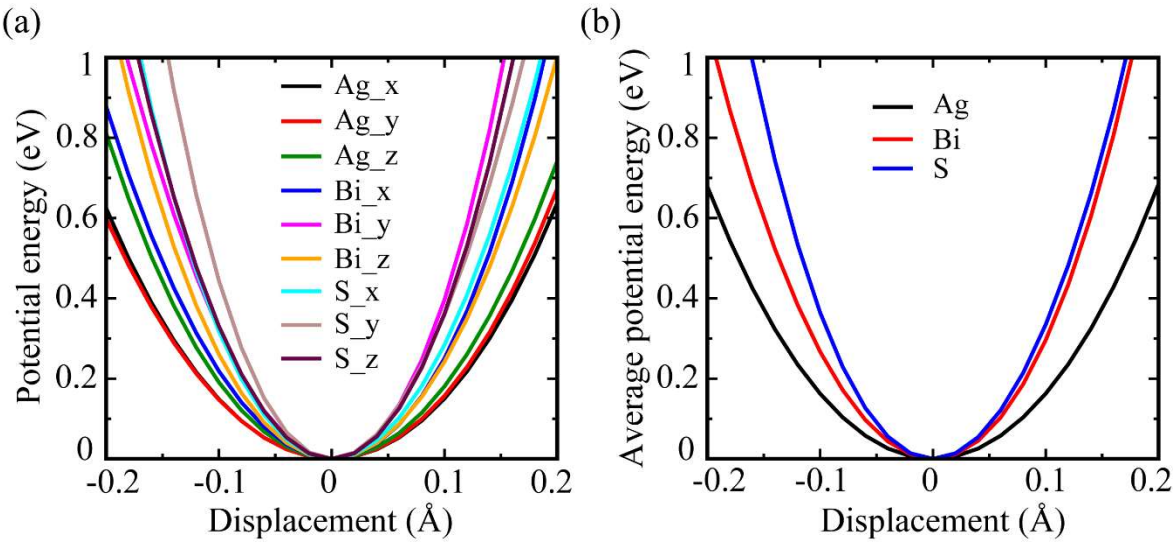

Figure 2.2.6. *(a) Potential energy versus displacement of Ag, Bi and S along x-, y- and z- directions, (b) average potential energy versus displacement.*

In PbQ (Q = S/Se/ Te), anharmonic displacement of the cations provides local structural distortions in the high-symmetry rocksalt structure.[74-76] It is generally believed that, the stereochemical expression of the $6s^2$ lone pair of Pb^{2+} is the reason for the displacement and local distortions.[55] While on average, these distortions do not seem to break long-range symmetry, thus preserving the average crystallographic structure,[77] inelastic neutron scattering suggests a dynamic nature and strong anharmonicity of the lattice vibrations.[78-79] Importantly, while it is frequently observed that the global structure does not agree with the local structure in a variety of materials,[80-82] the local differences observed in the case of PbQ originate from the ns^2 lone pair of Pb^{2+}. Herein, we expect similar local structural distortions in cubic $AgBiS_2$, as Bi^{3+} possesses a similar $6s^2$ lone pair, which may contribute to the low κ_{lat}. While simple XRD and TEM (Figure 2.2.7) show the global structure of $AgBiS_2$ is cubic but to probe the local structure, we have performed pair distribution function (PDF) analysis of synchrotron X-ray data of bulk cubic $AgBiS_2$ at room temperature.

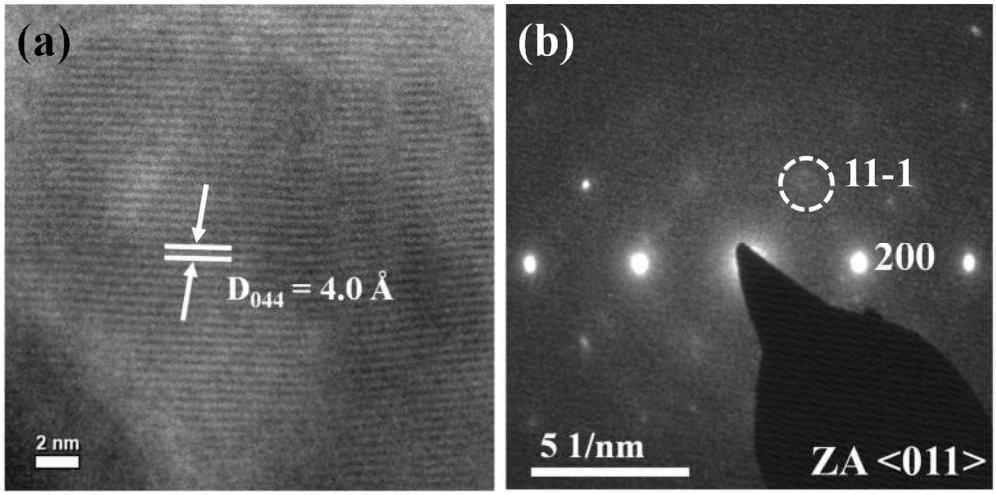

Figure 2.2.7. *(a) High resolution TEM image and (b) electron diffraction pattern of bulk $AgBiS_2$ sample.*

Figure 2.2.8 shows the X-ray PDF analysis results for $AgBiS_2$. Using the average rock salt structure ($Fm\bar{3}m$), the obtained G(r) could be fit well in the region of 4.5–25.5 Å (Figure 2.2.8c), however, some anomalies were observed in the low-r region (i.e., 2.5–4.5 Å Figure 2.2.8e), where the short-range M–S bond distances can be found. More specifically, a shoulder exists that cannot be explained by the average structural model. Upon reducing the symmetry to $P1$ and allowing the center of the octahedra (*i.e.,* the Ag/Bi positions) to refine freely, a mild distortion of the unit cell (Figure 2.2.8b) provided a better fit to the low-r region (Figure 2.2.8f), accompanied by a lower R_w value. These fits suggest the presence of a significant local distortion on a length scale of only a few unit cells, as the asymmetry can only be found in the low-r range. While in PbQ, the distortion seems to occur along the [100] direction,[75] here the distortion is slightly While the average structural model using $Fm\bar{3}m$ leads to a good fit of the data at higher r distances, the low-r range is not adequately described. Introducing small degrees of freedom for distortion leads to an improvement of the fit. The distortion is more pronounced in the [011] direction, *i.e.* towards the edge of the octahedra. Given that the distortion occurs on the local scale, the atomic fluctuations indeed do not break long-range symmetry and no significant changes in the Bragg data are expected. While Ag and Bi cannot be distinguished here, these distortions likely arise from the Bi^{3+} atoms, given that it is the only element with a $6s^2$ lone pair that can become stereochemically active.

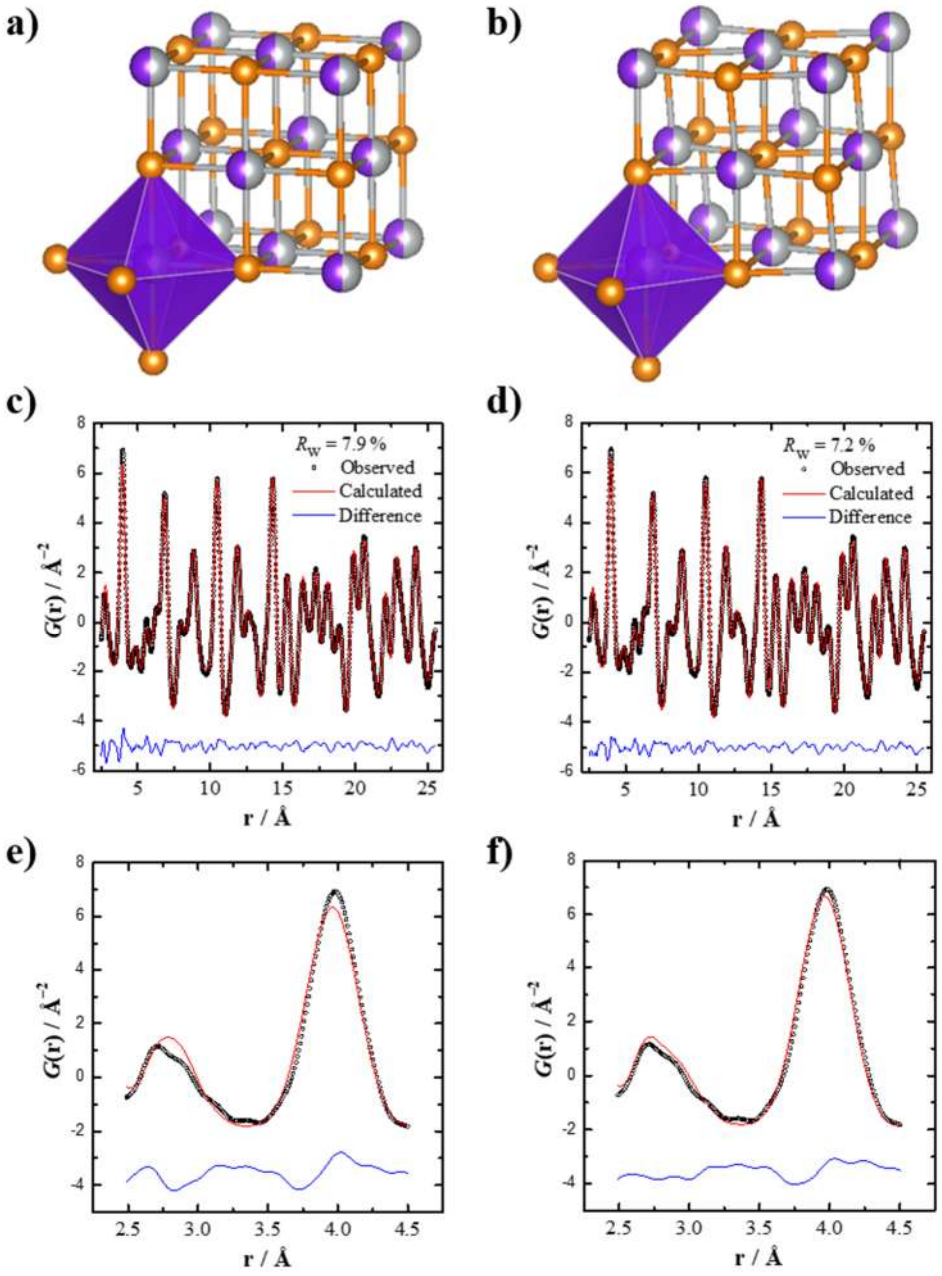

Figure 2.2.8. *(a) Undistorted structure of $AgBiS_2$ in the cubic unit cell with space group $Fm\bar{3}m$. (b) Refined $AgBiS_2$ with small distortions of the central cations away from the octahedral center in space group P1 (orange: S; violet: Bi; Grey: Ag). Experimentally obtained G(r) of the synchrotron total scattering data refined for the undistorted (c) and distorted unit cell (d), along with a zoom-in to the low-r range for the undistorted (e) and distorted (f) unit cells.*

The wave function of the Bi $6s^2$ lone pair is diffused and interact with the S p-orbitals with the extent of overlap scaling with bond ionicity. This Bi-s and S-p repulsion drives local structural distortion to a lower symmetry to stabilize the $6s^2$ lone pair, but the global structure remains cubic. However, just below this threshold where the local cubic $AgBiS_2$ is marginally stable, the $6s^2$ orbitals are very sensitive to small, local variations in bond distances induced by lattice vibrations. As a result of this local distortion, the bonds become strongly anharmonic with a high Grüneisen parameter (γ) of 2.1. The lone pair on Bi^{3+} plays an important role in deforming the lattice vibrations, which results in strong anharmonicity and thus, an ultra-low thermal conductivity in $AgBiS_2$.

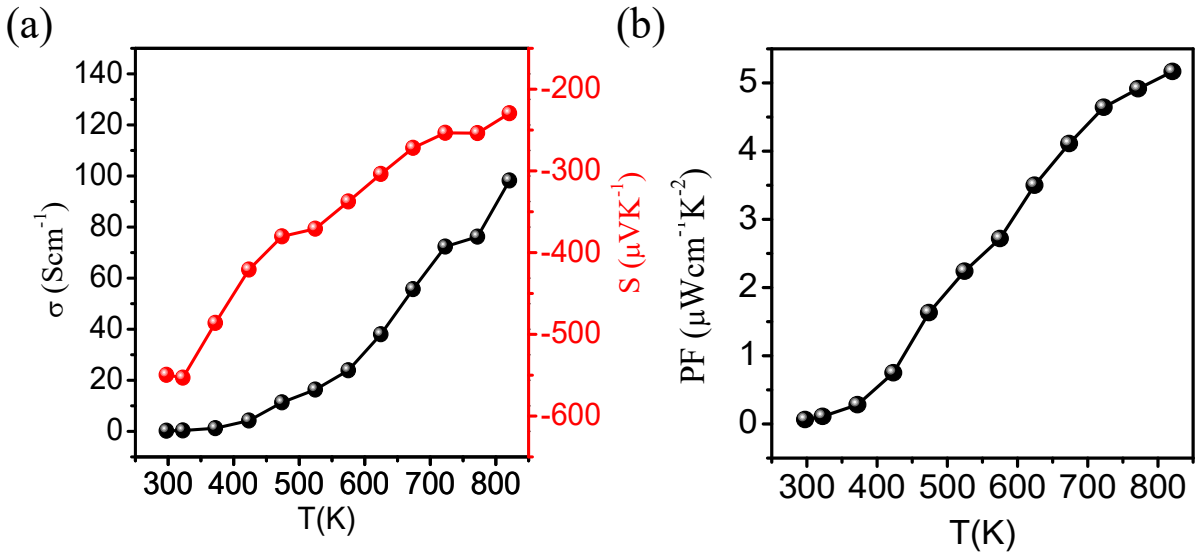

Figure 2.2.9. *Temperature-dependent (a) electrical conductivity (σ) and Seebeck coefficient (S) and (b) power factor of bulk $AgBiS_2$.*

Figure 2.2.9 shows the temperature-dependent electrical conductivity (σ) and Seebeck coefficient (S) for $AgBiS_2$ in the temperature range of 300-820 K. Typically, bulk $AgBiS_2$ has a σ of ~0.2 S cm^{-1} at 297 K, which rapidly increases to ~98 S cm^{-1} at 820 K. Moreover, the negative sign of S indicates an n-type conduction. The room temperature S for bulk $AgBiS_2$ is ~ – 549 μVK^{-1}, which decreases to ~ – 229 μVK^{-1} at 820 K. Additionally, a maximum power factor of 5.16 $\mu W\ cm^{-1}K^{-2}$ is achieved at 820 K (Figure 2.2.10). The temperature-dependent zT of $AgBiS_2$ is provided in Figure 2.2.9b

and a maximum zT of ~ 0.7 is achieved at 820 K, which is significant in terms n-type pristine nontoxic metal sulfides.

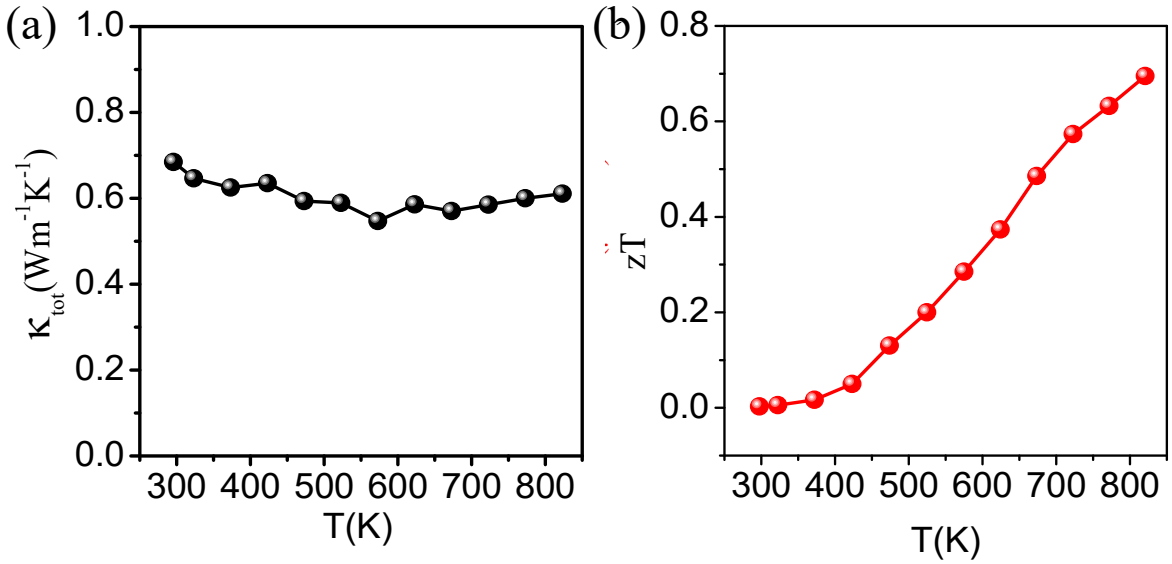

Figure 2.2.10. *Temperature-dependent (a) total thermal conductivity (κ_{tot}) and (b) thermoelectric figure of merit (zT) of cubic bulk $AgBiS_2$ sample.*

2.2.4. Conclusions

In summary, an ultra-low lattice thermal conductivity (κ_{lat}) of 0.68-0.48 W/mK in the temperature range 300- 820 K was found in bulk phase, *n*-type cubic $AgBiS_2$. The low κ_{lat} is attributed to the soft lattice vibrations of predominately Ag and strong lattice anharmonicity stemming from the $6s^2$ lone pair of Bi. $AgBiS_2$ possesses a locally distorted structure along the crystallographic [011] direction due the stereochemical activity of the Bi^{3+} lone pair, while the global structure remains cubic. Furthermore, the soft vibrations of Ag and the anharmonicity from Bi generate low energy optical phonon modes that strongly couple with the heat-carrying phonons, thereby providing a substantially low κ_{lat} in bulk cubic $AgBiS_2$. Ultimately, a zT of ~0.7 at 820 K was obtained for $AgBiS_2$. While further enhancements to the thermoelectric properties can also be achieved through the optimization of the *n*-type carrier concentration upon halide doping of the S^{2-} anion sublattice of $AgBiS_2$, the results presented herein are highly noteworthy among *n*-type metal sulfide thermoelectric materials.

2.2.5. References

[1] J. R. Sootsman, D. Y. Chung, M. G. Kanatzidis, *Angew. Chem. Int. Ed.* **2009**, *48*, 8616.

[2] G.Tan, L. -D. Zhao, M. G.Kanatzidis, *Chem. Rev.* **2016**, *116*, 12123.

[3] C. Chang, M. Wu, D. He, Y. Pei, C.-F. Wu, X.Wu, H. Yu, F. Zhu, K.Wang, Y.Chen, L.Huang, J.-F.Li, J . He, L.-D.Zhao, *Science* **2018**, 360, 778.

[4] K. Biswas, J. He, Q. Zhang, G. Wang, C.Uher, V. P. Dravid, M. G. Kanatzidis, *Nat. Chem.* **2011**, *3*, 160.

[5] L.-D. Zhao, S. Hao, S. -H. Lo, C. -I. Wu, X. Zhou, Y. Lee, H. Li, K. Biswas, T. P. Hogan, C. Uher, C. Wolverton, V.P. Dravid, M. G. Kanatzidis, *J. Am. Chem. Soc.* **2013**, *135*, 7364.

[6] K. Biswas, J. He, I. D. Blum, C. -I. Wu, T. P. Hogan, D. N. Seidman, V. P. Dravid, M. G. Kanatzidis, *Nature* **2012**, *489*, 414.

[7] B. Poudel, Q. Hao, Y. Ma, Y. Lan, A. Minnich, B. Yu, X. Yan, D. Wang, A. Muto, D. Vashaee, X. Chen, J. Liu, M. S. Dresselhaus, G. Chen, Z. Ren, *Science* **2008**, *320*, 634.

[8] M. K. Jana, K. Biswas, *ACS Energy Lett.* **2018**, 3, 1315.

[9] X. Shi, J. Yang, J. R. Salvador, M. Chi, J. Y. Cho, H. Wang, S. Bai, J. Yang, W. Zhang, L. Chen, *J. Am. Chem. Soc.* **2011**, 133, 7837.

[10] B. C. Sales, D. Mandrus, R. K. Williams, *Science* **1996**, *272*, 1325.

[11] T. Takabatake, K. Suekuni, T. Nakayama, E. Kaneshita, *Rev. Mod. Phys.* **2014**, *86*, 669.

[12] G. S. Nolas, J. L. Cohn, G. A. Slack, S. B. Schujman, *Appl. Phys. Lett.* **1998**, *73*, 178.

[13] M. Samanta, K. Pal, P. Pal, U. V. Waghmare, K. Biswas, *J. Am. Chem. Soc.* **2018**, 140, 5866.

[14] D. J. Voneshen, K. Refson, E. Borissenko, M. Krisch, A. Bosak, A. Piovano, E. Cemal, M. Enderle, M. J. Gutmann, M. Hoesch, M. Roger, *Nat. Mater.* **2013**, *12*, 1028.

[15] L. Bjerg, B. B. Iversen, G. K. Madsen, *Phys. Rev. B* **2014**, *89*, 24304.

[16] M. K. Jana, K. Pal, U. V. Waghmare, K. Biswas, *Angew. Chem. Int. Ed.* **2016**, 128, 7923.

[17] M. K. Jana, K. Pal, A.Warankar, P. Mandal, U. V. Waghmare, K. Biswas, *J. Am. Chem. Soc.* **2017**, 139, 4350.

[18] B. Jiang, P. Qiu, H. Chen, Q. Zhang, K. Zhao, D. Ren, X. Shi, L. Chen, *Chem. Commun.* **2017**, *53*, 11658.

[19] S. Lin, W. Li, S. Li, Z. Zhang, Z. Chen, Y. Xu, Y. Chen, Y. Pei, , *Joule* **2017**, *1*, 816.

[20] W. Qiu, L. Xi, P. Wei, X. Ke, J. Yang, W. Zhang, *Proc. Natl. Acad. Sci.* **2014**, *111*, 15031.

[21] S. N. Guin, J. Pan, A. Bhowmik, D. Sanyal, U. V. Waghmare, K. Biswas, *J. Am. Chem. Soc.* **2014**, *136*, 12712.

[22] A. A. Olvera, N. A. Moroz, P. Sahoo, P. Ren, T. P. Bailey, A. A. Page, C. Uher, P. F. P.Poudeu, *Energy Environ. Sci.* **2017**, 10, 1668.

[23] H. Liu, X. Shi, F. Xu, L. Zhang, W. Zhang, L. Chen, Q. Li, C. Uher, T. Day, G. J. Snyder, *Nat. Mater.* **2012**, *11*, 422.

[24] S. Roychowdhury, M. K. Jana, J. Pan, S. N. Guin, D. Sanyal, U. V. Waghmare, K.Biswas, *Angew. Chem. Int. Ed.* **2018**, 57, 4043.

[25] F. Gascoin, A. Maignan, *Chem. Mater.* **2011**, 23, 2510.

[26] L.-D. Zhao, S.-H. Lo, Y. Zhang, H. Sun, G. Tan, C. Uher, C. Wolverton, V. P. Dravid, M. G. Kanatzidis, *Nature* **2014**, *508*, 373.

[27] J. P. Heremans, V. Jovovic, E. S. Toberer, A. Saramat, K. Kurosaki, A. Charoenphakdee, S. Yamanaka, G. J. Snyder, *Science* **2008**, *321*, 554.

[28] K. F. Hsu, S. Loo, F. Guo, W. Chen, J. S. Dyck, C. Uher, T. Hogan, E. K. Polychroniadis, M. G. Kanatzidis, *Science* **2004**, *303*, 818.

[29] G.Tan, F. Shi, S. Hao, L.-D. Zhao, H. Chi, X. Zhang, C. Uher, C. Wolverton, V. P. Dravid, M. G. Kanatzidis, *Nat. Commun.* **2016**, *7*, 12167.

[30] Y. Sun, M. Christensen, S. Johnsen, N. V. Nong, Y. Ma, M. Sillassen, E. Zhang, A. E. C. Palmqvist, J. Bøttiger, B. B. Iversen, *Adv. Mater.* **2012**, *24*, 1693.

[31] A. Zevalkink, E. S. Toberer, W. G. Zeier, E. Flage-larsen, G. J. Snyder, *Energy Environ. Sci.* **2011**, *4*, 510.

[32] X. Lu, D. T. Morelli, Y. Xia, F. Zhou, V. Ozolins, H. Chi, X. Zhou, *Adv. Energy Mater.* **2013**, *3*, 342.

[33] P. Ying, X. Li, Y. Wang, J. Yang, C. Fu, W. Zhang, X. Zhao, T. Zhu, *Adv. Funct. Mater.* **2017**, 27, *1604145*.

[34] T. Yamada, H. Yamane, H. A. Nagai, *Adv. Mater.* **2015**, *27*, 4708.

[35] Z. Hu, S. Gao, , *Chem Geol.* **2008**, *253*, 205.

[36] K. Biswas, L. D. Zhao, M. G. Kanatzidis, *Adv. Energy Mater.* **2012**, 2, 634.

[37] S. N. Guin, K. Biswas, *Chem. Mater.* **2013**, *25*, 3225.

[38] M. Vázquez, E. Pallé, P. M. Rodríguez, *The Earth as a Distant Planet: A Rosetta Stone for the Search of Earth-Like Worlds, The Earth in Time* **2018** pp 35.

[39] J. Y. Ahn, J.-Y. Hwang, B. K. Ryu, M.-W. Oh, K. H. Lee, S. W. Kim, *CrystEngComm* **2016**, *18*, 1453.

[40] S. Bhattacharya, R. Chmielowski, G. Dennler, G. K. H. Madsen, *J. Mater. Chem. A* **2016**, *4*, 11086.

[41] H. Xie, X. Su, G. Zheng, T. Zhu, K. Yin, Y. Yan, C. Uher, M. G. Kanatzidis, X. Tang, *Adv. Energy Mater.* **2017**, 7, 1601299.

[42] M. Beaumale, T. Barbier, Y. Bréard, S. Hébert, Y. Kinemuchi, E. Guilmeau, *J. Appl. Phys.* **2014**, *115*, *43704*.

[43] H. Wang, E. Schechtel, Y. Pei, G. J. Snyder, *Adv. Energy Mater.* **2013**, *3*, 488.

[44] Z. Liu, H. Geng, J. Shuai, Z. Wang, J. Mao, D. Wang, Q. Jie, W. Cai, J. Sui, Z. Ren, *J. Mater. Chem. C* **2015**, *3*, 10442.

[45] E. Guilmeau, Y. Bréard, A. Maignan, *Appl. Phys. Lett.* **2011**, *99*, 52107.

[46] G. Tan, S. Hao, J. Zhao, C. Wolverton, M. G. Kanatzidis, *J. Am. Chem. Soc.* **2017**, *139*, 6467.

[47] P. Qiu, T. Zhang, Y. Qiu, L. Chen, *Energy Environ. Sci.* **2014**, 7, 4000.

[48] C. Bourgès, Y. Bouyrie, A. R. Supka, R. Al, O. I. Lebedev, M. Ohta, K. Suekuni, V. Nassif, R. Daou, Y. Miyazaki, M. Fornari, E. Guilmeau, *J. Am. Chem. Soc.* **2018,** 140, 2186.

[49] D. T. Morelli, V. Jovovic, J. P. Heremans, *Phys. Rev. Lett.* **2008**, *101*, 35901.

[50] M. D. Nielsen, V. Ozolins, J. P. Heremans, *Energy Environ. Sci.,* **2013**, 6, 570.

[51] R. Seshadri, N. A. Hill, *Chem. Mater.* **2001**, 13, 2892.

[52] A. F. May, G. J. Snyder, *Introduction to Modeling Thermoelectric Transport at High Temperatures. In Thermoelectrics Handbook: Thermoelectrics and its Energy Harvesting* Rowe, D. M., Ed. CRC Press: Boca Raton, FL, **2012**.

[53] O. L. Anderson, *J. Phys. Chem. Solids* **1963**, *24*, 909.

[54] L.-D. Zhao, J. He, D. Berardan, Y. Lin, J.-F. Li, C.-W. Nan, N. Dragoe, *Energy Environ. Sci.* **2014**, 7, 2900.

[55] W. G. Zeier, A. Zevalkink, Z. M. Gibbs, G. Hautier, M. G. Kanatzidis, G. J. Snyder, *Angew.Chem. Int. Ed.* **2016**, *55*, 6826.

[56] W. Kohn, L. Sham, *J. Phys. Rev.* **1965**, *140*, A1133.

[57] G. Kresse, Furthmüller, *Comput. Mater. Sci.* **1996**, *54*, 11169.

[58] G. Kresse, Furthmiiller, *J. Phys Rev B.* **1996**, 6, 15.

[59] P. E.Blöchl, *Phys. Rev. B* **1994**, *50*, 17953.

[60] G. Kresse, D. Joubert, *Phys. Rev. B* **1999**, *59*, 1758.

[61] J. P. Perdew, K. Burke, M. Ernzerhof, , *Phys. Rev. Lett.* **1996**, *77*, 3865.

[62] A. van de Walle, P. Tiwary, M. de Jong, D. L. Olmsted, M. Asta, A. Dick, D. Shin, Y. Wang, L. Q. Chen, Z. K. Liu, *Calphad* **2013**, *42*, 13.

[63] A. Togo, Tanaka, *Scr. Mater.* **2015**, 108, 1.

[64] A. Zunger, S.-H. Wei, L. G. Ferreira, J. E. Bernard, *Phys. Rev. Lett.* **1990**, *65*, 353.

[65] S.-H. Wei, L. G. Ferreira, J. E. Bernard, A. Zunger, *Phys. Rev. B* **1990**, *42*, 9622.

[66] X. Qiu, J. W.Thompson, S. J. L. Billinge, *J. Appl. Cryst.* **2004**, *37*, 678.

[67] C. L. Farrow, P. Juhas, J. W. Liu, D. Bryndin, E. S. Božin, J. Bloch, T. Proffen, S. J. L. Billinge, *J. Phys. Condens. Matter* **2007**, *19*, 335219.

[68] T. Egami, S. J. L. Billinge, *Underneath the Bragg Peaks: Structural Analysis of Complex Materials*, 7th ed. Cahn, R. W., Ed. Pergamon Materials Series: Oxford, **2003.**

[69] D. G. Cahill, S. K. Watson, R. O. Pohl, *Phys. Rev. B* **1992**, *46*, 6131.

[70] S. H. Lo, J. He, K. Biswas, M. G. Kanatzidis, V. P. Dravid, *Adv. Funct. Mater.* **2012,** *22,* 5175.

[71] Y. Xiao, C. Chang, Y. Pei, D. Wu, K. Peng, X. Zhou, S. Gong, J. He, Y. Zhang, Z. Zeng, L. D. Zhao, *Phys. Rev. B* **2016,** 94, 125203.

[72] J. O. Jenkins, J. A. Rayne, R. W. Ure, *Phys. Rev. B* **1972***, 5*, 3171.

[73] H. Liu, J. Yang, X. Shi, S. A. Danilkin, D. Yu, C. Wang, *J Mater.* **2016**, *2*, 187.

[74] B. Sangiorgio, E. S. Bozin, C. D. Malliakas, M. Fechner, A. Simonov, M. G. Kanatzidis, S. J. L. Billinge, N. A. Spaldin, T. Weber, *Phys. Rev. Mat.* **2018**, 2, 085402.

[75] E. S. Bozin, C. D. Malliakas, P. Souvatzis, T. Proffen, N. A. Spaldin, M. G. Kanatzidis, S. J. L. Billinge, *Science.* **2010**, *330*, 1660.

[76] R. Yu, E. S. Bozin, M. Abeykoon, B. Sangiorgio, N. A. Spaldin, C. D. Malliakas, M. G. Kanatzidis, S. J. L. Billinge, *Arxiv Cond-Mat* **2018**, 1805.01069v1.

[77] T. Keiber, F. Bridges, B. C. Sales, *Phys. Rev. Lett.* **2013**, *111*, 95504.

[78] O. Delaire, J.Ma, K.Marty, A. F. May, M. A.McGuire, M. H. Du, D. J. Singh, A. Podlesnyak, G. Ehlers, M. D. Lumsden, B. C. Sales, *Nat. Mater.* **2011**, 10, 614.

[79] T. Shiga, J. Shiomi, J. Ma, O. Delaire, T. Radzynski, A. Lusakowski, K. Esfarjani, G. Chen, *Phys. Rev. B - Condens. Matter Mater. Phys.* **2012**, *85*, 1.

[80] K. Page, T. Proffen, M. Niederberger, R. Seshadri, *Chem. Mater.* **2010**, 22, 4386.

[81] E. Aksel, J. S. Forrester, J. C. Nino, K. Page, D. P. Shoemaker, J. L. Jones, *Phys. Rev. B: Condens. Matter Mater. Phys.* **2013**, 87, 104113.

[82] T. Krauskopf, S. P. Culver, W. G. Zeier, *Inorg. Chem.* **2018**, 57, 4739.

Chapter 2.3

Enhancement of Thermoelectric Performance of *n*-Type $AgBi_{1+x}Se_2$ via Improvement of the Carrier Mobility by Modulation Doping†

†*Paper based on this has been published as* ***E. Rathore****, S.N. Guin, K. Biswas, Bull. Mater. Sci.* ***2020****, 43, 315.*

Chapter 2.3

Enhancement of thermoelectric performance of n-type $AgBi_{1+x}Se_2$ via improvement of the carrier mobility by modulation doping†

Summary: *High charge carrier mobility with low lattice thermal conductivity is one of the key factors for the design of a good thermoelectric material. Recent studies show that n-type $AgBiSe_2$ is a promising compound for thermoelectric energy conversion due to intrinsically low lattice thermal conductivity. However, low charge carrier mobility in $AgBiSe_2$ is the constraint for enhancement of its power factor. In this chapter, we have used a chemical modification way to realize modulation doping in $AgBiSe_2$. The addition of 2-6 mol % excess Bi in $AgBiSe_2$ results in formation of Bi-rich modulation doped microstructures of topological semimetal, Bi_4Se_3 in $AgBiSe_2$ matrix. We show that due to facile carrier transport via semi-metallic Bi_4Se_3 microstructure results in overall improvement of carrier mobility without compromising Seebeck coefficient in $AgBiSe_2$ system, which in turn result in a remarkable improvement in the power factor (σS^2) value. A highest σS^2 value ~6.35 $\mu W\ cm^{-1}\ K^{-2}$ at 800 K has been achieved in $AgBiSe_2$-3% Bi excess sample, which is higher than previously reported metal ion and halogen doped $AgBiSe_2$.*

S

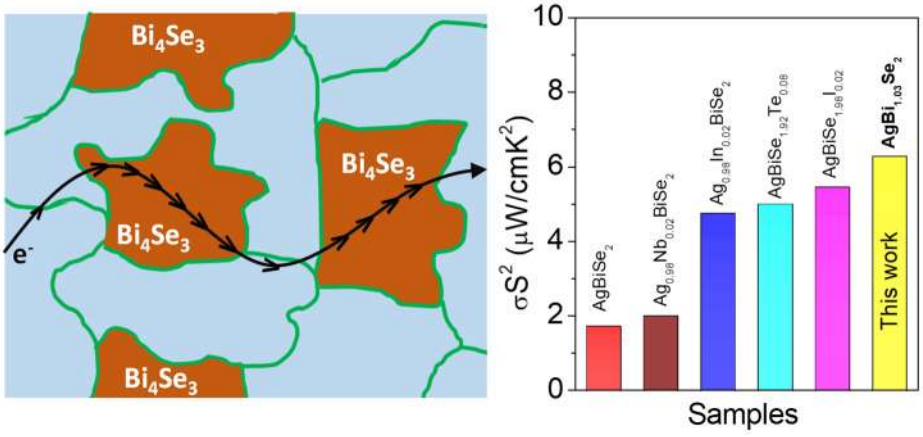

†*Paper based on this has been published as E. Rathore, S.N. Guin, K. Biswas, Bull. Mater. Sci.* ***2020****, 43, 315.*

2.3.1. Introduction

In the recent years, the energy and environment related concern intensified the research in the arena of efficient, cost-effective and pollution-free means of power generation. Thermoelectric materials are the all solid-state converters without any moving part, can directly and reversibly convert waste heat into electricity.[1–4] Over the last two decades, there has been an escalated interest in the field of thermoelectric materials research. The effectiveness of a thermoelectric material is governed by the thermoelectric figure of merit, $zT = \sigma S^2 T/\kappa$, where σ is the electrical conductivity, S is the Seebeck coefficient, T is the temperature in Kelvin, κ is the thermal conductivity.[1–4] The fundamental challenge for designing of a promising thermoelectric material is intriguing due to conflicting thermoelectric parameters. To improve the thermoelectric properties, different concepts have been employed via improvement of the Seebeck coefficient or reduction of the thermal conductivity or by simultaneous tailoring of both the parameters. The Seebeck coefficient can be improved by the introduction of resonant levels in the electronic structure or by electronic band convergence.[5,6] On the other hand, κ_{lat} can be reduced by solid solution alloying, nanostructuring and all-scale hierarchical structuring.[3,7,8] The inorganic solids with intrinsically low κ_{lat} [9] due to rattling modes,[10] soft phonon modes,[11] resonant bonding,[12] high lattice anharmonicity[13] are realized recently to be promising candidates for the thermoelectric application.

Among the intrinsically low κ_{lat} compounds, the copper and silver based Te-free I-V-VI_2 (where I = Cu, Ag or an alkali metal; V = Sb, Bi; and VI = S, Se) chalcogenide semiconductors have shown promise for enhanced thermoelectric properties.[14-20] The multiple soft phonon modes and strong phonon-phonon interaction caused by large bonding anharmonicity due to repulsion between the ns^2 lone pair of group V elements and valence p orbital of chalcogenide is the origin of high thermal resistance for these compounds.[14] In recent years, several new Te-free materials from this class has been discovered as potential candidate for thermoelectrics. In the p-type family, $AgSbSe_2$ and in n-type family $AgBiSe_2$ have established to be the most promising candidates.[15,18,19,21,22] At room temperature, $AgBiSe_2$ crystallizes in a centro-symmetric cation ordered hexagonal structure with space group $P\bar{3}m1$ and lattice parameter a = 4.194 Å, c = 19.65 Å.[23] It shows two structural transitions at higher temperature. The hexagonal (α) to rhombohedral (β) (space group $R\bar{3}m$, a = 7.022 Å) transition takes place at ~460 K

(Figure 2.3.1). During α-β transition the cation sublattice remains ordered but a slight atomic displacement and an elongation of the unit cell in the (001) direction of the hexagonal lattice takes place. The ordered rhombohedral (β) to cation-disordered cubic (γ) (space group *Fm-3m*, $a = 5.832$ Å) phase transition takes place ~580 K.[23]

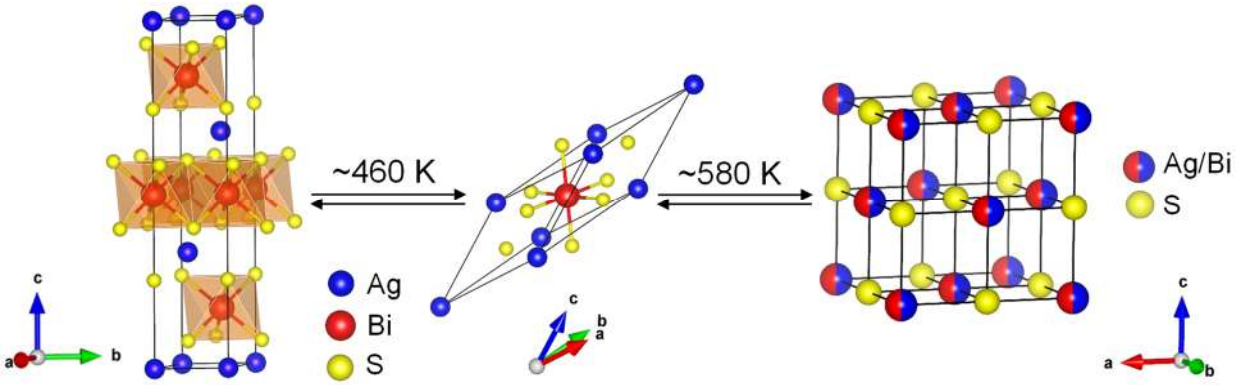

Figure. 2.3.1. *Temperature-dependent structural phase transitions in $AgBiSe_2$. The room temperature hexagonal and the intermediate rhombohedral phases are cation ordered structure. The high-temperature cubic phase is a cation disordered structure.*

Although pristine $AgBiSe_2$ exhibits low thermal conductivity, its thermoelectric performance is poor due to low electrical transport.[18] The thermoelectric property of $AgBiSe_2$ has been improved by regulating carrier concentration, using electron doping strategy in host cationic or anionic site. For instance, solid solution alloying of higher valent cation (Nb, In or Ge) in the Ag site optimizes the n-type carrier concentration and leads to enhancement of zT.[18,24,25] The doping of monovalent halide ion ($Cl^-/Br^-/I^-$) on the divalent selenium (Se^{2-}) site can act as an *n*-type dopant in $AgBiSe_2$ and results in the significant improvement in thermoelectric properties.[19] Furthermore, the effect of Ag vacancy defect and tellurium substitution on the transport property of $AgBiSe_2$ has been investigated.[26,27] However, low carrier mobility for pristine $AgBiSe_2$ (~67 $cm^2\,V^{-1}\,s^{-1}$) and doped samples still restrict to improve the electrical transport properties.

Generally, in heavily doped semiconductors, the high population of free carriers leads to a diminution of carrier mobility due to increased carrier-carrier scattering and ionized impurity scattering.[1] Recently, the concept of three-dimensional (3D) modulation doping (MD) has been introduced to improve the carrier mobility in thermoelectric materials.[1,20,28] Usually, modulation-doped samples are a physical mixture

of two-phase composites made of undoped and heavily doped counterparts. The undoped counterpart has low carrier concentration but high carrier mobilities, whereas the doped counterpart has high carrier concentrations but low carrier mobilities. In a heavily doped semiconductor, the high population of free carriers can spill over throughout the matrix. However, in a modulation doped sample one can force the charge carriers to spill over from the modulation doped region into the surrounding host matrix. Therefore, the ionized atoms remain spatially separated within the modulation doped region. Consequently, the ionized impurity scattering rate can be decreased in modulation doped sample and an overall improvement of carrier mobility can be achieved.[20, 28-30] Historically, this technique was first implemented in two-dimensional electron gas (2DEG) thin film devices for improving the carrier mobility and thus the electrical conductivity.[31] In thermoelectrics, using modulation doping, enhanced power factor was achieved in $Si_{1-x}Ge_x$ composites by mechanically mixing the doped and undoped $Si_{1-x}Ge_x$ nanograins.[30] The concept of modulation doping is successfully applied to BiCuSeO,[28] BiAgSeS[20] and Half-Heusler TiNiSn[31]. All these reports encouraged us to investigate the MD approach in intrinsically low thermal conductivity $AgBiSe_2$ system where electronic transport can be improved by enhancing the carrier mobility.

Herein, in this chapter we discuss large enhancement of power factor in $AgBiSe_2$ by enhancing carrier mobility by using modulation doping approach. The present modulation doping is quite different from conventional approach. In our study, we have used 2-6 mol % excess Bi as a modulation dopant in $AgBiSe_2$ to improve the carrier transport. We demonstrate a chemical modification way to realize modulation doping in $AgBiSe_2$ by embedding bismuth rich microstructure in $AgBiSe_2$ matrix through matrix encapsulation technique. We have chosen Bi for two reasons. Firstly, Bi is an *n*-type semimetal with a small Fermi surface (low carrier effective mass), long carrier mean free path and extremely high electron mobility (~10^4 cm^2 V^{-1} s^{-1} at 300 K).[32] Secondly, Bi is a constitute element of $AgBiSe_2$ and therefore it ruled out the aliovalent doping in the parent $AgBiSe_2$ phase and minimizes the possibility of ionize impurity scattering process. The diffusion of electrons from $AgBiSe_2$ matrix to Bi-rich semi-metallic precipitate results in an overall enhancement of carrier mobility in $AgBiSe_2$-x % Bi (x = 2-6 mol %) system. We show that the addition of small fraction of Bi in $AgBiSe_2$ results in a large effect on the microstructure and transport properties of $AgBiSe_2$. PXRD and

microstructure analysis reveals that $AgBiSe_2$-x % Bi samples are not single phase but rather forms a microstructure composed of well dispersed Bi-rich nano/micro-inclusion of topological semimetal, Bi_4Se_3 [33,34] in the matrix of $AgBiSe_2$. Electrical transport measurement shows that the MD approach enhances the carrier mobility and hence electrical conductivity in $AgBiSe_2$ which results in a remarkable improvement in the power factor (σS^2) value over a wide temperature. A maximum power factor value of ~6.35 μW cm^{-1} K^{-2} at 800 K was measured in $AgBiSe_2$-3 % Bi, which is higher than the metal ion and halogen doped $AgBiSe_2$ system.

2.3.2. Methods

2.3.2.1. Reagents. Elemental silver (Ag, 99.9999%, metal basis, Sigma Aldrich), elemental bismuth (Bi, 99.9999%, metal basis, Sigma Aldrich) and elemental selenium (Se, 99.999%, metal basis, Alfa Aesar) were used for synthesis without further purification.

2.3.2.2. Synthesis. Ingots (~7g) of pristine $AgBiSe_2$ and $AgBi_{1+x}Se_2$ (x= 2-6 mol %) were synthesized by melting reaction of stoichiometric amounts of high-purity elemental Ag, Bi, and Se, taken in quartz tubes which were sealed under high vacuum (~ 10^{-5} Torr). The sealed tubes were slowly heated up to 723 K in 12 h, then heated up to 1123 K in 4 h, soaked for 10 h, and eventually slow cooled to room temperature over a period of 12 h. For transport property measurements, the samples were cut using a low-speed diamond saw and polished using a polisher. The density of the samples was found to be ~ 97 % of the theoretical value of pristine $AgBiSe_2$.

2.3.2.3. Powder X-ray Diffraction. Powder X-ray diffraction patterns (PXRD) for finely powder samples were recorded using a Cu $K\alpha$ (λ = 1.5406 Å) radiation source on a Bruker D8 diffractometer.

2.3.2.4. Carrier Concentration. The room temperature carrier concentration of the samples was determined by Hall coefficient measurement system using a home build measurements set up.

2.3.2.5. Field Emission Scanning Electron Microscopy (FESEM). FESEM images were derived using NOVA NANO SEM 600 (FEI,

Germany) operated at 15 KV. The samples were prepared by polishing them with fine polishing paper.

2.3.2.6. Electrical Transport. Electrical conductivity and Seebeck coefficients were measured concurrently under a helium atmosphere from room temperature to ~823 K in a ULVAC RIKO ZEM-3 instrument system. The sample for the measurement is parallelepiped with dimensions of ~2 mm × 2 mm × 8 mm. The longer direction matches the direction in which the thermal conductivity was measured. Heating and cooling cycles gave repeatable electrical properties for a given sample. Electrical transport and thermal transport are measured in same direction. **2.3.2.7. Thermal transport.** The thermal diffusivity (D) was measured by laser flash method (Netzsch LFA-457) from room temperature to ~823 K. It was performed on carbon-coated disc samples of 8 mm in diameter and 2 mm thickness under an N_2 atmosphere. Temperature-dependent heat capacity, C_p, was derived using the standard sample (pyroceram) in LFA457. Cowan model with pulse correction was used to analyze the thermal diffusivity data. The total thermal conductivity, κ_{total}, was estimated using the formula: $\kappa_{total} = DC_p\rho$, where ρ is the density.

2.3.2.8. Calculation of Effective Mass. We have estimated the effective mass (m^*) assuming a single parabolic band model with acoustic phonon scattering, according to the following equation (1-3) using the measured S and Hall carrier concentration (n):

$$m^* = \frac{h^2}{2k_BT}\left[\frac{n}{4\pi F_{1/2}(\eta)}\right]^{2/3} \quad \text{Eq. 2.3.1.}$$

$$S = \frac{k_B}{e}\left(\frac{2F_1(\eta)}{F_0(\eta)} - \eta\right) \quad \text{Eq. 2.3.2.}$$

$$F_n(\eta) = \int_0^\infty \frac{x^n}{1 + e^{x-\eta}}\,dx \quad \text{Eq. 2.3.3.}$$

where k_B is the where, η is the reduced Fermi energy, $F_n(\eta)$ is the nth order Fermi integral, k_B is the Boltzmann constant, e is the electron charge, h is the Planck constant. The reduced Fermi energy was extracted based on fitting the respective Seebeck data.[35-39]

2.3.3. Results and Discussions

The crystalline ingots of $AgBiSe_2$ and $AgBiSe_2$- x% Bi (x= 2-6 mol %) were synthesized by elemental melting reaction in vacuum sealed quartz tubes followed by slow cooling. Figure 2.3.2a shows PXRD pattern of pristine and $AgBiSe_2$- x% Bi samples. The pattern for pristine sample could be indexed based on hexagonal $AgBiSe_2$.

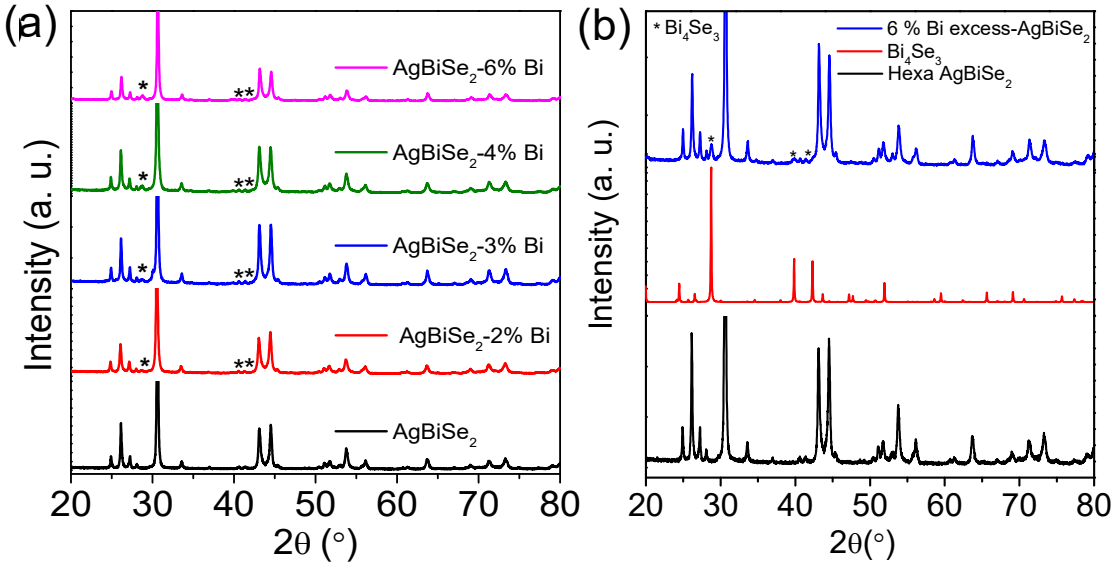

Figure 2.3.2. *(a) Room temperature powder XRD pattern of pristine $AgBiSe_2$-x% Bi (x=0-6 mol %) samples and (b) 6 % Bi excess sample, simulated Bi_4Se_3, $AgBiSe_2$. "*" indicates the second phase of Bi_4Se_3 in 6 % Bi excess-$AgBiSe_2$.*

The XRD patterns for Bi excess samples show additional reflections of the second phase of topological semimetal, Bi_4Se_3 ("*" marked in the plot). The intensity of the additional peaks increases with the rise of bismuth concentration which implies the increase of secondary phase of Bi_4Se_3 in the sample. Figure 2.3.3b shows that "*" peaks can be indexed to Bi_4Se_3 in 6 % Bi-excess sample.

To confirm these extra reflections of secondary phase of Bi_4Se_3 in PXRD data, we have carried out backscattered electron imaging (BSE) during FESEM and energy dispersive X-ray spectroscopy (EDAX) to understand the microstructure in $AgBiSe_2$- x% Bi (x= 2-6 mol%). The BSE-FESEM image of 3 % Bi modulation doped sample is presented in figure. 2.3.3a and b. The micrograph clearly shows two distinct regions with dark and bright contrast. The elements with the higher atomic number have greater

probability for elastic collision and looks brighter in BSE image. Thus, the region with bright contrast is related with heavier elements of the sample which is Bi_4Se_3 precipitates in the present case and EDAX analysis in Figure 2.3.4b, confirms that the precipitates are Bi- rich phases, Bi_4Se_3.

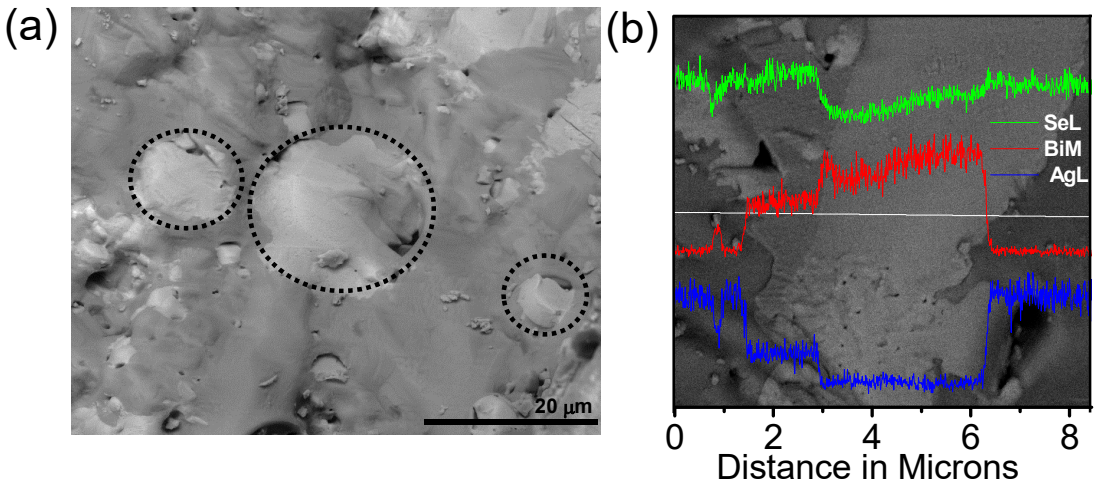

Figure 2.3.3. *(a) Backscattered FESEM image of the cleaved surface of $AgBiSe_2$- 3% Bi sample, the Bi rich precipitates with bright contrast are circled with black dotted line. (b) EDAX elemental line scan along the matrix and precipitate.*

The darker contrast regions correspond to the matrix in Figure 2.3.4a. To further evaluate the composition of the matrix and the precipitate, we have performed elemental line scanning which shows Bi-rich precipitate while the matrix is close to the composition of $AgBiSe_2$. Thus, the microstructure analysis further confirms the presence of Bi-rich secondary phase of Bi_4Se_3 in the $AgBiSe_2$ sample.

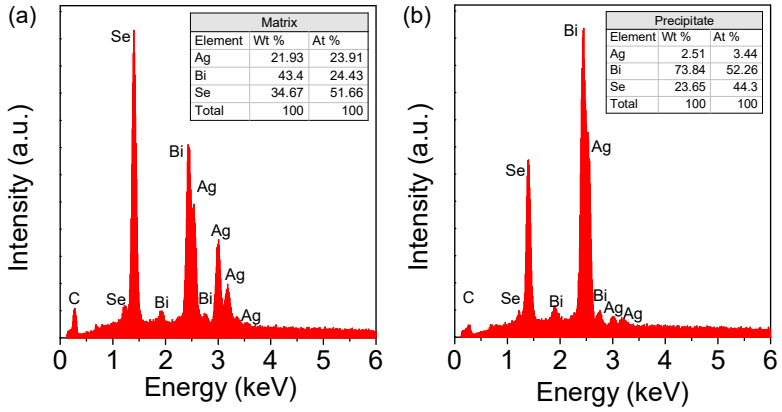

Figure 2.3.4. *EDAX analysis of $AgBiSe_2$ matrix (dark contrast) and precipitate (bright contrast).*

In Figure 2.3.5, we present temperature dependent electronic transport properties of $AgBiSe_2$ - x % Bi (x= 0-6 mol %). Pristine $AgBiSe_2$ exhibits a σ value of ~63 S cm^{-1} at room temperature (Figure. 2.3.5a, inset). The temperature-dependent, σ in the hexagonal phase maintain nearly constant value upto ~ 460 K. In the rhombohedral phase (temperature window of 460–580 K), the system exhibits metallic behavior with σ drops from ~52 S cm^{-1} at 460 K to ~16 S cm^{-1} at 580 K. In the cubic phase (above ~585 K), the σ value increases to ~24 S cm^{-1} at 708 K. The σ value for Bi- modulation doped samples are considerably higher than the pristine sample, which shows an increasing trend with rise of Bi concentration (Figure. 2.3.5a). The modulation doped samples show a similar metal to semiconductor type transition during rhombohedral to cubic phase transformation like in pristine $AgBiSe_2$, which is also observed in metal ion and halogen doped samples of $AgBiSe_2$[18,19,24,25]. Typically, for $AgBiSe_2$ - 3% Bi sample, the σ value changes from ~ 380 S cm^{-1} at room temperature to ~ 435 S cm^{-1} at 800 K.

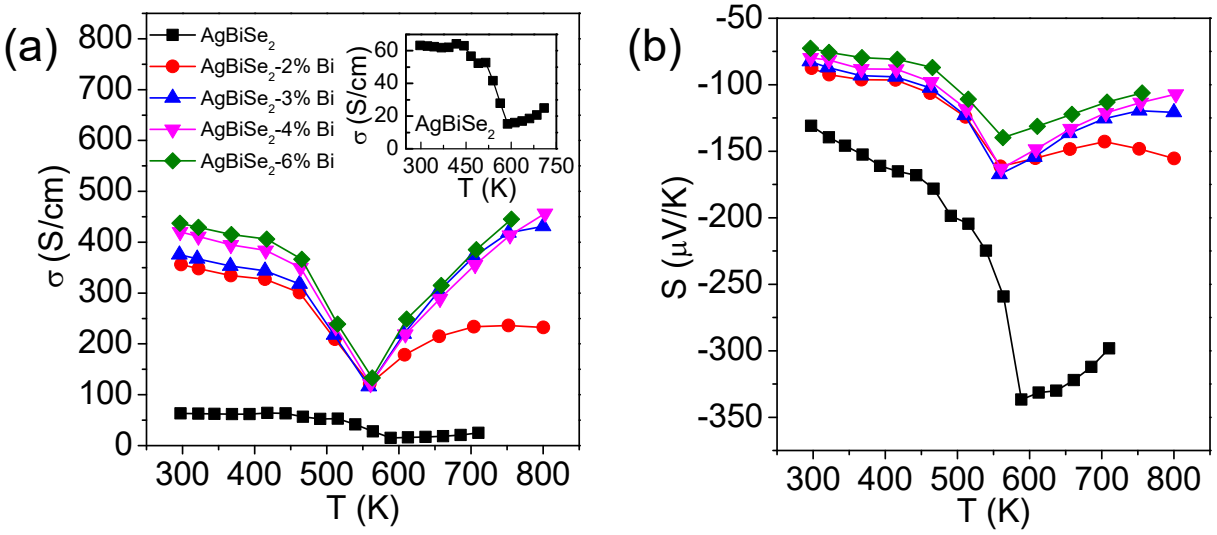

Figure. 2.3.5. *Temperature dependent (a) electrical conductivity (σ), and (b) Seebeck coefficient (S) of $AgBiSe_2$-x% Bi (x=0-6 mol %) samples. The inset in (a) shows zoomed data for pristine $AgBiSe_2$.*

To get better insights for the improvement of the electrical conductivity value, we have measured carrier concentration of the selected samples. The negative value of Hall coefficient (R_H), at ambient temperature for pristine and $AgBiSe_2$-x % Bi (x = 0-6 mol%) samples indicates *n*-type conduction in the system. We have estimated the carrier

concentration (n) and carrier mobility (μ) from the formula: $n = 1/eR_H$, and $\mu=\sigma/ne$ respectively, where e is the electronic charge. The electrical conductivity (σ) is related to n through the carrier mobility (μ) through the following expression.

$$\sigma = ne\mu \tag{4}$$

μ relies on the additional conditions shown in equation 5

$$\mu = \frac{e\tau}{m^*} \tag{5}$$

where, τ is the relaxation time, and m^* the carrier's effective mass. Notably, in the halogen and cation doped $AgBiSe_2$ the improvement in the carrier transport primarily due to the rise of carrier concentration. The Bi incorporation results in a slight increase in carrier concentration while the carrier mobility increases dramatically compared to pristine sample (Table 1). Typically, for $AgBiSe_2$- 3% Bi, μ shows a value of ~ 248 cm^2 V^{-1} s^{-1}, which is much higher than previously reported cation and anion doped $AgBiSe_2$ samples ranging from ~22 to ~ 63 cm^2 V^{-1} s^{-1} with similar carrier concentration [18,19] indicating that modulation doping suppresses the ionized impurity scattering. In addition, the diffusion of electrons to Bi_4Se_3 precipitate, where carrier mobility is higher than $AgBiSe_2$ matrix results in an overall improvement of μ in the system.

Table 2.3.1. *Room temperature carrier concentration (n), electrical conductivity (σ), carrier mobility (μ) and effective mass (m^*) of $AgBiSe_2$-x% Bi (x=0-6 mol %) samples.*

Sample	n (cm^{-3})	σ (S cm^{-1})	μ (cm^2 V^{-1} s^{-1})	m^*/m_0
$AgBiSe_2$	5.85×10^{18}	63	67	0.25
$AgBiSe_2$-2% Bi	7.97×10^{18}	355	278	0.18
$AgBiSe_2$-3% Bi	9.46×10^{18}	375	248	0.19
$AgBiSe_2$-4% Bi	1.02×10^{19}	420	257	0.20
$AgBiSe_2$-6% Bi	1.52×10^{19}	437	180	0.19

Temperature dependent Seebeck coefficient (S) of $AgBiSe_2$ and Bi modulation doped samples has been presented in Figure. 2.3.5b. Typically, $AgBiSe_2$- 3% Bi, sample shows an S value of -82.5 μV K^{-1} at room temperature which reaches a value of -100 μV K^{-1} at 460 K within the hexagonal phase. After the hexagonal to rhombohedral phase-transition, the Seebeck coefficient shows an increasing trend and reaches a value of the

maximum value of -160 μV K^{-1} at 560 K. In the cubic phase, the *S* value decreases and reaches -120 μV K^{-1} at 800 K. Although the trend of *S* in the present case of Bi-excess is similar to the metal ion and halogen doped $AgBiSe_2$, the value of *S* is lower in the measured temperature range. Below figure shows the heating and cooling cycle for electrical conductivity and Seebeck coefficient of $AgBiSe_2$-3% Bi sample.

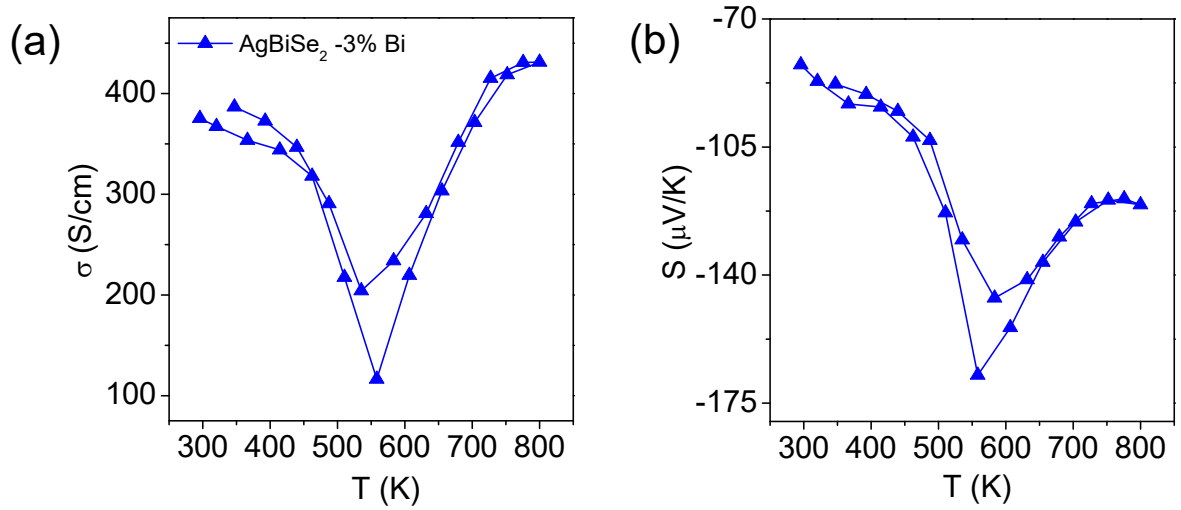

Figure. 2.3.6. *Temperature dependent heating-cooling cycle electrical conductivity (σ) and Seebeck coefficient (S) data for $AgBiSe_2$-3% Bi sample.*

To understand this, we have calculated carrier effective mass (m^*) assuming single parabolic band model with acoustic phonon scattering (r = -1/2). We have observed a large decrease of m^* compare to pristine sample (Table 2.3.1). Besides, the m^* value ranging from 0.18 to 0.20 is much smaller than halogen doped samples with m* ranging from 0.46 to 0.59. [19] Thus, lower *S* value in the present case is due to a combine effect of decreased m^* and increase in the carrier concentration (*n*), as given by Mott equation, where *S* is directly proportional to the m^* ($S \sim m^*$) and inversely proportional to *n* ($S \sim n^{2/3}$). [2] We would also like to mention that low carrier effective mass (m^*) in the modulation doped samples assist to increase overall carrier mobility (equation 2) which improve the σ in the present case.

The temperature-dependent power factor (σS^2) for all the samples, estimated from measured σ and *S* have been shown in figure. 2.3.7a. The Bi modulation doped samples show large improvement in σS^2 than the pristine sample. Typically, the $AgBiSe_2$-3 % Bi sample shows a σS^2 of ~ 2.6 μW $cm^{-1}K^{-2}$ at room temperature which reaches a

maximum value of ~ 6.35 μW $cm^{-1}K^{-2}$ at 800 K. Indeed, the maximum σS^2 value obtained in the present ingot samples is higher than that of the halogen and metal ion doped $AgBiSe_2$ ranging from ~2.0 to ~5.45 μW $cm^{-1}K^{-2}$ (Figure 2.3.7b). [18,19,24,27]

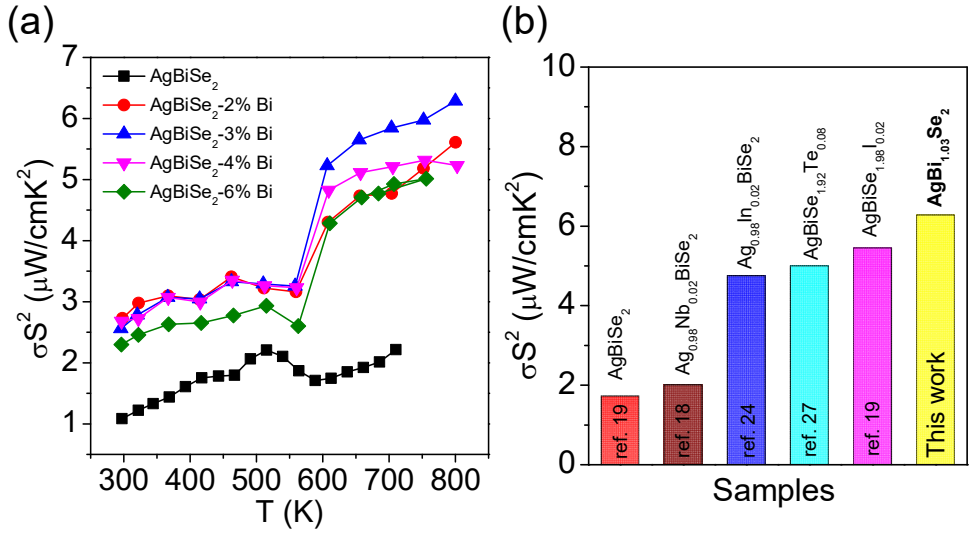

Figure. 2.3.7. *(a) Temperature dependent power factor of (σS^2) $AgBiSe_2$-x% Bi (x=0-6 mol %) samples and (b) comparison of power factors of the halogen and metal ion doped $AgBiSe_2$ samples.*

Figure. 2.3.9a, represent temperature-dependent total thermal conductivity, κ_{total}, of all the samples. κ_{total} has been estimated using the formula, $\kappa_{total} = DC_p\rho$, where D is the thermal diffusivity, Cp is specific heat and ρ is density of the sample (Figure. 2.3.8).

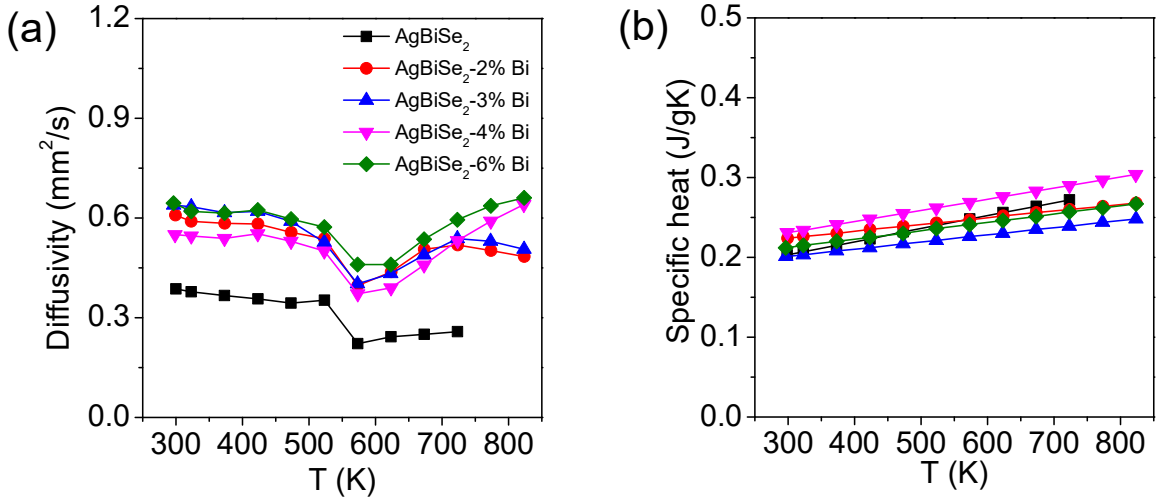

Figure. 2.3.8. *Temperature-dependent (a) thermal diffusivity (D) and (b) specific heat (C_p) of $AgBiSe_2$-x% Bi (x=0-6 mol %) samples*

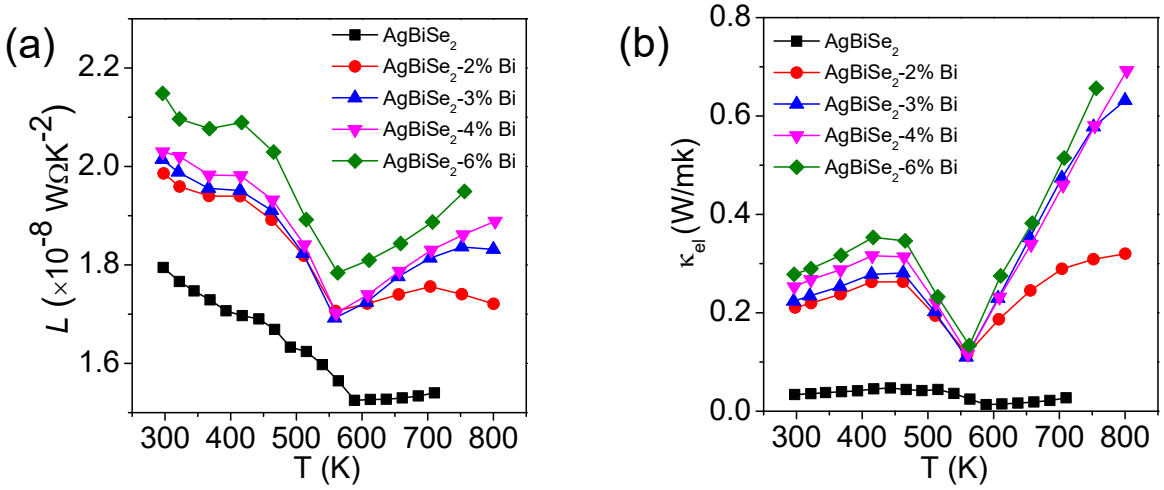

Figure. 2.3.9. *Temperature dependent (a) total thermal conductivity (κ_{total}) and (b) lattice thermal conductivity (κ_{lat}) of $AgBiSe_2$-x% Bi (x=0-6 mol %) samples.*

All the doped samples show an increasing trend of κ_{total} over the measurement temperature. Typically, for $AgBiSe_2$-3 % Bi sample a κ_{total} of ~ 0.95 W $m^{-1}K^{-1}$ has been measured at room temperature, which decreases to a minimum value of ~0.67 W $m^{-1}K^{-1}$ in the rhombohedral at 570 K. With further increasing temperature, in the cubic phase the κ_{total} initially show an increasing trend and then reaches to a value of ~0.93 W $m^{-1}K^{-1}$ at 823 K.

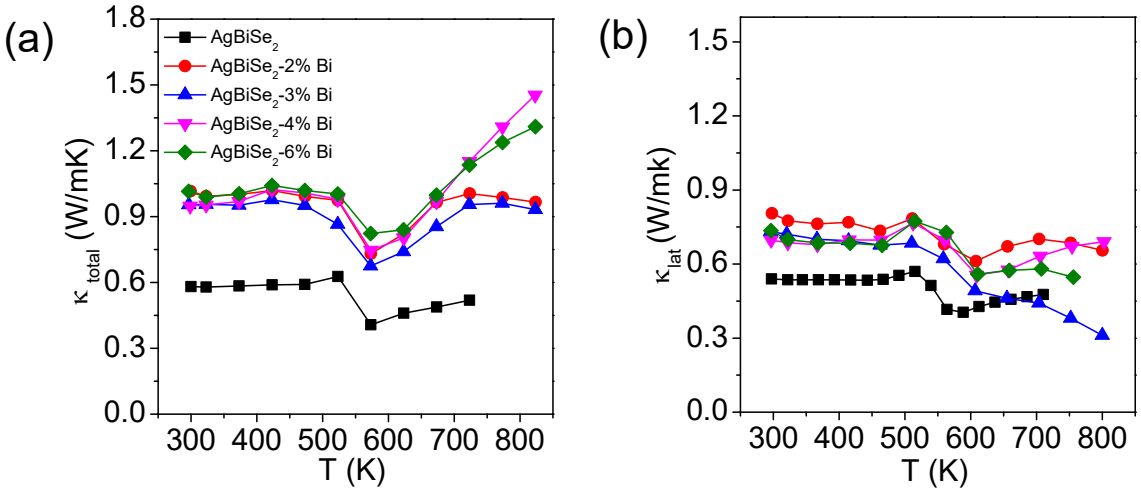

Figure. 2.3.10. *Temperature dependent (a) Lorenz number (L) and (b) electronic thermal conductivity (κ_{el}) of $AgBiSe_2$-x% Bi (x=0-6 mol %) samples.*

For higher concentration modulation doped samples, $AgBiSe_2$-x % Bi (x= 4-6 mol %), in the cubic phase the κ_{total} shows increasing trend. To understand this, we have extracted the contribution of lattice thermal conductivity (κ_{lat}) and electronic thermal conductivity (κ_{el}) (Figure. 2.3.10b) to the κ_{total} (Figure. 2.3.9b) using Wiedemann–Franz law: $\kappa_{el} = L\sigma T$, where Lorenz number, L (Figure. 2.3.10a). L has been calculated using single parabolic band model, which can be found elsewhere.[15] The analysis indicates a large contribution from the κ_{el} at higher temperature results in such an observation. We also observed a small increase in κ_{lat} value in the modulation doped sample compared to the pristine $AgBiSe_2$. Generally, in I-V-VI_2 family of compounds, the phononic contribution towards κ_{total} is already to a minimum value as the mean free path of the phonons is in the range of interatomic distance. Thus, the possibility of scattering of smaller mean free path phonons by the micrometer size precipitate can be ruled out here. We therefore attribute that the increase in κ_{lat} might be associated with the additional contribution of κ_{lat} from the microstructure phase of Bi_4Se_3 which probably has higher thermal conductivity.

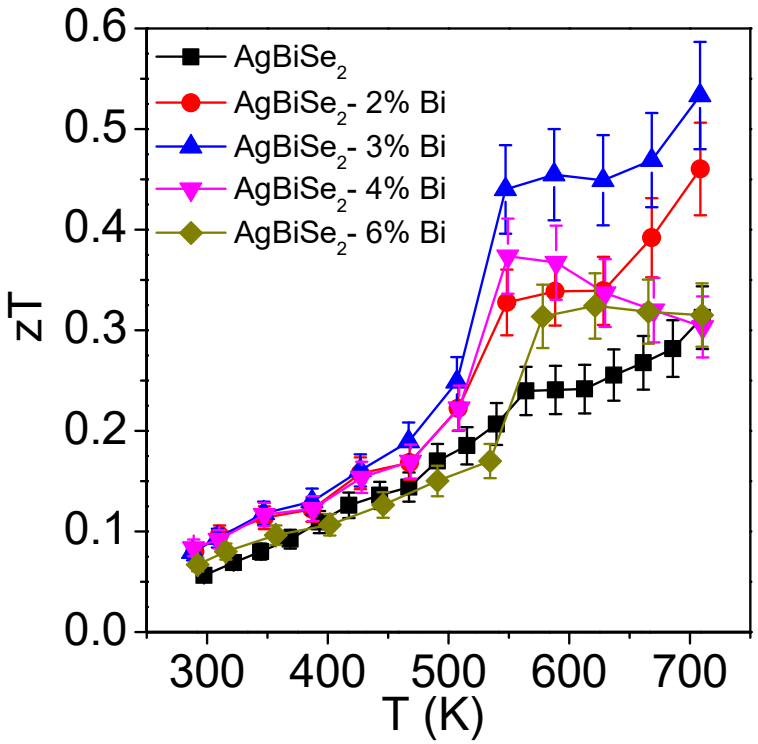

Figure. 2.3.11. *Temperature-dependent thermoelectric figure of merit (zT) of $AgBiSe_2$-x% Bi (x=0-6 mol %) samples. 10% error bar has been shown in zT estimation.*

The estimated temperature-dependent thermoelectric figure of merit, zT from the electrical and thermal transport data for all the samples have been given above in figure. 2.3.11. The estimation includes ~ 10 % error from the different measurement. The modulation doped samples show higher zT value compared to pristine sample. The improvement in the zT value is due to large enhancement of electrical conductivity and power factor value due to improved carrier mobility of the sample. A highest zT value of ~0.53 at 800 K has been achieved for $AgBiSe_2$-3% Bi sample.

2.3.4. Conclusions

In summary, our study shows that modulation doping is an effective way to improve carrier mobility in $AgBiSe_2$. We have shown that addition of small amount of Bi in $AgBiSe_2$ results in a large effect on the microstructure and transport properties of $AgBiSe_2$. The suppression of the ionized impurity scattering and injection of charge carrier to the precipitate of topological semimetal, Bi_4Se_3 from the $AgBiSe_2$ matrix results in large improvement of carrier mobility. As a consequence, we have observed an increase in thermoelectric power factor and zT in $AgBiSe_2$. In general, low carrier mobility in I-V-VI_2 class of materials is constraint for the improvement of power factor. Our study demonstrate that use of heterogeneous modulation doping approach could be an effective strategy for improvement of carrier transport in I-V-VI_2 class of compounds.

2.3.5. References

[1] G. Tan, L. D. Zhao, M. G. Kanatzidis, *Chem. Rev.* **2016**, 116, 12123.

[2] J. R. Sootsman, D. Y. Chung, M. G. Kanatzidis, *Angew. Chemie - Int. E.* **2009**, 48, 8616.

[3] L. D. Zhao, V. P. Dravid and M. G. Kanatzidis, *Energy Environ. Sci.* **2014**, **7**, 251.

[4] C. Chang, M. Wu, D. He, Y. Pei, C. F. Wu, X. Wu, H. Yu, F. Zhu, K. Wang, Y. Chen, L. Huang, J. F. Li, J He, L. D. Zhao, *Science* **2018**, 360, 778.

[5] Q. Zhang, B. Liao, Y. Lan, K. Lukas, W. Liu, K. Esfarjani, C. Opeil, D. Broido, G. Chen, Z Ren, *Proc. Natl. Acad. Sci. U.S.A* **2013**, 110, 13261.

[6] A. Banik, U. S. Shenoy, S. Saha, U. V. Waghmare, K. Biswas, *J. Am. Chem. Soc.* **2016**, 138, 13068.

[7] K. Biswas, J. He, Q. Zhang, G. Wang, C. Uher, V. P. Dravid, M. G. Kanatzidis, *Nat. Chem.* **2011**, 3, 160.

[8] K. Biswas, J. He, I. D. Blum, C. I. Wu, T. P. Hogan, D. N. Seidman, V. P. Dravid, M. G. Kanatzidis, *Nature* **2012**, 489, 414.

[9] M. K. Jana, K. Biswas, *ACS Energy Lett.* **2018**, 3, 1315.

[10] M. K. Jana, K. Pal, U. V. Waghmare, K. Biswas, *Angew. Chemie - Int. Ed.* **2016**, 55, 7792.

[11] E. Rathore, R. Juneja, S. P. Culver, N. Minafra, A. K. Singh, W. G. Zeier, K. Biswas *Chem. Mater.* **2019**, 31, 2106.

[12] S. Lee, K. Esfarjani, T. Luo, J. Zhou, Z. Tian, G. Chen, *Nat. Commun.* **2014**, 5, 3525.

[13] L. D. Zhao, S. H. Lo, Y. Zhang, H. Sun, G. Tan, C. Uher, C. Wolverton, V. P. Dravid, M. G. Kanatzidis, *Nature* **2014**, 508, 373.

[14] D. T. Morelli, V. Jovovic, J. P. Heremans, *Phys. Rev. Lett.* **2008**, 101, 35901.

[15] S. N. Guin, A. Chatterjee, D. S. Negi, R. Datta, K. Biswas, *Energy Environ. Sci.* **2013**, 6, 2603.

[16] K. T. Wojciechowski, M. Schmidt, *Phys. Rev. B - Condens. Matter Mater. Phys.* **2009**, 79, 184202.

[17] V. Jovovic, J. P. Heremans, *J. Electron. Mater.* **2009**, 38, 1504.

[18] L. Pan, D. Be, N. Dragoe, *J. Am. Chem. Soc.* **2013**, 135, 4914.

[19] S. N. Guin, V. Srihari, K. Biswas, *J. Mater. Chem. A* **2015**, 3, 648.

[20] D. Wu, Y. Pei, Z. Wang, H. Wu, L. Huang, L. D. Zhao, J. He, *Adv. Funct. Mater.* **2014**, 24, 7763.

[21] F. D. Rosi, E. F. Hockings, N. E. Lindenblad, *RCA Rev.* **1961**, 22, 82.

[22] C. Xiao, X. Qin, J. Zhang, R. An, J. Xu, K. Li, B. Cao, J. Yang, B. Ye, Y. Xie, *J. Am. Chem. Soc.* **2012**, 134, 18460.

[23] S. Geller, J. H. Wernick, *Acta Crystallogr.* **1959**, 12, 46.

[24] X. Liu, D. Jin, X. Liang, X. Liu, D. Jin, X. Liang, *Appl. Phys. Lett.* **2016,** 109, 133901.

[25] H. J. Wu, P. C. Wei, H. Y. Cheng, J. R. Deng, Y. Y. Chen, *Acta Mater.* **2017,** 141, 217.

[26] F. Böcher, S. P. Culver, J. Peilstöcker, K. S. Weldert, W. G. Zeier, *Dalt. Trans.* **2017,** 46, 3906.

[27] Y. Goto, A. Nishida, H. Nishiate, M. Murata, C. H. Lee, A. Miura, C. Moriyoshi, Y. Kuroiwa, Y. Mizuguchi, *Dalt. Trans.* **2018**, 47, 2575.

[28] Y. Pei, H. Wu, D. Wu, F. Zheng, J. He, *J. Am. Chem. Soc.* **2014**, 136, 13902.

[29] M Zebarjadi, G Joshi, G Zhu, B Yu, A Minnich, Y Lan, X Wang, M Dresselhaus, Z Ren, G Chen *Nano Lett.* **2011**, 11, 2225.

[30] T. Berry, C. Fu, G. Au, G. H. Fecher, W. Schnelle, F. Serrano-sanchez, Y. Yue, H. Liang, C. Felser, *Chem. Mater.* **2017**, 29, 7042.

[31] R. People, J. C. Bean, D. V. Lang, A. M. Sergent, H. L. Störmer, K. W. Wecht, R. T. Lynch, K. Baldwin, *Appl. Phys. Lett.* **1984**, 45, 1231.

[32] Y. Hasegawa, Y. Ishikawa, T. Saso, H. Shirai, H. Morita, T. Komine, H. Nakamura *Physica B: Condensed Matter* **2006**, 382, 140.

[33] Q. D. Gibson, L. M. Schoop, A. P. Weber, H. Ji, S. N. Perge, I. K. Drozdov, H. Beidenkopf, J. T. Sadowski, A. Fedorov, A. Yazdani, T. Valla, R. J. Cava, *Phys. Rev. B* **2013**, 88, 081108.

[34] T. Valla, H. Ji, L. M. Schoop, A. P. Weber, Z.-H. Pan, J. T. Sadowski, E. Vescovo, A. V. Fedorov, A. N. Caruso, Q. D. Gibson, L. Müchler, C. Felser, R. J. Cava, *Phys. Rev. B* **2012**, 86, 241101.

[35] Y. L. Pei, H. Wu, J. Sui, J. Li, D. Berardan, C. Barreteau, L. Pan, N. Dragoe, W. S. Liu, J. He , L. D. Zhao, *Energy Environ. Sci.* **2013**, 6, 1750.

[36] L. D. Zhao, S. H. Lo, J. He, H. Li, K. Biswas, J. Androulakis, C. I. Wu, T. P. Hogan, D. Y. Chung, V. P. Dravid, M. G. Kanatzidis, *J. Am. Chem. Soc.* **2011**, 133, 20476.

[37] J. Androulakis, I. Todorov, J. He, D. Y. Chung, V. P. Dravid, M. G. Kanatzidis *J. Am. Chem. Soc.* **2011**, 133, 10920.

[38] W. S. Liu, Q. Zhang, Y. Lan, S. Chen, X. Yan, Q. Zhang, H. Wang, D. Wang, G. Chen, Z. Ren, *Adv. Energy Mater.* **2011**, 1, 577.

[39] H. Wu, C. Chang, D. Feng, Y. Xiao, X. Zhang, Y. Pei, L. Zheng, D. Wu, S. Gong, Y. Chen, J. He, M. G. Kanatzidis, L. D. Zhao, *Energy Environ. Sci.* **2015**, 8, 3298.

Chapter 2.4

High Thermoelectric Performance in *n*-type PbS: Synergistic Role of Enhanced Covalency and Nanostructured Phonon Scattering†

† *Paper based on this is under review as* ***E. Rathore****, R. Juneja, S. Roychowdhury, M. Kofu, K. Nakajima A. K. Singh, K. Biswas xx* ***2021****, xx, xx.*

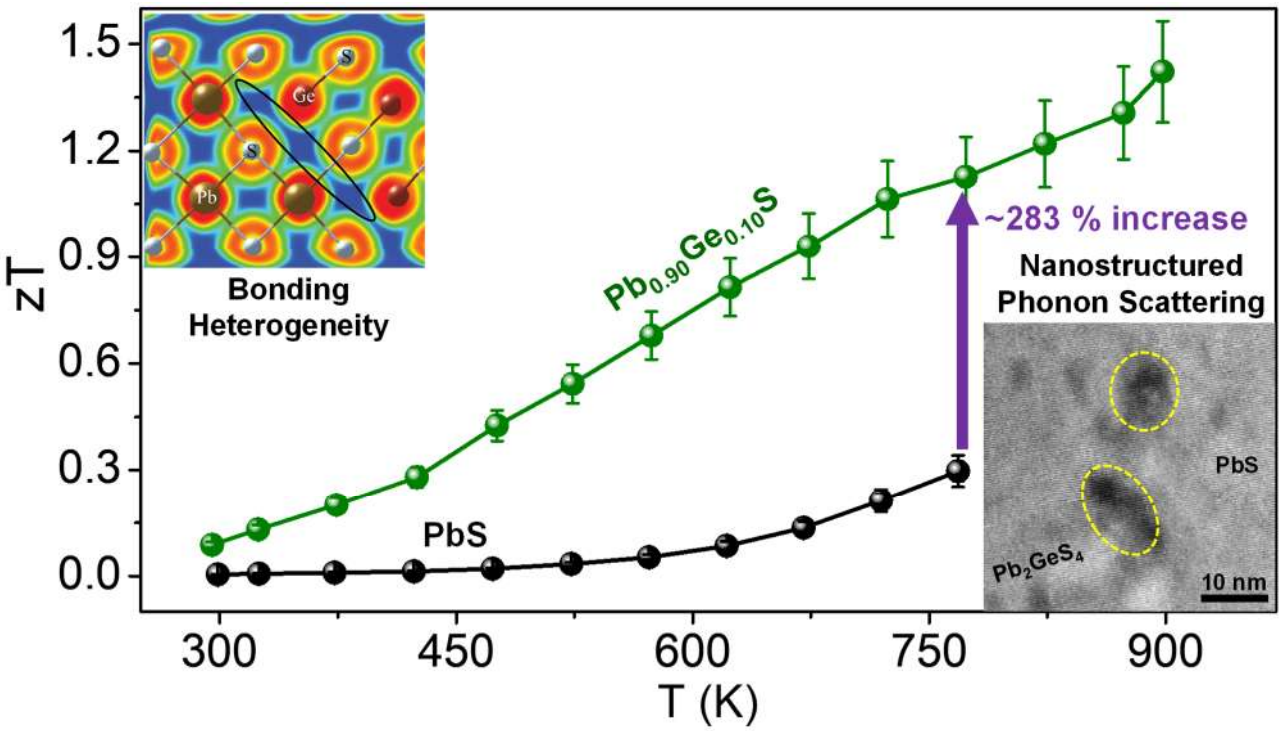
zT
T (K)
1.5
1.2
0.9
0.6
0.3
0.0
300
450
600
750
900
Pb0.90Ge0.10S
PbS
~283 % increase
Nanostructured
Phonon Scattering
Bonding
Heterogeneity
Ge
S
S
Pb
PbS
Pb2GeS4
10 nm

Chapter 2.4

High Thermoelectric Performance in *n*-type PbS: Synergistic Role of Enhanced Covalency and Nanostructured Phonon Scattering†

Summary: *Crystalline solids with a high thermoelectric performance at higher temperatures can convert waste heat to electricity without emitting any hazardous gas, which promises to play important role in energy management. High thermoelectric performance can be achieved either by tuning the electronic structure or by enhancement in scattering the heat-carrying phonons, which often affect each other. Thereby, a leap in the performance can be achieved by simultaneous modulation of electronic structure and lowering of thermal conductivity. Herein, we demonstrate a high thermoelectric figure of merit (zT) of 1.45 at 900 K for Ge doped (4-10 mol%) in n-type PbS, which is the highest value among all n-type PbS-based thermoelectric materials. This high performance is achieved by synergistic enhancement of covalency in chemical bonding which increases the electrical conductivity, and by introduction endotaxial nanometer-sized (5-10 nm) precipitates of Pb_2GeS_4 in PbS matrix which strongly scatter the heat-carrying phonons. The n-type $Pb_{0.90}Ge_{0.10}S$ demonstrates an ultra-low lattice thermal conductivity (κ_{lat}) of 0.56 Wm^{-1} K^{-1} at 900 K, which is close to theoretical minima of 0.45 Wm^{-1} K^{-1} of PbS. Transmission Electron Microscopy (TEM) investigation shows that Ge doping of ≥ 4 mol % Ge in PbS forms endotaxial nanoprecipitates in the PbS matrix which lowers the κ_{lat} by 40 % in $Pb_{0.90}Ge_{0.10}S$ compared to pristine PbS. The presence of low-lying transverse acoustic (TA) and longitudinal acoustic (LA) phonon modes at 48.24 cm^{-1} and 91.83 cm^{-1}, respectively are revealed from inelastic neutron scattering (INS) experiments. The softening of low-frequency modes at a higher temperature and ultra-short phonon lifetime (1-4.5 ps) further explain the ultra-low κ_{lat}. Electron localization function (ELF) analysis confirms chemical bonding hierarchy in Ge*

† *Paper based on this is under review as* ***E. Rathore****, R. Juneja, S. Roychowdhury, M. Kofu, K. Nakajima A. K. Singh, K. Biswas xx* ***2021****, xx, xx.*

doped PbS due to more covalent bonding character of Ge-S compared to Pb-S. Further, first-principles density functional theoretical (DFT) calculations of electronic structure demonstrate that Ge doping significantly lowers the deformation potential of n-type PbS, indicating weakened electron-phonon coupling, thereby increasing the electrical conductivity in Ge doped PbS. The simultaneous (a) decrease of κ_{lat} by phonon softening and nanostructured phonon scattering and (b) enhancement of electrical transport due to the enhanced covalency lead to highest zT of 1.45 in n-type Ge doped PbS.

2.4.1. Introduction

Nearly two-thirds of all utilized energy is being wasted as heat. Waste heat to electrical energy conversion using high performance and earth-abundant thermoelectric materials is alluring widespread interest for future energy sustainability and management.[1–3] The performance of thermoelectric material is determined by the dimensionless figure of merit, $zT = S^2\sigma T/(\kappa_{lat+}\ \kappa_{ele})$, where S is Seebeck coefficient, σ is electrical conductivity, κ_{lat} and κ_{ele} are the lattice and electronic thermal conductivity.[2,4-6] zT can be enhanced by boosting power factor ($S^2\sigma$) and/or lowering thermal conductivity.[7-10] Strategies to enhance the power factor include electronic bandstructure tuning by the convergence of multiple bands,[11-14] band alignment via endotaxial second phase,[9,15] creation of resonant levels [3,16,17] etc. While the strategies to decrease κ_{lat} involve the formation of all length scale hierarchical nano/meso-architectures,[9,10,18] guest atom rattling,[19] lattice anharmonicity.[20-22] Besides procuring excellent electronic performance as well as low thermal conductivity, thermoelectric energy conversion demands earth-abundant and low-cost constituent elements for mass-market applications.[23,24]

Lead chalcogenides such as PbTe and PbSe, have been considered to be champion materials in the temperature range of 600-900 K due to their unique electronic structure and intrinsically low thermal conductivity.[1-4,25,26] However, with concern regarding the high price and potential scarcity of Te and Se, it is essential to develop thermoelectric materials based on earth-abundant and low-cost elements.[27] On the contrary, sulfur is significantly lower in cost and earth-abundant compared to that of Te and Se. Lead sulfide, PbS, with a rock salt structure has the potential to be an alternative to PbTe and PbSe.[15,28,29] However, the high lattice thermal conductivity (2.75 $Wm^{-1}\ K^{-1}$ at 300 K) constrains thermoelectric performance in PbS.[30-32] Additionally, the lower performance in PbS is also attributed to its higher deformation potential as compared to PbSe and PbTe, which results in lower σ at similar doping level/concentration due to stronger electron-phonon coupling in PbS.[33-36] Recently, lattice thermal conductivity of PbS has been reduced by nano-structuring in *p*-type materials such as in PbS-(Sr,Ca)S,[29] PbS-(Zn,Cd)S[15] and in *n*-type PbS-Sn-PbTe,[37] PbS-Sb,[38] PbS-Cu,[39] PbS-Bi_2S_3,[29] etc. However, a maximum zT of 1.3 in *n*-type $Pb_{0.94}Sn_{0.06}S$-8% PbTe[37] and *n*-type $Pb_{0.93}Sb_{0.05}S$[38], and a maximum zT of 1.3 at 923 K for *p*-type $Pb_{0.975}Na_{0.025}S$-3.0% CdS[40] has been realized. Hence, the quest to achieve higher thermoelectric performance in low-

cost PbS material remains an open opportunity to explore, which could be achieved by simultaneously improving the electronic transport and lowering the thermal conductivity.

Herein, we demonstrate high thermoelectric performance (zT of 1.45 at 900 K) for Ge doped (4-10 mol%) *n*-type PbS, which is the highest value among all PbS-based thermoelectrics. One of the main reasons to achieve such high performance in 10 mol% Ge doped PbS is its significantly low lattice thermal conductivity (κ_{lat}) of ~0.56 Wm^{-1} K^{-1} at 900 K which is near to theoretical minima (κ_{min}) of 0.45 Wm^{-1} K^{-1} for PbS. Transmission electron microscopy (TEM) investigation shows that the Ge doping (≥4 mol%) in PbS forms endotaxial nano-precipitates (5- 10 nm) of Pb_2GeS_4 in PbS matrix, which scatters the heat-carrying phonons heavily and lowers the κ_{lat}. The κ_{lat} of $Pb_{0.90}Ge_{0.10}S$ is ~40% lower compared to the pristine PbS at room temperature. Low-lying transverse acoustic (TA) and longitudinal acoustic (LA) phonon modes at 48.24 cm^{-1} and 91.83 cm^{-1}, respectively, were experimentally evidenced from the inelastic neutron scattering (INS) measured. We also observed softening of low frequency phonon modes at a higher temperature. The short phonon life-time (1-4.5 ps) estimated from INS experiments indicates strong phonon scattering which accounts for the ultra-low κ_{lat} in 10 mol% Ge doped PbS sample. Electron localization function (ELF) calculations show bonding heterogeneity in the case of Ge doped PbS due to the more covalent bonding character of Ge-S compared to Pb-S. First-principles density functional theoretical (DFT) calculations of electronic band structure indicate that Ge doping significantly lowers the deformation potential of n-type PbS, signifying weakened electron-phonon coupling, thereby increasing the electrical conductivity in Ge doped PbS samples. The synergetic role of (a) decreased κ_{lat} by phonon softening and nanostructured phonon scattering and (b) enhanced electrical transport due to stronger covalency leads to high zT of 1.45 in n-type PbS.

2.4.2. Methods

2.4.2.1. Reagents. Elemental Pb (wire, 99.99% Sigma Aldrich), S (pieces, 99.99%, Sigma-Aldrich) and Ge (pieces, 99.99%, sigma) Alfa Aesar) were used for synthesis without further purification.

2.4.2.2. Synthesis. Polycrystalline samples of $Pb_{1-x}Ge_xS$ (x =0.00-0.10) were synthesized from high purity elements Pb, S and Ge using vacuum-sealed tube melting and spark plasma sintering (SPS). The stoichiometric amounts of these elements were sealed in 13 mm quartz tubes under vacuum (10^{-6} Torr). The tubes were heated to 723 K in 12 h, then eventually heated to 1423 K, kept at this temperature for 6 h and finally air quenched to room temperature. The samples were powdered and transferred into a graphite die (10 mm diameter). The powders were pelletized by using SPS (SPS211-LX, Dr. Sinter Lab) under the pressure of 45 MPa for 10 min at 823 K. Density of the sample was estimated to be ~ 99% of the theoretical crystallographic density of PbS.

2.4.2.3. Powder X-ray Diffraction. Powder X-ray diffraction patterns (PXRD) for finely powder samples were recorded using a Cu $K\alpha$ (λ = 1.5406 Å) radiation source on a Bruker D8 diffractometer.

2.4.2.4. Carrier Concentration. Room temperature hall measurement was carried out in custom-built equipment developed by Excel Instruments where up to a magnetic field of 0.57 T and 50 mA dc-current were used.

2.4.2.5. Electronic Transport Properties. The electrical conductivity and Seebeck coefficient of parallelepiped shaped samples of $Pb_{1-x}Ge_xS$ (x =0.00-0.10) with the dimensions of ~2 mm × 2 mm × 8 mm were measured simultaneously from in the 298-900 K range under a low pressure He atmosphere by a ZEM-3 instrument (ULVAC-RIKO). The samples were spray-coated with boron nitrate to avoid the liberation of sulfur and also to protect the instrument. Reproducible results were achieved in the heating and cooling cycle measurements.

2.4.2.6. Thermal Conductivity. The total thermal conductivity, κ_{total}, was estimated from the relationship: $\kappa_{total} = DC_p\rho$, where ρ is the density, D is thermal diffusivity and C_p is specific heat capacity. D was measured in the 298-900 K under a N_2 atmosphere using laser flash method (Netzsch LFA-457). The measurement was performed on carbon-coated coin-shaped samples with radius of ~10 mm and thickness of less than ~2 mm.

2.4.2.7. Field Emission Scanning Electron Microscopy (FESEM). Backscattered FESEM imaging and EDAX were performed using Zeiss Gemini 500 FESEM on fined polished pieces of $Pb_{1-x}Ge_xS$ (x =0.04, 0.10).

2.4.2.8. Transmission Electron Microscopy (TEM). The electron diffraction pattern and HRTEM images of the as-synthesized materials were acquired using a TEM instrument (FEI TECNAI G2 20 STWIN) which operates at 200 kV. TEM samples were prepared by conventional mechanical thinning and tripod polishing of small pieces of $Pb_{1-x}Ge_xS$ (x =0.04, 0.10) samples. Large electron transport area was obtained by subsequent Ar ion milling in the precision ion polishing system (PIPS) with the ion energy of 4 eV and beam angle of 7 deg. The thickness was restricted to 80-90 μm.

2.4.2.9. Inelastic Neutron Scattering (INS). This part of work was carried at J-PARC in Japan under the collaboration with Dr. Kenji Nakajima. Cold neutron disc chopper spectrometer BL14 AMATERAS[41], was used to perform multi-E_i time-of-flight INS measurements. E_i of 42.00 and 15.2 meV were selected. Powder samples of $Pb_{0.90}Ge_{0.10}S$ were encased in a thin-walled aluminum cylinder with a diameter of 14 mm. $Pb_{0.90}Ge_{0.10}S$ data were collected at 8-600 K and a top-loading cryofurnace was used to control temperatures. The data reduction and visualization were accomplished using UTSUSEMI version 0.3.7.[42] The neutron-weighted general density of state (GDOS) was calculated by using the integration results of $G(Q,E) = S(Q,E)\left[1 - e^{\frac{-E}{\kappa_B T}}\right]E$, where $\left[1 - e^{\frac{-E}{\kappa_B T}}\right]$ =<n>+1 describes the Bose population factor and G(E) ∝ S(E)*E/(<n>+1) for E>0. The integration Q region was 3.2–5.2 $Å^{-1}$ for E = 42.0 meV and 1.8-3.2 $Å^{-1}$ for E = 15.2 meV. The peak broadening or change in full width at half maximum (FWHM) was calculated as, FWHM(T)-FWHM(8K). The peak positions and the line width of acoustic phonons were calculated by the Gaussian fitting using fityk and the data was plotted using OriginPro 8.5. To get the scattering rate from the fitted data, the 8 K data was used as a standard to observe the change in parameters with the change in temperature. The phonon scattering was then obtained by adding Gaussian widths in quadrature, $\sigma_{scat} = \sqrt{\sigma_T^2 - \sigma_{8K}^2}$, where σ_{8K} is the width at base temperature 8 K, σ_T is

the width at the higher temperature.[43] We calculated phonon lifetime from the extracted width using, $\tau^{-1} = 2.355\pi\sigma_{scat}$, where τ is inverse lifetime.[43]

2.4.2.10. Computational methods. This part of work was carried at IISc, Bangalore, India under the collaboration with Prof. Abhishek K. Singh. The first-principles calculations were performed using density functional theory (DFT)[44] as implemented in the Vienna *Ab initio* Simulation Package (VASP).[45,46] Projector augmented wave (PAW) pseudopotentials [47,48] were employed to represent the ion-electron interactions, Perdew-Burke-Ernzerhof (PBE)[49] generalized gradient approximation was used to approximate the exchange and correlation part of the total energy. The special quasi-random structure (SQS) was generated using the Monte Carlo SQS tool as implemented in Alloy Theoretical Automated Toolkit (ATAT)[50]. All the structures were optimized using a conjugate gradient scheme until the Hellmann-Feynman forces on the atoms were less than 0.0001 eV/Å and using a plane wave energy cut-off of 450 eV. PbS crystallizes in Fm-3m space group with one Pb and one S in the primitive cell, occupying 4b (0.5, 0.5, 0.5) and 4a (0, 0, 0) Wyckoff positions, respectively. The optimized lattice parameters are a = b = c = 4.24 Å with $\alpha = \beta = \gamma = 60°$. Experimentally, n-type conductivity, good mobility, and low lattice thermal conductivity are observed upon Ge doping in PbS ($Pb_{1-x}Ge_xS$ where x = 0 - 0.10). To understand the origin of these from first-principles, Ge-doped PbS is modeled using the special quasi-random structure (SQS) algorithm[51,52]. The structure is generated by creating a 3x3x3 supercell and replacing the Pb sites with Ge. The structure with 3 Ge corresponding to 11% Ge doping is shown Figure 2.4. S4. The optimized lattice parameters for the doped structure are a = 12.64 Å, b = 12.61 Å, and c = 12.65 Å with $\alpha = 60.08°$, $\beta = 59.81°$, and $\gamma = 60.11°$. Additionally, the presence of nanoprecipitates of Pb_2GeS_4 is observed by the PXRD analysis. The secondary phase is monoclinic phase with space group $P2_1/c$ and the optimized lattice parameters for the secondary phase are a = 8.02 Å, b = 9.62 Å, and c = 10.96 Å with $\alpha = 90°$, $\beta = 114.98°$, and $\gamma = 90°$.

The deformation potential (D) is obtained by calculating the electronic band structure as a function of pressure. The slope of the change in valence band maxima or conduction band minima versus pressure curve gives the hole or electron deformation potential, respectively. To analyze the effect of doping on the lattice thermal conductivity, we analyzed the bonding characteristics through electron localization

function (ELF). ELF quantifies the bonding character by calculating the probability corresponding to finding the same spin electron near one reference electron.[53,54] The trend in bonding characteristics obtained from ELF is further confirmed by the crystal orbital Hamilton population (COHP) analysis, which gives the information on bonding and antibonding contribution.[55,56]

2.4.3. Results and Discussions

Polycrystalline samples of $Pb_{1-x}Ge_xS$ (x =0.00-0.10) were synthesized by vacuum (10^{-5} Torr) sealed tube melting followed by spark-plasma sintering (SPS) technique.

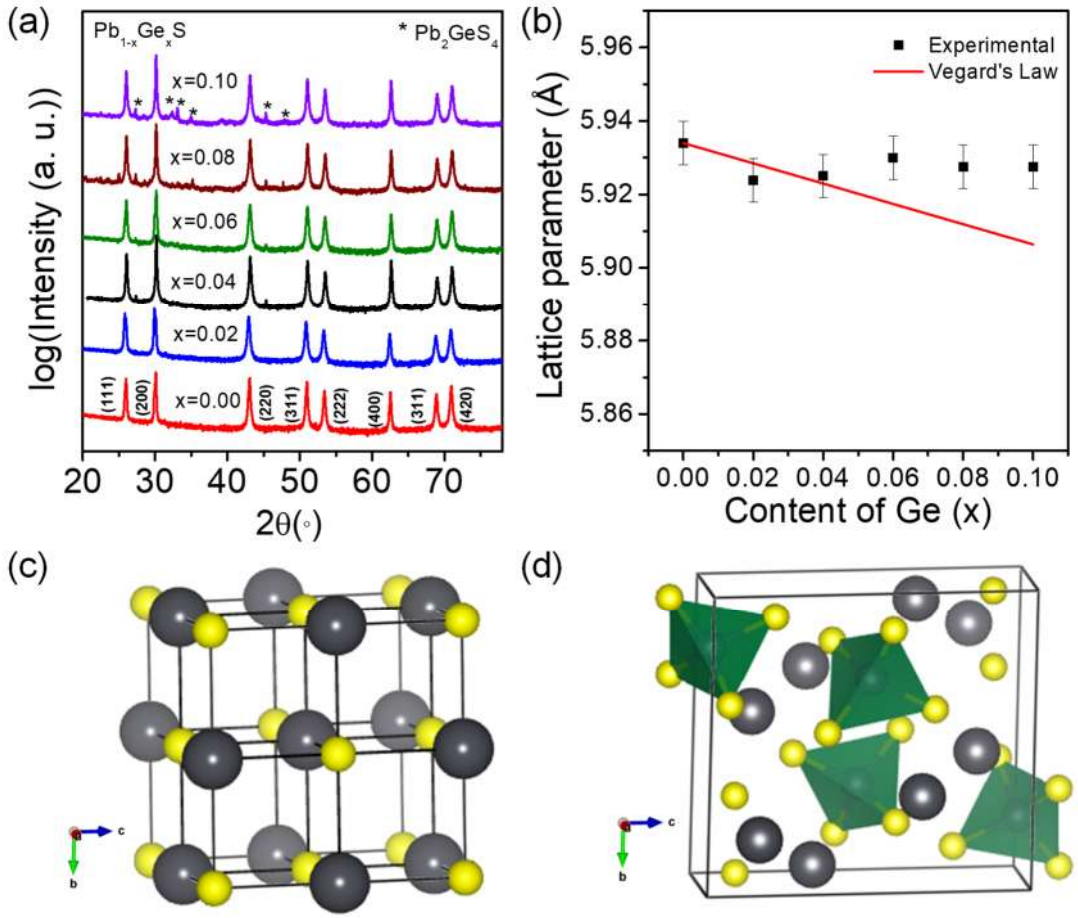

Figure 2.4.1. *(a) PXRD patterns of $Pb_{1-x}Ge_xS$ (x=0-0.10) samples. * indicates presence of Pb_2GeS_4 as minor secondary phase. (b) Lattice parameter vs. content of Ge (x) in $Pb_{1-x}Ge_xS$ (x=0-0.10) samples, indicating deviation from Vegard's Law (red line) (c) Cubic structure of rocksalt PbS. (d) Crystal structure of Pb_2GeS_4; black (Pb); yellow (S); green tetrahedral (GeS_4).*

The powder X-ray diffraction (PXRD) patterns of $Pb_{1-x}Ge_xS$ (where x = 0 - 0.10) show an excellent match to the rock salt phase of PbS with a space group of *Fm-3m* (Figure 2.4.1a, c). The lattice parameter slightly decreases with an increase in Ge concentration up to 4 mol% due to the replacement of Pb^{2+} (~1.2 Å) by Ge^{2+} (~0.65 Å) which has a smaller cationic radius. However, at Ge concentration ≥ 4 mol%, the lattice parameter diverges from Vegard's law (red line), signifying the solid solution limit of Ge in PbS is ~4 mol% (Figure 2.4.1b). Mention must be made that solid solution limits of Ge in PbSe and PbTe are ~12 % and ~ 13% respectively.[57,58] Ge doping in PbS beyond the solid-solution limit, leads to the formation of the secondary phase of Pb_2GeS_4, marked by "*" in the PXRD pattern shown in Figure 2.4. 1a, as low-intensity reflections. The secondary Pb_2GeS_4 phase, related K_2SO_4 type structure, crystallizes in monoclinic space group $P2_1/c$ comprising of isolated [GeS_4] tetrahedra and Pb^{2+} ions in six- and sevenfold coordination (see Figure 2.4.1d).[59] The advantage of this secondary phase on the thermoelectric properties of PbS is discussed later.

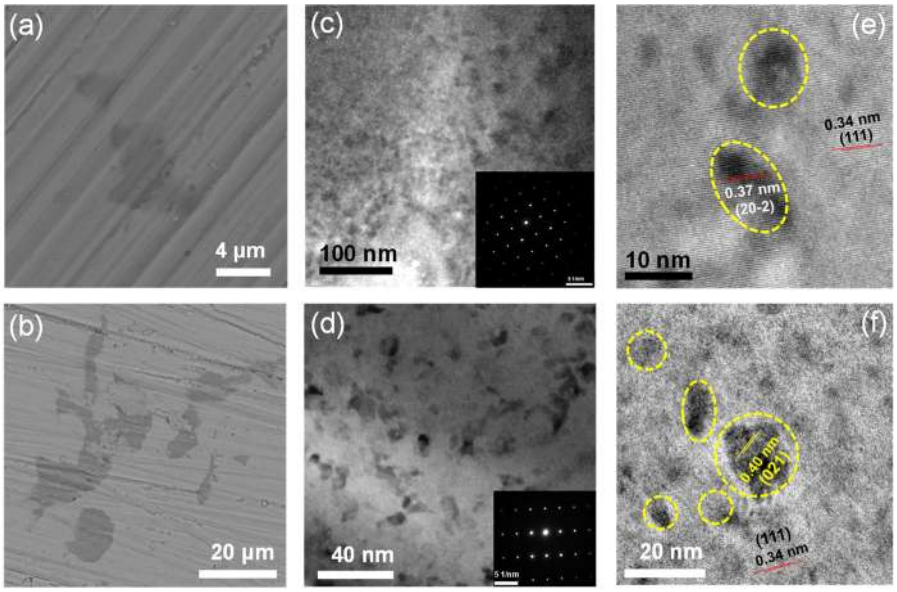

Figure 2.4.2. *(a) and (b) Backscattered FESEM images from polished surfaces of $Pb_{0.96}Ge_{0.04}S$ and $Pb_{0.90}Ge_{0.10}S$; (c) and (d) low magnification TEM images of $Pb_{0.96}Ge_{0.04}S$ and $Pb_{0.90}Ge_{0.10}S$, inset showing SAED pattern of PbS matrix; (e) and (f) HRTEM of $Pb_{0.96}Ge_{0.04}S$ and $Pb_{0.90}Ge_{0.10}S$. In (e), Pb_2GeS_4 nanoprecipitates (darker contrast, dotted in yellow circle) show d spacing of 0.37 nm for (20-2) planes and d spacing of 0.34 nm with (111) plane is corresponding to PbS matrix. In (f), Pb_2GeS_4 nanoprecipitates (darker contrast, dotted in yellow circle), show d spacing of 0.40 nm for (020) planes.*

To understand the nano/microstructure and chemical composition of secondary phases in Ge doped PbS samples ($Pb_{1-x}Ge_xS$, x=0.04, 0.10), backscattered electron imaging (BSE)- field emission scanning electron microscopy (FESEM), energy dispersive X-ray analysis (EDAX) and transmission electron microscopy (TEM) were performed. The BSE-FESEM image of $Pb_{0.96}Ge_{0.04}S$ shows the presence of dark contrast precipitates with the size of ~ 2-6 μm in PbS matrix (Figure 2.4.2a, 2.4.3a). The EDAX analysis (Figure 2.4.3b, c) confirms the darker contrast precipitates are Ge-rich whereas the lighter contrast matrix is PbS. TEM and high-resolution transmission electron microscopy (HRTEM) images in (Figure 2.4. 2c and 2e) of $Pb_{0.96}Ge_{0.04}S$ also show dark contrast nanoprecipitates (5–10 nm). The lattice with the *d*-spacing of 0.37 nm in the nanoprecipitates is corresponding to (20-2) planes of Pb_2GeS_4, which is nearly coherent with 0.34 nm *d*-spacing of (111) planes of PbS (Figure 2.4. 2e).

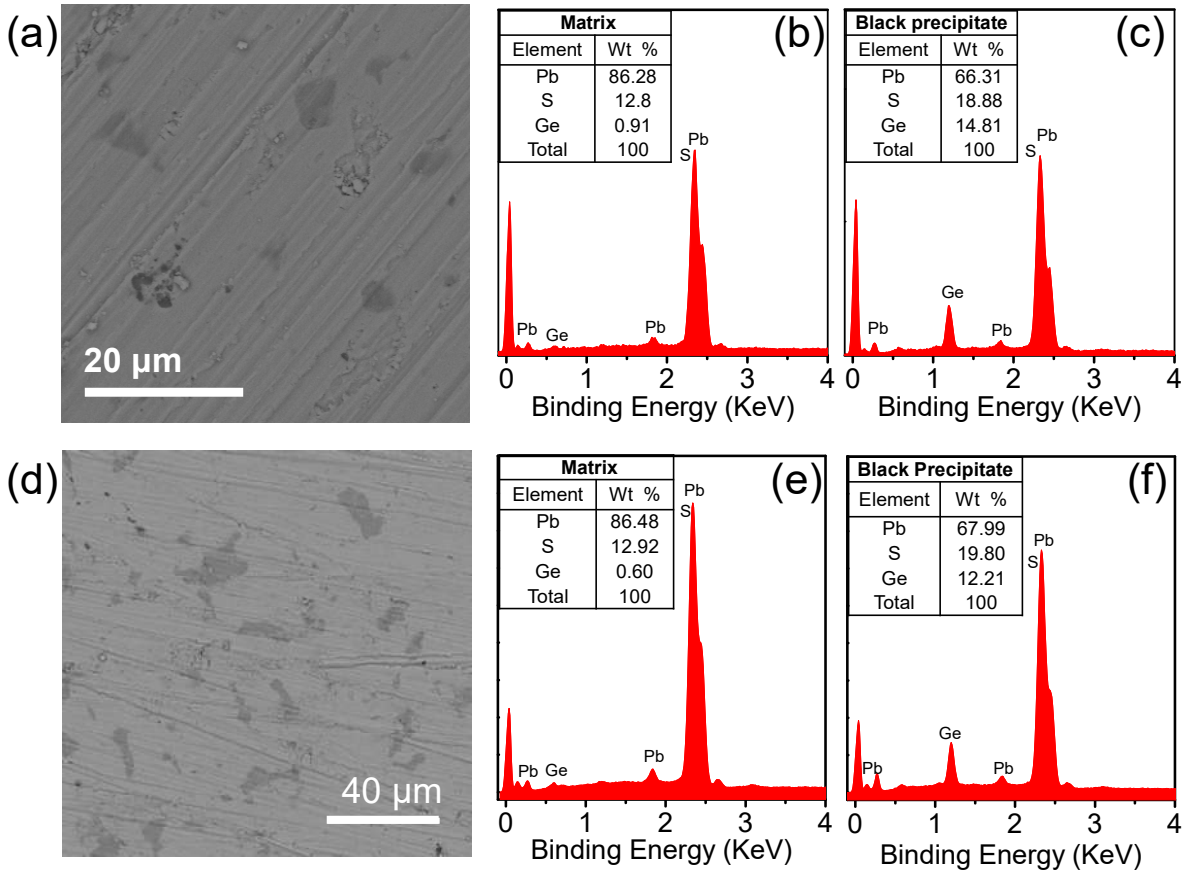

Figure 2.4.3. *Backscattered FESEM images from polished surface, EDAX of matrix and from black precipitate of (a-c) $Pb_{0.96}Ge_{0.04}S$ and (d-f) $Pb_{0.90}Ge_{0.10}S$ respectively.*

EDAX in scanning transmission electron microscopy (STEM) mode images also confirmed these nano-precipitates are Pb_2GeS_4 (Figure 2.4.4a). The selected area electron diffraction (SAED) pattern (inset of Figure 2.4.3c) shows the single-crystalline nature of the Ge doped PbS sample. The nanometer-sized inclusions of Pb_2GeS_4 can play a key role in scattering phonons without affecting electrons in PbS.

As we increase the concentration of Ge to x=0.10 in $Pb_{1-x}Ge_xS$, the BSE images show morphological differences. The size of dark contrast precipitates increased from 2-6 μm to 10-15 μm and are distributed uniformly in the PbS matrix, indicating consolidation of small precipitates into bigger precipitates (Figure 2.4. 2b and 2.4.3d).

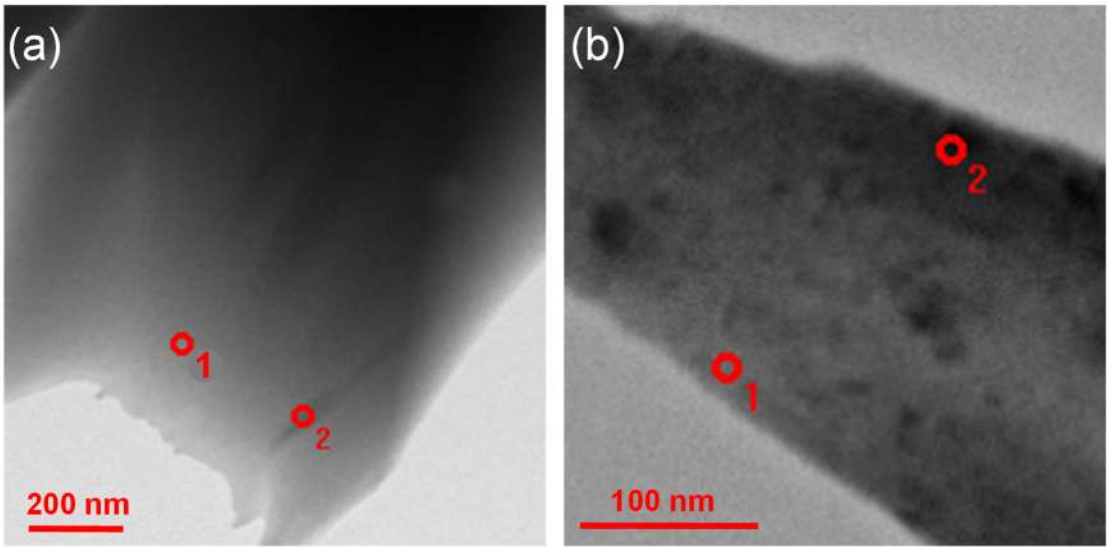

$Pb_{0.96}Ge_{0.04}S$	Bright Region (1)		Dark Region (2)	
Element	Wt%	At%	Wt%	At%
Pb	93.23	31.92	87.97	57.05
Ge	0	0	3.19	5.91
S	6.76	68.07	8.83	37.03
Total	100	100	100	100

$Pb_{0.90}Ge_{0.10}S$	Bright Region (1)		Dark Region (2)	
Element	Wt%	At%	Wt%	At%
Pb	90.12	65.17	79.57	46.05
Ge	4.33	8.94	10.75	17.77
S	5.53	25.88	9.66	36.17
Total	100	100	100	100

Figure 2.4.4. *Scanning transmission electron microscopy (STEM) images and EDAX from bright and dark regions of (a) $Pb_{0.96}Ge_{0.04}S$ and (b) $Pb_{0.90}Ge_{0.10}S$ samples showing dark region as Pb_2GeS_4 secondary phase.*

The EDAX analysis on the dark contrast precipitates (Figure 2.4.3f) corresponds to Pb_2GeS_4 phase, which is further confirmed by TEM analysis. Figure 2.4. 2b shows

that the size of the small endotaxial nano-inclusions has also increased from 5-10 nm to 5-20 nm for x=0.10 in $Pb_{1-x}Ge_xS$. The SAED pattern in the inset of Figure 2.4.3d shows intact crystal structure even though the Ge doping has been increased to 10 %. The calculated d-spacing of darker contrast precipitates (dotted in yellow circle) in $Pb_{0.90}Ge_{0.10}S$ matrix is 0.40 nm, attributed to the (021) planes of Pb_2GeS_4 phase (Figure 2.4.3f). STEM mode images and EDAX confirms the presence of Pb_2GeS_4 phase (Figure 2.4.4b). The presence of these endotaxial Pb_2GeS_4 nanoprecipitates in PbS matrix can effectively lower the lattice thermal conductivity by scattering the heat-carrying phonons of similar wavelengths.

Table 2.4.1. Room temperature carrier concentration (n), electrical conductivity (σ), and carrier mobility (μ) of $Pb_{1-x}Ge_xS$ (x=0-0.10) samples.

Sample	Carrier concentration (cm^{-3})	σ (S/cm)	μ (cm^2/Vs)
PbS	8.54×10^{17}	27	197
4% Ge	2.44×10^{19}	554	142
6% Ge	1.90×10^{19}	452	151
8% Ge	2.00×10^{19}	463	146
10% Ge	1.48×10^{19}	256	168

To observe the effect of Ge doping on thermoelectric properties of PbS, we measured the temperature-dependent electrical transport of $Pb_{1-x}Ge_xS$ samples. The electrical conductivity decreases with an increase in temperature due to carrier-phonon scattering, thereby showing the behavior of degenerate semiconductors (Figure 2.4.5a). At room temperature, the electrical conductivity (σ) of pristine PbS is ~27 S/cm. In contrast, upon Ge doping we observe tremendous increase of σ to ~555 S/cm at room temperature for x=0.04 in $Pb_{1-x}Ge_xS$ due to increase in the *n*-type carrier concentration (n) from 8.54×10^{17} cm^{-3} for pristine PbS to 2.44×10^{19} cm^{-3} for $Pb_{0.96}Ge_{0.04}S$ (Table 2.4.1). However, the electronic conductivity slightly decreases upon further increasing the doping concentration to x=0.10. Typically, at room temperature, electrical conductivity

becomes ~399 S/cm and ~117 S/cm at 900 K for $Pb_{0.90}Ge_{0.10}S$. The charge carrier mobility (μ_H) in Figure 2.4.5b shows that Ge doped samples exhibit μ_H in the range of 142-197 $cm^2V^{-1}s^{-1}$ and n in the range of 1.48-2.44 x 10^{19} cm^{-3}.

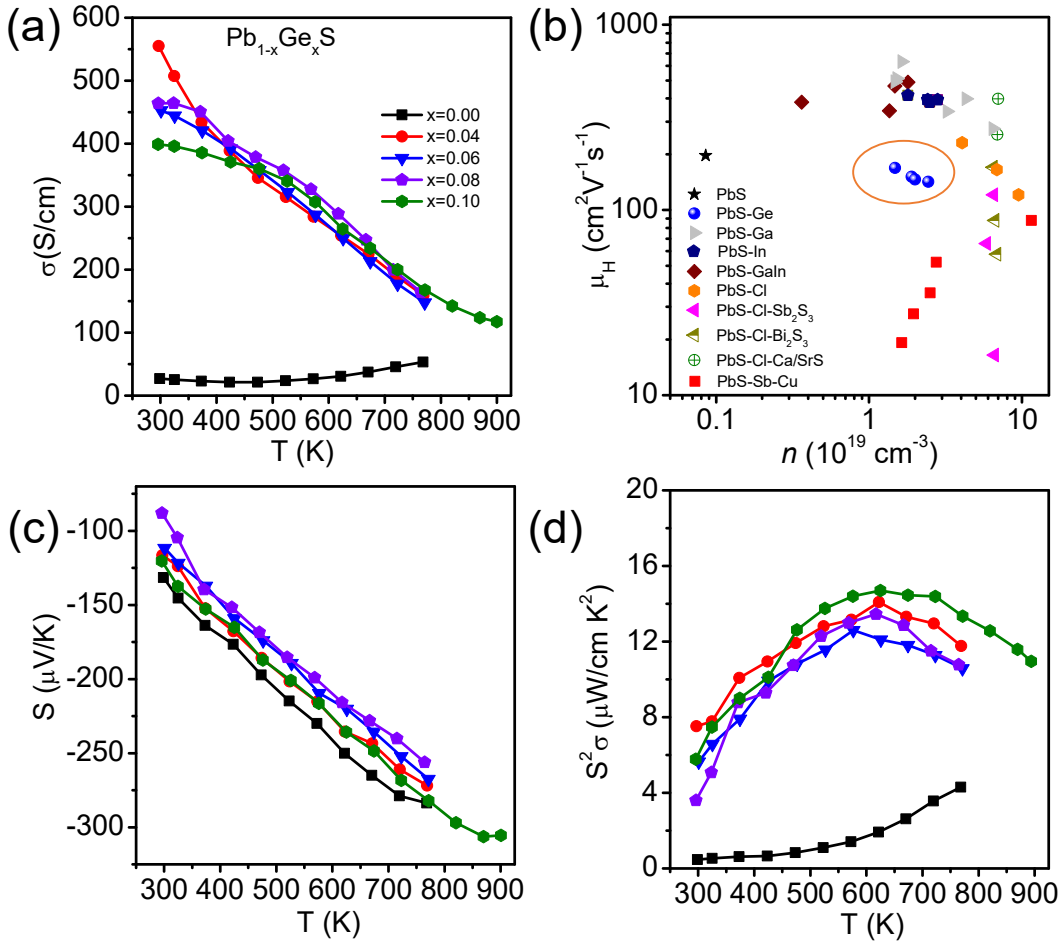

Figure 2.4.5. *Temperature-dependent (a) electrical conductivity (σ) of $Pb_{1-x}Ge_xS$ (x=0-0.10) samples. (b) Comparison of room temperature carrier mobility, μ_H, of PbS and Ge doped PbS (in this work) with previously reported samples, PbS—Ga,[32] PbS—In,[32] PbS—Ga-In,[32] PbS-Cl,[33] PbS-Cl-Sb_2S_3,[29] PbS-Cl-Bi_2S_3,[29] PbS-Cl-Ca/SrS,[29] PbS-Sb-Cu.[39] Temperature-dependent (c) Seebeck coefficients (S), (d) power factor ($S^2\sigma$) of $Pb_{1-x}Ge_xS$ (x=0-0.10) samples.*

Figure 2.4.5c shows temperature-dependent Seebeck coefficients for $Pb_{1-x}Ge_xS$ samples. The negative sign of the Seebeck coefficient specifies the electrons as the major carriers. All the Ge doped samples exhibit lower Seebeck coefficient values than the pristine PbS from room temperature to 770 K, validating the carrier concentration listed in Table 2.4.1. For $Pb_{0.90}Ge_{0.10}S$, the Seebeck coefficient value increases from ~ -120 μV/K

at room temperature to ~ -305 μV/K at 900 K. As a result of high electrical conductivity and Seebeck coefficient, the power factor for Ge doped samples is ~7 folds higher than pristine PbS sample at room temperature and a peak power factor of 14.7 μW/cmK^2 at 625 K is achieved for $Pb_{0.90}Ge_{0.10}S$, which decreases to ~11.0 μW/cmK^2 at 900 K (Figure 2.4.5d).

To understand the electronic properties for Ge-doped PbS samples, we performed first principles density functional theory calculations of electronic structure. Figure 2.4.6. shows the SQS unit cell of Ge doped PbS and secondary phase Pb_2GeS_4. The electronic band structures and corresponding atom-projected electronic density of states (DOS) of pristine, $Pb_{0.89}Ge_{0.11}S$, and the secondary phase Pb_2GeS_4 are shown in Figure 2.4.7. The electronic structure analysis reveals that the contribution of Ge is in the conduction band states in both the doped and secondary phase, implying Ge-doping as the plausible cause for *n*-type conductivity.

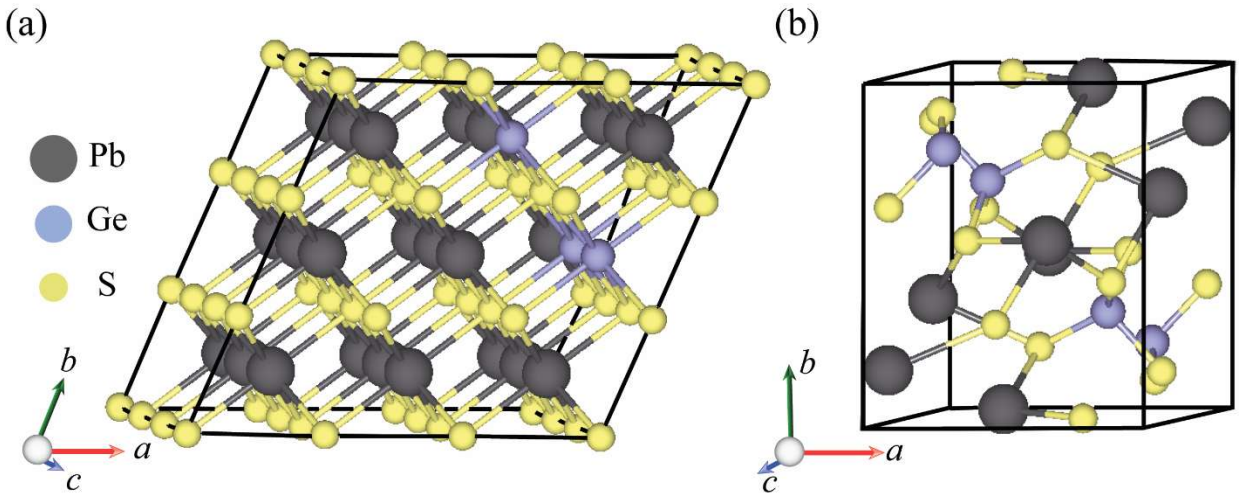

Figure 2.4.6. *(a) The SQS unit cell of Ge doped PbS and (b) Unit cell of secondary phase Pb_2GeS_4.*

To explain the origin of reasonably high mobility, we further analyzed the change in deformation potential upon Ge doping, which has inverse square dependence on mobility.[34,36] From the evolution of electronic band structure as a function of pressure, deformation potential (D) can be estimated. It is quantified by the change in the band edges as a function of pressure. The slope of the change in valence band maxima and

conduction band minima versus pressure curve gives the hole (D_h) and electron deformation potential (D_e), respectively. If the deformation potential is small, then it signifies that the bands are rigid as a function of pressure. Table 2.4.2 summarizes D_h and D_e calculated by applying hydrostatic pressure. D_e is lower than D_h in all the three compounds, namely, pristine PbS, $Pb_{0.89}Ge_{0.11}S$ and Pb_2GeS_4. This suggests that the carriers are less scattered in the conduction band than the valence band. Moreover, D_e for Ge doped PbS (8.94 eV) is smaller as compared to pristine PbS (9.31 eV). This may be attributed to stronger bonding in Ge-doped sample as compared to pristine PbS. In Ge-doped PbS, the Ge-S bond is more covalent than Pb-S bond and hence the deformation potential is smaller. This increase in bond covalency results in lowering of electron-phonon coupling, thereby contributing to the high electronic mobility and conductivity, and hence the power factor in Ge-doped PbS samples increases.

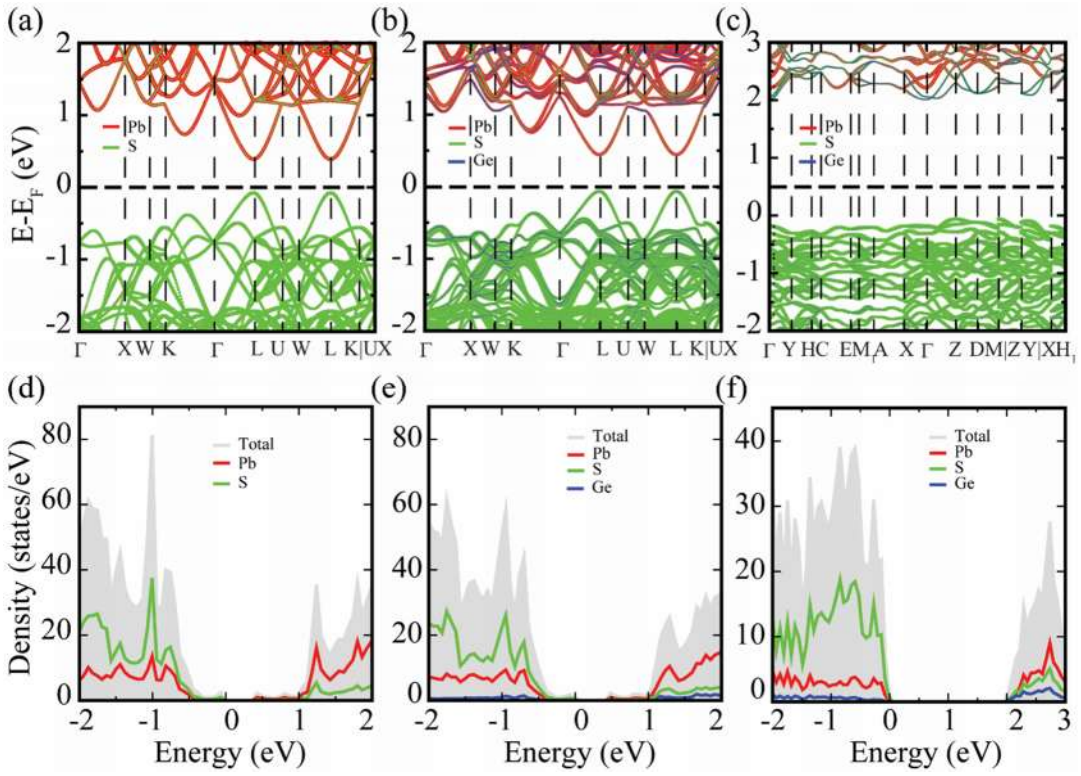

Figure 2.4.7. *Electronic band structures for (a) pristine, (b) Ge doped PbS ($Pb_{0.89}Ge_{0.11}S$), and (c) Pb_2GeS_4. The electronic density of states for (d) pristine, (e) doped, and (f) Pb_2GeS_4.*

Table 2.4.2. Hole and electron deformation potential (D_h and D_e) obtained by applying hydrostatic pressure for the pristine PbS, $Pb_{0.89}Ge_{0.11}S$, and secondary Pb_2GeS_4.

Case	Deformation Potential	
	D_h	D_e
Pristine	12.35	9.31
$Pb_{0.89}Ge_{0.11}S$	12.43	8.94
Pb_2GeS_4	8.98	6.79

The most striking finding in this work is that the introduction of Ge in the PbS lattice has profound effects on the reduction of thermal conductivity. For example, at room temperature, the total thermal conductivity value of $Pb_{0.90}Ge_{0.10}S$ (1.91 Wm^{-1} K^{-1}) is 1.5 times lower than that of pristine PbS (2.87 Wm^{-1} K^{-1}) (Figure 2.4. 8a). Upon increasing Ge doping, the thermal conductivity decreases drastically, and a minimum thermal conductivity of 0.68 Wm^{-1} K^{-1} is achieved at 900 K for x=0.10.

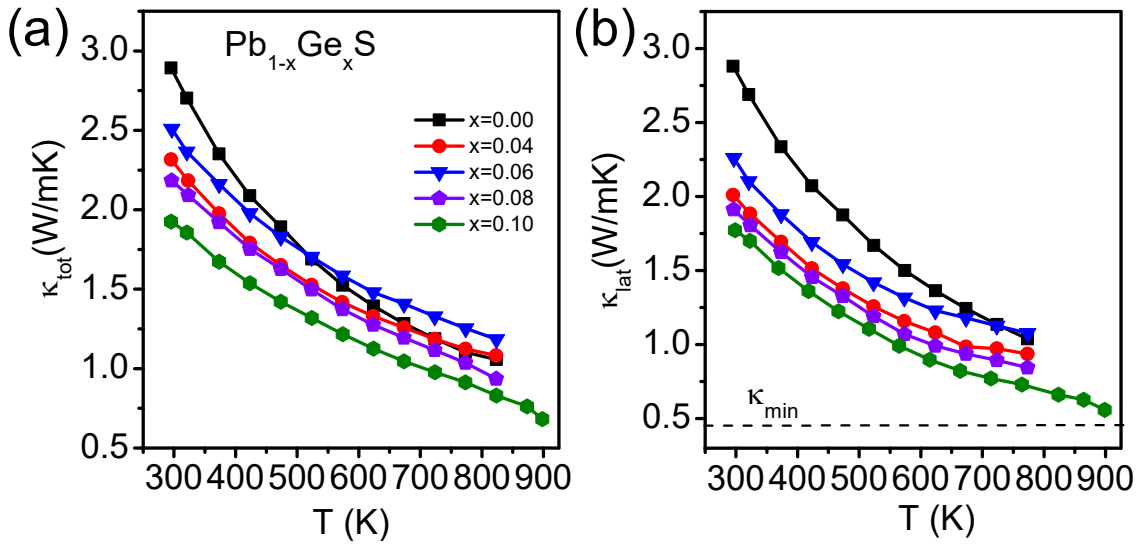

Figure 2.4.8. Temperature-dependent (a) total thermal conductivity (κ_{tot}) and, (b) lattice thermal conductivity (κ_{lat}) of Pb_{1-x} Ge_xS (x=0-0.10) samples.

The temperature-dependent lattice thermal conductivity (κ_{lat}) values of samples, estimated by subtracting κ_e from $\kappa_{tot,}$ is shown in Figure 2.4. 8b. At room temperature, κ_{lat} is 2.88 Wm^{-1} K^{-1} for PbS, decreases to 1.04 W m^{-1} K^{-1} at 773 K. For $Pb_{0.90}Ge_{0.10}S$, κ_{lat} decreases from 1.77 Wm^{-1} K^{-1} at room temperature to 0.56 W m^{-1} K^{-1} at 900 K, which is close to theoretical minimum lattice thermal conductivity (κ_{min}) of PbS (0.45 W m^{-1} K^{-1}). This substantial decrease of lattice thermal conductivity for $Pb_{0.90}Ge_{0.10}S$ in comparison to pristine PbS is ascribed to the extensive scattering of heat-carrying phonons of different wavelength by endotaxial nanoprecipitates of Pb_2GeS_4 present in $Pb_{0.90}Ge_{0.10}S$ matrix (see in Figure 2.4. 2). The phonon with mean free paths smaller than 10 nm contributes ~90% of κ_{lat} for IV-VI metal chalcogenides.[60] The precipitates of the Pb_2GeS_4 in $Pb_{0.90}Ge_{0.10}S$ sample are in the range of 5-20 nm which scatters heat-carrying phonons effectively, leading to suppression of lattice thermal conductivity. Previously, low κ_{lat} has been achieved in PbTe[61] and PbSe[62] via Ge doping due to nanoscale heterogeneities or lattice anharmonicity.

To investigate further the effect of doping on the thermal transport property, we analyzed the bonding characteristics through electron localization function (ELF) (Figure 2.4. 9). ELF quantifies the bonding character by calculating the probability corresponding to finding the same spin electron near one reference electron. ELF values lie in the range of 0-1, where 1 corresponds to covalent bonding and 0 corresponds to delocalized behavior. The calculated ELF along [110] plane for the pristine and Ge-doped is depicted in Figure 2.4.9a, b, respectively. We observe an increase in bonding heterogeneity in the case of Ge-doped PbS. Similar bonding heterogeneity is seen in the ELF for secondary phase Pb_2GeS_4, for [010] and [001] planes. Additionally, Ge-S bonding is stronger than Pb-S bonding for both the doped and secondary phase. Hence, the Ge doping leads to hierarchy in the chemical bonding, which results in low lattice thermal conductivity due to bonding heterogeneity. Additionally, crystal orbital Hamilton population (COHP) analysis[55,56]for PbS, Ge-doped PbS and Pb_2GeS_4, reveals that Ge and S bonds are contributing to bonding region as shown by the black arrows in Figure 2.4.10. This contribution is higher compared to that of Pb-S bonds, implying a more covalent bonding character of Ge-S compared to Pb-S.

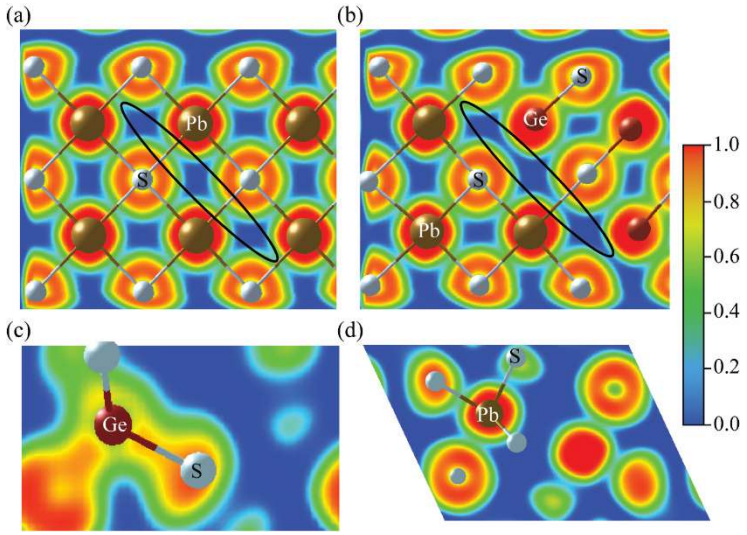

Figure 2.4.9. *ELF for (a) pristine PbS along [110] plane, (b) $Pb_{0.89}Ge_{0.11}S$ along [110] plane, (c) and (d) Pb_2GeS_4 along [010] and [001] plane, respectively.*

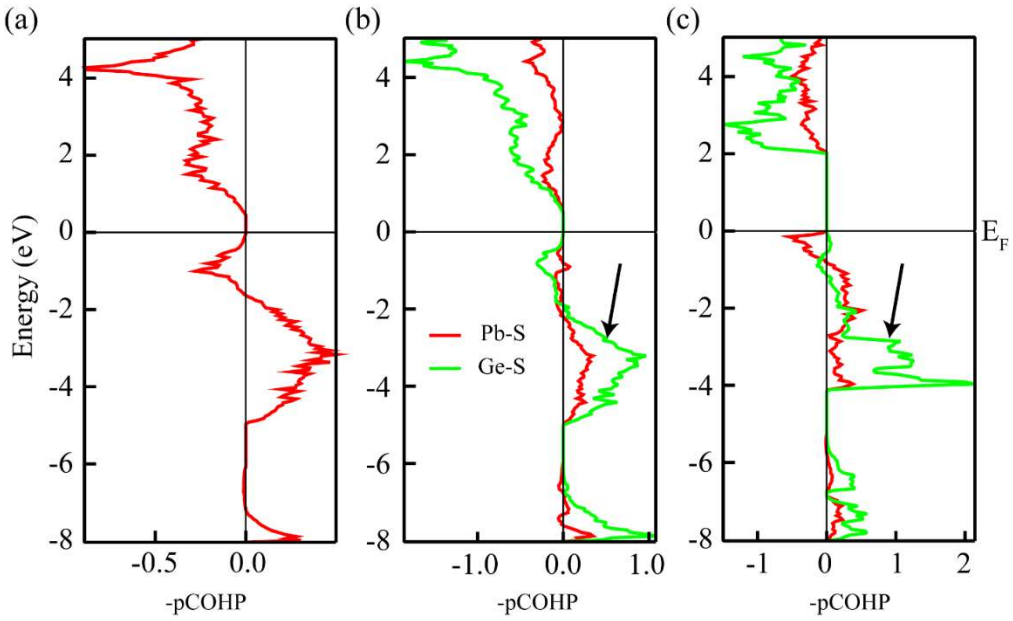

Figure 2.4.10. *Calculated COHP for (a) pristine PbS, (b) $Pb_{0.89}Ge_{0.11}S$, and (c) Pb_2GeS_4.*

Further, to understand this low lattice thermal conductivity for $Pb_{0.90}Ge_{0.10}S$, we quantified experimental phonon density of states using temperature-dependent inelastic neutron scattering measurements in the temperature range of 8-600 K. Figure 2.4.11a, b and 2.4.12a, shows the phonon density of states ($G(\omega)$) for $Pb_{0.90}Ge_{0.10}S$ for E_i=42 meV *and E_i=15.2 meV, respectively.*

Figure 2.4.11. *Temperature-dependent phonon DOS of $Pb_{0.90}Ge_{0.10}S$ sample, measured*

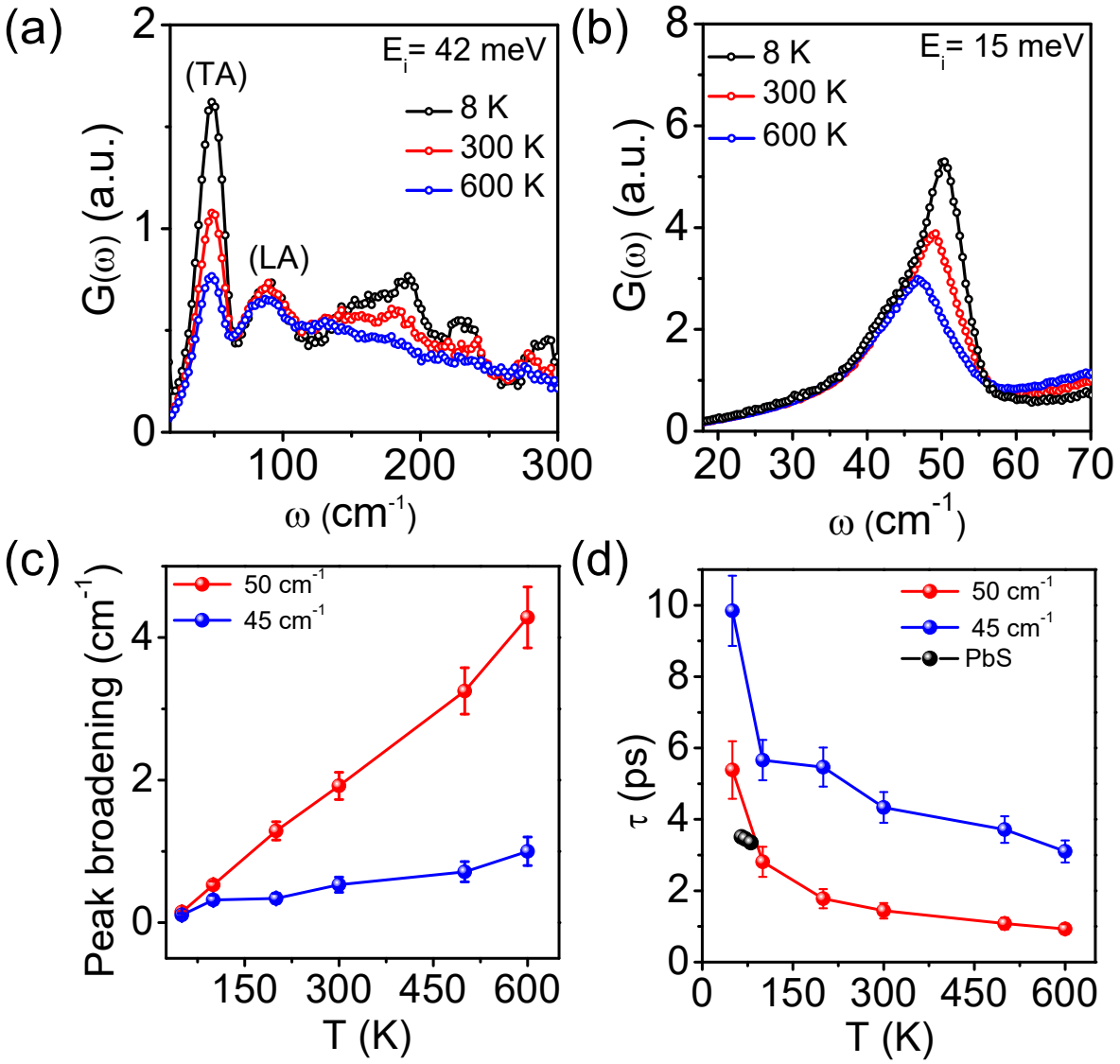

using INS at (a) E_i= 42 meV and (b) 15 meV. Temperature dependence of (c) peak broadening (FWHM) and (d) phonon lifetimes extracted using Gaussian fitting of peaks centered at 50 and 45 cm^{-1} for E_i =15 meV. Phonon lifetime for PbS is calculated using lattice thermal conductivity[49] and average sound velocity.[31]

The overall shape of G(ω) is consistent with calculations of the phonon density of states (PDOS) for bulk PbS[62], indicating the presence of low-lying modes. We observe transverse acoustic (TA) modes at ~ 48 cm^{-1} and longitudinal acoustic (LA) at ~ 91cm^{-1}.[62] Further, at high energy of E_i=42 meV, the modes above ~150 cm^{-1} corresponding from sulfur vibrations decrease the signature at high temperatures due to the high anharmonicity (Figure 2.4. 7a and S6a). In low energy of E_i=15.2 meV, we observe a shift of the TA mode from ~50 cm^{-1} at 8 K to ~46 cm^{-1} at 600 K (Figure 2.4.11b). The peak broadening increases with the increase in temperature for two deconvoluted peaks (Figure 2.4.11c and 12b), centered at 50 cm^{-1} and 45 cm^{-1}, signifying the softening of low-frequency phonon modes at high temperatures. Phonon lifetime measured from INS is in the range of 1-4.5 ps at room temperature for Ge-doped PbS, which is comparable with the values measured from average sound velocity[31] and low-temperature lattice thermal conductivity of PbS[63] (Figure 2.4.11d). This ultra-short phonon lifetime suggests strong phonon-phonon scattering which accounts for the ultra-low lattice thermal conductivity in Ge doped PbS.

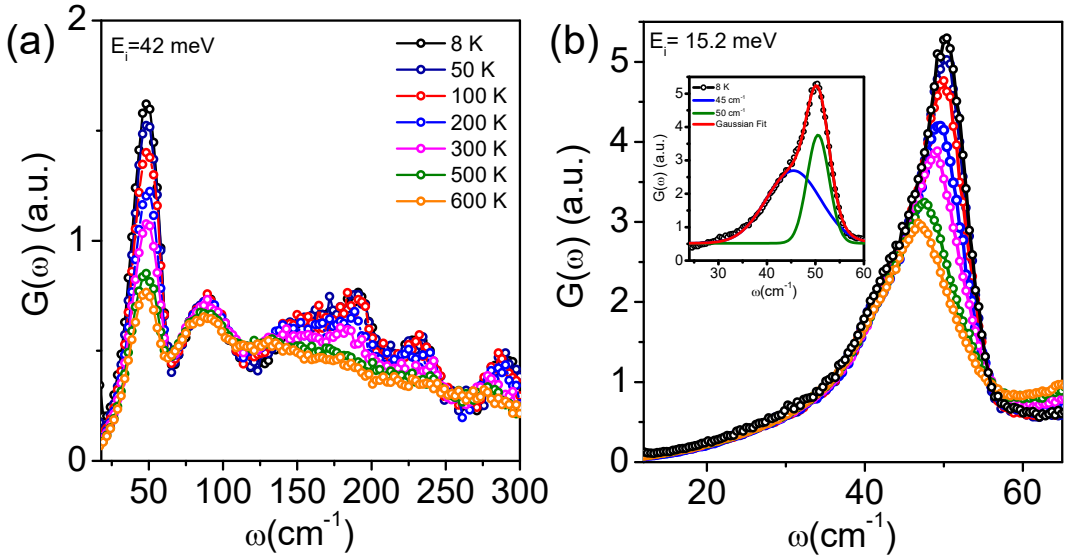

Figure 2.4.12. *Temperature-dependent phonon DOS of $Pb_{0.90}Ge_{0.10}S$ sample, measured using inelastic neutron scattering at (a) E_i= 42 meV and (b) 15 meV in the range 8-600 K range. Inset shows the Gaussian fitting of peak centered at 50 and 45 cm^{-1} for E_i =15 meV at 8 K.*

We observe a tremendous enhancement in zT due to synergistic optimization of electrical and thermal transport properties in $Pb_{1-x}Ge_xS$ samples via the presence of

enhanced covalency and endotaxial nanoprecipitates of Pb_2GeS_4 in PbS matrix. The temperature-dependent zT of $Pb_{1-x}Ge_xS$ clearly shows that Ge doping in PbS has been beneficial to improve the overall thermoelectric performance (Figure 2.4.13a). n-type $Pb_{0.90}Ge_{0.10}S$ sample exhibits the maximum zT of ~ 1.45 at 900 K, which is the highest among all n-type PbS-based thermoelectric materials (Figure 2.4. 13b).

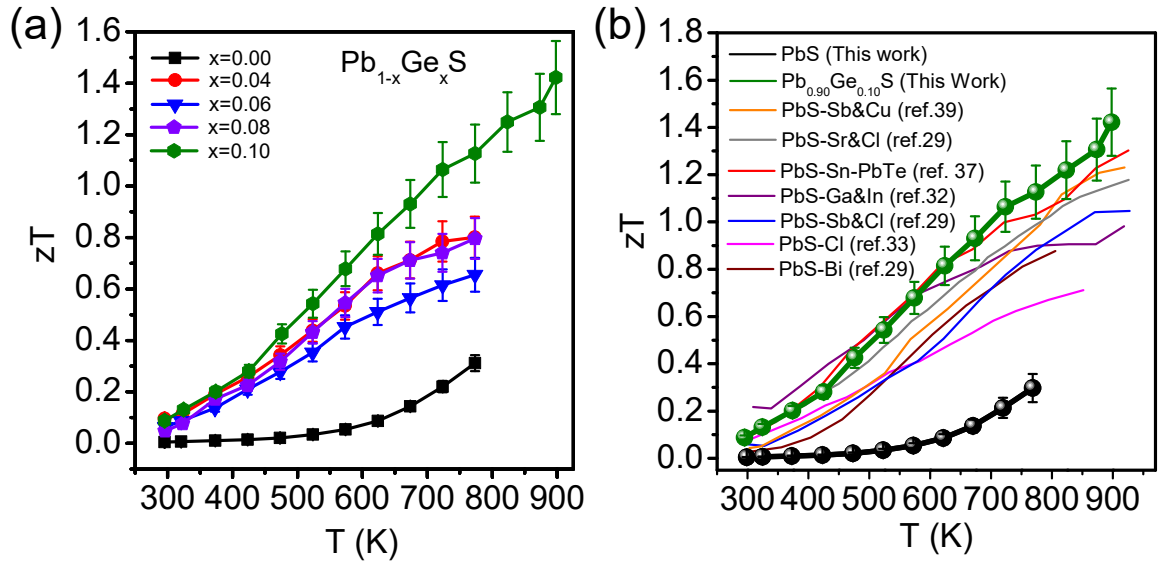

Figure 2.4.13. *(a) Thermoelectric fig. of merit (zT) of $Pb_{1-x}Ge_xS$ (x=0-0.10) samples and (b) comparison of zT values for n-type PbS with those in previously reported n-type PbS-based thermoelectric materials. The uncertainly in zT measurement is ~10 %.*

2.4.4. Conclusions

Our findings provide a fundamental understanding of chemical bonding, electronic structure modulation and nanostructured phonon scattering in n-type Ge doped PbS which resulted in significant enhancement of the thermoelectric performance. The Ge doping in PbS leads to ultra-low lattice thermal of 0.56 W m^{-1} K^{-1} at 900 K for n-type $Pb_{0.90}Ge_{0.10}S$. One of the main causes of such low lattice thermal conductivity is the strong phonon scattering by nanostructured (5-20 nm) Pb_2GeS_4 in Ge-doped PbS matrix. Inelastic neutron scattering (INS) measurement reveals the experimental low-lying TA and LA anharmonic phonon modes with ultra-short lifetime (1-4.5 ps), which further increased the phonon scattering and resulted in ultra-low lattice thermal conductivity. Electron localization functional (ELF) analysis confirms the enhanced

covalent and chemical bonding heterogeneity upon Ge doping in PbS. Further, DFT calculation electronic structure suggests the lowering of deformation potential upon Ge doping in PbS, due to weakened electron-phonon coupling, which improved the electrical transport. This synergetic decrease of (a) lattice thermal conductivity due to endotaxial nano precipitates of Pb_2GeS_4 and presence of anharmonic low energy phonons and (b) increase of electrical conductivity due to enhanced covalency in chemical bonding boost to high zT value of ~ 1.45 at 900 K in n-type Ge doped PbS, which is shown the promise as low cost and high-temperature alternative of PbTe and PbSe based thermoelectric materials.

2.4.5. References

[1] G. Tan, L.-D. Zhao, M. G. Kanatzidis, *Chem. Rev.* **2016**, 116, 12123.

[2] Y. Xiao , L.-D. Zhao, *Science.* **2020**, 367, 1196.

[3] X. -L. Shi, J. Zou , Z.-G. Chen, *Chem. Rev.* **2020**, 120, 7399.

[4] Z.-H. Ge, L.-D. Zhao, D. Wu, X. Liu, B.-P. Zhang, J.-F. Li , J. He, *Mater. Today* **2016,** 19, 227.

[5] S. Roychowdhury, T. Ghosh, R. Arora, M. Samanta, L. Xie, N. K. Singh, A. Soni, J. He, U. V. Waghmare, , K. Biswas, *Science*, **2021**, 6530, 722.

[6] L.-D. Zhao, S.-H. Lo, Y. Zhang, H. Sun, G. Tan, C. Uher, C. Wolverton, V. P. Dravid , M. G. Kanatzidis, *Nature*, **2014**, 508, 373.

[7] L.-D. Zhao, G. Tan, S. Hao, J. He, Y. Pei, H. Chi, H. Wang, S. Gong, H. Xu , V. P. Dravid, *Science* **2016**, 351, 141.

[8] D. Sarkar, T. Ghosh, S. Roychowdhury, R. Arora, S. Sajan, G. Sheet, U. V. Waghmare, , K. Biswas, *J. Am. Chem. Soc.* **2020**, 142, 12237.

[9] K. Biswas, J. He, Q. Zhang, G. Wang, C. Uher, V. P. Dravid , M. G. Kanatzidis, *Nat. Chem.* **2011**, 3, 160.

[10] K. Biswas, J. He, I. D. Blum, C.-I. Wu, T. P. Hogan, D. N. Seidman, V. P. Dravid , M. G. Kanatzidis, *Nature* **2012**, 489, 414.

[11] Y. Pei, X. Shi, A. LaLonde, H. Wang, L. Chen , G. J. Snyder, *Nature* **2011**, 473, 66.

[12] M. Dutta, T. Ghosh , K. Biswas, *APL Mater.* **2013**, 8, 040910.

[13] Q. Zhang, F. Cao, W. Liu, K. Lukas, B. Yu, S. Chen, C. Opeil, D. Broido, G. Chen , Z. Ren, *J. Am. Chem. Soc.* **2012**, 134, 10031.

[14] A. Banik, U. S. Shenoy, S. Saha, U. V. Waghmare, , K.Biswas, *J. Am. Chem. Soc.* **2016**, 138, 13068.

[15] L.-D. Zhao, J. He, S. Hao, C.-I. Wu, T. P. Hogan, C. Wolverton, V. P. Dravid , M. G. Kanatzidis, *J. Am. Chem. Soc.* **2012**, 134, 16327.

[16] J. P. Heremans, V. Jovovic, E. S. Toberer, A. Saramat, K. Kurosaki, A. Charoenphakdee, S. Yamanaka , G. J. Snyder, *Science* **2008**, 321, 554.

[17] Q. Zhang, B. Liao, Y. Lan, K. Lukas, W. Liu, K. Esfarjani, C. Opeil, D. Broido, G. Chen , Z. Ren, *Proc. Natl. Acad. Sci.* **2013**, 110, 13261.

[18] B. Poudel, Q. Hao, Y. Ma, Y. Lan, A. Minnich, B. Yu, X. Yan, D. Wang, A.

Muto, D.Vashaee, X. Chen, J. Liu, M. S. Dresselhaus, G. Chen , Z. Ren, *Science.* **2008**, 320, 634.

[19] X. Shi, J. Yang, J. R. Salvador, M. Chi, J. Y. Cho, H. Wang, S. Bai, J. Yang, W. Zhang , L. Chen, *J. Am. Chem. Soc.* **2011**, 133, 7837.

[20] M. Dutta, S. Matteppanavar, M.V.D. Prasad, J. Pandey, A. Warankar, P. Mandal, A. Soni, U.V. Waghmare , K. Biswas, *J. Am. Chem. Soc.* **2019**, 141, 20293.

[21] P.Acharyya, T.Ghosh, K.Pal, K.Kundu, K. S. Rana, J. Pandey, A. Soni, U.W.Waghmare , K. Biswas, *J. Am. Chem. Soc.* **2020**, 142, 15595.

[22] M. K. Jana , K. Biswas, *ACS Energy Lett.*, **2018**, 3, 1315.

[23] X. Lu, D. T. Morelli, Y. Xia, F. Zhou, V. Ozolins, H. Chi , X. Zhou, 2013, 342.

[24] A. Zevalkink, E. S. Toberer, W. G. Zeier, E. Flage-Larsen , G. J. Snyder, *Energy Environ. Sci.* **2011**, 4, 510.

[25] O. Delaire, J. Ma, K. Marty, A. F. May, M. A. McGuire, M. H. Du, D. J. Singh, A. Podlesnyak, G. Ehlers, M. D. Lumsden , B. C. Sales, *Nat. Mater.* **2011**, 10, 614.

[26] E. S. Božin, C. D. Malliakas, P. Souvatzis, T. Proffen, N. A. Spaldin, M. G. Kanatzidis , S. J. L. Billinge, *Science* **2010**, 330, 1660.

[27] Z. Hu , S. Gao, *Chemical Geology* **2008**, 253, 205.

[28] L.-D. Zhao, J. He, C.-I. Wu, T. P. Hogan, X. Zhou, C. Uher, V. P. Dravid , M. G. Kanatzidis, *J. Am. Chem. Soc.* **2012**, 134, 7902.

[29] L.-D. Zhao, S.-H. Lo, J. He, H. Li, K. Biswas, J. Androulakis, C.-I. Wu, T. P. Hogan, D.-Y. Chung, V. P. Dravid , M. G. Kanatzidis, *J. Am. Chem. Soc.* **2011**, 133, 20476.

[30] Y. Pei , Y. Liu, *J. Alloys Compd.*, **2012**, 514, 40.

[31] E. Rathore, M. Dutta , K. Biswas, *J. Chem. Sci.*, **2019**, 131, 116.

[32] Z.-Z. Luo, S. Hao, S. Cai, T. P. Bailey, G. Tan, Y.Luo, L.Spanopoulos, C.Uher, C.Wolverton, V. P. Dravid, Q.Yan, , M. G.Kanatzidis, *J. Am. Chem. Soc.* **2019**, 141, 6403.

[33] H. Wang, E. Schechtel, Y. Pei , G. J. Snyder, *Adv. Energy Mat.* **2013**, 488.

[34] H. Wang, Y. Pei, A. D. LaLonde , G. J. Snyder, *Proc. Natl. Acad. Sci. U. S. A.*, **2012**, 109, 9705.

[35] A. D. LaLonde, Y. Pei , G. J. Snyder, *Energy Environ. Sci.*, **2011**, 4, 2090.

[36] R. Cheng, S. Hao, J. Li, H. Bai, S. Xie, Y. Gong, W. Liu, J. Wu, G. Tan , X. Tang, *ACS Appl. Mater. Interfaces* **2020**, 12, 14203.

[37] Y. Xiao, D. Wang, Y. Zhang, C. Chen, S. Zhang, K. Wang, G. Wang, S. J. Pennycook, G. J. Snyder, H. Wu , L.-D. Zhao, *J. Am. Chem. Soc.* **2020**, 142, 4051.

[38] B. Jiang, X. Liu, Q. Wang, J. Cui, B. Jia, Y. Zhu, J. Feng, Y. Qiu, M. Gu, Z. Ge , J. He, *Energy Environ. Sci.* **2020**, 13, 579.

[39] M. Zhao, C. Chang, Y. Xiao, R. Gu, J. He , L. Zhao, *J. Alloys Compd.* **2019**, 781, 820.

[40] L.-D. Zhao, J. He, S. Hao, C. I. Wu, T. P. Hogan, C. Wolverton, V. P. Dravid , M. G. Kanatzidis, *J. Am. Chem. Soc.* **2012**, 134, 16327.

[41] K. Nakajima, S. Ohira-Kawamura, T. Kikuchi, M. Nakamura, R. Kajimoto, Y. Inamura, N. Takahashi, K. Aizawa, K. Suzuya, and K. Shibata, *J. Phys. Soc. Japan* **2011**, 80, SB028.

[42] Y. Inamura, T. Nakatani, J. Suzuki, and T. Otomo, *J. Phys. Soc. Japan* **2013**, 82, SA031.

[43] M. Dutta, M. Samanta, T. Ghosh, D. J. Voneshen and K. Biswas, *Angew. Chemie Int. Ed.*, 2020, DOI:https://doi.org/10.1002/anie.202013923.

[44] W. Kohn and L. J. Sham, *Phys. rev.* **1965**, 140, A1133.

[45] G. Kresse and J. Furthmüller, *Comput. Mater. Sci.* **1996,** 6, 15.

[46] G. Kresse and J. Furthmüller, *Phys. Rev. B* **1996**, 54, 11169.

[47] P. E. Blöchl, *Phys. Rev. B* **1994**, 50, 17953.

[48] G. Kresse and D. Joubert, *Phys. Rev. B* **1999**, 59, 1758.

[49] J. P. Perdew, K. Burke and M. Ernzerhof, *Phys. Rev. Lett.* **1996**, 77, 3865.

[50] A. Van De Walle, P. Tiwary, M. De Jong, D. L. Olmsted, M. Asta, A. Dick, D. Shin, Y. Wang, L. Chen, Z. Liu and M. Carlo, *Calphad* **2013**, 42, 13.

[51] A. Zunger, S.-H. Wei, L. G. Ferreira and J. E. Bernard, *Phys. Rev. Lett.* **1990**, 65, 353.

[52] S.-H. Wei, L. G. Ferreira, J. E. Bernard and A. Zunger, *Phys. Rev. B* **1990,** 42, 9622.

[53] A. D.Becke and K. E. Edgecombe, *J. Chem. Phys.* **1990**, 92, 5397.

[54] A.Savin, R. Nesper, S. Wengert, and T. F. Fässler, *Angew. Chemie Int. Ed.*

1997, 36, 1808.

[55] V. L. Deringer, A. L. Tchougréeff and R. Dronskowski, *J. Phys. Chem. A* **2011**, 115, 5461.

[56] R. Dronskowski and P. E. Bloechl, *J. Phys. Chem.* **1993**, 97, 8617.

[57] Z.-Z. Luo, S. Hao, X. Zhang, X. Hua, S. Cai, G. Tan, T. P. Bailey, R. Ma, C. Uher, C. Wolverton, V. P. Dravid, Q. Yan , M. G. Kanatzidis, *Energy Environ. Sci.* **2018**, 11, 3220.

[58] Z.-Z. Luo, X. Zhang, X. Hua, G. Tan, T. P. Bailey, J. Xu, C. Uher, C. Wolverton, V. P. Dravid, Q. Yan , M. G. Kanatzidis, *Adv. Funct. Mater.* **2018**, 28, 1801617.

[59] D. I. Bletskan, Y. V. Voroshilov, L. M. Durdinets, P. P. Migalko, V. A. Stefanovich , V. N. Kabatsii, *Crystallogr. Reports* **2003**, 48, 573.

[60] S. Roychowdhury, M. Samanta, S. Perumal , K. Biswas, *Chem. Mater.* **2018**, 30, 5799.

[61] J P. Jood, M. Ohta, P. Jood, M. Ohta, A. Yamamoto , M. G. Kanatzidis, *Joule* **2018**, *2*, 1339.

[62] D. Bozyigit, N. Yazdani, M. Yarema, O. Yarema, W. M. M. Lin, S. Volk, K. Vuttivorakulchai, M. Luisier, F. Juranyi , V. Wood, *Nature* **2016,** 531, 618.

[63] D. Greig, *Phys. Rev.* **1960**, 120, 358.

Chapter 2.5.

Origin of Ultralow Lattice Thermal Conductivity in Superconductive $SnMo_6S_8$ Cheverel Phase: Role of Sn Rattlers[†]

[†] *Manuscript under preparation*

Chapter 2.5

Origin of Ultralow Lattice Thermal Conductivity in Superconductive $SnMo_6S_8$ Cheverel Phase: Role of Sn Rattlers †

Summary: *Crystalline solids with ultralow thermal conductivity are essential for thermal barrier coating and thermoelectric waste heat to electricity conversion. Intrinsically low thermal conductive materials are important as extrinsic methods to reduce lattice thermal conductivity causes scattering of charge carriers which slashes the carrier mobility. Herein, we synthesized superconductive $SnMo_6S_8$ which belongs to Chevrel phase family and comprises of two subunits, Mo_6S_8 and SnS_8. $SnMo_6S_8$ exhibits an ultra-low lattice thermal conductivity (κ_{lat}) of 1.17 Wm^{-1} K^{-1} at room temperature which decreases to 1.00 Wm^{-1} K^{-1} at 818 K. Temperature Raman analysis shows the decrease of spectral line width of low frequency modes below 210 cm^{-1} and new peaks at 123 and 205 cm^{-1}appears at superconducting transition temperature ~11 K indicating the involvement of strong electron-phonon coupling in $SnMo_6S_8$. Further, first-principles density functional theoretical (DFT) calculations show Sn dominated low frequency modes, presence of flat bands corresponding to Sn rattler atoms and presence of avoided crossing between acoustic and optical modes which is hallmark of the soft modes. This contributes to scattering of phonons and leads to ultralow lattice thermal conductivity.*

† *Manuscript under preparation*

2.5.1. Introduction

The discovery of earth-abundant environmentally benign crystalline solids materials is necessary for the development of efficient thermoelectrics, thermal barrier coating, and refractories.[1–7] Reduction of lattice thermal conductivity (κ_{lat}) is usually achieved via extrinsically perturbing the lattice using point defects,[3,8,9] alloying,[10] nanostructuring or grain-boundary engineering,[11] multiscale hierarchical architectures, and mesoscale structuring.[12] These strategies are efficient in scattering a wide range of phonon frequencies to slash the κ_{lat} satisfactorily by reducing the phonon lifetime but unavoidably deteriorate the carrier transport by scattering the free charge carriers that are essential for improving the electrical conductivity of a material.[13] On the contrary, crystalline solids have emerged as an alternative due independent control over the electrical transport and ability to impede phonon flow intrinsically.

Crystalline metal sulfides have gained popularity due to the low cost and high earth abundance of sulfur although metal sulfides show higher κ_{lat} compared to that of the selenides and tellurides due to the lighter mass of S.[14–16] However, intrinsically low κ_{lat} have been achieved in solids with layered structure with lattice anharmonicity (e.g., BiSe, BiTe, SnSe, and SnS),[17–22] liquid-like cation disordering in superionic substructure resembling a "phonon glass-electron crystal (PGEC)" (e.g., Cu_2S, $Cu_{2-x}Se$, $Cu_{12}Sb_4S_{13}$ and AgCuTe),[23–26] intrinsic rattling (e.g., $Na_{0.8}CoO_2$, Tl_3VSe_4, TlSe, $AgBi_3S_5$, $TlInTe_2$, and $CsAg_5Te_3$),[27–34] resonant bonding,[35] stereochemical lone-pair driven anharmonicity (e.g., $AgPbBiSe_3$, $AgSbTe_2$, $CuBiS_2$, $AgBiS_2$),[4,36–39] ferroelectric instability[40] and complex crystal structures (e.g. skutterudites or clathrates)[41–43]. These studies show that materials with structures that can accommodate additional atoms in their lattice are likely to have low lattice thermal conductivity. Chevrel phases ($M_xT_6X_8$; X = chalcogen, T= Mo, Nb, Ta, Re, W; where M can be monovalent, divalent, or trivalent elements, with x varying from 0-4) are such kind of ternary molybdenum chalcogenides family materials.[44–46] They exhibit cavities which can greatly vary in size and contain large variety of atoms ranging from large ones such as Pb to small ones such at Cu. These inserted small atoms usually show large thermal parameters which indicate that they move around and can significantly scatter the phonons.[47] However, the origin of ultra-

low lattice thermal conductivity in Chevrel phase compounds with large ions like Pb or Sn has not been well understood.[48]

Herein, we investigate the origin of intrinsically low κ_{lat} (1.17–1.00 Wm^{-1} K^{-1} in the temperature range of 296–818 K) of an eco-friendly and earth-abundant *p*-type superconductive $SnMo_6S_8$ with critical temperature, T_c at ~11 K. Temperature dependent Raman analysis shows the decrease of spectral line width of low frequency modes below 210 cm^{-1} and new peaks at 123 and 205 cm^{-1} appears at superconducting transition temperature ~11 K indicating the involvement of strong electron-phonon coupling in $SnMo_6S_8$. Further, first-principles density functional theoretical (DFT) calculations show Sn dominated low frequency modes, presence of flat bands corresponding to Sn rattler atoms and presence of avoided crossing between acoustic and optical modes which is hallmark of the soft modes. This contributes to scattering of phonons and leads to ultralow lattice thermal conductivity.

2.5.2. Methods

2.5.2.1. Reagents. Elemental Sn (powder, 99.99% Sigma Aldrich), S (pieces, 99.99%, Sigma-Aldrich) and Mo (powder, 99.99%, sigma) Alfa Aesar) were used for synthesis without further purification.

2.5.2.2. Synthesis. Powder samples of $SnMo_6S_8$ were synthesized from high purity powder elements Sn, Mo and S using vacuum-sealed tube melting and spark plasma sintering (SPS). The stoichiometric amounts of these elements were weighed, and the powders were ground using pestle mortar. The powder was sealed in 13 mm quartz tubes under vacuum (10^{-6} Torr). The tubes were heated to 723 K in 4 h, kept for 24 h, then heated to 973 K in 4 h, kept at this temperature for 24 h and then eventually heated to 1323 K in 4 h, kept for 48 h and finally cooled down to room temperature in 9 h. The powdered samples were obtained and transferred into a graphite die (10 mm diameter). The powders were pelletized by using SPS (SPS211-LX, Dr. Sinter Lab) under the pressure of 45 MPa for 10 min at 1223 K. Density of the sample was estimated to be ~ 99% of the theoretical crystallographic density of $SnMo_6S_8$.

2.5.2.3. Powder X-ray Diffraction. Powder X-ray diffraction patterns (PXRD) for finely powder samples were recorded using a Cu $K\alpha$ (λ = 1.5406 Å) radiation source on a Bruker D8 diffractometer.

2.5.2.4. Electronic Transport Properties. The electrical conductivity and Seebeck coefficient of parallelepiped shaped samples of $SnMo_6S_8$ with the dimensions of ~2 mm × 2 mm × 8 mm were measured simultaneously from in the 298-818 K range under a low pressure He atmosphere by a ZEM-3 instrument (ULVAC-RIKO). The samples were spray-coated with boron nitrate to avoid the liberation of sulfur and also to protect the instrument. Reproducible results were achieved in the heating and cooling cycle measurements.

2.5.2.5. Thermal Conductivity. The total thermal conductivity, κ_{total}, was estimated from the relationship: $\kappa_{\text{total}} = DC_p\rho$, where ρ is the density, D is thermal diffusivity and C_p is specific heat capacity. D was measured in the 298-900 K under a N_2 atmosphere using laser flash method (Netzsch LFA-457). The measurement was performed on carbon-coated coin-shaped samples with radius of ~10 mm and thickness of less than ~2 mm.

2.5.2.6. Heat Capacity Measurement. Low temperature (2−33 K) specific heat of $SnMo_6S_8$ is measured in Quantum Design, Physical Property Measurement System (PPMS).

2.5.2.7. Low-Temperature Resistivity Measurement. Low temperature (2−33 K) resistivity of $SnMo_6S_8$ is measured in Physical Property Measurement System (PPMS).

2.5.2.8. Raman Spectroscopy. Micro-Raman measurements were performed using Horiba Jobin-Yvon LabRAM HR evolution Raman spectrometer in back scattering geometry with solid state laser excitation ~ 785 nm, 1800 gr/mm grating and Peltier cooled CCD detector. Temperature dependent Raman study was performed using Montana cryostat in the range of 3 - 300 K.

2.5.2.9. Computational methods. This part of work was carried under the collaboration with Prof. U. V. Waghmare, TSU, JNCASR. Our first-principles theoretical calculations are based on density functional theory (DFT) employing the

Quantum ESPRESSO[49] (QE) code. We used a generalised gradient approximation (GGA)[50] to the exchange-correlation energy functional as parametrized by Perdew, Burke, and Ernzerhof (PBE)[51]. The projector augmented wave (PAW) potentials[52] with valence configuration $4d^{10}\ 5s^2\ 5p^2$, $4s^2\ 4p^6\ 4d^4\ 5s^2$ and $3s^2\ 3s^4$ were adopted for Sn, Mo and S respectively. Electronic wave functions and charge density were represented in plane wave basis sets truncated with cut-off energies of 50 Ry and 400 Ry respectively. The discontinuity in occupation numbers of electronic states was smeared using a Fermi-Dirac distribution function with broadening of $k_BT = 0.003$ Ry and integrations over Brillouin Zone (BZ) were sampled on a uniform 6×6×6 mesh of k-points for relaxation of geometric structures and 8×8×8 for total energy calculations. We used scalar-relativistic PAW potentials to optimize the structure with respect to lattice constants and atomic coordinates. The structure was optimized to minimize the enthalpy, $H = E + PV$. Effects of spin-orbit coupling (SOC) were included in our calculations of electronic structure through the use of fully relativistic potentials,[53] while we used scalar-relativistic PAW potentials in calculation of phonons. Electronic spectrum was determined at Bloch vectors along high symmetry lines (Γ - M - K - Γ – A – L – H – A - L – M – K - H) in the Brillouin zone. Lattice dynamical properties were determined using density functional linear response (called as density functional perturbation theory[6]) as implemented in the QE package[49]. To obtain phonon dispersion, dynamical matrices were obtained on a 2x2x2 q-points grid in the Brillouin Zone. We Fourier interpolated these dynamical matrices to obtain the phonon dispersion along high symmetry lines (Γ - X - S - R - X) in the Brillouin zone. Our estimates of the optimized lattice constants of 45 atom conventional unit cell are $a = b = 9.22$ Å, $c = 11.44$ Å, which agree within the typical GGA errors with experimental lattice parameters ($a = b = 9.17$ Å, $c = 11.36$ Å). The relaxed lattice constant and bond angle of 15 atom primitive unit cell are $a = 6.51$ Å and $\alpha = 90^\circ$, in good agreement with experimental values.

2.5.3. Results and Discussions

$SnMo_6S_8$ belongs to Chevrel phase family which crystallizes the $R\bar{3}$ space group $SnMo_6S_8$ comprises of molecular building blocks of Mo_6S_8 units, composed of the octahedral cluster of Mo atoms inside the tetragonally distorted S_8 cube and distorted CsCl type SnS_8 units (Figure 2.5.1a).[54] The stacking of Mo_6S_8 units form three-

dimensional channels that are available for cation transport and the cavities are occupied by Sn atoms. Sn atoms are enveloped by 8 adjacent sulfur atoms from 8 Mo_6S_8 units located at the corners of a pseudo cube with $\bar{3}$ symmetry which is slightly compressed along threefold axis. Considering the crystal ionic radii for S^{2-} (~1.70 Å) and Sn^{2+}(~1.26 Å),[55] the larger interatomic Sn-S of the SnS_8 cube is larger than the anticipated value by 0.134 Å, which indicates for the delocalization of the Sn atom

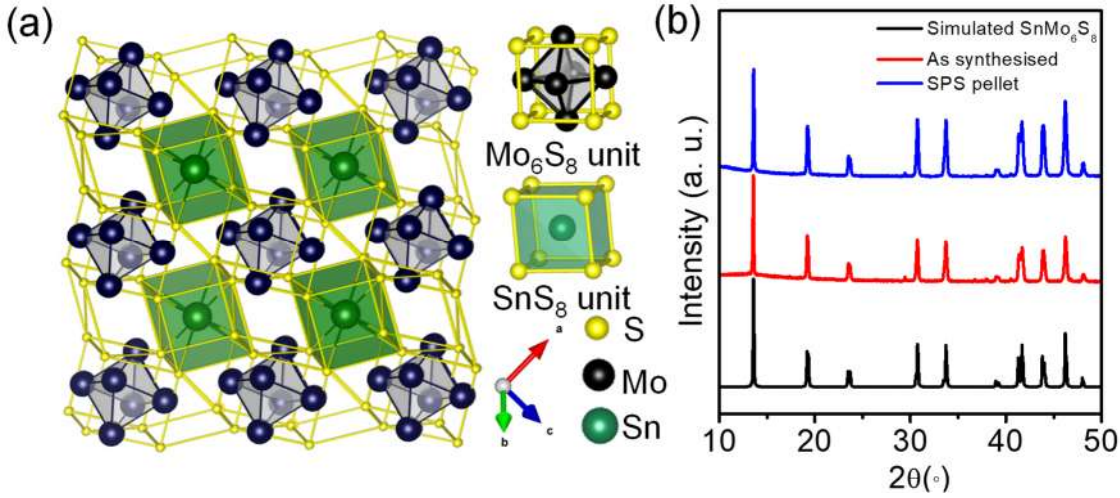

Figure 2.5.1. *(a) Stacking view of Mo_6S_8 units and SnS_8 cubic sites of rhombohedral $SnMo_6S_8$ with space group $R\bar{3}$ and (b) powder XRD patterns of powdered and spark plasma sintered pellet of $SnMo_6S_8$.*

$SnMo_6S_8$ was synthesized by vacuum sealed tube method as described in section 2.5.2.2. It was a challenge to synthesize $SnMo_6S_8$ due high melting point of elemental Mo (2896 K) and formation of more stable MoS_2 phase. The powder X-ray diffraction (PXRD) patterns of $SnMo_6S_8$ show an excellent match to rhombohedral phase of $SnMo_6S_8$ with a space group of $R\bar{3}$ (Figure 2.5.1b). Previously, the Chevrel-type compounds have been reported to have low sinterability that causes poorly dense structure.[48] The spark-plasma sintering technique was applied to sinter the samples which helped to achieve density above 99% and we were successful to make dense pellets without the formation of MoS_2 first time (Figure 2.5.1b).

To find out the superconductivity critical temperature we carried out low temperature resistivity and heat capacity measurements in the temperature range 2-33 K. Figure 2.5.2a shows that resistivity suddenly drops from 8.32 x 10^{-7} Ωm at ~11 K

indicating the obvious characteristic of a superconductor, *i.e.* the complete disappearance of its electrical resistance below a temperature that is known as its critical temperature. The low-temperature specific heat capacity measurements show a hump at ~11 K indicating the evidence of superconductivity. Jarlborg et. al have reported that the superconductivity in $SnMo_6S_8$ is driven by the unusual charge transfer from both Mo site and Sn sites to the chalcogens.[56]

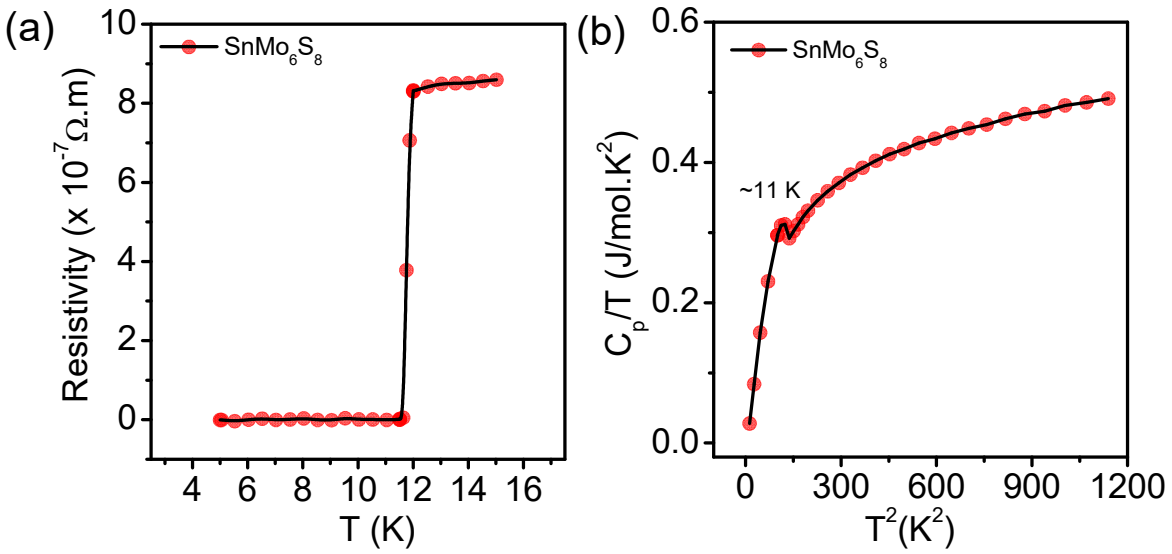

Figure 2.5.2. *(a) Resistivity vs T plot showing superconducitiviy transition at ~ 11 K and (b) C_p/T vs T^2 plot in temperature range 2-33 K observes T_c at ~ 11 K.*

We measured the temperature dependent total thermal conductivity, and the lattice thermal conductivity was estimated by subtracting κ_e from κ_{tot} values. The most striking finding in this work is intrinsically low κ_{lat} which is 1.17 at room temperature and reduces to 1.00 Wm^{-1} K^{-1} at 818 K which is 52 % lower than the κ_{tot} value at room temperature. We observed 1/T dependence of lattice thermal conductivity, suggesting dominant anharmonic phonon scattering which may be arising due to the delocalization of Sn atoms occupied in the cavities of host formed by the stacking of Mo_6S_8. These Sn atoms can move freely or vibrate in the channels and can scatter the heat carrying phonons, thereby slashing the lattice thermal conductivity. Previously, Kimball et. al have studied vibrational motion of Sn with ^{119}Sn Mossbauer effect and reported large

anharmonicity and soft vibrational modes, thereby softening the lattice and creating anisotropy at ^{119}Sn sites in $SnMo_6S_8$.[57]

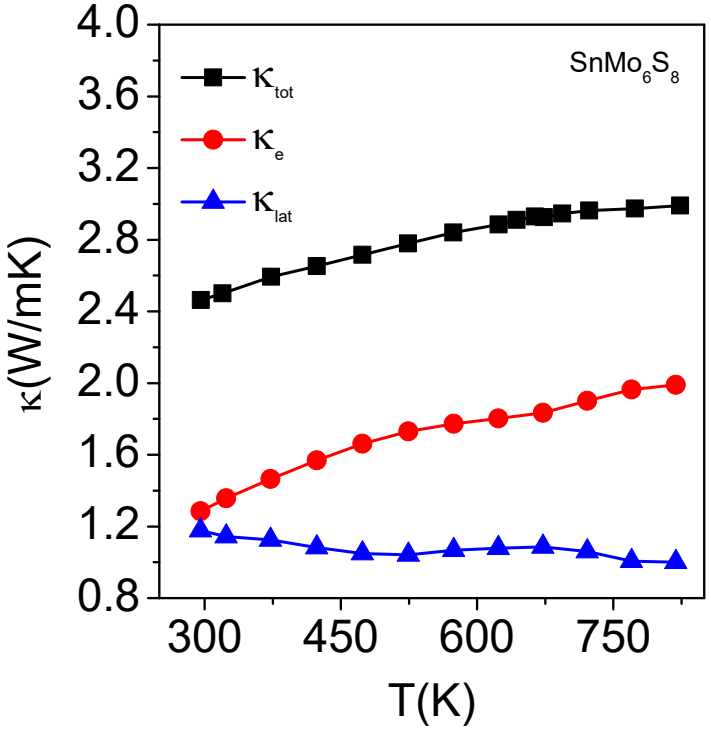

Figure 2.5.3. *Temperature-dependent total thermal conductivity (κ_{tot}, black), lattice thermal conductivity (κ_{lat}, blue) and electronic thermal conductivity (κ_e, red).*

To understand this intrinsically low thermal conductivity arising from the soft modes of Sn, we carried out Raman spectroscopy to investigate low frequency modes and the results are shown in Figure 2.5.4. $SnMo_6S_8$ crystallizes in $R\bar{3}$ space group with 42 zone center optical modes. The Raman active modes consist of seven doubly degenerate E_g and seven A_g modes. The room temperature Raman data are shown in Figure 2.5. where all the Raman modes are fitted with Lorentz peak function represented with blue color. The red color curve shows the cumulative fit of the overall Raman spectra. Origin of the peaks observed ~ 111 cm^{-1}, 145 cm^{-1}, 254 cm^{-1} and 366 cm^{-1} are assigned to E_g symmetry. Modes appearing ~ 187 cm^{-1}, 243 cm^{-1} and 284 cm^{-1} are related to A_g symmetry[58] are shown in Figure 2.5.4a.

The superconducting transition temperature of $SnMo_6S_8$ is ~ 11 K and theoretical arguments suggest that phonons of low frequency are most effective in electron-phonon coupling and hence are important to superconductivity. The commonly known Chevrel

phase compounds such as $PbMo_6S_8$, $Cu_{1.8}Mo_6S_8$, $SnMo_6S_8$ are characterized by a strong electron-phonon interaction with the largest coupling involving phonon modes with energies in the frequency range from 11 to 17 meV and with a strong intermolecule Peierls character.[59] At the zone center (Γ point) and the zone bounday (X point), the external torsional modes have been suggested to be important for superconductivity. The involvement of electron-phonon coupling in superconductivity can be manifested in temperature dependent Raman study.

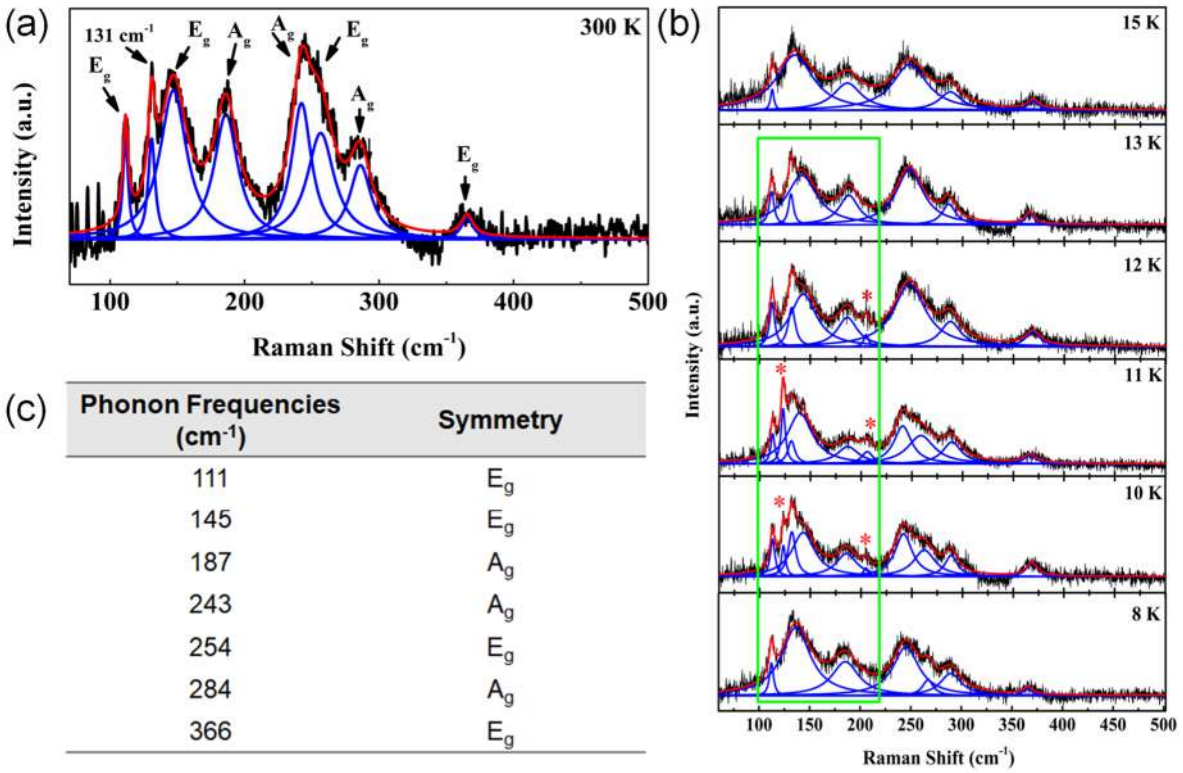

(c)

Phonon Frequencies (cm^{-1})	Symmetry
111	E_g
145	E_g
187	A_g
243	A_g
254	E_g
284	A_g
366	E_g

Figure 2.5.4. *Raman spectra of $SnMo_6S_8$ at (a) 300 K, (b) at 8, 10, 11, 12, 13, 15 K using 785 nm excitation. Each Raman modes are fitted with Lorentz function shown with blue color and the red curve represents cumulative fit. "*" represents the new modes appearing at the onset of superconducting transition due to electron-phonon coupling and (c) Table indicates the measured frequencies of Eg and Ag modes.*

Figure 2.5.4b shows the temperature dependent Raman spectra near superconducting temperature from 15 K to 8 K. Similar to Raman spectra at 300 K, all the Raman modes are observed up to 15 K but interestingly below 15 K, the spectral linewidth of the low frequency modes below 210 cm^{-1} decreases and new modes ~ 123

cm^{-1} and ~ 205 cm^{-1} appears (marked with * in Figure 2.5.4b) near superconducting transition temperature ~ 11 K. Surprisingly, these modes are observed only at and near superconducting transition and absent at further lower temperatures confirming the involvement of strong electron-phonon coupling in superconductivity of $SnMo_6S_8$ compound.

To better understand this low lattice thermal conductivity and superconductivity for $SnMo_6S_8$, we carried out first-principle DFT calculation. Fig. 2.5.5 (a) shows the band structure both without and with inclusion of the spin-orbit coupling and 2.5.5 (b) shows the atom projected density of states (PDOS) of $SnMo_6S_8$. Electronic structure of $SnMo_6S_8$ calculated at the optimized lattice constants reveals bands crossing the Fermi level. It is clear that conduction bands and valence bands are not affected significantly with inclusion of spin orbit coupling (SOC) in our calculations. The band gap estimated both without and with inclusion of the spin-orbit coupling is 0.7 eV is consistent with the experimental bandgap of 0.5 eV, which is typical of DFT calculations of band gaps. For deeper understanding of the electronic properties, we examined the projected density of states (PDOS) (see Figure 2.5.5 b). Examination of the projected density of states (PDOS) reveals that its valence band (VB) is contributed mostly by d orbitals of Mo and by p orbitals of S. Its conduction band (CB) is contributed primarily by d orbitals of Sn and p orbitals of Sn. The lone pair of Sn atom is intact, this is observed from the projected density of states (PDOS) where the contribution of lone pair of s-orbital of Sn is at ~ -8 eV, very deeper in the valence band region.

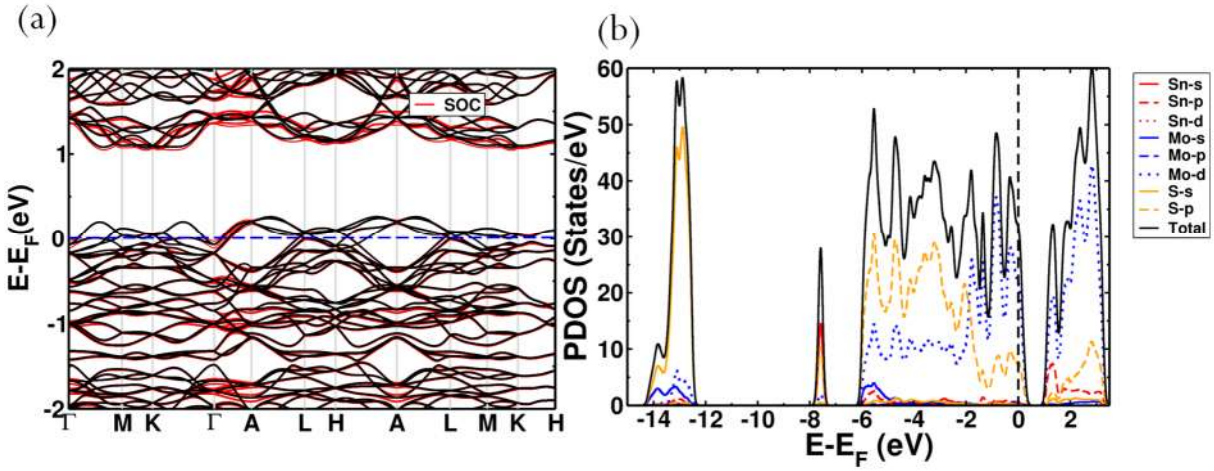

Figure 2.5.5. *(a) Electronic structure of $SnMo_6S_8$ calculated at the theoretical lattice constant with the inclusion of spin-orbit interaction (SOC) (red line) and without SOC (black lines). (b) Corresponding projected density of states (PDOS) of $SnMo_6S_8$.*

To investigate the low lattice thermal conductivity and superconductivity for $SnMo_6S_8$ we determined the phonon dispersion using first-principles Density Functional Perturbation Theory (DFPT) (Figure 2.5.6 a). The optical phonons of $SnMo_6S_8$ exhibit triply degenerate instability at a frequency of 4.5 i cm^{-1} at Γ point. An interesting feature evident in the phonon dispersion is the presence of unstable modes at all wave vectors except near the R point (= π/a (1,1,1)). This is linked through Fourier analysis with the local distortions with chain-like short-range order[60,61], and size of the distorted region ~ $1/q_c$.

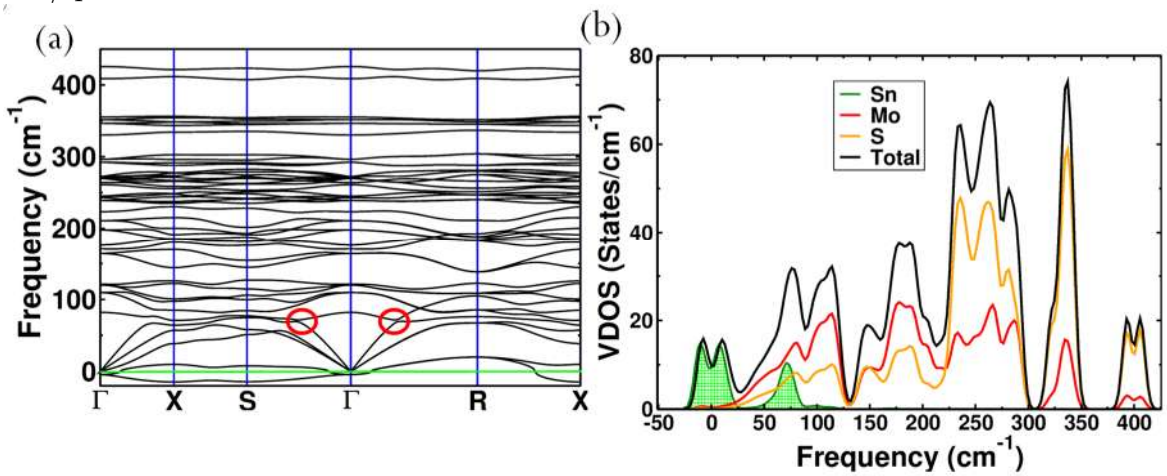

Figure 2.5.6. *(a) Phonon dispersion of $SnMo_6S_8$ revealing two negative phonon branches with frequencies at 4.5 cm^{-1} near the Γ point. Avoided-crossing between branches of TA and TO phonons highlighted in the low frequency phonon dispersion along Γ to S/R are encircled in red. (b) The associated total and atom-projected phonon density of states (Ph-DOS) of $SnMo_6S_8$.*

Another interesting feature is the large number of "soft" optical modes with frequencies < 110 cm^{-1} evident in the phonon density of states (Ph-DOS) showing a peak at ~70 cm^{-1} and 100 cm^{1}. We examined the atom-projected phonon DOS (see Figure 2.5.6 b) to investigate the contribution of atoms to these "soft" optical modes. While the structural instability in *$SnMo_6S_8$* involves dominant displacements of only Sn atoms, Mo and S displacements dominate the higher frequency regions (see Fig. 2.5.6 b). Projected phonon density of states, DOS reveals that low frequency optical modes (<100 cm^{-1}) are dominated by vibrations of Sn atoms followed by the contributions from Mo and S atoms. We also examine the eigen displacements of the unstable phonon modes (those having imaginary frequencies) at the Γ point as well as few low frequency soft modes of *$SnMo_6S_8$* to access the relative roles of Sn, Mo and S (see Figure 2.5.7 b). Our results signify the presence of a rattler kind of behavior of Sn in $SnMo_6S_8$. The role of

the cations in the optical–acoustic phonon scattering processes is evident from the avoided crossing between the branches of acoustic and low frequency optical modes in the phonon dispersion.

To get an insight into atomic-level dynamics, we have calculated the potential energy curves by displacing the atoms relative to the eigen displacements ($\hat{e}_u$) of unstable optical phonon modes modes at Γ point. It is clear from Figure 2.5.7 (a) that Sn atoms are confined in a very shallow double well potential wells suggesting that Sn atoms would easily rattle within shallow well with large amplitudes. This rattler band which is weakly unstable having imaginary frequency of ~ i 4.5 cm $^{-1}$ will get stabilized in its displaced structure along the eigen displacement i.e u(0.06) X $\hat{e}_u$.

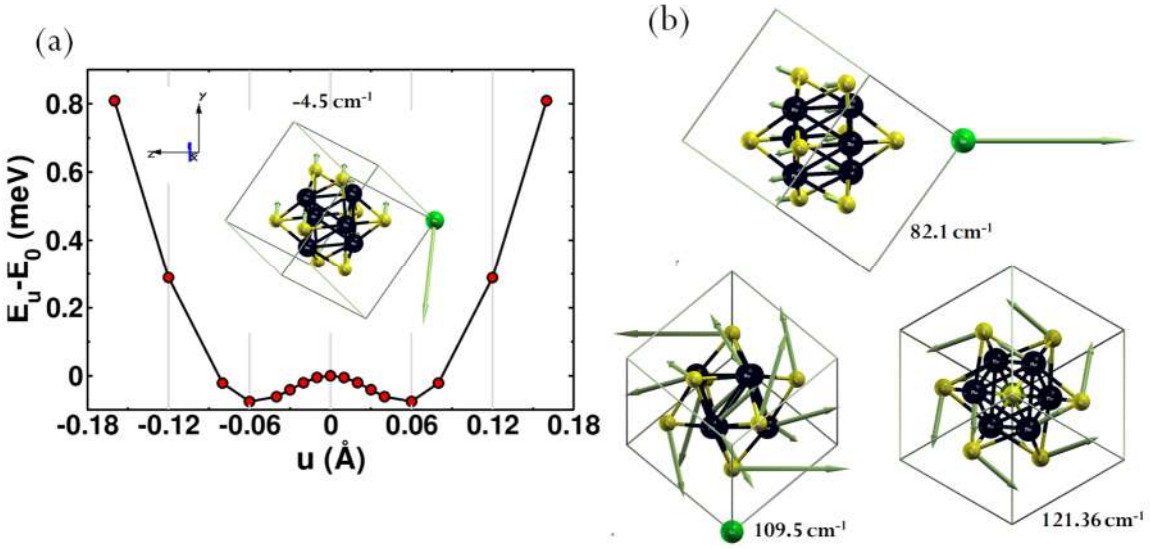

Figure 2.5.7. *(a) Plot of total energy governing the dynamics of atomic displacements along eigen displacements of the unstable optical phonon mode at Γ. (b) Visualization of few low frequency optical mode phonons of $SnMo_6S_8$ at Γ (Black, Green and Yellow atoms represent Mo, Sn and S respectively).*

2.5.4. Conclusions

In summary, an intrinsically ultralow lattice thermal conductivity of 1.17–1.00 Wm^{-1} K^{-1} in the temperature range of 296–818 K of an eco-friendly and earth-abundant *p*-type superconductive $SnMo_6S_8$ with critical temperature, T_c at ~11 K have been investigated. Temperature dependent Raman analysis shows the decrease of spectral line width of low frequency modes below 210 cm^{-1} and appearance of new peaks at 123 and 205 cm^{-1} superconducting transition temperature ~11 K indicates the involvement of strong electron-phonon coupling in $SnMo_6S_8$. The collective rattling

vibrations of Sn cations manifest as weakly localized branches with imaginary frequencies in the phonon dispersion; they are strongly anharmonic and scatter the heat carrying acoustic phonons to effectively lower k_L. Anomalously high lattice anharmonic interaction between acoustic modes and the rattler TO modes arises from the freely vibrating Sn rattler. Our results of TA and TO phonons indicated avoided-crossing between themselves, which indicates rattling dynamics that leads to ultralow lattice thermal conductivity in ternary molybdenum chalcogenides family materials.

2.5.5. References

[1] G. Tan, L.-D. Zhao, M. G. Kanatzidis, *Chem. Rev.* **2016**, *116*, 12123–12149.

[2] J. R. Sootsman, D. Y. Chung, M. G. Kanatzidis, *Angew. Chemie Int. Ed.* **2009**, *48*, 8616–8639.

[3] K. Biswas, J. He, Q. Zhang, G. Wang, C. Uher, V. P. Dravid, M. G. Kanatzidis, *Nat. Chem.* **2011**, *3*, 160–166.

[4] S. Roychowdhury, T. Ghosh, R. Arora, M. Samanta, L. Xie, N. K. Singh, A. Soni, J. He, U. V Waghmare, K. Biswas, *Science (80-.).* **2021**, *371*, 722 LP – 727.

[5] X.-L. Shi, J. Zou, Z.-G. Chen, *Chem. Rev.* **2020**, *120*, 7399–7515.

[6] Y. Xiao, L.-D. Zhao, *Science (80-.).* **2020**, *367*, 1196–1197.

[7] N. P. Padture, M. Gell, E. H. Jordan, *Science (80-.).* **2002**, *296*, 280.

[8] J. He, L.-D. Zhao, J.-C. Zheng, J. W. Doak, H. Wu, H.-Q. Wang, Y. Lee, C. Wolverton, M. G. Kanatzidis, V. P. Dravid, *J. Am. Chem. Soc.* **2013**, *135*, 4624.

[9] L.-D. Zhao, S. Hao, S.-H. Lo, C.-I. Wu, X. Zhou, Y. Lee, H. Li, K. Biswas, T. P. Hogan, C. Uher, C. Wolverton, V. P. Dravid, M. G. Kanatzidis, *J. Am. Chem. Soc.* **2013**, *135*, 7364–7370.

[10] S. Roychowdhury, R. K. Biswas, M. Dutta, S. K. Pati, K. Biswas, *ACS Energy Lett.* **2019**, *4*, 1658.

[11] B. Poudel, Q. Hao, Y. Ma, Y. Lan, A. Minnich, B. Yu, X. Yan, D. Wang, A. Muto, D. Vashaee, *Science (80-.).* **2008**, *320*, 634–638.

[12] K. Biswas, J. He, I. D. Blum, C.-I. Wu, T. P. Hogan, D. N. Seidman, V. P. Dravid, M. G. Kanatzidis, *Nature* **2012**, *489*, 414–418.

[13] M. K. Jana, K. Biswas, *ACS Energy Lett.* **2018**, *3*, 1315–1324.

[14] H. Wang, E. Schechtel, Y. Pei, G. J. Snyder, *Adv. Energy Mater.* **2013**, *3*, 488.

[15] H. Xie, X. Su, G. Zheng, T. Zhu, K. Yin, Y. Yan, C. Uher, M. G. Kanatzidis, X. Tang, *Adv. Energy Mater.* **2017**, *7*, 1601299.

[16] M. Beaumale, T. Barbier, Y. Bréard, S. Hébert, Y. Kinemuchi, E. Guilmeau, *J. Appl. Phys.* **2014**, *115*, 43704.

[17] M. Samanta, K. Pal, P. Pal, U. V Waghmare, K. Biswas, *J. Am. Chem. Soc.* **2018**, *140*, 5866.

[18] M. Samanta, K. Pal, U. V Waghmare, K. Biswas, *Angew. Chem., Int. Ed.* **2020**, *59*, 4822.

[19] L.-D. Zhao, S.-H. Lo, Y. Zhang, H. Sun, G. Tan, C. Uher, C. Wolverton, V. P. Dravid, M. G. Kanatzidis, *Nature* **2014**, *508*, 373.

[20] C. Chang, M. Wu, D. He, Y. Pei, C. F. Wu, X. Wu, H. Yu, F. Zhu, K. Wang, Y. Chen, L. Huang, J. F. Li, J. He, L. D. Zhao, *Science (80-.).* **2018**, *360*, 778.

[21] Y. K. Lee, Z. Luo, S. P. Cho, M. G. Kanatzidis, I. Chung, *Joule* **2019**, *3*, 719.

[22] W. He, D. Wang, H. Wu, Y. Xiao, Y. Zhang, D. He, Y. Feng, Y.-J. Hao, J.-F. Dong, R. Chetty, L. Hao, D. Chen, J. Qin, Q. Yang, X. Li, J.-M. Song, Y. Zhu, W. Xu, C. Niu, X. Li, G. Wang, C. Liu, M. Ohta, S. J. Pennycook, J. He, J.-F. Li, L.-D. Zhao, *Science (80-.).* **2019**, *365*, 1418.

[23] T. Takabatake, K. Suekuni, T. Nakayama, E. Kaneshita, *Rev. Mod. Phys.* **2014**, *86*, 669–716.

[24] Y. He, T. Day, T. Zhang, H. Liu, X. Shi, L. Chen, G. J. Snyder, *Adv. Mater.* **2014**, *26*, 3974–3978.

[25] H. Liu, X. Shi, F. Xu, L. Zhang, W. Zhang, L. Chen, Q. Li, C. Uher, T. Day, G. J. Snyder, *Nat. Mater.* **2012**, *11*, 422–425.

[26] S. Roychowdhury, M. K. Jana, J. Pan, S. N. Guin, D. Sanyal, U. V Waghmare, K. Biswas, **2018**, 2–7.

[27] D. J. Voneshen, K. Refson, E. Borissenko, M. Krisch, A. Bosak, A. Piovano, E. Cemal, M. Enderle, M. J. Gutmann, M. Hoesch, M. Roger, L. Gannon, A. T. Boothroyd, S. Uthayakumar, D. G. Porter, J. P. Goff, *Nat. Mater.* **2013**, *12*, 1028.

[28] S. Mukhopadhyay, D. S. Parker, B. C. Sales, A. A. Puretzky, M. A. McGuire, L. Lindsay, *Science (80-.).* **2018**, *360*, 1455.

[29] M. Dutta, S. Matteppanavar, M. V. D. Prasad, J. Pandey, A. Warankar, P. Mandal, A. Soni, U. V Waghmare, K. Biswas, *J. Am. Chem. Soc.* **2019**, *141*, 20293–20299.

[30] G. Tan, S. Hao, J. Zhao, C. Wolverton, M. G. Kanatzidis, *J. Am. Chem. Soc.* **2017**, *139*, 6467–6473.

[31] M. Dutta, M. Samanta, T. Ghosh, D. J. Voneshen, K. Biswas, *Angew. Chem., Int. Ed.* **2021**, *60*, 4259.

[32] M. K. Jana, K. Pal, A. Warankar, P. Mandal, U. V Waghmare, K. Biswas, *J. Am. Chem. Soc.* **2017**, *139*, 4350–4353.

[33] H. Lin, G. Tan, J.-N. Shen, S. Hao, L.-M. Wu, N. Calta, C. Malliakas, S. Wang, C. Uher, C. Wolverton, M. G. Kanatzidis, *Angew. Chem., Int. Ed.* **2016**, *55*, 11431.

[34] W. Lee, H. Li, A. B. Wong, D. Zhang, M. Lai, Y. Yu, Q. Kong, E. Lin, J. J. Urban, J. C. Grossman, P. Yang, *Proc. Natl. Acad. Sci. U. S. A.* **2017**, *114*, 8693.

[35] S. Lee, K. Esfarjani, T. Luo, J. Zhou, Z. Tian, G. Chen, *Nat. Commun.* **2014**, *5*.

[36] M. Dutta, K. Pal, U. V Waghmare, K. Biswas, *Chem. Sci.* **2019**, *10*, 4905.

[37] D. T. Morelli, V. Jovovic, J. P. Heremans, *Phys. Rev. Lett.* **2008**, *101*, 35901.

[38] Z. Feng, T. Jia, J. Zhang, Y. Wang, Y. Zhang, *Phys. Rev. B Condens. Matter Mater. Phys.* **2017**, *96*, 235205.

[39] E. Rathore, R. Juneja, S. Culver, N. Minafra, A. Singh, W. Zeier, K. Biswas,

Chem. Mater. **n.d.**, *31*, 2106–2113.

[40] D. Sarkar, T. Ghosh, S. Roychowdhury, R. Arora, S. Sajan, G. Sheet, U. V Waghmare, K. Biswas, *J. Am. Chem. Soc.* **2020**, *142*, 12237.

[41] G. J. Snyder, E. S. Toberer, *Nat. Mater.* **2008**, *7*, 105.

[42] H. Xie, X. Su, X. Zhang, S. Hao, T. P. Bailey, C. C. Stoumpos, A. P. Douvalis, X. Hu, C. Wolverton, V. P. Dravid, C. Uher, X. Tang, M. G. Kanatzidis, *J. Am. Chem. Soc.* **2019**, *141*, 10905.

[43] V. Pavan Kumar, G. Guélou, P. Lemoine, B. Raveau, A. R. Supka, R. Al Rahal Al Orabi, M. Fornari, K. Suekuni, E. Guilmeau, *Angew. Chemie Int. Ed.* **2019**, *58*, 15455–15463.

[44] O. Peña, *Phys. C Supercond. its Appl.* **2015**, *514*, 95–112.

[45] Ø. Fischer, *Appl. Phys.* **1978**, *16*, 1–28.

[46] R. Chevrel, M. Sergent, in *Supercond. Ternary Compd. I*, Springer, **1982**, pp. 25–86.

[47] T. Caillat, J.-P. Fleurial, G. J. Snyder, *Solid State Sci.* **1999**, *1*, 535–544.

[48] T. Tsubota, M. Ohtaki, K. Eguchi, *J. Ceram. Soc. Japan* **1999**, *107*, 697–701.

[49] Quantum-ESPRESSO is a community project for high-quality quantum-simulation software, based on density-functional theory, and coordinated by P. Giannozzi. See http://www. quantum-espresso.org.

[50] X. Hua, X. Chen, W. A. Goddard, *Phys. Rev. B* **1997**, *55*, 16103.

[51] J. P. Perdew, K. Burke, M. Ernzerhof, *Phys. Rev. Lett.* **1996**, *77*, 3865–3868.

[52] G. Kresse, D. Joubert, *Phys. Rev. B* **1999**, *59*, 1758–1775.

[53] A. Dal Corso, *Comput. Mater. Sci.* **2014**, *95*, 337–350.

[54] R. Chevrel, C. Rossel, M. Sergent, *J. Less Common Met.* **1980**, *72*, 31–43.

[55] R. D. t Shannon, *Acta Crystallogr. Sect. A Cryst. physics, diffraction, Theor. Gen. Crystallogr.* **1976**, *32*, 751–767.

[56] T. Jarlborg, A. J. Freeman, *Phys. Rev. Lett.* **1980**, *44*, 178.

[57] C. W. Kimball, L. Weber, G. Van Landuyt, F. Y. Fradin, B. D. Dunlap, G. K. Shenoy, *Phys. Rev. Lett.* **1976**, *36*, 412.

[58] D. J. Holmgren, R. T. Demers, M. V Klein, D. M. Ginsberg, *Phys. Rev. B* **1987**, *36*, 1952.

[59] J. Chen, A. J. Millis, D. R. Reichman, *Phys. Rev. Mater.* **2018**, *2*, 114801.

[60] H. Krakauer, R. Yu, C.-Z. Wang, K. M. Rabe, U. V Waghmare, *J. Phys. Condens. Matter* **1999**, *11*, 3779.

[61] A. Banik, T. Ghosh, R. Arora, M. Dutta, J. Pandey, S. Acharya, A. Soni, U. V Waghmare, K. Biswas, *Energy Environ. Sci.* **2019**, *12*, 589–595.

PART 3

Layered Materials for Selective Capture of Toxic Heavy Metal Ions and Radioactive Ions from Contaminated Water

Chapter 3.1

Layered Metal Chalcophosphate, $K_{0.48}Mn_{0.76}PS_3$. H_2O, for Efficient Selective and ppb Level Sequestration of Pb from Water

---

†*Paper based on this has been published as* ***E. Rathore****, P. Pal, K. Biswas,. J. Phys. Chem. C* ***2017****, 121, 14, 7959–7966.*

Chapter 3.1

Layered Metal Chalcophosphate, $K_{0.48}Mn_{0.76}PS_3$. H_2O, for Efficient, Selective and ppb level Sequestration of Pb from Water up to ppb Level†

Summary: *Sequestration of heavy metal ions from water is an important issue in chemistry and environmental science. In this chapter, we have discussed the detailed Pb^{2+} adsorption and ion exchange kinetics of a potassium intercalated layered metal thiophosphate, $K_{0.48}Mn_{0.76}PS_3.H_2O$ (K-MPS-1), which is capable of efficient removal of Pb^{2+} (>99 %) from very dilute concentration (1-100 ppb). K-MPS-1 can selectively capture Pb^{2+} even in presence of other monovalent and divalent cations such as Na^+, Ca^{2+}, Mg^{2+} with high separation factor. K-MPS-1 can operate within a broad pH range of 2-12 effectively with high distribution co-efficient (K_d^{Pb}) of 5.36 x10^5 mL/g, following pseudo second order kinetics. Initially, K^+ intercalation in $MnPS_3$ (MPS-1) increases the interlayer spacing and subsequently creates a Mn^{2+} vacancy to maintain charge neutrality and destroy the center of symmetry of P_2S_6 unit. Finally, Pb^{2+} kicks out K^+ ions from the interlayer and sits into Mn^{2+} vacant sites in MPS-1 which further helps to regain the center of symmetry of the structure. K-MPS-1 has achieved Pb^{2+} removal capacity of 393.5±8 mg/g following Langmuir-Freundlich adsorption model. K-MPS-1 is effective to capture Pb^{2+} far below the mark of tolerance level (15 ppb, USA-EPA) of drinking water.*

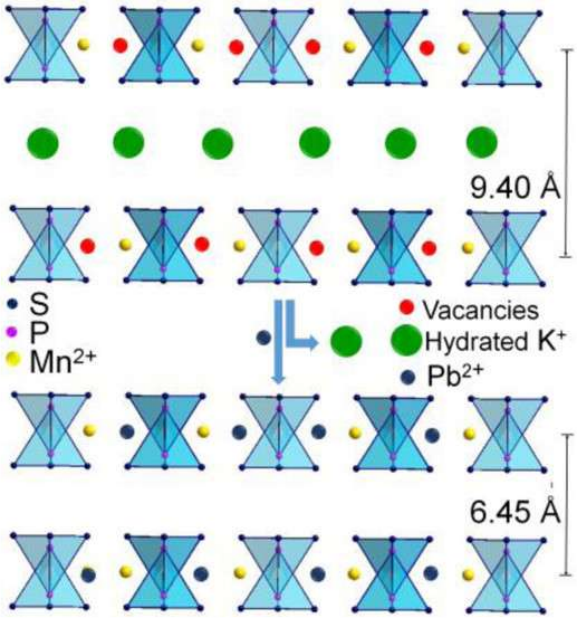

†*Paper based on this has been published as* ***E. Rathore****, P. Pal, K. Biswas, J. Phys. Chem. C* ***2017****, 121, 14, 7959–7966.*

3.1.1. Introduction

Rapid industrialization has led to discharge of heavy metal ions into water resources. Presence of heavy metal ions such as Pb^{2+}, Hg^{2+} and Cd^{2+} in water is detrimental to human health and environment due to toxicity, non-biodegradability and bioaccumulation.[1-7] Traditional methods i.e. ion exchange, chemical precipitation, flocculation, membrane separation and evaporation are unable to selectively and effectively remove the heavy metal ions up to the mark of tolerance level (ppb level) of drinking water.[8] Although, natural hydrophilic adsorbents like clays, zeolites and activated carbon are the promising candidate in this field because of high surface area and low cost, but suffers from weak binding affinity for heavy metal ions, low efficiency and selectivity from dilute solutions.[9-14] However, intercalated zeolites, layered metal oxides, hydroxides, mesoporous silica, metal organic frameworks and metal chalcogenides have drawn attention with respect to the other materials due to higher removal capacity and selectivity.[15-24]

Heavy metal ions forms strong covalent bond with sulfides.[25-27] Specially, in layered metal sulfides, the higher capacity of heavy metal ion absorption arises due to both the open sulfide framework structure and soft Lewis base nature of sulfide anions which has higher affinity towards soft Lewis acidic heavy metal ion center.[28-36] This strategy is the basis for designing effective adsorbent materials based on inorganic sulfides (e.g. $K_{2x}Mn_xSn_{3-x}S_6$ and $K_{2x}Sn_{4-x}S_{8-x}$) for incarceration of heavy metal ions.[28-36] Trailing this idea, recently, introduction of polysulfide anions $[S_x]^{2-}$ into layered double hydroxides gallery has proved to be effective in selective capture of heavy metals, but the lack of stability due to oxidation of $[S_x]^{2-}$ species to $[SO_4]^{2-}$ and unsatisfied removal capacity resists the practical utilization.[37-39] Therefore, it remains a challenge to find a novel stable material which can work in wide pH range with fast kinetics, large adsorption capacity and is capable of removing Pb^{2+} ions selectively from water which is below the drinking water limit (< 15 ppb, USA-EPA).[40]

In this chapter, we demonstrate an elaborate Pb^{2+} ion adsorption and ion-exchange kinetics studies of a potassium intercalated layered metal chalcophosphate, $K_{0.48}Mn_{0.76}PS_3 \cdot H_2O$ (K-MPS-1). We have determined the nature of sorption by calculating the rate constants. The Pb^{2+} sorption isotherm follows the Langmuir-Freundlich model, which indicates the multilayer adsorption. Further, we have

characterized the Pb^{2+} adsorbed K-MPS-1 in detail by IR, Raman spectroscopy, band gap measurement, X-ray photoelectron spectroscopy and zeta potential analysis to provide mechanistic path of Pb^{2+} adsorption and ion exchange. K-MPS-1 rapidly and efficiently captures Pb^{2+} over 99 % even when the concentration of Pb^{2+} is very low (1-100 ppb). Moreover, K-MPS-1 is stable and captures Pb^{2+} within a broad pH range of 2-12. K-MPS-1 removes Pb^{2+} effectively with a high distribution coefficient of ~10^5 mL/g, following pseudo second order kinetics. K-MPS-1 has an enormous Pb^{2+} capturing capacity of 393.5 mg/g, which is the respectable compared to the other reported materials.[29,39,41-54] K-MPS-1 selectively captures Pb^{2+} even in presence of other mono and divalent cations such as Na^+, Ca^{2+} and Mg^{2+}, which makes it a promising candidate for decontamination of Pb in wide variety of water wastes. Potassium intercalation increases layer spacing and creates Mn^{2+} vacancy in $MnPS_3$. Insertion of Pb^{2+} pulls out K^+ and fills vacancy by forming Pb-S covalent bond, which is generally governed by the strong interaction of soft Lewis acidic sulfide and soft Lewis basic Pb^{2+}.

3.1.2. Methods

3.1.2.1. Reagents. Manganese (Mn, Alfa Aesar 99.95 %), red phosphorous (P, Alfa Aesar 98.9 %), sulphur (S, Alfa Aesar 99.999 %), lead nitrate ($Pb(NO_3)_2$, Sigma Aldrich 99.999%), and potassium chloride (KCl, Alfa Aesar 99.5 %) were used for synthesis without further purification.

3.1.2.2 Synthesis. $MnPS_3$ (MPS-1) was prepared by mixing appropriate ratio of elements Mn, P, S followed by sealing under vacuum (10^{-5} Torr) in quartz tube. The tube was slowly heated to 723 K over 12 h, then heated up to 923 K in 2 h, soaked for 144 h, and subsequently cooled to room temperature in 8h. Deep green color reported MPS-1 was obtained.[55] 1 g MPS-1 was stirred with 50 mL 2M KCl aq. solution for 24 h at room temperature and the light green $K_{0.48}Mn_{0.76}PS_3.H_2O$ (K-MPS-1) was separated by centrifugation [56, 57] , washed with water and ethanol and checked the phase purity by XRD.

3.1.2.3. Powder X-ray Diffraction. Powder X-ray diffraction for all of the samples were recorded using a Cu K_α (λ = 1.5406 Å) radiation on a Bruker D8 diffractometer.

3.1.2.4. Band Gap Measurement. To estimate optical band gap of the finely grinded powder samples at room temperature, diffuse reflectance measurements were carried out over the range of 250 nm to 2500 nm using a Perkin Elmer Lambda 900, UV/Vis/NIR spectrometer in reflectance mode. Absorption (α/ S) data were calculated from reflectance data using Kubelka-Munk equation: $\alpha/S = (1-R)^2/(2R)$, where R is the reflectance, α and S are the absorption and scattering coefficient, respectively. The energy band gaps were derived from α/S vs E (eV) plot.

3.1.2.5. Fourier Transform Infrared Spectroscopy. FTIR spectra of powder sample was recorded using a Bruker IFS 66v/S spectrometer.

3.1.2.6. Raman Spectroscopy. Raman spectroscopy measurements of powder sample were carried out with a HORIBA LABRAM HR800 spectrometer. The excitation wavelength of the laser was 514 nm.

3.1.2.7. Thermogravimetric Analysis. TGA was performed using a TGA/DSC 2 STAR instrument in the temperature range of 300–773 K under nitrogen atmosphere with a ramp rate of 5 K min^{-1}.

3.1.2.8. Field Emission Scanning Electron Microscopy and Energy Dispersive Spectroscopy Analysis. FESEM of the synthesized and lead adsorbed materials were performed using NOVA NANO SEM 600 (FEI, Germany) operated at 15 KV. EDAX compositional analysis was performed during FESEM imaging.

3.1.2.9 X-Ray Photoelectron Spectroscopy. XPS measurement has been performed with Mg−Kα (1253.6 eV) X-ray source with a relative composition detection better than 0.1% on an Omicron Nanotechnology spectrometer.

3.1.2.10 Zeta Potential Measurement. The zeta potential measurements were carried out using a NanoZS (Malvern UK) employing a 532 nm laser.

3.1.2.11. ICP-AES. Actual concentration of the lead containing solutions (1ppm-1000ppm) were measured by ICP-AES. ICP-AES measurements were carried out using Perkin-Elmer Optima 7000DV instrument. Pb standard (1000mg/L, Sigma-Aldrich), Mn standard (1000mg/L, Sigma-Aldrich) and multi-element standard (Ca 2000 mg/L,

Na 1000 mg/L , K 200 mg/L and Mg 400 mg/L, Sigma-Aldrich) were used to determine the concentration of various cations.

3.1.2.12. ICP-MS. Element concentrations in ppb level (1-1000 ppb) were measured using a quadrupole inductively coupled plasma- mass spectrometer (ICP-MS, Thermo Scientific X-Series II) at CEaS, IISc equipped with Nickel sample and skimmer cones. Samples were introduced using a 100 ml/min PFA nebulizer connected to a peristaltic pump running at 30 rpm into an ESI-PC3 Peltier cooled spray chamber. A CETAC ASX-520 auto-sampler was used. Uptake time for samples and standards was 60 seconds while the rinse time (in 2% HNO_3) was 90 seconds.

3.1.2.13. Pb^{2+} Sorption and Ion-Exchange Kinetics. Sorption studies is carried out by batch method at V:m~1000 mL/g. 10 mL of Pb^{2+} aqueous solution (1 ppb-1000 ppm) is taken in a 15 mL centrifuging tube. 10 mg of K-MPS-1 was added and shaken for 24 hrs. The solid material is removed by centrifugation or filtration by Whatman filter paper No. 41 and then measured the initial and final Pb^{2+} concentrations in the supernatant by using ICP-AES and ICP-MS. The obtained data is used for determination of Pb^{2+} sorption isotherm.

Kinetic studies are carried out to study the rate and path ways of sorption until the equilibrium has reached. Initially, 10 mL of 30 ppm Pb^{2+} aqueous solution and 10 mg of K-MPS-1 is shaken in an individual tube. After a certain time interval, the suspension of each tube is centrifuged and the final concentration is measured by ICP.

3.1.3. Results and Discussion

Layered transition metal thiophosphates MPS_3, where M is a divalent metal cation, have the similar structural connectivity of $CdCl_2$ structure, where metal ions and P-P pairs occupy the Cd positions and sulphur atoms occupies the chloride positions.[55] Previously, Clement et.al. have reported that layered $MnPS_3$ can intercalate wide range of cations, including organometallic species, ammonium and alkali metal cations.[56, 57]

3.1.3.1 Sythesis and Characterization

We have synthesized dark green powder of $MnPS_3$ (MPS-1) and light green color K^+ intercalated $MnPS_3$ (K-MPS-1) by stirring a suspension of MPS-1 in 2M KCl solution for 24 h at room temperature (Figure 3.1.1).[56]

$$MnPS_3 + 2x\ KCl\ (aq) \longrightarrow Mn_{1-x}K_{2x}PS_3.nH_2O + xMnCl_2\ (x=0.24)$$

The Pb^{2+} sorption properties are explored by stirring $Pb(NO_3)_2$ solution with the as synthesized K-MPS-1. The synthesized Pb^{2+} sorbed K-MPS-1 (Pb-MPS-1) is distinct in color compared to MPS-1.

$$K_{2x}Mn_{1-x}PS_3.nH_2O + xPb(NO_3)_2\ (aq) \longrightarrow Pb_xMn_{1-x}PS_3.nH_2O + 2xKNO_3(x=0.24)$$

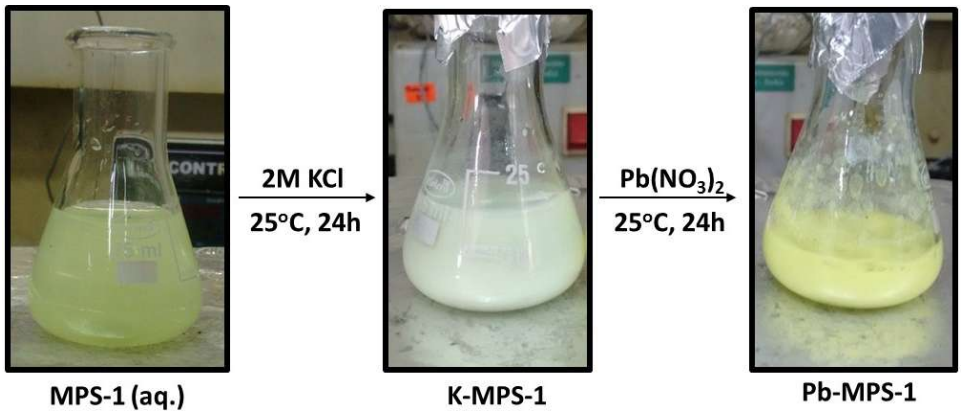

Figure 3.1.1 *Color change during ion-exchange reactions.*

Initial elemental analysis by energy-dispersive X-ray analysis (EDAX) of K-MPS-1 and Pb-MPS-1 shows significant amount of Pb^{2+} sorption by K-MPS-1 (see Table 3.1.1 and Figure 3.1.2)

Table 3.1.1 *Elemental identification and quantification by EDX.*

K-MPS-1			Pb-MPS-1		
Element	Wt %	At %	Element	Wt %	At %
P	17.74	20.45	P	11.87	17.88
S	51.82	57.71	S	38.49	56.00
Mn	22.59	14.68	Mn	23.94	20.33
K	7.85	7.17	Pb	25.69	5.78
Total	**100**	**100**	**Total**	**100**	**100**

More accurate quantification of the elements in K-MPS-1 and Pb-MPS-1 was carried out by inductively coupled plasma (ICP)-AES and ICP-MS analysis. The chemical

formula of K-MPS-1 derived by both ICP and thermogravimetric analysis (TGA, Figure 3.1.3), which is to be $K_{0.48}Mn_{0.76}PS_3.H_2O$.

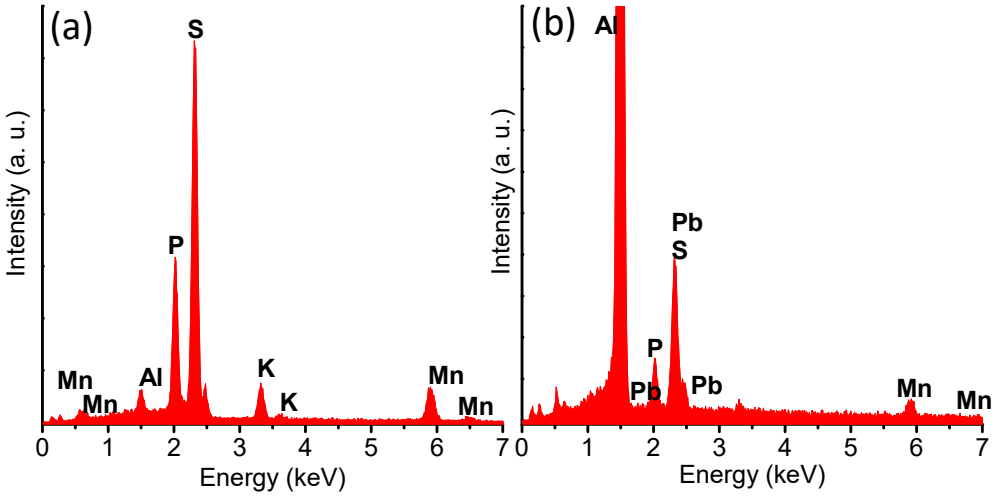

Figure 3.1.2. *EDX spectrum of (a) K-MPS-1 and (b) Pb-MPS-1*

The phase identification and inter layer spacing of K-MPS-1 and Pb^{2+} adsorbed MPS-1 were probed by powder X-ray diffraction (PXRD, see Figure 3.1.4). K^+ intercalation in MPS-1 increases the inter-layer spacing from 6.45 to 9.40 Å, retaining the monoclinic layered crystal structure. After Pb^{2+}sorption, the inter-layer spacing is decreased back to 6.45 Å, which is similar to pristine MPS-1 (Figure 3.1.4 and Table 3.1.2). [58]

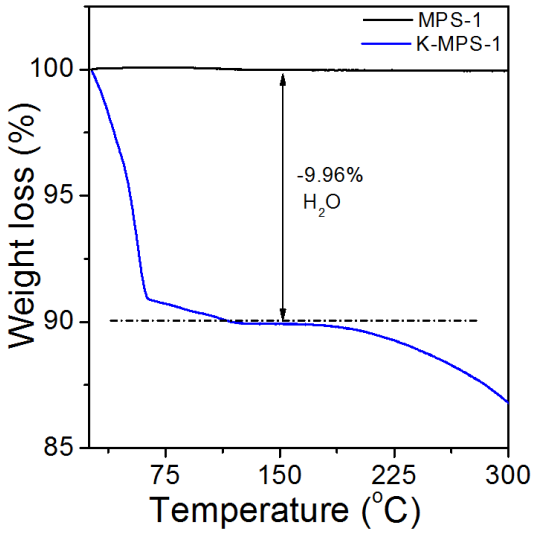

Figure 3.1.3. *TGA analysis of MPS-1 and K-MPS-1*

Table 3.1.2. Interlayer spacing and band gap.

Material	Interlayer spacing (Å)	Band gap energy (eV)
MPS-1	6.45	2.39
K-MPS-1	9.40	2.54
Pb-MPS-1	6.45	2.45

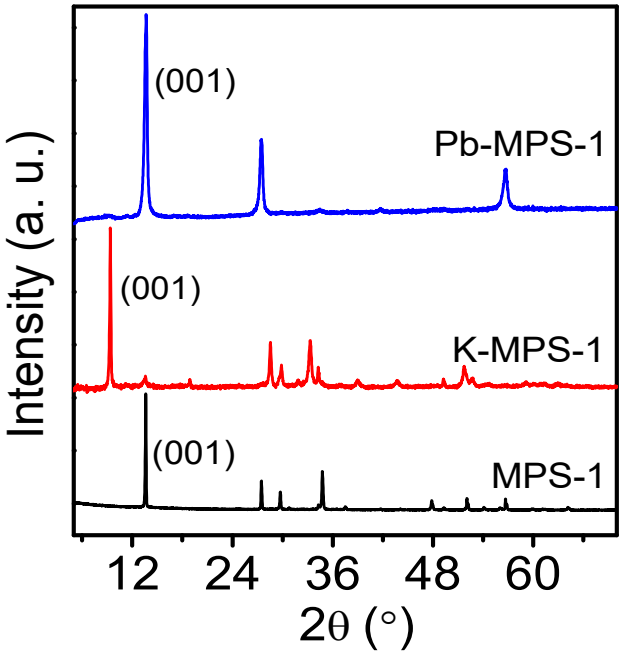

Figure 3.1.4. PXRD patterns of the MPS-1, K-MPS-1 and Pb-MPS-1.

The binding nature of Pb in K-MPS-1 is derived by infrared (IR) and Raman spectroscopy. In the pristine MPS-1, P-S bond shows single asymmetric P-S stretching at 565 cm^{-1} and P-P bond stretching occurs at 445 cm^{-1} (Figure 3.1.5a). K^+ ion intercalation in MPS-1 removes few Mn^{2+} from the solid layer for keeping the balance in total charge, which results in intra-layer Mn^{2+} vacancies in K-MPS-1. This destroys the inversion center in structure and the three S atoms do not stay in the same plane. As a result, asymmetric P-S stretching splits into two components (in-plane and out-

plane), which are appearing at 604 and 550 cm^{-1}, respectively (Figure. 3.1.5a).[59,60] Interestingly, Pb-MPS-1 shows a single P-S stretching at 565 cm^{-1}. Pb^{2+} adsorption removes K^+ ions from interlayer space of $MnPS_3$ and Pb^{2+} occupies the Mn^{2+} vacancy site, which regenerates the center of symmetry and makes the three S atoms coplanar in the structure. This attributes to merging of two P-S stretching modes in a single peak at 565 cm^{-1}.

The strong Raman band at about 386 cm^{-1} is assigned to the PS_3 stretching mode in MPS-1 (Figure 3.1.5b).[59, 60] K^+ intercalation creates an intra-layer Mn^{2+} vacancy and decreases the P-S bond length, which leads to a red shift in the P-S stretching frequency by 2 cm^{-1} K-MPS-1. After Pb^{2+} sorption, this P-S stretching is blue shifted to 384 cm^{-1} due to fill up of Mn^{2+} vacancies (Figure 3.1.5b). This is attributed to the slight increase in P-S bond length in Pb-MPS-1 with respect to P-S bond length in MPS-1. Another band appearing at 275 cm^{-1} is assigned to degenerate bending modes of the PS_3 unit. Two others bands at 247 and 227 cm^{-1} are assigned to translational, T'_{xy}, and rotational, $R'_{xy,}$ motions of the PS_3 unit, respectively (Figure 3.1.5b).[59, 60]

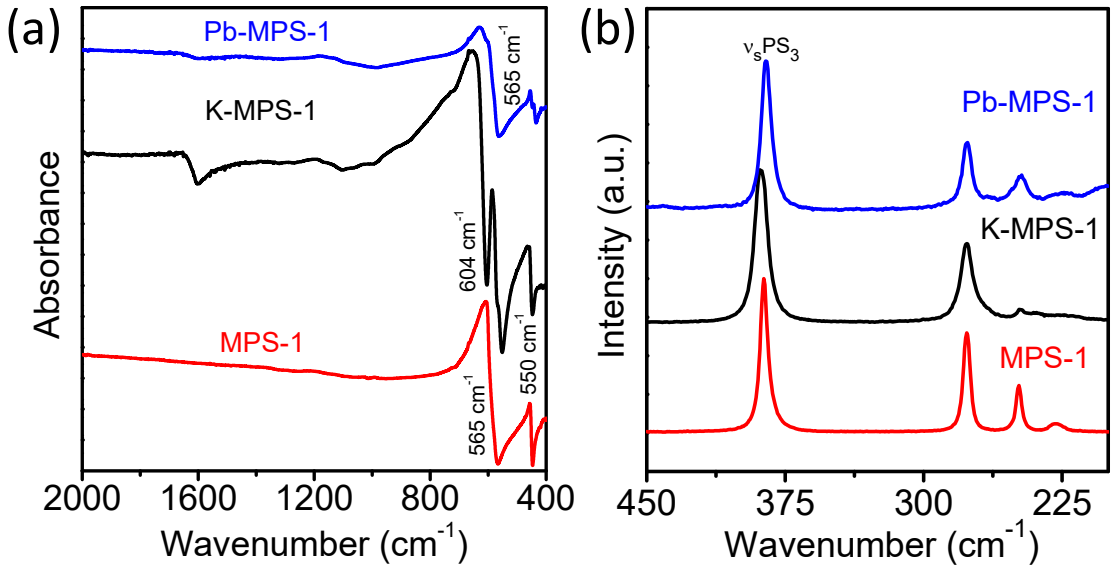

Figure 3.1.5. *(a) Infrared spectra and (b) Raman spectra of the MPS-1, K-MPS-1 and Pb-MPS-1.*

These modes of vibration (275, 247 and 227 cm^{-1}) are strongly sulfur sensitive. The motions of PS_3 in xy plane (layer plane) are affected due to K-intercalation via loss of

symmetry, thus the intensity of the translational (T'_{xy}) and rotational (R'_{xy}) modes decrease in case of KMPS-1 with respect to MPS-1. Pb sorption helps to regain the symmetry in P_2S_6 unit, which further increases the intensity. [61]

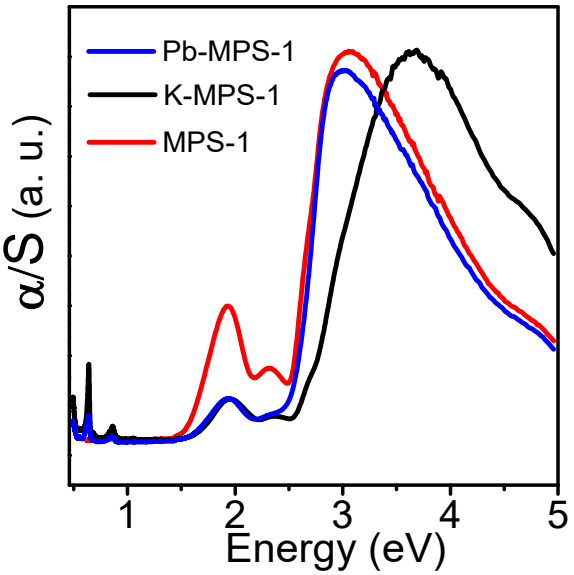

***Figure 3.1.6**. Electronic absorption spectra of MPS-1, K-MPS-1 and Pb-MPS-1.*

Intercalation of K^+ in $MnPS_3$ increases the band gap from 2.38 eV to 2.54 eV indicating increase the gap between the layers due to K^+ intercalation (Figure 3.1.6). Sorption of Pb^{2+} in K-MPS-1 leads to removal of K^+ from the interlayer space and Pb^{2+} occupies the Mn^{2+} vacancy in the $MnPS_3$ layer. The larger covalent interaction between Pb and S with respect to K and S destabilizes the valance band resulting to a further reduction in band gap to 2.45 eV. While the covalent character of Pb-S in Pb-MPS-1 is smaller than that of the Mn-S in MPS-1, depicts band gap of Pb-MPS-1 is 0.06 eV higher than that of MPS-1.

The morphology of the materials is studied by field emission scanning electron microscopy (FESEM) analysis (Figure 3.1.7). The K-intercalated layers are still stacked to each other in K-MPS-1 due to weak van der Waals' force of attraction and the smooth surface are clearly shown in Figure 3.1.7 (a, b). Pb^{2+} sorption keeps the layer as intact as before, but surface roughness increases in Pb-MPS-1, which might be due to additional surface adsorption. (Figure 3.1.7. (c, d)).

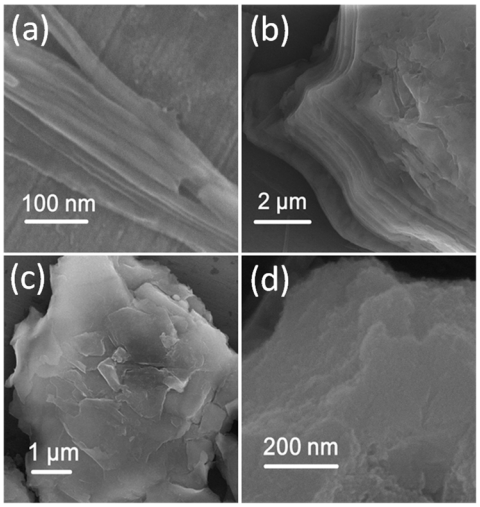

Figure 3.1.7. *FE-SEM images before (a, b) and after (c, d) Pb^{2+} sorption.*

3.1.3.2. Mechanism of Pb capture by K-MPS-1

We propose a qualitative mechanism of Pb^{2+} sorption in K intercalated $MnPS_3$ (K-MPS-1) by the above XRD, IR, Raman, electronic absorption spectroscopy and FESEM studies (Figure 3.1.8 and 3.1.9). Initially, intercalation of hydrated K^+ in MPS-1 increases the inter-lamellar spacing and creates a Mn^{2+} vacancy for maintaining the overall charge balance.

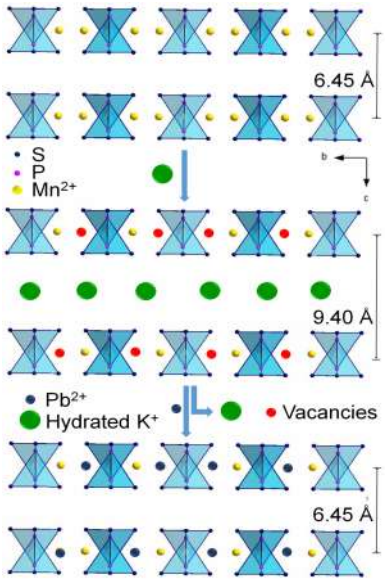

Figure 3.1.8. *Schematic representation displaying the qualitative ion exchange mechanism.*

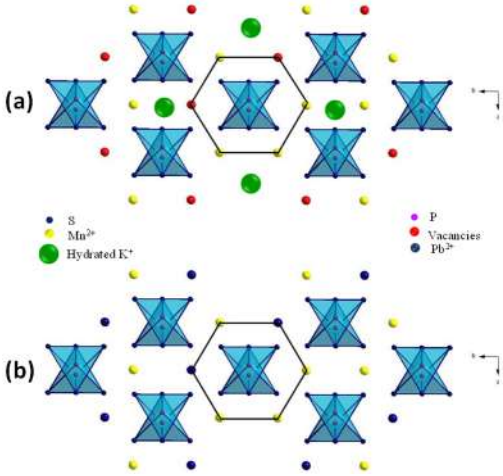

Figure 3.1.9. *Top view of schematic representation displaying the ion exchange mechanism of synthesized and lead adsorbed material.*

Additionally, excess Mn^{2+} vacancy formation creates extra negative charges which are balanced by self aerial oxidation of Mn^{2+} to Mn^{3+} in K-MPS-1.[31] The coexistence of Mn^{2+} and Mn^{3+} in K-MPS-1 is shown in Mn2p X-ray photo electron spectra (XPS) (Figure 3.1.10a).

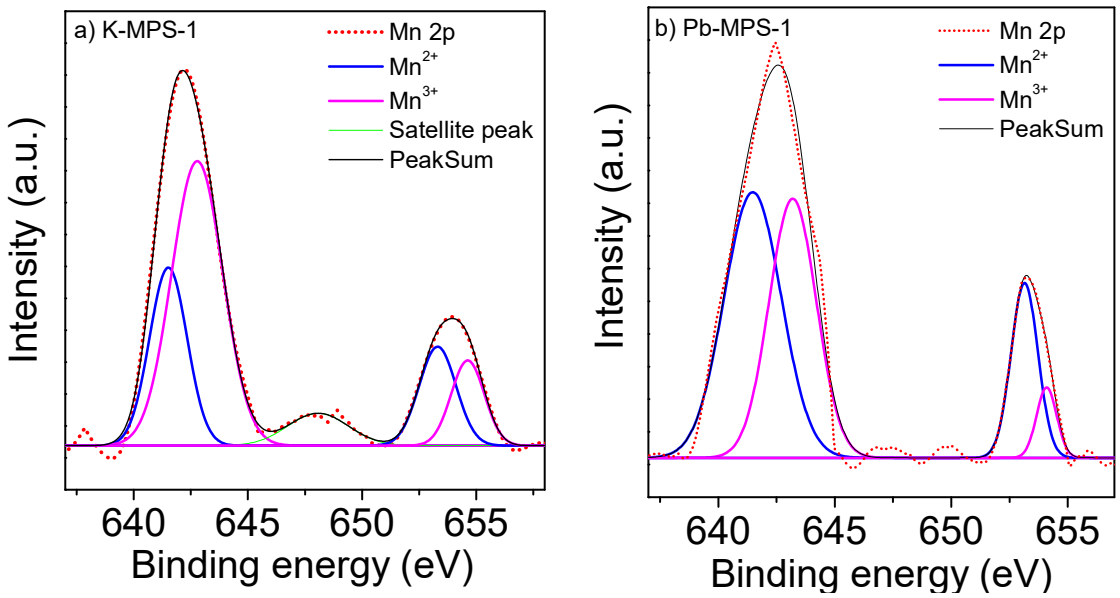

Figure 3.1.10. *Mn2p peak in the XPS spectrum of (a) K-MPS-1 and (b) Pb-MPS-1.*

In the Pb^{2+} sorption process, Pb^{2+} goes into the Mn^{2+} vacancy site in the layer and pulls out the intercalated hydrated K^+ ions from interlayer, which decreases the inter-

lamellar spacing. Moreover, the formation of an excess Mn^{2+} vacancy during K intercalation creates the excess negative charge on surface S atoms. The additional surface charge on the S atoms promotes the adsorption of extra Pb^{2+} over the surface and makes the surface rough. Surface adsorption of Pb^{2+} diminishes the Mn^{3+} concentration in Pb-MPS-1 which is again confirmed by XPS studies (see Figure 3.1.10b). Thus, Pb^{2+} adsorbs both in the Mn^{2+} vacancy site and surfaces. The formation excess negative charge on the surface after K-intercalation was further confirmed by the zeta potential measurement. It was found that the negative charge of the MPS-1 increases upon intercalation of K^+, but it diminishes by sorption of Pb^{2+} into K-MPS-1 (Figure 3.1.11).

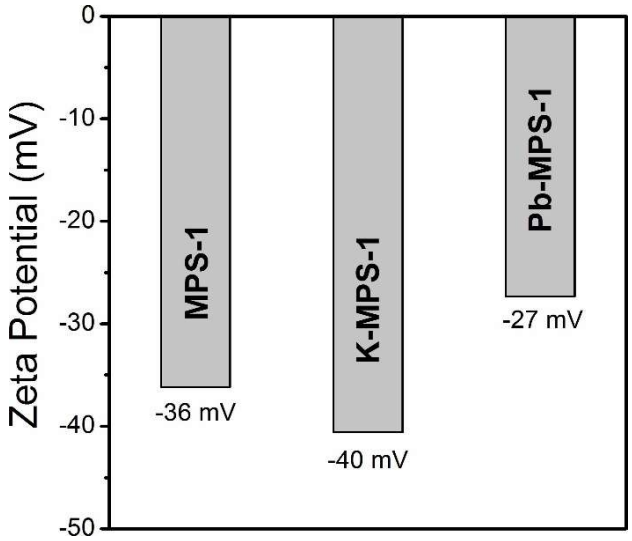

Figure 3.1.11. *Zeta potential of MPS-1, K-MPS-1, Pb-MPS-1 at pH 7 and room temperature.*

3.1.3.3 Sorption Studies

To determine the quantitative sorption capacity of K-MPS-1, we performed ion-exchange batch studies at room temperature within a broad range of Pb^{2+}concentrations from ppb to ppm (*V:m = 1000 mL/g*; pH ~ 6.5, Milli-Q water). The initial and final concentration of Pb^{2+} in the aqueous solution are measured by ICP analysis and maximum sorption capacity (q_m) and the distribution co-efficient (K_d) are calculated by using Eq. (1) and (2).

The equilibrium data and K_d are shown in Figure 3.1.12a and Table 3.1.3, respectively, which can be fitted using Langmuir and Langmuir-Freundlich adsorption isotherm models.[31] The equilibrium data were best fitted (R^2 = 0.991) with the Langmuir-Freundlich model (see Figure 4a) expressed as below:

$$q = q_m \frac{(bC_e)^{1/n}}{1+(bC_e)^{1/n}} \quad (1)$$

$$K_d = \left(\frac{V}{m}\right)\frac{(C_o - C_e)}{C_e} \quad (2)$$

where q (mg/g) is the amount of the cation sorbed at equilibrium concentration C_e (ppm), q_m is the maximum sorption capacity of the adsorbent, C_o is the initial concentration, b (L/mg) is the Langmuir-Freundlich constant assigned to the affinity of the ions towards the adsorbents. $1/n$ is a measure of the intensity of adsorption where n is a constant.

Table 3.1.3. *Sorption results of K-MPS-1 toward* Pb^{2+}.

Initial concentration, C_0 (ppm)	Final concentration, C_f (ppm)	Removal (%)	q (mg/g)	K_d (mL/g)
402.60	1.70	99.6	400.9	2.35 X 10^5
349.90	1.55	99.5	351.9	2.26 X 10^5
319.30	1.09	99.6	318.2	2.90 X 10^5
244.00	0.82	99.7	240.8	2.95 X 10^5
146.30	0.68	99.5	145.6	2.14 X 10^5
104.10	0.56	99.4	103.5	1.83 X 10^5
70.34	0.42	99.4	70.6	1.69 X 10^5
19.85	0.32	98.4	19.5	6.14 X 10^4
5.37	0.23	95.6	5.2	2.21 X 10^4
7.86	0.15	98.0	7.7	5.16 X 10^4
0.49	0.11	76.7	0.3	3.23 X 10^3
0.29	0.08	73.2	0.2	2.65 X 10^3
0.30	0.04	87.7	0.3	6.99 X 10^3
m = 0.010 g, V = 10 mL, V:m = 1000 mL/g				

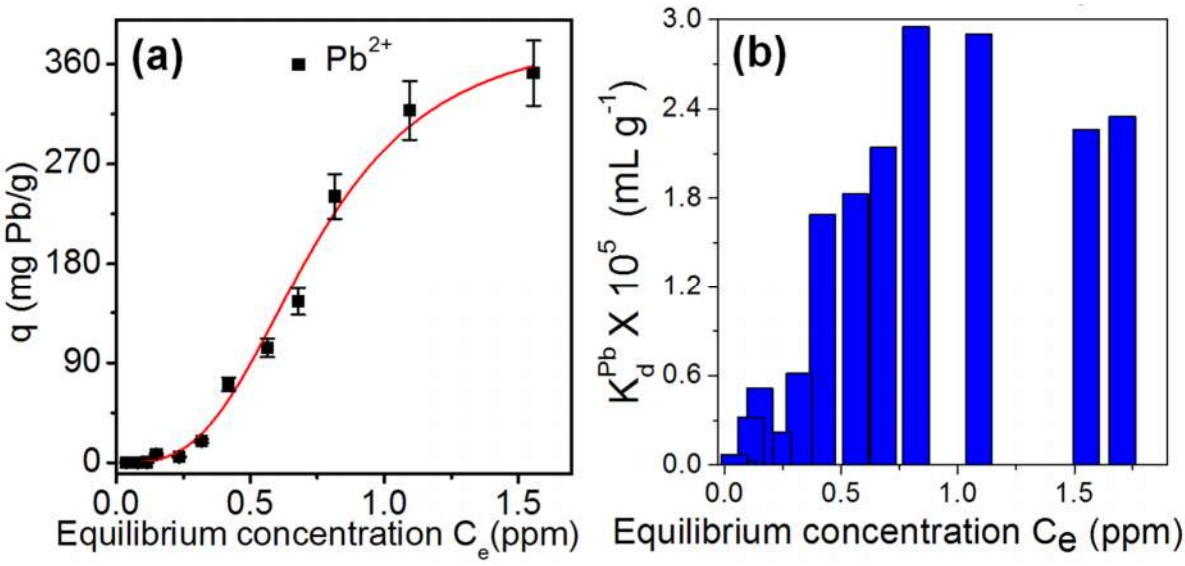

Figure 3.1.12. *(a) Sorption isotherm for the sorption of Pb^{2+} in K-MPS-1 (pH ~ 6.5, RT). The solid (red line) represents the fitting of the data with Langmuir- Freundlich model (fitting data for Pb^{2+}: b =1.35 Lmg^{-1}, n=0.32, R^2=0.992) and (b) Distribution coefficient (K_d^{Pb}) of Pb^{2+} ion exchange at ppm level concentration of Pb^{2+}.*

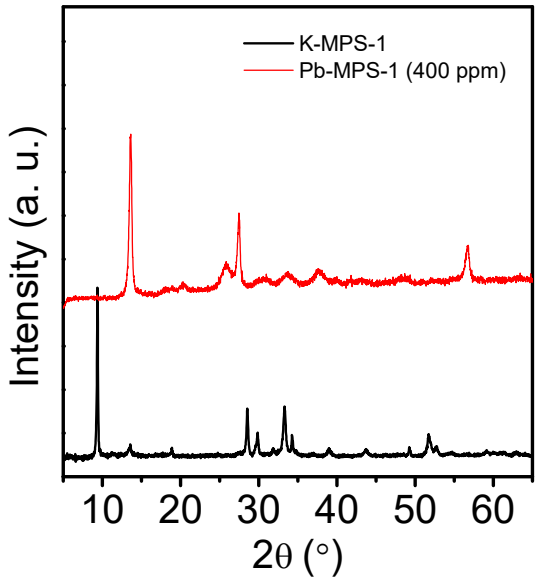

Figure 3.1.13. *XRD of sorbed Pb^{2+} sample at 400 ppm concentration on K-MPS-1.*

The K_d is found in a range of 0.4x10^4 to 2.95 x10^5 mL/g (see Figure 3.1.12b and Table 3.1.3). The layered material is intact even if the initial concentration of Pb^{2+} (400 ppm) is higher than that of the saturation level of the K-MPS-1 (Figure 3.1.13). The

sorption data revealed that K-MPS-1 can capture Pb^{2+} rapidly, showing 97% removal within 4.5 h and ≥99 % removal within 12 h (see Table 3.1.4 below).

Table 3.1.4. *Kinetics data of Pb^{2+} sorption using K-MPS-1.*

Initial concentration, C_o (ppm)	Time (min)	Final concentration, C_f, (ppm)	Removal (%)	K_d (mL/g)	q_t (mg/g)
28.64	15	17.63	38.4	6.25 X 10^2	11.0
	180	3.19	88.9	7.98 X 10^3	25.5
	240	1.04	96.4	2.66 X 10^4	27.6
	270	0.71	97.5	3.93 X 10^4	27.9
	1920	0.37	98.7	7.75 X 10^4	28.3
	3180	0.08	99.7	3.62 X 10^5	28.6
m=0.040g, V= 40mL, V:m=1000mL/g					

We have achieved a maximum Pb sorption capacity q_m of 393.5±8 mg/g for K-MPS-1, which is comparable for Pb sorption capacity for other leading materials (see Table 3.1.5), with 99.8 % removal within 12h (Figure 3.1.14a and b). The high value of b (1.35 L/mg) indicates that K-MPS-1 has a strong affinity towards the Pb^{2+} and the rate of removal is rapid with high distribution co-efficient 2.95×10^5 mL/g.[35] The observed Pb^{2+} exchange capacity (1.91 mmol/g) is almost two times higher than that the theoretical exchange capacity (1.17 mmol/g) of K-MPS-1, which indicates that Pb^{2+} occupies Mn^{2+} vacancy as well as the surface to form multilayer layers.

Table 3.1.5. Comparison of Pb^{2+} sorption capacities between different adsorbents.

Adsorbents	q_m (mg/g)	pH, Temperature	Working pH range	Ref.
K-MPS-1	393.5	6.5, RT	2-12	this work
KMS-1	319	5, RT	2-9	29
MoS_4-LDH	290	RT	2-10	39
Edta-LDH	180	5, RT	3-6	41
DTPA-LDH	170	5.4, RT	3-5.5	42
Cl-LDH	74	5.4, RT	3-5.5	42
LS-LDH	123	5, RT	-	43
LS-GH	1210	5, RT	2-6	44
MNP-CTS	140	6, RT	2-6	45
H100-LDH	128	5, 35° C	-	46
CDpoly-MNPs	65	5.5, RT	2-6	47
Fe_3O_4-GS	158	6-7, RT	2-7.5	48
Titanate-architecture	366	5, RT	-	49
CeO_2 nanowires	642	RT	-	50
EDTA-GO	479	6.8, RT	6.5-7	51
GO–Zr-P	363	6	1-8	52
Graphene oxide	1119	5, RT	3-7	53
NC–FeMg LDH	345	RT	3-7	54

3.1.3.4 Kinetics Study

Kinetics of the ion exchange of layered K-MPS-1 is also explored. The sorption for Pb^{2+} reaches equilibrium within ~8 h (Figure 3.1.14c) and the rate of Pb^{2+} sorption is

calculated by using two different rate equations: pseudo-first-order [Eq. (3)] and pseudo-second-order [Eq. (4)] as stated by the equation below

$$\ln(q_e - q_t) = \ln q_e - k_1 t \qquad (3)$$

$$\frac{t}{q_t} = \frac{1}{k_2 q_e^2} + \frac{t}{q_e} \qquad (4)$$

where q_e (mg/g) is the amount of Pb^{2+} adsorbed per unit mass of adsorbent at equilibrium, q_t is Pb^{2+} ions adsorbed at time t, k_1 and k_2 (g/mg min^{-1}) are the rate constants of pseudo-first-order and pseudo-second-order adsorption interactions. The value of k_1 and k_2 are estimated by plotting $\ln(q_e\text{-}q_t)$ vs. t and t/q_t vs t plot by using Eq. (3) and (4), respectively (see Table 3.1.6).

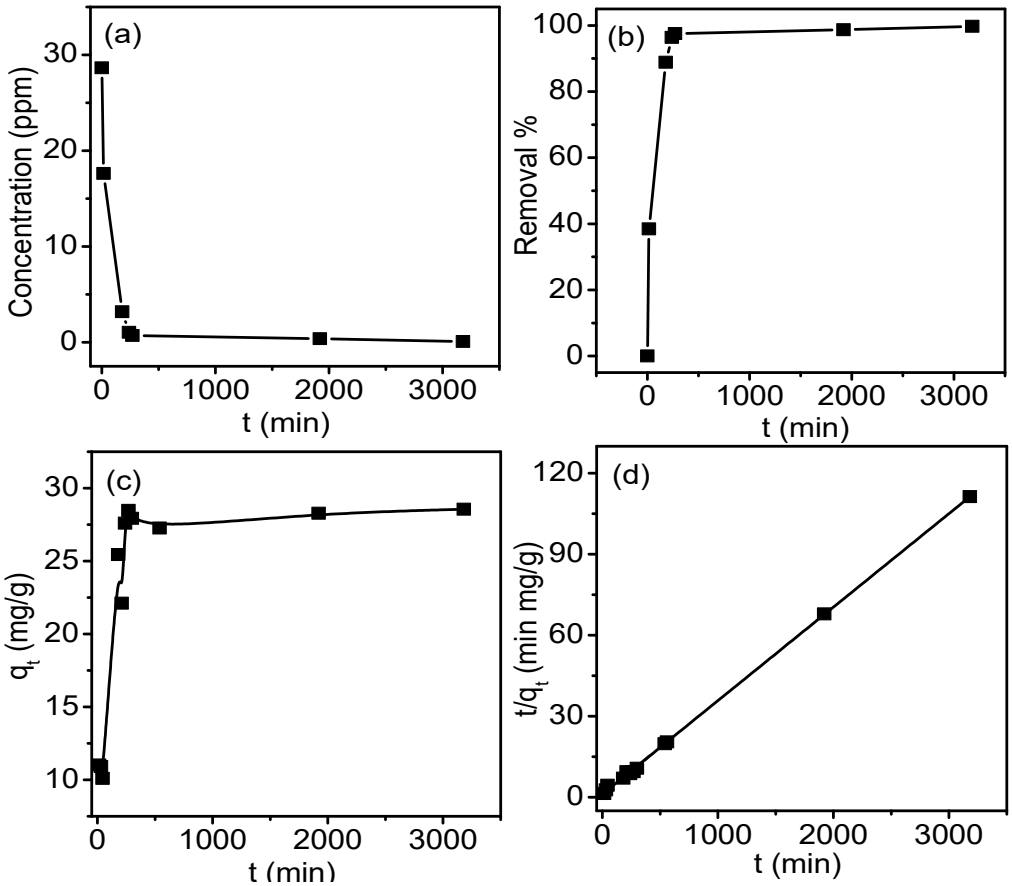

Figure 3.1.14. *Sorption kinetics curve for Pb^{2+}: (a) ion concentration change with contact time, (b) removal % of Pb^{2+} as a function of contact time, (c) sorption capacity (q_t) with contact time and d) pseudo-second-order kinetic plots for Pb^{2+} sorption.*

The values of rate constants (k) and correlation coefficient (R^2) revealed the feasibility of kinetic path of Pb^{2+} sorption. [39] Hence, the goodness of fit R^2 (0.991)

obtained from the Eq. (4), which very close to unity indicates the sorption of Pb^{2+} on K-MPS-1 follows pseudo-second-order kinetics suggesting the process is chemisorption and irreversible (Figure 3.1.14d).

Table 3.1.6 *Kinetic parameters for sorption of Pb^{2+} by K-MPS-1 with two different models.*

Order	Adsorbate	R^2	q_e (exp) (mg g^{-1})	q_e (cal) (mg g^{-1})	k (g/mg/min)
Pseudo-2nd	Pb^{2+}	0.9993	28.2	28.9	1.00 X 10^{-3}
Pseudo-1st	Pb^{2+}	0.2801	28.2	8.1	2.29 X 10^{-3}

Irreversibility of Pb^{2+} sorption in K-MPS-1 is further proved by the ICP analysis during desorption obtained by stirring Pb-MPS-1 with saturated KCl solution (Table 3.1.7). Generally, the Pb contamination is in very low concentration level (ppb) in water. At such a low concentration, K-MPS-1 can take an ample amount of Pb ~393.5 mg/g for long time usage.

Table 3.1.7. *Desorption studies of Pb-MPS-1 by using saturated KCl.*

C_0, (ppm)	C_0, (ppm)	Removed %	Adsorbed on K-MPS-1	Pb^{2+} released, (ppm)	Released %
402.6	1.705	99.6	400.895	0.97	0.2
349.9	1.556	99.6	348.344	0.824	0.2
244	0.815	99.7	243.185	1.005	0.4
146.3	0.679	99.5	145.621	0.579	0.4
70.34	0.419	99.4	69.921	0.044	0.1
m = 0.010 g, V = 10 mL KCl solution, V:m = 1000 mL/g					

3.1.3.5. Competitive Ion-Exchange and Selectivity Studies

The affinity and selectivity of the material are expected to be unaffected in presence of other monovalent and divalent cations. Thus, we have performed sorption studies using a solution containing a mixture of Pb^{2+}, Na^+, Ca^{2+} and Mg^{2+}. K-MPS-1 is capable of discriminating Pb^{2+} ions selectively without a change in K_d^{Pb} value ($0.4x10^5$ mL/g) and the results are depicted in Table 3.1.8.

Moreover, the material shows selective sorption of Pb^{2+} even in the presence of high concentration ratio between Ca^{2+} and Pb^{2+} (see Figure 3.1.15a). This happens due to strong affinity between soft acidic Pb^{2+} and soft basic S^{2-} ligand according to the Hard Soft Acid Base (HSAB) principle [62], whereas the interaction weakens drastically for the hard Ca^{2+} and Mg^{2+} ions. The ability of an ion-exchange media to separate two ions from one another can be expressed by the separation factor, SF (K_d^a/ K_d^b). At lower concentration of Pb such as 30 ppm in presence of Ca (30 ppm) and Mg (20 ppm), the SF (Pb^{2+}/Ca^{2+}) is $4.8x10^3$ and SF (Pb^{2+}/Mg^{2+}) is $5.11x10^3$, respectively.[36] The affinity and selectivity order of cations, determined by comparison of K_d value are to be in the order: $Pb^{2+} >> Ca^{2+} \approx Mg^{2+} >> Na^+$.

Table 3.1.8 Summary of the competitive ion-exchange data of K-MPS-1.

Exchange cations	V:m (mL/g)	Initial concentration (ppm)	Final concentration (ppm)	% Removal	K_d (mL/g)
Pb^{2+} + Ca^{2+} + Mg^{2+}	990	28.16 (Pb) 32.82 (Ca) 20.92 (Mg)	0.70 (Pb) 32.55 (Ca) 20.76 (Mg)	97.5 (Pb) 0.8 (Ca) 0.8 (Mg)	3.90×10^4 8.21 7.63
Pb^{2+} + Ca^{2+} + Mg^{2+}	980	33.42 (Pb) 65.28 (Ca) 37.78 (Mg)	0.59 (Pb) 63.32 (Ca) 35.77 (Mg)	98.2 (Pb) 3.0 (Ca) 5.3 (Mg)	5.45×10^4 3.03×10^1 5.51×10^1

3.1.3.6 pH Studies

The interaction between the K-MPS-1 and Pb^{2+} is persistent in a broad pH range 2-12 (Table 3.1.9) and interaction strength is unaltered with a K_d^{Pb} of the order of ~10^4 to 10^5 mL g^{-1} in the 2-10 pH range (Figure 3.1.15b). PXRD analysis shows that the K-MPS-1 is stable within a pH range 2-12 (Figure 3.1.15c) which indeed indicates the structure and composition is stable in such broad pH range. A maximum K_d^{Pb} value of 5.36 x10^5 mL g^{-1} with the highest Pb^{2+} removal capacity of 99.81% is observed at pH 1.75. In acidic condition, hard protons have the lower affinity for soft basic S^{2-}, thus soft acidic Pb^{2+} sorption will be dominant. Thus, Pb^{2+} uptake increases in lower pH. We have performed the Mn leaching experiment at different pH and observed there is the negligible quantity of Mn leaching (Table 3.1.10), which suffices the stability of the material in different pH.

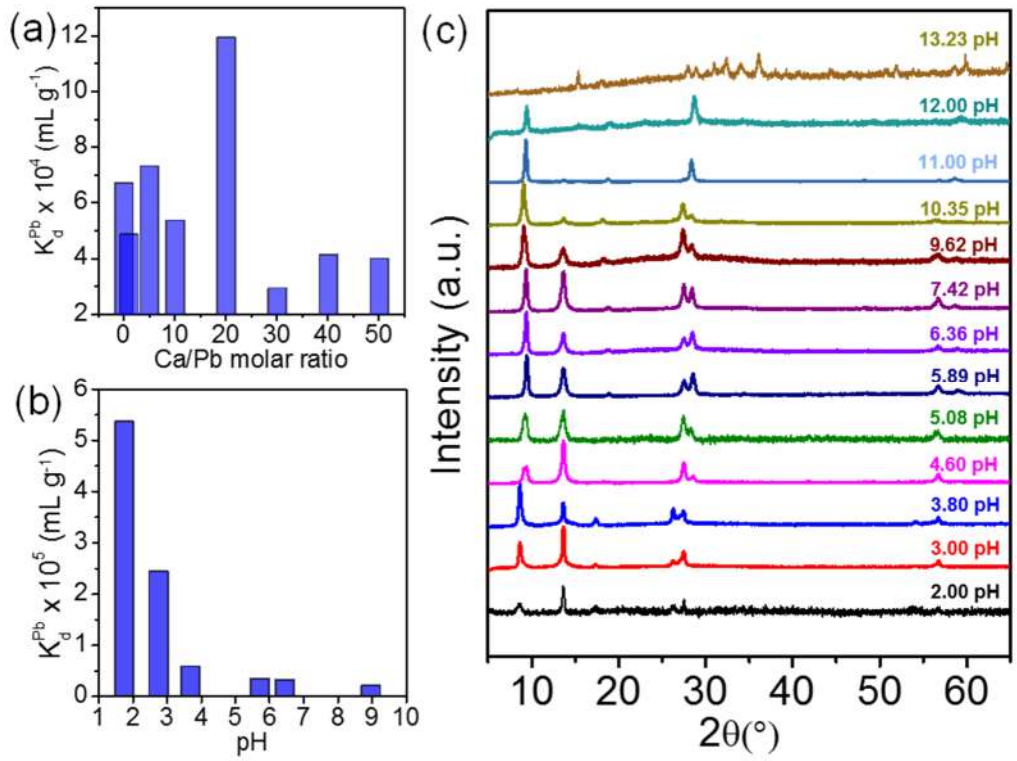

Figure 3.1.15. *(a) Variation of distribution coefficient (K_d^{Pb}) with Ca/Pb molar ratios. (b) Distribution coefficient (K_d^{Pb}) of Pb^{2+} ion exchange at different pH and (c) PXRD patterns of K-MPS-1 in pH range 2-13.2.*

Table 3.1.9. *Summary of Pb^{2+} sorption by K-MPS-1 in different pH.*

pH	Initial concentration, C_o (ppm)	Final concentration, C_f (ppm)	% Removed	q (mg/g)	K_d (mL/g)
1.75	35.62	0.07	99.8	35.9	5.36 X 10^5
2.75	35.85	0.14	99.6	34.7	2.44X 10^5
3.68	35.17	0.58	98.3	34.2	5.88X 10^4
5.71	30.46	0.84	97.2	29.0	3.47X 10^4
6.44	24.40	0.71	97.1	23.0	3.25X 10^4
8.96	13.80	0.60	95.7	12.8	2.14X 10^4
10.75	14.00	2.16	84.6	11.7	5.44X 10^3
11.39	19.01	3.63	80.9	15.3	4.24X 10^3

Table 3.1.10 *Mn^{2+} leaching study in different pH showing negligible Mn leaching.*

pH	Mn^{2+} Leaching (mmole/mg)
2.2	0.0017
3.0	0.0015
4.9	0.0014
7.1	0.0014
9.3	0.0015
11.9	0.0012
m = 10 mg, V = 10 mL, V:m = 1000 mL/g	

3.1.3.7 Low Concentration (ppb Level) Pb Capture and Capture of Pb from a Lake in Bangalore

At lower concentration of Pb^{2+} (1-1000 ppb), the removal capacity and K_d values remain as high as 99 % and ~10^5 mL/g, respectively (Figure 3.1.16 and Table 3.1.11).

We have used ICP-MS, Thermo Scientific X-Series II for detecting the ppb level concentration of Pb as it has really low detection limit. Finally, we have tested Pb^{2+} sequestration from the water samples collected from the local Rachenahalli lake, Jakkur, Bangalore, India. The K-MPS-1 is able to selectively remove 99.2% of Pb^{2+} from the potable water sample containing 68 ppb Pb^{2+} and Pb^{2+} concentration reaches below the tolerance level (15 ppb, USA-EPA) (Table 3.1.11).

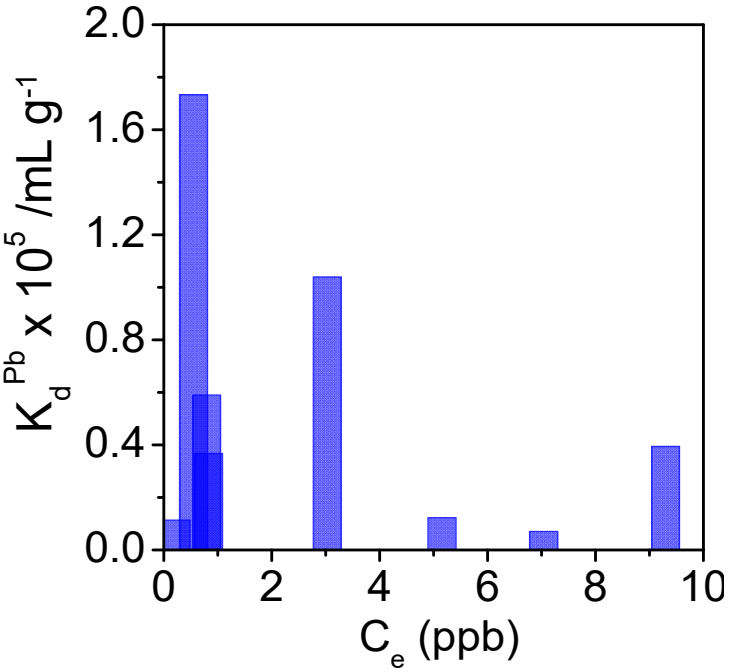

Figure 3.1.16. *Distribution coefficient (K_d^{Pb}) of Pb^{2+} ion exchange at ppb level of Pb^{2+}.*

3.1.4. Conclusions

In summary, Pb^{2+} sorption and ion-exchange kinetics of K-MPS-1 were studied in detail. K-MPS-1 removes Pb^{2+} with a remarkably high capacity (393.5 mg/g) following Langmuir-Freundlich model. It has high distribution co-efficient of 5.96 x 10^5 mL g^{-1} for Pb^{2+} which follows pseudo-second order kinetics, indicates the sorption is chemisorption. K-MPS-1 demonstrates efficient Pb removal (>99 %) from the dilute concentration of aqueous Pb^{2+} solutions (1-1000 ppb). K-MPS-1 exhibits high selectivity towards Pb^{2+} in presence of other hindering hard cations such as Na^+, Ca^{2+}, Mg^{2+} due to strong soft acid-soft base Pb-S interactions, according to the HSAB principle. K-MPS-1 can operate even in broad pH range of 2-12. Intercalation of K^+ in $MnPS_3$ creates a Mn^{2+} vacancy, which is occupied by Pb^{2+} during Pb^{2+} sorption in K-MPS-1. Interestingly, K-MPS-1 is effective

for removing Pb^{2+} from the potable water collected from the lake in Bangalore and can make the Pb^{2+} concentration below the tolerance level of drinking water. Further, the present study can be extended to capture rare earth elements and radionuclides by using K-MPS-1.

Table 3.11. *Removal of Pb^{2+} at lower ppb level.*

Initial concentration, C_0 (ppb)	Final concentration, C_f (ppb)	% Removed
0.95	0.10	89.5
2.84	0.23	91.7
11.36	0.40	96.5
31.14	0.83	97.3
47.84	0.80	98.3
68.57	5.16	92.5
56.45	7.05	87.5
96.50	0.55	99.4
375.60	9.30	97.5
318.00	3.03	99.0
834.20	36.52	95.6
68.00 (Rachenahalli lake water)	0.552	99.2
m = 0.010 g, V = 10 mL, V:m = 1000 mL/g		

3.1.5. References

[1] M. J. Manos, M. G. Kanatzidis, *Chem. Sci.* **2016**, *7*, 4804.

[2] T. W. Clarkson in Heavy metals in the environment (Ed.: B. Sarkar), Marcel Dekker, New York, **2002**, pp. 457.

[3] A. P. Carnizello, L. Marcal, P. S. Calefi, E. J. Nassar, K. J.Ciuffi, R. Trujillano, M. A. Vicente, S. A. Korili, A. J. Gil, *Chem. Eng. Data* **2009**, *54*, 241.

[4] M. A. Shannon, P. W. Bohn, M. Elimelech, J. G. Georgiadis, B. J. Marinas, A. M. Mayes, *Nature* **2008**, *452*, 301.

[5] R. P. Schwarzenbach, B. I. Escher, K. Fenner, T. B. Hofstetter, C. A. Johnson, U. von Gunten and B. Wehrli, *Science* **2006**, *313*, 1072.

[6] S. Majumder, S. Gupta and S. Raghuvanshi in *Heavy Metals In Water: Presence, Removal and Safety* (Eds.: S. Sharma), The Royal Society of Chemistry, Cambridge, **2015**, pp. 44.

[7] M. A. Barakat and R. Kumar in *Heavy Metals In Water: Presence, Removal and Safety* (Eds.: S. Sharma), The Royal Society of Chemistry, Cambridge, 2015, pp. 193.

[8] D. R. Tonini, D. A. Gauvin, R. W. Soffel, W. P. Freeman, *Environ. Prog.* **2003**, *22*, 167.

[9] A. Benhammou, A. Yaacoubi, L. Nibou, B. J. Tanouti, *Colloid Interface Sci.* **2005**, *282*, 320.

[10] Y. El Mouzdahir, A. Elmchaouri, R. Mahboub, A. ElAnssari, A. Gil, S. A. Korili, M. A. Vicente, *Appl. Clay Sci.* **2007**, *35*, 47.

[11] G. Blanchard, M. Maunaye, G. Martin, *Water Res.* **1984**, *18*, 1501.

[12] W. Du, L. B.Yin, Y. Q. Zhuo, Q. S. Xu, L. Zhang, C. H. Chen, *Ind. Eng. Chem. Res.* **2014**, *53*, 582.

[13] X. W. Zhao, Q. Jia, N. Z. Song, W. H. Zhou, Y. S. Li, *J. Chem. Eng. Data* **2010**, *55*, 4428.

[14] D. Mohan, K. P. Singh, *Water Res.* **2002**, *36*, 2304.

[15] H.S. Sherry, *J. Phys. Chem.* **1968**, *72*, 4086.

[16] C.-H. Lin, D. S.-H. Wong, S.-Y. Lu, *ACS Appl. Mater. Interfaces* **2014**, *6*, 16669.

[17] Z. Liu, R. Ma, M. Osada, N. Iyi, Y. Ebina, K. Takada, T. Sasaki *J. Am. Chem. Soc.* **2006**, *128*, 4872.

[18] L. Mercier, T.J. Pinnavaia, *Adv Mater.* **1997**, *9*,500.

[19] X. Feng, G. E. Fryxell, L.-Q. Wang, A. Y. Kim, J. Liu, K. M. Kemner, *Science* **1997**, *276*, 923.

[20] C.W. Abney, J.C. Gilhula, K. Lu, W. Lin, *Adv Mater.* **2014**, *26*, 7993.

[21] M. J. Manos, C. D. Malliakas, M. G. Kanatzidis, *Chem. Eur. J.* **2007**, *13*, 51.

[22] X.-F. Yu, J.-W. Liu, H.-P. Cong, L. Xue, M. N. Arshad, H. A. Albar, T. R. Sobahi, Q. Gao, S.-H. Yu, *Chem. Sci.* **2015**, *6*, 2511.

[23] H. Xue, Q. Chen, F. Jiang, D. Yuan, G. Lv, L. Liang, L. Liu, M. A Hong, *Chem. Sci.* **2016**, *7*, 5983.

[24] A. Chakraborty, S. Bhattacharyya, A. Hazra, A. C. Ghosh, T. K. Maji, *Chem. Commun.* **2016**, *52*, 2831.

[25] N. Ding, M. G. Kanatzidis, *Nat Chem.* **2010**, *2*,187.

[26] S. Bag, P. N. Trikalitis, P. J. Chupas, G. S. Armatas, M. G. Kanatzidis, *Science* **2007**,*317,* 490.

[27] S. Bag, A.F. Gaudette, M.E. Bussell, M.G. Kanatzidis, *Nat Chem.* **2009**, *1*,217.

[28] M. J. Manos, N. Ding, M. G. Kanatzidis, *Proc. Natl. Acad. Sci. U. S. A.* **2008**, *105*, 3696.

[29] M. J. Manos, M. G. Kanatzidis, *Chem. Eur. J.* **2009**, *15*, 4779.

[30] M. J. Manos, M. G. Kanatzidis, *J. Am. Chem. Soc.* **2012**, *134*, 16441.

[31] M. J. Manos, M. G. Kanatzidis, *J. Am. Chem. Soc.* **2009**, *131*, 6599.

[32] M. J. Manos, V. G. Petkov, M. G. Kanatzidis, *Adv. Funct. Mater.* **2009**, *19*, 1087.

[33] Z. H. Fard, C. D. Malliakas, J. L. Mertz, M. G. Kanatzidis, *Chem. Mater.* **2015**, *27*, 1925.

[34] D. Sarma, C. D. Malliakas, K. S. Subrahmanyam, S. M. Islam, M. G. Kanatzidis, Chem. Sci. 2016, 7, 1121.

[35] X. M Zhang, D. Sarma, Y. Q. Wu, L. Wang, Z. X. Ning, F.Q. Zhang, M. G. Kanatzidis, J. Am. Chem. Soc. 2016, 138, 5543.

[36] D. Sarma, S. M. Islam, K. S. Subrahmanyam, M. G. Kanatzidis, J. Mater. Chem. A, 2016, *J. Mater. Chem. A* **2016**, *4*, 16597.

[37] S. L. Ma, Q. M. Chen, H. Li, P. L. Wang, S. M. Islam, Q. Y. Gu, X. J. Yang, Kanatzidis, M. G. J. Mater. Chem. A 2014, 2, 10280.

[38] S. L. Ma, Y. Shim, S. M. Islam, K. S. Subrahmanyam, P. L. Wang, H. Li, S. C. Wang, X. J. Yang, M. G. Kanatzidis, Chem. Mater. 2014, 26, 5004.

[39] L. Ma, Q. Wang, S.M. Islam, Y. Liu, S. Ma, M.G. Kanatzidis, J. Am. Chem. Soc. 2016, 138, 2858.

[40] https://www.epa.gov/dwreginfo/lead-and-copper-rule

[41] M. R. Perez, I. Pavlovic, C. Barriga, J. Cornejo, M. C. Hermosin, M. A. Ulibari, *Appl. Clay Sci.* **2006**, *32*, 245.

[42] X. F. Liang, W. G. Hou, Y. M. Xu, G. H. Sun, L. Wang, Y. Sun, X. Qin, *Colloids Surf. A* **2010**, *366*, 50.

[43] G. L. Huang, D. Wang, S. L. Ma, J. L. Chen, L. Jiang, P. Y. Wang, *J. Colloid Interface Sci.* **2015**, *445*, 294.

[44] F. Li, X. Wang, T. Yuan, R. A. Sun, *J. Mater. Chem. A* **2016**, *4*, 11888.

[45] L. C. Zhou, L. Q. Ji, P. C. Ma, Y. M. Shao, H. Zhang, W. J. Gao, Y. F. Li, *J. Hazard. Mater.* **2014**, *265*, 104.

[46] M. A. Gonzalez, I. Pavlovic, C. Barriga, *Chem. Eng. J.* **2015**, *269*, 221.

[47] A. M. Badruddoza, Z. B. Shawon, T. W. J. Daniel, K. Hidajat, M. S. Uddin, *Carbohydr. Polym.* **2013**, *91*, 322.

[48] X. Y. Guo, B. Du, Q. Wei, J. Yang, L. H. Hu, L. G.Yan, W. Y. Xu, *J. Hazard. Mater*. **2014**, *278*, 211.

[49] C.-H. Lin, D. S.-H. Wong, S.-Y. Lu, *ACS Appl. Mater. Interfaces* **2014**, *6*, 16669.

[50] X.-F. Yu, J.-W. Liu, H.-P. Cong, L. Xue, M. N. Arshad, H. A. Albar, T. R. Sobahi, Q. Gao, S.-H.Yu, *Chem. Sci.* **2015**, *6*, 2511.

[51] C. J. Madadrang, H. Y. Kim, G. Gao, N. Wang, J. Zhu, H. Feng, M. Gorring, M. L. Kasner, S. Hou, *Appl. Mater. Interfaces* **2012**, *4*, 1186.

[52] S. Pourbeyram, *Ind. Eng. Chem. Res.* **2016**, *55*, 5608.

[53] R. Sitko, E. Turek, B. Zawisza, E. Malicka, E. Talik, J. Heimann, A. Gagor, B. Feist, R. Wrzalik, *Dalt. Trans.* **2013**, *42*, 5682.

[54] L. Ling, W.-J. Liu, S. Zhang, H. Jiang, *J. Mater. Chem. A* **2016**, *4*, 10336.

[55] W. Klingen, R. Ott, H. Hahn, *Z. Anorg. Allg. Chem* **1973**, *396*, 271.

[56] R. Clement, *J. Chem. Soc., Chem. Commun.*, 1980, 647.

[57] R. Clement, J. J. Girerd, I. Morgenstern-Badarau, *Inorg. Chem.* **1980**, *19*, 2852.

[58] L.Silipigni, G.D. Marco, G. Salvato, V.Grasso, *Appl. Surf. Sci.* **2005**, *252,* 1998.

[59] Y. Mathey, R. Clement, C. Sourisseau, G. Lucazeau, *Inorg. Chem.* **1980**, *19*, 2773.

[60] P. A. Joy, S. Vasudevan, *J. Am. Chem. Soc.* **1992**, *114*, 7792

[61] R. Clement, O. Gamier, J. Jegoudez, *Inorg. Chem* **1986**, *25*, 1404.

[62] R. G. Pearson, *J. Am. Chem. Soc.* **1963**, *85*, 3533.

Chapter 3.2

Selective and ppb Level Removal of Hg (II) from Water: Synergistic Role of Graphene Oxide and SnS_2[†]

[†]*Paper based on this has been published as* ***E. Rathore****, K. Biswas, J. Mater. Chem. A* ***2018****, 6, 13142.*

Chapter 3.2

Selective and ppb level removal of Hg (II) from water: synergistic role of graphene oxide and SnS_2[†]

Summary: *Mercury (Hg) contamination can cause serious health issues like brain damage, skin diseases and birth defects. An upper limit of 2 ppb for Hg in drinking water has been allowed by the United States Environmental Protection Agency (EPA). Thus, selective removal of Hg below 2 ppb is an important challenge in the treatment of wastewater. Herein, we report the tremendous selectivity and ppb level removal of $Hg^{(II)}$ from water by using a graphene oxide and tin (IV) disulfide (SnS_2) composite ($GO@SnS_2$). The material can remove 99.1 % of $Hg^{(II)}$ from a concoction of $Na^{(I)}$, $K^{(I)}$, $Cs^{(I)}$, $Rb^{(I)}$, $Ca^{(II)}$, $Mg^{(II)}$, $Co^{(II)}$, $Cu^{(II)}$, $Ni^{(II)}$, $Zn^{(II)}$, $Pb^{(II)}$, $Cd^{(II)}$, $Mn^{(II)}$, $Fe^{(III)}$ and $As^{(III)}$ with a high separation factor of the order 10^2-10^3. We have achieved a capacity of 342.02 ± 8.02 mg/g with a distribution coefficient (K_d) value of 8.68 X 10^5 mL/g and the $GO@SnS_2$ is stable in the pH range 0.5 – 11. The material can remove $Hg^{(II)}$ from even 0.3 ppb $Hg^{(II)}$ contaminated water. Further, the mechanism behind the synergistic $Hg^{(II)}$ adsorption is due to the interaction between $Hg^{(II)}$ and –COOH of GO and the soft Lewis acid-base chemistry between S^{2-} of SnS_2 and $Hg^{(II)}$. For convenient application, we have designed a tea bag filled with $GO@SnS_2$ powder which can capture 99.9% of $Hg^{(II)}$ from contaminated water economically.*

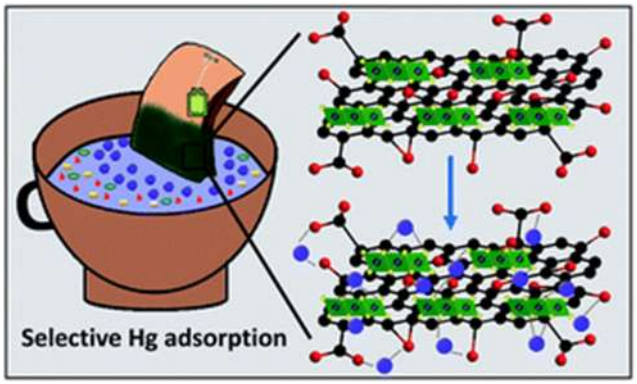

[†]*Paper based on this has been published as* ***E. Rathore****, K. Biswas, J. Mater. Chem. A* ***2018****, 6, 13142.*

3.2.1. Introduction

Clean and fresh water is pivotal to the existence of life. However, the world's supply of fresh water is dwindling and the contaminants level are increasing rapidly.[1,2] World Health Organization (WHO) has listed heavy metal ions like mercury, cadmium, lead and arsenic as major toxic contaminants in industrial wastewater as well as in groundwater.[3] Conventional methods of heavy metal ion removal are classified as electrochemical treatments (electrocoagulation, electrodeposition and elector-floatation), physicochemical processes (chemical precipitation and ion exchange) and adsorption.[4–6] However, precipitation methods show practical limitations to reduce the concentration of heavy metals up to the legal limits in drinking water.[7] Selective sequestration of heavy metals from water bodies using sorbent materials have been a challenging goal due to low capacity, low surface area, moderate affinity towards heavy metal ions and pH stability of the materials.[5,8–14] Thus, the challenge is attracting researchers to develop innovative and improved materials/methods for efficient removal of heavy metal ions.

One of the most cost-effective methods of removing heavy metal is selective metal ion adsorption using high surface area natural adsorbents such as clays,[10–13] zeolites,[14] activated carbon, 3D RGO aerogel[15] and graphene-oxide nanosorbents[16] but it suffers from weak affinity, selectivity, and pH stability due to the oxidic framework. To tackle these problems, researchers have designed new materials like thiol-functionalized PAF-1-SH,[17] MOFs,[18] COFs,[19,20] clays[21] and thioether based TAPB-BMTTPA-COF[22] by introducing soft Lewis basic thiol groups to the oxidic materials. However, thiols based adsorbents have high propensity to oxidize to disulfide under ambient conditions and suffer from long-term use.[23,24] Recently, sulfide-based solid-state materials materials like KMS-1,[25] KMS-2,[26] K-MPS-1,[27,28] LHMS-1,[29] S_x–LDH[30], MoS_4-LDH[31], Fe-MoS_4 LDH[9], porous amorphous chalcogenides,[32] chalcogels[33], 3D MoS_2 aerogels[34], ZnS nanoparticle gel[35] have been implied for removal of heavy metals including Hg. They are effective due to the high affinity of the soft Lewis base sulfur framework towards the soft Lewis acids. However, removal of Hg below the legal limit of 2 ppb (United States Environmental Protection Agency, USA-EPA),[36] selectively and conveniently in a broad pH range is still a challenge.

Here in this chapter, we have used graphene oxide (GO) for anchoring tin (IV) sulfide (SnS_2) to introduce soft Lewis basic framework and increase the binding affinity

of GO for the selective removal of $Hg^{(II)}$ from the water. The GO@SnS_2 material can remove $Hg^{(II)}$ from even 0.3 ppb $Hg^{(II)}$ contaminated water with a capacity of 342.02 ± 8.02 mg/g with a distribution coefficient (K_d) value of 8.68 X 10^5 mL/g. We have studied the adsorption of $Hg^{(II)}$ thoroughly and observed a synergistic increase in capacity of $Hg^{(II)}$ removal by the incorporation of SnS_2 grafts onto GO. We have investigated the synergistic $Hg^{(II)}$ adsorption mechanism, which indicates two adsorption processes are responsible for the removal of $Hg^{(II)}$ by GO@SnS_2 composite: interaction between $Hg^{(II)}$ and –COOH of GO and the soft Lewis acid-base chemistry between S^{2-} of SnS_2 and $Hg^{(II)}$. GO@SnS_2 is stable in the pH range 0.5 – 11 and removes $Hg^{(II)}$ efficiently ~99 % in wide pH range. It distinguishes $Hg^{(II)}$ efficiently from a mixture of $Na^{(I)}$, $K^{(I)}$, $Cs^{(I)}$, $Rb^{(I)}$, $Ca^{(II)}$, $Mg^{(II)}$, $Co^{(II)}$, $Cu^{(II)}$, $Ni^{(II)}$, $Zn^{(II)}$, $Pb^{(II)}$, $Cd^{(II)}$, $Mn^{(II)}$, $Fe^{(III)}$ and $As^{(III)}$; and shows tremendous selectivity towards $Hg^{(II)}$ with high separation factor of the order 10^2-10^3. We have also designed a tea-bag comprising GO@SnS_2 powder for the practical application of $Hg^{(II)}$ removal and found that it can remove up to 99.9 % $Hg^{(II)}$ efficiently from contaminated solution.

3.2.2. Methods

3.2.2.1. Reagents. Graphite powder (SD fine- chem, 99.5 %) $SnCl_4.5H_2O$ (Sigma-Aldrich, 99.995 %), graphite powder (SD fine- chem, 99.5 thiourea (CH_4N_2S, Sigma-Aldrich, ≥ 99.0 %) and mercury nitrate ($Hg(NO_3)_2$, Sigma Aldrich 99.999%) were used for synthesis without further purification.

3.2.2.2 Synthesis. To synthesize GO, oxidation of graphite powder (SD fine- chem, 99.5 %) was performed using the Hummer's method.[37] 1.5 mmol $SnCl_4.5H_2O$ (Sigma-Aldrich, 99.995 %) was added to 40 mL dispersion of GO (1mg/ mL) and ultrasonicated for 4h. Then, 8 mmol thiourea (CH_4N_2S, Sigma- Aldrich, ≥ 99.0 %) as the sulfur source was added to the above solution and stirred for 30 min. The solution was autoclaved and heated to 160 °C for 16 h. The obtained greenish black residue was centrifuged, washed several times and freeze dried.

3.2.2.3. Powder X-ray Diffraction. Powder X-ray diffraction for all of the samples were recorded using a Cu K_α (λ = 1.5406 Å) radiation on a Bruker D8 diffractometer.

3.2.2.4. Raman Spectroscopy. Raman spectroscopy measurements of powder sample were carried out with a HORIBA LABRAM HR800 spectrometer. The excitation wavelength of the laser was 514 nm.

3.2.2.5. Thermogravimetric Analysis. TGA was performed using a TGA/DSC 2 STAR instrument in the temperature range of 300–773 K under nitrogen atmosphere with a ramp rate of 5 K min^{-1}.

3.2.2.6. Field Emission Scanning Electron Microscopy and Energy Dispersive Spectroscopy Analysis. FESEM of the synthesized and lead adsorbed materials were performed using NOVA NANO SEM 600 (FEI, Germany) operated at 15 KV. EDAX compositional analysis was performed during FESEM imaging.

3.2.2.7. Zeta Potential Measurement. The zeta potential measurements were carried out using a NanoZS (Malvern UK) employing a 532 nm laser.

3.2.2.8. Surface area analysis. Surface area and porosity measurements were carried out using QUNATACHROME QUADRASORD-SI analyzer at 77 K for N_2.

3.2.2.9. ICP. The initial and final concentration of the elements in aqueous samples (5 ppm-3000 ppm) was measured by Perkin-Elmer Optima 7000DV ICP AES instrument. The calibration solutions were prepared by ICP standards of Hg, Co, Cu, Ni, Zn, Pb, Cd, Mn, Fe, Rb, Cs (1000mg/L, Sigma-Aldrich) and multi-element standard (Ca 2000 mg/L, Na 1000 mg/L, K 200 mg/L and Mg 400 mg/L, Sigma-Aldrich). To detect the concentration in ppb level (0.2-5000 ppb), a quadrupole inductively coupled plasma- mass spectrometer (ICP-MS, Thermo Scientific X-Series II) was used.

3.2.2.10. Adsorption Experiments with GO@SnS_2. The adsorption studies of GO@SnS_2 were carried out using batch method (V: m~1000 mL/g). 10 mg of adsorbent was added to 10 mL of $Hg^{(II)}$ aqueous solution (0.2 ppb-3000 ppm) and shaken for 24 h using the tube-rotator. The $Hg^{(II)}$ adsorbed material (GO@SnS_2) was separated from the mixture by centrifugation and dried at 70 °C. The analysis of supernatant solution for target metal ion was done by using inductively coupled plasma-atomic emission spectroscopy (ICP-AES) and inductively coupled plasma- mass spectrometry (ICP-MS). The obtained concentrations were used to calculate absorption capacity of

GO@SnS_2 (q_e, from eq 1) and the binding affinity of $Hg^{(II)}$ towards GO@SnS_2 in terms of distribution coefficient (K_d, from eq 2).

$$q_e = \frac{(C_o - C_e)V}{m} \quad \text{Eq. 3.2.1.}$$

$$K_d = \left(\frac{V}{m}\right)\frac{(C_o - C_e)}{C_e} \quad \text{Eq. 3.2.2.}$$

where, V, m, C_e, and C_o indicates the volume of $Hg^{(II)}$ aqueous solution (mL), amount of adsorbent taken, equilibrium concentration (ppm) and initial concentration (ppm) respectively.

3.2.2.11. Adsorption Kinetics. Kinetic studies of $Hg^{(II)}$ adsorption by GO@SnS_2 were conducted till it reached equilibrium. 10 mg of the GO@SnS_2 was added into 15 mL centrifugal tube, a 10 mL aqueous solution containing ~93 ppm $Hg^{(II)}$ was added (V/m = 1000 mL/g) and shaken. After a definite time interval, ~4 mL of supernatant was taken and analyzed by ICP.

3.2.2.12. Uptake of Hg(II) in Different pH. The influence of pH on the adsorption of $Hg^{(II)}$ from aqueous solution was examined over the pH range 0.5-13.9. For each experiment, 10 mL solution of 80-100 ppm $Hg^{(II)}$ with varying pH was shaken with 10 mg of GO@SnS_2 for 24 h. The supernatant was analyzed by ICP-AES.

3.2.2.13. Selectivity Experiments. To test the effect of co-existing ions like $Na^{(I)}$, $K^{(I)}$, $Cs^{(I)}$, $Rb^{(I)}$, $Ca^{(II)}$ and $Mg^{(II)}$ and selectivity of $Hg^{(II)}$ capture, competitive adsorption studies were carried out with 10 mg of GO@SnS_2, with V: m~1000 mL/g, using 10 mL of ~20 ppm mixture of these cations with $Hg^{(II)}$, at room temperature with 24 h contact time. A separate study was carried out to examine the effect of $Hg^{(II)}$ removal in presence of competitive ions, $Co^{(II)}$, $Cu^{(II)}$, $Ni^{(II)}$, $Zn^{(II)}$, $Pb^{(II)}$, $Cd^{(II)}$, $Mn^{(II)}$, $Fe^{(III)}$ and $As^{(III)}$.

3.2.2.14. Tea Bag Experiment. For the practical application of this material, 1 g of GO@SnS_2 powder was packed in a tea bag paper. The tea bag was dipped in a 100 mL beaker containing ~100 ppm of $Hg^{(II)}$ solution. After a certain time, 3 mL of solution was taken out, and the concentration of $Hg^{(II)}$ was measured using ICP.

3.2.3. Results and Discussion

3.2.3.1. Synthesis and characterizations. Initially, the negatively charged surface of GO facilitates the adsorption of $Sn^{(II)}$ on GO surface via Coulombic attraction. The high temperature (160 °C) condition release of S^{2-} from CH_4N_2S and leads to the formation of SnS_2 nanoparticles on GO. PXRD of the GO@SnS_2 shows the incorporation of SnS_2 grafts on GO as all the diffraction peaks can be indexed with respect to hexagonal SnS_2 (Figure. 3.2.1). The (001) diffraction peak indicates crystalline nature of SnS_2 on GO.[38] The average crystallite size of SnS_2 on GO is estimated from peak broadening of PXRD to be 13.3 nm. However, the broad (002) peak of graphite at 26.6° in GO and GO@SnS_2 suggests few-layer nature of GO sheets (Figure. 3.2.1). Adsorption of $Hg^{(II)}$ was carried out using the batch method. PXRD shows that $Hg^{(II)}$ adsorbed GO@SnS_2 composite is still intact as there is no separation of GO and SnS_2.

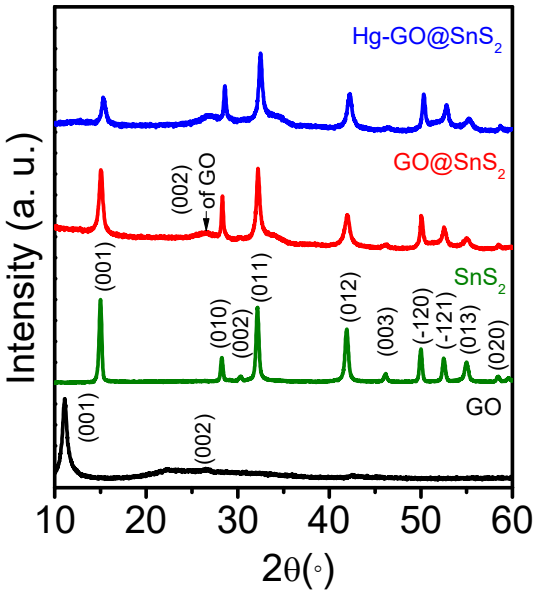

Figure. 3.2.1. *PXRD patterns for GO, SnS_2, GO@SnS_2 and Hg adsorbed GO@SnS_2 material.*

FESEM images show that layers SnS_2 are deposited on the graphene oxide (Figure. 3.2. 2a). The layers remain intact even after adsorption of $Hg^{(II)}$ (Figure. 3.2.2b). The EDAX confirms the presence of Hg in Hg-GO@SnS_2 (Figure. 3.2.2c and Table 3.2.1). The EDAX line scan in Figure. 3.2.2d shows even distribution of $Hg^{(II)}$ in the composite. TEM and HRTEM images in Figure. 3.2.3a-c of Hg- GO@SnS_2 shows the thin sheet of GO, textured with small nanocrystals of SnS_2 in size range of 2-5 nm, which is smaller

than that the size estimated from PXRD. This indicates the formation of predominately small SnS_2 nanoparticles on GO sheets along with few relatively bigger particles. The lattice plane distance matches with (101) and (102) planes of SnS_2 (Figure. 3.2.3c). However, we did not observe any HgS nanoparticles which indicate direct metal ion adsorption. SAED pattern shows polycrystalline nature due to SnS_2 and GO (Figure. 3.2.3d).

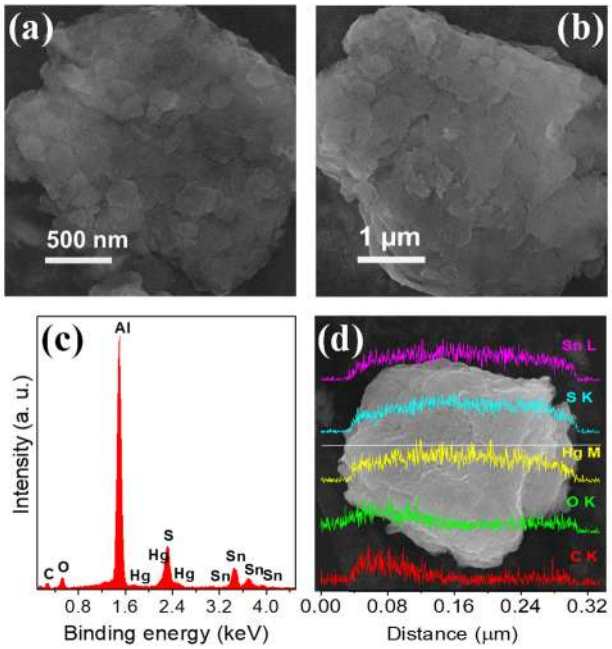

Figure. 3.2.2. *SEM images (a) GO@SnS_2, (b) Hg adsorbed GO@SnS_2 material, (c) EDAX analysis and (d) line scan of Hg adsorbed GO@SnS_2.*

Table 3.2.1.: *Elemental identification and quantification by EDAX spectra analysis.*

GO@SnS_2			Hg-GO@SnS_2		
Element	Wt %	At %	Element	Wt %	At %
C	10.92	21.40	C	23.98	55.37
O	41.49	61.03	O	11.48	19.90
Sn	15.19	11.15	Sn	38.2	8.93
S	32.39	6.42	S	16.74	14.48
Hg	0	0	Hg	9.61	1.33
Total	100	100	Total	100	100

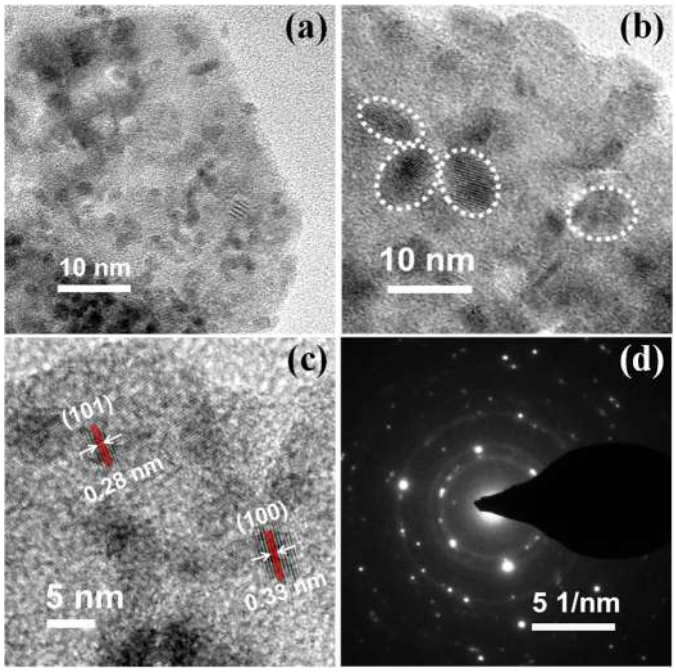

Figure. 3.2.3. *TEM, HRTEM and SAED pattern of Hg adsorbed material (white dotted circles indicate SnS_2 and red parallel lines denote lattice planes of SnS_2).*

The surface of GO@SnS_2 was characterized by N_2 adsorption and desorption isotherm (see Figure. 3.2.4). The isotherm obtained is defined by type IV, suggestive of mesopores which in turn facilitates condensation with pore volume 4.6 x 10^{-2} cm^3/g.

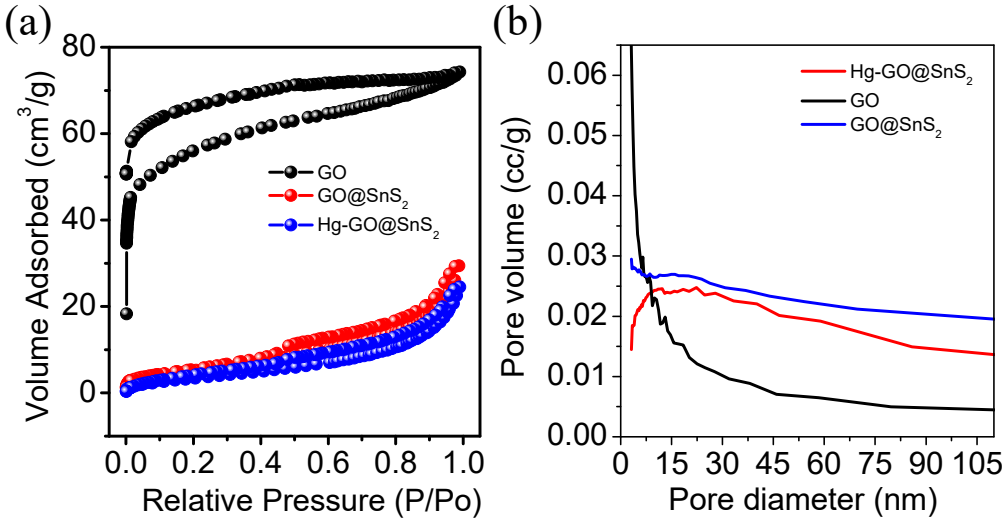

Figure. 3.2.4. *(a) N_2 adsorption and desorption isotherms at 77 K and (b) pore width distribution of GO, GO@SnS_2 and Hg adsorbed GO@SnS_2.*

The surface area of GO decreases significantly after SnS_2 loading which decreases further after $Hg^{(II)}$ sorption (Figure 3.2.4 and Table 3.2.2). This indicates that the SnS_2 nanoparticle covers the surface of GO in GO@SnS_2. $Hg^{(II)}$ sorption further occupies the surface, which results in further decrease in the specific surface.

Table 3.2.2. *Nitrogen adsorption and desorption results.*

Material	Surface Area (m^2/g)	Pore volume (cc/g)	Pore diameter (nm)
GO	174.02	0.115	3.1
GO@SnS_2	19.54	0.046	3.9
Hg-GO@SnS_2	11.75	0.037	3.4

TGA and zeta potential studies were carried out to understand the mechanism of $Hg^{(II)}$ adsorption. In TGA, The GO@SnS_2 composite shows 9.06% weight loss at ~200 ^oC corresponding to a conversion of SnS_2 to SnO_2 (Figure. 3.2. 5a).[39] Further, weight loss from ~540 ^oC is due to the removal of GO.[36] In case of Hg-GO@SnS_2, 15.3 % additional weight loss was measured at ~200 ^oC which corresponds to the removal of water from hydrated $Hg^{(II)}$ adsorbed on the composite. The zeta potential values confirm that the negative surface charge of GO decreases upon formation of a composite with SnS_2 indicating the anchoring of SnS_2 on GO as the $Sn^{(IV)}$ acts as Lewis acid and carbonyl oxygen in GO as Lewis base (Figure. 3.2. 5b). The negative charge on GO@SnS_2 can be attributed to the free S^{2-}. $Hg^{(II)}$ adsorption further decreases the negative charge due to binding of $Hg^{(II)}$ to unsaturated sulfurs. These observations suggest that SnS_2 nanocrystals graft on GO surface, which can dramatically increase the affinity of $Hg^{(II)}$ adsorption on GO@SnS_2 surface.

Further, we have investigated GO, GO@SnS_2 and $Hg^{(II)}$ adsorbed GO@SnS_2 by FT-IR spectra (Figure. 3.2. 6a). The characteristics peak of GO for C=O, C=C, carboxy C-O, epoxy C-O, C-O-C and O-H occurs at 1720, 1622, 1410, 1227, 1058, 856 and 3500 cm^{-1} respectively.[40] After incorporation of SnS_2 on GO, the shift of these peaks to lower

wavenumber occurs which indicates the weakening of C-O bond and binding of $Sn^{(IV)}$. The structural O-H peak diminishes and there is the appearance of two new peaks at 645 and 530 cm^{-1} corresponding to Sn–S asymmetric stretching[41] and Sn–O asymmetric stretching.[40]

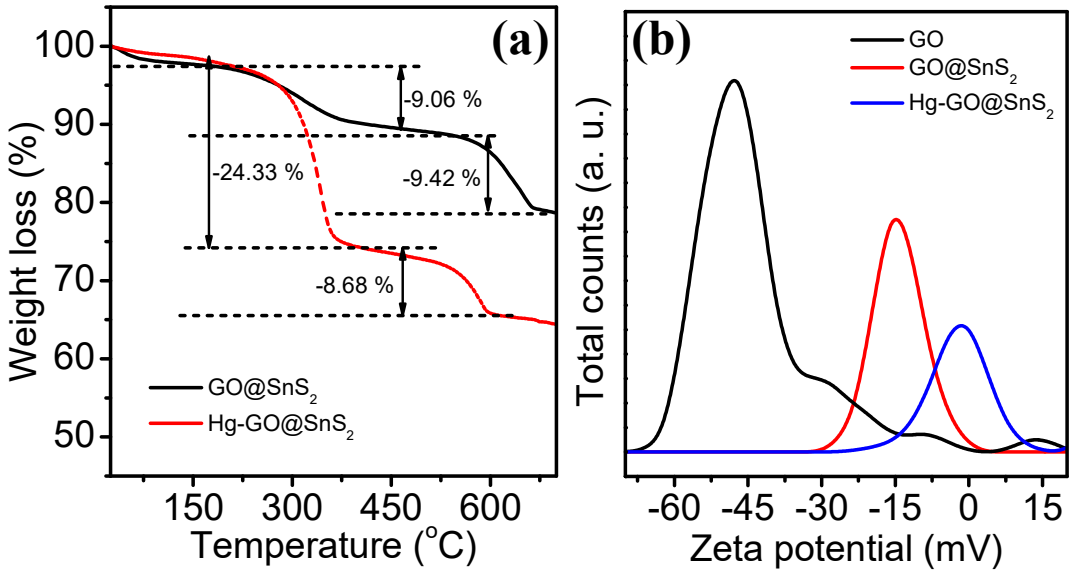

Figure. 3.2.5. *(a) TGA of GO@SnS_2 and Hg adsorbed composite and (b) zeta potential of GO, GO@SnS_2 and Hg adsorbed GO@SnS_2.*

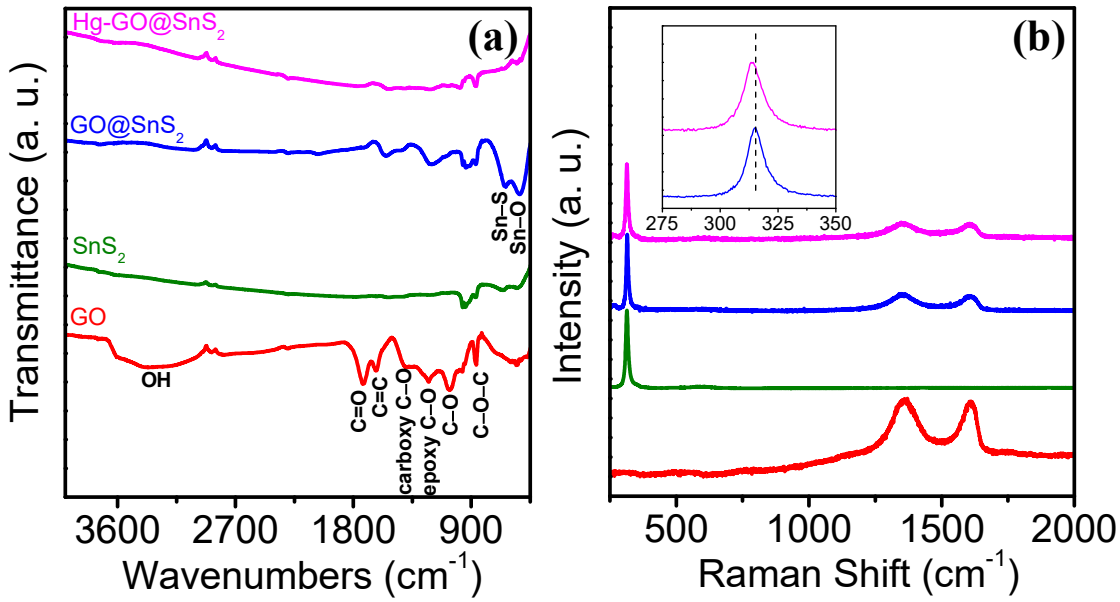

Figure. 3.2.6. *(a) FT-IR and (b) Raman spectra of GO, SnS_2, GO@SnS_2 and Hg-GO@SnS_2.*

Further, Raman spectroscopy was performed on GO, GO@SnS_2 and $Hg^{(II)}$ adsorbed GO@SnS_2 (Figure. 3.2. 6b). The characteristic peak of GO at 1362 and 1609 cm^{-1} corresponds to the graphitic-G band and the D band. The intensity ratio of the D-band to G-band of GO (I_D/I_G) for GO@SnS_2 and GO are 1.04 and 0.97 respectively, which indicates an electronic interaction between GO and SnS_2 nanoparticles.[40, 42] The attachment of SnS_2 is confirmed by the sharp A_{1g} mode at ~315.4 cm^{-1} in GO@SnS_2. The slight blue shift by 2 cm^{-1} in $Hg^{(II)}$ adsorbed GO@SnS_2 spectra indicates the binding of $Hg^{(II)}$.

3.2.3.2. Adsorption experiments. To investigate the capacity of GO@SnS_2 for $Hg^{(II)}$ uptake, adsorption isotherm experiments were carried out using the batch method. Figure. 3.2.7 shows experimental $Hg^{(II)}$ adsorption isotherms data for GO@SnS_2 and controlled GO and SnS_2. The observed experimental data were best fitted using Langmuir isotherm model, which is suitable for heterogeneous surfaces.

Langmuir isotherm:

$$q = q_m \frac{(bC_e)}{1+(bC_e)} \qquad \text{Eq.3.2.3.}$$

where q (mg/g) is the amount of $Hg^{(II)}$ adsorbed at equilibrium concentration, q_m is the maximum $Hg^{(II)}$ adsorption capacity, b (L/ mg) is the Langmuir constant related to interaction energy of $Hg^{(II)}$ and material; and C_e (ppm) is the equilibrium concentration. The equilibrium adsorption results were best fitted with Langmuir isotherm with a good agreement of $R^2 \geq 0.98$ and the adsorption constants are listed in Table 3.2.3.

Table 3.2.3. *Adsorption parameters obtained by fitting the isotherm Langmuir model.*

Material	q_m (mg/g)	b	R^2
SnS_2	185.83 ± 2.76	0.100	0.991
GO	255.10 ± 3.07	0.035	0.993
GO@SnS_2	342.02 ± 8.02	0.045	0.980

The q_m values for $Hg^{(II)}$ adsorption are 185.83 ± 2.76, 255 ± 3.07 and 342.02 ± 8.02 mg/g for SnS_2, GO and GO@SnS_2 respectively, indicating favorable adsorption of $Hg^{(II)}$ on GO@SnS_2. The highly oxidized groups on GO provide hydrophilic surface structure, facilitates adsorption and is responsible for the high capacity in aqueous solutions. These values are higher than most of the GO-based materials.[43-46]

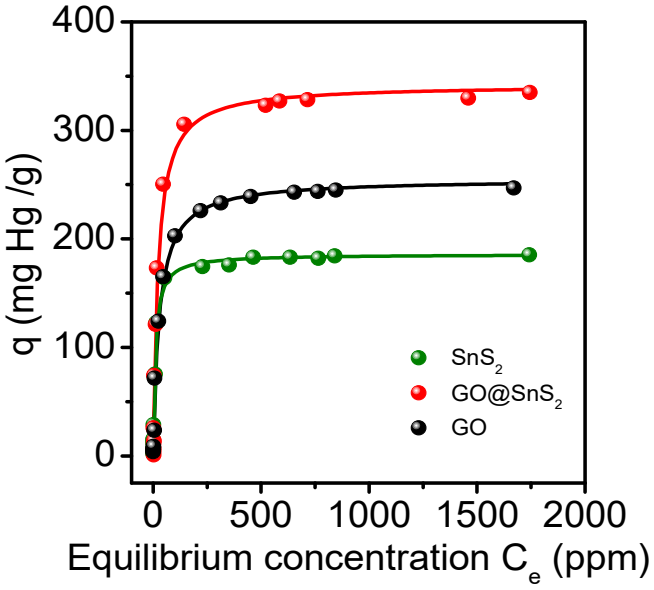

Figure. 3.2.7. *Adsorption isotherms of $Hg^{(II)}$ on SnS_2, GO and GO@SnS_2 (solid line corresponds to Langmuir fitting).*

The considerable increase in capacity for GO@SnS_2 arises due to synergistic adsorption of Hg(II) on GO as well as on SnS_2 present in the composite. Electrostatic attraction and chemical absorption play an essential role in improving the adsorption performance of an adsorbent. These two factors are regulated by the nature and concentration of the surface functional groups present on the material. Here, two adsorption processes are responsible for the removal of $Hg^{(II)}$ by GO@SnS_2 composite: interaction between $Hg^{(II)}$ and –COOH[15] of GO and the soft Lewis acid-base chemistry between S^{2-} of SnS_2 and $Hg^{(II)}$.

(1) Electrostatic attraction: $Hg^{(II)}$ replaces with $H^{(I)}$ in –COOH and binds with –COO- groups on GO surface.

$GO - COOH + Hg^{(II)} \rightarrow GO–COO^{-} - Hg^{(II)} + H^{(I)}$

$(GO - COOH)_2 + Hg^{(II)} \rightarrow (GO–COO^{-})_2 – Hg^{(II)} + 2H^{(I)}$

(2) Chemical absorption: In the composite, terminal S^{2-} in SnS_2 acts as soft Lewis base and $Hg^{(II)}$ acts as soft Lewis acid to form covalent interactions.
GO-O-$Sn^{(IV)}$-$(S^{2-})_2$ + $Hg^{(II)}$ → GO-O-Sn^{4+}-$(S^{2-})_2$ — $Hg^{(II)}$

Table 3.2.4. *Summary of the low ppb level removal of $Hg^{(II)}$ using GO@SnS_2 composite.*

Initial concentration (ppb)	Final concentration (ppb)	% Removed	q (mg/g)	K_d (mL/g)
0.268	0.112	58.2	0.15	1.38 X 10^3
0.406	0.078	80.9	0.32	4.12 X 10^3
1.283	0.060	95.3	1.21	2.02 X 10^4
28.620	6.508	77.7	21.68	3.33 X 10^3
37.660	5.076	86.5	32.26	6.36 X 10^3
95.100	9.600	89.9	84.65	8.82 X 10^3
675.900	7.931	98.8	654.87	8.26 X 10^4
4889.000	5.568	99.9	4835.08	8.68 X 10^5

In addition to the high capacity of GO@SnS_2, it can even remove $Hg^{(II)}$ from low contaminated water ($Hg^{(II)}$ initial concentration of 0.268 ppb) up to 0.112 ppb, which is far below the acceptable drinking water limit of 2 ppb, given by USA-EPA.[36] The results of low ppb removal of $Hg^{(II)}$ are summarised in Table 3.2.4. K_d values obtained are in the range of 10^3 to 10^5 which indicates that $Hg^{(II)}$ binds efficiently to the material (see Table 3.2.4). We have achieved a maximum K_d value of 8.68 X 10^5 mL/g. We have performed the Sn-leaching experiment on GO@SnS_2 during $Hg^{(II)}$ adsorption and found negligible leaching (Table 3.2.5).

Further, $Hg^{(II)}$ capture efficiency of GO@SnS_2 from aqueous solutions has been inspected by exploring adsorption kinetics of GO@SnS_2 (100.0 mg) in ~100 ppm solution (pH ~ 6.5) of $Hg(NO_3)_2$ (100.0 mL). Within 15 min, the concentration decreases from 92.62 ppm to 40.44 pm.

Table 3.2.5*. Sn^{2+} leaching study at different time for SnS_2 and GO@SnS_2 during Hg removal.*

Time (min)	Sn Leaching in mmole/L	
	SnS_2	GO@SnS_2
5	4.6 X 10^{-3}	7.6 X 10^{-5}
50	8.5 X 10^{-3}	12.7 X 10^{-5}
200	8.8 X 10^{-3}	27.9 X 10^{-5}

Figure. 3.2.8 shows the fast kinetics for GO@SnS_2, which can remove up to ~95% $Hg^{(II)}$ within 210 min. To understand the kinetics of adsorption, the experimental data were fitted with two kinetics model: pseudo-second-order and pseudo-first-order model using the following equation:

$$\ln(q_e - q_t) = \ln q_e - k_1 t \quad \text{Eq. 3.2.4}$$

$$\frac{t}{q_t} = \frac{1}{k_2 q_e^2} + \frac{t}{q_e} \quad \text{Eq. 3.2.5}$$

where q_e (mg/g) is the amount of $Hg^{(II)}$ adsorbed per unit mass of GO@SnS_2 at equilibrium, q_t is Hg (II) ions adsorbed at time t, k_1,(min^{-1}) and k_2 (g $mg^{-1}min^{-1}$) are the rate constants of pseudo-first-order and pseudo-second-order adsorption kinetics model. Plotting $\ln(q_e\text{-}q_t)$ vs. t and t/q_t vs. t by using Eq. (3.2.4) and (3.2.5), respectively gives the value of k_1 and k_2.

Table 3.2.6*. Kinetic parameters for adsorption of $Hg^{(II)}$ by GO@SnS_2*

Order	R^2	q_e (exp) (mg/g)	q_e (cal) (mg/g)	k (g/mg/min)
Pseudo-2nd	0.999	8.18	8.54	10^{-2}
Pseudo-1nd	0.953	8.18	5.21	2.18 X 10^{-2}

As seen from, Table 3.2. 6, pseudo-second-order model is suitable for $Hg^{(II)}$ adsorption since the value of R^2 is 0.999. k_2 is of the order of 10^{-2}, indicating fast kinetics due to the availability of favorable sites for $Hg^{(II)}$ adsorption. In order to understand the individual role of GO and SnS_2 in Hg capture, we have performed comparative Hg

sorption kinetics for GO, SnS_2 and GO@SnS_2 (Figure 3.2.9) GO@SnS_2 removes Hg at slightly faster rate compared to others which is mainly due to the influence of GO, while the selectivity to Hg arises due to SnS_2 (discussed later).

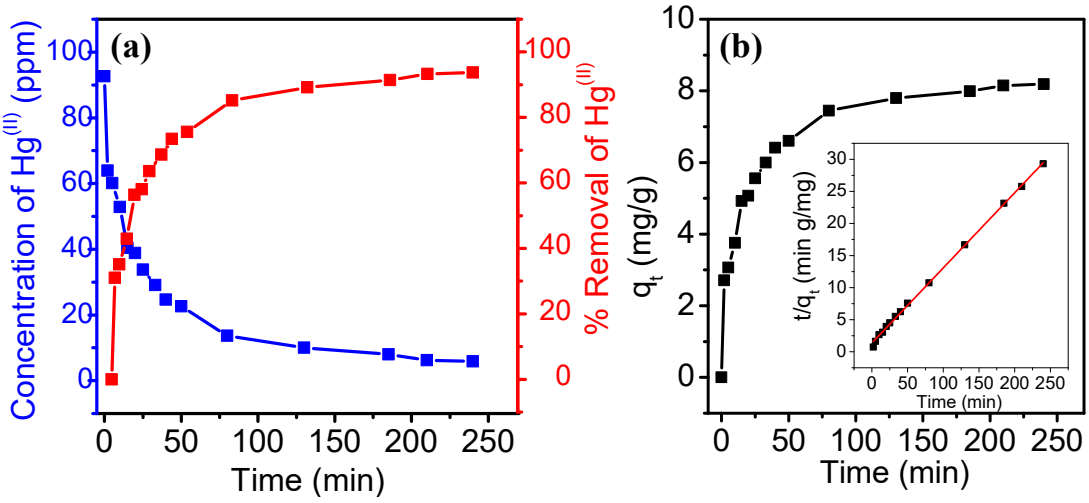

Figure. 3.2. 8. $Hg^{(II)}$ adsorption kinetics curves for GO@SnS_2: (a) concentration and removal % of $Hg^{(II)}$ as a function of time and (b) adsorption capacity (q_t) with contact time; (inset) pseudo-second-order kinetics plot for $Hg^{(II)}$ adsorption.

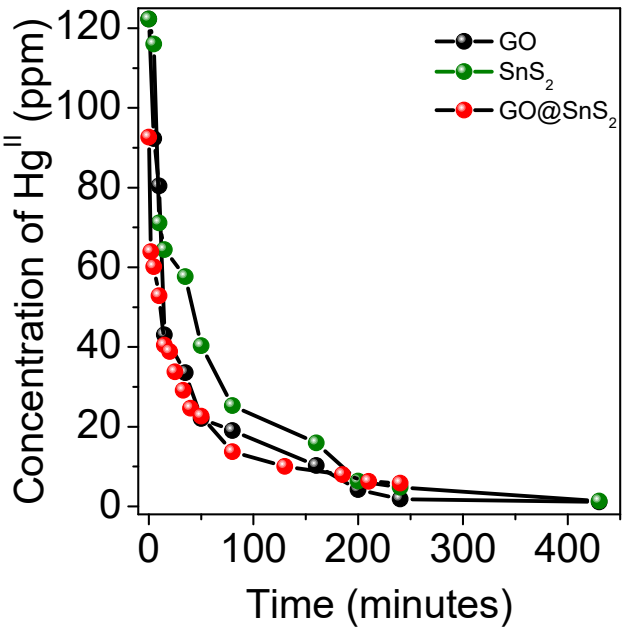

Figure. 3.2.9. Comparison of uptake of Hg with time by GO, SnS_2 and GO@SnS_2.

3.2.3.3. pH Based Ion Exchange Experiments. pH plays a vital role in the adsorption of adsorbents onto GO.[47] Interestingly, GO@SnS_2 is stable in pH ranging from 0.66 to 11 (Figure. 3.2. 10a). The $Hg^{(II)}$ removal grafts (SnS_2) are anchored to the backbone of GO and thus prevent the leaching of binding sites in extreme pH range. To study the effect of pH on adsorption of $Hg^{(II)}$ on GO@SnS_2, we have tested a series of aqueous solutions of $Hg^{(II)}$ (80-100 ppm) with pH ranging from 0.46 to 13.9.

Table 3.2.7. *Selected data for adsorption studies in different pH.*

pH	Initial concentration (ppm)	Final concentration (ppm)	% Removed	q (mg/g)	K_d (mL/g)
0.46	89.43	3.52	96.1	85.1	2.42 X 10^4
1.04	85.04	3.038	96.4	81.2	2.67 X 10^4
2.38	70.23	1.217	98.3	68.3	5.61 X 10^4
2.7	80.64	1.545	98.1	79.1	5.12 X 10^4
3.82	84.76	2.176	97.4	83.4	3.83 X 10^4
5.05	91.78	1.195	98.7	88.8	7.43 X 10^4
6.6	85.37	3.937	95.4	79.8	2.03 X 10^4
7.3	87.18	3.24	96.3	83.9	2.59 X 10^4
8.6	93.02	0.01	96.8	89.1	2.98 X 10^4
10.06	92.57	1.114	98.8	89.7	8.05 X 10^4
11.24	104.4	30.71	70.6	72.2	2.35 X 10^3
12.41	95.5	35.59	62.7	59.3	1.67 X 10^3
13.96	161.9	62.84	61.2	99.1	1.58 X 10^3

Figure. 3.2. 10b shows ~98 % removal of $Hg^{(II)}$ in the pH range 1 to 10 (Table 3.2.7), which is remarkable. Generally, at low pH, materials like Fe_3O_4-GS,[48] PAGF,[49] MGO,[44] $PAN_{AP}F$,[50] $CoFe_2O_4$-rGO[46], etc suffer from poor removal efficiency due to surplus $H^{(I)}$, which compete with $Hg^{(II)}$ binding O^- sites, but here this possibility is ruled out as soft Lewis acid $Hg^{(II)}$ binds with soft Lewis base S^{2-}. However, there are thiol functionalized adsorbents which can remove $Hg^{(II)}$ efficiently but have high tendency to oxidize to disulfide under ambient conditions, leading to loss of capacity.[23,24] In contrast,

$GO@SnS_2$ composite is exceptionally stable in air as well as in acidic and basic aqueous medium. At pH >10, although the material removes $Hg^{(II)}$ reasonably but not efficiently as the material starts degrading.

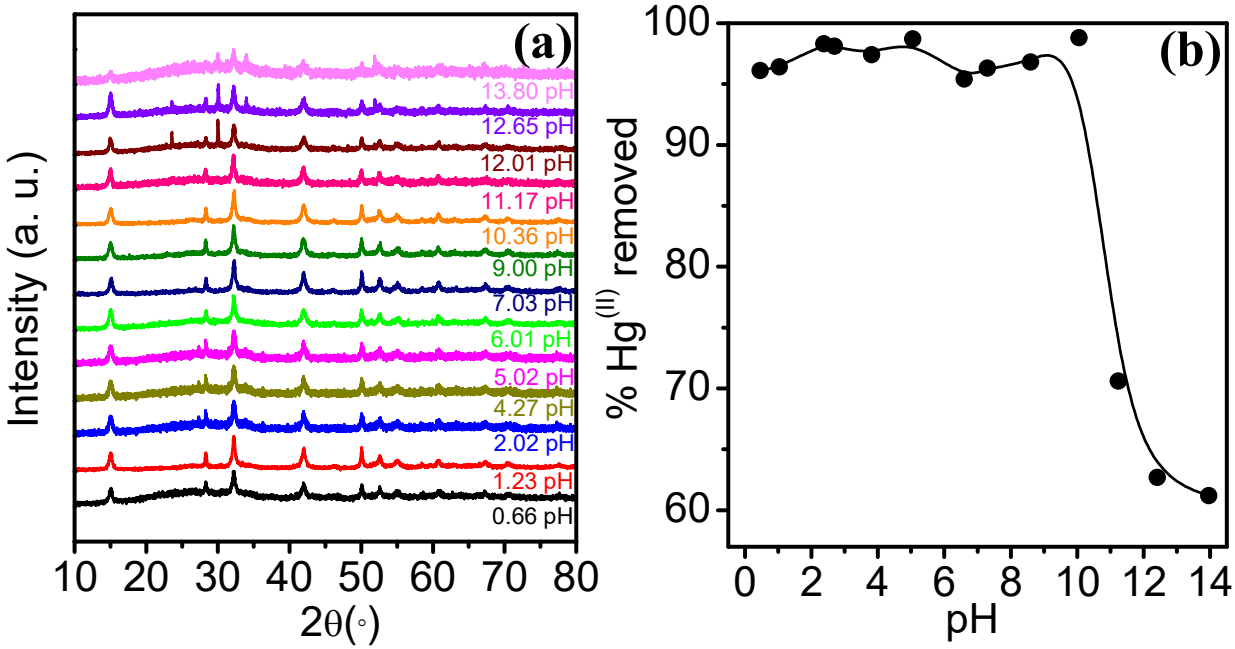

Figure. 3.2.10. *(a) Stability of $GO@SnS_2$ with respect to pH and (b) removal of $Hg^{(II)}$ in different pH.*

3.2.3.4. Selectivity of $GO@SnS_2$ for $Hg^{(II)}$. It is necessary for a material to selectively capture $Hg^{(II)}$ from water for practical use. The selectivity of $Hg^{(II)}$ adsorption towards $GO@SnS_2$ was studied by taking 10 mL of mixture of cations ($Hg^{(II)}$, $Na^{(I)}$, $K^{(I)}$, $Cs^{(I)}$, $Rb^{(I)}$, $Ca^{(II)}$ and $Mg^{(II)}$) and treating it with 10 mg of adsorbent. Table 3.2.8 depicts the initial and final concentration of competitive ions, and it is clear that $GO@SnS_2$ selectively removes $Hg^{(II)}$.

The degree of selectivity for $Hg^{(II)}$ in the presence of competing metal ions is evaluated by separation factor (α^{Hg})[9,51,52] which is determined by:

$$\alpha_M^{Hg} = \frac{K_d^{Hg}}{K_d^M}$$

The separation factor is extremely high, of the order 10^2, indicating high selectivity of $Hg^{(II)}$ towards $GO@SnS_2$ in the presence of co-existing cations (Figure. 3.2. 11a). To further check the selectivity, we performed adsorption study in presence of 20 ppm solution of $Hg^{(II)}$, $Co^{(II)}$, $Cu^{(II)}$, $Ni^{(II)}$, $Zn^{(II)}$, $Pb^{(II)}$, $Cd^{(II)}$, $Mn^{(II)}$, $Fe^{(III)}$ and $As^{(III)}$.

$GO@SnS_2$ can remove 99.1% of $Hg^{(II)}$ selectively from the mixture of the elements (Table 3.2.9). Figure. 3.2.11b shows extremely high α^{Hg} of order 10^4. We have studied the comparative $Hg^{(II)}$ selectivity between GO, SnS_2 and $GO@SnS_2$, which indicates that the separation factors for $GO@SnS_2$ are significantly higher than that of individual GO and SnS_2 (Figure. 3.2.12).

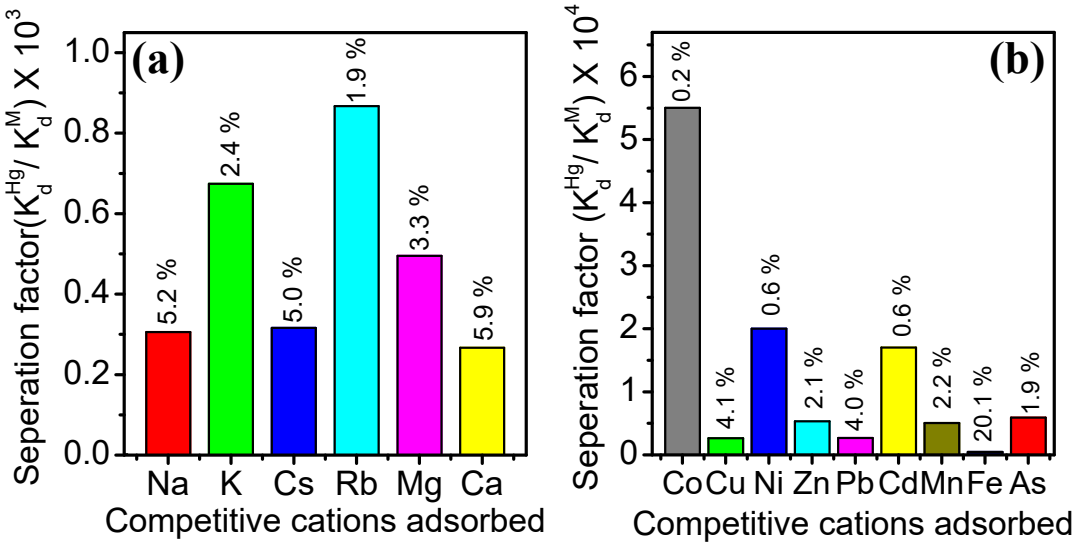

Figure. 3.2. 11. *(a)-(b) Bar plots of separation factor of different competitive ions and removal % of cations in the mixture containing ~20 ppm of elements.*

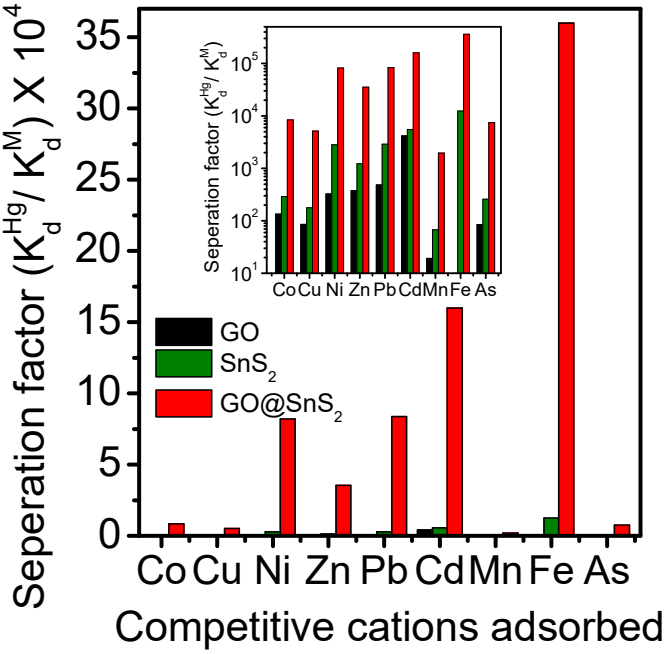

Figure. 3.2.12. *Comparison of separation factors of different competitive ions with GO, SnS_2 and $GO@SnS_2$. Inset shows the expanded view in log scale.*

Table 3.2.8. Summary of the competitive adsorption data of GO@SnS_2 composite.

Exchange cations	Initial concentration (ppm)	Final concentration (ppm)	% Removal	K_d^M (mL/g)	Separation factor, α^{Hg} (K_d^{Hg}/ K_d^M)
$Hg^{(I)}$	17.08	0.96	94.4	1.68 X 10^4	1
$Na^{(I)}$	27.47	26.04	5.2	54.9	3.05 X 10^2
$K^{(I)}$	21.39	20.87	2.4	24.91	6.73 X 10^2
$Cs^{(I)}$	22.41	21.28	5.0	53.1	3.16 X 10^2
$Rb^{(I)}$	33.18	32.55	1.9	19.35	8.67 X 10^2
$Mg^{(II)}$	19.21	18.58	3.3	33.91	4.95 X 10^2
$Ca^{(II)}$	20.43	19.22	5.9	62.95	2.66 X 10^2
m = 0.010 g, V = 10 mL, V:m = 1000 mL/g					

Table 3.2.9. Summary of the competitive adsorption $Hg^{(II)}$ using GO@SnS_2 composite in presence of $Co^{(II)}$, $Cu^{(II)}$, $Ni^{(II)}$, $Zn^{(II)}$, $Pb^{(II)}$, $Cd^{(II)}$, $Mn^{(II)}$, $Fe^{(III)}$ and $As^{(III)}$.

Exchange cations	Initial concentration (ppm)	Final concentration (ppm)	% Removal	K_d^M (mL/g)	Separation factor, α^{Hg} (K_d^{Hg}/ K_d^M)
$Hg^{(II)}$	19.58	0.173	99.1	5.58 X 10^4	1
$Co^{(II)}$	19.66	19.62	0.2	1.01	5.5 X 10^4
$Cu^{(II)}$	19.65	18.85	4.1	21.11	2.6 X 10^3
$Ni^{(II)}$	19.72	19.61	0.6	2.79	2.0 X 10^4
$Zn^{(II)}$	20.35	19.93	2.1	10.48	5.3 X 10^3
$Pb^{(II)}$	19.86	19.06	4.0	20.88	2.7 X 10^3
$Cd^{(II)}$	19.85	19.72	0.6	3.27	1.7 X 10^4
$Mn^{(II)}$	20.32	19.88	2.2	11.01	5.0 X 10^3
$Fe^{(III)}$	21.29	17.02	20.1	124.81	4.5 X 10^2
$As^{(III)}$	19.79	19.42	1.9	9.48	5.9 X 10^3
m = 0.010 g, V = 10 mL, V:m = 1000 mL/g					

Further, SnS_2 demonstrates better selectivity compared to GO. Thus, we believe the remarkable selectivity towards $Hg^{(II)}$ for GO@SnS_2 is due to mainly SnS_2 via soft Lewis acid-base interactions. When SnS_2 nanoparticles are decorated on GO surface the active S^{2-} increases, which enhanced the selectivity synergistically.

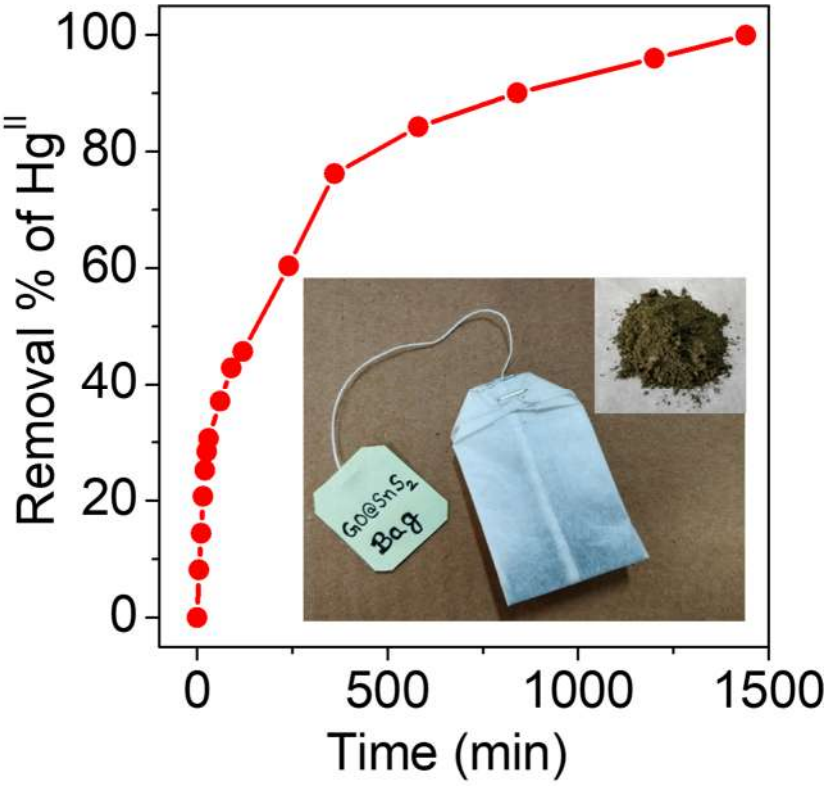

Figure. 3.2.13. *Removal of $Hg^{(II)}$ using a GO@SnS_2 tea bag from 100 mL solution containing ~84.5 ppm of $Hg^{(II)}$.*

With this incredibly high selectivity, pH stability and low ppb level removal of $Hg^{(II)}$, for practical use, we designed a tea bag filled with GO@SnS_2 powder (inset in Figure. 3.2. 13). Figure. 3.2. 12 shows that the concentration of Hg(II) decreases 50 % within 120 minutes. This tea bag can be used to capture $Hg^{(II)}$ conveniently from the effluent waste before it goes for further treatment.

3.2.4. Conclusions

In summary, GO@SnS_2 exhibits highly selective and efficient removal of $Hg^{(II)}$ from water with a capacity of 342.02 ± 8.02 mg/g. It can remove $Hg^{(II)}$ even from 0.3 ppb level. The highly accessible $Hg^{(II)}$ binding sites, S^{2-} from SnS_2 and COO- on the

surface of GO plays a synergistic role in the effective $Hg^{(II)}$ capture. It can sequester 99% $Hg^{(II)}$ selectively even in presence of $Na^{(I)}$, $K^{(I)}$, $Cs^{(I)}$, $Rb^{(I)}$, $Mg^{(II)}$, $Co^{(II)}$, $Cu^{(II)}$, $Ni^{(II)}$, $Zn^{(II)}$, $Pb^{(II)}$, $Cd^{(II)}$, $Mn^{(II)}$, $Fe^{(III)}$ and $As^{(III)}$ with extremely high separation factor. Although the GO shows higher $Hg^{(II)}$ adsorption capacity and slightly faster kinetics of $Hg^{(II)}$ sorption compared to SnS_2 alone, the selectivity of Hg removal is mainly enhanced due to SnS_2 via soft Lewis acid-base interactions, which demonstrates the synergistic property of GO@SnS_2. Moreover, this material can be used in pH range from 0.4 to 10 efficiently. The fundamental mechanism behind the synergistic $Hg^{(II)}$ on GO@SnS_2 is two-fold: interaction between $Hg^{(II)}$ and –COOH of GO and the soft Lewis acid-base chemistry between S^{2-} of SnS_2 and $Hg^{(II)}$. Further, the tea bags consisting GO@SnS_2 powder can be used for the application in removal of heavy metals from the effluent discharge conveniently and economically.

3.2.5. References

[1] M. A. Shannon, P. W. Bohn, M. Elimelech, J. G. Georgiadis, B. J. Marinas, A. M. Mayes, *Nature* **2008**, 452, 301.

[2] R. P. Schwarzenbach, B. I. Escher, K. Fenner, T. B. Hofstetter, C. A. Johnson, U. Von Gunten, B. Wehrli, *Science* **2016**, 313, 1072.

[3] Ten chemicals of major public health concern, http://www.who.int/ipcs/assessment/public_health/chemicals_phc/en/.

[4] M. A. Barakat, *Arab. J. Chem.* **2011**, 4, 361.

[5] D. D. Bailey, S.E., Olin, T.J., Bricka, R.M. Adrian, *Wat. Res.* **1999**, 33, 2469.

[6] A. Azimi, A. Azari, M. Rezakazemi, M. Ansarpour, *Chem. Bio. Eng. Rev.* **2017**, 4, 37.

[7] *Heavy Metal Waste Regulation: Which Substances Make Up the RCRA 8 Metals?*, https://www.hazardouswasteexperts.com/heavy-metal-waste-regulation-which-substances-make-up-the-rcra-8-metals/.

[8] A. Benhammou, A. Yaacoubi, L. Nibou, B. Tanouti, *J. Colloid Interface Sci.* **2005**, 282, 320.

[9] Z. Chen, A. Jawad, Z. Liao, Z. Zhou, A. Khan, T. Wang, J. Ifthikar, A. Shahzad, Z. Chen, *ACS Appl. Mater. Interfaces* **2017**, 9, 28451.

[10] I. L. Lagadic, M. K. Mitchell, B. D. Payne, *Environ. Sci. Technol.* **2001,** 35, 984.

[11] R. Celis, M. Carmen Hermosín , J. Cornejo, *Environ. Sci. Technol.* **2000**, 34, 4593.

[12] A. Sayari, S. Hamoudi, Y. Yang, *Chem. Mater.* **2005**, 17, 212.

[13] M. Jaber, J. Miehé-Brendlé, L. Michelin, L. Delmotte, *Chem. Mater.* **2005**, 17, 5275.

[14] M. J. Zamzow, B. R. Eichbaum, K. R. Sandgren, D. E. Shanks, *Separation Science and Technology* **1990**, 25, 1555.

[15] S. Wu, L. Kong, J. Liu, *Res. Chem. Intermed.* **2016**, 42, 4513.

[16] A. Gopalakrishnan, R. Krishnan, S. Thangavel, G. Venugopal, S. J. Kim, *J. Ind. Eng. Chem.* **2015**, 30, 14.

[17] B. Li, Y. Zhang, D. Ma, Z. Shi, S. Ma, *Nat. Commun.* **2014**, 5, 1.

[18] K. K. Yee, N. Reimer, J. Liu, S. Y. Cheng, S. M. Yiu, J. Weber, N. Stock, Z. Xu, *J. Am. Chem. Soc.* **2013**, 135, 7795.

[19] Q. Sun, B. Aguila, J. Perman, L. D. Earl, C. W. Abney, Y. Cheng, H. Wei, N.

Nguyen, L. Wojtas, S. Ma, *J. Am. Chem. Soc.* **2017**, 139, 2786.

[20] L. Merí-Bofí, S. Royuela, F. Zamora, L. Ruiz-Gonzales, J. Segura, R. Muñoz-Olivas, M. J. Mancheño, *J. Mater. Chem. A* **2017**, 17973.

[21] A. J. Tchinda, E. Ngameni, I. T. Kenfack , A. Walcarius, *Chem. Mater.* **2009**, 21, 4111.

[22] N. Huang, L. Zhai, H. Xu, D. Jiang, *J. Am. Chem. Soc.* **2017**, 139, 2428.

[23] J. S. Lee, S. Gomez-Salazar, L. L. Tavlarides, *React. Funct. Polym.* **2001**, 49, 159.

[24] A. M. Nam, S. Gomez-Salazar, L. L. Tavlarides, *Ind. Eng. Chem. Res.* **2003**, 42, 1955.

[25] M. J. Manos , M. G. Kanatzidis, *Chem. - A Eur. J.* **2009**, 15, 4779.

[26] Z. H. Fard, C. D. Malliakas, J. L. Mertz , M. G. Kanatzidis, *Chem. Mater.* **2015**, 27, 1925.

[27] E. Rathore, P. Pal, K. Biswas, *J. Phys. Chem. C* **2017**, 121, 7959.

[28] E. Rathore, P. Pal, K. Biswas, *Chem. - A Eur. J.* **2017**, 23, 11085.

[29] M. J. Manos, V. G. Petkov, M. G. Kanatzidis, *Adv. Funct. Mater.* **2009**, 19, 1087.

[30] S. Ma, Q. Chen, H. Li, P. Wang, S. M. Islam, Q. Gu, X. Yang, M. G. Kanatzidis, *J. Mater. Chem. A* **2014**, 2, 10280.

[31] L. Ma, Q. Wang, S. M. Islam, Y. Liu, S. Ma, M. G. Kanatzidis, *J. Am. Chem. Soc.* **2016**, 138, 2858.

[32] Z. Hassanzadeh Fard, S. M. Islam, M. G. Kanatzidis, *Chem. Mater.* **2015**, 27, 6189.

[33] Y. Oh, S. Bag, C. D. Malliakas, M. G. Kanatzidis, *Chem. Mater.* **2011**, 23, 2447.

[34] L. Zhi, W. Zuo, F. Chen, B. Wang, *ACS Sustain. Chem. Eng.* **2016**, 4, 3398.

[35] I. R. Pala, S. L. Brock, *ACS Appl. Mater. Interfaces* **2012**, 4, 2160.

[36] *National Primary Drinking Water Regulations*, https://www.epa.gov/ground-water-and-drinking-water/national-primary-drinking-water-regulations#Inorganic.

[37] W. S. Hummers , R. E. Offeman, *J. Am. Chem. Soc.***1958**, 80, 1339.

[38] J. Yin, H. Cao, Z. Zhou, J. Zhang, M. Qu, *J. Mater. Chem.* **2012**, 22, 23963.

[39] N. Du, X. Wu, C. Zhai, H. Zhang, D. Yang, *J. Alloys Compd.* **2013**, 580, 457.

[40] A. Kumar, L. Rout, R. S. Dhaka, S. L. Samal, P. Dash, *Rsc Adv.* **2015**, 5, 39193.

[41] G. Kiruthigaa, C. Manoharan, C. Raju, J. Jayabharathi, S. Dhanapandian, *Spectrochim. Acta - Part A Mol. Biomol. Spectrosc.* **2014**, 129, 415.

[42] S. Li, W. Xie, S. Wang, X. Jiang, S. Peng, D. He, *J. Mater. Chem. A* **2014**, 2, 17139.

[43] P. N. Diagboya, B. I. Olu-Owolabi, K. O. Adebowale, *RSC Adv.* **2015**, 5, 2536.

[44] Y. Guo, J. Deng, J. Zhu, X. Zhou, R. Bai, *RSC Adv.* **2016**, 6, 82523.

[45] J. Bao, Y. Fu, Z. Bao, *Nanoscale Res. Lett.* **2013**, 8, 1.

[46] Y. Zhang, L. Yan, W. Xu, X. Guo, L. Cui, L. Gao, Q. Wei, B. Du, *J. Mol. Liq.* **2014**, 191, 177.

[47] C. J. Madadrang, H. Y. Kim, G. Gao, N. Wang, J. Zhu, H. Feng, M. Gorring, M. L. Kasner, S. Hou, *ACS Appl. Mater. Interfaces* **2012**, 4, 1186.

[48] X. Guo, B. Du, Q. Wei, J. Yang, L. Hu, L. Yan, W. Xu, *J. Hazard. Mater.* **2014**, 278, 211.

[49] B. Tan, H. Zhao, Y. Zhang, X. Quan, Z. He, W. Zheng, B. Shi, *J. Colloid Interface Sci.*, **2017**, 512, 853.

[50] G. Xu, L. Wang, Y. Xie, M. Tao, W. Zhang, *J. Hazard. Mater.*, **2018**, 344, 679.

[51] D. Sarma, S. M. Islam, K. S. Subrahmanyam, M. G. Kanatzidis, *J. Mater. Chem. A* **2016**, 4, 16597.

[52] J. L. Mertz, Z. H. Fard, C. D. Malliakas, M. J. Manos, M. G. Kanatzidis, *Chem. Mater.* **2013**, 25, 2116.

Chapter 3.3

Nature-Inspired Coral like Layered Double Hydroxide for Selective ppb Level Capture of Cr(VI) from Contaminated Water†

†*Paper based on this is under review as* ***E. Rathore****, K. Maji, K. Biswas xxx* ***2021****, xx, xx.*

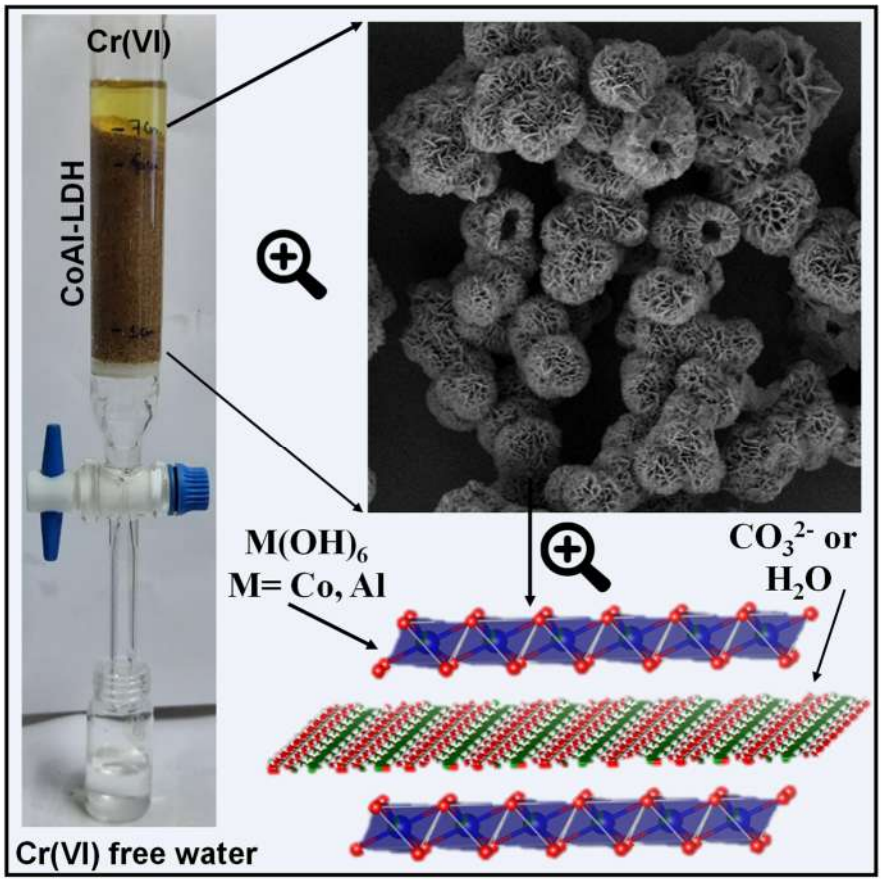
Cr(VI)
CoAl-LDH
M(OH)6
M= Co, Al
CO3 2- or
H2O
Cr(VI) free water

Chapter 3.3

Nature-Inspired Coral like Layered Double Hydroxide for Selective ppb Level Capture of Cr(VI) from Contaminated Water †

Summary: *Rapid industrialization has led to the release of hexavalent chromium, a "Class A" human carcinogen, mutagen, teratogen in the biological systems. Current adsorbents like layered double hydroxides (LDHs), anionic-exchange resins, metal-organic frameworks (MOFs), can remove harmful heavy metal oxyanions from water but are not stable in broad pH range, suffers from selectivity, and cannot capture them from trace values below the tolerance limits given by USA-EPA (100 ppb) and WHO(50 ppb). Herein, we have designed nature-inspired coral-like three-dimensional hierarchical structures of* $[Co_{0.79}Al_{0.21}(OH)_2(CO_3)_{0.11}] \cdot mH_2O$ *(CoAl-LDH) that sets a new benchmark for sequestering oxyanions of hexavalent chromium. CoAl-LDH shows a broad pH working range (1.93-12.22), high selectivity towards highly saturated water samples containing monovalent anions (*Cl^-*,* F^-*,* Br^-*,* NO_3^-*) and divalent (*SO_4^{2-}*) anions with fast kinetics (reaches equilibrium in a minute), high capacity (93.4 ± 7.8 mg* g^{-1}*), and high distribution coefficient of 1.09 x* 10^6 mLg^{-1}*. Unlike other materials, it can reduce Cr(VI) concentration up to 0.012 ppb. This high selectivity for Cr(VI) is linked to the weak bonding interaction between* $Cr_2O_7^{2-}$ *and brucite-like layers as revealed from thermogravimetric and infra-red spectroscopy. With these countless features coupled with low-cost and environmentally friendly nature, we have also designed an anion-exchange column that can remove > 99 % Cr(VI) with just 1 % wt. of CoAl-LDH and 99% wt. sand and is a promising candidate for the removal of Cr(VI) from industrial effluents.*

† *Paper based on this is under review as* ***E. Rathore****, K. Maji, K. Biswas xxx* ***2021****, xx, xx.*

3.3.1. Introduction

Excessive heavy metal discharge in the water bodies is a serious worldwide problem that causes health and environmental hazards.[1] Chromium is a highly toxic element in water that generates toxicity in plants and other life forms as it bioaccumulates in the body by entering into food chains.[2,3] Cr(VI) is more soluble, toxic, and listed as a "Class A" human carcinogen, mutagen, teratogen in the biological systems as compared to other less soluble Cr(III).[4–6] Depending on the pH of water, hexavalent chromium exists in various oxoanionic species like dichromate ($Cr_2O_7^{2-}$), hydrogen chromate ($HCrO_4^-$), chromate (CrO_4^{2-}), and hence it is difficult to remove from water.[7] Cr(VI) is released in the environment from industrial anthropogenic processes in metal plating, leather tanneries, dyes, cement, steel, textile, wood-preserving industries, etc.[1,8] Therefore, the efficient and economical eradication of chromium from the industrial wastewater and sewage before discharging it into the water streams has become an emergent issue.

Ion exchange and adsorption are robust technologies to sequester toxic water pollutants due to their low cost, simplicity for application, and high efficiency. Activated carbon,[9] cationic inorganic framework oxides,[5,7,10] hydroxides,[8] graphene composites,[4,11] zeolites,[12] functionalized magnetic nanoparticles[13,14], and resins[15,16] have shown effectiveness towards removing chromium but suffer from low-capacity, pH stability, selectivity, and low- ppb level removal ability. Recently, cation metal-organic frameworks (MOFs)[10,17–19], cationic polymeric network(CPN),[20] cationic covalent organic frameworks (COFs),[21,22] metal-organic resins (MORs)[23] have also been effective in capturing chromium but are expensive, also organic component causes poor thermal and chemical stability, sometimes gets oxidized by Cr(VI) causing safe-disposal issues as it can't be regenerated or reused and some suffer from cytotoxicity that limits their robustness for practical applications.[24,25]

On the contrary, layered double hydroxides (LDHs), two-dimensional nanostructured anionic clays have emerged as low-cost inorganic framework-based clay materials that facilitate the removal of toxic oxyanions.[26–28] LDHs have general formula, $[M^{a+}_{1-x}M^{b+}_{x}(OH)_2]^{q+}[A^{n-}_{q/n}]^{q-} \cdot mH_2O$, with $a = 1$ or 2, $b = 3$ or 4, $q = a+(b-a)x-2$, where M^{a+} and M^{b+}, A, x, and m are metal cations, interlayer anions with charge n, the molar ratio of $M^{a+}/(M^{a+}+M^{b+})$ and molar amount of interlayer water, respectively.[29] The

positively charged metal hydroxide layers, exchangeable anions like CO_3^{2-}, Cl^- or NO_3^- and water molecules present in the interlayer spaces or the surface help in absorption of oxyanion of Cr(VI) within the layers as well as on the surface of LDHs.[30] Recently, LDHs[27,31–33], calcinated LDHs,[27,34] and their composites with graphene oxide,[35,36] MOFs,[37] MoS_4,[38] polyacrylonitriles (PAN)[37] have been explored for Cr(VI) capture. Calcinated carbonate-containing LDHs have been shown to improve Cr(VI) adsorption but calcination requires a large amount of energy.[34] While NO_3^- and Cl^- as A^{n-} are better than calcined-LDHs but the release of NO_3^- causes environmental hazard[39] and Cl^- based LDH takes a long time to reach adsorption equilibrium.[34] Hence, it is necessary to develop low-cost high surface area materials for Cr(VI) sequestration which can remove Cr(VI) selectively from low ppb level, with high capacity, fast adsorption rate, and can work in a wide pH range.

Here in this chapter, we have synthesized nature-inspired coral-like three-dimensional hierarchical morphology of $[Co_{0.79}Al_{0.21}(OH)_{2(}CO_3)_{0.11}] \cdot mH_2O$ (CoAl-LDH) with higher structural orders compared with 2D hexagonal plates. CoAl-LDH contains carbonate (CO_3^{2-}) anions and interlayer water molecules that can easily be exchanged by oxyanions of Cr(VI) ($Cr_2O_7^{2-}$) species. Also, the positively charged layers of metal hydroxide layer facilitate the surface adsorption of $Cr_2O_7^{2-}$ on mesoporous CoAl-LDH. This material exhibits exceptional sequestering performance for Cr(VI) which is superior in terms of pH stability, regeneration-recycle ability, removing in both high (~500 ppm) and trace amounts (~5 ppb) of Cr (VI) with high selectivity from simulated contaminated samples. CoAl-LDH works in a broad 1.93-12.22 pH range, reduces Cr(VI) in water up to 0.012 ppb with a very high distribution coefficient of 1.09 x 10^6 mLg^{-1}, and shows rapid sorption kinetics where the equilibrium reaches within a minute. CoAl-LDH shows an extraordinary selectivity towards eliminating oxyanions of Cr(VI) even in the presence of a highly saturated concoction of monovalent anions (Cl^-, F^-, Br^-, NO_3^-) and divalent (SO_4^{2-}) anions. The exceptional adsorption properties of CoAl-LDH for Cr(VI) sequestration are linked to the weak bonding interaction between $Cr_2O_7^{2-}$ and brucite-like layers as revealed from thermogravimetric and infra-red spectroscopy. With these remarkable hexavalent chromium sorption properties, we designed an anion-exchange column with CoAl-LDH as a stationary phase. It can remove >99 % Cr(VI)

with just 1 % wt of CoAl-LDH in the column and is a promising candidate for a potential application.

3.3.2. Methods

3.3.2.1. Reagents. $Co(NO_3)_2 \cdot 6H_2O$ (Sigma- Aldrich, 99.999% trace metals basis), $Al(NO_3)_3 \cdot 9H_2O$ (Sigma- Aldrich, 99.997% trace metals basis), urea (Sigma- Aldrich, ACS reagent, 99.0-100.5%), and NH_4F (Sigma- Aldrich, ≥99.99% trace metals basis) were used for synthesis without further purification.

3.3.2.2 Synthesis. 3D coral-like CoAl-LDH hollow spheres were synthesized by solvothermal technique. Typically, 9 mmol of $Co(NO_3)_2 \cdot 6H_2O$, 3mmol of $Al(NO_3)_3 \cdot 9H_2O$, 21 mmol of urea and 100 mg of NH_4F were dissolved in 30 mL of methanol, and the mixture was stirred for 2 h. Then, the solution was transferred into a 50 mL Teflon-lined autoclave and was kept at 150 °C for 10 h. Finally, the product was collected by washing with deionized water and ethanol.

3.3.2.3. Characterizations. Powder X-ray diffraction (PXRD) patterns of CoAl-LDH and Cr(VI) adsorbed samples were obtained by using a Cu Kα (λ = 1.5406 Å) radiation on a Bruker D8 diffractometer in the 2θ scale range of 5-70°. Fourier-transform infrared spectroscopy (FT-IR) spectra of the samples were collected using a Bruker IFS 66v/S spectrometer in the range 4000-400 cm^{-1}. Thermogravimetric analysis (TGA) for CoAl-LDH and Cr(VI) adsorbed samples was performed using a TGA/DSC 2 STAR instrument in the temperature range of 30–800 ^oC under nitrogen atmosphere with a ramp rate of 2 ^oC min^{-1}. Field emission scanning electron microscopy (FESEM) and energy dispersive X-ray analysis (EDAX) elemental analysis for the CoAl-LDH and Cr(VI) adsorbed samples was done using ZEISS GeminiSEM 500 operated at 15 KV. Cr(VI)-adsorbed material was sonicated in ethanol, and 2 μL of the dispersion was drop-casted onto a carbon-coated copper grid and JEOL JEM2100 PLUS instrument was used to obtain TEM images, and selected area electron diffraction pattern. Surface area and porosity measurements were carried out using a QUNATACHROME QUADRASORD-SI analyzer at 77 K for N_2.

The initial and final concentration of the elements in aqueous samples (1-500 ppm) were measured by Perkin-Elmer Optima 7000DV ICP AES instrument. The

calibration solutions were prepared by ICP standards of Cr (1000mg/L, Sigma-Aldrich). To detect the concentration in ppb level (0.2-1000 ppb), a quadrupole inductively coupled plasma- mass spectrometer (ICP-MS, Thermo Scientific X-Series II) was used.

3.3.2.4. Adsorption Experiments with CoAl-LDH. The adsorption studies of CoAl-LDH were carried out using batch method (V: m~500 mL/g). 20 mg of CoAl-LDH was added to 10 mL of Cr(VI) aqueous solution (4.5 ppb-500 ppm), prepared from potassium dichromate ($K_2Cr_2O_7$) and shaken for 24 h using the tube-rotator. The Cr(VI) adsorbed material (CoAl-LDH) was removed from the suspension by centrifugation at 7000 rpm. The examination of supernatant solution for Cr(VI) metal ion was performed by using inductively coupled plasma-optical emission spectroscopy (ICP-OES) and inductively coupled plasma- mass spectrometry (ICP-MS). The obtained concentrations in ppm and ppb were used to estimate sorption capacity of CoAl-LDH (q_m, from Eq 3.3.1) and the binding affinity of Cr^{VI} towards CoAl-LDH in terms of distribution coefficient (K_d, from Eq 3.3.2).

$$q_m = \frac{(C_o - C_e)V}{m} \quad \text{(Eq. 3.3.1)}$$

$$K_d = \left(\frac{V}{m}\right)\frac{(C_o - C_e)}{C_e} \quad \text{(Eq. 3.3.2)}$$

where, C_e, C_o, V and m, indicates the equilibrium concentration (ppm), initial concentration (ppm), volume of Cr^{VI} aqueous solution (mL) and amount of adsorbent taken (g), respectively.

3.3.2.5. Adsorption Kinetics. Kinetic studies of Cr(VI) adsorption by CoAl-LDH were conducted till it reached equilibrium. 200 mg of the CoAl-LDH was added into 250 mL beaker, a 100 mL aqueous solution containing ~104.1 ppm Cr^{VI} was added (V/m = 500 mL/g) and shaken. After a definite time interval, ~4 mL of supernatant was taken out using pipet, centrifuged at 7000 rpm and analyzed by ICP-AES.

3.3.2.6. Sequestration of Cr(VI) in Different pH. Different pH solutions ranging from 1.93 to 12.82 were prepared using 2M NaOH and 2M HCl solutions. The stability of CoAl-LDH was checked in different pH by taking 20 mg of CoAl-LDH in a vial with desired pH water and kept for 24 hours. The resultant was centrifuged, collected, dried and PXRD was recorded. The influence of pH on the adsorption of Cr(VI) from aqueous solution was examined over the pH range 1.93-12.82.

For each experiment, 10 mL solution of 10 ppm Cr(VI) with varying pH was shaken with 20 mg of CoAl-LDH for 24 h. The supernatant was collected using centrifuge and analyzed by ICP-AES.

3.3.2.7. Selectivity Experiments. To test the effect of co-existing anions Cl^-, F^-, Br^-, NO_3^- and SO_4^{2-} and selectivity of dichromate anion ($Cr_2O_7^{2-}$) capture, competitive adsorption studies were carried out with 20 mg of CoAl-LDH, with V: m~500 mL/g. 10 mL of ~50 ppm Cr(VI) solution was taken in varying concentration of Cl^-, F^-, Br^-, NO_3^- and SO_4^{2-} anions in 0.025-0.25 M range and stirred for 24 h at room temperature.

3.3.2.8. Column Bed Preparation and Study. For the practical application of this material, 0.2 g of CoAl-LDH powder and 19.8 g of sieved sand was ground finely to get an even mixture. To a 2 cm diameter column, ~ 4-5 g of sand was first added to fill around 1 cm height. Then 20 g of this finely ground mixture was added to the column so as to reach a height of 5 cm. Then again ~4-5 g of sand was added to make the final height of column around 7 cm to completely pack the column tightly. A similar column of height 7 cm was prepared with only sand as a reference column to understand if sand is absorbing any Cr(VI) anions. The packed columns were washed with water once to see if the particles were clogging the column or not or the small particles are leaking out from the column. The column was attached to a valve to control the flow of contaminated water entering the column. A dichromate solution of ~100 ppm at pH 7 was used to conduct the study. The initial and final concentrations were obtained using ICP-OES.

3.3.2.9. Regeneration of CoAl-LDH. The material can be regenerated by treating the used CoAl-LDH with 2M potassium carbonate to remove adsorbed $Cr_2O_7^{2-}$ oxyanions by shaking for 24 h. The solution is centrifuged and collected material is washed with water and ethanol. The supernatant was analysed with ICP to calculate amount of Cr^{VI} released in 2M potassium carbonate solution. This replenished material can be used again to extract $Cr_2O_7^{2-}$ oxyanions.

3.3.3. Results and discussion

Layered double hydroxide comprises positively charged layers of brucite-type octahedra ($M(OH)_6$, M: Co, Al) sheets with negatively charged carbonate anions (CO_3^{2-}) and water molecules in the interlayers as shown in Figure 3.3.1a, which provides an opportunity to explore anion-exchange for capturing toxic oxyanions like dichromate ($Cr_2O_7^{2-}$).

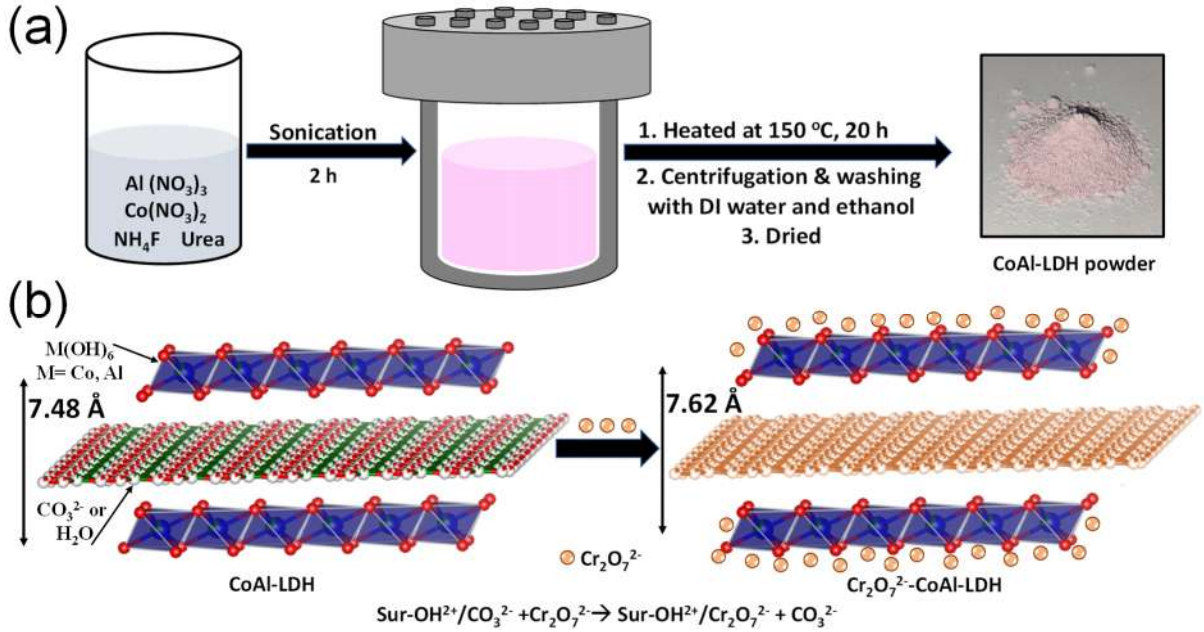

Figure 3.3.1. *(a) Hydrothermal synthesis scheme of CoAl-LDH and (b) Cr(VI) ion-exchange-sorption scheme.*

Hydrothermal synthesis of light pink coloured CoAl-LDH, carried out using $Co(NO_3)_2 \cdot 6H_2O$, $Al(NO_3)_3 \cdot 9H_2O$ as precursors for Co^{2+} and Al^{3+} cations, urea for providing OH^- and CO_3^{2-}, and NH_4F as structure mediating agent. The contents were stirred in water, sealed in Teflon-lined autoclave and kept at 150 °C as shown in the scheme in Figure 3.3.1b. The thermal decomposition of urea and mechanism of CoAl-LDH growth can be expressed as follows in Eq. 3.3.3--3.3.6:

$$CO(NH_2)_2 + H_2O \rightarrow NH_4^+ + OH^- + CO_2 \quad \text{(Eq. 3.3.3)}$$

$$CO_2 + OH^- \rightarrow CO_3^{2-} + H_2O \quad \text{(Eq. 3.3.4)}$$

$$Co^{2+} + Al^{3+} + OH^- + CO_3^{2-} \rightarrow \text{CoAl-LDH} \quad \text{(Eq. 3.3.5)}$$

$$\text{LDHSurface-}OH^{2+}/CO_3^{2-} + Cr_2O_7^{2-} \rightarrow \text{LDHSurface-}OH^{2+}/Cr_2O_7^{2-} + CO_3^{2-} \quad \text{(Eq. 3.3.6)}$$

The Cr(VI) sorption properties were explored by stirring a solution of potassium dichromate with CoAl-LDH using the batch method as shown in Eq. 4. The powder X-ray diffraction (PXRD) pattern of CoAl-LDH samples in Figure 3.3.2a show the classic nature of hydrotalcite materials, where diffraction peaks at 2θ of 11.81, 23.71, 34.66, 39.21° are ascribed to 003, 006, 012, and 015 diffraction planes, respectively, matching with the hexagonal phase of $(Co_4Al_2(OH)_{12}CO_3(H_2O)_3)_{0.5}$, (JCPDS card no. 97-017-2995).[40] The Co/Al molar ratio is obtained 3.76: 1 using inductively coupled plasma (ICP) and the LDH formula is $[Co_{0.79}Al_{0.21}(OH)_2(CO_3)_{0.11}] \cdot mH_2O$. Chromium ion exchange in CoAl-LDH shifts the (003) peak to lower 2θ, indicating an increase in interlamellar spacing from 7.48 to 7.62 Å due to ion-exchange of CO_3^{2-} with dichromate ions ($Cr_2O_7^{2-}$) (see zoomed PXRD in Figure 3.3.3a)

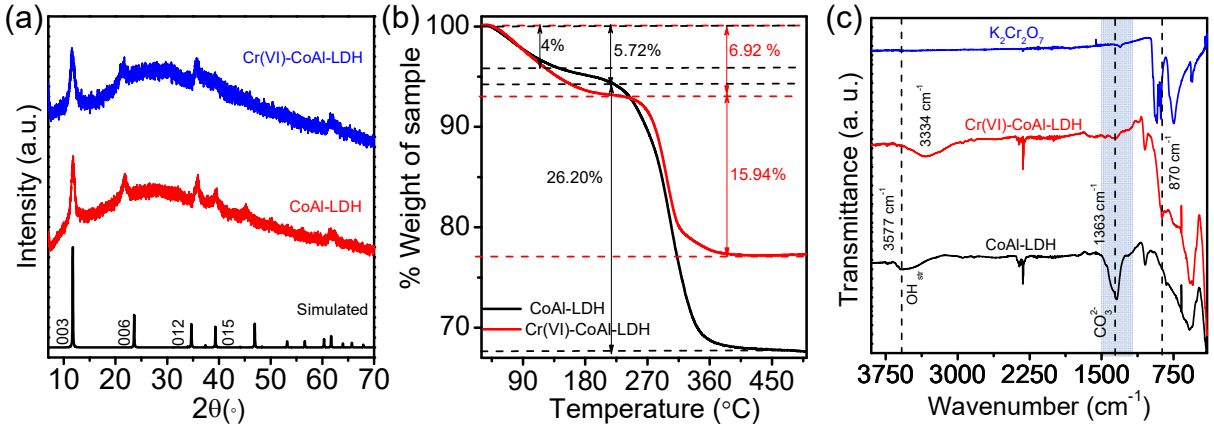

Figure 3.3.2. *(a) PXRD pattern (b) TGA of the prepared CoAl-LDH and after Cr(VI) adsorption on CoAl-LDH; and (c) FTIR spectra of the prepared CoAl-LDH, after Cr(VI) adsorption on CoAl LDH and potassium dichromate indicating removal of CO_3^{2-} and adsorption of $Cr_2O_7^{2-}$ on CoAl-LDH.*

Further to understand this ion-exchange, we performed a thermogravimetric study as shown in Figure 3.3.2b. For CoAl-LDH, we observed that the first weight loss between 30–125 °C was mainly because of the water release from the surface. The second weight loss in 125–225 °C was assigned to the removal of interlayer water molecules and intercalated CO_3^{2-}. While extreme weight loss of 26.2 % in the third stage at 262 °C was ascribed to the thermal decomposition of brucite-like layers through the removal of OH groups as water molecules leading to the formation of $CoAl_2O_4$.[41] On the contrary in the

case of Cr(VI) adsorbed CoAl-LDH, 6.92 weight % was lost as surface and interlayer water. The weight loss at 262 °C decreases to 15.94 %, indicating that some interaction between $Cr_2O_7^{2-}$ and brucite-like layers that inhibit the complete removal of OH groups as water molecules.

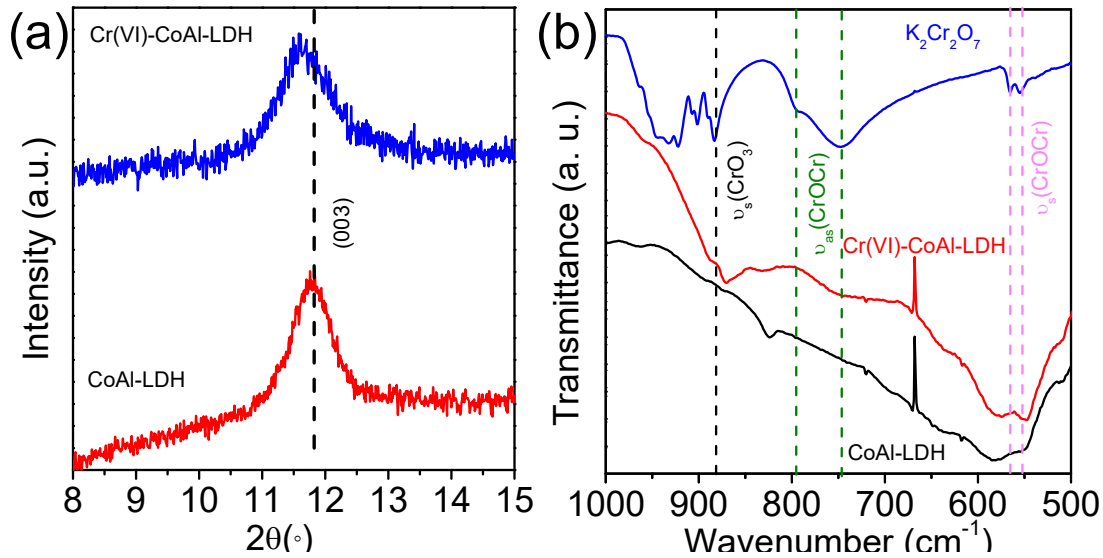

***Figure 3.3.3**. Zoomed PXRD pattern and FTIR spectra of the prepared CoAl-LDH, after Cr(VI) adsorption on CoAl-LDH and $K_2Cr_2O_7$.*

Mechanistic study of oxyanion of Cr(VI) sorption is of paramount importance in understanding the interaction or bonding between dichromate as adsorbate and CoAl-LDH as adsorbent as it leads to optimization of the sorption process and helps to understand desorption or regeneration. To find out the mechanism of sorption, we carried out Fourier-transform infrared spectroscopy (FTIR) analysis, shown in Figure 3.3.2c. The sharp peak at 1363 cm^{-1} corresponding to CO_3^{2-} in CoAl-LDH, diminishes when Cr(VI) is adsorbed on CoAl-LDH.[40] The broad band at 3577 cm^{-1}, occurring because of stretching vibrations of the O–H group of interlayered water molecules and metal bonded hydroxyl groups of CoAl-LDH, redshifts to 3334 cm^{-1} indicating a weakening of this bond and formation of new hydrogen bonding with $Cr_2O_7^{2-}$ molecules and metal bonded hydroxyl groups of CoAl-LDH. Two new peaks arise at 870 cm^{-1} and 747 cm^{-1} corresponding to $\upsilon_s(CrO_3)$ and $\upsilon_{as}(CrOCr)$[42] in Cr(VI) adsorbed CoAl-LDH as shown in Figure 3.3.3b.

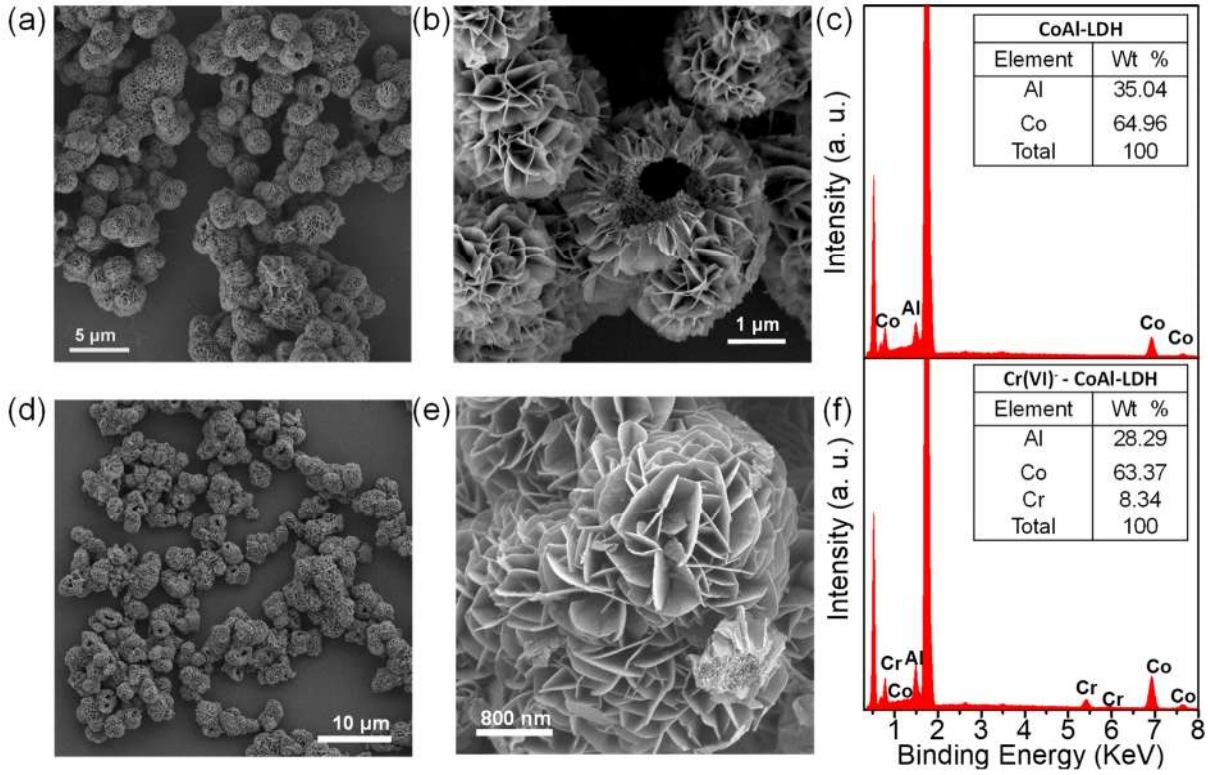

Figure 3.3.4. *SEM images of (a,b) coral like CoAl-LDH (d,e) after Cr(VI) adsorption on CoAl-LDH and (c,f) EDAX analysis of before and after Cr(VI) adsorption on CoAl-LDH respectively.*

The overview field emission scanning electron microscope (FESEM) images of porous CoAL-LDH show well-defined distinct microspheres of ~ 1-3 µm in diameter (Figure 3.3.4a, b), different from traditional hexagonal platelet crystallite morphology of LDHs[41] which upon drying form irregular stone-like aggregates that hinders the adsorption performances. Here, the addition of a small amount of ammonium fluoride (NH_4F) in the synthesis protocol acts as a structure mediating agent and crystal-forming agent that is responsible for the formation of these 3D-crystalline coral-like structures.[43] The higher magnification SEM images depict that the microspheres have nature-inspired coral-like hierarchical morphology comprising from self-organized hexagonal nanoplates extending from the centre of microspheres, distributing uniformly in all directions leading to hollow coral-like structures as shown in the transmission electron microscopy (TEM) image in Figure 3.3.5a.

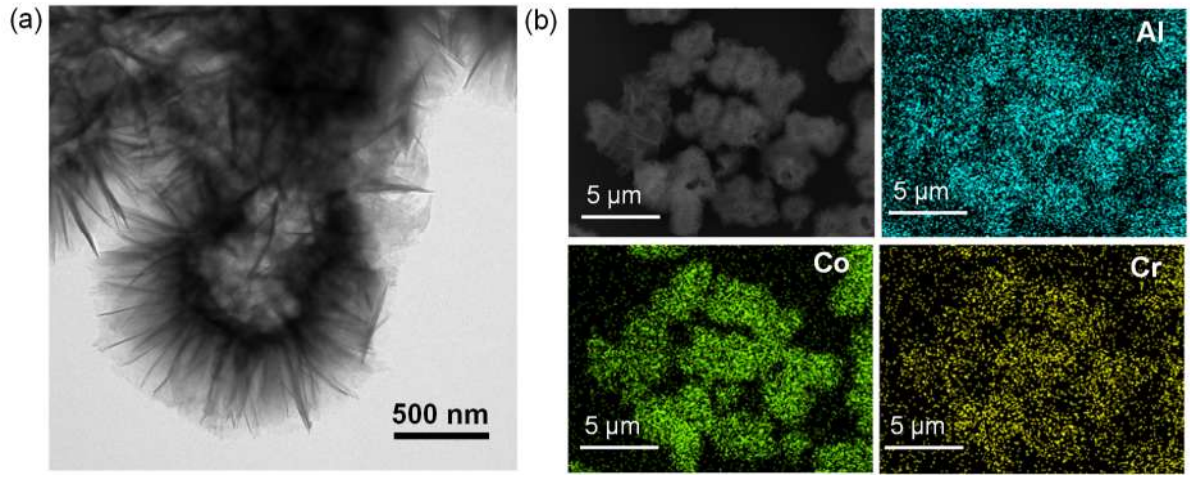

Figure 3.3.5. (a) Transmission electron microscopy (TEM) image and (b) EDS analysis showing the elemental distribution of Cr(VI) adsorbed CoAl-LDH.

The N_2 isotherm obtained for CoAl-LDH is of type II multilayer adsorption, with mesopores in 3-15 nm range, which in turn allows condensation with a pore volume of 2.63×10^{-1} cm^3 g^{-1} and BET surface area of 47.4 m^2/g (Figure 3.3.6). The Cr(VI) intercalated LDH retains the morphology of coral-like microspheres as seen in Figure 3.3.4 d,e.

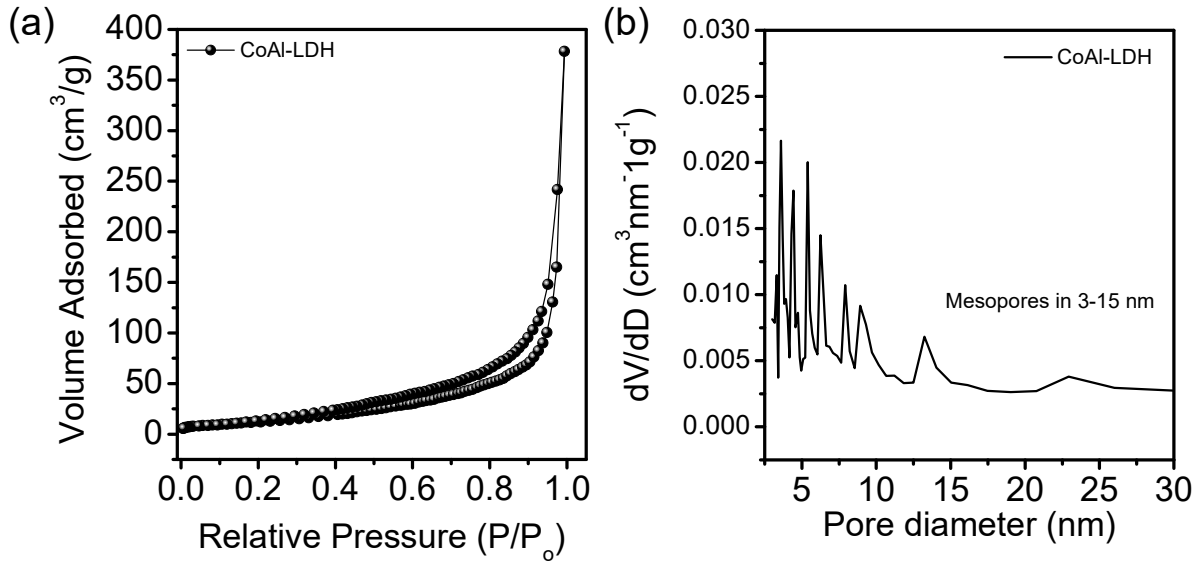

Figure 3.3.6*. (a) Type-II multilayer N_2 adsorption and desorption isotherms at 77 K of CoAl LDH and (b) pore size distribution of CoAl-LDH.*

The energy-dispersive X-ray spectroscopy (EDAX) analysis shows the successful incorporation of chromium in CoAl-LDH. The color mapping analysis from the TEM study in Figure 3.3.5b shows the Cr(VI) sorption occurs uniformly which is due to the high surface area of CoAl-LDH, indicating that $Cr_2O_7^{2-}$ molecules not only ion-exchange with CO_3^{2-}, but are also distributed uniformly on the surface of LDH.

***Table 3.3.1**. Summary of Cr(VI) adsorption isotherm data (m = 0.020 g, V = 10 mL, and V/m = 500 mL g^{-1}).*

Initial Concentration (ppm)	Final Concentration (ppm)	% Cr (VI) removed	q (mg/g)	K_d (mLg^{-1})
3.5	2.5	28.7	0.49	1.99×10^2
4.8	2.4	48.9	1.17	4.76×10^2
7.2	2.4	65.9	2.33	9.52×10^2
12.3	2.4	80.1	4.86	1.99×10^3
27.8	2.4	91.2	12.88	5.25×10^3
51.3	2.5	95.2	24.05	9.68×10^3
78.7	2.6	96.7	38.44	1.49×10^4
112.4	5.9	94.7	53.25	9.02×10^3
149.6	20.8	86.1	65.37	3.14×10^3
190.3	46.8	75.4	72.14	1.54×10^3
221.7	63.5	71.4	78.32	1.23×10^3
270.3	107.0	60.4	80.44	7.52×10^2
334.5	167.9	49.8	82.89	4.94×10^2
481.2	284.0	41.0	97.14	3.42×10^2

The porous coral-like morphology and labile exchangeable CO_3^{2-} motivated us to examine the sorption capacity of CoAl-LDH for Cr(VI) oxyanions uptake. The adsorption isotherm experiments were performed using the batch method. Figure 3.3.7a shows experimental Cr(VI) adsorption isotherm data, best fitted using the Langmuir isotherm model for heterogeneous surfaces.

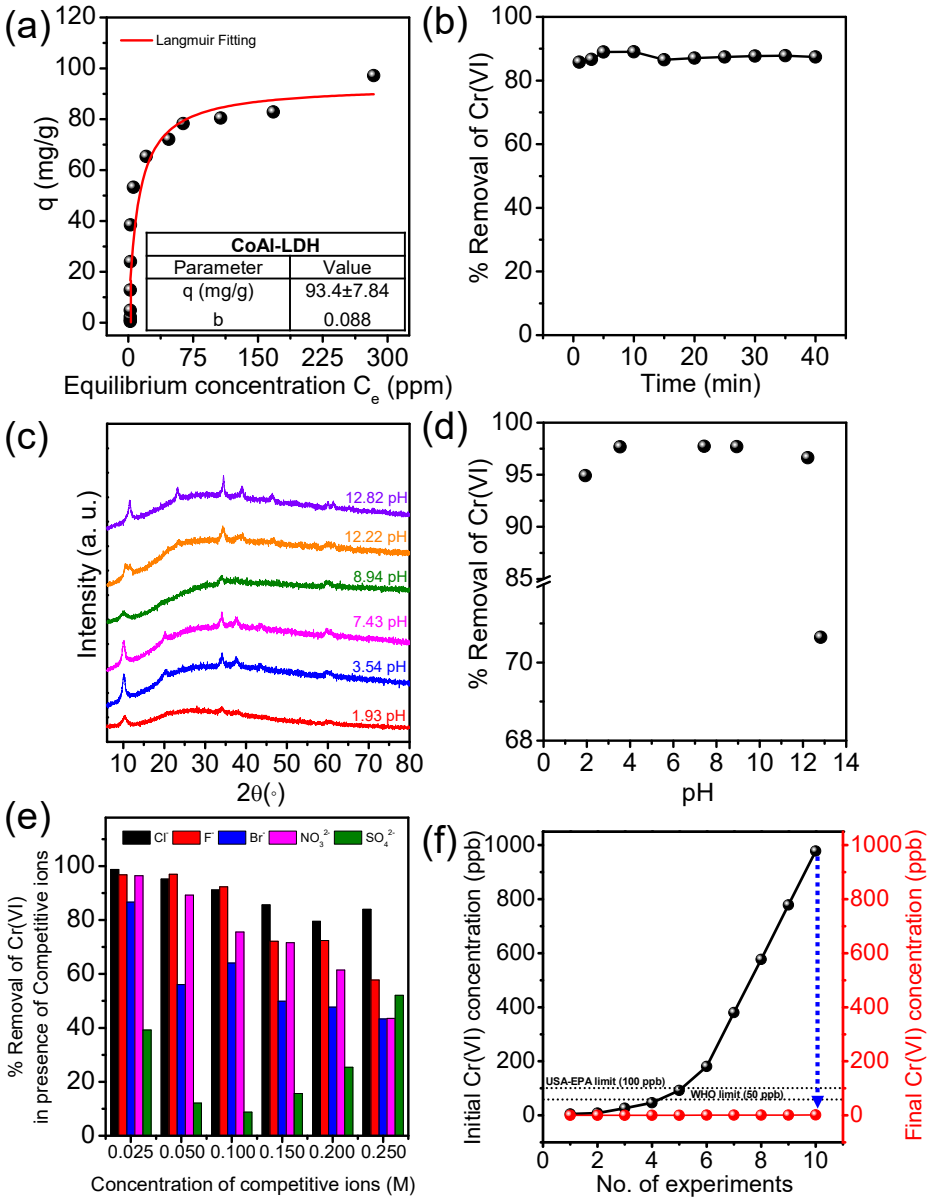

Figure 3.3.7*. (a) Equilibrium data for $Cr_2O_7^{2-}$ ion exchange with CO_3^{2-} on CoAl-LDH (pH ~7, V/m= 1000 mLg^{-1}). The solid red line represents fitting with the Langmuir model, (b) Ion-exchange kinetics plot showing % Cr(VI) removal as a function of contact time, (c) PXRD showing the stability of CoAl-LDH in pH range 1.93–12.82 and (d) removal percentage of Cr (VI) at different pH (~10 ppm Cr(VI) solution, V/m= 1000 mLg^{-1}). (e) Selective removal of Cr(VI) in presence of competitive anions in a concoction of different molar solutions of Cl^-, F^-, Br^-,NO_3^{2-}, SO_4^{2-} and 50 ppm of Cr(VI) anion and (f) removal of Cr(VI) from low ppb contamination using CoAl-LDH.*

Table 3.3.2. *Comparison table describing adsorption properties of various LDH, oxides, anion-exchange resins and MOFs.*

Type	Adsorbents	q_m (mg/g) at RT	Equilibrium time	Working pH range	Lowest limit of removal reported	Selectivity	Ref.
LDH	CoAl-LDH	93.4	1 min	1.93-12.32	4.5 ppb	Cl^-, F^-, Br^-, NO_3^-, SO_4^{2-}	-
	MoS_4-LDH	130	5 min	4-10	10 ppm	SO_4^{2-}, NO_3^-, Cl^-	38
	TJU-1	279	NA	3-12	16 ppm	Cl^-, HCO_3^-, NO_3^- , SO_4^{2-}	7
	CH–Mg/Al	63.6	120 min	3-7	NA	NA	33
	Ni/Mg/Al-LDH	103.4	150 min	NA	NA	CO_3^{2-}, SO_4^{2-}, $H_2PO_4^-$, Cl^-	32
	AMH	105.3	50 min	1-10	NA	NA	8
	Li/Al LDH	187	20 h	4-10	NA	NA	27
Cationic aluminum oxy-hydroxide	JU-11	105.4	30 min	3-10	10 ppm	NO_3^-, Br^-, Cl^-, HCO_3^-, F^-, CO_3^{2-}	5
Anion exchange resins	IRN78	63.57	90 min	7	NA	NA	5
	Lewatit MP 64	20.8	90 min	2-7	NA	NA	15
	IRA 96	23.9	50 min	2-7	NA	NA	16
MOFs	**ZJU-101**	245	10 min	NA	NA	Cl^-, Br^-, NO_3^-, SO_4^{2-}, I^- and F	17
	MOF-867	53.4	12 h	NA	NA	NA	17
	SLUG-21	60	NA	NA	NA	NA	10
	MOR-1–HA	242	60 min	3	6 ppm	Cl^-, NO_3^-, Br^- and SO_4^{2-}	23
	Zn/Co-SLUG-35	68.5	2 h	NA	NA	Cl^-, NO_3^-, SO_4^{2-}	19
	FIR-53	74.2	60 min	NA	NA	Cl^-, Br^-, NO_3^-	18

Langmuir isotherm:

$$q = q_m \frac{(bC_e)}{1+(bC_e)}$$

(Eq. 5)

where q (mgg^{-1}) is the quantity of Cr(VI) adsorbed at equilibrium concentration C_e (ppm), q_m is the maximum Cr(VI) adsorption capacity, b (Lmg^{-1}) is the Langmuir constant related to the interaction energy of Cr(VI) and CoAl-LDH.

The q_m value for Cr(VI) sorption is 93.4 ± 7.8 mg g^{-1} with b value of 0.088 Lmg^{-1} and distribution coefficient (K_d) values ~ 10^2-10^4 mLg^{-1}. The q_m value is higher than most of the materials mentioned in Table 3.3.2.[5,10,15–19,33] The Cr(VI) sequestration efficiency of CoAl-LDH from aqueous solutions has also been inspected by exploring the adsorption kinetics of CoAl-LDH in ~104 ppm solution (pH ~6.5) of $K_2Cr_2O_7$. Within a minute, the concentration decreases from 104 ppm to 14.83 ppm which is 85.8 % removal, indicating strong interactions between $Cr_2O_7^{2-}$ and the structure of LDH due to fast kinetics of sorption and it outperforms than other materials mentioned in Table 3.3.2., (see Figure 3.3.7b). A maximum K_d value of 8.12 x 10^3 mLg^{-1} has been obtained.

Table 3.3.3*. Kinetics data of Cr(VI) adsorption on CoAl-LDH (m = 0.020 g, V = 10 mL, and V/m = 500 mL g^{-1}).*

Time (min)	Initial concentration (ppm)	Final concentration (ppm)	% $Cr_2O_7^{2-}$ Removed	q (mg/g)	K_d (mL/g)
0	104.1	104.1	0.0	0.00	0.00 x 10^0
1	104.1	14.8	85.8	44.64	6.02 x 10^3
3	104.1	13.9	86.6	45.09	6.48 x 10^3
5	104.1	11.5	89.0	46.31	8.06 x 10^3
10	104.1	11.4	89.0	46.34	8.12 x 10^3
15	104.1	14.00	86.6	45.05	6.44 x 10^3
25	104.1	13.1	87.4	45.48	6.92 x 10^3
35	104.1	12.7	87.8	45.72	7.22 x 10^3
40	104.1	13.1	87.4	45.48	6.92 x 10^3

Metal adsorption is largely influenced by the pH stability of the adsorbent and the metal chemistry in the solution. Interestingly, CoAl-LDH is stable at pH ranging from 1.93 to 12.22 compared to other materials mentioned in Table 3.3.2. Hexavalent chromium exists as $HCrO_4^-$ at pH < 6.5 and as CrO_4^{2-}at pH > 6.5 as shown in (Eq.3.3..7-3.3.10). CoAl-LDH shows 95-98 % removal of Cr(VI) in the pH range from 1.93 to 12.22. At low pH, the removal efficiency is high due to protonated and positively charged surface which favours electrostatic attraction with $HCrO_4^-$(Eq. 3.3.10).

Table 3.3.4*. Summary of Cr(VI) adsorption data using the CoAl-LDH at different pH.*

pH	Initial concentration (ppm)	Final concentration (ppm)	% Cr (VI) Removed	q (mg/g)	K_d (mL/g)
1.93	11.47	0.58	94.9	5.44	9.34 x 10^3
3.54	12.59	0.29	97.7	6.18	2.12x 10^4
7.43	12.36	0.28	97.7	5.95	2.12x 10^4
8.94	11.01	0.27	97.5	5.32	1.95x 10^4
12.22	10.03	0.34	96.6	4.82	1.43x 10^4
12.82	8.04	2.36	70.6	2.80	1.19x 10^3

However, with the increase of the solution pH above pH 12.22 the adsorption efficiency decreased slightly (~70 % removal) due to the change of the major species of Cr(VI) from $HCrO_4^-$ to CrO_4^{2-} leading to sorption competition arising from surplus OH^- present in solution and a slight modification in the surface of LDH after 12.22 pH which repels CrO_4^{2-} (Eq. 10). CoAl-LDH has an exceptional acidic/basic buffer ability in a broad pH range of 1.93-12.22 due to OH^- and CO_3^{2-} and outperforms other pH-dependent materials like LDHs,[27,31–33,38] anion exchange resins,[5,16,17,15] cationic MOFs,[10,17–19,23] cationic aluminium oxyhydroxides,[5] which usually remove Cr(VI) in 3-10 pH.

$$H_2CrO_4 \rightleftharpoons H^+ + HCrO_4^- \quad \text{(Eq. 3.3.7)}$$

$$HCrO_4^- \rightleftharpoons H^+ + CrO_4^{2-} \quad \text{(Eq. 3.3.8)}$$

$$2HCrO_4^- \rightleftharpoons Cr_2O_7^{2-} + H_2O \quad \text{(Eq. 3.3.9)}$$

$$\text{Low pH :- LDH-surface-OH} + H_3O^+ \rightarrow \text{LDH-surface-}OH_2^+ + H_2O \quad \text{(Eq.3.3.10)}$$

High pH :- LDH-surface-OH + OH^- → LDH-surface-O^- + H_2O (Eq. 3.3.11)

CoAl-LDH has exceptional selectivity for Cr(VI) in the pool of competing anions, Cl^-, F^-, Br^-, NO_3^- and SO_4^{2-} with a concentration in 0.025-0.25 M. The monovalent cations Cl^-, F^-, Br^- and NO_3^- have an insignificant effect on the Cr(VI) removal efficiency of CoAl-LDH as seen in Figure 3.3.7e. However, divalent SO_4^{2-} competes with $Cr_2O_7^{2-}$ oxyanions due to similar charges but the ratio of the concentration of SO_4^{2-} (4.3×10^3 - 4.3×10^7 ppm) and $Cr_2O_7^{2-}$ (50 ppm) is much higher and even seawater contains ~ 2700 ppm of SO_4^{2-}.[44] Hence, CoAl-LDH is a promising selective sequestrant of Cr(VI) that can work efficiently even in the presence of a highly saturated concoction of Cl^-, F^-, Br^-, NO_3^- and SO_4^{2-} anions.

While previously reported adsorbents display exceptional sorption capacity for Cr(VI), it still remains a major challenge to remove trace levels of Cr(VI) up to the maximum permissible drinking water limit of 50 ppb (WHO)[45] and 100 ppb (USA-EPA)[46].

Table 3.3.4*. Low ppb Cr(VI) adsorption data using CoAl-LDH.*

Initial concentration (ppb)	Final concentration (ppb)	% Cr (VI) removed	K_d (mLg^{-1})
4.502	0.361	92.0	5.57×10^3
8.373	0.162	98.1	2.52×10^4
26.290	0.012	99.9	1.09×10^6
46.290	0.023	99.9	1.01×10^6
91.970	0.202	99.8	2.24×10^5
180.500	0.471	99.7	1.89×10^5
380.200	0.528	99.9	3.58×10^5
576.900	0.605	99.9	4.69×10^5
778.600	0.697	99.9	5.55×10^5

CoAl-LDH can remove 99.8 % of Cr(VI) even from 5-1000 ppb and can reduce the Cr(VI) levels up to such a low value of 0.012 ppb as shown in Figure 3.3.7f and

Table 3.3.4. The K_d values are very high with ~ 10^3-10^6 mLg^{-1} range and a maximum K_d of 1.09 x 10^6 mLg^{-1} have been obtained.

The most problematic and expensive part of application of an adsorption technology is the desorption/regeneration of adsorbents. We performed a regeneration study by treating the used-LDH with 2M potassium carbonate to remove $Cr_2O_7^{2-}$ oxyanions and replenish the LDH framework with CO_3^{2-} ions. We were able to desorb ~60-85 % of $Cr_2O_7^{2-}$ from used LDH and the material can be used again (Table 3.3.5). This process successfully restores the properties of adsorption similar to its initial properties for cost effective reuse rather than disposing it in the environment.

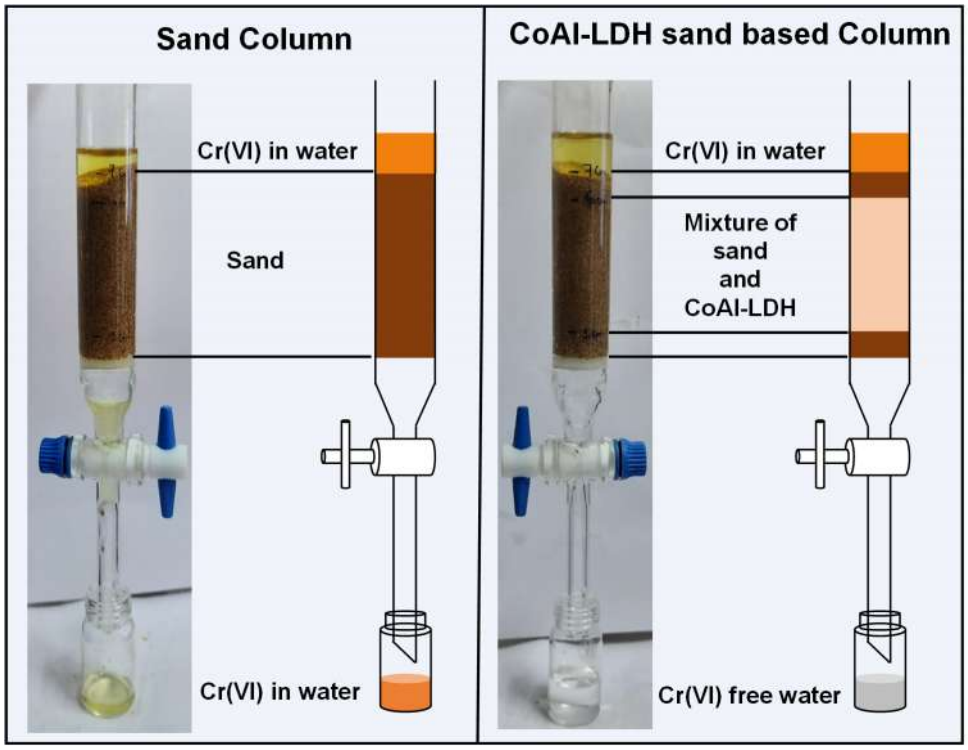

Figure 3.3.8*. Dichromate sorption by CoAl-LDH/ sand column (Initial $Cr_2O_7^{2-}$ concentration = 100 ppm; pH~7; CoAl-LDH/ sand= 0.2: 19.8 g).*

With this extremely high selectivity, pH stability, low ppb level removal efficiency, and regeneration properties of CoAl-LDH, for practical application, we designed a CoAl-LDH/ sand column (Figure 3.3.8). CoAl-LDH and sand act as stationary phase and the mobile phase is the contaminated water.

Table 3.3.5*. Regeneration study of CoAl-LDH adsorbent by replenishing CO_3^{2-} by 2M K_2CO_3.*

Initial Cr(VI) (ppm)	Final Cr(VI) (ppm)	% Cr(VI) removed	Total amount of Cr(VI) expected in ppm to be released (ppm)	Amount of Cr(VI) removed in saturated K_2CO_3 (ppm)	Cr(VI) % Desorbed
12.7	1.5	87.9	11.2	4.0	63.9
52.7	1.5	97.2	51.2	22.5	56.0
228.0	15.2	93.3	212.8	36.7	82.8
482.7	236.4	51.0	246.3	50.7	79.4

Table 3.3.6*. Summary of Cr(VI) adsorption data using sand column as reference and CoAl-LDH/ sand column (50 mL ~100 ppm Cr(VI) solution passed through two columns; one with only sand and another with mixture sand and CoAl-LDH).*

S. No.	Only Sand			Mixture of sand and CoAl-LDH Sand: CoAl-LDH = 19.8: 0.2		
	Initial concentration (ppm)	Final concentration (ppm)	% Cr (VI) Removed	Initial concentration (ppm)	Final concentration (ppm)	% Cr (VI) Removed
1.	99.7	99.1	0.6	99.7	0.60	99.4
2.	99.7	95.2	4.5	99.7	0.65	99.3
3.	99.7	96.0	3.7	99.7	0.67	99.3

The main logic behind using a mixture of LDH and an inexpensive-stable supporting matrix of sand is that the LDH sorbent is restricted, undisturbed by the water flow, and separated by sand which safeguards the continuous water flow, preventing clogging of the column. Also, the pressure exerted by water on LDH will be reduced as most of it will be exerted by sand, ensuring a continuous flow. We observed more than 99 % removal of Cr(VI) for ~100 ppm Cr(VI) contaminated solution with just 1 % wt loading of CoAl-LDH in 99 % wt of sand. To ensure that the efficiency is mainly due to CoAl-LDH, not sand, we also explored only the sand column as a blank and found that it could not remove Cr(VI) at all (see Table 3.3.6).

3.3.4. Conclusions

In summary, nature-inspired coral-like CoAl-LDH can selectively and efficiently sequester oxyanions of toxic Cr(VI) up to such a low value of 0.012 ppb unlike other material in a very broad pH range from 1.93 to 12.22 with a high capacity of is 93.4 ± 7.8 mg g^{-1}. Weak bonding interaction between $Cr_2O_7^{2-}$ and brucite-like layers promotes selectivity towards oxyanions of Cr(VI). Interestingly, this material can be regenerated and recycled and no pre-treatment of wastewater is required. The anion-exchange column designed can remove 99 % Cr(VI) from contaminated water. Furthermore, this low-cost column consisting of a mixture of CoAl-LDH and sand can be used for the removal of toxic oxyanions from effluent discharge conveniently and economically.

3.3.5. References

[1] V. Kumar, R. D. Parihar, A. Sharma, P. Bakshi, G. P. Singh Sidhu, A. S. Bali, I. Karaouzas, R. Bhardwaj, A. K. Thukral, Y. Gyasi-Agyei, J. Rodrigo-Comino, *Chemosphere* **2019**, *236*, 124364.

[2] M. Costa, C. B. Klein, *Crit. Rev. Toxicol.* **2006**, *36*, 155.

[3] F. Brito, J. Ascanio, S. Mateo, C. Hernandez, L. Araujo, P. Gili, P. Martín-Zarza, S. Dominguez, A. Mederos, *Polyhedron* **1997**, *16*, 3835.

[4] H. Jabeen, V. Chandra, S. Jung, J. W. Lee, K. S. Kim, S. Bin Kim, *Nanoscale*, **2011**, *1*, 3583.

[5] P. Bai, Z. Dong, S. Wang, X. Wang, Y. Li, Y. Wang, Y. Ma, W. Yan, X. Zou, J. Yu, *Angew.Chem. Int. Ed.* **2020**, *59*, 19539.

[6] Q. L. and X. W. Jian Zhao, Zhenyu Li, Jinfeng Wang, *J. Mater. Chem. A* **2015**, *3*, 15124.

[7] H. Yang, H. Fei, *Chem. Commun.* **2017**, *53*, 7064.

[8] Y. Li, B. Gao, T. Wu, D. Sun, X. Li, B. Wang, F. Lu, *Water Res.* **2009**, *43*, 3067.

[9] D. Mohan, C. U. Pittman, *J. Hazard. Mater.* **2006**, *137*, 762.

[10] H. Fei, M. R. Bresler, S. R. J. Oliver, *J. Am. Chem. Soc.* **2011**, *711*, 11110.

[11] L. Fan, C. Luo, M. Sun, H. Qiu, *J. Mater. Chem.* **2012**, *22*, 24577.

[12] M. Pansini, C. Colella, M. De Gennaro, *Desalination* **1991**, *83*, 145.

[13] L. Zhang, Q. Sun, D. Liu, A. Lu, *J. Mater. Chem. A* **2013**, *1*, 9477.

[14] J. Huang, Y. Li, Y. Cao, F. Peng, Y. Cao, Q. Shao, H. Liu, Z. Guo, *J. Mater Chem. A* **2019**, *6*, 13062.

[15] E. Pehlivan, S. Cetin, *J. Hazard. Mater.* **2009**, *163*, 448.

[16] S. Edebali, E. Pehlivan, *Chem. Eng. J.* **2010**, *161*, 161.

[17] Q. Zhang, J. Yu, J. Cai, L. Zhang, Y. Cui, Y. Yang, B. Chen, G. Qian, *Chem. Commun.* **2015**, *51*, 14732.

[18] H.-R. Fu, Z.-X. Xu, J. Zhang, *Chem. Mater.* **2015**, *27*, 205.

[19] H. Fei, C. S. Han, J. C. Robins, S. R. J. Oliver, *Chem. Mater.* **2013**, *25*, 647.

[20] J. Li, X. Dai, L. Zhu, C. Xu, D. Zhang, M. A. Silver, P. Li, L. Chen, Y. Li, D. Zuo, *Nat. Commun.* **2018**, *9*, 1.

[21] H. Ma, B. Liu, B. Li, L. Zhang, Y.-G. Li, H.-Q. Tan, H.-Y. Zang, G. Zhu, *J. Am. Chem. Soc.* **2016**, *138*, 5897.

[22] Y.-J. Cheng, R. Wang, S. Wang, X.-J. Xi, L.-F. Ma, S.-Q. Zang, *Chem. Commun.* **2018**, *54*, 13563.

[23] S. Rapti, A. Pournara, D. Sarma, I. T. Papadas, G. S. Armatas, A. C. Tsipis, T. Lazarides, M. G. Kanatzidis, M. J. Manos, *Chem. Sci.* **2016**, *7*, 2427.

[24] A. A. Zagorodni, *Ion Exchange Materials: Properties and Applications*, Elsevier, **2006**.

[25] M. McGuire, N. Blute, L. Fong, D. Froelich, P. Kavounas, G. Qin, *Hexavalent Chromium Removal Using Anion Exchange and Reduction with Coagulation and Filtration*, Water Environment Research Foundation, **2008**.

[26] K. Goh, T. Lim, Z. Dong, *Water research*, **2008**, *42*, 1343.

[27] N. Chubar, R. Gilmour, V. Gerda, M. Mi, M. Omastova, K. Heister, P. Man, J. Fraissard, V. Zaitsev, *Adv. Colloid Interface Sci.* **2017**, *245*, 62.

[28] K.-H. Goh, T.-T. Lim, Z. Dong, *Water Res.* **2008**, *42*, 1343.

[29] M. K. Uddin, *Chem. Eng. J.* **2017**, *308*, 438.

[30] V. R. L. Constantino, T. J. Pinnavaia, *Inorg. Chem.* **1995**, *34*, 883.

[31] N. K. Lazaridis, D. D. Asouhidou, *Water Res.* **2003**, *37*, 2875.

[32] C. Lei, X. Zhu, B. Zhu, C. Jiang, Y. Le, J. Yu, *J. Hazard. Mater.* **2017**, *321*, 801.

[33] L. Xiao, W. Ma, M. Han, Z. Cheng, *J. Hazard. Mater.* **2011**, *186*, 690.

[34] D. Carriazo, M. del Arco, C. Martín, V. Rives, *Appl. Clay Sci.* **2007**, *37*, 231.

[35] X. Lv, X. Qin, K. Wang, Y. Peng, P. Wang, G. Jiang, *J. Hazard. Mater.* **2019**, *373*, 176.

[36] Y. Zheng, B. Cheng, W. You, J. Yu, W. Ho, *J. Hazard. Mater.* **2019**, *369*, 214.

[37] R. Soltani, A. Marjani, S. Shirazian, *Dalt. Trans.* **2020**, *49*, 5323.

[38] L. Ma, S. M. Islam, H. Liu, J. Zhao, G. Sun, H. Li, S. Ma, M. G. Kanatzidis, *Chem. Mater.* **2017**, *29*, 3274.

[39] S. V Prasanna, R. A. P. Rao, P. V. Kamath, *J. Colloid Interface Sci.* **2006**, *304*, 292.

[40] H. Gao, R. Cao, X. Xu, J. Xue, S. Zhang, T. Hayat, N. S. Alharbi, J. Li, *ACS Sustain. Chem. Eng.* **2019**, *7*, 905.

[41] X. Zhao, L. Zhang, P. Xiong, W. Ma, N. Qian, W. Lu, *Microporous Mesoporous Mater.* **2015**, *201*, 91.

[42] H. S. H. Stammreich, D. Bassi, O. Sala, *Spectrochim. Acta* **1990**, *10*, 147.

[43] W. Y. Lim, G. W. Ho, *Procedia Eng.* **2017**, *215*, 163.

[44] "Sulfate in drinking water" https://www.who.int/water_sanitation_health/dwq/chemicals/sulfate.pdf

[45] Guidelines for drinking-water quality: second addendum. **2008**, https://www.who.int/water_sanitation_health/publications/gdwq3rev/en/

[46] "Chromium in drinking water" https://www.epa.gov/sdwa/chromium-drinking-water.

Chapter 3.4

Reversible and Efficient Sequestration of Cs from Water by Layered Metal Chalcophosphate, K-MPS-1†

†*Paper based on this has been published as* ***E. Rathore,*** *P. Pal, K. Biswas, Chem. Eur. J.* ***2017****, 23, 11085.*

Chapter 3.4

Reversible and Efficient Sequestration of Cesium from Water by Layered Metal Chalcophosphate, K-MPS-1†

Summary: *Water body contamination with radioactive species is an important issue due to significant development in nuclear energy. Cesium (^{137}Cs) radioisotope is a non-actinide fission product of the uranium and plutonium; and it is long-lived. Hence, selective removal/capture of Cs is essential for managing radioactive waste. Herein, we report a detailed Cs^+ ion-exchange study of potassium intercalated layered metal thiophosphate, $K_{0.48}Mn_{0.76}PS_3.H_2O$ (K-MPS-1). The sorption of Cs^+ by K-MPS-1 follows Langmuir model with a high capacity of 337.5 mg/g and high distribution coefficients in the order of ~ 10^4 mL/g. K-MPS-1 can sequester Cs^+ efficiently even from very low concentration (ppb level). K-MPS-1 exhibits high Cs uptake in a broad pH range of 2-12 and the ion exchange process reaches equilibrium within a short time (~15 min) following pseudo-second order kinetics. Moreover, K-MPS-1 demonstrates selectivity towards Cs^+ capture in the presence of complex solutions containing excess Na^+, Ca^{2+} and Mg^{2+} ions, which is due to the favorable interaction between Cs (soft Lewis acid) and S (soft Lewis base). K-MPS-1 reversibly captures Cs^+ and it can be regenerated by treating Cs-MPS-1 by KCl solution.*

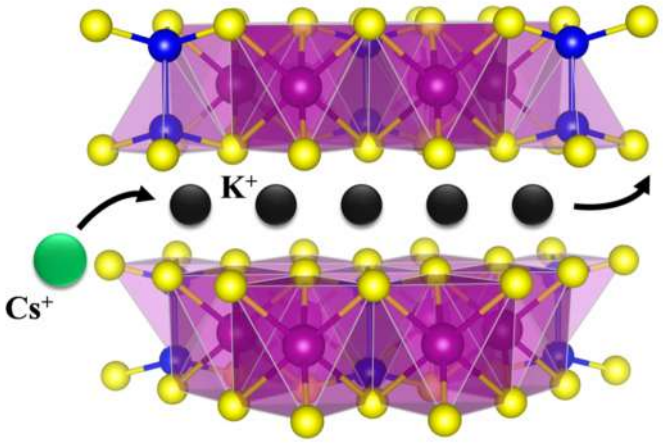

†*Paper based on this has been published as* ***E. Rathore,*** *P. Pal, K. Biswas, Chem. Eur. J.* ***2017****, 23, 11085.*

3.4.1. Introduction

Nuclear energy has emerged as one of the low-cost alternatives for electrical power with no emission of greenhouse gases.[1] But the management and disposal of radioactive wastes is the key issue with this developing nuclear energy. Radioactive cesium, ^{137}Cs, a non-actinide fission product of the uranium and plutonium, emits harmful gamma radiations, high energy beta particles and has long half-life ($t_{1/2}$) of ~30.17 years.[2,3] ^{137}Cs accumulates in ecosystems, assimilates in living organisms and plants due to high water solubility and analogous physicochemical properties of K^+.[4] In 2013, Castrillejo *et al.* have shown that there is a major increase in radioactive ^{137}Cs levels in the seawater samples taken from the Fukushima Dai-ichi nuclear power plant compared to pre-Fukushima ^{137}Cs levels.[5,6] Thus, design and synthesis of stable materials is necessary for treatment of the discharged nuclear effluents comprising of inhomogeneous samples with high salt concentration and extreme pH conditions.

Dissolved inorganic and organic ligands (e.g., EDTA) are generally not capable of binding strongly to Cs^+.[7] Biosorption *i.e.* using biopolymers like alginates, isolated from bacteria fungi, yeast, algae have also been used to remove Cs^+.[8-10] Methods like coprecipitate flotation, coagulation/sedimentation, evaporation, reverse osmosis, sand filtration, ultrafiltration, microfiltration, electro dialysis and solvent extractions suffer from selectivity in presence of high salt concentrations and can't reduce concentration of Cs^+ below ~50 ppb level.[3,11-13]Ion-exchange is an inexpensive efficient method, can selectively adsorb Cs^+ and proves to be potential for storage of Cs^+ ions from solidified waste and reductive nuclear discharges.[14,15] Inorganic ion exchangers are preferred over organic ion exchangers due to superior chemical, thermal and radiation stability.[16] Tremendous ion-exchange studies of Cs^+ have been done in natural minerals (zeolites and clays)[7,17], insoluble transition metal ferrocyanides[18–20], titanium silicates[21,22], metal oxides (TiO_2, MnO_2)[23], MOFs[24], PAN (polyacrylonitrile) based exchangers,[25–27] but they lack stability in extreme pH as well selectivity due to presence of other inhibiting cations present in nuclear wastes containing water.

Solid state metal chalcogenides have shown improved ion-exchange properties for soft metal ions in comparison to the sulfur-functionalized non-chalcogenide materials.[28] Recently, researchers have explored layered and three-dimensional open framework metal chalcogenides for ion-exchange applicatios.[29–34] The soft Lewis base nature of

sulfide and selenide anions provide higher affinity towards soft Lewis acidic metal ion centers[35,36] Nuclear discharge waste containing high salt concentration of hard ions (H^+, Na^+, Ca^{2+},Mg^{2+}) cannot inhibit the ion-exchange properties of these materials, but some of them suffers from stability due to non-stoichiometry, presence of unbalanced charges[37] and organic moiety;[38] and low Cs^+ ion removal capacity[33,39,40], weak affinity towards Cs^+ in presence of others mono and di-valent cations.[38] Therefore, there is plenty of room to be explored about the ion-exchange properties of stable inorganic chalcogenides, which can have high capacity and effective distribution co-efficient in the broad pH range in presence of high salt concentration. Alkali metal intercalated metal chalcophosphate ($A_{2x}M_{1-x}PS_3.(H_2O)_y$; A=K, Na; M = Mn, Cd, etc.) is a layered material which can be readily synthesized and it is stable in a broad pH range.[41] In chapter 3.1, we have shown that $K_{0.48}Mn_{0.76}PS_3.H_2O$ is capable of selective sequestration of Pb from the water up to low ppb in 2-10 pH range.

In this chapter, we discuss a detailed Cs^+ ion-exchange investigation of potassium intercalated layered metal thiophosphate, $K_{0.48}Mn_{0.76}PS_3.H_2O$ (K-MPS-1). The sorption of Cs^+ by K-MPS-1 follows Langmuir adsorption model with a high capacity of 333.1±17 mg/g (at pH ~7) and distribution coefficients in order of ~10^4 mL/g. K-MPS-1 exhibits high cesium uptake both under strongly acidic and strongly basic conditions (pH 2-12). Cs uptake reaches equilibrium within 15 min following the pseudo second order kinetics and the distribution coefficients remain unaffected (~10^4 mL/g) even in the presence of complex solutions containing excess Na^+, Ca^{2+}, Mg^{2+}ions. The selectivity over other common cations originates from Cs-S soft Lewis acid-Lewis base interactions rather than size effects. K-MPS-1 can sequester Cs^+ from low ppb level (5-100 ppb). Cs^+ occupies K^+ site and forms a Cs^+ intercalate (Cs-MPS-1). Further, K-MPS-1 reversibly takes Cs^+ and can be regenerated by treating it to 2M KCl solution. The results show that layered K-MPS-1 can be considered as a selective and inexpensive sorbent for ^{137}Cs radioactive isotope which is generally formed during nuclear reactions.

3.4.2. Methods

3.4.2.1 Reagents. Manganese (Mn, Alfa Aesar 99.95 %), red phosphorous (P, Alfa Aesar 98.9 %), sulphur (S, Alfa Aesar 99.999 %), cesium chloride ($CsCl_2$, Sigma Aldrich

99.999%) and potassium chloride (KCl, Alfa Aesar 99.5 %) were used for synthesis without further purification.

3.4.2.2 Synthesis. A stoichiometric quantity of Mn, P and S were mixed and heated in vacuum sealed (10^{-5} Torr) quartz tube to synthesize $MnPS_3$ (MPS-1) which is explained in section 2.2.2.[42] Potassium intercalated $MnPS_3$ (K-MPS-1) was synthesized by stirring $MnPS_3$ powder with saturated KCl solution.[43,44]

3.4.2.3 Characterizations. Powder X-ray diffraction of samples were done using a Cu Kα (λ = 1.5406 Å) radiation on a Bruker D8 diffractometer. To estimate optical band gap of the finely grinded powder samples at room temperature, diffuse reflectance measurements were carried out over the range of 250 nm to 2500 nm using a Perkin Elmer Lambda 900, UV/Vis/NIR spectrometer in reflectance mode. Absorption (α/ S) data were calculated from reflectance data using Kubelka-Munk equation: $\alpha/S = (1-R)^2/(2R)$, where R is the reflectance, α and S are the absorption and scattering coefficient, respectively. The energy band gaps were derived from α/S vs E (eV) plot. FTIR spectra of powder sample was recorded using a Bruker IFS 66v/S spectrometer. Raman spectroscopy measurements of powder sample were carried out with a HORIBA LABRAM HR800 spectrometer. The excitation wavelength of the laser was 514 nm. TGA was performed using a TGA/DSC 2 STAR instrument in the temperature range of 300–773 K under nitrogen atmosphere with a ramp rate of 5 K min^{-1}. FESEM of the synthesized and lead adsorbed materials were performed using NOVA NANO SEM 600 (FEI, Germany) operated at 15 KV. EDAX compositional analysis was performed during FESEM imaging. XPS measurement has been performed with Mg−Kα (1253.6 eV) X-ray source with a relative composition detection better than 0.1% on an Omicron Nanotechnology spectrometer. The zeta potential measurements were carried out using a NanoZS (Malvern UK) employing a 532 nm laser. Actual concentration of the lead containing solutions (1ppm-1000ppm) were measured by ICP-AES. ICP-AES measurements were carried out using Perkin-Elmer Optima 7000DV instrument. Cs standard (1000mg/L, Sigma-Aldrich), Mn standard (1000mg/L, Sigma-Aldrich) and multi-element standard (Ca 2000 mg/L, Na 1000 mg/L , K 200 mg/L and Mg 400 mg/L, Sigma-Aldrich) were used to determine the concentration of various cations. Element concentrations in ppb level (1-1000 ppb) were measured using a quadrupole inductively coupled plasma- mass spectrometer (ICP-MS, Thermo Scientific X-Series II) equipped

with Nickel sample and skimmer cones. Samples were introduced using a 100 ml/min PFA nebulizer connected to a peristaltic pump running at 30 rpm into an ESI-PC3 Peltier cooled spray chamber. A CETAC ASX-520 auto-sampler was used. Uptake time for samples and standards was 60 seconds while the rinse time (in 2% HNO_3) was 90 seconds.

3.4.2.4 Cs^+ Sorption and Ion-Exchange Kinetics. Typical ion-exchange studies of K-MPS-1 with non-radioactive Cs^+ (which mimics radioactive $^{137}Cs^+$ due to the same size) were carried out using batch method (V:m~1000 mL/g). 10 mg of K-MPS-1 was added to 10 mL of Cs^+ aqueous solution (5 ppb-1300 ppm) in a 15 mL centrifuging tube and shaken for 15 min in tube rotator. The Cs^+ ion-exchanged material (Cs-MPS-1) was separated by centrifugation or filtration (through filter paper, Whatman No. 41) and dried in an oven at 60 ^oC. The filtrate was collected and the concentration of Cs^+ was measured using ICP-AES and ICP-MS. The obtained concentrations were used to determine the sorption isotherms and calculate maximum sorption capacity.

Kinetic studies of Cs^+ sorption by K-MPS-1 were carried out until the equilibrium was reached. Ion exchange experiments of various reaction time (5, 10 and 15 min) were performed. For each experiment, 10 mL of ~45 ppm Cs^+ aqueous solution and 10 mg of K-MPS-1 is taken in a 15mL centrifugation tube and the contents were shaken. After a certain time interval, the suspension of each tube is centrifuged and collected filtrates were analyzed for the final concentration by ICP.

To test the effect of inhibiting ions like Ca^{2+}, Mg^{2+} and Na^+ on Cs^+ ions, competitive ion exchange studies were carried out with a *V/m* ratio of 1000 mL/g using solution containing these cations (80ppm Cs^+, 25ppm Ca^{2+}, Mg^{2+}, Na^+) at room temperature with 15 min contact time.

3.4.3. Results and Discussion

3.4.3.1. Characterizations of Cs-MPS-1

The Cs^+ sorption properties are explored by stirring $CsNO_3$ solution with the as synthesized K-MPS-1, where V: m is 1000 mL/g. The ion-exchange process is very fast and almost all K^+ ions were exchanged with Cs^+ in K-MPS-1 within 15 min which we will discuss in detail later part of this chapter. EDAX analysis of cesium exchanged K-

MPS-1 (Cs-MPS-1) showed complete removal of K^+ ions and insertion of Cs has taken place in K-MPS-1. Cs^+ insertion does not change the layered morphology of the K-MPS-1 (Figure 3.4.1).

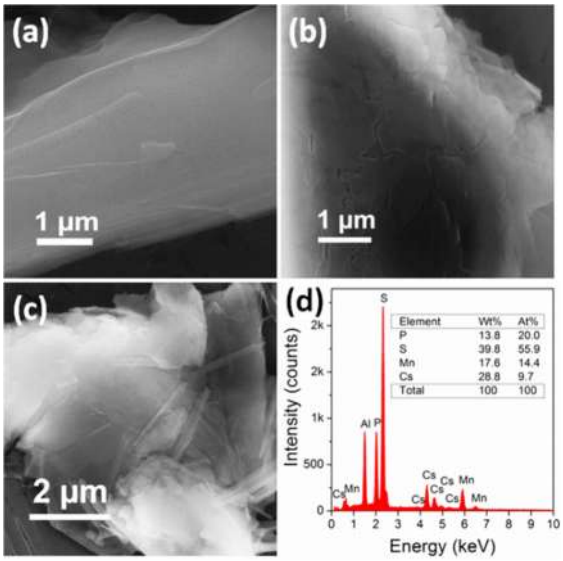

Figure 3.4.1. *(a) FESEM images of K-MPS-1, (b) Cs adsorbed K-MPS-1, (c) Zomed version of Cs-MPS-1 and (d) EDX spectra of Cs-MPS-1.*

We have characterized MPS-1, K-MPS-1 and Cs-MPS-1 by PXRD to confirm the K^+ intercalation into MPS-1 and Cs^+ ion exchange in K-MPS-1. First, a significant shift of the (001) Bragg peak to the lower 2 was observed when K^+ intercalated in $MnPS_3$ due to the expansion of the layer in K-MPS-1(Figure 3.4.2a).

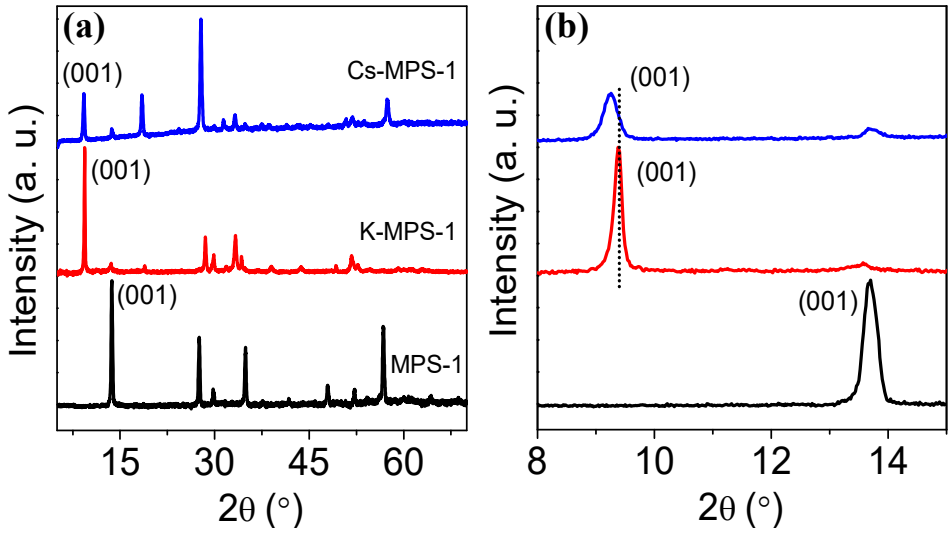

Figure 3.4.2. *(a) PXRD patterns of MPS-1, K-KPS-1 and Cs-MPS-1. (b) Zoomed version of PXRD in the 2θ range of 8-15°.*

Cs^+ ion exchange in K-MPS-1 further shifts the (001) to lower 2 with respect to K-MPS-1, indicating the increase in inter-lamellar spacing. Cs^+ insertion into K-MPS-1 increases the interlayer spacing from 9.42 to 9.54 Å which is clearly shown in zoomed version of PXRD (Figure 3.4.2b). Insertion of larger Cs^+ ions (3.06 Å) in place of K^+ (2.80 Å) increases the interlayer spacing by 0.12 Å and shift (001) Bragg peak.

Figure 3.4.3 shows the schematics of the ion-exchange reaction in K-MPS-1. Chemical equation below describes the ion-exchange process that takes place in K-MPS-1.

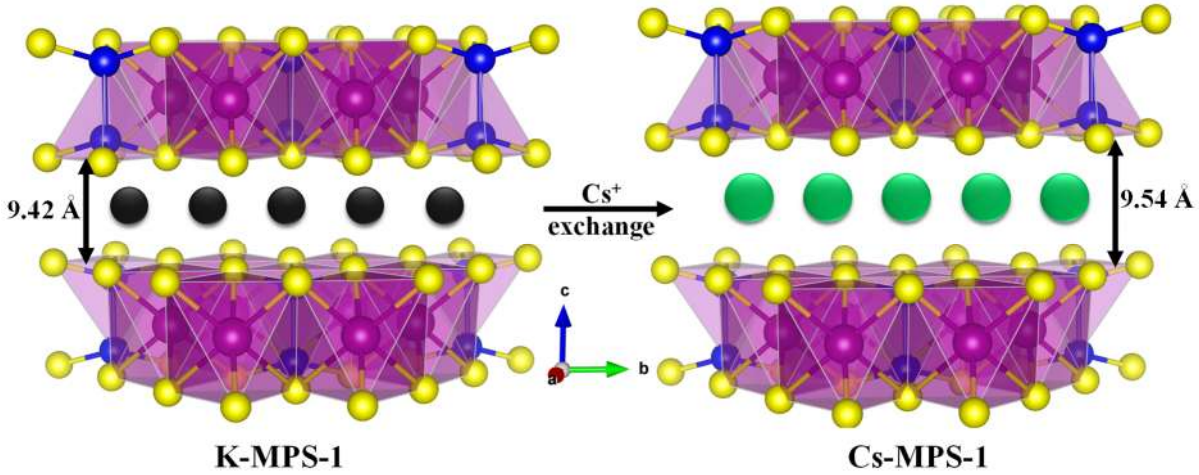

Figure 3.4.3. *Schematic for the mechanism of Cs^+ capture by K-MPS-1. Mn, purple; P, blue; S, yellow; K, black; Cs, green.*

$$K_{2x}Mn_{1-x}PS_3.nH_2O + 2xCsCl\ (aq) \longrightarrow Cs_{2x}Mn_{1-x}PS_3.nH_2O + 2xKCl$$

Figure 3.4.4a and b represents the FT-IR and Raman spectra of MPS-1, K-MPS-1, and Cs sorbed K-MPS-1, respectively. In FT-IR spectra, MPS-1 shows two distinct peaks at 445 and 565 cm^{-1}, arising from P-P and symmetric P-S stretching of the P_2S_6 unit, respectively.[45] Intercalation of K^+ doesn't affect the lower energy band (445 cm^{-1}), but splits the higher energy band (565 cm^{-1}) into two bands at 605 and 552 cm^{-1} including a weak band at 565 cm^{-1}. Intercalation of K^+ in MPS-1 pulls out Mn^{2+} and creates a Mn^{2+} vacancy in the layer to maintain the charge balance, which leads to distortion of the symmetric P_2S_6 unit. [46] As a result, asymmetric P-S stretching splits into two components (in-plane and out-plane), which are appearing at 605 and 552 cm^{-1}, respectively. While, sorption of Cs in K-MPS-1 results in the complete disappearance of

the weak symmetric P-S band and intensification of two strong distorted P-S bands. This indicates that Cs^+ replaces K^+ ions in the interlayer space, thereby slightly increasing the extent of distortion due to the large size effect.

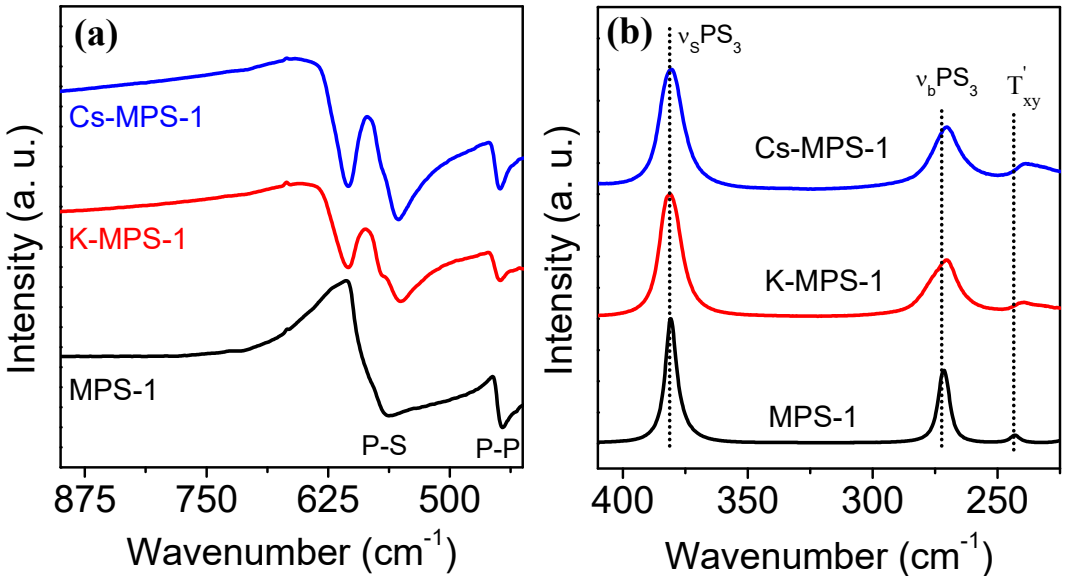

Figure 3.4.4. *(a) IR spectra of MPS-1, potassium intercalated K-MPS-1 and Cs exchanged Cs-MPS-1. (b) Raman spectrum of MPS-1, K-MPS-1 and Cs-MPS-1.*

Table 3.4.1 *Interlayer spacing and band gap*

Material	Interlayer spacing (Å)	Band gap energy (eV)
MPS-1	6.45	2.39
K-MPS-1	9.42	2.53
Cs-MPS-1	9.54	2.68

Raman spectra show the higher energy stretching mode of PS_3 unit is unaltered in all cases because it is metal independent (Figure 3.4.4b). The lower energy vibration modes of K-MPS-1 and Cs-MPS-1 has changed in position and intensity due to less charge density of K and Cs with respect to Mn^{2+}. However, these lower energy bands are highly sulfur and metal ions sensitive.[45] The $_b$ (PS_3) and T_{xy} (PS_3) are red shifted 2 cm^{-1} and 4 cm^{-1} with respect to that of MPS-1, respectively. Metal vacancies formed by intercalation of K^+ ions in MPS-1 distorts the symmetric P_2S_6 units, thereby decreasing

the frequency.[47] In the case of Cs-MPS-1, Cs^+ larger than K^+ ion, which enhances the distortion and reduces the frequency further.

Insertion of K^+ and Cs^+ into MPS-I and K-MPS-1 are further analyzed by UV-Vis study. Figure 3.4.5 shows the electronic absorption spectra of MPS-1, K-MPS-1 and Cs-MPS-1. Intercalation of K^+ in $MnPS_3$ increases the band gap from 2.38 eV to 2.53 eV indicating increase the gap between the layers due to K^+ intercalation (Table 3.4.1). Cs exchanged material exhibits a small increase in band gap with respect to K-MPS-1. Cs-MPS-1 shows a band gap 2.68 eV which is 0.15 eV greater than that of the K-MPS-1. This can be attributed to the weak interaction between Cs and S with respect to K and S. The interaction follows in the order of electronegativity ($X_{Cs}<X_K$). The weaker interaction between Cs and S stabilizes the bonding sulfur orbital and increase the band gap in Cs-MPS-1.

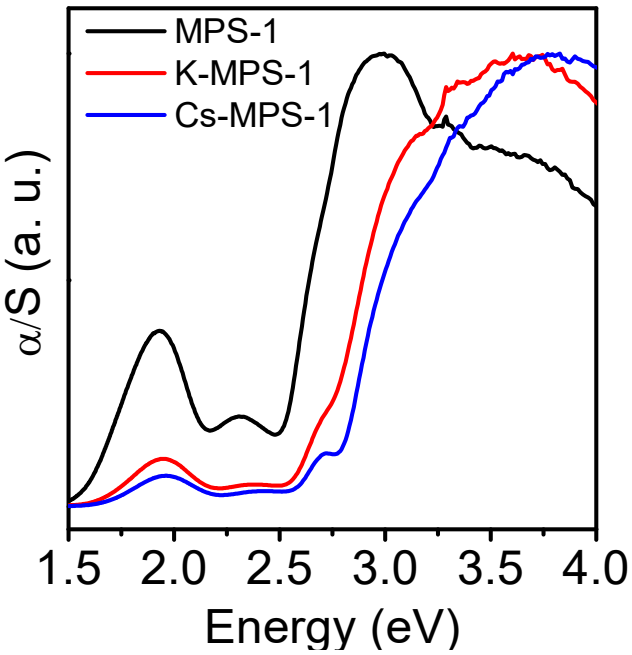

Figure 3.4.5. *Solid state electronic absorption spectra of MPS-1, K-MPS-1 and Cs-MPS-1.*

3.4.3.2. Cs^+ Sorption Studies

In order to establish a relationship between the amount of cesium ions sorbed in the K-MPS-1 and the concentration of remaining Cs^+ ions in the aqueous phase, the adsorption isotherm studies were performed and ion exchange capacity of K-MPS-1 for

Cs^+ was calculated. To determine the quantitative Cs^+ sorption capacity of K-MPS-1, we performed ion-exchange batch studies at room temperature within a broad range of Cs^+ concentrations from ppb to ppm (*V:m = 1000 mL/g*, pH ~ 6.5, Milli-Q water). The initial and final concentration of Cs^+ in the aqueous solution are measured by ICP analysis. Adsorption isotherm generally provides information about adsorption mechanism, surface properties, affinity and capacity of adsorbent. The sorbent, K-MPS-1, was contacted with varying concentrations of Cs^+ until equilibrium was reached and the data is tabulated in Table 3.4.2 and Table 3.4.3.

Table 3.4.2 *Sorption results of K-MPS-1 toward* Cs^+

Initial concentration C_0, (ppm)	Final concentration C_f, (ppm)	Removal (%)	q (mg/g)	K_d (mL/g)
7.87	0.739	90.6	7.1	9.7 X 10^3
10.83	3.159	70.8	7.7	2.4 X 10^3
103.3	45.37	56.1	57.4	1.3 X 10^3
154.4	49.03	68.2	105.4	2.2 X 10^3
263	70.77	73.1	188.5	2.7 X 10^3
389.5	175.4	55.0	212.0	1.2 X 10^3
827.1	537.8	35.0	286.4	0.5 X 10^3
1296	989.7	23.6	303.3	0.3 X 10^3
m = 0.010 g, V = 10 mL, V:m = 1000 mL/g				

Figure 3.4.6a shows the fitting of equilibrium data by two binding models, Langmuir and Langmuir-Freundlich.

Langmuir isotherm $$q = q_m \frac{(bC_e)}{1+(bC_e)}$$ (Eq. 3.4.1)

Langmuir-Freundlich isotherm $$q = q_m \frac{(bC_e)^{1/n}}{1+(bC_e)^{1/n}}$$ (Eq, 3.4.2)

where q (mg g^{-1}) is the amount of Cs^+ adsorbed at equilibrium concentration, q_m is the maximum Cs^+ adsorption capacity, b (L mg^{-1}) is the Langmuir constant related to adsorption energy, C_e (ppm) is the equilibrium concentration and $1/n$ is a measure of intensity of adsorption where n is a constant.

Table 3.4.3. *Removal of Cs^+ at ppb level.*

Initial concentration $C_{0,}$ (ppb)	Final concentration $C_{f,}$ (ppb)	% Removed	K_d (mL/g)
5.0	0.7	86.0	6.1 X 10^3
18.5	2.6	85.9	6.1 X 10^3
72.7	11.0	84.9	5.6 X 10^3
120.10	17.9	85.1	5.7 X 10^3
245.8	12.0	95.1	1.95 X 10^4
562.5	36.8	93.5	1.43 X 10^4
693.5	46.9	93.2	1.38 X 10^4
965.9	57.3	94.1	1.59 X 10^4
1420	84.8	94.0	1.57 X 10^4
m = 0.010 g, V = 10 mL, V:m = 1000 mL/g			

The affinity of K-MPS-1 towards Cs^+ is expressed in terms of distribution coefficient (K_d):

$$K_d = \left(\frac{V}{m}\right)\frac{(C_o - C_e)}{C_e} \qquad (3)$$

where, V is the volume (mL) of Cs^+ aqueous solution, m is the amount of K-MPS-1 ion exchanger taken, C_e is equilibrium concentration (ppm) and C_o is the initial concentration (ppm). K_d values in the range of 10^3 to 10^4 which is considered to be good and reversible ion exchange process (see Table 3.4.2 and Table 3.4.3). We have observed the maximum K_d value is 1.6 x 10^4 mL/g (see Table 3.4.3).

The experimental equilibrium data were well fitted with both Langmuir and Langmuir-Freundlich isotherm with a good agreement of $R^2 \geq 0.95$ and the ion-exchange sorption constants are given in Table 3.4.4. The value of Langmuir-Freundlich constant n = 0.9 was found to be closer to 1 suggesting that the adsorption behavior follows the Langmuir adsorption model. This result indicates that the exchangeable Cs^+ ions form monolayer assuming that sorption occurs on a structurally homogeneous adsorbent and all the sorption sites are energetically identical. Thus, the adsorption sites for Cs^+ ions

are fixed in between the layers due to weak electrostatic interaction between the S^{2-} ions and interlayer Cs^{+}.

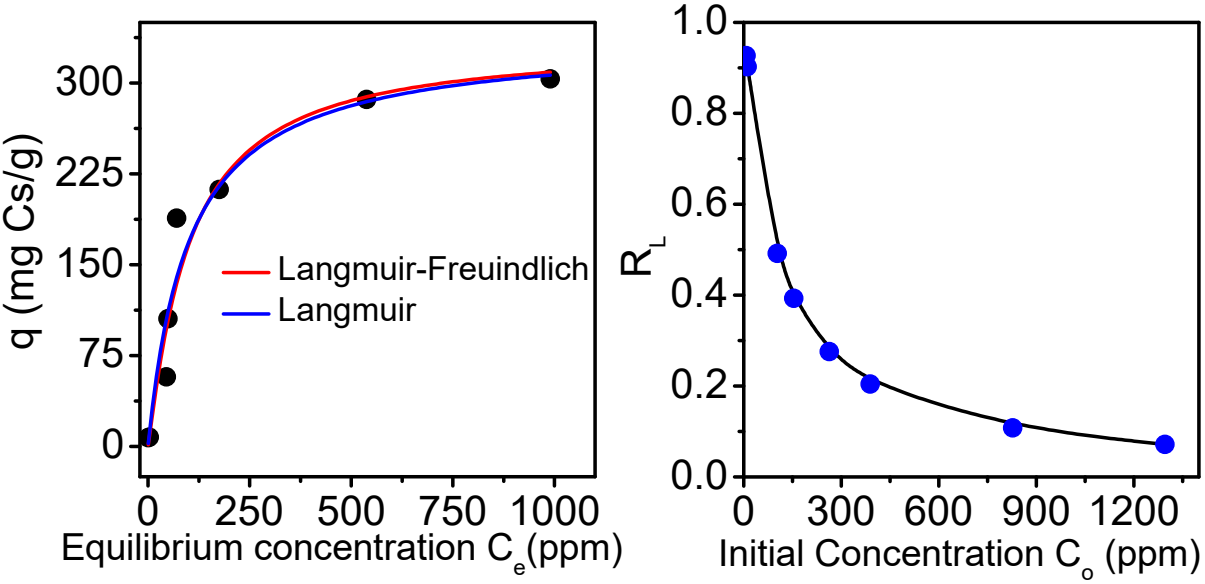

Figure 3.4.6. *(a) Equilibrium data for Cs^{+} ion exchange (pH~ 7, V:m= 1000 mL/g). The solid blue and red line represents the fitting with Langmuir and Langmuir-Freundlich model. (b) Variation of R_L with initial cesium concentration of K-MPS-1.*

Table 3.4.4 *The ion-exchange sorption constants obtained by fitting the isotherm data with different models.*

Parameters	Langmuir	Langmuir-Freundlich
q_m (mg/g)	337.5(17)	333.11(17)
b (L/mg)	0.01	0.01
n	-	0.9
R^2	0.952	0.953

The theoretical capacity of K-MPS-1 for Cs^{+} uptake is calculated to be 310.7 mg/g which is comparable to the maximum ion exchange capacity, q_m, obtained from Langmuir and Langmuir-Freundlich isotherm model (Table 3.4.4). In the EDAX study of Cs-MPS-1, we have also observed the complete removal of K^{+}. Thus, these observation further supports that the Cs^{+} ions occupy the position of K^{+} ions which are intercalated between the $MnPS_3$ slabs of K-MPS-1. Moreover, Langmuir isotherm model for Cs sorption indicates the homogeneous nature of K-MPS-1, i.e. each Cs^{+} adsorption has

equal adsorption activation energy and demonstrates the formation of mono layer coverage of Cs^+ in between the layers of ion-exchanger. The observed Cs uptake capacity, q_m, 337.5±17 mg/g obtained from Langmuir model compares well with state of art of materials listed in Table 3.4.5.

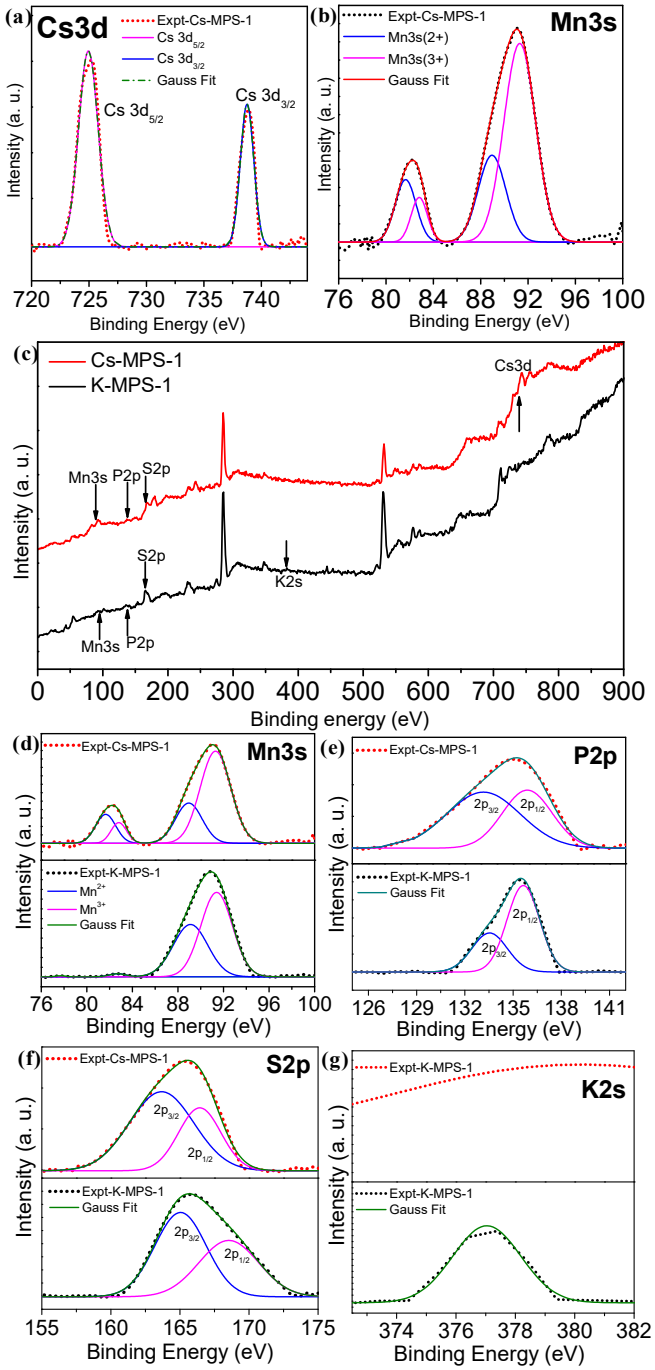

Figure 3.4.7. *XPS spectra for (a) Cs3d; (b) Mn3s of Cs-MPS-1; (c) Survey scan; (d) Mn3s; (e) P2p; (f) S2p and (g) K2s of before and after Cs exchange.*

Further, XPS spectra of Cs-MPS-1 shows two distinct peaks at the position 730 and 744 eV for the Cs $3d_{5/2}$ and $3d_{3/2}$ (Figure 3.4.7a) including other elemental peaks as in K-MPS-1. Note that there was no XPS peak observed for K^+ for exchanged materials, indicating effective exchange of K^+(Figure 3.4.7). K^+ intercalation creates an excess negative charge on the surface of MPS-1 due to Mn^{2+} vacancy, which further confirmed by Zeta potential measurement. However, Cs^+ insertion in K-MPS-1 does not affect the surface charge (Figure 3.4.8). This further supports that Cs exchange takes place only in the position of K^+ in between the layer.

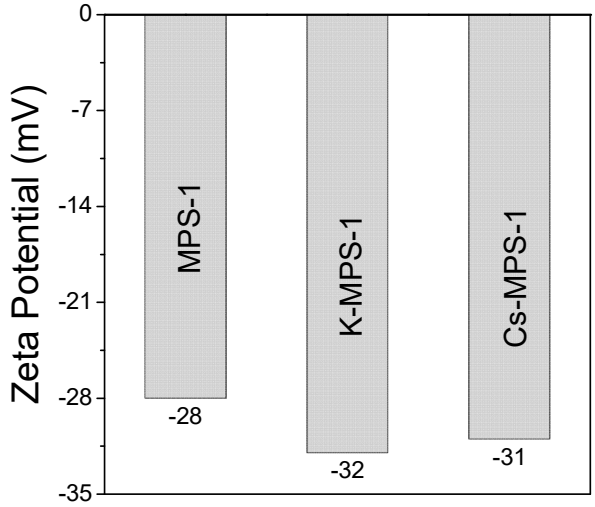

Figure 3.4.8. *Surface charge analysis of MPS-1, K-MPS-1 and Cs-MPS-1 by zeta potential measurements.*

The nature of Langmuir isotherm was further verified by the analysis of the dimensionless constant separation factor or equilibrium parameter, R_L,[48] which is given by

$$R_L = \frac{1}{1+(bC_o)} \qquad \text{(Eq. 3.4.3)}$$

where b (L/mg) is Langmuir constant and C_o is initial concentration of adsorbate in mg/L. The R_L indicates about the nature of adsorption isotherm accordingly: $R_L > 1$ unfavorable adsorption; $0 < R_L < 1$ favorable adsorption; $R_L = 0$ irreversible adsorption and $R_L = 1$ linear adsorption. From the Langmuir fitting data, the present R_L value ranges from 0.07 to 0.92, (see Figure 3.4.6b) indicating favorable adsorption of Cs^+ in K-MPS-1.

Table 3.4.5 Comparison of Cs^+ ion-exchange properties of K-MPS-1 with other materials.

Material	q_m(mg/g) (Langmuir)	K_d(mL/g) (pH~ 7)	Active pH range	Equilibrium study time (min)	Ref.
K-MPS-1	337.48±17	~ 10^4	2-12	15	This work
KMS-1	226±2	≥ 10^4	0.8-12	5	[37]
KMS-2	531±28	≥ 10^3	3-10	-	[50]
KTS-1	205±6	≥ 10^5	-	-	[40]
KTS-3	280±11	≥ 10^4	2-12	5	[39]
PB/Fe_3O_4/GO	55.56	≥ 10^3	4-10	720	[20]
Na alginate	80.64	-	2-6	120	[9]
PAN-KNiCF	157.729	≥ 10^4	-	1440	[25]
PATiW	217	≥ 10^3	2-9	180	[51]
γ-Zr phosphate	180.7	≥ 10^3		14400	[16]
MnO_2–PAN	321.6	944	1-9	35	[26]
HexaCNFe-Fe	240-380	10^2 -10^3	-	2880	[52]
K_6MS	66±4	≥ 10^4	2.5-12	-	[33]
K@RWY	310	≥ 10^5	1.6-11.8	5	[53]
Maghemite PVA-Alginate Beads	28.32	≥ 10^4	2-12	330	[8]
Magnetite PB nanocomposites	280.82 (10 °C)	≥ 10^5	2-9	240	[18]
FJSM-SnS	409±29 (65 °C)	≥ 10^3	0.7-11	5 (65 °C), 30 (RT)	[38]
GeSbS-2	231±15 (65 °C)	≥ 10^3	2.8-11	2 (65 °C)	[54]
T3NT	200	≥ 10^3	1-7	10	[55]

The value of Langmuir constant b (L/mg) for Cs^+ is 0.01 L/mg which indicates the binding affinity of Cs^+ towards K-MPS-1 is moderate. This weak binding nature of Cs^+ was proved by the reversibility of the ion-exchange reaction. 89 % of Cs^+ released from Cs-KMPS-1 in desorption studies with KCl solutions (Table 3.4.6). Hence, the material can be regenerated and used repeatedly for Cs^+ capturing.

Table 3.4.6. *Reversibility studies of Cs-MPS-1 by using saturated KCl.*

C_0, (ppm)	C_0, (ppm)	Cs^+ Removed %	Cs^+ Adsorbed on K-MPS-1 (ppm)	KCl added (ppm)	Cs^+ released, (ppm)	Released %
150.2	40.3	73.2	109.9	634.4	79.2	72.1
150.2	26.3	82.5	123.9	1692	109.7	88.5
m = 0.010 g, V = 10 mL KCl solution, V:m = 1000 mL/g						

3.4.3.3 Kinetics Study

To understand the dynamics of Cs^+ sorption, kinetics studies were carried out. Figure 3.4.9 shows that equilibrium is reached within 15 min, indicating that Cs^+ exchange takes place rapidly and the data are tabulated in Table 3.4.7.

Table 3.4.7. Kinetics data of Cs^+ sorption using K-MPS-1.

Initial concentration C_o, (ppm)	Time (min)	Final concentration C_f, (ppm)	Removal (%)	K_d (mL/g)	q_t (mg/g)
45.97	0	45.97	0	-	-
	5	12.54	72.7	2.69 X 10^3	33.77
	10	10.75	76.6	3.31 X 10^3	35.58
	15	10.32	77.6	3.42 X 10^3	35.30
m=0.010g, V= 10mL, V:m=1000mL/g					

The extremely high mobility of K^+ ions and high affinity of the soft Lewis basic sulfide site for soft Cs Lewis acids sites resulted in the fast ion exchange kinetics in K-MPS-1. To determine the adsorption rate and pathway of Cs^+ exchange, pseudo first order and pseudo second order model were used.

$$\ln(q_e - q_t) = \ln q_e - k_1 t \qquad \text{(Eq. 3.4.4)}$$

$$\frac{t}{q_t} = \frac{1}{k_2 q_e^2} + \frac{t}{q_e} \qquad \text{(Eq. 3.4.5)}$$

where q_e (mg/g) is the amount of Cs^+ exchanged per unit mass of K-MPS-1 at equilibrium, q_t is Cs^+ ions adsorbed at time t, k_1 and k_2 (g/mg min^{-1}) are the rate constants of pseudo-first-order and pseudo-second-order adsorption interactions. k_1 and k_2 are calculated by plotting $\ln(q_e\text{-}q_t)$ vs. t and t/q_t vs t plot by using Eq. (3.3.4) and (3.4.5), respectively (Table 3.4.9).[39]

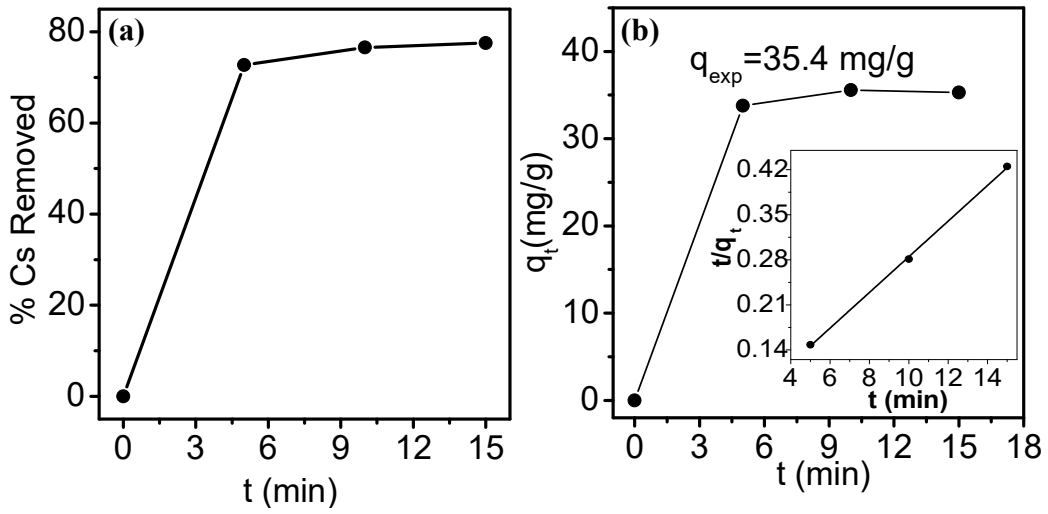

Figure 3.4.9. *Ion- exchange kinetics curve for Cs^+: (a) removal % of Cs^+ as a function of contact time, (b) ion-exchange capacity (q_t) with contact time and pseudo-second-order kinetic plots (inset) for Cs^+ sorption.*

Table 3.4.8. *Kinetic parameters for sorption of Cs^+ by K-MPS-1 with two different models.*

Order	Adsorbate	R^2	q_e (exp) (mg g^{-1})	q_e (cal) (mg g^{-1})	k (g/mg/min)
Pseudo-2nd	Cs^+	0.999	35.4	36.1	9.82 X 10^{-2}
Pseudo-1st	Cs^+	0.933	35.4	21.6	3.75 X 10^{-1}

The goodness of fit, R^2, is to be 0.999 for the Eq. (4), which is very close to unity, indicates the sorption of Cs^+ on K-MPS-1 follows pseudo-second-order kinetics (Figure 3.4.9b).

3.4.3.4. pH and Competitive Ion-Exchange Studies

Nuclear discharge containing Cs^+ generally has extreme pH condition, thus it is important to have a material that can withstand within a broad pH range. Therefore, we have carried out ion-exchange studies in the pH range of 2-12 and observed that the K-MPS-1 removes Cs rapidly and effectively. Distribution coefficient, K_d was calculated at various pH (Figure 3.4.10), which shows that even in extreme pH conditions K_d remains unaffected. Hence, K-MPS-1 proves to retain Cs removal capabilities and it is stable in a wide range of pH compared to other materials in Table 3.4.5.

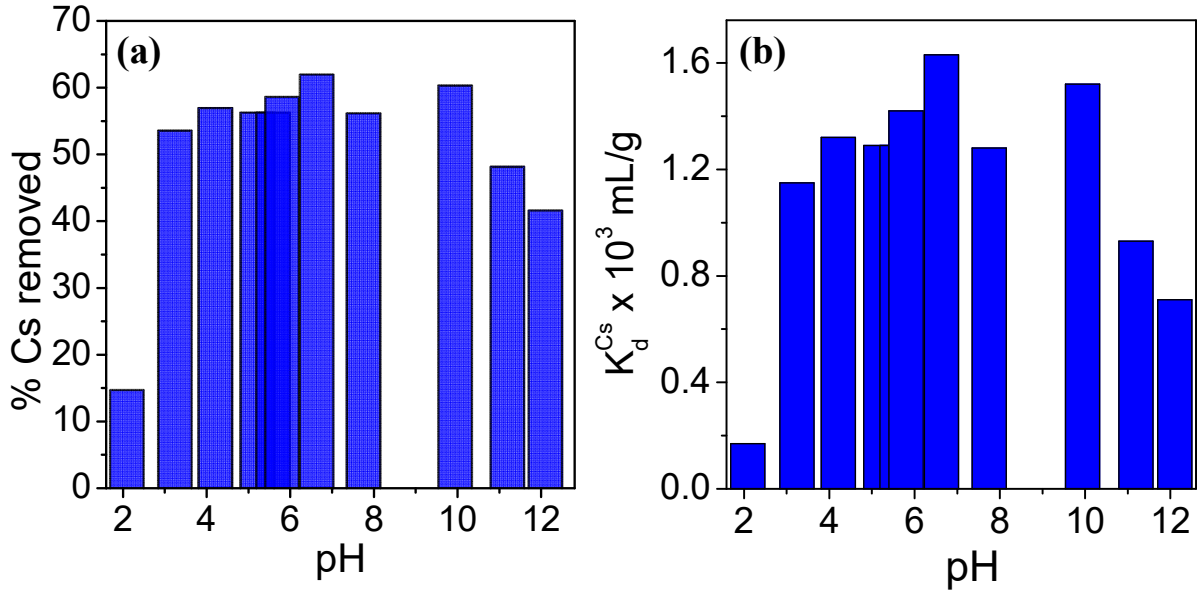

Figure 3.4.10. *pH Studies: (a) removal % of Cs^+ ions by K-MPS-1 and (b) distribution coefficient (K_d^{Cs}) of ion exchange.*

Further, K_d (~10^4 mL/g) remains unaffected even in presence of other hard mono and divalent ions (Na^+, Ca^{2+} and Mg^{2+}), which proves the selectivity of K-MPS-1 for Cs^+ uptake. Moreover, even in presence of Cl^-, Br^-, I^- and CO_3^{2-} sequestration of Cs remains unaffected (Table 3.4.10).The affinity between soft Cs^+ and soft S^{2-} is the reason for the selective sorption.

Table 3.4.9. Selected data for Cs^+ competitive ion-exchange experiments of K-MPS-1.

Exchange cations	V:m (mL/g)	Initial concentration (ppm)	Final concentration (ppm)	% Removal	K_d (mL/g)
Cs^+	1000	31.42 (Cs)	15.51 (Cs)	50.6 (Cs)	1.03 X 10^3 (Cs)
Na^+		20.41 (Na)	20.06 (Na)	1.71 (Na)	17.44 (Na)
Rb^+		25.43 (Rb)	22.86 (Rb)	10.11 (Rb)	112.42 (Rb)
Ca^{2+}		9.70 (Ca)	8.03 (Ca)	17.22 (Ca)	207.97 (Ca)
Mg^{2+}		0.29 (Mg)	0.22 (Mg)	22.50 (Mg)	290.18(Mg)

Table 3.4.10. Effect of anions on sequestration of Cs^+ from water.

Cesium salt used	C_o, (ppm)	C_e, (ppm)	q (mg/g)	K_d (mL/g)
CsCl	146.6	19.5	127.2	6.5 X 10^3
CsBr	155.9	23.4	132.5	5.6 X 10^3
CsI	148.8	22.7	126.1	5.6 X 10^3
Cs_2CO_3	150.2	26.3	123.9	4.7 X 10^3
m=0.010 g, V= 10 mL, V:m=1000 mL/g				

3.4.3.5. Low Concentration (ppb level) Cs^+ Capture

Cs^+ contamination is generally in very low concentration.[49] We have also carried out experiments in a low concentration ranging from 5-1000 ppb of Cs^+. Interestingly, we found that K-MPS-1 is able to remove ~85-95 % of Cs^+ in low concentration and K_d is unaltered which is tabulated in Table 3.4.3. Previously, KMS-1,[29] KMS-2[50] and FJSM-SnS[38] has shown excellent Cs^+ removal properties (Table 3.4.5). KMS-1 has lower capacity for Cs^+ removal as compared to that of present K-MPS-1. KMS-2 has higher Cs^+ removal capacity compared to K-MPS-1 and K_d value is 1.52 × 10^4 mL/g for Cs^+ uptake in presence of Sr^{2+} and Ni^{2+} at pH 10. Moreover, KMS-2 can operate in pH range of 3-10.[50] While FJSM-SnS showed higher Cs^+ removal capacity compared to K-MPS-1,

organic moieties like $[Me_2NH_2]^+$ or $[Me_3NH]^+$ are released during Cs^+ exchange in water, which is not desirable. K-MPS-1 is stable material which has reasonably good capacity, operates in 2-12 pH range with a high distribution coefficient ~10^4 mL/g which release non-toxic K^+ upon Cs^+ exchange.

3.4.3.6. Reversibility and Regeneration Study

Further, K-MPS-1 can be regenerated by treating with 2M KCl. We have used 10 mg of K-MPS-1 and added ~150 ppm of Cs^+ ion solution. Ion-exchange studies were performed to remove Cs^+ ions. The suspension was centrifuged and filtrate was measured for the final concentration of Cs^+ using ICP. The filtered product (Cs-MPS-1) was dried and washed with water. This product was then treated with different concentrations of KCl solution for 30 min. Then, it was filtered and the filtrate was analyzed using ICP for the amount of Cs^+ ion released in the solution (Table 3.4.11).

Table 3.4.11. *Reversibility studies of K-MPS-1 by using different concentration of KCl solutions.*

C_o, (ppm)	C_e, (ppm)	Cs^+ Removed from solution (%)	Cs^+ Adsorbed on K-MPS-1 (ppm)	Concentration of K^+ ions added to regenerate K-MPS-1 (ppm)	Cs^+ released, (ppm)	Released %
150.2	40.3	73.2	109.9	634.4	79.2	72.1
150.2	26.3	82.5	123.9	1692	109.7	88.5
m = 0.010 g, V = 10 mL KCl solution, V:m = 1000 mL/g						

We have observed that the amount of Cs released is more when the concentration of KCl in high. We have performed the regeneration investigation up to 4 cycles by using 2M KCl solution to regenerate K-MPS-1 and the same material is used again and again for removing Cs^+ ions (Table 3.4.12).

Table 3.4.12. Regeneration studies (4 cycles) of K-MPS-1 by using 2M KCl solution.

Cycle No.	C_o, (ppm)	C_e, (ppm)	% Removed	q (mg/g)
1	1070	568.5	46.9	250.7
2	1070	576.3	46.1	246.9
3	1070	605.7	43.4	226.1
4	1070	636.8	40.5	202.1
V:m = 500 mL/g				

3.4.4. Conclusions

K-MPS-1 is capable of selective, efficinet and reversible sequestration of Cs from the water. The sorption of Cs^+ by K-MPS-1 follows Langmuir model with a capacity of 333.1±17 mg/g. K-MPS-1 can retain the Cs caputuring ability even in extreme pH conditions and reaches ion-exchange equilibrium within a very short period of time (~15 min) with high distribution co-efficient. The sorption kinetics follows pseudo second order rate law. The adsorbed Cs^+ ion occupies the intercalation site of K^+ ions in K-MPS-1, which is proven by several characterization techniques such as PXRD, Raman, IR, XPS, zeta potential measuremnet and Langmuir isotherm model. Ion exchange is reversible and the K-MPS-1 can be regenerated by treating the Cs-MPS-1 with KCl solution. The higher K_d values originate from the favourable interaction between soft acidic Cs and soft Lewis basic S rather than just due to the space filling effects of the layered K-MPS-1. K_d for Cs capture remains unaffected even in presence of mono and di-valent cations (Na^+, Ca^{2+} and Mg^{2+}), which indicates the selectivity. K-MPS-1 can effectively remove upto 95% of Cs^+ from trace (ppb) concentrations of Cs^+ ions in water samples. Thus, K-MPS-1 can be considered as a cost-effective, inexpensive, environmental friendly and resuable ion-exchanger for remediation of radioactive $^{137}Cs^+$.

3.4.5. References

[1] World Statistics: Nuclear Energy Around the World, http:// www.nei.org/Knowledge-Center/Nuclear-Statistics/World- Statistics.

[2] V. N. Romanovskiy, I. V Smirnov, V. A. Babain, T. A. Todd, R. S. Herbst, J. D. Law, K. N. Brewer, *Solvent Extr. Ion Exch.* **2001**, *19*, 1.

[3] X. Liu, G. R. Chen, D. J. Lee, T. Kawamoto, H. Tanaka, M. L. Chen, Y. K. Luo, *Bioresour. Technol.* **2014**, *160*, 142.

[4] S. Yoshida, Y. Muramatsu, A. M. Dvornik, T. A. Zhuchenko, I. Linkov, *J. Environ. Radioact.* **2004**, *75*, 301.

[5] et. al. Yasunari T, Stohl A, Hayano R, Burkhart J, Eckhardt S, *Proc. Natl. Acad. Sci.* **2011**, *108*, 19530.

[6] M. Castrillejo, N. Casacuberta, C. F. Breier, S. M. Pike, P. Masqu, K. O. Buesseler, *Environ. Sci. Technol.* **2016**, *50*, 173.

[7] B. C. Bostick, M. A. Vairavamurthy, K. G. Karthikeyan, J. Chorover, *Environ. Sci. Technol.* **2002**, *36*, 2670.

[8] Z. Majidnia, A. Idris, *Chem. Eng. J.* **2015**, *262*, 372.

[9] M. Y. Khotimchenko, E. A. Podkorytova, V. V. Kovalev, E. V. Khozhaenko, Y. S. Khotimchenko, *J. Environ. Sci. Technol.* **2013**, *7*, 30.

[10] H. A. Omar, A. S. Abdel-Razek, M. S. Sayed, *Nat. Sci.* **2010**, *8*, 140.

[11] K. Shakir, M. Sohsah, M. Soliman, *Sep. Purif. Technol.* **2007**, *54*, 373.

[12] R. O. Abdel Rahman, H. A. Ibrahium, Y. T. Hung, *Water (Switzerland)* **2011**, *3*, 551.

[13] H. Luo, S. Dai, P. V. Bonnesen, A. C. Buchanan, J. D. Holbrey, N. J. Bridges, R. D. Rogers, *Anal. Chem.* **2004**, *76*, 3078.

[14] J. Lehto, R. Harjula, *Radiochim. Acta* **1999**, *86*, 65.

[15] D. V. Marinin, G. N. Brown, *Waste Manag.* **2000**, *20*, 545.

[16] S. Komarneni, R. Roy, *Nature* **1982**, *299*, 707.

[17] T. H. Wang, T. Y. Liu, D. C. Wu, M. H. Li, J. R. Chen, S. P. Teng, *J. Hazard. Mater.* **2010**, *173*, 335.

[18] J. Jang, D. S. Lee, *Ind. Eng. Chem. Res.* **2016**, *55*, 3852.

[19] S.-C. Jang, S.-B. Hong, H.-M. Yang, K.-W. Lee, J.-K. Moon, B.-K. Seo, Y. Huh, C. Roh, *Nanomaterials* **2014**, *4*, 894.

[20] H. Yang, L. Sun, J. Zhai, H. Li, Y. Zhao, H. Yu, *J. Mater. Chem. A*, **2014**, 2, 326.

[21] M. Ishfaq, H. Karim, M. Khan, *J. Radioanal. Nucl. Chem.* **1993**, *170*, 321.

[22] I. M. Ali, E. S. Zakaria, H. F. Aly, *J. Radioanal. Nucl. Chem.* **2010**, *285*, 483.

[23] A. Dyer, M. Pillinger, J. Newton, R. Harjula, T. Möller, S. Amin, *Chem. Mater.* **2000**, *12*, 3798.

[24] B. Aguila, D. Banerjee, Z. Nie, Y. Shin, S. Ma, P. K. Thallapally, *Chem. Commun.* **2016**, *52*, 5940.

[25] Z. Du, M. Jia, X. Wang, *J. Radioanal. Nucl. Chem.* **2013**, *298*, 167.

[26] A. Nilchi, R. Saberi, S. Rasouli Garmarodi, A. Bagheri, *Appl. Radiat. Isot.* **2012**, *70*, 369.

[27] B. J. Riley, D. A. Pierce, J. Chun, J. Matyáš, W. C. Lepry, T. G. Garn, J. D. Law, M. G. Kanatzidis, *Environ. Sci. Technol.* **2014**, *48*, 5832.

[28] J. Qian, J. Ma, W. He, D. Hua, *Chem. Asian J.* **2015**, *10*, 1738.

[29] M. J. Manos, M. G. Kanatzidis, *J. Am. Chem. Soc.* **2012**, *134*,16441.

[30] N. Ding, M. G. Kanatzidis, *Nat. Chem.* **2010**, *2*, 187.

[31] M. J. Manos, M. G. Kanatzidis, *J. Am. Chem. Soc.* **2009**, *131*, 6599.

[32] M. J. Manos, N. Ding, M. G. Kanatzidis, *Proc. Natl. Acad. Sci.* **2008**, *105*, 3696.

[33] M. J. Manos, K. Chrissafis, M. G. Kanatzidis, *J. Am. Chem. Soc.* **2006**, *128*, 8875–.

[34] M. J. Manos, R. G. Iyer, E. Quarez, J. H. Liao, M. G. Kanatzidis, *Angew. Chemie Int. Ed.* **2005**, *44*, 3552.

[35] M. J. Manos, C. D. Malliakas, M. G. Kanatzidis, *Chem. Eur. J.* **2007**, *13*, 51.

[36] N. Ding, M. G. Kanatzidis, *Chem. Mater.* **2007**, *19*, 3867.

[37] M. J. Manos, M. G. Kanatzidis, *J. Am. Chem. Soc.* **2009**, *131*, 6607.

[38] X.-H. Qi, K.-Z. Du, M.-L. Feng, J.-R. Li, C.-F. Du, B. Zhang, X.-Y. Huang, *J. Mater. Chem. A* **2015**, *3*, 5665.

[39] D. Sarma, C. D. Malliakas, K. S. Subrahmanyam, S. M. Islam, M. G. Kanatzidis, *Chem. Sci.* **2016**, *7*, 1121.

[40] N. (CY) Mercouri G. Kanatzidis, Wilmette, IL (US); Joshua L. Mertz, Evanston, IL (US); Emmanouil Manos, *Chalcogenide Compounds for the Remediation of Nuclear and Heavy Metal wastes,US Patent, US2011290735-A1.*, **2011**.

[41] R. Brec, *Solid State Ionics* **1986**, *22*, 3.

[42] W. Klingen, R. Ott, H. Hahn, *Zeitschrift für Anorg. und Allg. Chemie* **1973**, *396*, 271.

[43] R. Clement, *J. Chem. Soc., Chem. Commun.*, **1980**, 647.

[44] R. Clement, J. J. Girerd, I. Morgenstern-Badarau, *Inorg. Chem.* **1980**, *19*, 2852.

[45] Y. Mathey, R. Clement, C. Sourisseau, G. Lucazeau, *Inorg. Chem.* **1980**, *19*, 2773.

[46] P. Fuentealba, C. Cortés, N. Audebrand, E. Le Fur, V. Paredes-García, D. Venegas-Yazigi, J. Manzur, E. Spodine, *Dalt. Trans. Commun. Cite this Dalt. Trans* **2015**, *44*, 12493.

[47] I. Lagadic, R. Clément, *Microsc. Microanal. Microstruct.* **1993,** *4*, 453.

[48] T. W. Weber, R. K. Chakravorti, *AIChE J.* **1974**, *20*, 228.

[49] T. Mizuno, H. Kubo, *Sci. Rep.* **2013**, *3*, 1742.

[50] J. L. Mertz, Z. H. Fard, C. D. Malliakas, M. J. Manos, M. G. Kanatzidis, *Chem. Mater.* **2013**, *25*, 2116.

[51] I. M. El-Naggar, *Adv. Chem. Eng. Sci.* **2012**, *2*, 166.

[52] T. Vincent, C. Vincent, Y. Barre, Y. Guari, G. Le Saout, E. Guibal, *J. Mater. Chem. A* **2014**, *2*, 10007.

[53] H. Yang, M. Luo, L. Luo, H. Wang, D. Hu, J. Lin, X. Wang, Y. Wang, S. Wang, X. Bu, et al., *Chem. Mater.* **2016**, *28,* 8774.

[54] B. Zhang, M. L. Feng, H. H. Cui, C. F. Du, X. H. Qi, N. N. Shen, X. Y. Huang, *Inorg. Chem.* **2015**, *54*, 8474.

[55] D. Yang, S. Sarina, H. Zhu, H. Liu, Z. Zheng, M. Xie, S. V Smith, S. Komarneni, *Angew. Chemie Int. Ed.* **2011**, *50*, 10594.

PART 4

Heterostructures of Halide Perovskites and their Optical Properties

Chapter 4.1

Charge Transfer in the Heterostructure of $CsPbBr_3$ Nanocrystals with Nitrogen-Doped Carbon Dots

*Paper based on this has been published as **E. Rathore**, K. Maji, D. Rao, B. Saha, and K. Biswas, J. Phys. Chem. Lett. **2020**, 11, 19, 8002-8007.*

Chapter 4.1

Charge Transfer in the Heterostructure of $CsPbBr_3$ Nanocrystals with Nitrogen-Doped Carbon Dots†

Summary: *Heterostructures of inorganic halide perovskites with mixed-dimensional inorganic nanomaterials have shown great potential not only in the field of optoelectronic energy devices and photocatalysis but also for improving our fundamental understanding of the charge transfer across the heterostructure interface. Herein, we present for the first time the heterostructure integration of the $CsPbBr_3$ nanocrystal with an N-doped carbon dot. We explore the photoluminescence (PL) and photoconductivity of the heterostructure of $CsPbBr_3$ nanocrystals and N-doped carbon dots. PL quenching of $CsPbBr_3$ nanocrystals with the addition of N-doped carbon dots was observed. The photoexcited electrons from the conduction band of $CsPbBr_3$ are trapped in the N-acceptor state of N-doped carbon dots, and the charge transfer occurs via quasi type II-like electronic band alignment. The charge transfer in the halide perovskite-based heterostructure should motivate further research into the new heterostructure synthesis with perovskites and the fundamental understanding of the mechanism of charge/energy transfer across the heterostructure interface.*

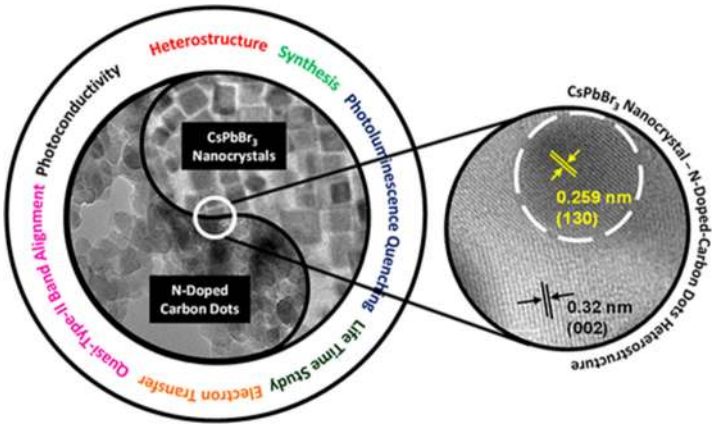

†*Paper based on this has been published as* ***E. Rathore****, K. Maji, D. Rao, B. Saha, and K. Biswas, J. Phys. Chem. Lett.* ***2020****, 11, 19, 8002-8007.*

4.1.1. Introduction

Recent advances in all-inorganic halide perovskites have created sensation in the diverse optoelectronic applications like photovoltaics, photodetectors, light-emitting diodes and lasers.[1-10] The high absorption coefficient, wide absorption range, high photoluminescence quantum efficiencies (>90%) and long electron-hole diffusion lengths of halide perovskites make them attractive in these fields.[6-17] However, diminution in dimensionality from bulk perovskites to nanocrystals (zero-dimensional, 0D) and other low-dimensional (1D and 2D) structures have persuaded more attention due to their tunable band gap, optoelectronic properties, etc. [18,19]

Parallelly in the last decade, two dimensional (2D) materials like graphene, phosphorene, MoS_2 and MXenes have gained significant attention in optoelectronics due to layer dependent electronic structure and tunable electronic gap through doping.[20-25] Recently, mixed dimensional nano-heterostructures of different inorganic compounds demonstrate great potential to discover new materials and properties.[1,26-28] Enhancement in optoelectronic properties, photo-response and efficient CO_2 reduction capability has been achieved by the formation of heterostructures between 2D layered materials (graphene oxide, MXene and phosphorene) and $CsPbBr_3$ nanocrystals (NCs).[29-33] Heterostructure of metal chalcogenide semiconductors like ZnS, CdS, CdSe, PbS, PbSe with $CsPbBr_3$ and $CsPbI_3$ NCs exhibited type I or type II band alignments, which showed tremendous impact on tuning the photo-responsivity and luminescent properties.[34-38] However, the heterostructure integration of $CsPbBr_3$ nanocrystals with the 0D carbon dots has not been explored so far. 0D carbon dots (CDs) have unique electrical, optical and chemical properties.[39-41] By doping with various elements (e.g., nitrogen, boron, or sulphur), the optical properties of CDs can be modulated.[42] Interestingly, N-doping in CDs produced electron accepting trap states, which enhanced the charge separation as well as quantum efficiency.[43-47] Hence, N-doped CDs has attracted attention in diverse fields such as in electrocatalytic oxygen reduction reaction,[48] light-driven water splitting,[49] and photocatalysis.[50]

Here in this chapter, we have synthesized the heterostructure of $CsPbBr_3$ nanocrystals (NCs) with N- doped carbon dots (CD) and investigated the charge transfer between the two systems. $CsPbBr_3$ NCs anchored on the N-doped CDs *via* H-bonding interactions of $-NH_2$ /-COOH group present in oleylamine/oleic acid ligands on $CsPbBr_3$

surface with the functional groups (C=O, C-O, O-H, -NH_2, O=C-OH, etc) on the N-doped CDs. N-doping forms the trap states below the conduction band of CD. We noted momentous quenching of photoluminescence of $CsPbBr_3$ within the heterostructure systems. To explore the mechanism of PL quenching in the heterostructure, we have carried out time-resolved PL spectroscopy and measured the photoconductivity of $CsPbBr_3$-N-doped CD device. PL quenching occurs due to the electron transfer from the conduction band of halide perovskite to the N-acceptor state of the N-doped CDs *via* a quasi-type-II electronic band alignment.

4.1.2. Methods

4.1.2.1. Reagents. Cesium carbonate (Cs_2CO_3, 99.9%, Sigma-Aldrich), lead (II) bromide ($PbBr_2$, 99.9%, Sigma-Aldrich), oleic acid (OA, tech. 90%, Sigma-Aldrich), oleylamine (OAm, tech. 70%, Sigma-Aldrich), 1-octadecene (ODE, tech. 90%, Sigma Aldrich), and toluene (AR, 99.0%, SDFCL), citric acid (99.5%, Sigma-Aldrich), thiourea (99%, Sigma-Aldrich), dialysis membrane were used for the synthesis without further purification.

4.1.2.2 Synthesis.

4.1.2.2.1. Synthesis of Cs-Oleate. In a 50 mL 3-necked round-bottom flask, 410 mg (1.26 mmol) Cs_2CO_3 and 20 mL ODE were taken and heated at 120 °C with continuous stirring under vacuum for 1 h to get a homogeneous solution. After 1 h, 1.30 mL of OA was added, and the solution was kept for another 30 min at the same condition. The vacuum was replaced with nitrogen atmosphere and kept for 5 min to get a clear Cs-oleate solution. This Cs-oleate solution was stored at room temperature under nitrogen atmosphere for further use.

4.1.2.2.2. Synthesis of $CsPbBr_3$ nanocrystals. In a typical synthesis, 0.376 mmol (137 mg) of $PbBr_2$ and 10 mL of ODE were taken in a 25 mL 3-necked RB flask and dried under vacuum for about 1 h. Then the RB is filled with N_2 and 1 mL each of OA and OAm were added. Again, the flask was kept under vacuum until $PbBr_2$ dissolved and a transparent solution is formed. The reaction temperature is raised to 140°C under N_2 atm and 0.8 ml of previously heated (at 100°C) Cs-oleate solution was swiftly injected. The reaction mixture become fluorescent green and after 5 min the

reaction was quenched by ice bath. The synthesized $CsPbBr_3$ NCs were then washed with toluene and precipitated by centrifugation at 8000 rpm for 15 min, followed by dispersing the products in toluene for further studies.

4.1.2.2.3. Synthesis of Nitrogen-Doped Carbon Dots. 1g of citric acid and 500 mg of urea were dissolved in 25 mL of distilled water. The solution mixture was taken to an autoclave and heated at 160°C for 6 h. The prepared reaction mixture was centrifuged at 9000 rpm for 10 min to discard the larger particles. Then, the dispersion solution was dialyzed against pure water for 24 h. At the end, the final dispersed solution was vacuum- dried at 70 °C for 3 days.

4.1.2.3. Powder X-ray Diffraction. Powder X-ray diffraction for all of the samples were recorded using a Cu K_α (λ = 1.5406 Å) radiation on a Bruker D8 diffractometer.

4.1.2.4. Transmission Electron Microscopy. The transmission electron microscopy (TEM) images of the synthesized $CsPbBr_3$ NCs and CDs were taken using a JEOL (JEM3010) TEM instrument (300 kV accelerating voltage) fitted with a Gatan CCD camera and also with a FEI TECNAI G2 20 STWIN TEM instrument (operating at 200 kV).

4.1.2.5 Fourier Transform Infrared Spectroscopy (FTIR). FTIR spectra were recorded in the range of 400-4000 cm^{-1} by using a Bruker Optics Alpha-P FTIR spectrophotometer equipped with an attenuated total reflectance (ATR) module.

4.1.2.6. X-ray Photoelectron Spectroscopy (XPS). The measurement was done on AXIS ULTRA in the range of 0-1100 eV.

4.1.2.7. Optical Measurement. Electronic absorption spectra were recorded using Perkin-Elmer Lambda 900. A FluoroMax-4 spectrofluorometer (Horiba JobinYvon Inc.) with a 5 nm slit width was used to record the photoluminescence (PL) spectrum.

4.1.2.8. Photoluminescence (PL) Quenching Study. 2 mL $CsPbBr_3$ NCs solution in toluene with 1.97 x 10^{-6} M concentration was initially taken in a PL-cuvette and PL spectra was recorded. Then 20 µl solution in toluene of dispersed N doped CDs ((12.37 - 92.59 mg/L) was added to it in each step and after the sonication at room temperature PL spectra was recorded.

4.1.2.9. Fluorescent Lifetime Measurement. The time-correlated single photon counting (TCSPC) method was implemented during the fluorescence lifetime measurements using the FluoroCube (Horiba Jobin Yvon, formerly IBH product) with a 373 nm LED excitation source. The TBX-04 picosecond photon-detection module was used to detect the fluorescence signal. The DAS 6 decay analysis software package (HORIBA Jobin Yvon IBH) was used to analyze the fluorescence decay, where the best decay curve fit was achieved by monitoring the reduced χ^2 values and the weighted residuals. A multi-exponential decay model was used to fit the life-time data. We obtained reduced χ^2 values in the range 0.9-1.2.

$$I(t) = \alpha_1 e^{-t/\tau_1} + \alpha_2 e^{-t/\tau_2} + \alpha_3 e^{-t/\tau_3} \quad \text{Eq. 4.1.1}$$

$$\tau_{avg} = \sum_i \alpha_i \, \tau_i^2 \, / \sum_i \alpha_i \, \tau_i \quad \text{Eq. 4.1.2}$$

4.1.2.10. Determination of Molar Extinction Coefficient ($\boldsymbol{\varepsilon}$). To determine ε, the absorption of dilute solution of $CsPbBr_3$ and CDs was collected with different concentrations. ε was then calculated using Beer-Lambert Law: $A = \varepsilon \times C \times L$, where, A is the absorbance, and L is the optical path length (1 cm) taken from cuvette dimension.

4.1.2.11. Current-Voltage (I-V) Measurement. This part of work was done under collabotation with Dr. Bivas Saha and Ms. Dheemahi Rao. The samples were made into square shaped pellets of uniform size and gold contacts were deposited using e-beam evaporation method. The I-V measurement was performed using Kiethley-2450 source meter. The Xe arc lamp (Oriel Newport) was used as light source to study the photo enhancement in current. The lamp was set to 150W and placed 20 cm away from the samples during measurement.

4.1.2.12. Electrochemical Measurements. To calculate the electrochemical band edge energies for N-doped CD and $CsPbBr_3$, the cyclic voltammogram was recorded under non-aqueous conditions. The following formula was

utilized to determine the experimental electrochemical HOMO and LUMO levels in terms of eV unit:

$$E\ (LUMO) = -e\ [E_{red}^{onset} + 4.4]$$
$$E\ (HOMO) = E\ (LUMO) - E_{0\text{-}0}$$

where E_{0-0} represent the 0–0 energy, which is defined as the lowest energy transition and that we can estimate from UV–vis and fluorescence emission spectra. We obtained a value 2.37 eV for $E_{0\text{-}0}$ corresponding to 523 nm for $CsPbBr_3$.

For $CsPbBr_3$,

$$E\ (CB) = -e\ [-0.71 + 4.4] = -3.69\ eV$$
$$E\ (VB) = [-3.69\ -2.37]\ eV = -6.06\ eV$$

We obtained of 2.32 eV, 3.65 eV and 4.15 eV for E_{0-0} corresponding to 534 nm, 339 nm and 298 nm for N-doped CDs.

For N-doped CDs,

$$E_{\pi^*}\ (LUMO) = -e\ [-0.73 + 4.4] = -3.67\ eV$$
$$E_n^{C=N}\ (HOMO) = [-3.67\ -2.32]\ eV = -5.99\ eV$$
$$E_n^{C=O}\ (HOMO\text{-}1) = [-3.67\ -3.65]\ eV = -7.32\ eV$$
$$E_{\pi}\ (HOMO\text{-}2) = [-3.67\ -4.15]\ eV = -7.82\ eV$$

4.1.3. Results and Discussion

$CsPbBr_3$ nanocrystals (NCs) were synthesized by solution-based hot-injection method with Cs-oleate and $PbBr_2$ as precursors.[3] Powder X-ray diffraction (PXRD) pattern of synthesized $CsPbBr_3$ NCs matched well with the simulated orthorhombic phase (*Pbnm*) (see Figure 4.1.1a). The nearly monodispersed square-shaped morphology of $CsPbBr_3$ NCs with average particle size of 15.2 nm can be visualized in the transmission electron microscopy (TEM) image (Figure 4.1.1c). These nanocrystals of $CsPbBr_3$ are well dispersed in toluene but unstable in water. To achieve successful heterostructure integration of $CsPbBr_3$ NC with 0D carbon dots, the challenge was to

select a suitable common solvent as carbon dots are usually dispersible in aqueous medium.

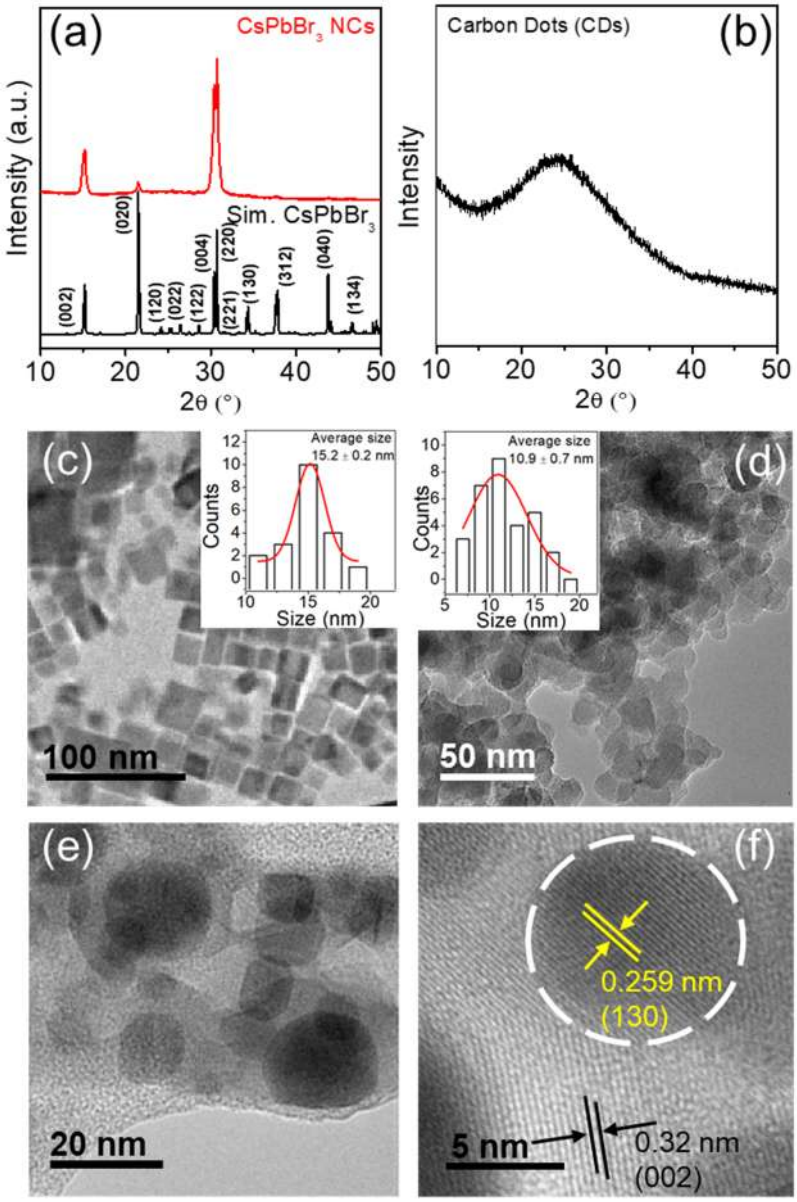

Figure 4.1.1. *Powder X-ray diffraction (PXRD) and TEM images of (a, c) $CsPbBr_3$ nanocrystals (NCs) and (b, d) N-doped carbon dots (CDs), respectively. The inset shows the particle size distribution for $CsPbBr_3$ NCs and N-doped CDs and the red line indicates Gaussian fitting. (e) TEM (f) HRTEM of heterostructure of $CsPbBr_3$ NCs -N-doped CDs system. The white circle (darker contrast) denotes $CsPbBr_3$ NC with 0.259 nm d-spacing and light contrast region corresponds to N-doped CDs with 0.32 nm d-spacing.*

Hence, we have synthesized N-doped carbon dots (CDs) with controlled amino-passivated surfaces, which could be dispersed in toluene as well. The N-doped CDs were synthesized by using hydrothermal reaction with citric acid and urea as precursors.The product of the hydrothermal reaction was centrifuged at 9000 rpm to discard the larger particles. Then, the dispersion solution was dialyzed against distilled water for 24 h. At the end, the final dispersed solution was vacuum-dried. PXRD pattern of CD samples show broad peak centered at 24.5° (Figure 4.1.1b), indicating disordered graphitic layers [i.e. (002) planes] in the CDs.[45]

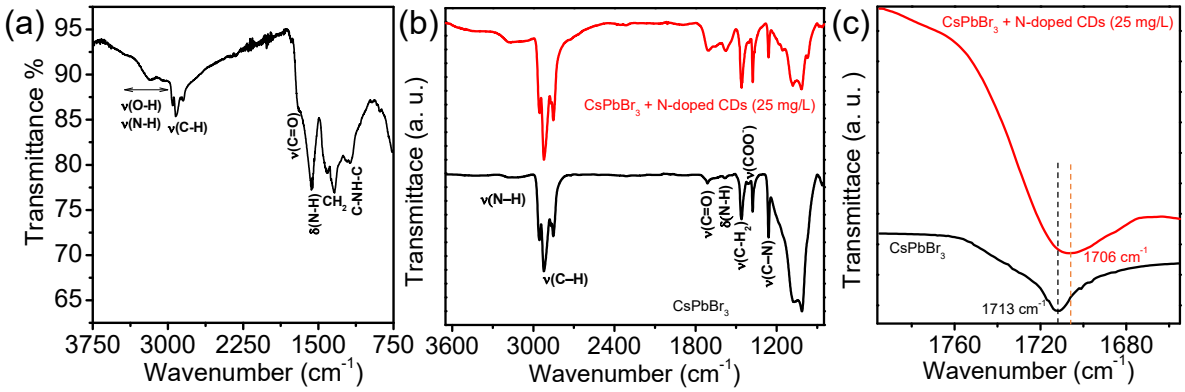

Figure 4.1.2. *FTIR spectrum of (a) N-doped CDs, (b) $CsPbBr_3$ (black) and heterostructure of $CsPbBr_3$ and N-doped CDs (red), and (c) zoomed version of ν(C=O) region.*

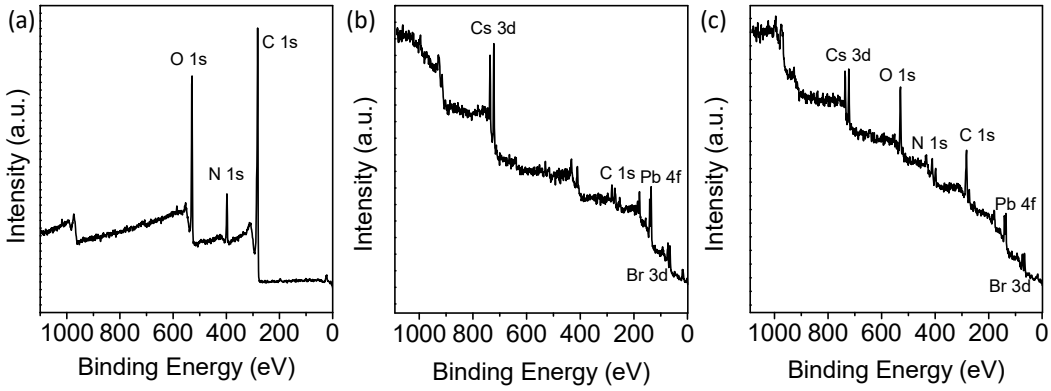

Figure 4.1.3. *XPS full survey scan of (a) N-doped CDs, (b) $CsPbBr_3$ and (c) heterostructure of $CsPbBr_3$ and N-doped CDs.*

In the Fourier transform infrared spectroscopy (FTIR) spectrum (Figure 4.1.2a), the intensity of N-H peak at 1572 cm^{-1} is stronger than C=O peak at 1698 cm^{-1}, signifying that the synthesized CDs have more amino groups on the surface of CDs.[44] The XPS peaks at 398.2 and 399.4 eV for N1s shown in Figure 4.1.4b,c and 4.1.5c,f reveal that nitrogen presents in the form of $(C)_3$-N (sp^3) and N-H (sp^3), respectively, which confirm the N doping in CDs. The N-doped CDs were found to exist as clusters and have nearly uniform size distribution with an average diameter of 10.9 nm (see TEM image in Figure 4.1.1d). To form the heterostructures between $CsPbBr_3$ NCs and N-doped CDs, the toluene dispersed N-doped CDs with different concentrations were added to the $CsPbBr_3$ solution in toluene and the mixture was sonicated at room temperature to induce anchoring of $CsPbBr_3$ NCs with N-doped CDs. PXRD of the integrated heterostructure shows the presence of both the $CsPbBr_3$ NCs and the N-doped CDs (Figure 4.1.4).

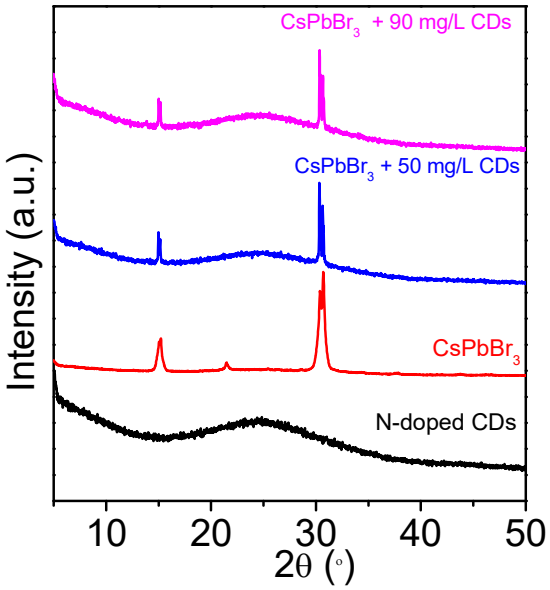

Figure 4.1.4. *PXRD of N-doped CDs, $CsPbBr_3$ and heterostructure of $CsPbBr_3$ NCs -N- doped CDs system.*

The assembly of $CsPbBr_3$ NCs on N-doped CDs can also be seen from the TEM image (Figure 4.1.1e). The high-resolution TEM (HRTEM) image of the heterostructure shows the (130) lattice planes of $CsPbBr_3$ NCs with interplanar distance of 0.259 nm, and (002) graphitic planes with 0.32 nm distance for N-doped CDs (Figure 4.1.1f). Further, we have measured the FTIR spectra of pure $CsPbBr_3$ NCs and the

heterostructure of $CsPbBr_3$ NCs-N-doped CDs (Figure 4.1.2b, c). FTIR of $CsPbBr_3$ NCs is dominated mainly by the ν_{C-H} (~ 3000 cm^{-1}), $\nu_{C=O}$ (~1715 cm^{-1}), ν_{N-H} (~3139 cm^{-1}) and ν_{COO-} (~1407 cm^{-1}) of oleylamine and oleic acid (Figure 4.1.2b).[51-53] Formation of the heterostructures between $CsPbBr_3$ NCs and N-doped CDs is possibly due to the H-bonding interactions of $-NH_2$ / -COOH group present in oleylamine/ oleic acid capping ligands on the surface of $CsPbBr_3$ NCs with the functional groups (C=O, C-O, O-H,-NH_2, O=C-OH, etc.) of N-doped CDs. The characteristic shift of $\nu_{C=O}$ mode from oleic acid on $CsPbBr_3$ NCs (1713 cm^{-1}) toward the lower wavenumber at 1706 cm^{-1} in $CsPbBr_3$-N-doped CDs heterostructure along with the mode broadening imply the possible H-bonding interaction in the heterostructures (Figure 4.1.2c). We have also performed the XPS of $CsPbBr_3$ and $CsPbBr_3$-N-doped CDs heterostructure, which are represented in Figure 4.1.4, and 4.1.6. In Figure 4.1.5b, we observed a slight shift in C-O peak for O1s from 531.0 eV for pure N-doped CDs to 530.7 eV for the heterostructure. For N1s, N-H peak shifts from 399.4 eV for pure N-doped CDs to 398.95 eV for the heterostructure (Figure 4.1.5c, f). These slight lower shifts in binding energy are an indicative of H-bonding interaction present in the heterostructure.[54]

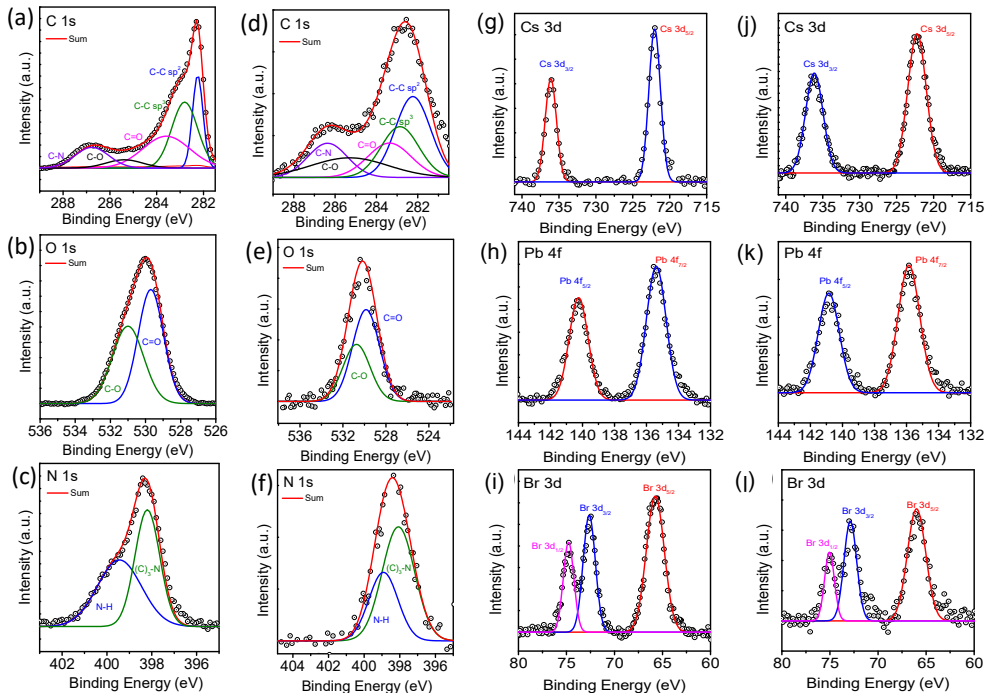

Figure 4.1.5. *XPS high resolution scan of C1s, N1s, and O1s for N-doped CDs (a, b, c) and the heterostructure of $CsPbBr_3$ and N-doped CDs (d, e, f), Cs3d, Pb4f, and Br3d for pristine $CsPbBr_3$ (g, h, i) and the heterostructure of $CsPbBr_3$ and N-doped CDs (j, k, l).*

To visualize further the interaction between the $CsPbBr_3$ and N-doped CDs, first the optical properties of N-doped CDs were studied using UV-Vis absorption and photoluminescence (PL) spectroscopy (see Figure 4.1.7). In the electronic absorbance spectrum of N-doped CD in aqueous solution, we observed sp^2-carbon network band at ~220 nm (π - π^* transition), absorbance band in 325-400 nm range corresponding to n - π^* transition of C=O and shoulder band in 550-620 nm range attributed to n - π^* transition of C=N arising from functional groups present on the surface of N-doped CDs (Figure 4.1.7a).[47,55]

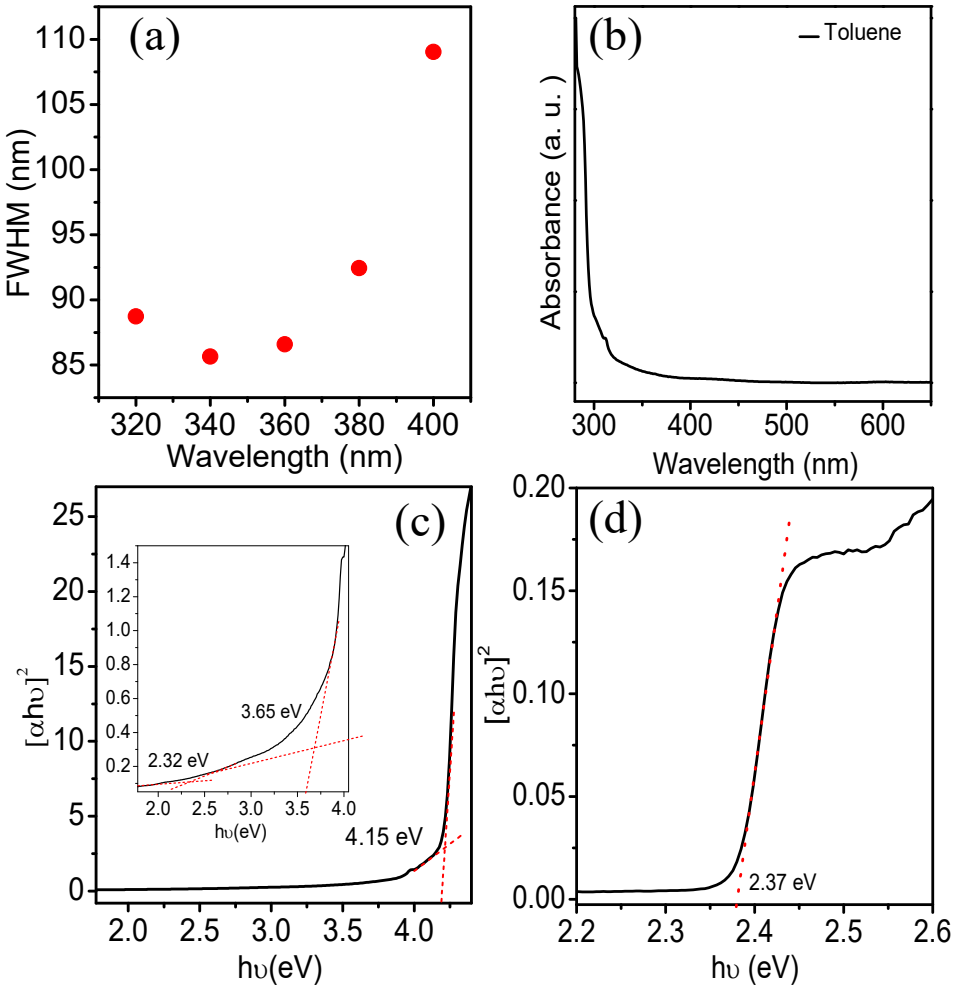

Figure 4.1.8. *(a) Change in peak-width (FWHM) of PL peak as a function of excitation wavelength. (b) Absorbance of N-doped CDs in toluene. Tauc plot from the electronic absorption data with band energies for (c) N-doped CDs (inset shows the zoom version) and (d) $CsPbBr_3$ NCs.*

PL spectra of N-doped CDs slightly vary with the excitation wavelength (from 320 to 400 nm), in which the emission maxima is red-shifted with increasing the excitation wavelength (Figure 4.1.7a).[39,40,56,57] Further, the peak-width of PL emission is increased with increasing the excitation wavelength (Figure 4.1.8a), which is attributed to the activation of trap states.[58] The N-doping leads to electron trapping N-surface states in CDs (below conduction band) which accelerates high yield of radiative recombination.[44,55] Figure 4.1.7b shows absorption and PL spectra of $CsPbBr_3$ NCs with absorption band peak at 507 nm and band edge emission at 517 nm. The absorption edges estimated from Tauc plots of the absorption data taken in toluene medium are 2.32 eV, 3.65 eV, 4.15 eV for N-CDs and 2.37 eV for $CsPbBr_3$ (Figure 4.1.8 b-d). Electronic absorbance and PL spectra of $CsPbBr_3$ NCs with different concentration of N-doped CDs in toluene are shown in Figure 4.1.8c and d, respectively. The concentration of $CsPbBr_3$ (1.97×10^{-6} M) is kept constant and different concentration of N-doped CDs is added. Absorbance retained the feature of $CsPbBr_3$ NCs with the successive addition of N-CDs, while PL intensity gradually decreases with slight blue shift. The formation of heterostructure $CsPbBr_3$ with the N-doped CDs leads to the quenching of PL and may be attributed to the transfer of photo-generated carriers between them. A maximum PL quenching efficiency of about 95% was achieved when 92.59 mg/L of N-doped CDs were added to 1.97×10^{-6} M $CsPbBr_3$ solution.

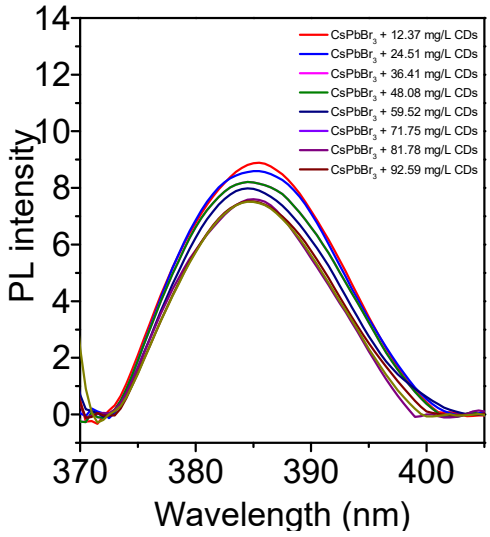

Figure 4.1.9. *Zoomed PL spectra (focusing N doped CD emission) of the heterostructure with variable concentrations of carbon dots (12.37-92.59) mg/L in 1.97 x 10^{-6} M $CsPbBr_3$ NCs in toluene medium.*

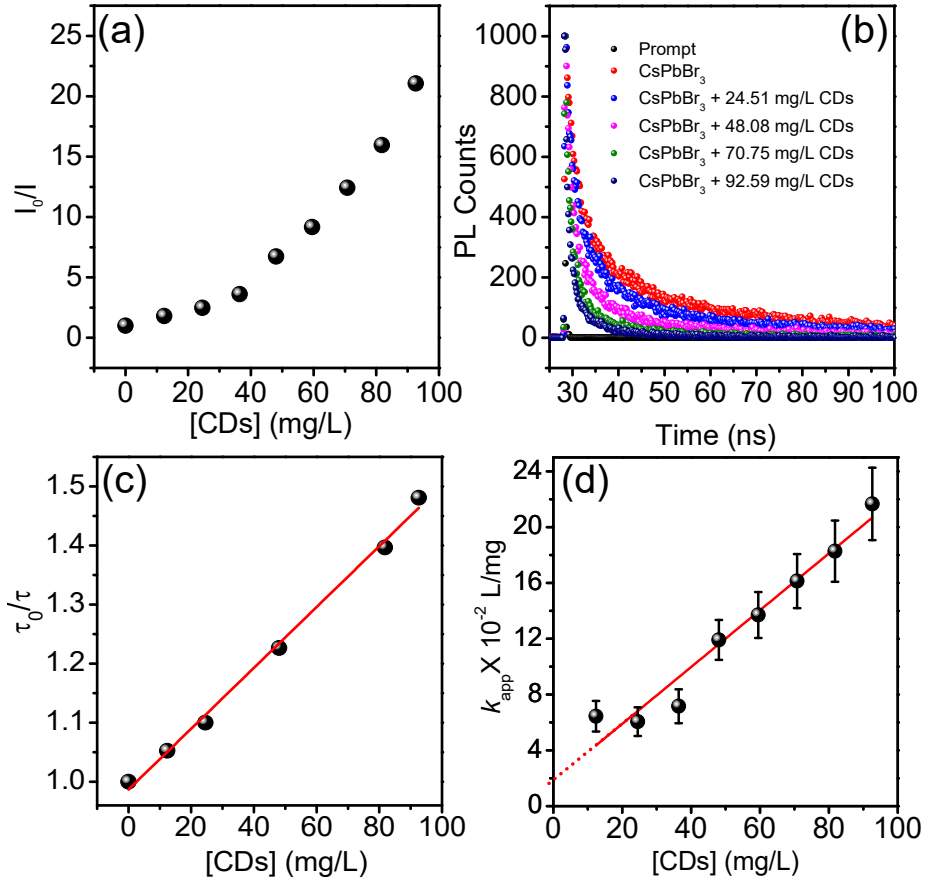

Figure 4.1.10. *(a) Stern-Volmer plot for PL quenching of $CsPbBr_3$ NCs in the presence of varying concentration of N-doped CDs. (b) Time resolved PL spectra of 1.97 x 10^{-6} M $CsPbBr_3$ NCs in toluene medium with different concentration of N-CDs. (c) Stern-Volmer plot in terms of photoluminescence lifetime of $CsPbBr_3$ NCs in the presence of N-CDs. (d) Modified Stern-Volmer plot showing the variation of k_{app} as a function of varying concentration of N-CDs.*

The nature of quenching processes that leads to the reduction in PL intensity in general can be governed by various factors like collision (dynamic quenching), formation of complexes in the ground state (static quenching), energy transfer and charge transfer reaction.[29] To understand the mechanism in the present case, we performed well-known Stern–Volmer analysis (Figure 4.1.10a). The non-linear nature of the plot follows the modified Stern-Volmer equation, Eq. 1, which shows upward curvature due to $[Q]^2$ term in Eq. 2.

$$\frac{I_O}{I} = (1 + k_s[Q])(1 + k_D[Q]) \qquad \text{Eq. 4.1.1}$$

$$\frac{I_O}{I} = 1 + (k_s + k_D)[Q] + k_s k_D [Q]^2 \quad \text{Eq. 4.1.2}$$

$$\frac{I_O}{I} = 1 + k_{app}[Q] \quad \text{Eq. 4.1.3}$$

$$k_{app} = k_S + k_D + k_S k_D[\mathrm{Q}] \quad \text{Eq. 4.4.4}$$

where I_O and I are the PL intensities of $CsPbBr_3$ NCs in the absence and presence of N-doped CDs, respectively, k_S and k_D are static and dynamic quenching constant, [Q] is the concentration of the N-doped CDs.

This upward curvature might be attributed to the presence of both dynamic and static quenching mechanism, thereby we observe fall in the PL intensity. Nevertheless, the measurement of PL lifetime is more robust than the PL intensity as it depends on the intensity of excitation and not on the concentration in $CsPbBr_3$-N-CD heterostructure system. Thus, we performed time-resolved PL spectroscopy. PL decay of $CsPbBr_3$-N-CD heterostructure could be fitted with the use of multicomponent decay kinetics (Figure 4.1.10b) and the fitting parameters are represented in Table 4.1.1.

Table 4.1.1. *Photoluminescence decay analysis of $CsPbBr_3$ NCs and N-doped CD heterostructure.*

Concentration of CDs in $CsPbBr_3$ solution (mg/L)	τ_1 (ns)	τ_2 (ns)	τ_3 (ns)	α_1	α_2	α_3	τ_{avg} (ns)
0	20.6	125.4	2.7	40.41	45.25	14.34	111.3
12.37	19.6	117.4	3.1	39.15	42.93	17.92	103.5
24.51	15.4	99.5	2.4	40.87	40.52	18.60	48.6
36.41	10.8	66.9	1.7	39.77	41.46	18.78	58.8
48.08	9.2	59.2	1.4	42.25	34.28	23.47	50.5
59.52	7.49	45.3	1.0	40.53	30.08	29.38	37.7
81.78	3.22	18.5	0.5	43.68	28.77	27.55	15.0
92.59	2.75	15.8	0.4	42.96	26.28	30.76	12.6

The $CsPbBr_3$-N-CD heterostructure decayed relatively faster than pristine $CsPbBr_3$ with average PL lifetime decreasing from 111.3 ns to 12.6 ns upon addition of 92.59 mg/L CD solution (Figure 4.1.10b). This difference between τ_{avg} of $CsPbBr_3$-N-

doped CD heterostructure and pristine $CsPbBr_3$ indicates the origin of non-radiative pathway from the substantial electronic interaction between $CsPbBr_3$ NCs and π electrons of N-doped CDs.[29] In case of pure static quenching, the lifetime should be unaffected in the presence of N-doped CD quenchers. The slope of τ_o/τ with [Q] in Figure 4. 3c gives dynamic quenching constant, k_D value as 0.51×10^4 μL/mg from Eq. 5.

$$\frac{\tau_o}{\tau} = 1 + k_D[Q] \qquad \text{Eq. 4.4.5}$$

where τ_o and τ are the excited state lifetimes of $CsPbBr_3$ in the absence and presence of N-CD, respectively. We have further estimated the static quenching constant, k_s as 1.32×10^4 μL/mg by plotting k_{app} with [Q] by using Eqs. 3 and 4 (see Figure 4.1.10d).

PL quenching is usually ascribed to either a non-radiative energy transfer or electron transfer mechanism. During the non-radiative energy transfer, generally intensity of the donor emission decreases and acceptor emission increases. As evidenced from both Figure 4.1.7d and Figure 4.1.9, both the $CsPbBr_3$ NC and N-doped CD emissions show decrease in intensity due to lack of overlap between the emission spectra of $CsPbBr_3$ and CDs, which rules out the possibility of energy transfer.[29] Thus, photo-induced electron transfer from the photoexcited $CsPbBr_3$ NCs to N-doped CDs is the most probable mechanism that is involved in the quenching of the PL of $CsPbBr_3$ NC. The photoexcited electrons can be injected from $CsPbBr_3$ NC to N-doped CD as it has N acceptor level. Subsequently, band gap of $CsPbBr_3$ will decrease a bit, which is observed in slight blue shift in PL (see Figure 4.1.7d). Similar blue shift of the PL of electron donor was previously observed in $CsPbBr_3$-phosphorene and $CsPbBr_3$-MXene composites.[29,32]

To understand the electron transfer between N-doped CDs and $CsPbBr_3$ NCs, we estimated band edges by cyclic voltammetry. The onset reduction potentials were found to be -0.73 V and -0.71 V for N-doped CDs and $CsPbBr_3$ NCs, respectively (Figure 4.1.11). Positions of VB and CB levels of the $CsPbBr_3$ are at -6.06 eV and -3.69 eV, respectively, while for N-doped CD, HOMOs are at -7.82 eV (π), -7.32 eV ($n_{C=O}$), -5.99 eV($n_{C=N}$), and LUMO is at -3.67eV (π*), (see Figure 4.1.12a). It is well known that N-doping in CDs introduces an accepter state below the conduction band (as shown in Figure 4.1.12a), [43-44] which provides quasi type-II like band alignment with $CsPbBr_3$

NC.[59-60] Such trap states act as acceptor centers for electrons from conduction band of $CsPbBr_3$.

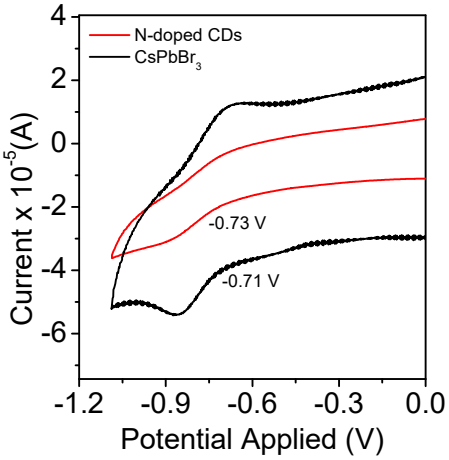

Figure 4.1.11. *Cyclic voltammograms of $CsPbBr_3$ NCs and CDs in 0.1 M tetrabutylammonium perchlorate (TBAP) solution of acetonitrile. The scan rate used was 50 mV/s.*

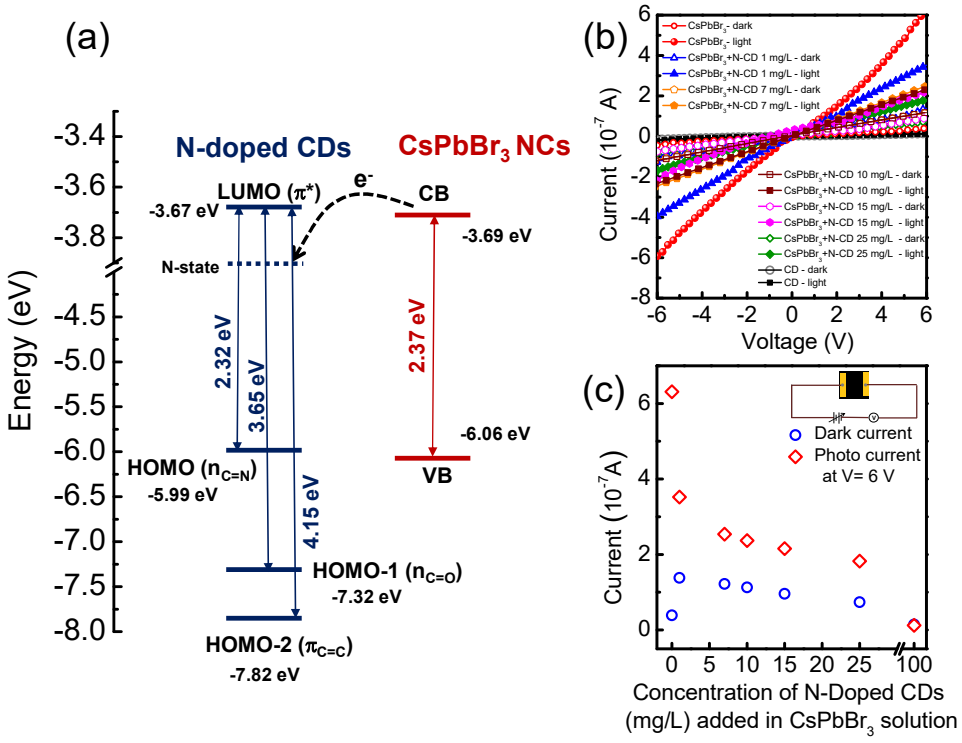

Figure 4.1.12. *(a) Band energies of $CsPbBr_3$ NCs and N-doped CDs. (b) Current vs. voltage (I-V) characteristics $CsPbBr_3$ NCs with different concentrations of N-doped CDs under dark and illuminated conditions measured from -6V to 6V. (c) Plot of dark current and photocurrent of different concentrations of N-doped CDs (mg/L) in 1.72 X 10^{-4} M $CsPbBr_3$ and the inset shows the schematic device representation.*

To understand the charge transfer between $CsPbBr_3$ NC and N-doped CD, we have fabricated photoconductivity device. From the current-voltage (I-V) measurement both in the dark and in presence of light (shown in Figure 4.1.12b, c), it is evident that the pure $CsPbBr_3$ NC shows higher photocurrent enhancement due to high absorption coefficient (931 $cm^{-1}g^{-1}L$) than that of the N-doped CD (low absorption coefficient of 22 $cm^{-1}g^{-1}$ L), which has almost no photo-response. In the $CsPbBr_3$-N-doped CD heterostructure, the photoexcited electrons from $CsPbBr_3$ NC are trapped in the acceptor states of N-doped CD (as shown in Figure 4.1.12a) and it becomes less available for photoconduction. This is evident from the decrease in photocurrent with increasing the concentration of N-doped CDs (mg/L) in the heterostructure system (Figure 4.1.12b, c).

4.1.4. Conclusions

In summary, we have successfully demonstrated the heterostructure between $CsPbBr_3$ NCs and N-doped CDs, which exhibited PL quenching of the halide perovskite. N-doping in the CD generated trap state below the conduction band. The mechanism of PL quenching of $CsPbBr_3$ is due to charge transfer from the conduction band of perovskite nanocrystal to the N-acceptor state of the CD arising because of quasi type II band alignment. Photoconductivity measurement showed that the photocurrent decreases in the heterostructure system compared to $CsPbBr_3$ NCs as the photo-excited electrons from $CsPbBr_3$ are trapped in N-acceptor in the N-doped CDs. The present work showed the synthesis and fundamental understanding of charge transfer mechanism in the all-inorganic halide perovskite-carbon dot heterostructure, which will activate further research into exploration of new heterostructures with other halide perovskite and mixed dimensional nanostructures.

4.1.5. References.

[1] P. V. Kamat, N. Pradhan, K. Schanze, P. S. Weiss, J. Buriak, P. Stang, T. W. Odom, G. Hartland, *ACS Energy Lett.* **2020**, 5, 2253.

[2] C. C. Stoumpos, M. G. Kanatzidis, *Adv. Mater.* **2016**, *28,* 5778.

[3] L. Protesescu, S. Yakunin, M. I. Bodnarchuk, F. Krieg, R. Caputo, C. H. Hendon, R. X. Yang, A. Walsh, M. V. Kovalenko, *Nano Lett.* **2015**, *15*, 3692

[4] A. Swarnkar, R. Chulliyil, V. K. Ravi, M. Irfanullah, A. Chowdhury, A. Nag, *Angew. Chem. Int. Ed.* **2015**, *54,* 15424.

[5] S. D. Stranks, H. J. Snaith, *Nat. Nanotechnol.* **2015**, *10*, 391.

[6] K. M. McCall, Z. Liu, G. Trimarchi, C. C. Stoumpos, W. Lin, Y. He, I. Hadar, M. G. Kanatzidis, B. W. Wessels, *ACS Photonics* **2018**, *5*, 3748.

[7] S. Seth, T. Ahmed, A. De, A. Samanta, *ACS Energy Lett.* **2019**, *4*, 1610.

[8] Y. Wu, X. Li, H. Zeng, *ACS Energy Lett.*, **2019**, *4*, 673.

[9] C. C. Stoumpos, L. Frazer, D. J. Clark, Y. S. Kim, S. H. Rhim, A. J. Freeman, J. B. Ketterson, J. I. Jang, M. G. Kanatzidis, *J. Am. Chem. Soc.* **2015**, *137*, 6804.

[10] A. H. Slavney, T. Hu, A. M. Lindenberg, H. I. Karunadasa, *J. Am. Chem. Soc.* **2016**, *138*, 2138.

[11] K. Kundu, P. Acharyya, K. Maji, R. Sasmal, S. S. Agasti, K. Biswas, *Angew. Chem. Int. Ed.* **2020**, 10.1002/anie.202005966.

[12] A. Sarkar, P. Acharyya, R. Sasmal, P. Pal, S. S. Agasti, K. Biswas, *Inorg. Chem.* **2018**, *57*,15558.

[13] Y. Tong, E. Bladt, M. F. Aygüler, A. Manzi, K. Z. Milowska, V. A. Hintermayr, P. Docampo, S. Bals, A. S. Urban, L. Polavarapu, J. Feldmann, *Angew. Chem. Int. Ed.* **2016**, *55*, 13887.

[14] A. K. Guria, S. K. Dutta, S. D. Adhikari, N. Pradhan, *ACS Energy Lett.* **2017**, *2*, 1014.

[15] D. Yang, M. Cao, Q. Zhong, P. Li, X. Zhang, Q. Zhang, *J. Mater. Chem. C* **2019**, *7*, 757.

[16] S. Yakunin, L. Protesescu, F. Krieg, M. I. Bodnarchuk, G. Nedelcu, M. Humer, G. D. Luca, M. Fiebig, W. Heiss, M. V. Kovalenko, *Nat. Commun.* **2015**, *6*, 8056.

[17] Q. A. Akkerman, V. D. Innocenzo, S.Accornero, A. Scarpellini, A. Petrozza, M. Prato, L. Manna, *J. Am. Chem. Soc.* **2015**, *137*, 10276.

[18] A. Swarnkar, A. R. Marshall, E. M. Sanehira, B. D. Chernomordik, D. T. Moore, J. A. Christians, T. Chakrabarti, J. M. Luther, *Science* **2016**, *354*, 92.

[19] H. Lin, C. Zhou, Y. Tian, T. Siegrist, B. Ma, *Energy Lett.* **2017**, *3*, 54.

[20] K. S. Novoselov, V. I. Fal'ko, L. Colombo, P. R. Gellert, M. G. Schwab, K. Kim, *Nature* **2012**, *490*, 192.

[21] C. N. R. Rao, A. K. Sood, K. S. Subrahmanyam, A. Govindaraj, *Angew. Chem. Int. Ed.* **2009**, *48*, 7752.

[22] H. Liu, A. T. Neal, Z. Zhu, Z. Luo, X. Xu, D. Tománek, P. D. Ye, *ACS Nano* **2014**, *8*, 4033.

[23] M. Chhowalla, H. S. Shin, G. Eda, L.-J. Li, K. P. Loh, H. Zhang, *Nat. Chem.* **2013**, *5*, 263.

[24] M. Naguib, V. N. Mochalin, M. W. Barsoum, Y. Gogotsi, *Adv. Mater.* **2013**, 992.

[25] C. Tan, X. Cao, X.-J. Wu, Q. He, J. Yang, X. Zhang, J. Chen, W. Zhao, S. Han, G.-H. Nam, *Chem. Rev.* **2017**, *117*, 6225.

[26] K. Geim, I. V. Grigorieva, *Nature* **2013**, *499*, 419.

[27] D. Jariwala, T. J. Marks, M. C. Hersam, *Nat. Mater.* **2017**, *16*, 170.

[28] Banik, K. Biswas, *Angew. Chem. Int. Ed.* **2017**, *129*, 14753.

[29] S. Muduli, P. Pandey, G. Devatha, R. Babar, M. Thripuranthaka, D. C. Kothari, M. Kabir, P. P. Pillai, S. Ogale, *Angew. Chem. Int. Ed.* **2018**, *130,* 7808.

[30] X. Tang, Z. Zu, Z. Zang, Z. Hu, W. Hu, Z. Yao, W. Chen, S. Li, S. Han, M. Zhou, *Sensors Actuators B. Chem.* **2017**, *245*, 435.

[31] Y. Xu, M. Yang, B. Chen, X. Wang, H. Chen, D. Kuang, C. A. Su, *J. Am. Chem. Soc.* **2017**, *139*, 5660.

[32] Pan, X. Ma, S. Huang, Y. Wu, M. Jia, P. Wangyang, Y. Liu, Y. Shi, L. He, Y. Liu, *J. Phys. Chem. Lett.* **2019**, *10*, 6590.

[33] M. Ou, W. Tu, S. Yin, W. Xing, S. Wu, H. Wang, S. Wan, Q. Zhong, R. Xu, *Angew. Chem. Int. Ed.* **2018**, *130*, 13758.

[34] V. K. Ravi, S. Saikia, S. Yadav, V.V. Nawale, A. Nag, *ACS Energy Lett.* **2020**, *5*, 1794.

[35] X. Liu, X. Zhang, L. Li, J. Xu, S. Yu, X. Gong, J. Zhang, H. Yin, *ACS Appl. Mater. Interfaces* **2019**, *11*, 40923.

[36] Brumberg, B. T. Diroll, G. Nedelcu, M. E. Sykes, Y. Liu, S. M. Harvey, M. R. Wasielewski, M. V. Kovalenko, R. D. Schaller, *Nano Lett.* **2018**, *18*, 4771.

[37] X. Zhang, X. Wu, X. Liu, G. Chen, Y. Wang, J. Bao, X. X, Xu, X. X. Liu, Q. Zhang, K. Yu, W. Wei, J. Liu, J. Xu, H. Jiang, P. Wang, X. Wang, *J. Am. Chem. Soc.* **2020**, *142*, 4464.

[38] S. Wang, C. Bi, A. Portniagin, J. Yuan, J. Ning, X. Xiao, X. Zhang, Y. Y. Li, S. V. Kershaw, J. Tian, A. L. Rogach, *ACS Energy Lett.* **2020**, 5, 2401.

[39] H. Li, Z. Kang, Y. Liu, S.T. Lee, *J. Mater. Chem.* **2012**, *22*, 24230.

[40] S. N. Baker, G. A. Baker, *Angew. Chem. Int. Ed.* **2010**, *49*, 6726.

[41] Pal, M.P. Sk, A. Chattopadhyay, *Mater. Adv.* **2020,** *1*, 525.

[42] K. Holá, M. Sudolská, S. Kalytchuk, D. Nachtigallová, A. L. Rogach, M. Otyepka, R. Zbořil, *ACS Nano* **2017**, *11*, 12402.

[43] Sharma, J. Das, *J. Nanobiotechnology* **2019**, 1.

[44] Y. Dong, H. Pang, H. B. Yang, C. Guo, J. Shao, Y. Chi, *Angew. Chem. Int. Ed.* **2013,** *52*, 7800.

[45] X. Li, S. Zhang, S. A. Kulinich, Y. Liu, H. Zeng, *Sci. Rep.* **2014,** *4*, 4976.

[46] D. Qu, M. Zheng, L. Zhang, H. Zhao, Z. Xie, X. Jing, R. E. Haddad, H. Fan, Z. Sun, *Sci. Rep.* **2014**, *4*, 1.

[47] Y. Choi, B. Kang, J. Lee, S. Kim, G.T. Kim, H. Kang, B.R. Lee, H. Kim, S.H. Shim, G. Lee, O. H. Kwon, *Chem. Mater.* **2016**, *28*, 6840.

[49] Y. Li, Y. Zhao, H. Cheng, Y. Hu, G. Shi, L. Dai, L. Qu, *J. Am. Chem. Soc.* **2012**, *134*, 15.

[50] T. F. Yeh, C. Y. Teng, S. H. Chen, H. Teng, *Adv. Mater.* **2014**, *26*, 3297.

[51] Y. Q. Zhang, D. K. Ma, Y.G. Zhang, W. Chen, S. M. Huang, *Nano Energy* **2013**, *2*, 545.

[52] L. M. Wheeler, E. M. Sanehira, A. R. Marshall, P. Schulz, M. Suri, N. C. Anderson, J. A. Christians, D. Nordlund, D. Sokaras, T. Kroll, S. P. Harvey, J. J. Berry, L. Y. Lin, J. M. Luther, *J. Am. Chem. Soc.* **2018**, *140*, 10504.

[53] S. Wang, L. Du, Z. Jin, Y. Xin, H. Mattoussi, *J. Am. Chem. Soc.* **2020**, *142*, 12669.

[54] S. Peng, Q. Wei, B. Wang, Z. Zhang, H. Yang, G. Pang, K. Wang, G. Xing, X. Sun, Z. Tang, *Angew. Chem. Int. Ed.* **2020** 10.1002/anie.202009193.

[55] H. S. Casalongue, S. Kaya, V. Viswanathan, D. J. Miller, D. Friebel, H. A. Hansen, J. K. Nørskov, A. Nilsson, H. Ogasawara, *Nat. Commun.* **2013**, *4*, 1.

[56] D. Chen, W. Wu, Y. Yuan, Y. Zhou, Z. Wana, P. Huang, *J. Mater. Chem. C,* **2016***, 4,* 9027.

[57] S. Dey, P. Chithaiah, S. Belawadi, K. Biswas, C. N. R. Rao, *J. Mater. Res.* **2014**, *29*, 383.

[58] X. Michalet, F.F. Pinaud, L.A. Bentolila, J.M. Tsay, S. Doose, J. J. Li, G. Sundaresan, A.M. Wu, S.S. Gambhir, S. Weiss, *Science* **2005**, *307*, 538.

[59] J. Cui, A. P. Beyler, I. Coropceanu, L. Cleary, T. R. Avila, Y. Chen, J. M. Cordero, S. L. Heathcote, D. K. Harris, O. Chen, J. Cao, M. G. Bawendi, *Nano Lett.* **2016**, *16*, 289.

[60] N. G. Pavlopoulos, J. T. Dubose, Y. Liu, X. Huang, N. Pinna, M. G. Willinger, T. Lian, K. Chare, J. Pyun, *CrystEngComm*, **2017**, 19, 6443.

[61] Teitelboim, N. Meir, M. Kazes, D. Oron, *Acc. Chem. Res.* **2016,** 49, 5, 902.

Chapter 4.2

Charge Transfer in the Heterostructure of $CsPbBr_3$ Nanocrystals with Layered Bismuth Oxychalcogenides (Bi_2O_2Se) Nanosheets†

†*Manuscript under preparation*

Chapter 4.2

Charge Transfer in the Heterostructure of $CsPbBr_3$ Nanocrystals with Layered Bismuth Oxychalcogenides (Bi_2O_2Se) Nanosheets †

Summary: *Semiconductor heterostructures have been an elementary unit for high-performance optoelectronic devices like light-emitting diodes, photodetectors, and solar cells. Recently, heterostructures comprising of zero-dimensional (0D) quantum dots (QDs) or nanocrystals (NCs) positioned on the surface of two-dimensional (2D) materials have appealed widespread attention, which provides synergetic effects and additional degrees of freedom to orient hetero-junctions and unfolds innovative prospects to apprehend high-performance optoelectronic devices. Herein, we present the heterostructure integration of 0D $CsPbBr_3$ NCs and 2D Bi_2O_2Se nanosheets (NSs) to explore their electronic coupling and the nature of photo-generated charge transfer between them. We observed that $CsPbBr_3$ NCs systematically self-assembled on the surface of 2D Bi_2O_2Se NSs. The heterostructures have been visualized by transmission electron microscopic (TEM) images and the bonding interactions have been studied by Fourier-transform infrared spectroscopy (FTIR). We have studied the photoluminescence (PL) quenching of $CsPbBr_3$ NCs in these heterostructures at room temperature. Time-resolved photoluminescence (TR-PL) spectroscopic techniques were implemented to investigate the nature of charge transfer in these 0D/2D nano-composites with variable concentrations of $CsPbBr_3$ NCs and Bi_2O_2Se NSs at 298 K. It is evident that the PL quenching occurred owing to the charge transfer from the conduction band of $CsPbBr_3$ to the Bi_2O_2Se via type-I electronic band alignment.*

† *Manuscript under preparation*

4.2.1. Introduction

Semiconductor heterostructures are appraised as an elementary unit for high-performance optoelectronic devices, like light-emitting diodes, photodetectors, and solar cells.[1–3] When two or more materials are employed by combining in a specific construction, heterostructures are formed, which were widely investigated owing to their outstanding properties[2,4] and extensively employed for improving the photovoltaic proficiency, photo-brightening, and intensifying catalytic activities[2] In general, photocatalysis and photovoltaics associated with the heterostructures have fascinated vast consideration, wherein the photogenerated charge carriers at the interface played an essential role. [5,6] These heterostructures can be achieved either by type-I or type-II band alignments, wherein the charge carriers can recombine or transfer from one semiconductor to another.[2] An essential approach can be achieved to construct these heterostructures for better device efficiency by promoting charge extraction and suppressing charge recombination.[7] In recent times, heterostructures comprising of zero-dimensional (0D) quantum dots (QDs) or nanocrystals (NCs) positioned on the surface of two-dimensional (2D) materials have appealed widespread attention, which can provide synergetic effects and additional degrees of freedom to orient hetero-junctions and unfolds innovative prospects to apprehend high-performance optoelectronic devices.[8]

So far, most of the research was directed towards the heterostructures chalcogenide semiconductors, noble metals, metal oxides, and their diverse combinations,[2] whereas fewer efforts were focused on the heterostructures with *all-inorganic* perovskite NCs. It is renowned that all-inorganic perovskite NCs have experienced colossal recognition as a result of their distinctive properties like enhanced photoluminescence quantum yield, narrow emission line-widths, an extensive color range, greatly tunable band-gaps, and improved stability,[9–13] which established them as excellent candidates for next-generation optoelectronic applications.[14] Heterostructures assimilating perovskite NCs with other low-dimensional materials were accomplished by photoluminescence (PL) quenching, and charge transfer, enhanced photoelectric detection, improved photocatalytic CO_2 reduction, tunable dual emission, exceptional thermal and water stability,[15–24] as established for composites consisting of $CsPbX_3$ with either N-doped carbon dots, or black phosphorus, or graphene oxide, or MXene, or porous g-

C_3N_4, or PbS, or Bi_2WO_6, or TiO_2. Since the success is restricted, more investigations involving new combinations of materials for designing novel heterostructures are indispensable. Recently, an emergent 2D layered material, Bi_2O_2Se has shown noticeable potential in device applications for instance phototransistors, ultrafast photodetection, and near-IR photodetectors[25–27] owing to their characteristic narrow bandgap, high air stability, and carrier mobility.[28] Thus, for high-performance optoelectronic devices, fabricating Bi_2O_2Se-based mixed-dimensional heterostructures is of immense significance. Recently, the combination of Bi_2O_2Se nanoplates with PbSe QDs in the form of mixed-dimensional 2D/0D heterostructures was utilized as high-performance and broadband photodetectors.[29] However, studies involving Bi_2O_2Se-based mixed-dimensional heterostructures are still in the early stage.

Herein, we establish a facile approach for the integration of a heterostructure based on the 0D $CsPbBr_3$ NCs and 2D Bi_2O_2Se nanosheets (NSs) to explore their electronic coupling and the nature of photogenerated charge transfer between them. We also observed that the $CsPbBr_3$ NCs systematically self-assembled on the surface of 2D NSs from TEM measurement and the bonding interaction was further verified from the FTIR study. Significant photoluminescence (PL) quenching of $CsPbBr_3$ NCs in these heterostructures was perceived both at room temperature and cryogenic temperature (77 K). Time-resolved photoluminescence (TR-PL) spectroscopic techniques were implemented to investigate the nature of charge transfer in these 0D/2D nano-composites with variable concentrations of $CsPbBr_3$ NCs and Bi_2O_2Se NSs at 298 K as well as at 77 K. It is evident that the PL quenching occurred owing to the charge transfer from the conduction band of $CsPbBr_3$ to the Bi_2O_2Se *via* type-I electronic band alignment, where the energy states were determined from the cyclic voltammetric study.

4.2.2. Methods

4.2.2.1. Reagents. Cesium carbonate (Cs_2CO_3, 99.9%, Sigma-Aldrich), lead (II) bromide ($PbBr_2$, 99.9%, Sigma-Aldrich), oleic acid (OA, tech. 90%, Sigma-Aldrich), oleylamine (OAm, tech. 70%, Sigma-Aldrich), 1-octadecene (ODE, tech. 90%, Sigma Aldrich), and toluene (AR, 99.0%, SDFCL), Bismuth nitrate ($Bi(NO_3)_3{\cdot}5H_2O$, Alfa Aesar, 99.9%), selenourea ($SeC(NH_2)_2$, Alfa Aesar, 99.9%), potassium hydroxide (KOH,

S D Fine-Chem Limited (SDFCL)), sodium hydroxide (NaOH, SDFCL), and ethanol were used without any further purification.

4.2.2.2 Synthesis.

4.2.2.2.1. Synthesis of Cs-Oleate. In a 50 mL 3-necked round-bottom flask, 410 mg (1.26 mmol) Cs_2CO_3 and 20 mL ODE were taken and heated at 120 °C with continuous stirring under vacuum for 1 h to get a homogeneous solution. After 1 h, 1.30 mL of OA was added, and the solution was kept for another 30 min at the same condition. The vacuum was replaced with a nitrogen atmosphere and kept for 5 min to get a clear Cs-oleate solution. This Cs-oleate solution was stored at room temperature under a nitrogen atmosphere for further use.

4.2.2.2.2. Synthesis of $CsPbBr_3$ Nanocrystals. In a typical synthesis, 0.376 mmol (137 mg) of $PbBr_2$ and 10 mL of ODE were taken in a 25 mL 3-necked RB flask and dried under vacuum for about 1 h. Then the RB is filled with N_2 and 1 mL each of OA and OAm were added. Again, the flask was kept under vacuum until $PbBr_2$ dissolved and a transparent solution is formed. The reaction temperature is raised to 140°C under N_2 atm and 0.8 ml of previously heated (at 100°C) Cs-oleate solution was swiftly injected. The reaction mixture becomes fluorescent green and after 5 min the reaction was quenched by an ice bath. The synthesized $CsPbBr_3$ NCs were then washed with toluene and precipitated by centrifugation at 8000 rpm for 15 min, followed by dispersing the products in toluene for further studies.

4.2.2.2.3. Synthesis of Few Layers of Bi_2O_2Se. 100 mg (0.206 mmol) of $Bi(NO_3)_3{\cdot}5H_2O$ and 12.7 mg (0.103 mmol) of $SeC(NH_2)_2$ were sequentially added at a 5 minutes interval into 20 ml water in a glass beaker. The solution was stirred continuously. The addition of $Bi(NO_3)_3{\cdot}5H_2O$ into water results in a milky white color solution which turns into an orange color solution after the addition of $SeC(NH_2)_2$. Finally, 120 mg (2.14 mmol) of KOH and 320 mg (8 mmol) of NaOH were added into the solution which turns the solution color black. After 10 minutes of stirring, the solution was put to rest which results in precipitation of the dark brown color nanosheets. These were then washed with alcohol and water and centrifuged. The purified product was then dried in a vacuum oven at 150 °C.

4.2.2.3. Powder X-ray Diffraction. Powder X-ray diffraction for all of the samples was recorded using a Cu K_α (λ = 1.5406 Å) radiation on a Bruker D8 diffractometer.

4.2.2.4. Transmission Electron Microscopy. The transmission electron microscopy (TEM) images of the synthesized $CsPbBr_3$ NCs and CDs were taken using a JEOL (JEM3010) TEM instrument (300 kV accelerating voltage) fitted with a Gatan CCD camera and also with an FEI TECNAI G2 20 STWIN TEM instrument (operating at 200 kV).

4.2.2.5 Fourier Transform Infrared Spectroscopy (FTIR). FTIR spectra were recorded in the range of 400-4000 cm^{-1} by using a Bruker Optics Alpha-P FTIR spectrophotometer equipped with an attenuated total reflectance (ATR) module.

4.2.2.6. Optical Measurement. Electronic absorption spectra were recorded using Perkin-Elmer Lambda 900. A FluoroMax-4 spectrofluorometer (Horiba JobinYvon Inc.) with a 5 nm slit width was used to record the photoluminescence (PL) spectrum.

4.2.2.7. Photoluminescence (PL) Quenching Study. 2.5 mL $CsPbBr_3$ NCs solution in toluene with 1.29 × 10^{-5} M concentration was initially taken in a PL-cuvette and PL spectra were recorded. Then 20-120 µL solution in toluene of dispersed Bi_2O_2Se (1.89 x 10^{-3} M) was added to it in each step and after the sonication at room temperature, PL spectra were recorded.

4.2.2.8. Fluorescent Lifetime Measurement. Edinburgh FLS1000 spectrofluorometer coupled with EPL-405 picosecond pulsed diode laser (wavelength 405 nm ± 10 nm, maximum average power 5 mW) was employed to collect time-resolved decay plots at 298 K and 77 K using a vacuum liquid-nitrogen cryostat. A multi-exponential decay model was used to fit the lifetime data. We obtained reduced χ^2 values in the range 0.9-1.2.

$$I(t) = \alpha_1 e^{-t/\tau_1} + \alpha_2 e^{-t/\tau_2} + \alpha_3 e^{-t/\tau_3} \quad \text{Eq. 1}$$

$$\tau_{avg} = \sum_i \alpha_i \tau_i^2 / \sum_i \alpha_i \tau_i \quad \text{Eq. 2}$$

4.2.2.9. Electrochemical Measurements. To calculate the electrochemical band edge energies for Bi_2O_2Se and $CsPbBr_3$, the cyclic voltammogram was recorded

under non-aqueous conditions. The following formula was utilized to determine the experimental electrochemical HOMO and LUMO levels in terms of eV unit:

$$E_{Ag/AgCl} = E^0_{Ag/AgCl} + 0.059 \times pH$$
$$\text{At pH=5.6, } E_{Ag/AgCl} = 0.222 + (0.059 \times 5.6) = 0.552 \text{ V}$$

$$E\ (LUMO) = -e\ [E_{red}^{onset} + E_{Ag/AgCl} + 4.4]$$
$$E\ (HOMO) = E\ (LUMO) - E_{0\text{-}0}$$

where $E_{0\text{–}0}$ represents the 0–0 energy, which is defined as the lowest energy transition and that we can estimate from UV–vis and fluorescence emission spectra. We obtained a value of 2.37 eV for $E_{0\text{-}0}$ corresponding to 523 nm for $CsPbBr_3$.

For $CsPbBr_3$,

$$E\,(CB) = -e\ [-0.71 + 4.4] = -3.69 \text{ eV}$$
$$E\ (VB) = [-3.69\ -2.37] \text{ eV} = -6.06 \text{ eV}$$

We obtained 0.839 eV for $E_{0\text{–}0}$ corresponding to 1478 nm for Bi_2O_2Se.

For Bi_2O_2Se,

$$E\,(CB) = -e\ [-0.309 + 0.552 + 4.4] = -4.643 \text{ eV}$$
$$E\ (VB) = [-4.643\ -0.839] \text{ eV} = -5.482 \text{ eV}$$

4.2.3. Results and Discussion

The mixed-dimensional heterostructures of 0D $CsPbBr_3$ NCs/2D Bi_2O_2Se NSs were synthesized by adding the toluene dispersed Bi_2O_2Se NSs with different concentrations to the $CsPbBr_3$ solution in toluene. The mixture was sonicated at room temperature to induce the anchoring of $CsPbBr_3$ NCs with Bi_2O_2Se 2D NSs. PXRD of as-synthesized nanocrystals of $CsPbBr_3$, few-layer nanosheets of Bi_2O_2Se, and the integrated heterostructures formed by the two are shown in Figure 4.2.1. The powder X-ray diffraction (PXRD) pattern of synthesized $CsPbBr_3$ NCs (solution-based hot-injection method where Cs oleate and $PbBr_2$ used as precursors, mentioned in section 4.2.2.2.) matched well with the simulated orthorhombic phase (*Pbnm*). The room temperature PXRD pattern of the as-synthesized vacuum dried nanosheets could be indexed with the pristine Bi_2O_2Se tetragonal structure (space group *I*4/*mmm*).[30] The

agglomeration of the nanosheets during vacuum drying results in such a clear depiction of the XRD pattern. The PXRD of heterostructures shows the presence of major peaks of both the $CsPbBr_3$ NCs and the Bi_2O_2Se NSs.

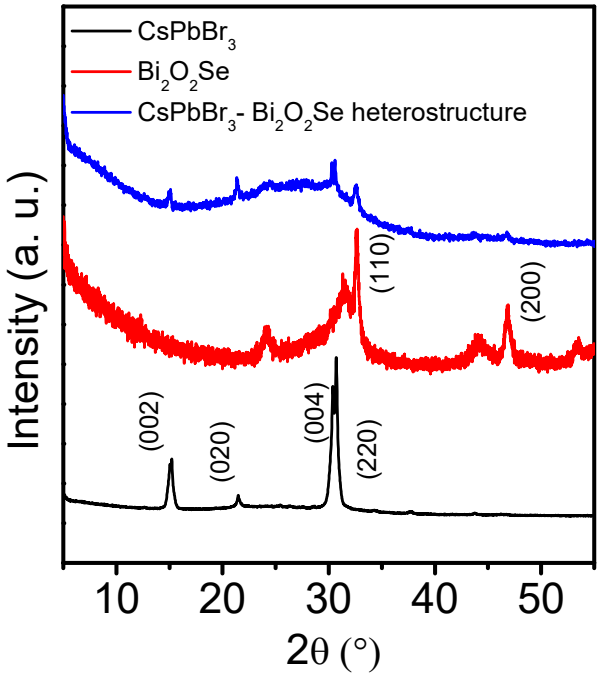

Figure 4.2.1. *Powder X-ray diffraction (PXRD) of $CsPbBr_3$ nanocrystals (NCs), vacuum dried Bi_2O_2Se NSs, and the heterostructure.*

The morphological studies were carried out using transmission electron microscopy (TEM) (Figure 4.2.2.). The low-magnification TEM image in Figure 4.2.2a noticeably shows the ultrathin morphology of the Bi_2O_2Se nanosheets with the lateral dimensions of the individual nanosheets ranging from ~80 to 200 nm. This layered arrangement is along the crystallographic *c*-axis with a spacing of ~0.68 nm[30] which is evident from the high-resolution TEM (HRTEM) image in Figure 4.2.2d. This lateral spacing between the two $[Bi_2O_2]^{2+}$ layers is slightly more than the bulk which has 0.61 nm. This difference is attributed to the structural relaxation in free-standing few layers of NSs as observed in previous studies where Bi_2O_2Se NSs were grown using the chemical vapor deposition (CVD) technique.[31] Figure 4.2.2b visualizes monodispersed square-shaped morphology of $CsPbBr_3$ NCs with an average particle size of ~15-20 nm. HRTEM image in Figure 4.2.2e shows the (101) lattice planes of $CsPbBr_3$ NCs with an interplanar

distance of 0.66 nm. Figure 4.2.2c shows the integration of $CsPbBr_3$ NCs on the Bi_2O_2Se 2D NSs. The HRTEM image of the heterostructure in Figure 4.2.2f shows the (021) lattice planes of $CsPbBr_3$ NCs with an interplanar distance of 0.39 nm, and (002) planes with a d-spacing of 0.67 nm.

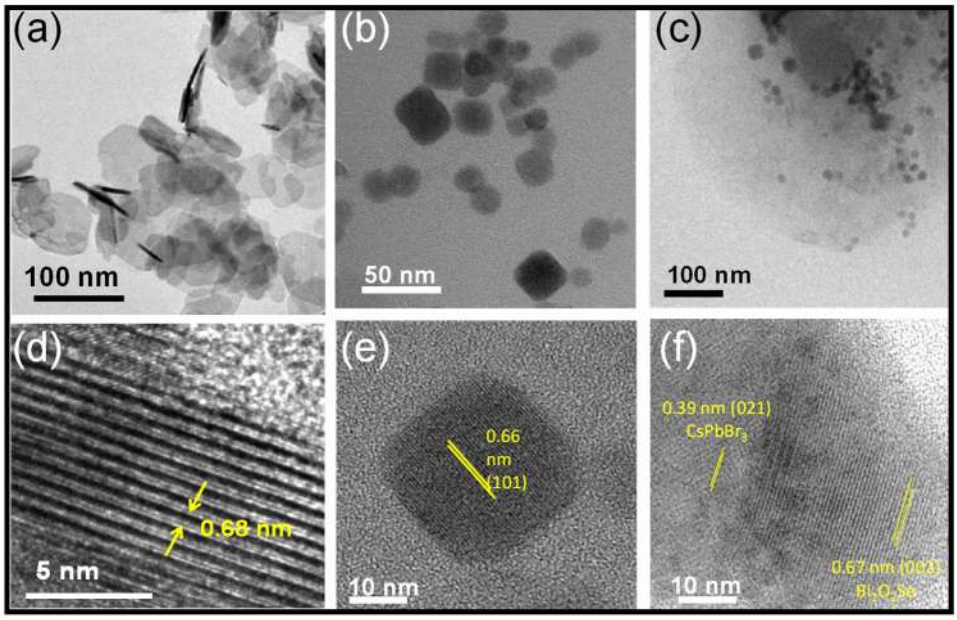

Figure 4.2.2. *Transmission electron microscopy (TEM) images of (a) Bi_2O_2Se 2D NSs (b) $CsPbBr_3$ NCs and (c) $CsPbBr_3$-Bi_2O_2Se heterostructures, respectively. HRTEM images of (d) Bi_2O_2Se 2D NSs with 0.68 nm d spacing (e) $CsPbBr_3$ NCs with 0.66 nm d spacing for (101) plane and (f and g) $CsPbBr_3$-Bi_2O_2Se heterostructures, respectively, where $CsPbBr_3$ NCs with a 0.39 nm d spacing for (021) plane, and Bi_2O_2Se with a 0.67 nm d spacing for (002) plane have been obtained.*

In addition, to understand the bonding interactions in these heterostructures we carried out Fourier transform infrared spectroscopy (FTIR). FTIR of $CsPbBr_3$ NCs is dominated mainly by modes arising from the oleyl group used in the synthesis of $CsPbBr_3$ NCs (ν(C–H_x) = 2852–2956 cm^{-1} and ν(C–H_2) = 1461 cm^{-1})[16,32,33]. These modes have been shifted to lower wavenumbers (ν(C–H_x) = 2845–2952 cm^{-1} and ν(C–H_2) = 1457 cm^{-1}) along with the mode broadening imply the possible interactions between $CsPbBr_3$ NCs and Bi_2O_2Se NSs. Formation of the heterostructures between $CsPbBr_3$ NCs and Bi_2O_2Se NSs is possibly due to the H-bonding interactions between the capping ligands on the surface of $CsPbBr_3$ NCs with $[Bi_2O_2]_n^{2n+}$ or $[Se]_n^{2n-}$ in Bi_2O_2Se NSs.

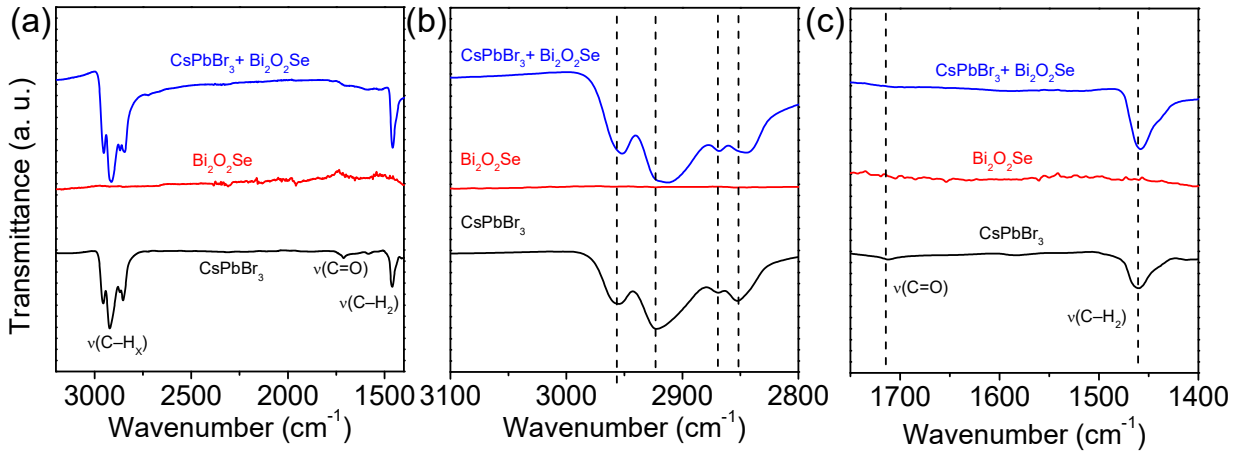

Figure 4.2.3. *FTIR spectra of $CsPbBr_3$ (black) Bi_2O_2Se NSs (red) and heterostructure of $CsPbBr_3$ and Bi_2O_2Se NSs (blue).*

Further to comprehend the interaction between the $CsPbBr_3$ NCs and Bi_2O_2Se NSs, first the optical properties of individual $CsPbBr_3$ NCs and Bi_2O_2Se NSs were studied using UV-Vis absorption and photoluminescence (PL) spectroscopic techniques (see Figure 4.2.4). The nanocomposites are prepared by adding (20-120µL) stock solution of 1.89 x 10^{-3} M Bi_2O_2Se in 2.5 mL of 1.29 × 10^{-5} M $CsPbBr_3$ NCs in toluene and optical spectra are recorded. The absorbance of heterostructures retained the feature of $CsPbBr_3$ NCs with the successive addition of Bi_2O_2Se solution, while PL intensity gradually decreased.

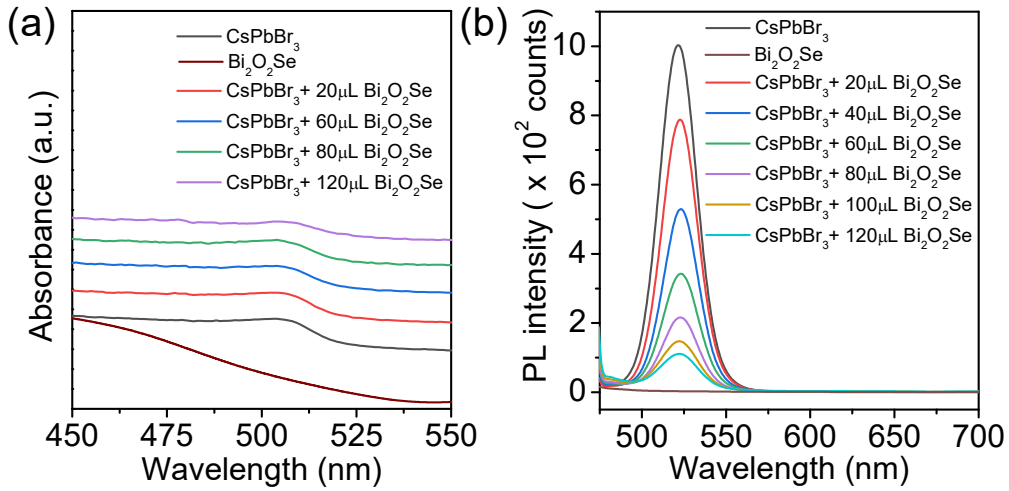

Figure 4.2.4. *(a) UV–vis absorption and (b) PL spectra of $CsPbBr_3$ NCs, Bi_2O_2Se NSs and $CsPbBr_3$ NC–Bi_2O_2Se heterostructure system synthesized by adding (20-120µL) stock solution of 1.89 x 10^{-3} M Bi_2O_2Se in 2.5 mL of 1.29 × 10^{-5} M $CsPbBr_3$NCs in toluene.*

The formation of heterostructure of $CsPbBr_3$ with the Bi_2O_2Se NSs leads to the quenching of PL and may be attributed to the transfer of photo-generated carriers between them. A maximum PL quenching efficiency of about 89% was achieved when 120 µL of 1.89 x 10^{-3} M Bi_2O_2Se NSs was added to 1.29 × 10^{-5} M $CsPbBr_3$ NC solution. The absorption edges estimated from Tauc plots of the absorption data taken in toluene medium are 2.37 eV for $CsPbBr_3$ and 0.84 eV Bi_2O_2Se NSs (Figure 4.2.5).

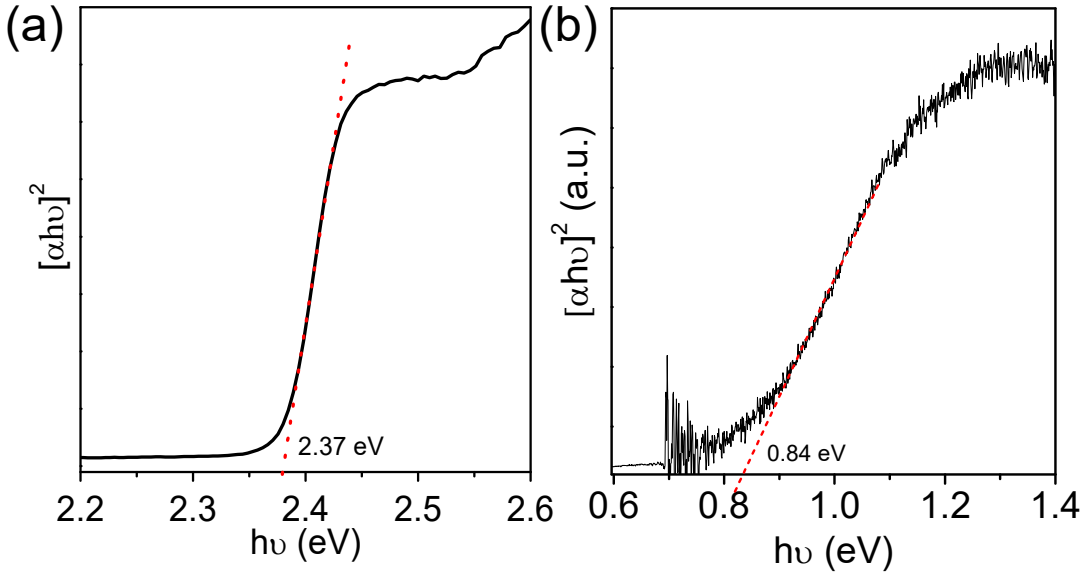

Figure 4.2.5. *Tauc plot from the electronic absorption data with band energies for (a) $CsPbBr_3$ NCs and (b) Bi_2O_2Se NSs.*

The nature of quenching processes that resulted in the reduction in PL intensity may normally be ruled out by numerous factors like the formation of complexes in the ground state (static quenching), collision (dynamic quenching), energy transfer, and charge transfer reactions.[29] To comprehend the mechanism in the current case, we implemented the familiar Stern–Volmer analysis (Figure 4.2.6a). The non-linear nature of the plot follows the modified Stern-Volmer equation, Eq. 1, which shows upward curvature due to $[Q]^2$ term in Eq. 4.2.2.

$$\frac{I_O}{I} = (1 + k_s[Q])(1 + k_D[Q]) \qquad \text{Eq. 4.2.1}$$

$$\frac{I_O}{I} = 1 + (k_s + k_D)[Q] + k_s k_D[Q]^2 \qquad \text{Eq. 4.2.2}$$

$$\frac{I_O}{I} = 1 + k_{app}[Q] \qquad \text{Eq. 4.2.3}$$

$$k_{app} = k_S + k_D + k_S k_D[Q] \qquad \text{Eq. 4.2.4}$$

where I_0 and I are the PL intensities of $CsPbBr_3$ NCs in the absence and presence of Bi_2O_2Se NSs, respectively, k_S and k_D are static and dynamic quenching constant, respectively, [Q] is the concentration of the Bi_2O_2Se NSs.

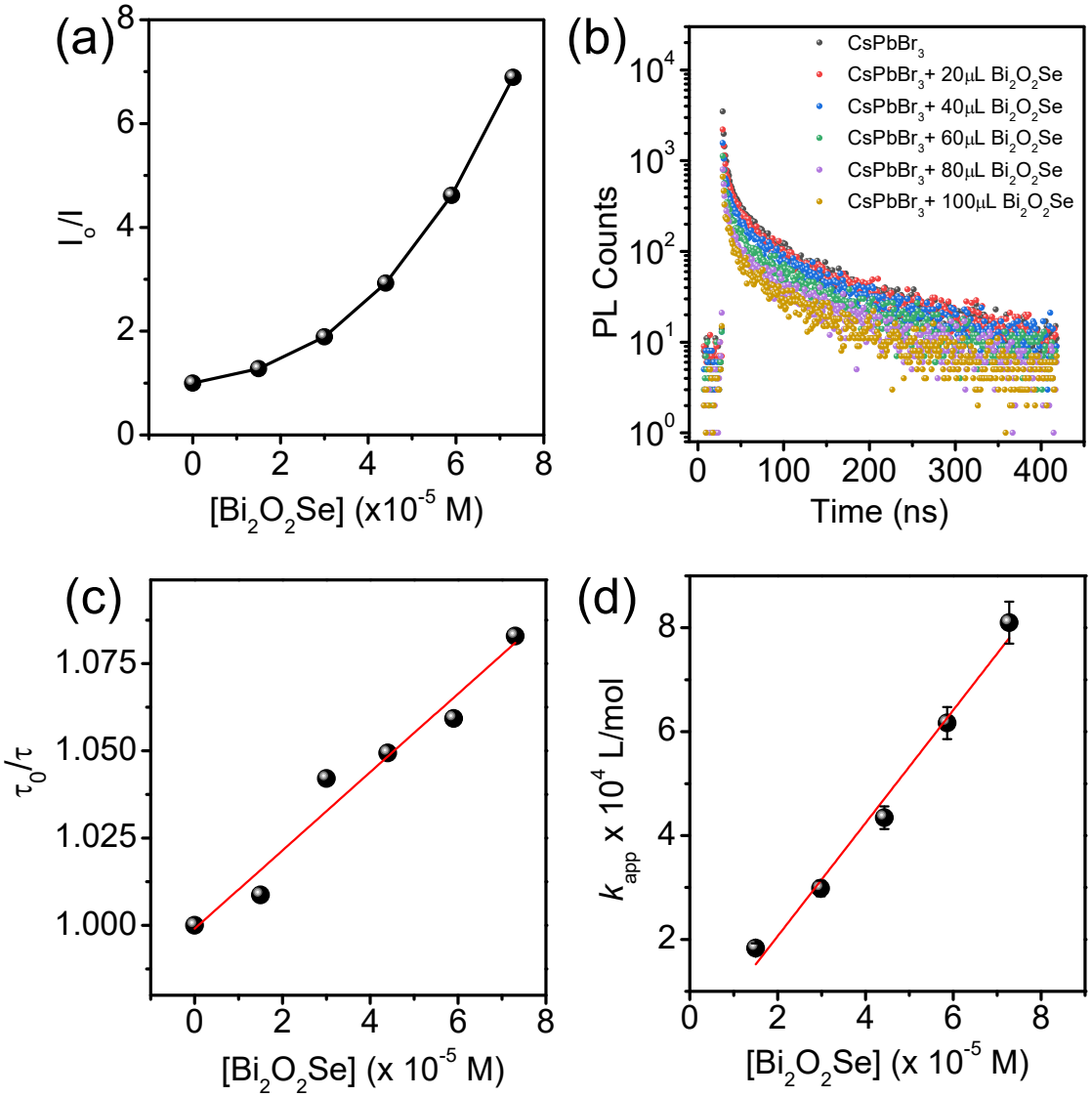

Figure 4.2.6. *(a) Stern–Volmer plot for PL quenching of $CsPbBr_3$ NCs in the presence of varying concentrations of Bi_2O_2Se. (b) Time-resolved PL spectra at 298 K for 1.29 × 10^{-5} M $CsPbBr_3$NCs in toluene medium with different amount (20-120μL) of 1.89 x 10^{-3} M Bi_2O_2Se added. (c) Stern–Volmer plot in terms of photoluminescence lifetime of $CsPbBr_3$ NCs in the presence of Bi_2O_2Se (d) Modified Stern–Volmer plot showing the variation of k_{app} as a function of the varying concentration of Bi_2O_2Se.*

This upward curvature may be ascribed to the existence of both dynamic and static quenching mechanisms and we observed a decrease in the PL intensity. However, the PL lifetime measurement is a more robust technique than the steady-state PL measurement as it is dependent on the excitation wavelength and independent of concentration of $CsPbBr_3$-Bi_2O_2Se heterostructure. Therefore, we executed time-resolved PL spectroscopy. PL decay of $CsPbBr_3$-Bi_2O_2Se heterostructure could be fitted with the use of multicomponent decay kinetics (Figure 4.2.7b) and the fitting parameters are represented in Table 4.2.1.

Table 4.2.1. *Photoluminescence decay analysis of $CsPbBr_3$ NCs and Bi_2O_2Se NSs heterostructure.*

Amount of 1.89 x 10^{-3} M Bi_2O_2Se added (µL)	Concentration of Bi_2O_2Se in $CsPbBr_3$ solution (x 10^{-5}M)	τ_1 (ns)	τ_2 (ns)	τ_3 (ns)	α_1	α_2	α_3	τ_{avg} (ns)
0	0	16.4	95.7	2.4	26.7	63.0	10.3	90.0
20	1.5	15.9	95.9	2.3	30.0	58.9	11.1	89.3
40	3.0	13.7	90.9	1.9	25.8	65.7	8.5	86.4
60	4.4	14.2	90.9	2.0	27.2	63.7	9.1	85.8
80	5.9	12.1	89.0	1.6	25.7	66.7	7.6	85.0
100	7.3	13.6	87.5	1.7	25.1	65.4	9.5	83.1

The $CsPbBr_3$ NCs-Bi_2O_2Se NSs heterostructure exhibited relatively faster decay than pristine $CsPbBr_3$ with average PL lifetime decreasing from 90.0 ns to 83.1 ns upon addition of 100 µL of 1.89 x 10^{-3} M Bi_2O_2Se NSs solution (Figure 4.2.7b). This difference between τ_{avg} of $CsPbBr_3$ NCs-Bi_2O_2Se NSs heterostructure and pristine $CsPbBr_3$ reveals the origin of the non-radiative pathway from the substantial electronic interaction between $CsPbBr_3$ NCs and Bi_2O_2Se NSs.[29] The slope of τ_o/τ with [Q] in Figure 4.2.7c gives the dynamic quenching constant, k_D value as 1.12 × 10^3 L/mol from Eq. 5.

$$\frac{\tau_o}{\tau} = 1 + k_D[Q] \qquad \text{Eq. 4.2.5}$$

where τ_o and τ are the excited-state lifetimes of $CsPbBr_3$ in the absence and presence of Bi_2O_2Se, respectively. We have further estimated the static quenching constant, k_s as 9.7×10^5 L/mol by plotting k_{app} with [Q] by using Eqs. 3 and 4 (see Figure 4.2.7d).

Typically, PL quenching is attributed to either a non-radiative energy transfer or electron transfer mechanism. Throughout the non-radiative energy transfer, usually the intensity of the donor emission decreases and acceptor emission increases. As evidenced from Figure 4.2.4, there is no overlap in the broad region 450-700 nm, and even the bandgap for Bi_2O_2Se is 0.84 eV, which rules out the possibility of energy transfer. Therefore, photo-induced electron transfer from the photoexcited $CsPbBr_3$ NCs to Bi_2O_2Se NSs is the most plausible mechanism in the quenching of the PL of $CsPbBr_3$ NCs.

To understand the electron transfer between Bi_2O_2Se NSs and $CsPbBr_3$ NCs, we estimated band edges by cyclic voltammetry. The onset reduction potentials were found to be -0.71 V and -0.31 V for $CsPbBr_3$ NCs and Bi_2O_2Se NSs, respectively (Figure 4.2.8). Positions of VB and CB levels of the $CsPbBr_3$ are at -6.06 eV and -3.69 eV, respectively, while for Bi_2O_2Se, VB and CB levels are at -5.48 eV and -4.64 eV, respectively (see Figure 4.2.9).

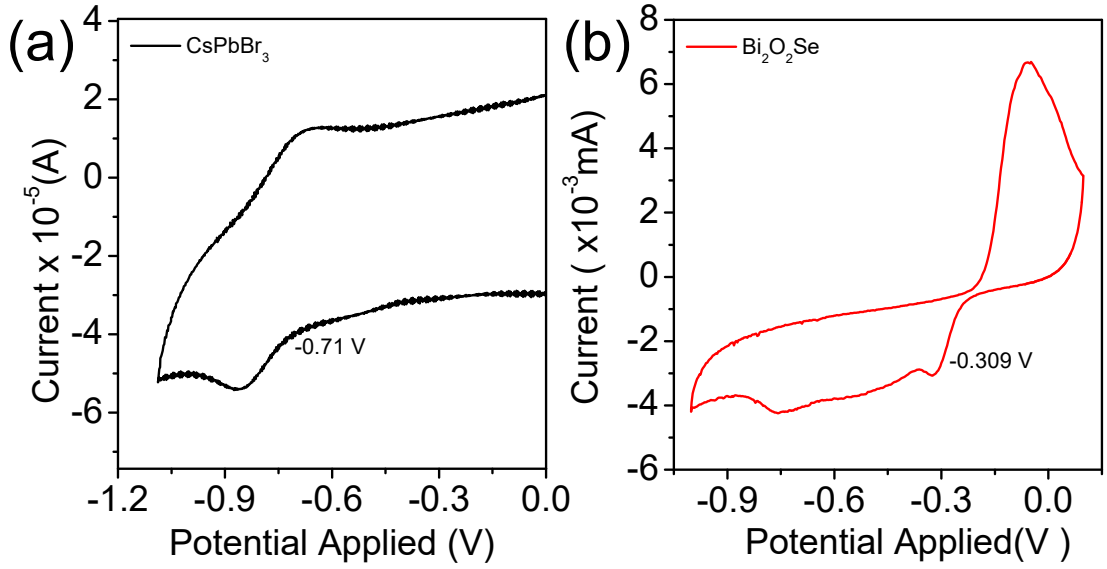

Figure 4.2.8. *Cyclic voltammograms of $CsPbBr_3$ NCs and Bi_2O_2Se NSs. The scan rate used was 50 mV/s.*

Due to the high optical absorption of $CsPbBr_3$ (931 cm^{-1} g^{-1} L), a large amount of carriers can be generated at the interface of the $CsPbBr_3$ and Bi_2O_2Se under the excitation at 450 nm. This type-I band alignment facilitates the injection of photo-generated carriers from CB of $CsPbBr_3$ into CB of Bi_2O_2Se. A similar type of charge transfer has been obtained previously in 2D Bi_2O_2Se nanoplates/1D $CsPbBr_3$ nanowires heterostructures grown epitaxially by a facile vertical vapor deposition method.[28]

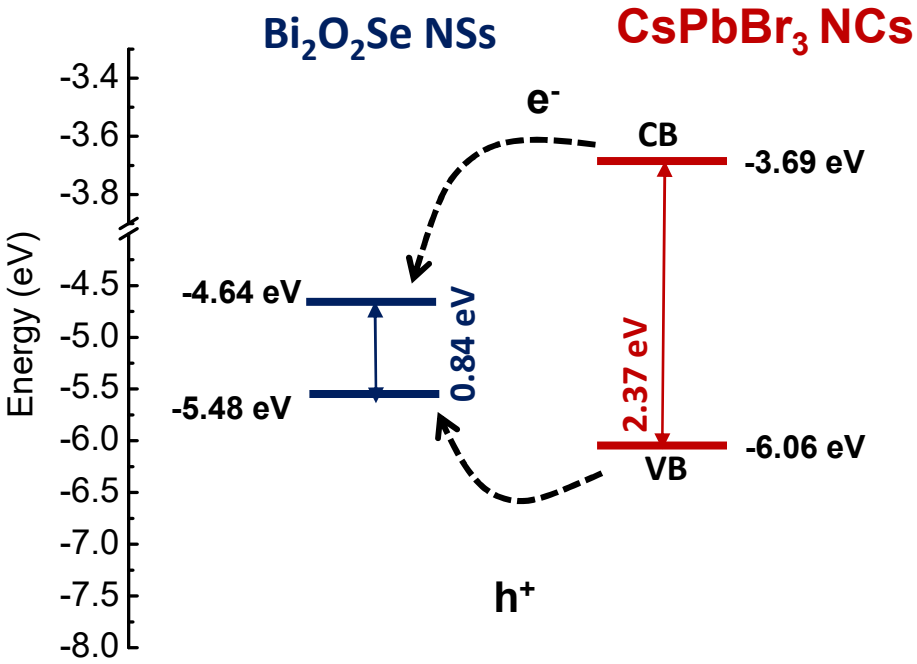

Figure 4.1.12. *Band energies of $CsPbBr_3$ NCs and Bi_2O_2Se NSs and depiction of type-I band alignment.*

4.2.4. Conclusions

In summary, we have successfully demonstrated a facile solution-based synthesis approach to form mixed-dimensional heterostructures of $CsPbBr_3$ NCs and Bi_2O_2Se NSs to understand the electronic coupling and the nature of photogenerated charge transfer between them. We visualized these self-assembled $CsPbBr_3$ NCs on the surface of 2D NSs from our TEM measurements and confirmed the bonding interactions by FTIR. We observed significant PL quenching of the halide perovskite when it forms heterostructure with Bi_2O_2Se NSs. TR-PL spectroscopic techniques were used to understand the dynamic

quenching. The charge transfer from the conduction band of $CsPbBr_3$ to conduction band of Bi_2O_2Se occurs due to type-I band alignment calculated from our cyclic voltammetric study. The present work indicated the synthesis and fundamental understanding of charge transfer mechanism in the all-inorganic halide perovskite-Bi_2O_2Se heterostructure, which will motivate further research into the exploration of new heterostructures with other halide perovskite and mixed dimensional nanostructures.

4.2.5. References

[1] R. S. Fishman, J. A. Fernandez-Baca, T. Rõõm, *Spin-Wave Theory and Its Applications to Neutron Scattering and THz Spectroscopy*, Morgan & Claypool Publishers, **2018**.

[2] S. Bera, N. Pradhan, *ACS Energy Lett.* **2020**, *5*, 2858–2872.

[3] P. V Kamat, N. Pradhan, K. Schanze, P. S. Weiss, J. Buriak, P. Stang, T. W. Odom, G. Hartland, *ACS Energy Lett.* **2020**, 2253–2255.

[4] M. Ha, J.-H. Kim, M. You, Q. Li, C. Fan, J.-M. Nam, *Chem. Rev.* **2019**, *119*, 12208–12278.

[5] A. J. Nozik, M. C. Beard, J. M. Luther, M. Law, R. J. Ellingson, J. C. Johnson, *Chem. Rev.* **2010**, *110*, 6873–6890.

[6] H. Wang, L. Zhang, Z. Chen, J. Hu, S. Li, Z. Wang, J. Liu, X. Wang, *Chem. Soc. Rev.* **2014**, *43*, 5234–5244.

[7] C. Gao, J. Wang, H. Xu, Y. Xiong, *Chem. Soc. Rev.* **2017**, *46*, 2799–2823.

[8] D. Kufer, G. Konstantatos, *Acs Photonics* **2016**, *3*, 2197–2210.

[9] L. Protesescu, S. Yakunin, M. I. Bodnarchuk, F. Krieg, R. Caputo, C. H. Hendon, R. X. Yang, A. Walsh, M. V Kovalenko, *Nano Lett.* **2015**, *15*, 3692–3696.

[10] S. Yakunin, L. Protesescu, F. Krieg, M. I. Bodnarchuk, G. Nedelcu, M. Humer, G. De Luca, M. Fiebig, W. Heiss, M. V Kovalenko, *Nat. Commun.* **2015**, *6*, 8056.

[11] Q. A. Akkerman, V. D'Innocenzo, S. Accornero, A. Scarpellini, A. Petrozza, M. Prato, L. Manna, *J. Am. Chem. Soc.* **2015**, *137*, 10276–10281.

[12] A. Swarnkar, R. Chulliyil, V. K. Ravi, M. Irfanullah, A. Chowdhury, A. Nag, **2015**, *400076*, 15424–15428.

[13] P. Acharyya, K. Kundu, K. Biswas, *Nanoscale* **2020**,*12*, 21094-21117.

[14] Y. Fu, H. Zhu, J. Chen, M. P. Hautzinger, X.-Y. Zhu, S. Jin, *Nat. Rev. Mater.* **2019**, *4*, 169–188.

[15] S. Muduli, P. Pandey, G. Devatha, R. Babar, M. Thripuranthaka, D. C. Kothari, M. Kabir, P. P. Pillai, S. Ogale, **2018**, *411008*, 7682–7686.

[16] E. Rathore, K. Maji, D. Rao, B. Saha, K. Biswas, *J. Phys. Chem. Lett.*, **2020**, *11*, 8002–8007.

[17] A. Pan, X. Ma, S. Huang, Y. Wu, M. Jia, Y. Shi, Y. Liu, P. Wangyang, L. He, Y. Liu, *J. Phys. Chem. Lett.* **2019**, *10*, 6590–6597.

[18] X.-H. Qi, K.-Z. Du, M.-L. Feng, J.-R. Li, C.-F. Du, B. Zhang, X.-Y. Huang, *J. Mater. Chem. A* **2015**, *3*, 5665–5673.

[19] J. Wang, J. Wang, N. Li, X. Du, J. Ma, C. He, Z. Li, *ACS Appl. Mater. Interfaces* **2020**, *12*, 31477–31485.

[20] Y. Liu, Y. Yang, P. Chen, Y. Shan, Y. Li, J. Shi, J. Hou, N. Zhang, G. Zhao, J. Xu, *Small* **2020**, *16*, 2004126.

[21] Z. Li, E. Hofman, J. Li, A. H. Davis, C. Tung, L. Wu, W. Zheng, *Adv. Funct. Mater.* **2018**, *28*, 1704288.

[22] X. Zhang, X. Wu, X. Liu, G. Chen, Y. Wang, J. Bao, X. Xu, X. Liu, Q. Zhang, K. Yu, *J. Am. Chem. Soc.* **2020**, *142*, 4464–4471.

[23] Y.-F. Xu, M.-Z. Yang, B.-X. Chen, X.-D. Wang, H.-Y. Chen, D.-B. Kuang, C.-Y. Su, *J. Am. Chem. Soc.* **2017**, *139*, 5660–5663.

[24] M. Ou, W. Tu, S. Yin, W. Xing, S. Wu, H. Wang, S. Wan, Q. Zhong, R. Xu, *Angew. Chemie* **2018**, *130*, 13758–13762.

[25] U. Khan, Y. Luo, L. Tang, C. Teng, J. Liu, B. Liu, H. Cheng, *Adv. Funct. Mater.* **2019**, *29*, 1807979.

[26] J. Li, Z. Wang, Y. Wen, J. Chu, L. Yin, R. Cheng, L. Lei, P. He, C. Jiang, L. Feng, *Adv. Funct. Mater.* **2018**, *28*, 1706437.

[27] J. Yin, Z. Tan, H. Hong, J. Wu, H. Yuan, Y. Liu, C. Chen, C. Tan, F. Yao, T. Li, *Nat. Commun.* **2018**, *9*, 1–7.

[28] C. Fan, B. Dai, H. Liang, X. Xu, Z. Qi, H. Jiang, H. Duan, Q. Zhang, *Adv. Funct. Mater.* **2021**, 2010263.

[29] P. Luo, F. Zhuge, F. Wang, L. Lian, K. Liu, J. Zhang, T. Zhai, *ACS Nano* **2019**, *13*, 9028–9037.

[30] T. Ghosh, M. Samanta, A. Vasdev, K. Dolui, J. Ghatak, T. Das, G. Sheet, K. Biswas, *Nano Lett.* **2019**, *19*, 5703–5709.

[31] J. Wu, C. Tan, Z. Tan, Y. Liu, J. Yin, W. Dang, M. Wang, H. Peng, *Nano Lett.* **2017**, *17*, 3021–3026.

[32] I. P. De Berti, M. V. Cagnoli, G. Pecchi, J. L. Alessandrini, S. J. Stewart, J. F. Bengoa, S. G. Marchetti, **2013**, *24*, 175601-175612.

[33] L. M. Wheeler, E. M. Sanehira, A. R. Marshall, P. Schulz, M. Suri, N. C. Anderson, J. A. Christians, D. Nordlund, D. Sokaras, T. Kroll, S. P. Harvey, J.

J. Berry, L. Y. Lin, J. M. Luther, *J. Am. Chem. Soc.* 2018, *140*, 10504–10513.

Summary of the Thesis

This section discusses the overall summary of the thesis. In this thesis, metal chalcogenides, chalcophosphates, halides have been explored for various intriguing properties for their application in thermoelectric energy conversion, water purification, and fundamental understanding of the charge transfer mechanisms in the heterostructures. In **Part-1**, I have given a brief introduction to metal chalcogenides, chalcophophates, halides, synthesis techniques used, and characterization methods that I have carried out. **Part-2** is related to the design and synthesis of metal chalcogenides for high-performance thermoelectric energy conversion. **Part 3** of my thesis is related to the environment and is focused on water purification using layered materials. **Part 4** of my thesis is directed towards the synthesis of heterostructures and understanding the charge-transfer mechanism.

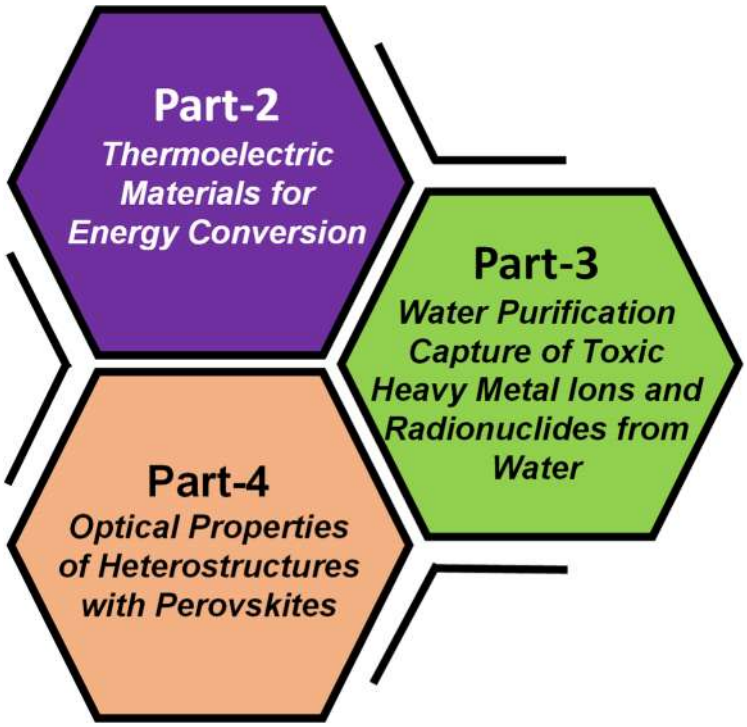

My thesis addresses the current important energy and environmental challenges and has immense societal importance. I have employed different synthesis routes to synthesize various metal chalcogenides, metal chalcophosphates, layered materials, and halide perovskites heterostructures and examined their properties.

Overall, the work presented in this thesis can be summarized based on the below three categories:

(1) High-Performance Thermoelectric Energy Conversion:

Decoupling of electronic and phonon transport is a key issue in thermoelectrics. **Part 2** of my thesis, comprising of 5 chapters, has discussed on modulation of electronic and phonon-transport to achieve high-performance thermoelectric energy conversion. I have understood the underlying reasons behind the low thermal conductivity arising from soft vibrations, stereochemical active lone-pair, rattler atoms, bonding heterogeneity, and phonon-scattering via endotaxial precipitates. I have improved the electronic properties by modulation doping and using aliovalent dopants. In **chapter 2.1**, I have discussed the influence of the periodic table in designing solid-state metal chalcogenides for thermoelectric energy conversion. In **Chapter 2.2,** I have shown stabilization of cubic $AgBiS_2$ at room temperature and understood the origin of ultralow thermal conductivity in n-type cubic $AgBiS_2$ caused by the soft vibrations and local structure distortion in [011] direction induced by the Bi $6s^2$ lone pair. In **chapter 2.3**, I have enhanced the electrical transport properties in Bi excess samples of $AgBiSe_2$ by modulation doping using microstructures of topological semi-metal Bi_4Se_3 which injects the charge carriers to the precipitates of Bi_4Se_3 from the AgBiSe2 matrix and results in a large improvement of carrier mobility. In **chapter 2.4,** I have reported the highest zT of 1.45 for the first time in low-cost and earth-abundant element-based lead sulfide, PbS thermoelectric material, an alternative to champion lead chalcogenides, PbTe, and PbSe. Ge doping in PbS synergistically brings out extremely low lattice thermal conductivity (κ_L) in PbS via endotoxic nano precipitates of Pb_2GeS_4 which scatter heat-carrying phonon and the electrical conductivity increases due to enhanced covalency in chemical bonding. In **chapter 2.5**, I have reported the synthesis of superconductive Chevrel phase compound $SnMo_6S_8$ and discussed the origin of ultra-low thermal conductivity arising from tin rattler atoms.

(2) Layered Materials for Water Purification

Clean and fresh water is pivotal to the existence of life, but the contaminant levels are increasing rapidly due to rapid industrialization. **Part 3** of my thesis,

comprising of 4 chapters, has discussed a detailed adsorption study for the removal of heavy metal ions and radionuclides selectively from *ppb* level contamination in water. In **chapter 3.1**, I have captured toxic lead (II) from water, efficiently and selectively from ppb level using layered metal chalcophosphate, $K_{0.48}Mn_{0.76}PS_3$. H_2O (K-MPS-1). This material is stable in 2-12 pH and can remove lead even from 1 ppb level. In **chapter 3.2**, I have studied the selective and ppb level removal of toxic mercury (II) from water using the composite of high surface area graphene oxide and tin sulfide which induces selectivity towards Hg(II) adsorption. The material is stable in pH 0.5-11 and can remove Hg(II) even from 0.3 ppb level. I have designed a prototype tea bag with a composite that can remove 99.9 % Hg(II) from water. In **chapter 3.3**, I have synthesized nature-inspired coral-like morphology of CoAl-Layered Double Hydroxide and used it to remove hexavalent chromium (VI) from the water up to 4.5 ppb level in a broad pH range of 1.93-12.22. Interestingly, it can be regenerated and recycled. With these great properties, I have designed a low-cost column for the treatment of effluent discharge, with 1 weight % of material and 99 weight % sand, and removed ~99% Cr(VI). In **chapter 3.4**, I have discussed the removal of radionuclide Cesium from water by the ion-exchange process using K-MPS-1. Ion-exchange of Cs(I) is reversible, shows fast kinetics and removal occurs at ppb level. In summary, this part of the thesis has described the removal of heavy metal ions, Pb(II), Hg(II), Cr(VI), and radionuclides of Cs(I) using layered materials.

(3) Charge Transfer in Heterostructures of Halide Perovskites

Part 4 of my thesis has shown the synthesis of heterostructures with all-inorganic halide perovskites and discussed the fundamental understanding of the charge-transfer mechanism. In **Chapter 4.1,** I have studied the charge transfer, the driving force for synthesis, photoluminescence quenching, and photoconductivity in the heterostructure of $CsPbBr_3$ nanocrystals with nitrogen-doped carbon dots. In **chapter 4.2**, I have synthesized the heterostructure of $CsPbBr_3$ nanocrystals with few layers of layered metal oxy-chalcogenide, Bi_2O_2Se, and studied the photoluminescence quenching mechanism.

List of publications

- Included in thesis

1. **E. Rathore**, K. Maji, K. Biswas, "Charge Transfer in the Heterostructure of $CsPbBr_3$ Nanocrystals with Nitrogen-Doped Carbon Dots", *J. Phys. Chem. Lett. 2020,* 11, 19, 8002.
2. **E. Rathore**, S. N. Guin, K. Biswas, Enhancement of thermoelectric performance of n-type $AgBi_{1+x}Se_2$ via improvement of the carrier mobility by modulation doping, *Bull. Mater. Sci.* 2020, 43, 315.
3. **E. Rathore,** R. Juneja, Sean Culver, N. Minafara, Abhishek Singh, W. Zeier, Kanishka Biswas, "Origin of ultra-low thermal conductivity in n-type cubic bulk $AgBiS_2$: Soft Ag vibrations and local structural distortion induced by Bi $6s^2$ lone pair", *Chem. Mater., 20*19, 31, 2106.
4. **E. Rathore**, M. Dutta, K. Biswas, "Influence of periodic table in designing solid-state metal chalcogenides for thermoelectric energy conversion", *J. Chem. Sci.*, 2019, 131, 1. (Review Article)
5. **E. Rathore,** K. Biswas, "Selective and ppb Level Removal of Hg(II) from Water: Synergistic Role of Graphene Oxide and SnS_2", *J. Mater. Chem. A,* 2018, 6, 13142.
6. **E. Rathore**, P. Pal, K. Biswas, "Reversible and efficient sequestration of Cs from water by layered metal thiophosphate, $K_{0.48}Mn_{0.76}PS_3.H_2O$", *Chem. Eur. J.*, 2017, 23, 11085.
7. **E. Rathore,** P. Pal, K. Biswas, "Layered Metal Chalcophosphate (K-MPS-1) for Efficient, Selective and ppb Level Sequestration of Pb from Water", *J. Phys. Chem. C*, 2017, 121, 7959.
8. **E. Rathore**, R. Juneja, S. Roychowdhury, M. Kofu, K. Nakajima, A. K. Singh, K. Biswas, "Enhancement of Thermoelectric Performance for n-Type PbS through Weak Electron Phonon Coupling and Strong Phonon Scattering by Pb_2GeS_4", *Manuscript under review 2021.*
9. **E. Rathore,** R. Arora, J. Pandey, A. Soni, U.V. Waghmare, K. Biswas, "Ultra-low thermal conductivity in Chevrel Phase compound", *Manuscript under preparation* 2021.

10. **E. Rathore**, K. Maji, K. Biswas, "Nature-Inspired Coral like Layered Double Hydroxide for Selective ppb Level Capture of Cr(VI) from Contaminated Water", *Manuscript under review* **2021.**
11. **E. Rathore,** K. Kundu, K. Maji, K. Biswas**,** **"**Photoluminescence quenching in perovskite and Bi_2O_2Se heterostructures"**,** *Manuscript under preparation* **2021.**

- Not included in thesis

1. **E. Rathore**, P. Dutta, K. Biswas, "Low Cost and Earth Abundant Metal Sulfides for Thermoelectric Energy Conversion", *Manuscript under submission* **2021**. (Review)
2. K. Mitra, G. K. Goyal, **E. Rathore**, K. Biswas, S. Vitta, S. Mahapatra, T. Dasgupta, "Enhanced Thermoelectric Performance in Mg_2Si by Functionalized Co-Doping", ***Phys. Status Solidi A.***, **2018**, 0, 1700829-1700839.

Biography

Ekashmi Rathore was born in Rawatbhata, Rajasthan (India). She received her B.Sc. Hons. Chemistry (2014) degree from Hindu College, University of Delhi (India) and M.S. in Chemical Science (2017) degree from New Chemistry Unit of Jawaharlal Nehru Center for Advanced Scientific Research (JNCASR, India). She has been awarded Best MS Thesis (2017). Her research work focuses on high-performance thermoelectric materials based on chalcogenides, removal of heavy metals and radionuclide using chalcophosphates, graphene oxide-metal sulfides, and studying optical properties of perovskite heterostructures. She has represented India in **Falling Walls Lab (2017), Germany, among 100 innovators from different countries, pitched water purification research innovation in just 3 minutes**! She is the recipient of the **best poster** awards at the "International Winter School on Frontiers in Material Science (2019), JNCASR, India", "First Indian Materials Conclave and 30th Annual General Meeting of Material Research Society India (MRSI) (2019), IISc, India", "Annual In-House Symposium (2018), JNCASR, India." Her Ph.D. story has been highlighted by PhDs of India on Quora, Medium, Instagram. She has also been highlighted in female **STEM role models in the Million STEM project, London** to inspire the next generation. In her leisure time, she loves to network with new people, travel around and paint the world with her creativity.